

Iran's fusion program:  
Poised to ignite *p. 1086*

Autumn books  
to fall for *p. 1088*

Political bias in Internet  
provision *p. 1151*

# Science

\$15  
9 SEPTEMBER 2016  
[sciencemag.org](http://sciencemag.org)

AAAS

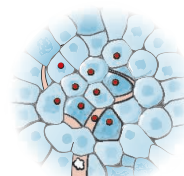


## PATHS TO A ZIKA VACCINE

*pp. 1073, 1094, & 1129*

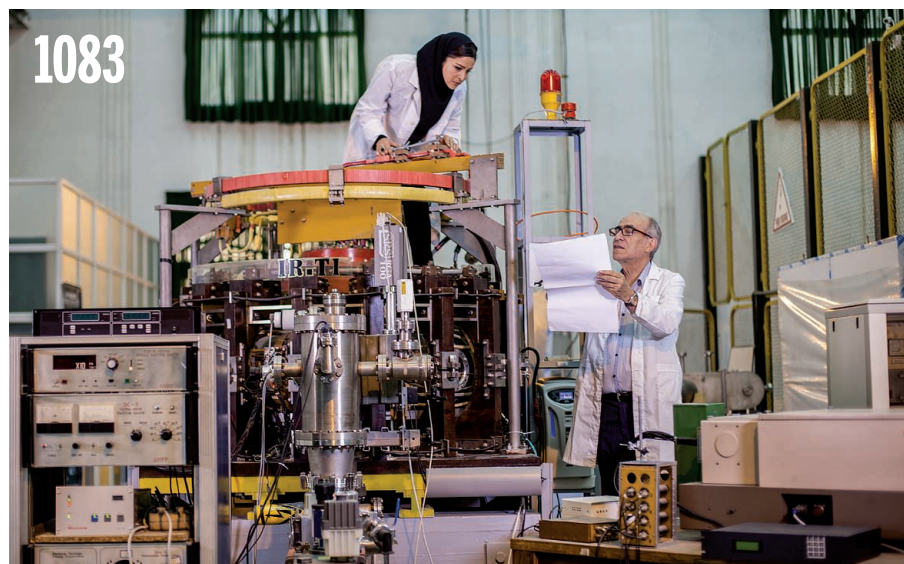
# CONTENTS

9 SEPTEMBER 2016 • VOLUME 353 • ISSUE 6304



## 1095 & 1161

Location influences tumor metabolism



Iran's tokamaks could see action in country's budding relationship with the ITER fusion experiment.

## NEWS

### IN BRIEF

**1074** News at a glance

### IN DEPTH

**1077** CAMPAIGN SETS OUT TO FIND A HOT LIMIT TO LIFE

Deep-sea drilling expedition off Japan to probe microbial boundary beneath sea floor *By P. Voosen*

**1078** CANNONBALL! CHINA'S MEGASPLASH IN OCEAN RESEARCH

Huge new national lab's research priorities remain sketchy *By K. McLaughlin*

**1079** THE ATMOSPHERE'S PACEMAKER SKIPS A BEAT

Hiccup bodes wet winter weather for Europe *By B. Mason*

**1080** NO PROOF THAT PREDATOR CULLS SAVE LIVESTOCK, STUDY CLAIMS

New analysis calls for more rigorous studies *By B. Goldfarb*

**1081** ACCUSATIONS FLY AFTER BIG GATES GRANT

Panel promises verdict on old dispute between WHO and the University of Oxford *By K. Kupferschmidt*

### FEATURES

**1083** IRANIAN SUN

A fusion research program nurtured in isolation could blossom as Iran joins the ITER megaproject  
*By R. Stone*

**1085** A year after the deal, nuclear collaborations languish  
*By R. Stone*

**1086** The reactor that triggered a nuclear crisis  
*By R. Stone*

## INSIGHTS

### BOOKS ET AL.

**1088** AUTUMN BOOKS TO FALL FOR

### PERSPECTIVES

**1094** ZIKA VACCINE TRIALS

There are new and familiar challenges in the race for timely and effective vaccines  
*By M. Lipsitch and B. J. Cowling*

► EDITORIAL P. 1073; RESEARCH ARTICLE P. 1129

**1095** LOCATION, LOCATION, LOCATION

Tissue of origin is important in determining how tumors rewire their metabolism *By K. H. Vousden and M. Yang*

► REPORT P. 1161

**1096** VISUALIZING EVOLUTION AS IT HAPPENS

A meter-scale growth plate allows the evolution of antibiotic resistance to be tracked *By L. McNally and S. P. Brown*  
► REPORT P. 1147

**1098** ASYMMETRY IN SUPRAMOLECULAR ASSEMBLY

Photoresponsive organic nanowires connect to gold nanomesh and silicon electrodes *By S. Slim and F. Rosei*

**1099** HOW DAMS CAN GO WITH THE FLOW

Small changes to water flow regimes from dams can help to restore river ecosystems *By N. L. Poff and J. C. Schmidt*

**1101** LENTIVIRAL VECTORS, TWO DECADES LATER

A deadly virus became an effective gene delivery tool *By L. Naldini et al.*

**1103** AHMED H. ZEWAEL (1946–2016)

A Nobel laureate, who pioneered femtochemistry, promoted a scientific renaissance in the Middle East  
*By P. B. Dervan*

**1104** DONALD A. HENDERSON (1928–2016)

A pragmatic and tireless epidemiologist led the international eradication of smallpox *By D. L. Heymann*

### POLICY FORUM

**1105** A U.S. "CANCER MOONSHOT" TO ACCELERATE CANCER RESEARCH

Patient engagement and data sharing must improve *By D. S. Singer et al.*

### LETTERS

**1107** NUCLEAR ENERGY: IMPROVE COLLABORATION

*By H. Yang et al.*

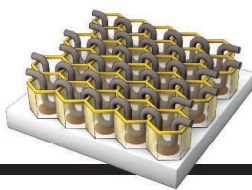
**1107** CANCEL YULIN'S ANNUAL DOG MEAT FESTIVAL

*By Q. Meng et al.*

**1108** TECHNICAL COMMENT ABSTRACTS

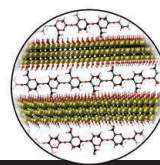
**1108** ONLINE BUZZ: BIODIVERSITY BOUNDARIES





1098

A nanoscaffold  
for solar cells



1137

An electromagnetic  
shield

## RESEARCH

### IN BRIEF

**1109** From *Science* and other journals

### REVIEWS

#### 1112 SOCIAL SCIENCES

Social and economic impacts of climate  
*T. A. Carleton and S. M. Hsiang*  
REVIEW SUMMARY; FOR FULL TEXT:  
[dx.doi.org/10.1126/science.aad9837](https://doi.org/10.1126/science.aad9837)

#### 1113 CLIMATE CHANGE

Improving the forecast for biodiversity  
under climate change *M. C. Urban et al.*  
REVIEW SUMMARY; FOR FULL TEXT:  
[dx.doi.org/10.1126/science.aad8466](https://doi.org/10.1126/science.aad8466)



1113

### RESEARCH ARTICLES

#### 1114 MACROPHAGES

Specification of tissue-resident  
macrophages during organogenesis  
*E. Mass et al.*

RESEARCH ARTICLE SUMMARY; FOR FULL TEXT:  
[dx.doi.org/10.1126/science.aaf4238](https://doi.org/10.1126/science.aaf4238)

#### 1115 BIOENGINEERING

Continuous genetic recording with self-  
targeting CRISPR-Cas in human cells  
*S. D. Perli et al.*  
RESEARCH ARTICLE SUMMARY; FOR FULL TEXT:  
[dx.doi.org/10.1126/science.aag0511](https://doi.org/10.1126/science.aag0511)

#### 1116 BIOPHYSICS

Single-molecule dissection of stacking  
forces in DNA *F. Kilchherr et al.*  
RESEARCH ARTICLE SUMMARY; FOR FULL TEXT:  
[dx.doi.org/10.1126/science.aaf5508](https://doi.org/10.1126/science.aaf5508)

#### 1117 MEMORY

Synaptic mechanisms of pattern  
completion in the hippocampal CA3  
network *S. J. Guzman et al.*

#### 1123 INHIBITORY SYNAPSES

Identification of an elaborate complex  
mediating postsynaptic inhibition  
*A. Uezu et al.*

#### 1129 VACCINES

Protective efficacy of multiple vaccine  
platforms against Zika virus challenge in  
rhesus monkeys *P. Abbink et al.*  
► EDITORIAL P. 1073; PERSPECTIVE P. 1094

### REPORTS

#### 1133 GEOPHYSICS

Local near instantaneously dynamically  
triggered aftershocks of large earthquakes  
*W. Fan and P. M. Shearer*

#### 1137 MATERIALS SCIENCE

Electromagnetic interference shielding  
with 2D transition metal carbides  
(MXenes) *F. Shahzad et al.*

#### 1141 GEOCHEMISTRY

Highly siderophile elements were  
stripped from Earth's mantle by iron  
sulfide segregation *D. C. Rubie et al.*

#### 1144 ORGANIC CHEMISTRY

Dirhodium-catalyzed C-H arene  
amination using hydroxylamines  
*M. P. Paudyal et al.*

#### 1147 ANTIBIOTIC RESISTANCE

Spatiotemporal microbial evolution on  
antibiotic landscapes *M. Baym et al.*  
► PERSPECTIVE P. 1096

#### 1151 INTERNET ACCESS

Digital discrimination: Political bias in  
Internet service provision across ethnic  
groups *N. B. Weidmann et al.*

#### 1155 ANIMAL BEHAVIOR

Optic flow odometry operates  
independently of stride integration in  
carried ants *S. E. Pfeiffer and M. Wittlinger*  
► PODCAST

#### 1157 CELL MIGRATION

Collective cell durotaxis emerges  
from long-range intercellular force  
transmission *R. Sunyer et al.*

#### 1161 TUMOR METABOLISM

Tissue of origin dictates branched-  
chain amino acid metabolism in mutant  
*Kras*-driven cancers *J. R. Mayers et al.*  
► PERSPECTIVE P. 1095

### DEPARTMENTS

#### 1073 EDITORIAL

Ebola and Zika: Cautionary tales  
*By Michael T. Osterholm*  
► PERSPECTIVE P. 1094;  
RESEARCH ARTICLE P. 1129

#### 1174 WORKING LIFE

Newton and the Big Apple  
*By E. S. Levine*

### ON THE COVER



Schematic illustration  
showing three paths to  
a vaccine for Zika virus.  
The Zika epidemic has  
recently exploded in the  
Americas and has been  
shown to cause devastat-  
ing birth defects, as well  
as neurological problems

in adults. See page 1129 for a description of  
three separate vaccine platforms that provide  
complete protection against Zika infection  
in rhesus monkeys. These findings lay a  
clear path for Zika vaccine development in  
humans. For related coverage, see pages 1073  
and 1094. *Illustration: Davide Bonazzi*

Science Staff .....1070  
New Products ..... 1166  
Science Careers .....1167

SCIENCE (ISSN 0036-8075) is published weekly on Friday, except the last week in December, by the American Association for the Advancement of Science, 1200 New York Avenue, NW, Washington, DC 20005. Periodicals mail postage (publication No. 484460) paid at Washington, DC, and additional mailing offices. Copyright © 2016 by the American Association for the Advancement of Science. The title SCIENCE is a registered trademark of the AAAS. Domestic individual membership and subscription (\$1 issues): \$165 (\$74 allocated to subscription). Domestic institutional subscription (\$1 issues): \$1622. Foreign postage extra: Mexico, Caribbean (surface mail) \$55; other countries (air assist delivery) \$89. First class, airmail, student, and emeritus rates on request. Canadian rates with GST available upon request. GST #1254 88122. Publications Mail Agreement Number 1069624. Printed in the U.S.A.  
Change of address: Allow 4 weeks, giving old and new addresses and 8-digit account number. Postmaster: Send change of address to AAAS, P.O. Box 96178, Washington, DC 20090-6178. Single-copy sales: \$15.00 current issue, \$20.00 back issue prepaid includes surface postage; bulk rates on request. Authorization to photocopy material for internal or personal use under circumstances not falling within the fair use provisions of the Copyright Act is granted by AAAS to libraries and other users registered with the Copyright Clearance Center (CCC) Transactional Reporting Service, provided that \$35.00 per article is paid directly to CCC, 222 Rosewood Drive, Danvers, MA 01923. The identification code for Science is 0036-8075. Science is indexed in the Reader's Guide to Periodical Literature and in several specialized indexes.

**Editor-in-Chief** Jeremy Berg

**Executive Editor** Monica M. Bradford **News Editor** Tim Appenzeller

**Deputy Editors** Lisa D. Chong, Andrew M. Sugden(UK), Valda J. Vinson, Jake S. Yeston

## Research and Insights

**DEPUTY EDITOR, EMERITUS** Barbara R. Jasny **SR. EDITORS** Caroline Ash(UK), Gilbert J. Chin, Julia Fahrenkamp-Uppenbrink(UK), Pamela J. Hines, Stella M. Hurlley(UK), Paula A. Kiberstis, Marc S. Lavine(Canada), Kristen L. Mueller, Ian S. Osborne(UK), Beverly A. Purnell, L. Bryan Ray, Guy Riddihough, H. Jesse Smith, Jelena Stajic, Peter Stern(UK), Phillip D. Szuromi, Sacha Vignieri, Brad Wible, Nicholas S. Wigginton, Laura M. Zahn **ASSOCIATE EDITORS** Brent Grocholski, Keith T. Smith **ASSOCIATE BOOK REVIEW EDITOR** Valerie B. Thompson **LETTERS EDITOR** Jennifer Sills **LEAD CONTENT PRODUCTION EDITORS** Harry Jach, Lauren Kmec **CONTENT PRODUCTION EDITORS** Jeffrey E. Cook, Chris Filiatreau, Cynthia Howe, Barbara P. Ordway, Catherine Wolner **SR. EDITORIAL COORDINATORS** Carolyn Kyle, Beverly Shields **EDITORIAL COORDINATORS** Aneera Dobbins, Joi S. Granger, Jeffrey Hearn, Lisa Johnson, Maryrose Madrid, Anita Wynn **PUBLICATIONS ASSISTANTS** Nida Masulis, Dona Mathieu, Le-Toya Mayne Flood, Shannon McMahon, Scott Miller, Jerry Richardson, Alice Whaley(UK), Brian White **EXECUTIVE ASSISTANT** Anna Bashkirova **ADMINISTRATIVE SUPPORT** Janet Clements(UK), Lizanne Newton(UK)

## News

**NEWS MANAGING EDITOR** John Travis **INTERNATIONAL EDITOR** Richard Stone **DEPUTY NEWS EDITORS** Elizabeth Culotta, David Grimm, Eric Hand David Malakoff, Leslie Roberts **CONTRIBUTING EDITOR** Martin Enserink(Europe) **SR. CORRESPONDENTS** Daniel Clery(UK), Jeffrey Mervis, Elizabeth Pennisi **NEWS WRITERS** Adrian Cho, Jon Cohen, Jennifer Couzin-Frankel, Carolyn Gramling, Jocelyn Kaiser, Catherine Maticic, Kelly Servick, Robert F. Service, Erik Stokstad(Cambridge, UK), Paul Voosen, Meredith Wadman **INTERNS** Jessica Boddy, Ben Panko **CONTRIBUTING CORRESPONDENTS** John Bohannon, Warren Cornwall, Ann Gibbons, Mara Hvistendahl, Sean Kean, Eli Kintisch, Kai Kupferschmidt(Berlin), Andrew Lawler, Mitch Leslie, Charles C. Mann, Eliot Marshall, Virginia Morell, Dennis Normile(Shanghai), Heather Pringle, Tania Rabesandratana(London), Emily Underwood, Gretchen Vogel(Berlin), Lizzie Wade(Mexico City) **CAREERS** Donisha Adams, Rachel Bernstein(Editor), Maggie Kuo **COPY EDITORS** Julia Cole, Dorie Chevlen, Jennifer Levin (Chief) **ADMINISTRATIVE SUPPORT** Jessica Adams

**Executive Publisher** Rush D. Holt

**Publisher** Bill Moran **Chief Digital Media Officer** Rob Covey

**BUSINESS OPERATIONS AND PORTFOLIO MANAGEMENT DIRECTOR** Sarah Whalen **PRODUCT DEVELOPMENT DIRECTOR** Will Schweitzer **PRODUCT DEVELOPMENT ASSOCIATE** Hannah Heckner **BUSINESS SYSTEMS AND FINANCIAL ANALYSIS DIRECTOR** Randy Yi **SENIOR SYSTEMS ANALYST** Nicole Mehmedovich **DIRECTOR, BUSINESS OPERATIONS & ANALYSIS** Eric Knott **MANAGER, BUSINESS OPERATIONS** Jessica Tierney **SENIOR BUSINESS ANALYST** Cory Lipman **SENIOR BUSINESS ANALYSTS** David Garrison, Michael Hardesty Meron Kebede, Sandy Kim **FINANCIAL ANALYST** Drew Sher **DIRECTOR, COPYRIGHTS LICENSING SPECIAL PROJECTS** Emilie David **PERMISSIONS ASSOCIATE** Elizabeth Sandler **RIGHTS, CONTRACTS, AND LICENSING ASSOCIATE** Lili Kiser **RIGHTS & PERMISSIONS ASSISTANT** Alexander Lee

**MARKETING DIRECTOR** Elise Swinehart **ASSOCIATE MARKETING DIRECTOR** Stacey Burke Bowers **MARKETING ASSOCIATE** Steven Goodman **CREATIVE DIRECTOR** Scott Rodgers **SENIOR ART ASSOCIATES** Paula Fry art ASSOCIATE Kim Huynh

**FULFILLMENT SYSTEMS AND OPERATIONS** membership@aaas.org **MANAGER, MEMBER SERVICES** Pat Butler **SPECIALISTS** Terrance Morrison, Latasha Russell **MANAGER, DATA ENTRY** Mickie Napoleoni **DATA ENTRY SPECIALISTS** Brenden Aquilino, Fiona Giblin **MARKETING ASSOCIATE** Isa Sesay-Bah

**PUBLISHER RELATIONS, EASTERN REGION** Keith Layson **PUBLISHER RELATIONS, WESTERN REGION** Ryan Rexroth **SALES RESEARCH COORDINATOR** Aiesha Marshall **ASSOCIATE DIRECTOR, INSTITUTIONAL LICENSING OPERATIONS** Iquo Edim **SENIOR OPERATIONS ANALYST** Lana Guz **MANAGER, AGENT RELATIONS & CUSTOMER SUCCESS** Judy Lillibridge

**WEB TECHNOLOGIES PORTFOLIO MANAGER** Trista Smith **TECHNICAL MANAGER** Chris Coleman **PROJECT MANAGER** Nick Fletcher **DEVELOPERS** Ryan Jensen, Jimmy Marks, Brandon Morrison **BUSINESS ANALYST** Christina Wofford

**DIGITAL MEDIA DIRECTOR OF ANALYTICS** Enrique Gonzales **DIGITAL REPORTING ANALYST** Eric Hossinger **SR. MULTIMEDIA PRODUCER** Sarah Crespi **MANAGING DIGITAL PRODUCER** Alison Crawford **PRODUCER** Liana Birke **VIDEO PRODUCER** Chris Burns, Nguyễn Hoài Nguyễn **DIGITAL SOCIAL MEDIA PRODUCER** Brice Russ

**DIRECTOR OF OPERATIONS PRINT AND ONLINE** Lizbeth Harman **DIGITAL/PRINT STRATEGY MANAGER** Jason Hillman **QUALITY TECHNICAL MANAGER** Marcus Spiegler **PROJECT ACCOUNT MANAGER** Tara Kelly **DIGITAL PRODUCTION MANAGER** Lisa Stanford **ASSISTANT MANAGER DIGITAL/PRINT** Rebecca Doshi **SENIOR CONTENT SPECIALISTS** Steve Forrester, Antoinette Hodal, Lori Murphy, Anthony Rosen **CONTENT SPECIALISTS** Jacob Hedrick, Kimberley Oster **ADVERTISING OPERATIONS SPECIALIST** Ashley Jeter

**DESIGN DIRECTOR** Beth Rakouskas **DESIGN EDITOR** Marcy Atarod **SENIOR DESIGNERS** Garvin Grullón, Chrystal Smith **GRAPHICS MANAGING EDITOR** Alberto Cuadra **SENIOR SCIENTIFIC ILLUSTRATORS** Chris Bickel, Katharine Sutliff **SCIENTIFIC ILLUSTRATOR** Valerie Altounian **INTERACTIVE GRAPHICS EDITOR** Jia You **SENIOR GRAPHICS SPECIALISTS** Holly Bishop, Nathalie Cary **PHOTOGRAPHY MANAGING EDITOR** William Douthitt **SENIOR PHOTO EDITOR** Christy Steele **PHOTO EDITOR** Emily Petersen

**DIRECTOR, GLOBAL COLLABORATION, CUSTOM PUBLICATIONS, ADVERTISING** Bill Moran **EDITOR, CUSTOM PUBLISHING** Sean Sanders: 202-326-6430 **ADVERTISING MARKETING MANAGER** Justin Sawyers: 202-326-7061 science\_advertising@aaas.org **ADVERTISING SUPPORT MANAGER** Karen Foote: 202-326-6740 **ADVERTISING PRODUCTION OPERATIONS MANAGER** Deborah Tompkins **SR. PRODUCTION SPECIALIST/GRAPHIC DESIGNER** Amy Hardcastle **SR. TRAFFIC ASSOCIATE** Christine Hall **SALES COORDINATOR** Shirley Young **ASSOCIATE DIRECTOR, COLLABORATION, CUSTOM PUBLICATIONS/CHINA/TAIWAN/KOREA/SINGAPORE** Ruolei Wu: +86-186 0082 9345, rwu@aaas.org **COLLABORATION/CUSTOM PUBLICATIONS/JAPAN** Adarsh Sandhu + 81532-81-5142 asandhu@aaas.org **EAST COAST/E. CANADA** Laurie Faraday: 508-747-9395, FAX 617-507-8189 **WEST COAST/W. CANADA** Lynne Stickrod: 415-931-9782, FAX 415-520-6940 **MIDWEST** Jeffrey Dembski: 847-498-4520 x3005, Steven Loerch: 847-498-4520 x3006 **UK EUROPE/ASIA** Roger Gonçalves: TEL/FAX +41 43 243 1358 **JAPAN** Katsuyoshi Fukamizu(Tokyo): +81-3-3219-5777 fukamizu@aaas.org **CHINA/TAIWAN** Ruolei Wu: +86-186 0082 9345, rwu@aaas.org

**WORLDWIDE ASSOCIATE DIRECTOR OF SCIENCE CAREERS** Tracy Holmes: +44 (0) 1223 326525, FAX +44 (0) 1223 326532 tholmes@science-int.co.uk **CLASSIFIED** advertise@sciencecareers.org **U.S. SALES** Tina Burks: 202-326-6577, Nancy Toema: 202-326-6578 **EUROPE/ROW SALES** Sarah Lelarge **SALES ASSISTANT** Kelly Grace **JAPAN** Hiroyuki Mashiki(Kyoto): +81-75-823-1109 hmashiki@aaas.org **CHINA/TAIWAN** Ruolei Wu: +86-186 0082 9345 rwu@aaas.org **MARKETING MANAGER** Allison Pritchard **MARKETING ASSOCIATE** Aimee Aponte

**AAAS BOARD OF DIRECTORS, CHAIR** Geraldine L. Richmond **PRESIDENT** Barbara A. Schaaf **PRESIDENT-ELECT** Susan Hockfield **TREASURER** David Evans **SHAW CHIEF EXECUTIVE OFFICER** Rush D. Holt **BOARD** Cynthia M. Beall, May R. Berenbaum, Carlos J. Bustamante, Stephen P.A. Fodor, Claire M. Fraser, Michael S. Gazzaniga, Laura H. Greene, Elizabeth Loftus, Mercedes Pascual

**SUBSCRIPTION SERVICES** For change of address, missing issues, new orders and renewals, and payment questions: 866-434-AAAS (2227) or 202-326-6417, FAX 202-842-1065. Mailing addresses: AAAS, P.O. Box 96178, Washington, DC 20090-6178 or AAAS Member Services, 1200 New York Avenue, NW, Washington, DC 20005

**INSTITUTIONAL SITE LICENSES** 202-326-6730 **REPRINTS:** Author Inquiries 800-635-7181 **COMMERCIAL INQUIRIES** 803-359-4578 **PERMISSIONS** 202-326-6765, permissions@aaas.org **AAAS Member Services** 202-326-6417 or http://membercentral.aaas.org/discounts

Science serves as a forum for discussion of important issues related to the advancement of science by publishing material on which a consensus has been reached as well as including the presentation of minority of conflicting points of view. Accordingly, all articles published in Science—including editorials, news and comment, and book reviews—are signed and reflect the individual views of the authors and not official points of view adopted by AAAS or the institutions with which the authors are affiliated.

**INFORMATION FOR AUTHORS** See pages 624 and 625 of the 5 February 2016 issue or access [www.sciencemag.org/authors/science-information-authors](http://www.sciencemag.org/authors/science-information-authors)

## SENIOR EDITORIAL BOARD

Gary King, *Harvard University*, Susan M. Rosenberg, *Baylor College of Medicine*, Ali Shalatifard, *Northwestern University Feinberg School of Medicine*

## BOARD OF REVIEWING EDITORS

(Statistics board members indicated with \$)

Adriano Aguzzi, *U. of Hospital Zürich*  
Takuzo Aida, *U. of Tokyo*  
Leslie Aiello, *Wenner-Gren Foundation*  
Judith Allen, *U. of Edinburgh*  
Sonia Altizer, *U. of Georgia*  
Sebastian Amigorena, *Institut Curie*  
Kathryn Anderson, *Memorial Sloan-Kettering Cancer Center*  
Meinrat O. Andreae, *Max-Planck Inst. Mainz*  
Paola Arlotta, *Harvard U.*  
Johan Auwerx, *EPFL*  
David Awschalom, *U. of Chicago*  
Clare Baker, *University of Cambridge*  
Nenad Ban, *ETH Zürich*  
Jordi Bascompte, *University of Zurich*  
Franz Bauer, *Pontificia Universidad Católica de Chile*  
Ray H. Baughman, *U. of Texas, Dallas*  
David Baum, *U. of Wisconsin*  
Carlo Beenakker, *Leiden U.*  
Kamran Behnia, *ESPCI-ParisTech*  
Yasmine Belkaid, *NIAID, NIH*  
Philip Benfey, *Duke U.*  
May Berenbaum, *U. of Illinois*  
Gabriele Bergers, *U. of California, San Francisco*  
Bradley Bernstein, *Massachusetts General Hospital*  
Peer Bork, *EMBL*  
Bernard Bourdon, *Ecole Normale Supérieure de Lyon*  
Chris Bowler, *Ecole Normale Supérieure*  
Ian Boyd, *U. of St. Andrews*  
Emily Brodsky, *U. of California, Santa Cruz*  
Ron Brookmeyer, *U. of California Los Angeles (\$)*  
Christian Büchel, *U. Hamburg-Eppendorf*  
Joseph A. Burns, *Cornell U.*  
Carter Tribley Butts, *U. of California, Irvine*  
Gyorgy Buzsáki, *New York U. School of Medicine*  
Blanche Capel, *Duke U.*  
Mats Carlsson, *U. of Oslo*  
Ib Chorkendorff, *U. of Denmark*  
David Clapham, *Children's Hospital Boston*  
Joel Cohen, *Rockefeller U., Columbia U.*  
James J. Collins, *MIT*  
Robert Cook-Deegan, *Duke U.*  
Lisa Coussens, *Oregon Health & Science U.*  
Alan Cowman, *Walter & Eliza Hall Inst.*  
Robert H. Crabtree, *Yale U.*  
Roberta Croce, *Vrije Universiteit*  
Janet Currie, *Princeton U.*  
Jeff L. Dangel, *U. of North Carolina*  
Tom Daniel, *U. of Washington*  
Frans de Waal, *Emory U.*  
Stanislas Dehaene, *Collège de France*  
Robert Desimone, *MIT*  
Claude Desplan, *New York U.*  
Dennis Discher, *U. of Pennsylvania*  
Gerald W. Dorn II, *Washington U. School of Medicine*  
Jennifer A. Doudna, *U. of California, Berkeley*  
Bruce Dunn, *U. of California, Los Angeles*  
William Dunphy, *Caltech*  
Christopher Dye, *WHO*  
Todd Ehlers, *U. of Tuebingen*  
David Ehrhardt, *Carnegie Inst. of Washington*  
Tim Elston, *U. of North Carolina at Chapel Hill*  
Jennifer Elisseeff, *U. of N*  
Gerhard Ertl, *Fritz-Haber-Institut, Berlin*  
Barry Everitt, *U. of Cambridge*  
Ernst Fehr, *Johns Hopkins U.*  
Anne C. Ferguson-Smith, *U. of Cambridge*  
Michael Feuer, *The George Washington U.*  
Toren Finkel, *NHLBI, NIH*  
Kate Fitzgerald, *U. of Massachusetts*  
Peter Fratzl, *Max-Planck Inst.*  
Elaine Fuchs, *Rockefeller U.*  
Daniel Geschwind, *UCLA*  
Karl-Heinz Glassmeier, *TU Braunschweig*  
Ramon Gonzalez, *Rice U.*  
Julia R. Greer, *Caltech*  
Elizabeth Grove, *U. of Chicago*  
Nicolas Gruber, *ETH Zurich*  
Kip Guy, *St. Jude's Children's Research Hospital*  
Taekjip Ha, *U. of Illinois at Urbana-Champaign*  
Wolf-Dietrich Hardt, *ETH Zurich*  
Christian Haass, *Ludwig Maximilians U.*  
Sharon Hammes-Schiffer, *U. of Illinois at Urbana-Champaign*  
Michael Hasselmo, *Boston U.*  
Martin Heimann, *Max-Planck Inst. Jena*  
Yka Helariutta, *U. of Cambridge*  
James A. Hendler, *Rensselaer Polytechnic Inst.*  
Janet G. Hering, *Swiss Fed. Inst. of Aquatic Science & Technology*  
Kai-Uwe Hinrichs, *U. of Bremen*  
David Hodell, *U. of Cambridge*  
Lora Hooper, *UT Southwestern Medical Ctr. at Dallas*  
Tamas Horvath, *Yale University*  
Raymond Huey, *U. of Washington*  
Fred Hughson, *Princeton U.*  
Auke Ijspeert, *EPFL Lausanne*  
Stephen Jackson, *USGS and U. of Arizona*  
Steven Jacobsen, *U. of California, Los Angeles*  
Kai Jonsson, *EPFL Lausanne*  
Peter Jonas, *Inst. of Science & Technology (IST) Austria*  
Matt Kaeberlein, *U. of Washington*  
William Kaelin Jr., *Dana-Farber Cancer Inst.*  
Daniel Kahne, *Harvard U.*  
Daniel Kammen, *U. of California, Berkeley*  
Abby Kavner, *U. of California, Los Angeles*  
Hitoshi Kawakatsu, *U. of Tokyo*  
Masashi Kawasaki, *U. of Tokyo*  
V. Narry Kim, *Seoul National U.*  
Robert Kingston, *Harvard Medical School*  
Etienne Kochlin, *Ecole Normale Supérieure*  
Alexander Kolodkin, *Johns Hopkins U.*  
Thomas Langer, *U. of Cologne*  
Mitchell A. Lazar, *U. of Pennsylvania*  
David Lazer, *Harvard U.*  
Thomas Lecuit, *IBDM*  
Virginia Lee, *U. of Pennsylvania*  
Stanley Lemon, *U. of North Carolina at Chapel Hill*  
Ottoline Leyser, *Cambridge U.*  
Wendell Lim, *U.C. San Francisco*  
Marcia C. Linn, *U. of California, Berkeley*  
Jianguo Liu, *Michigan State U.*  
Luis Liz-Marzan, *CIC biomaGUNE*  
Jonathan Losos, *Harvard U.*  
Ke Lu, *Chinese Acad. of Sciences*  
Christian Lüscher, *U. of Geneva*  
Laura Machesky, *CRUK Beatson Inst. for Cancer Research*  
Anne Magurran, *U. of St. Andrews*  
Oscar Marin, *CSIC & U. Miguel Hernández*  
Charles Marshall, *U. of California, Berkeley*  
C. Robertson McClung, *Dartmouth College*  
Rodrigo Medellín, *U. of Mexico*  
Graham Medley, *U. of Warwick*  
Tom Misteli, *NCI*  
Yasushi Miyashita, *U. of Tokyo*  
Mary Ann Moran, *U. of Georgia*  
Richard Morris, *U. of Edinburgh*  
Alison Mutsaers-Reif, *NC State U. (\$)*  
Thomas Muringer, *The Hastings Center*  
Daniel Neumark, *U. of California, Berkeley*  
Kitty Nijmeijer, *U. of Twente*  
Helga Nowotny, *European Research Advisory Board*  
Ben Olken, *MIT*  
Rachel O'Reilly, *Warwick U.*  
Joe Orenstein, *U. of California Berkeley & Lawrence Berkeley National Lab*  
Harry Orr, *U. of Minnesota*  
Pilar Ossorio, *U. of Wisconsin*  
Andrew Oswald, *U. of Warwick*  
Isabella Pagano, *Istituto Nazionale di Astrofisica*  
Margaret Palmer, *U. of Maryland*  
Steve Palumbi, *Stanford U.*  
Jane Parker, *Max-Planck Inst. of Plant Breeding Research*  
Giovanni Parmigiani, *Dana-Farber Cancer Inst. (\$)*  
John H. J. Petrini, *Memorial Sloan-Kettering Cancer Center*  
Samuel Pfaff, *Salk Institute for Biological Studies*  
Joshua Plotkin, *U. of Pennsylvania*  
David Polman, *FOI Institute AMOLF*  
Philippe Polman, *CNRS*  
Jonathan Pritchard, *Stanford U.*  
Wim van der Putten, *Netherlands Institute of Ecology*  
David Randall, *Colorado State U.*  
Felix Rey, *Institut Pasteur*  
Trevor Robbins, *U. of Cambridge*  
Jim Roberts, *Fred Hutchinson Cancer Research Ctr.*  
Amy Rosenzweig, *Northwestern University*  
Mike Ryan, *U. of Texas, Austin*  
Mitsunori Saitou, *Kyoto U.*  
Shimon Sakaguchi, *Kyoto U.*  
Miquel Salmeron, *Lawrence Berkeley National Lab*  
Jürgen Sandkühn, *Medical U. of Vienna*  
Alexander Schlier, *Harvard U.*  
Vladimir Shalae, *Purdue U.*  
Robert Siliciano, *Johns Hopkins School of Medicine*  
Denis Simon, *Arizona State U.*  
Uri Simonson, *U. of Pennsylvania*  
Alison Smith, *John Innes Centre*  
Richard Smith, *U. of North Carolina (\$)*  
John Speakman, *U. of Aberdeen*  
Allan C. Spradling, *Carnegie Institution of Washington*  
Jonathan Sprent, *Garvan Inst. of Medical Research*  
Eric Steig, *U. of Washington*  
Paula Stephan, *Georgia State U. and National Bureau of Economic Research*  
Molly Stevens, *Imperial College London*  
V. S. Subrahmanian, *U. of Maryland*  
Ira Tabas, *Columbia U.*  
Sarah Teichmann, *Cambridge U.*  
John Thomas, *North Carolina State U.*  
Shubha Tole, *Tata Institute of Fundamental Research*  
Christopher Tyler-Smith, *The Wellcome Trust Sanger Inst.*  
Herbert Virgin, *Washington U.*  
Bert Vogelstein, *Johns Hopkins U.*  
Janice Volkert, *U. of Göttingen*  
David Wallace, *Weizmann Inst. of Science*  
Ian Walsmsley, *U. of Oxford*  
Jane-Ling Wang, *U. of California, Davis (\$)*  
Daniel Waxman, *Fudan U.*  
Jonathan Weissman, *U. of California, San Francisco*  
Chris Wilk, *U. of Missouri (\$)*  
Ian A. Wilson, *The Scripps Res. Inst. (\$)*  
Timothy D. Wilson, *U. of Virginia*  
Rosemary Wyse, *Johns Hopkins U.*  
Jan Zaenen, *Leiden U.*  
Kenneth Zaret, *U. of Pennsylvania School of Medicine*  
Jonathan Zehr, *U. of California, Santa Cruz*  
Len Zon, *Children's Hospital Boston*  
Maria Zuber, *MIT*

## BOOK REVIEW BOARD

David Bloom, *Harvard U.*, Samuel Bowring, *MIT*, Angela Creager, *Princeton U.*, Richard Sweder, *U. of Chicago*, Ed Wasserman, *DuPont*



# Ebola and Zika: Cautionary tales

**T**he emergence of Zika in the Americas is a stark reminder of how quickly public health challenges of infectious diseases can change. The need for a safe and effective vaccine is immediate. Yet, like the Ebola epidemic 2 years ago, we find ourselves without a vaccine to combat this latest threat.

When surveillance points to a possible emergence of a new infectious disease of potential public health importance, we need procedural and funding mechanisms that can quickly identify candidate vaccines and drive research and development toward licensure and production. Even if such a vaccine is not yet licensed, having it ready for immediate large trials when a regional crisis occurs will be a major advantage over our current reactive system.

Two years ago, amidst the Ebola epidemic in West Africa, the international health community was laser-focused on finding an effective and safe vaccine. By heroic public health actions and luck, the crisis was curtailed without one. Today, hardly a word is mentioned about that crisis or the current status of vaccine development.

Yet tomorrow, we could experience another explosive Ebola epidemic that begins in the slums of one of equatorial Africa's megacities and spreads in deadly waves, where only the availability of an effective vaccine could halt its ruinous progression.

Now, Zika transmission in Florida dominates news in the United States, along with partisan political theater regarding government funding for the country's response. However, we must not take our eye off the most pressing problem of Zika: the explosive transmission in the Americas outside the continental United States. For example, it is estimated that up to 5% of Puerto Rico's population is getting infected with Zika each month, including thousands of pregnant women, for whom infection could result in fetal microcephaly.

I fear the road to a Zika vaccine may be long and bumpy. Despite optimistic predictions, demonstrating safety will be an immense challenge. It likely will be necessary to conduct studies involving many thousands

of participants to determine if Guillain-Barré syndrome (GBS), a serious autoimmune condition caused by natural Zika virus, is also related to vaccine candidates. And recent follow-up of a vaccine efficacy study for dengue, Zika's cousin flavivirus, suggests a diminishing vaccine-induced antibody response over time. This means that antibody-dependent enhancement disease may occur upon infection with a new dengue strain, or possibly even another flavivirus such as Zika or yellow fever.

The handwriting is on the wall regarding the current Zika outbreak in the Americas. High human infection rates in the major impact regions, caused by virus-carrying mosquitoes and human sexual transmission, will continue for several more years. Eventually, the number of cases will drop as more of the community develops immunity. Zika vaccine trials in the Americas may be too late to be tested on the current high number of cases.

The Coalition for Epidemic Preparedness Innovations (CEPI) is a new international effort that includes the Wellcome Trust; Bill & Melinda Gates Foundation; World

Economic Forum; U.S., Indian, and Norwegian governments; GAVI; academic researchers; international vaccine manufacturers; and the World Health Organization. CEPI ([www.cepi.net](http://www.cepi.net)) is the best hope to fill the vaccine preparedness hole.

These experiences demand better answers than our current vaccine research, development, manufacturing, and distribution system has provided. Based on observation, we could, and should, have anticipated that agents like Zika and Ebola virus would emerge as serious pathogens. The 2013 to 2014 Zika outbreak in French Polynesia produced nearly 9000 suspected cases and a strong association with GBS. How much more incentive is needed to develop candidate vaccines? With the growth of megacities in the developing world and prevalence of *Aedes aegypti* mosquitoes in many areas, this disease should not have come as a surprise—nor should the host of others yet to come that we would be foolish not to expect.

—Michael T. Osterholm



*Michael T. Osterholm is a Regents Professor; McKnight Endowed Presidential Chair in Public Health; and director of the Center for Infectious Disease Research and Policy; all at the University of Minnesota, Minneapolis, MN. Email: [mto@umn.edu](mailto:mto@umn.edu)*



***“How much more incentive is needed to develop candidate vaccines?”***

“We were beginning to think that Philae would remain lost forever.”

**Patrick Martin, the European Space Agency's Rosetta mission manager.** Photos from Rosetta finally revealed the lander this week; it is wedged into a dark crack on comet 67P/Churyumov-Gerasimenko.

## IN BRIEF

## A swoop past the stormy planet

NASA's Juno spacecraft has returned its first close-up images of Jupiter, from a unique vantage above and below the planet's poles. This image of the south pole, taken on 27 August in the first of the probe's 36 orbits, shows some of the giant storms that roil the atmosphere in both clockwise and counterclockwise directions. Juno began orbiting Jupiter on 4 July and will spend a year studying the planet from a swooping, polar orbit that brings it close to the upper atmosphere. The orbit was designed to thread the needle between Jupiter's cloud tops and radiation belts, which can fry electronics and interfere with the spacecraft's microwave detector. Mission scientists plan to use this instrument to peer beneath the planet's veil of haze and ammonia clouds in order to map a suspected water layer. The roots of storm systems are expected to be seen in this layer, and measuring water's abundance in relation to other elements can help scientists determine whether Jupiter formed in its current location, or migrated in from a more distant, colder birthplace.

The "JunoCam" captured giant storms roiling Jupiter's surface.

## AROUND THE WORLD

### China tackles superbugs

**BEIJING** | China, the world's largest consumer of human and animal antibiotics, has pledged to step up research and development into new antimicrobials and to rein in overuse of existing medicines to counter growing global antimicrobial resistance. Antibiotics are currently widely available without prescriptions in China for both human and livestock use. As part of a national action plan unveiled on 26 August, the Chinese central government said that it would mobilize the efforts of 14 ministries and departments including health, food and drugs, and agriculture. By 2020, the government aims to develop new

antimicrobials, make sales of the drugs by prescription only, ramp up surveillance of human and veterinary usage, and increase training and education for both medical professionals and consumers on their proper use. No details were available on funding for the new measures.  
<http://scim.ag/Chinaresistance>

### Ancient dig shut by politics

**SELÇUK, TURKEY** | A major archaeological project in the ancient city of Ephesus in Turkey has been shut down early, an apparent victim of international politics. Researchers with the Austrian Archaeological Institute in Vienna were notified last week by the Turkish Ministry

of Culture and Tourism that their project at Ephesus would have to end immediately. No reason was given, but Austria's chancellor had antagonized the Turkish government in August by saying the



Turkish officials ended an Austrian dig at Ephesus.



country was not fit to join the European Union. The archaeologists had already wrapped up their excavations, but had planned to work on restoration of the site for another 2 months to protect structures from winter storms. “We are concerned about the potential for damage,” says Sabine Ladstätter, director of the institute. A smaller excavation at Limyra, Turkey, was also ordered to shut down. Ladstätter does not know whether the institute will be allowed to apply for a permit to resume work next year.

## Sri Lanka malaria-free

**COLOMBO, SRI LANKA** | Sri Lanka has gone 3 years without a locally transmitted case of malaria, making the country officially free of the disease, the World Health Organization declared 5 September. A bloody, 30-year civil war disrupted health services, but the island has one advantage: Its surrounding waters help protect it against disease-carrying mosquitoes. The country has been close to eliminating endemic malaria before: After a huge epidemic with up to 5.5 million cases and 80,000 deaths in 1934 and 1935, Sri Lanka wrestled the disease down to 20 cases a year in the early 1960s. Then attention shifted and malaria resurged, with more than half a million cases in 1969. Elimination efforts resumed in earnest in 2009, with indoor residual spraying, widespread distribution of insecticide-treated bed nets, and surveillance to find and treat every case. The last locally transmitted case was reported in September 2012. Today, the only cases occur in travelers—but imported cases pose an ongoing threat to re-establishing the disease.

## New reports slam Karolinska

**STOCKHOLM** | The Karolinska University Hospital and the Karolinska Institute (KI) in Stockholm ignored warning signs when they hired surgeon Paolo Macchiarini in 2010, two independent panels concluded last week. The hospital and university commissioned the investigations in the wake of an ongoing misconduct scandal surrounding Macchiarini and the artificial tracheae he implanted in three patients at the hospital. Two have died, and a third has been hospitalized since receiving an implant in 2012. The hospital terminated Macchiarini’s employment in 2013, but KI stood by the surgeon until revelations in a television documentary led to his dismissal in March. The reports found that the procedures did not have proper ethical approval and were not based on adequate

Nine subspecies, such as *Giraffa camelopardalis rothschildi*, may represent four separate species.

## DNA divides giraffes into four species

**F**ew conservationists have worried about the giraffe. The gangly, charismatic creatures with long legs, longer necks, and prehensile purple tongues still number 90,000. But a closer look at the genetics of Africa’s nine giraffe subspecies suggests that *Giraffa camelopardalis* really represents four distinct species, one of which has fewer than 5000 individuals. Researchers from the Giraffe Conservation Foundation in Namibia collected skin samples from 190 giraffes throughout Africa and asked Axel Janke, a geneticist at the Senckenberg Biodiversity and Climate Research Centre and Goethe University Frankfurt in Germany, and his colleagues to analyze the animals’ DNA. Given how mobile giraffes are, Janke was surprised by the diversity he found—some genetic differences were greater than those between grizzly and polar bears. The nine giraffe subspecies should be reorganized into four true species, the team proposed this week in *Current Biology*, arguing the species separated between 1.25 million and 2 million years ago.



science. In response, this week the Swedish government dismissed the chancellor in charge of Sweden’s university system, who had led the effort to recruit the star surgeon. It also said it would replace KI’s entire board of directors.  
[http://scim.ag/\\_Klscandal](http://scim.ag/_Klscandal)

## Vaccine R&D coalition launched

**OSLO** | A new public-private coalition that aims to derail epidemics by speeding

development of vaccines launched its website last week. Backed by the Wellcome Trust and the Bill & Melinda Gates Foundation, the Coalition for Epidemic Preparedness Innovations (CEPI) grew out of the widespread conviction that vaccines languishing in R&D could have prevented the recent Ebola epidemic in West Africa. John-Arne Røttingen is interim CEO of CEPI after stepping down as head of the infectious disease division of the Norwegian Institute of Public Health in

Oslo, Norway and India are also partners in CEPI, which Røttingen says hopes to raise enough money in its early years to spend “a couple of hundred million dollars” annually. CEPI will consider proposals from independent investigators and issue requests for proposals that target specific opportunities. Its initial focus is on two or three vaccines against emerging pathogens that are on a list of 11 compiled by the World Health Organization.

## NEWSMAKERS

### UC doc to run gun violence center

As widely expected, **Garen Wintemute**, an epidemiologist at the University of California Davis Medical Center in Sacramento, has been picked to run the country’s first state-funded research center to study firearm violence. U.S. support for gun-related research has been scarce since 1996, when gun advocates in Congress threatened the funding of federal agencies trying to study the causes and prevention

of gun violence. Wintemute, who has spent more than \$1 million of his own funds to sustain his gun research in the past, calls the new center a “stark example” for Congress, which recently rejected amendments to provide new federal funds to study gun violence. The 5-year, \$5 million state grant, approved back in June, will allow his team to investigate questions such as why California’s annual death rate from gun violence has dropped by roughly 20% since 2000 whereas the nationwide rate has not changed.

### Three Qs

On 30 August, **Andrew Mude**, a Kenyan economist at the International Livestock Research Institute in Nairobi, was named the winner of the 2016 Norman Borlaug Award for under-40 scientists from the World Food Prize for an innovative livestock insurance program. More than 3 million pastoralist households in northern Kenya depend on goats, cows, sheep, and camels, and the high rate of livestock

losses during droughts is a major cause of childhood malnutrition.

#### Q: How does the program work?

**A:** We use satellite readings called the Normalized Differen[ce] Vegetation Index to calculate the level of greenness and how much foliage is available in an area. We use this data to predict the number of livestock that will be affected [by its disappearance], which triggers a payment to the herders.

#### Q: How is it financed?

**A:** Insurances are purchased annually before the onset of the rainy season, and herders are paid regardless of whether or not they lose animals. The payouts depend on the degree of drought and range from 5% to 100% of the total insured value.

#### Q: What’s next?

**A:** We hope to expand the program into Somalia, Mali, and Senegal. We are also looking into marshaling locals to collect and send verifiable data, such as the incidence of livestock diseases, through smartphones.

## BY THE NUMBERS

# 10%

Proportion of global wilderness lost in the past 20 years. That’s 3.3 million square kilometers—an area twice the size of Alaska (*Current Biology*).

# 565

Days that a man had Ebola virus fragments in his semen after recovering from the disease, according to preliminary results from Liberia’s Men’s Health Screening Program (*The Lancet Global Health*).

# 715%

Increase in gonorrhea in Utah women between 2011 and 2014, the U.S. Centers for Disease Control and Prevention reports.



Oklahoma ordered three dozen wastewater injection wells closed following a powerful earthquake.

### Injection wells shut down in earthquake’s wake

**A** magnitude-5.6 earthquake—possibly triggered by the underground disposal of wastewater from oil and gas production—rocked central Oklahoma on 3 September, tying a record set in 2011 for the strongest temblor in the state’s history. Previous research has shown that high rates of fluid injection, which can increase the hydraulic pressure along a fault, are responsible for the rapid increase in earthquakes in the central and eastern United States in recent years (*Science*, 19 June 2015, p. 1299). The U.S. Geological Survey said in a statement that it could not now say definitively that this earthquake was caused by human activities, although fluid injection has triggered many earthquakes in the state. Oklahoma state regulators have ordered 37 well operators, all within an area of about 1870 square kilometers around the quake’s epicenter, to shut down operations. Oklahoma currently has more than 3000 active wastewater injection wells across the state; since 2013, the state has monitored operators and occasionally restricted disposal volume in earthquake-prone regions. The quake damaged buildings but caused no serious injuries.





## MICROBIOLOGY

# Campaign sets out to find a hot limit to life

Deep-sea drilling expedition off Japan to probe microbial boundary beneath sea floor

By Paul Voosen

**S**omewhere in the sediments and rocks beneath the ocean floor, it gets too hot for living things. But how far down? Even after drilling kilometers into the ocean floor, scientists have found that microbes persist. “We keep digging and digging and digging deeper and have not hit the bottom of the biosphere,” says Jan Amend, a geochemist at the University of Southern California in Los Angeles.

A new ocean drilling expedition will try to settle the question by drilling into crust where high temperatures are found unusually close to the sea floor, bringing life’s thermal limit within reach. On 13 September, the research vessel *Chikyu* will set sail from Shimizu, Japan, and sink its bits into a patch of ocean floor where the sediments should reach 130°C at the maximum drill depth of 1260 meters. Somewhere along the way, the team expects, life should succumb to rising temperatures.

Finding that limit—the goal of the 62-day T-Limit campaign, part of the International Ocean Discovery Program—could guide estimates of the abundance and diversity of ocean floor microbes, which play large roles in biogeochemical cycles. For instance, the deep microbes, estimated to hold one-third of Earth’s total biomass, take carbon out of the ocean and sequester it when they die.

“We need to understand who they are and how they make a living,” says Bo Jørgensen, a geomicrobiologist at Aarhus University in Denmark.

Over the past decade, awareness of the abundance of life in the watery pores of the deep biosphere has turned microbiology into a primary focus of scientific ocean drilling. Expeditions have discovered microbes in nutrient-poor clays and hard bedrock. And,

---

***“We keep digging and digging and digging deeper and have not hit the bottom of the biosphere.”***

Jan Amend, University of Southern California

in 2012, the same team behind the T-Limit expedition found microbes 2.5 kilometers beneath the sea floor, a record depth, eking out a living from coal beds fossilized more than 20 million years ago.

T-Limit’s target is the Nankai Trough, perched atop the subduction zone where the Philippine Sea Plate dives beneath the Eurasian Plate. That tectonic action boosts temperatures in the layers of mudstone and volcanic ash that fill in the trough. T-Limit will drill all the way through this sediment

and then 50 meters into the basalt underneath. It’s not an easy target, as the drill may encounter clays transformed into cementlike pockets by high temperatures. “They’re drilling through some really awkward sediment,” says Beth Orcutt, a biogeochemist at the Bigelow Laboratory for Ocean Sciences in East Boothbay, Maine. The drilling itself will heat nearby sediments, so the team will leave a probe in place for a year to discover the borehole’s true heat gradient.

Demonstrating that life really is absent below a certain depth will be tough. Beyond philosophical debates about proving a negative, contamination in core samples has been a chronic problem. But the *Chikyu* will use a new drilling technology, stabilizing and lubricating its borehole with seawater instead of the drilling muds that have often caused contamination in the past. The team will also x-ray the cores to choose those whose interiors appear pristine, evacuating those by helicopter to the Kochi Core Center in Nankoku, Japan. There, any microbes will be sequenced and cultured.

All told, the T-Limit team expects to detect traces of life as sparse as six microbial cells per cubic centimeter of sediment. “This is a fantastic challenge for geochemistry and microbiology,” says Kai-Uwe Hinrichs, one of the expedition’s lead scientists and a geochemist at the University of Bremen in Germany.

If the effort does reveal a thermal limit



to life, it won't be the only boundary. Other hostile conditions deep in ocean sediments, such as scarce nutrients, high pressure, or extreme salinity, probably set life's limit in some places. And the Nankai Trough sediments are starkly different from another high-temperature environment, the hydrothermal vents on midocean ridges. Bacteria and archaea discovered at these vents have been grown in the lab at up to 122°C. But the vents, which are rich in energy sources for microbes, are poor proxies for most ocean floor sediments, where scarce nutrients could mean a lower thermal limit. It would be a surprise to see life in the Nankai linger at temperatures close to that lab-set record, Jørgensen says.

The best existing evidence for a heat limit beneath the ocean comes from the oil and gas industry, says Victoria Orphan, a geobiologist at the California Institute of Technology in Pasadena. Researchers learned decades ago that petroleum reservoirs formed at 85°C or higher underwent "paleo-pasteurization," which killed off microbes that would have degraded the oil. Crude oil found at cooler temperatures, even deep down, often bears the sulfuric detritus left by busy microbes.

The Nankai cores could reveal more than a temperature limit. Microbes cultivated from them could also help settle whether bacteria or archaea are more dominant in the subsurface, and they could also offer a glimpse of the microbes' lifestyles. Current evidence suggests they live extraordinarily long lives thanks to glacial metabolisms. Some reproduce as little as once a century, Jørgensen says. But that evidence, based on metabolic products and cell counts, is uncertain: It's possible that only a fraction of the bugs are active and the rest dormant. If so, the metabolisms of active microbes could resemble those of their surface cousins.

Nor do investigators know precisely how heat limits life in a nutrient-poor environment. At high temperatures, DNA and amino acids become difficult to maintain: The bond between DNA's backbone and bases tends to fail, and amino acids become more prone to flipping into their mirror image structures, which are mostly unusable for building proteins. Jørgensen suspects the failure of mechanisms that repair such damage could be a primary reason for a thermal limit.

He looks forward to learning whether the inhabitants of the deep cores confirm his hunch. But most microbiologists are eagerly awaiting what amounts to the ultimate bottom line: an end to Earth's habitable zone. As Steve D'Hondt, a geobiologist at the University of Rhode Island, Narragansett Bay, puts it, "Whatever their temperature limit is, it sets a new boundary." ■



## MARINE SCIENCE

## Cannonball! China's megasplash in ocean research

Huge new national lab's research priorities remain sketchy

By **Kathleen McLaughlin**,  
in Qingdao, China

**C**hina is massing an army of researchers to attack the mysteries of the ocean. The Qingdao National Laboratory for Marine Science and Technology, a venture taking shape in this seaside city in northeastern China, will consolidate much of the nation's ocean research and host 10,000 researchers and support staff, making it one of the largest national labs in the world.

The Qingdao laboratory, run by the science ministry, is "meant to mobilize the resources of the country" and heal a fragmentation that many Chinese officials believe hampers scientific research, says Director Wu Lixin, a physical oceanographer. As the first of several national laboratories that China intends to launch in the coming years—others will be devoted to brain research, physics, and environmental science—the Qingdao lab will also be a bellwether for efforts to persuade scientists to accept greater government scrutiny and direction in exchange for ample resources.

Foreign scientists will get their first glimpse of the lab when it hosts a global conference on climate and oceans later

this month. For now, the \$200 million ultramodern campus, set here on well-manicured grounds near the Yellow Sea, is largely empty; only about a third of the 1500 scientists now affiliated with the lab work on site. Planners hope formidable resources will entice Chinese and international scientists to sign on. "It's a build-it-and-they-will-come model, which is very different from what we do," says Huntington Willard, director of the Marine Biological Laboratory in Woods Hole, Massachusetts. "This may all work out wonderfully, but at the moment, we don't know what the objective or goal is."

Wu says a major attraction of the new lab will be a research vessel for deep-sea drilling. The *Dream*, as it will be named, would be the third vessel of its kind after Japan's *Chikyu* and the United States's *JOIDES Resolution*. Wu expects construction to begin later this year. The lab, which will bring 11 existing marine research centers under its wing, will also inherit a fleet of manned submersibles, including the *Jiaolong*, which in 2012 dove more than 7000 meters into the Mariana Trench, setting a world depth record. Another attraction is likely to be the cuisine: One of Wu's first hires is a top chef poached from a luxury hotel to head the lab's dining facilities.



Algae blooms off Qingdao, China, are a prime research target for a new national laboratory.

Its research priorities are hazier. Wu and the Chinese Academy of Sciences, which will relinquish thousands of researchers to the lab, list several strategic missions: ocean and climate, marine life, energy and mineral resources, extreme environments in the deep sea and at the poles, and ecosystem health. Tsunami prediction will be another focus, says Wu, who declined to elaborate on specific research questions the national lab intends to tackle. He also demurred when asked whether the lab will extend China's recent work in mapping and exploring the politically charged waters of the South China Sea. "The only interest we have is to represent our country," Wu says.

Still, the Qingdao lab is well situated to investigate the impact of China's development on its coastal waters, notes Laurence P. Madin, research director at the Woods Hole Oceanographic Institution. It recently signed a research agreement with the Ocean University of China here in Qingdao, one of the institutions now under the national lab's authority. For many years, massive algae blooms have plagued Qingdao's waters, and researchers have yet to fully untangle the web of pollution and nutrients that feeds the blooms.

Wu says the lab will aggressively recruit overseas talent, as both staff and collaborators. The *Dream* drill ship, for example, will offer free berths to international scientists as an incentive to work on projects approved by the national lab. But the lack of specific goals gives some potential foreign collaborators pause. "Our scientists would need to be convinced that the questions being asked, and the opportunities for questions to address, are compelling questions that cannot be addressed here or elsewhere," Willard says.

Working at the national lab is also a tough sell for some prominent Chinese marine scientists, says Cui Weicheng, a former project director for the *Jiaolong* who serves on the lab's advisory board. Cui now runs the Hadal Science and Technology Research Center at Shanghai Ocean University in China, where he is using private funding to build advanced submersibles. "When you get a lot of money from the central government, the government assesses you frequently and they want you to produce very big discoveries," he says. "This is not a good atmosphere for scientific research." Wu is betting that top-notch facilities and sheer strength in numbers will prove Cui wrong. ■

Kathleen McLaughlin is a writer in Beijing.

## ATMOSPHERIC SCIENCE

# The atmosphere's pacemaker skips a beat

## Hiccup bodes wet winter weather for Europe

By Betsy Mason

**H**igh in the stratosphere, winds whip around Earth's equator, switching from westerlies to easterlies and back again roughly every 28 months. Although the length of the cycle varies from year to year, the quasi-biennial oscillation (QBO), as it is known, is as dependable as they come: It had not skipped a beat since scientists first reported its existence in 1960.

Until now.

Earlier this year, westerly winds did not yield smoothly to easterlies, as expected, sending scientists scrambling to understand both cause and consequences. One repercussion is already clear: The accuracy of seasonal forecasting could take a hit. But scientists don't know whether the break in the pattern was a one-off thing, or a more ominous sign of the things to come in a warming world. One thing is for sure: One of atmospheric science's most durable precepts has cracked. "All the textbooks will have to be rewritten," says Kevin Hamilton, an atmospheric scientist at the University of Hawaii's International Pacific Research Center in Honolulu, and a co-author of a study published online this week in *Science* that describes the unprecedented disturbance.

The QBO consists of bands of strong stratospheric winds that appear in the mid-

stratosphere and slowly descend, weakening until they dissipate near the base of the stratosphere around an altitude of 16 kilometers. As each band of wind moves down, a new band heading in the opposite direction begins forming above it, with each cycle lasting between 22 and 36 months.

But in February, scientists began to notice something strange in the data from a weather balloon above Singapore. A band of easterly winds began to form above the westerlies, as expected, at the end of 2015, but it was cut off by a new band of westerly winds that appeared below it, keeping the QBO from completing a normal cycle. "This is really, really unexpected," says Steven Pawson, an earth scientist at NASA's Goddard Space Flight Center in Greenbelt, Maryland, and a co-author of a study published last week in *Geophysical Research Letters* that also describes the disruption.

A capricious QBO would deprive scientists of a seasonal forecasting tool. Although it occurs in the tropics, the QBO affects global weather through teleconnections: interactions with large-scale waves in the stratosphere that project its influence to higher latitudes. This reach, coupled with its regularity, has made the QBO a stabilizing force on global weather patterns. So the QBO's unexpected deviation is "kind of a shock" to forecasters' ability to predict weather, Hamilton says.



The quasi-biennial oscillation may have played a role in bringing floods to the United Kingdom this past winter.

For example, there's a strong statistical suggestion that the QBO influences the North Atlantic Oscillation, a pattern of seesawing atmospheric pressures that dominates European weather. When the QBO winds are in a westerly phase, pressure differences over the North Atlantic tend to be more extreme. That strengthens the jet stream and boosts the chances that northern Europe will experience warmer, stormier winters like this past one, which brought floods to the United Kingdom. The expected easterly phase at the end of this year would have given northern Europe a good shot at a colder, drier winter. Instead, the return to westerly winds means that Europeans are more likely to see another stormy winter. "It's not a sure thing that that would be the forecast, but it loads the dice toward those sorts of conditions," says Scott Osprey, a climate scientist at the University of Oxford in the United Kingdom and lead author of the *Science* study.

Scientists have identified several possible causes for the break. The QBO is thought to be driven by tropical waves—generated by warm, circulating air—that propagate up from the troposphere into the stratosphere. But when Osprey's team plugged the anomalous QBO data into a climate model, the disruption appeared to originate outside of the tropics. One possible culprit is this past winter's strong El Niño, which not only brought unusually warm waters to the eastern equatorial Pacific Ocean, but also shook up atmospheric waves and weather patterns well beyond the tropics. A "blob" of warm water that has been growing in the northern Pacific Ocean since 2013 is another possible cause, as is a sudden stratospheric warming event that occurred this past winter in the high latitudes of the Northern Hemisphere.

The two teams are not yet ready to indict climate change as the more fundamental culprit, but they are concerned. "You can't encounter any new phenomenon without wondering if there's some impact of climate change," says Anne Smith, an atmospheric scientist at the National Center for Atmospheric Research in Boulder, Colorado. Osprey's team suspects that global warming will slow down the QBO and make it more vulnerable to future disruptions.

And indeed, they found hints of this, in one of the three climate models they studied. Under an extreme climate change scenario that forecasts warming of about 3.7°C by the end of the century, the model suggested QBO disruptions could occur up to three times every 100 years. If warming is playing a role, this first break in the QBO might not be the last. ■

*Betsy Mason is a freelance writer in the San Francisco Bay Area in California.*

## WILDLIFE BIOLOGY

# No proof that predator culls save livestock, study claims

## New analysis calls for more rigorous studies

By Ben Goldfarb

**O**n 5 August, biologists from the Washington Department of Fish and Wildlife ascended in a helicopter to shoot two members of the Profanity Peak wolf pack, which had been preying on cattle in the state's northeast corner. After the cull failed to end predation, the state removed four more members of the 11-wolf pack. Some conservationists were outraged, but the logic behind such lethal control seems airtight: Remove livestock-killing wolves, coyotes, bears, and other predators, and you'll protect farmers and ranchers from future losses.

A new study, however, claims that much of the research underpinning that common sense notion is flawed—and that the science of predator control needs a methodological overhaul. Adrian Treves, a conservation biologist at the University of Wisconsin, Madison, and his colleagues examined more than 100 peer-reviewed studies, searching for ones that randomized study sites, intervening on some by removing or deterring predators while leaving others untouched. Not a single experiment in which predators were killed has

ever successfully applied this randomized controlled design, they report this week in *Frontiers in Ecology and the Environment*. "Lethal control methods need to be subjected to the same gold standard of science as anything else," Treves says. He argues that policymakers should suspend predator management programs that aren't backed by rigorous evidence.

David Mech, a wolf expert at the University of Minnesota (UM), Twin Cities, isn't persuaded. He notes that many of the studies Treves scrutinized "met some pretty good scientific standards, but just weren't quite perfect. ... Drawing the conclusion that therefore all these depredation management programs should stop until gold standard studies are done—that's a very big leap."

Lethal control has long been a staple of wildlife management. Eurasian lynx have

been culled by hunters in Norway, wolves killed in Spain and Sweden, jackals and caracals eliminated in South Africa. In the United States, predator control often falls to the federal APHIS Wildlife Services, a branch of the U.S. Department of Agriculture. In 2015, the agency killed 385 gray wolves, 284 mountain lions, and more than 68,000 coyotes. Unlike the Profanity Peak wolf pack, which wasn't targeted until it began killing livestock, coyote populations in many states are subject to preemptive thinning.

Treves says he was inspired to look at the science behind predator control by a book unrelated to wild carnivores: *The Emperor of All Maladies: A Biography of Cancer*, Siddhartha Mukherjee's epic history of cancer. As Treves paged through it, he says, "a light bulb went off in my head." He suspected that predator

---

**"Lethal control methods need to be subjected to the same gold standard of science as anything else."**

**Adrian Treves**, University of Wisconsin, Madison

management was plagued by the same methodological problems that had once led cancer researchers to promote ineffective cures—particularly a dearth of randomized controlled trials. Although removing carnivores to ease livestock loss makes intuitive sense, Treves and other scientists were skeptical: For instance, some research suggests that coyote populations subject to culling have higher pup survival rates, and that male cougars expand their ranges in response to hunting.

What Treves found when he and his co-authors—Miha Krofel, a wildlife researcher at Slovenia's University of Ljubljana, and Jeannine McManus, a researcher at the Landmark Foundation in Riversdale, South Africa—dived into the literature confirmed his suspicions. Only 12 studies came close to Treves's gold standard or even a lesser "silver" standard, in which livestock losses before and after predator management were monitored, or analyzed in retrospect. Many other studies had flaws that he says make it impossible to draw reliable inferences. A 1999 experiment purporting to show the effectiveness of shooting coyotes from helicopters, for instance, had a higher density of sheep in its control pastures, which could have made them more attractive to hungry coyotes. Oth-





Federal officials shot four pack members after wolves killed cattle in Montana.

ers failed to properly randomize intervention and control sites or described their methods inadequately, making replication impossible.

"There are so many ways that these studies could have been improved," says Robert Crabtree, a carnivore ecologist and founder of the Yellowstone Ecological Research Center in Bozeman, Montana. "Not by spending more money, but by paying careful attention to standardization protocols, transparency, and replication."

Some of the authors whose studies Treves critiques object to his analysis. He discounted a 2008 study suggesting that trapping male wolves reduces livestock loss, for instance, in part because it excluded certain data points. But lead author Elizabeth Harper, then at UM, says that the paper thoroughly explains why each data point was excluded, and that the omissions kept misleading data from contaminating the results. Harper adds that she isn't convinced Treves's own study lives up to his standards: The authors assessed the validity of studies themselves, rather than asking independent experts. "That could create their own bias," Harper says.

Others say that Treves is setting an impractically high bar. The complexity of field biology precludes most gold standard experiments, argues Adrian Wydeven, Timber Wolf Alliance coordinator at Northland College in Ashland, Wisconsin. Scientists face countless variables, including subtle differences in habitat, weather, and the unpredictable movements of animals themselves. "I just don't see that it's an attainable standard—it's not like being in the lab," Wydeven says. Such research also relies on the cooperation of farmers and ranchers, who may not be ea-

ger to take part in a randomized, controlled study. When wolves are at the door, who wants their flock to be one that doesn't get help?

Treves counters that two of the studies he and his colleagues analyzed did meet the standard. Both evaluated nonlethal predator deterrence techniques: guard dogs and strings of flapping red flags that scare off wolves and coyotes. Performed by Tom Gehring, a biologist at Central Michigan University in Mount Pleasant, they showed that wolves and coyotes both steered clear of cattle farms patrolled by Great Pyrenees dogs, and that the flags deterred wolves, but not coyotes.

To prepare for the studies, done on Michigan's Upper Peninsula, Gehring combed through data on the ranges of local wolf packs to identify vulnerable farms, then visited each operation to secure its commitment. He paired farms based on attributes like size and location and randomly assigned one to the treatment group and one to the control group. "It was an ordeal," Gehring acknowledges. "It took months."

In the end, he claims, the rigorous design was well worth the trouble. Before his experiments, he says, many ranchers and biologists were skeptical that guard dogs could protect stock against wolves. By the end, though, the ranchers who had been assigned to the control group were clamoring for dogs of their own. "You don't hear anybody question that guard dogs work in Michigan anymore," Gehring says. ■

*Ben Goldfarb is a freelance writer in New Haven, Connecticut.*

## SCIENTIFIC INTEGRITY

# Accusations fly after big Gates grant

Panel promises verdict on old dispute between WHO and the University of Oxford

By Kai Kupferschmidt

**W**hen a big consortium led by University of Oxford researchers José Villar and Stephen Kennedy in the United Kingdom bagged a \$29 million grant from the Bill & Melinda Gates Foundation in March 2008, it seemed a cause for celebration. Their goal was to develop global standards to assess whether a fetus is on a healthy growth trajectory. Such standards would allow doctors to spot problems early and help prevent deaths in babies as well as mothers.

But the announcement shocked and angered some researchers at the World Health Organization's (WHO's) Department of Reproductive Health and Research in Geneva, Switzerland. Since late 2006, they had been heading a major effort to do the same thing in which Villar and Kennedy both participated; Kennedy had even signed a contract for Villar to develop a key protocol for the study, which Villar had yet to deliver. But members of the WHO group now say that the Oxford duo were using ideas developed in the WHO project in their competing grant proposal; some accuse them of deliberately delaying their WHO work while they were courting the Gates Foundation.

Thus began a bitter dispute involving three important players in global health that is still awaiting a resolution 8 years later. An independent panel is now looking into the matter and may soon arrive at a verdict, a WHO spokesperson says. WHO decided to commission the investigation last year after seeking advice from Frank Wells, an independent consultant on research ethics based in Ipswich, U.K.

In the executive summary of his report for WHO, which *Science* has obtained, Wells cautioned that the case was tangled. But he warned that doing nothing could create the impression that WHO didn't take misconduct allegations seriously. He found it "surprising" that the organization lacked a formal policy to deal with such allegations, and

that the Gates Foundation had steadfastly refused to investigate alleged misconduct by its grantees.

The University of Oxford, meanwhile, denies any wrongdoing by Kennedy and Villar. It looked into the matter three times—in 2008, 2009, and 2011—and concluded on each occasion “that there was no substance to the accusations,” the university wrote to *Science*, although it refused to elaborate. Kennedy and Villar declined to comment.

WHO set out to do a fetal growth study because existing growth curves were based mostly on European and U.S. cohorts, and it was unclear whether they applied elsewhere. The agency recruited dozens of scientists to work on a study to measure fetal growth around the globe. And it paid Villar \$31,350, in part to write a protocol for the study.

That protocol was supposed to be delivered in December 2007, but it was never finished. In an email seen by *Science*, Kennedy informed WHO in March 2008 that Villar had not been able to complete the task and offered to reimburse the money. In January of that year, recalls Paul Chamberlain, an Oxford expert in scanning fetuses who was also involved in the WHO project, Kennedy and Villar told him that they had submitted their own grant proposal to measure fetal growth to the Gates Foundation. “The decision surprised me,” Chamberlain says. “I had always understood that this was a study that would be run under the auspices of WHO.”

The grant was awarded, and the pair started what has become known as the Intergrowth-21<sup>st</sup> consortium. Not long after, Wells wrote in his report, WHO expressed concerns to the University of Oxford that the protocol for the Gates-funded study was “closely related, if not identical, to the WHO protocol.” Oxford disagreed, and demanded that the allegations be withdrawn. The two organizations tangled over the issue for several years, Wells notes, but WHO pursued the matter “without any specific direction,” and in the end WHO dropped the matter. The Gates Foundation, meanwhile, tried to stay out of the dispute, writing in August 2009 that “this type of situation is most appropriately addressed by Oxford and WHO.” (The foundation declined to answer *Science*’s questions about its handling of the dispute.)

But WHO remained under heavy pressure from three external scientists to seek redress: Lawrence Platt, a gynecologist at the University of California, Los Angeles, who heads the executive committee for the WHO study; Torvid Kiserud of the University of Bergen in Norway, a member of the executive committee and the study’s steering committee; and Marshall Lindheimer, a nephrologist from the University of Chicago in Illinois who, although not a party in the dispute himself, became a champion for the WHO panel. “The three frustrated professors,” as Wells calls



A Gates-funded study headed by University of Oxford researchers and a similar effort by the World Health Organization both set out to develop worldwide standards for fetal growth.

them in his report, kept lobbying for an independent investigation. The Oxford investigations were “not transparent, none of us in the research group ... was ever consulted or asked to explain,” Kiserud says.

WHO eventually asked Wells to look into the matter in 2014. Wells didn’t hear all sides of the story—the Oxford scientists refused to talk to him—but he recommended that WHO ask an independent panel to look at the similarities between the WHO and Oxford protocols. Among the risks of not doing so, he wrote: “Professors publish in *The Wall Street Journal* or similar, implicating WHO for condoning academic misconduct.” (That did not happen, but Lindheimer did alert *Science* to the dispute in March of this year.)

WHO has not revealed who’s doing the investigation, and it says the report won’t be made public. But if the panel finds that the Oxford researchers engaged in misconduct, WHO will refer the issue to the United

Kingdom’s General Medical Council, which could impose sanctions if it agrees with the findings, a WHO spokesperson says. The three professors say they’re pleased about the investigation, but say it should also ask whether Kennedy and Villar dragged their feet on the WHO project as they prepared their Gates proposal.

Intergrowth-21<sup>st</sup> has already resulted in a series of papers. When the first batch came out in *BJOG*, an obstetrics and gynecology journal, Chamberlain asked the journal to remove his name as a co-author. “I did not

want my name associated with that study,” he says. More papers were published in 2014 and 2015 in *The Lancet*. They showed that babies of healthy mothers show similar growth patterns irrespective of ethnicity. Growth standards developed by the consortium are now used, for instance, to see whether the babies of pregnant women infected with Zika might be suffering from microcephaly.

Last year, a study that had followed more than 2300 pregnant women in the United States came to a different conclusion: that fetal growth differs significantly between four ethnic groups. The WHO group—minus Villar and Kennedy—has yet to publish conclusions from its own study. In its statement to *Science*, the University of Oxford expressed

concern that the dispute about the Gates grant could fuel a scientific controversy. “It would be a tragedy if reopening a matter that has repeatedly been declared closed by WHO delayed the introduction of international standards with potential health benefits every year to more than 20,000,000 of the most vulnerable infants worldwide,” its statement said. Platt calls that “an exaggerated claim with no substance.”

As a result of the case, WHO has drafted a formal policy for dealing with alleged research misconduct; it will be publicly available before the end of the year. That’s a positive step, says Lindheimer, who has warned WHO that scientists would shun its panels if they believe others could make off with their ideas. WHO, he says, was “in the dark ages when this affair began.” Platt agrees. “Each of us at this stage of our careers seeks no personal gain but rather do our small part in ensuring the integrity of science,” he says. ■





Islamic Azad University's Chinese-made tokamak could see action as an ITER test bed.

# IRANIAN SUN

A fusion research program nurtured in isolation could blossom as Iran joins the ITER megaproject

By Richard Stone, in Tehran

**T**he Damavand tokamak is an unlikely emblem of hope for Iranian science. Named after Iran's tallest mountain, it looks like an antique bathysphere studded with metal barnacles. Its heritage is retro, too; Iran purchased the machine, which confines and heats plasma within powerful magnetic fields,

from Russia in 1994, and its toroidal hull is vintage Soviet. Only the barnaclelike adornments—Iranian-made devices for probing and shaping plasma—are newer.

For more than a decade, the 110 scientists in the fusion department of the Atomic Energy Organization of Iran (AEOI) here in north Tehran experimented on their aging tokamak and other devices

in seclusion, cut off from the global fusion community because of Iran's status as a nuclear pariah. Their isolation is about to end. In early 2017, Iran is expected to join the world's most expensive physics experiment, ITER, a mammoth tokamak now under construction near Cadarache in southern France. The Damavand device would add to a menagerie of small toka-





At Cadarache in France on 1 July, ITER chief Bernard Bigot (far left) briefs Iranian delegates Ali Akbar Salehi, Sorena Sattari, and Mahmood Ghoranneviss (left to right).

maks around the globe now being used as test beds for ITER, which aims to achieve the first controlled, self-sustaining fusion reaction within a decade or two, at a cost of tens of billions of dollars.

ITER Director-General Bernard Bigot plans to lead a delegation here as early as next month to begin formal talks on ties that, Iranian science officials hope, will boost the nation's fusion program and expose Iranian experts to global norms in science. An ITER partnership "will solve many cultural problems" that hinder Iran's efforts to create a knowledge-based economy, says Sorena Sattari, Iran's vice president for science and technology, who, with AEIO President Ali Akbar Salehi, went to Cadarache in July for informal discussions about Iran's potential contributions.

An agreement with ITER would be the first big scientific fruit of a landmark international deal—the Joint Comprehensive Plan of Action (JCPOA)—in which Iran agreed to limits on its nuclear program in exchange for the lifting of economic sanctions imposed by the United Nations and individual countries after revelations of covert nuclear facilities in 2003. It would also mark fusion research as an exception to the generally lackluster progress on the scientific cooperation envisioned in the agreement (see sidebar, p. 1085), which has been hampered by growing distrust between Iran and the United States.

A year after the deal was signed in July 2015, Iranian officials complain that the

United States has not sent an emphatic signal to international banks that it is okay to do business with Iran again, delaying an expected economic bounce. And although Iran on 29 August paroled a young laser physicist, Omid Kokabee, convicted of "communicating with a hostile government" in 2012 and sentenced to 10 years in prison, U.S. officials are wringing their hands over a fresh wave of arrests of Iranian-Americans visiting family in Iran.

With the mood souring, the JCPOA's fate hangs in the balance. "We should keep it as we keep a baby: Make sure no harm reaches the nuclear deal," Salehi says. "Everything is at stake." He hopes that the prospect of cooperation on fusion will help blunt domestic criticism. If the fusion ties help save the deal, decades of quiet persistence by Iranian researchers, backing from top politicians, and the influence of scientists who maintained overseas ties in Iran's darkest times will have a very public payoff.

**IRAN'S PURSUIT OF FUSION** started nearly a half-century ago. In the mid-1960s, Masud Naraghi, then a young plasma physicist, was working in the United States on space-ship re-entry technologies for a NASA contractor in New York. In 1965, he and other Iranian expatriates met the last shah of Iran, Mohammad Reza Pahlavi, at the Waldorf Astoria New York in New York City. "He told me, 'Why don't you come back to Iran, and help your country?'" Naraghi says. "It really affected me. I was

homesick." Naraghi, now president of Torr International in New Windsor, New York, returned to Iran and joined the faculty of Aryamehr University here, renamed Sharif University of Technology after the 1979 revolution that ousted the shah.

Pahlavi was intent on developing nuclear power in Iran, which in 1967 acquired a research fission reactor from the United States under the Atoms for Peace Program (see sidebar, p. 1086). At that time, research on fusion power was in its infancy, and Naraghi saw a chance for Iran to get in on the ground floor. He started a plasma research group in 1971, and, 4 years later, oversaw construction of Iran's first tokamak—called Alvand—at AEIO's nascent Tehran Nuclear Research Center. Science in Iran sputtered during the Iran-Iraq War in the 1980s, however, and Naraghi emigrated to the United States in 1989.

The next big boost for Iranian fusion came at a private university in the foothills of the Alborz Mountains north of here. Plasma physicist Mahmood Ghoranneviss moved to the arid aerie in 1993. At the time, he recalls, "there was no road here. Only land." He had come to start his own plasma physics center at Islamic Azad University (IAU).

He had a powerful patron: Akbar Hashemi Rafsanjani, the university's founder and then-president of Iran. Rafsanjani "understood the importance of fusion for our country's future," Ghoranneviss says. As a sweetener to lure him from AEIO, where



# A year after the deal, nuclear collaborations languish

By **Richard Stone**

In Iran, the nuclear agreement signed last year with world powers isn't popular. Economic payoffs have been slow to materialize, and resentment over years of isolation and sanctions remains strong. Ali Akbar Salehi, president of the Atomic Energy Organization of Iran (AEOI) in Tehran, believes that getting Iranian and foreign scientists to work together is a potential salve. It "will recover lost trust and build up confidence," he says. Joint projects could also make up for the loss of opportunities for Iranian nuclear scientists under the deal, says Salehi, who says he has upward of 15,000 nuclear scientists and engineers to worry about. "I have to be mindful of them. I shouldn't let them feel, 'Look, everything is slowing down,' or 'We are running out of jobs.'"

But except for projects in fusion (see main story, p. 1083), scientific cooperation is lagging. One initiative that is slow off the mark is the transformation of the underground Fordow Fuel Enrichment Plant, which housed about 2700 centrifuges for enriching uranium, into an international physics center. Under the nuclear agreement—officially known as the Joint Comprehensive Plan of Action (JCPOA)—Russia is helping Iran reconfigure 358 of the centrifuges at Fordow to produce stable isotopes for medicine and industry.

"The modification of the design is not an easy job," says Salehi, who predicts it could take another year to complete the work. One challenge: Iran has not settled on which radioisotopes to produce. "We want to produce isotopes that are needed on the market," Salehi says. "It's not research for the sake of research."

In the meantime, Iran has proposed turning a second wing at Fordow—emptied of its centrifuges—into a nuclear research lab that, Salehi says, would "replicate and be complementary" to an International Atomic Energy Agency lab in Seibersdorf, Austria. He would like Iranian and foreign experts "to come up with different proposals and see what we can do there."

Another JCPOA task intended to bring together nuclear scientists is re-engineering the Arak heavy water reactor, originally designed to burn natural uranium, which could generate about a bomb's worth of plutonium a year. Iran agreed to switch to low-enriched uranium—which yields only traces of plutonium when burned—and use a smaller calandria, the vessel holding the reactor core, which would make it harder to switch back to natural uranium fuel. In

January, workers removed the existing calandria and filled it with concrete. "There were people here [at AEOI] in mourning over that," AEOI Vice President Behrooz Kamalvandi says.

China and the United States are co-chairing a working group that will review Iran's new reactor design. The goal is to ensure, as a U.S. Department of Energy official put it, that the reactor "will allow effective peaceful uses but not rapid accumulation of plutonium suitable for weapons." But Salehi complains that the group is moving slowly. "The working group is not doing what it is expected to do," he says. "We need our design to be certified by more advanced countries. ... But if they don't, so be it. We will go on with our work."

European labs are one bright spot for Iranian researchers, says Javad Rahighi, director of the Iranian Light Source Facility (ILSF) in Tehran, which aims to build an advanced synchrotron. He is about to ink a deal to buy 500 hours of beam time in 2017 at the ALBA synchrotron near Barcelona, Spain. Next year ILSF will also start building a beamline at ELETTRA, a synchrotron in Trieste, Italy.

The JCPOA has melted other barriers between Europe and

Iran. In April in Tehran, a senior EU delegation that included Carlos Moedas, European commissioner for research, innovation and science, agreed to welcome Iranian involvement in research on food security, climate change, and rare diseases, and to step up Iranian engagement in Horizon 2020, the European Union's flagship research program. The European Union also invited Iranian nuclear scientists to submit proposals to the Euratom research program in areas such as nuclear medicine and reactor safety.

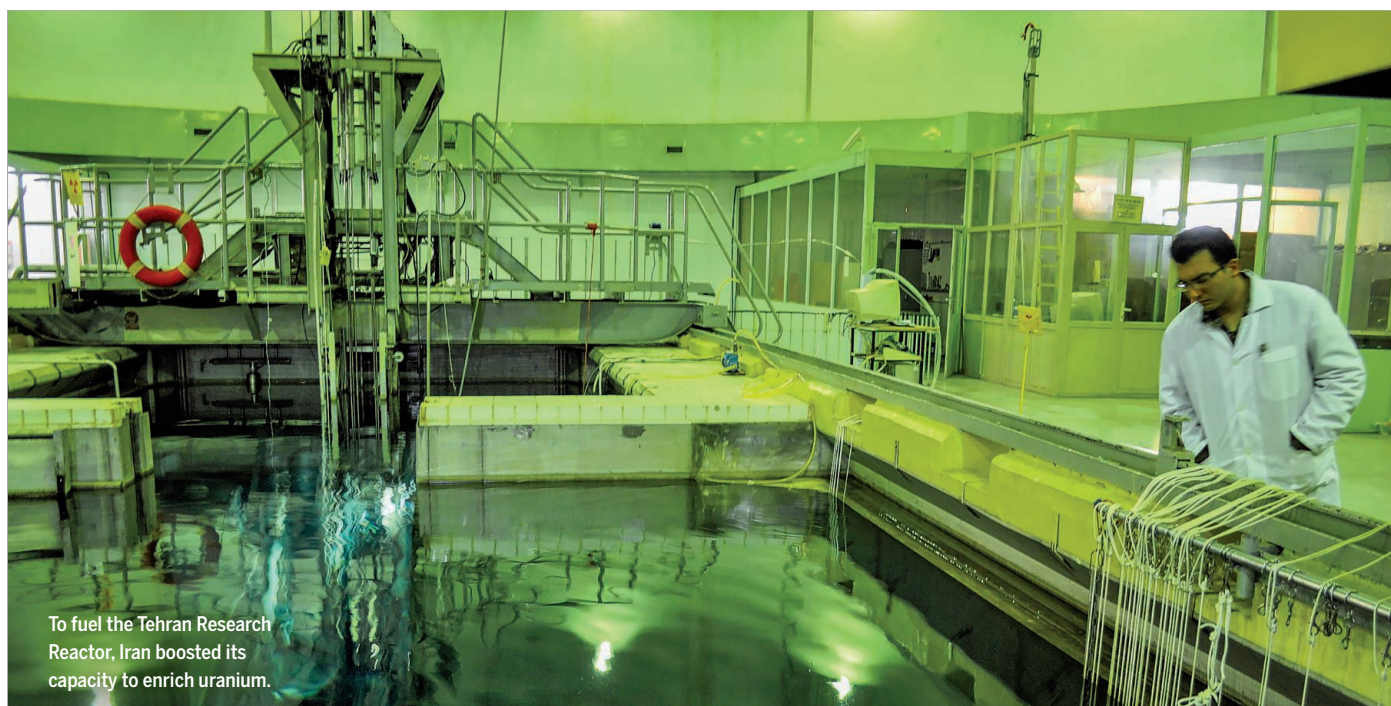
Iran's scientific community isn't getting much

help from the United States, however. Current U.S. law limits cooperation on nuclear research, and U.S. Department of the Treasury regulations bar spending money in Iran for most purposes, including research, without a license. Last month, the treasury department rejected an application from Biruni Inc., a foundation in Los Angeles, California, for a license to transfer funds to help pay for construction of Iran's national astronomical observatory near Kashan.

Many Iranian scientists are disappointed that the U.S. scientific community remains on the sidelines. "Americans sitting back and doing nothing for us is not a pleasant thing to see," Rahighi says. "We took very bold steps," Kamalvandi adds. "The nuclear deal is still alive, but it needs a lot of work and a lot of help in order to succeed." ■



European labs are aiding Javad Rahighi's quest to build an advanced synchrotron in Tehran. Rahighi is disappointed that U.S. collaborations have not materialized.



To fuel the Tehran Research Reactor, Iran boosted its capacity to enrich uranium.

## The reactor that triggered a nuclear crisis

By **Richard Stone**

**F**rom high on the wall of a rotunda at the Tehran Nuclear Research Center, portraits of Iran's supreme leader, Ali Khamenei, and his predecessor, grand ayatollah Ruhollah Khomeini, gaze down on an emerald-green pool. Eight meters below the surface is the machine that sparked the latest international crisis over Iran's nuclear ambitions—and helped motivate the July 2015 nuclear deal to constrain them.

The Tehran Research Reactor (TRR) is used mainly for producing medical radioisotopes, not weapons, but Iran's concerted effort to produce fuel for it “precipitated a security crisis that led to Israel's push for military action and, as a result, the White House decision to finally make a serious effort at negotiations,” says R. Scott Kemp, an expert on Iran's nuclear program at the Massachusetts Institute of Technology in Cambridge. “The rest is history.”

Ironically, the TRR was a gift from the United States. Under the Atoms for Peace program that promoted civilian nuclear research around the world, the United States provided the reactor in 1967, along with bomb-grade fissile material—highly enriched uranium (HEU)—to fuel it. It came online 2 years later, with a 25-year design life. But Iran kept its nuclear jalopy running decades longer than expected by scrounging for spare parts—and by finding ways around international sanctions.

After Iran's 1979 revolution, the United States and other nuclear powers refused to provide it with HEU. So Iran enlisted Argentina in 1989 to convert the TRR to run on low-enriched uranium (LEU), containing 19.75% of the fissile isotope uranium-235; a few years later, Argentina sold Iran 115.8 kilograms of LEU fuel.

Revelations in 2003 of Iran's covert nuclear activities posed new complications. That year, the International Atomic Energy

Agency (IAEA) discovered that a decade earlier Iran had secretly irradiated about 7 kilograms of uranium oxide in the reactor and extracted a small amount of plutonium. Those and other activities eventually led the United Nations and individual countries to tighten sanctions.

In 2009, when the TRR was running low on fuel, Iran asked IAEA to authorize an LEU purchase, but negotiations broke down. “I told the president at the time, Dr. [Mahmoud] Ahmadinejad, ‘Look, we will have to do something. Put up our sleeves and start working,’” says Ali Akbar Salehi, the president of the Atomic Energy Organization of Iran in Tehran. He launched a crash effort to learn how to make LEU fuel plates.

Some Western experts say fueling the TRR was not Iran's only motivation. “They used the Tehran reactor as an excuse,” contends Olli Heinonen, a senior fellow at Harvard University's Belfer Center for Science and International Affairs. Within 2 years, Iran was making its own LEU fuel, thanks to a technological leap: Its engineers had learned how to link centrifuge cascades to enrich uranium to ever-higher levels.

It was an ominous milestone, Kemp says, because reaching 20% low enrichment represents roughly 90% of the effort needed to make the HEU needed for a bomb. It was “an important step in HEU production,” he says, and it quickly precipitated the crisis that led to the nuclear deal.

Now, the TRR may help Salehi and others assuage domestic critics of the agreement. Salehi, who says he finds himself these days in a “very acute position,” points to LEU fuel fabrication and other achievements as proof that Iran won't lose its edge. “Certainly we have accepted some constraints,” he says. However, he notes, Iran continues to mine and enrich uranium, produce heavy water, experiment on advanced centrifuges, and, of course, make radioisotopes at the TRR. “All of our nuclear activities are still going on.” ■



he had apprenticed for a decade, the university bought a small, used tokamak from China. But at first, it was difficult to staff his center. “People didn’t know what plasma is. They thought I was talking about blood.” Step by step, he says, he recruited students and assembled a team that began using the tokamak to probe plasma instabilities.

Ten years later, sanctions over Iran’s nuclear program began to bite and a cloud of suspicion descended on collaborations with Iranian nuclear scientists. Magnetic confinement fusion “has no relevance to nuclear weapons,” notes R. Scott Kemp, an expert on Iran’s nuclear program at Massachusetts Institute of Technology in Cambridge. But Ghoranneviss worried that his center would also fall under suspicion. He contacted the International Atomic Energy Agency (IAEA) in Vienna. “I explained, ‘I am not a government man, my university is private. Please help me.’” IAEA threw him a lifeline: In 2006, the agency brought Ghoranneviss into its Coordinated Research program for fusion, which connected him with researchers in other countries.

Through the IAEA program he met Heinrich Hora, a theoretical physicist at the University of New South Wales, Sydney, in Australia. Hora was nervous about getting involved with the sanctioned country. “I was very cautious,” he says. But he and Ghoranneviss discovered a common passion for a radical alternative to tokamaks.

Tokamaks like ITER burn deuterium and tritium, hydrogen isotopes that, when fused, spew high-energy neutrons and intense radioactivity. Hora and collaborators envisioned combining magnetic confinement with powerful laser pulses to ignite a different fuel: hydrogen and boron-11, which does not produce damaging neutrons during fusion. With George Milev, a nuclear physicist at the University of Illinois, Urbana-Champaign, they laid out the theoretical basis for the approach in *Energy and Environmental Sciences* in 2010, in a paper that got wide attention. Hora says calculations by one of Ghoranneviss’s students—Babak Malekynia—were “crucial and important.”

A second collaboration with a U.S. fusion effort soon blossomed. In April 2012, Voice of America ran a report on its Persian language television channel about a “fusion for peace” proposal, in which Eric Lerner, the president of LPP Fusion in Middlesex, New Jersey, and two colleagues proposed that the U.S. and Iranian governments work together. Ghoranneviss got in touch with Lerner, and a month later the two agreed to work on joint pa-

pers from studies on a kind of compact fusion machine that both IAU and LPP used: a plasma focus device that relies on a current-induced magnetic field—rather than external magnets like a tokamak—to contain tiny plasma globs. IAU dispatched a senior fusion expert, Hamid Yousefi, for stints at LPP in 2012 and 2014.

The collaboration hit a pothole in early 2013, after a website, Forbidden Knowledge TV, claimed that LPP had developed fusion “generators” and was selling six to Iran for \$70,000 apiece. What Lerner calls “misinformation” caught the eye of the U.S. Department of Commerce and the Federal Bureau of Investigation, which opened an inquiry. LPP was quickly cleared of any wrongdoing, Lerner says. Experiments with the plasma physics team at IAU are continuing.

**NOW, GHORANNEVISS IS EMBARKING** on a far grander collaboration. In February, Sattari appointed him Iran’s chief representative to ITER.

Some Iranian officials think that in starting out with a modest partnership outlined in a memorandum of understanding, Iran is aiming too low. Ghoranneviss says that Rafsanjani, still an influential politician, earlier this year suggested that Iran become a full member of ITER, coequal with China, the European Union, India, Japan, Russia, South Korea, and the United States. “He loves fusion,” Ghoranneviss says. “He said, ‘Don’t worry about money.’”

Salehi, however, says it’s too early for

***“We would be a weak full member [of ITER]. We need to build up indigenous capacity.”***

**Ali Akbar Salehi**, Atomic Energy Organization of Iran

full membership. The cost to Iran—which he estimates at about \$120 million a year—is daunting. Moreover, Salehi says, Iran is simply not ready. “We would be a weak full member. We still need to build up indigenous capacity,” both in training researchers and upgrading Iran’s aging tokamaks.

AEOI’s nuclear fusion department, for example, has been handicapped not only by Iran’s isolation, but also by security concerns. As suspicions grew that Iran may have been pursuing nuclear weapons, assassins started targeting researchers with links to Iran’s nuclear program. Over 3 years, four were slain in an effort widely thought to have been orchestrated by Israel. The government assigned security personnel to escort hundreds of scientists, including top fusion researchers, wherever

they ventured in public.

Even so, AEOI’s fusion program has been building its human capital. It hosts university students, giving them experimental problems to solve on Iran’s small tokamaks. Trainees also work on AEOI’s “Iranian Sun” plasma focus. The device “is handy and cheap for studying plasma behavior,” says plasma physicist Seyed Mahmud Sadat Kiai, who with 32 AEOI co-authors wrote a 2010 paper in the *Journal of Fusion Energy* describing how they used the plasma focus to generate short-lived radioisotopes.

The result is a homegrown plasma physics community, a few hundred researchers and graduate students strong, ready for new collaborations in the wake of the nuclear deal. Among the JCPOA parties, France has taken the lead in reaching out to Iran on fusion; in July, six fusion experts from the Paris-based French Alternative Energies and Atomic Energy Commission visited AEOI and IAU to explore possibilities for Iran to contribute to France’s work on ITER’s divertor, a structure that removes helium—the “ash” from fusion—from a burning plasma.

Bigot in July asked for the blessings of the ITER Council, made up of representatives of the seven full members, to pursue a relationship with Iran that would begin with work in diagnostics: defined measurements for observing and characterizing plasma. As *Science* went to press, Bigot says he was waiting for a final council member to weigh in; the six responses so far, including the United States’s, are positive. Provided he gets what he calls a “full green light,” Bigot will lead a team here that will assess Iran’s capacity in diagnostics.

Once the agreement is finalized, Salehi says, Iran will dispatch fusion experts for training at Cadarache and other fusion installations. If things go smoothly, Iran could negotiate associate membership in ITER, which would expand the relationship beyond diagnostics. Around 2020, perhaps with French assistance, Iran intends to build a larger tokamak, similar in scale to machines in China and South Korea. Full membership, Salehi hopes, could come around the time ITER is expected to start operating, in late 2025.

For Ghoranneviss, joining ITER is a dream come true. But the responsibility of leading Iran’s bid to help capture the sun’s energy source is weighing on him. “I cannot sleep at night. My troubles are increasing,” he says, with a smile. After decades of adversity, they are welcome troubles. ■



## BOOKS *et al.*

### FALL READING

# Autumn books to fall for

A mother sets out to discover how her late son's organs helped to advance scientific research. A data scientist reveals how invisible algorithms perpetuate inequality. A citizen scientist delights in the contributions of enthusiastic volunteers. Taking a cue from the season, the books on this year's fall reading list are poignant, crisp, and reflective. Learn how to combat medical science denial and why we tempt fate by building in disaster-prone areas. Join an awe-inspiring journey through the cosmos, delve into a light-hearted exploration of profanity, or contemplate the path forward for autonomous vehicles and animal agriculture.

## Driverless

Reviewed by **Tim Athan**

Everyone is talking about driverless cars. Recent advancements in power storage, computational power, sensory technology, communication bandwidth, algorithm efficiency, and more have moved autonomous vehicles from the realm of science fiction into the real world. In *Driverless*, authors Hod Lipson and Melba Kurman delve into these and other contributing technologies.

Included is an exhaustive review of one such advance, "deep learning," that allows a

computer to learn from experience. One boggling potential application in the context of driverless cars is "hive learning," in which everything a vehicle learns about road conditions can theoretically be instantaneously shared with all other vehicles, enabling a new vehicle to possess the experience of millions of miles of driving. Yet, deep learning is only as comprehensive as its training. The deadly Tesla accident that occurred in May seems to have resulted from an encounter with a "corner case," a condition not included in training.

Humans are vulnerable to corner cases, too. A driver who faces a new situation without preparation is experiencing a cor-

### Driverless Intelligent Cars and the Road Ahead

Hod Lipson and Melba Kurman  
MIT Press, 2016. 322 pp.



ner case. And human information sharing is not instantaneous, meaning that any lessons learned will benefit only the individual driver.

Unlike traditional computer algorithms, deep learning creates a nonexplicit, black-box intelligence that cannot be reverse-engineered. For this reason, trying to determine





why a driverless system made a decision can be as difficult as ascertaining a human's decision process. This, write the authors, will have implications for liability assessment.

The book also delves into advances in machine vision. Only recently have we developed pattern-recognition software and hardware capable of recognizing real road challenges such as shadows. The Tesla accident, which appears to have involved difficulty discerning the side of a turning tractor-trailer, highlights that there is still work to do.

"Human-in-the-loop" computation automates most, but not all, functions. It is the approach used by pilots and surgeons. But the authors contend that drivers will be unable to maintain sufficient alertness over the course of a lengthy trip. It was reported, for example, that the driver of the Tesla was watching a movie at the time of the fatal accident.

The authors acknowledge that an autonomous future is not guaranteed and discuss potential problems, both in technology and in policy. Yet they are clearly rooting for it. After reading this book, you will be knowledgeable enough to make your own informed opinion.

*The reviewer works in software reliability and accident reconstruction for Engineering Systems, Inc., Ann Arbor, MI 48108, USA. Email: twathan@engsys.com*

## Weapons of Math Destruction

Reviewed by **Kalpana Shankar**

Are data neutral? In *Weapons of Math Destruction*, Cathy O'Neil, a math blogger, former Barnard professor, and former quantitative analyst for the hedge fund D. E. Shaw, answers with a resounding "no."

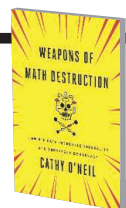
In this extremely approachable book, O'Neil looks closely at how invisible algorithms and Big Data are used to make decisions for and about us in almost every arena of our lives. The result, she argues, further disenfranchises those with the least power in our society and entrenches the "comfortable classes in their own marketing silo."

The least transparent and most troubling algorithms she terms "weapons of math destruction" (WMDs). She describes such models as black boxes that cannot easily be challenged but that, nevertheless, can have devastating consequences, particularly for the poorest and most marginalized groups and individuals.

O'Neil begins by discussing her own professional work with the development and deployment of mathematical models. She then describes her disillusionment following the housing crash that led her to quit

**Weapons of Math Destruction**  
How Big Data Increases Inequality  
and Threatens Democracy

Cathy O'Neil  
Crown, 2016. 272 pp.



her hedge fund job, launch a blog to combat sloppy and biased statistics, and join the Occupy Wall Street movement. The rest of the book delves into specific cases of troubling data practices in areas including credit scores, predictive policing, auto insurance pricing, the for-profit college industry, and work scheduling.

O'Neil's talent for breaking down complex issues is enviable for its narrative power; I finished reading each chapter enlightened but disturbed. She weaves together the actions of relevant industries with stories of the real effects of algorithms on the lives of individuals, distinguishing potentially "good" uses of data analytics from WMDs throughout. This approach gives nuance to the problems she is addressing. She concludes with some concrete prescriptions for bringing more regulation, transparency, and

*The reviewer is at the School of Information and Communication Studies at University College, Dublin, Dublin 4, Ireland. Email: kalpana.shankar@ucd.ie*



equity to mathematical models and Big Data.

As someone who is familiar with the discourse of models, algorithms, and data, I had no trouble jumping right into the book, but a formal introduction to these terms as she is using them might have been useful for readers who are less familiar with this terrain. However, this structural issue is minor, and overall the book is an excellent overview of a large and complex topic.

### What the F What Swearing Reveals About Our Language, Our Brains, and Ourselves

Benjamin K. Bergen  
Basic Books, 2016. 280 pp.



## What the F

Reviewed by **Tina Masciangioli**

“F bombs” come in and out of earshot as I walk down the hallway of my school. I ask my students if they are going to talk like that in their jobs. Would they say that word in front of their mothers? They shrug. If I’m lucky, I get an apologetic “my bad” or at least a look of embarrassment.

In *What the F*, a self-proclaimed “book-length love letter to profanity,” cognitive scientist Benjamin K. Bergen succeeds in bringing me around to appreciate the broader context, as well as the finer points, of the role “bad” words play in human society. Bergen takes the reader through the many dimensions of swearing—from definitions, etymology, and usage trends to the relationship between profanity and language

*The reviewer teaches chemistry at Falls Church High School, Falls Church, VA 22042, USA. Email: tinamasc@verizon.net*

more broadly. He even addresses the merits of ignoring profanity, as well as many other questions I have had over the years, such as, where do swear words come from? Is swearing harmful to children? And should people—whether a mother in a grocery store or an athlete on the basketball court—be punished for using profanity?

As one might expect given the provocative title, *What the F* is often very entertaining. At times, however, the book can be quite “in the reeds,” as Bergen admits, and will appeal more to linguists than to casual readers. However, nonexperts will likely still enjoy Bergen’s skillful use of analogies and pop-culture references and learning about the unique challenges of doing research on a taboo subject.

Although Bergen admits to having a “special affection” for swearing, he does an admirable job of staying objective throughout his analysis. He also voices concern about a troubling trend in the increased use of slurs and name calling and offers guidance for how individuals and society might respond to minimize the insults while still enjoying an expletive now and again.

## Welcome to the Universe

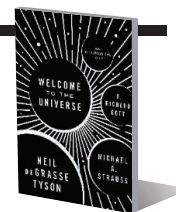
Reviewed by **Kanwal Singh**

“Every time we make an argument that we’re special in the cosmos ... we learn that the opposite is true. In fact, we occupy a humble corner of the galaxy, which occupies its own humble corner in the universe.” The grand size and scale of the cosmos is one of the recurring themes of *Welcome to the Universe*.

Written by three astrophysicists—Neil deGrasse Tyson, Michael A. Strauss, and

### Welcome to the Universe An Astrophysical Tour

Neil deGrasse Tyson,  
Michael A. Strauss,  
J. Richard Gott  
Princeton University Press,  
2016. 470 pp.



J. Richard Gott—the book is based on a course the authors cotaught for several years at Princeton University. It is organized into three sections—the first (Stars, planets, and life) largely belongs to Tyson, the second (Galaxies) to Strauss, and the third (Einstein and the universe) to Gott. Along the way, the reader is taken on a journey from relatively familiar territory—the organization of the solar system and galaxies and the life cycles of stars—through discussions of the Big Bang and the early universe and into recent hypotheses about the future of the universe and our little corner of it.

It is easy to imagine these authors presenting their chapters as lectures to introductory students. All three write in informal, conversational tones, and the text is sprinkled with genuinely funny non sequiturs, such as a brief rumination on dwarfs versus dwarves and commentary on English-speaking aliens in *Star Trek*.

At the same time, the casual reader may find it difficult to follow some of the book’s quantitative arguments, which are largely presented in the narrative rather than being set apart. In these instances, pulling out pencil and paper may help. In addition, in some sections the authors assume prior knowledge of concepts familiar only to those who have had some introduction to modern physics.

What this book does very well is to present not just what we know about the universe but how we know it. The chapter “Why Pluto is not a planet” is particularly good at showing how our organization of knowledge about the universe changes as that knowledge grows. The last third of the book does a wonderful job of presenting some very complex theories, such as inflation and density fluctuations in the cosmic background radiation.

Despite the almost incomprehensible vastness and complexity of the universe, Tyson’s observation that understanding astrophysics can be empowering resonates. “No, I don’t feel small,” he writes. “I feel large, because the human brain ... figured this stuff out.”

*The reviewer is dean of the college and in the Department of Physics at Sarah Lawrence College, Bronxville, NY 10708, USA. Email: ksingh@sarahlawrence.edu*



“In the universe, we’re always looking back in time,” writes Neil deGrasse Tyson in *Welcome to the Universe*.



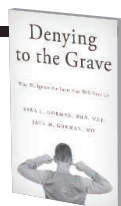


Evacuations forced more than 13,000 residents from their homes as the Cocos wildfire burned through the foothills around San Marcos, California, in 2014.

### Denying to the Grave Why We Ignore the Facts That Will Save Us

Sara E. Gorman and  
Jack M. Gorman

Oxford University Press, 2016. 324 pp.



## Denying to the Grave

Reviewed by **Susan Douglas**

When Thomas Duncan died from Ebola in a Dallas hospital on 8 October 2014, Americans panicked: calling off work, avoiding public transit, closing businesses and schools. In their new book, *Denying to the Grave*, authors Sara Gorman and Jack Gorman introduce the concept of medical science denial by demonstrating how the actual risk of contracting and dying from Ebola in America was negligible compared with the risk of dying from heart disease, cancer, automobile accidents, and gunshot wounds. Citing an estimate calculated by NPR journalist Michaela Doucette, they write that “the risk of contracting Ebola in the United States was one in 13.3 million, far less than the risk of dying in a plane crash, from a bee sting, by being struck by lightning, or being attacked by a shark.” And yet, the panic persisted.

In *Denying to the Grave*, Gorman and Gorman outline the reasons for this disconnect. In six chapters, the authors describe how conspiracy theories, charismatic leaders, confirmation bias, ignorance, complexity, and risk perception contribute to the problem and how our emotions, neurobiology, and psychology make us susceptible to

misguided health decisions.

Gorman and Gorman illustrate how our psychology has influenced our perception of everything from HIV and human papilloma virus to childhood vaccinations, gun violence, nuclear power, antibiotic treatment, and electroconvulsive therapy. They show that, in the face of irrefutable evidence, the public reaction to these issues is largely fear-based and outline both the underlying emotions and the anatomical locations in the brain that are associated with these responses.

The book suggests that scientists and medical professionals must change how they communicate health risks to address the factors that influence how people make decisions. The authors argue that those of us in these professions need to challenge people to think for themselves by asking them to imagine a range of scenarios in which the issue at hand could play out, including those with which they disagree.

One way to do this might be to ask skeptics how they would handle a given situation if the scientific evidence were indeed correct. The authors suggest encouraging these individuals to write down what they think would happen, how they would feel, and what the consequences would be. The next step is to help them recognize when their emotions are guiding their decisions.

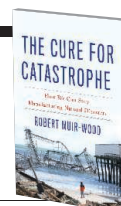
The authors correctly assert that, without a change in how we communicate health-related science, the public will remain vulnerable to influences that could negatively influence life-and-death decisions.

*The reviewer is at the UCLA School of Medicine, Department of Neurology, Los Angeles, CA 90045, USA. Email: sdouglas@mednet.ucla.edu*

### The Cure for Catastrophe How We Can Stop Manufacturing Natural Disasters

Robert Muir-Wood

Basic Books, 2016. 367 pp.



## The Cure for Catastrophe

Reviewed by **Timothy A. Cohn**

In the opening pages of *The Cure for Catastrophe*, the author describes a harrowing scene from the aftermath of a devastating earthquake: “Ruins spilled into the street. Second-floor rooms missing a wall, wallpaper torn, a child’s artwork flapping, a bed covered with debris. Clothes, a saucepan, school bags, family photographs strewn in the dirt...” Mother Nature provides a rich source of material for novelists. But this is no work of fiction.

The book, by Robert Muir-Wood, is a welcome and long-overdue addition to the disaster literature that recognizes and confronts the paradox of societies’ mostly sluggish approach to dealing with vulnerabilities to natural hazards. This is in stark contrast, for example, to our rapid response to aviation safety or terrorist threats. “Repetitive loss” is common for floods, for example.

In eloquent prose, Muir-Wood recounts

*The reviewer is in the Office of Surface Water at the United States Geological Survey, Reston, VA 20192, USA. Email: tacohn@usgs.gov*





Animal agriculture is in desperate need of reform, argues Ellen Silbergeld in *Chickenizing Farms and Food*.

disasters of the past millennium from a variety of perspectives: historical accounts; natural process science; structural engineering; building codes; land-use regulation; risk estimation; risk management; insurance and reinsurance; and, perhaps above all, political processes and priorities. His message for the future is hopeful but demands changes in both policy and culture.

Is it realistic to believe there is a “cure for catastrophe?” Muir-Wood acknowledges that it won’t happen soon. Changing a culture takes time and political will. Even where resources are abundant, there are plenty of incentives to maintain the status quo. For example, the wealthiest individuals and communities often choose to live in harm’s way so as to enjoy the benefits it confers. As Kaye Shedlock noted, “active tectonics makes for beautiful landscapes,” and, despite the risks, oceanfront property is undeniably desirable.

*The Cure for Catastrophe* is beautifully written, thoughtful, and rigorous. Although the book includes 63 pages of notes, which will serve future scholars, the main text is accessible to a general audience. I found it a pleasure to read.

## Chickenizing Farms and Food

Reviewed by **Sarah Edwards**

On a Sunday morning trip to the farmer’s market, I joyfully saunter up to a woman selling local free-range organic poultry:

The chickens run free for the duration of their lives! No antimicrobial drugs or growth hormones are administered! The chickens are slaughtered as humanely as possible! How could I not support this alternative to industrial agriculture?

I am what Ellen Silbergeld calls a “wet.” In terms borrowed from Margaret Thatcher, Silbergeld describes wets as valuing agriculture systems that emphasize “social and biological ecology.” “Dries,” on the other hand, see economic efficiency as the main goal and therefore place value on industrial production methods and new technologies. Silbergeld uses this analogy to set the stage for the conflict between these factions in modern animal agricultural practices.

Throughout 12 chapters, Silbergeld’s book touches on topics inexorably linked by modern food production: industrial practices, veterinary practices, the roles of government regulatory agencies, superbugs, worker safety, food safety, and food security.

Although the title would suggest otherwise, Silbergeld does not take a firm stand against industrial meat production; rather, she makes the case that this model will ultimately prevail. She describes how the wets’ plan to feed the world through alternative practices focused on rural communities fails to recognize that the world is becoming increasingly more urbanized.

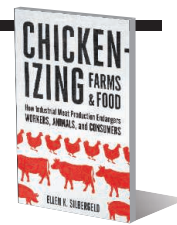
In chapter 9, Silbergeld’s discussion of worker safety features a processing plant

*The reviewer is at the Food Safety and Inspection Service, United States Department of Agriculture, Washington, DC 20250, USA. Email: sarah.rose.edwards.phd@gmail.com*

### Chickenizing Farms and Food How Industrial Meat Production Endangers Workers, Animals, and Consumers

Ellen K. Silbergeld

Johns Hopkins University  
Press, 2016. 333 pp.



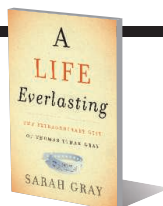
worker, Olga, covered in animal parts as she clocks out for the evening. In keeping with her frequent references to Upton Sinclair’s *The Jungle*, here Silbergeld aimed at (and hit) my heart. Her goal, however, was not only to reach my heart but also to “connect heart and stomach” and reconcile discussions of worker and food safety. “Simply put, by eliminating the humanity of workers in food production and reducing food safety to an engineering principle, neither food safety nor worker safety was protected,” she writes.

Silbergeld devotes two chapters to the growing danger of antimicrobial resistance. She describes how and when the use of veterinary drugs as a prophylaxis for disease became commonplace in food animal practices and the impact that this practice has had on global public health. Here, the reader would have benefited from a more thorough discussion of how, exactly, a farmer lacing animal feed with antimicrobial drugs can lead to life-threatening drug-resistant infections in humans.

Little doubt exists that meat production is fraught with problems. After reading Silbergeld’s book, my next visit to the farmer’s market will be a more enlightened one.



**A Life Everlasting**  
The Extraordinary Story  
of One Boy's Gift to  
Medical Science  
Sarah Gray  
HarperOne, 2016. 286 pp.



## A Life Everlasting

Reviewed by **Šeila Selimovic**

"I don't believe in putting anything of value in the ground. Whether it's a diamond ring that can be passed down to another generation, or if it's tissue for transplant or for research," Rebecca Cummings-Suppi, a manager at the Philadelphia-based Gift of Life Donor Program, told Sarah Gray at the 2014 annual meeting of the American Association of Tissue Banks. "That's how cures happen."

In *A Life Everlasting*, Gray recounts her journey to learn how donating her late son's organs might have helped advance scientific research. The book is heart-wrenching at times, to be sure, but those who would pass it over for this reason are denying themselves the opportunity to meet Sarah's son, Thomas Ethan Gray, and learn about his ultimate gift to science.

Throughout the book, Gray expertly weaves the story of her son's terminal condition—anencephaly, diagnosed in utero—and the decision to donate his organs with her quest to determine the donation's effect on research. The cord blood of Thomas and his healthy twin, Callum, was used in the search for the genetic roots of anencephaly. Thom-

as's liver went to a laboratory working to develop a liver-cell transplantation technique, a treatment suitable for newborns too small for liver transplants. His corneas were included in a study to help regenerate certain eye cells and prevent vision loss.

Gray's desire to find meaning in personal tragedy, and her motherly pride in her late son's contributions to research, permeate every page. So does her belief in science: Interspersed throughout the book are references to research studies; organ, tissue, and eye banks; organ procurement organizations; and institutions specializing in donations for research, training, and education. A comprehensive resource list for future donors is included in the appendix.

Both poignant and uplifting, *A Life Everlasting* is not just the story of Thomas Gray; it is also the story of researchers and donation facilitators. Most of all, it is a story of how science can give meaning to both life and death.

### NOTES

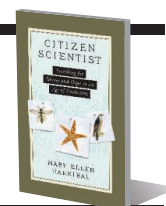
This material should not be interpreted as representing the viewpoint of the U.S. Department of Health and Human Services, the National Institutes of Health, or the National Institute of Biomedical Imaging and Bioengineering.

## Citizen Scientist

Reviewed by **Gillian Bowser**

The bighorn ram lounging on a rock watched as a group of people searched the desert floor. "I hear a signal!" someone shouted. The small group scurried around, never looking up, intent in their search for a radio-collared desert tortoise. This expedition in 1998, sponsored by the Earthwatch Institute, served as my introduction to citizen science, a growing phenomenon in ecological research wherein noncreden-

**Citizen Scientist**  
Searching for Heroes and  
Hope in an Age of Extinction  
Mary Ellen Hannibal  
The Experiment, 2016. 432 pp.



tial observers participate in scientific data collection.

Public involvement in scientific fieldwork is hardly new. From the "armchair" naturalist Charles Darwin to the California couple who spotted sea otters returning to Big Sur in 1938, *Citizen Scientist* frames the participation of both professionals and casual observers as an essential part of ecological science history.

Author and avid citizen scientist Mary Ellen Hannibal traces an astonishing diversity of volunteer-enabled projects from tidal pool surveys to databases such as Nature's Notebook, Fern Watch, Bee Watch, and Cricket Crawl. She also reveals how smartphones have given citizens the power to contribute to huge data sets, linked in time and space. Newer cellphone apps like iNaturalist or eBird, for example, use crowdsourcing to verify and document biodiversity.

Efforts to recruit more participants are on the rise as citizen science gains traction as a tool to document planetary biodiversity. *Citizen Scientist* made me want to jump off the couch and download everything from the Spotter Pro app, intended to keep ships from colliding with whales, to Story Maps, which allows users to create and annotate interactive maps.

Citizen scientists are not limited to counting dead birds or scanning wildlife cams. "Extreme citizen science" initiatives seek to connect western science and indigenous cultures to create new kinds of knowledge. Hannibal describes one such project, in which archaeologists have partnered with the Amah Mutsun tribe of the San Juan Valley to restore cultural and ecological connections that have been lost over time.

Back in Joshua Tree National Park, the bighorn ram got to his feet, dislodging a chuckwalla. The sound caught our attention, and we watched as it disappeared into the desert haze. Just then, the radio-collared desert tortoise moved out of the shadows and, with whoops of joy, we pounced to collect data. Examples of the wonder and excitement I felt that day dance from every page of *Citizen Scientist*. ■

10.1126/science.aah4996

The reviewer is at the Natural Resource Ecology Laboratory, Colorado State University, Fort Collins, CO 80523, USA. Email: gbowser@colostate.edu

The reviewer is at the National Institute of Biomedical Imaging and Bioengineering, National Institutes of Health, Bethesda, MD 20892, USA. Email: seila.selimovic@nih.gov



Citizen scientists participate in the National Park Service Centennial BioBlitz at Bandelier National Monument.

## PERSPECTIVES

## INFECTIOUS DISEASE

# Zika vaccine trials

## There are new and familiar challenges in the race for timely and effective vaccines

By **Marc Lipsitch<sup>1</sup>** and  
**Benjamin J. Cowling<sup>2</sup>**

**P**romising data for candidate vaccines against Zika virus infection reported by Abbink *et al.* (1) on page 1129 of this issue raise hopes that one or more Zika virus vaccines may soon be ready for efficacy trials. Recent years have seen a barrage of emerging infectious diseases, including those caused by new pathogens such as Middle East respiratory syndrome (MERS) coronavirus, and those that are newly salient because of increased geographic spread, higher incidence, or genetic change, such as influenza A(H1N1)pdm09, Ebola virus, and Zika virus. Developing effective vaccines is a central goal for such pathogens.

Repeatedly, emerging infections have caught us by surprise, with no vaccine candidate or only very early-stage candidates available. Human safety and immunogenicity must be established before starting large-scale efficacy studies. These studies consume valuable time while the epidemic spreads. During the 2014–2015 Ebola epidemic, the urgency of exponentially growing incidence gave way to the urgency of declining incidence, which threatened the ability to test vaccine efficacy. The effectiveness of one Ebola vaccine was proven just as the epidemic ended (2). During the 2009–2010 influenza A(H1N1) pandemic, efficacy testing was not required because demonstrating immunogenicity for influenza vaccines is accepted as indicative of efficacy (3). Yet, delays in vaccine availability in many locations meant that the vaccine arrived too late to affect the course of the first pandemic waves.

A key principle of preparedness is to do as much work as possible before an emergency happens, so that the response can be decisive and efficient. Several approaches would speed vaccine availability in future emergencies. For pathogens we have not yet encountered, there is a need for platform technologies that rapidly produce test vaccine lots and, if successful, mass-produce vaccines against a new pathogen (4). Further, innovative proposals for performing human safety and immunogenicity studies on candidate vaccines against



Earlier this year, the U.S. National Institute of Allergy and Infectious Diseases launched a safety and immunogenicity clinical trial of a vaccine candidate to prevent Zika virus infection.

a range of pathogens before the next emergency (5, 6) would enhance preparedness against known pathogens that could become greater threats if they become more common or geographically widespread. Moreover, for pathogens (3, 7) that have at least one proven efficacious vaccine, discovering correlates of protection (8) could justify initial reliance on immunogenicity (and safety) data in the use of subsequent vaccines or formulations against the same pathogen. The new field of systems vaccinology, which uses thousands of measurements on vaccinated persons to identify correlates and possible mechanisms of immune protection (9), could accelerate such discovery.

Continued innovation during “peacetime” in designing and studying (through simulation) vaccine efficacy trials that address the challenges of emergencies is needed to enhance quick responses. Getting results rapidly for emerging-disease vaccine candidates sometimes calls for innovative trial designs, such as the ring-vaccination trial used to test an Ebola vaccine (2), or for adapting existing designs to meet the logistical challenges of the disease and the populations in which it is spreading (10). Adaptive designs that test multiple candidate vaccines and put more resources toward those showing the most promise may be needed, particularly for emerging-disease vaccines, to avoid ethical issues that could arise in testing vaccines after one has been proven effective. The properties of such trial designs should be understood before they are needed.

Trials for emerging infectious disease countermeasures pose novel ethical questions. For Ebola, there was an intense debate about the ethics and political acceptability of individually randomized or placebo-controlled trials in the context of a highly lethal infection (11). Zika virus raises a different spectrum of challenges. As with trial design, a concerted effort is needed, during a period when there is not an immediate emergency, to raise, debate, and reach consensus about ethical issues that can arise in trials of countermeasures. For example, the World Health Organization defined conditions under which placebos could be used in vaccine trials (12). Future efforts will require not only analytic rigor and openness to multiple perspectives, but also imagination to anticipate distinctive ethical challenges that could be raised by future emergencies caused by different types of pathogens.

Many challenges for Ebola vaccines arose from the severity of the infection. Zika virus infection, by contrast, is mild or asymptomatic in most patients but severe in a few, causing congenital malformations in the fetuses of some women infected during pregnancy (13). This pattern raises distinct challenges: What is the most relevant outcome for clinical trials? We do not yet know how much a mild or asymptomatic infection contributes to transmission or whether it could harm fetuses if it occurs in a pregnant woman. Therefore, infection, rather than symptoms, could be an important trial end point. However, this raises challenges for monitoring trial participants, especially because serologic tests for Zika virus infection are im-

<sup>1</sup>Center for Communicable Disease Dynamics, Department of Epidemiology, Harvard T.H. Chan School of Public Health, Boston, MA, USA. <sup>2</sup>World Health Organization Collaborating Centre for Infectious Disease Epidemiology and Control, School of Public Health, Li Ka Shing Faculty of Medicine, The University of Hong Kong, Hong Kong. Email: mlipsitc@hsph.harvard.edu



perfect. What should be given to those in the control arm of a trial? Placebo may be appropriate, whereas other flavivirus vaccines (for yellow fever, dengue, or Japanese encephalitis) could complicate interpretation, particularly given the possible interactions of immunity to one flavivirus with susceptibility to other strains or species (14). Where should trials be planned? As with Ebola, local epidemics of Zika virus will wane, but unlike Ebola they are expected to recur in synchrony with mosquito seasonality (15). This may necessitate planning trials in multiple sites and activating them rapidly where incidence resurges (15). The cross-reactive immune response between Zika and dengue also complicates the ability to generalize results from one population to another: the immunogenicity and efficacy of a Zika virus vaccine in a flavivirus-naïve person might differ from that of a person with a history of flavivirus infection. Women of childbearing age who have not had Zika virus infection and are not known to be pregnant will be a priority group for vaccination, but trials will be complicated by incident pregnancies. How can trials study this group without creating undue risk for the fetuses of participants, who may not yet be conceived at the time of trial entry?

The severity profile of Zika virus infection may also provide opportunities. Deliberate infection of humans is an efficient way to test vaccine efficacy when risks can be minimized; could this strategy be used for Zika virus infection? Because of the low severity in healthy adults, placebo use in trials may be acceptable to those who opposed it for Ebola (11).

These challenges and opportunities will occupy those working to hasten availability of a safe, effective Zika virus vaccine (see the photo). Meanwhile, Zika virus is another reminder of the need to enhance our preparedness to develop and approve vaccines for emerging and re-emerging infectious diseases. ■

#### REFERENCES

1. P. Abbink *et al.*, *Science* **353**, 1129 (2016).
2. A. M. Henao-Restrepo *et al.*, *Lancet* **386**, 857 (2015).
3. M. E. Greenberg *et al.*, *N. Engl. J. Med.* **361**, 2405 (2009).
4. P. R. Dormitzer *et al.*, *Sci. Transl. Med.* **5**, 185ra68 (2013).
5. S. A. Plotkin *et al.*, *N. Engl. J. Med.* **373**, 297 (2015).
6. World Health Organization, "An R&D blueprint for action to prevent epidemics" (2016), pp. 1–44.
7. N. J. Andrews *et al.*, *Lancet Infect. Dis.* **14**, 839 (2014).
8. World Health Organization, "Correlates of vaccine-induced protection: Methods and implications" (2013), pp. 1–65.
9. B. Pulendran, *Proc. Natl. Acad. Sci. U.S.A.* **111**, 12300 (2014).
10. M. Lipsitch *et al.*, *Science* **348**, 46 (2015).
11. J. Cohen, K. Kupferschmidt, *Science* **346**, 289 (2014).
12. A. Rid *et al.*, *Vaccine* **32**, 4708 (2014).
13. M. A. Johansson *et al.*, *N. Engl. J. Med.* **375**, 1 (2016).
14. L. Priyamvada *et al.*, *Proc. Natl. Acad. Sci. U.S.A.* **113**, 7852 (2016).
15. N. M. Ferguson *et al.*, *Science* **353**, 353 (2016).

10.1126/science.aai8126

#### CANCER

## Location, location, location

Tissue of origin is important in determining how tumors rewire their metabolism

By Karen H. Vousden and Ming Yang

**T**here was a time when cancers were almost entirely defined by their tissue of origin. Patients were diagnosed with a cancer of a particular organ and treated—with varying degrees of success—according to these classifications. However, research over the past 50 years has revolutionized our understanding of malignant progression at the genomic level and established the view that cancers could also be grouped by the genetic alterations that drove their development. While this work has uncovered a bewildering complexity of genetic and epigenetic

**“...cancers from different organs are dissimilar in many important ways.”**

alterations in tumors, it also showed that mutations in the same oncogenes and tumor suppressor genes are found time and again in multiple types of cancer. These driver mutations play a fundamental causative role in the development of almost all cancers, suggesting that under the hood, even cancers of diverse origins have key similarities. An extension of this concept is that the presence of frequently occurring genetic drivers can be used to dictate the optimal therapeutic approach, regardless of whether the tumor derives from breast, lung, colon, or pancreas. While such reductionism is attractive, it remains clear that cancers from different organs are dissimilar in many important ways. Now, on page 1161 of this issue, Mayers *et al.* (1) provide further evidence that the tissue of origin is as important as the driving oncogenic mutations in determining how a tumor behaves and—by extension—how to treat it.

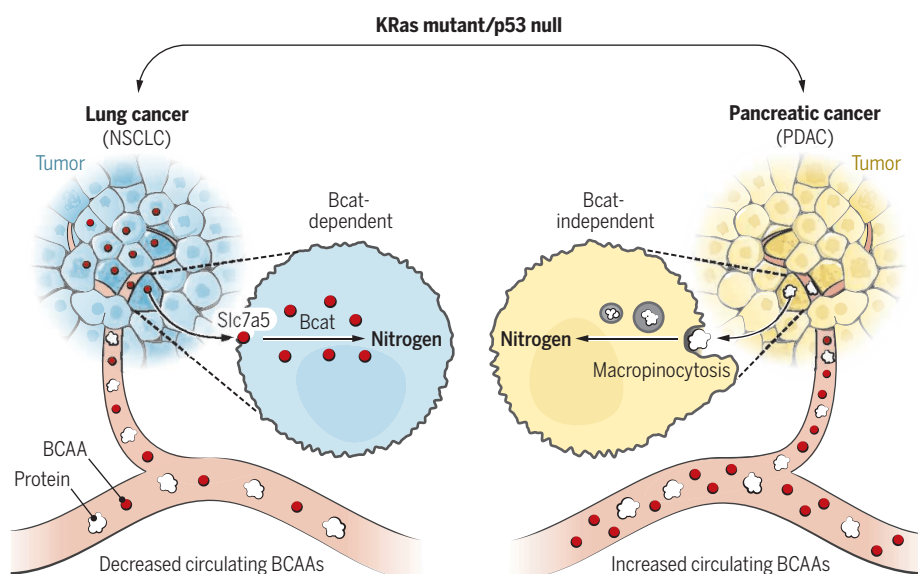
The work focuses on the metabolic changes that promote tumor growth and survival. We already know that there is tremendous plasticity in the ability of cancer cells to rewire their metabolic pathways, allowing them to adapt to different signals and environments.

For example, some cancer cells grown in two-dimensional culture show a strong reliance on a supply of exogenous glutamine (2), whereas their counterparts growing in vivo are much less dependent on glutamine uptake (3, 4). The origin of the tumor can also dictate how nutrients are acquired (5).

To explore this further, Mayers *et al.* made use of well-established genetically engineered mouse models (6, 7) that allow for the activation of *KRas* and loss of *Trp53*, specifically in the lung (resulting in non-small cell lung carcinoma, NSCLC) or the pancreas (resulting in pancreatic ductal adenocarcinoma, PDAC), and recapitulate the genetic changes seen in many human pancreas and lung cancers. In previous work using these models, this group showed that the early stages of pancreatic cancer were associated with increased circulating branched-chain amino acid (BCAA) levels resulting from increased tissue breakdown, although this was not seen in the lung model (8). Now, Mayers *et al.* show that the NSCLCs take up BCAAs much more avidly than do the PDACs, leading to a decrease in circulating BCAA levels. In vivo metabolic tracing revealed that despite being driven by the same oncogenic mutations, lung and pancreatic cancers satisfy their need for nitrogen to produce nonessential amino acids and nucleotides in different ways (see the figure).

At a molecular level, these differences were reflected in higher expression of *Slc7a5* (encoding the transporter for BCAAs) and *Bcat2* (encoding a transaminase that allows the cells to capture the nitrogen from this source) in the lung tumors. By comparison, the PDACs showed none of these changes. The authors went to the effort to confirm these observations in isolated pancreatic tumor cells, to avoid possible dilution of the gene expression signal by stromal cells that heavily infiltrate this cancer type. Similar patterns of changes in gene expression were seen in human lung and pancreatic cancers. Consistent with the suggestion that these tumors use BCAAs primarily to provide nitrogen, there was no increased contribution of carbon from this source to the tricarboxylic acid (TCA) cycle, which was fueled by enhanced glycolysis in both lung and pancreatic cancers. However, the study did not suggest that the entire nitrogen demand was met by BCAAs in the NSCLCs; rather, its results implied that

Cancer Research UK Beatson Institute, Switchback Road, Glasgow G61 1BD, UK. Email: k.vousden@beatson.gla.ac.uk



**Metabolic differences in tumors of different origins.** Despite being driven by the same initiation mutations in *KRAS* and *Trp53*, NSCLCs and PDACs acquire nitrogen differently. NSCLCs induce pathways that allow for the use of BCAAs, including up-regulation of the transporter *Slc7a5* and the BCAA transaminase *Bcat*. PDACs, by contrast, increase protein uptake through macropinocytosis and release nitrogen from nonessential amino acids. These cancers also promote tissue protein breakdown. As a consequence, animals bearing NSCLCs show a depletion of circulating BCAAs, whereas animals bearing PDACs show increased plasma BCAA levels.

the relative contribution compared to other sources (such as glutamine) was increased.

Finally, the authors show that these metabolic changes have functionally important consequences. Deletion of the cytosolic and mitochondrial *Bcat* genes resulted in a profound defect in the ability of NSCLC cells to form tumors but had much less impact on the tumorigenicity of the PDAC cells. This effect was not seen in cells grown in culture, where both lung and pancreas cells were indifferent to *Bcat* expression, most likely because under these conditions glutamine is the preferred source of nitrogen. Interestingly, the difference in tumor growth was seen whether the cells were transplanted orthotopically (i.e., the NSCLC cells into the lung and the PDAC cells into the pancreas) or subcutaneously, suggesting that the difference in behavior is truly a reflection of the origin of the tumor rather than the tissue environment. The work provides a nice counterpoint to previous studies showing that PDAC cells use macropinocytosis to engulf protein and liberate the nonessential amino acids glutamine, alanine, and serine that are preferentially used to support nitrogen demand and other requirements of these tumors (9, 10). In this case, BCAAs were not used, again consistent with the increase in circulating BCAAs detected in mice carrying these tumors. As might be expected, much less macropinocytosis was seen in the lung cancer cells, which presumably do not depend on this process. Whether these metabolic changes are also

seen in pancreatic or lung cancers driven by different genetic drivers is an open question.

The work provokes the interesting possibility that, at least in the context of mutant *KRAS* and *TP53* tumors, NSCLC would be selectively sensitive to *Bcat* inhibitors, whereas inhibitors of macropinocytosis would preferentially affect PDACs. Whether similar metabolic dependencies are manifest in early or premalignant lesions—which might be more easily treated—remains to be determined. Furthermore, the observation that lung cancers deplete BCAAs from serum while PDAC tumors are associated with increased circulating BCAA levels may even provide an important and simple biomarker, especially if changes in the levels of these amino acids can be detected before a clinical manifestation of the tumor is evident (8). ■

#### REFERENCES AND NOTES

1. J. R. Mayers *et al.*, *Science* **353**, 1161 (2016).
2. D. R. Wise, C. B. Thompson, *Trends Biochem. Sci.* **35**, 427 (2010).
3. I. Marin-Valencia *et al.*, *Cell Metab.* **15**, 827 (2012).
4. S. M. Davidson *et al.*, *Cell Metab.* **23**, 517 (2016).
5. M. O. Yuneva *et al.*, *Cell Metab.* **15**, 157 (2012).
6. N. Bardeesy *et al.*, *Proc. Natl. Acad. Sci. U.S.A.* **103**, 5947 (2006).
7. M. DuPage, A. L. Dooley, T. Jacks, *Nat. Protoc.* **4**, 1064 (2009).
8. J. R. Mayers *et al.*, *Nat. Med.* **20**, 1193 (2014).
9. C. Commisso *et al.*, *Nature* **497**, 633 (2013).
10. J. J. Kamphorst *et al.*, *Cancer Res.* **75**, 544 (2015).

#### ACKNOWLEDGMENTS

Supported by Cancer Research U.K. grant C596/A10419 and European Research Council grant 322842-METABOp53.

10.1126/science.aai7629

## EVOLUTION

# Visualizing evolution as it happens

A meter-scale growth plate allows the evolution of antibiotic resistance to be tracked

By Luke McNally<sup>1,2</sup> and Sam P. Brown<sup>3</sup>

One of the greatest symbols of the birth of evolutionary biology is Darwin's first sketch of an evolutionary tree, above which he wrote: "I think." Not only are evolutionary trees central to how scientists conceptualize evolutionary processes, Darwin's words also capture a key aspect of evolutionary science: It is difficult to observe, forcing researchers to rely heavily on inference. In recent decades, studies of fast-growing microorganisms have allowed hypotheses about evolutionary processes to be tested experimentally (1). On page 1147 of this issue, Baym *et al.* (2) report a device for visualizing evolutionary branching as bacteria grow across a meter-scale agar slab. The results offer important insights into evolutionary dynamics in spatially extended systems.

The device, the microbial evolution and growth arena (MEGA) plate, is elegantly simple in its construction. It consists of a 120- by 60-cm dish with regions of agar containing different antibiotic concentrations. The plate's large size enables an antibiotic concentration gradient to be maintained for the ~10 days it takes *Escherichia coli* to grow and evolve across the plate. Furthermore, it allows for sufficiently large population sizes to maintain a supply of mutations.

The ancestral bacteria initially grow to occupy the inoculation area, where antibiotic concentrations are low. When a more resistant mutant arises at the growing front, a fan-shaped burst of growth occurs as the mutant expands into areas of higher antibiotic concentrations, until it reaches concentrations at which it can no longer grow. The process

<sup>1</sup>Centre for Immunity, Infection and Evolution, School of Biological Sciences, University of Edinburgh, Edinburgh EH9 3FL, UK. <sup>2</sup>Institute of Evolutionary Biology, School of Biological Sciences, University of Edinburgh, Edinburgh EH9 3FL, UK. <sup>3</sup>School of Biology, Georgia Institute of Technology, Atlanta, GA 30332, USA. Email: luke.mcnelly@ed.ac.uk; sam.brown@biology.gatech.edu



then repeats, creating a pattern of branching fans of growth down the plate (see the figure). The patterns are reminiscent of the abstract Muller plots (3) that are often used to represent evolutionary dynamics. The advent of evolutionary innovations via mutation and the subsequent selection of these mutants are thus imprinted on the plate, providing an unprecedented visualization of evolution through time and space.

The striking beauty of the images and videos of Baym *et al.*'s experiments belies the gravity of the evolutionary problem that they address. The unabated rise of antimicrobial resistance is one of the greatest challenges that society faces (4). The results illustrate the scale of the challenge: The *E. coli* in the

microspatial environments, the genetic changes underlying evolved resistance appear to be highly reproducible; in contrast, evolution on the MEGA plate showed a large diversity of resistance mechanisms. As well as mutations in pathways directly targeted by the antibiotic, putatively adaptive mutations were also found in several other pathways, including those involved in stress responses, transcription, and translation. Future experiments should investigate how the size of the MEGA plate (and thus mutational supply), choice of antibiotic, and gradient steepness combine to determine the diversity of evolutionary pathways by which bacteria can evolve resistance.

A key factor slowing the spread of antibiotic resistance is the cost of resistance;

resistance mutations generally reduce growth in the absence of the antibiotic. However, resistant bacteria often overcome this problem via "compensatory mutations" that reduce the cost of the resistance mechanism (6). Baym *et al.* observed frequent compensatory mutations in their experiments. However, they also highlight a critical constraint on compensatory adaptation: Compensatory mutations could only expand when they occurred on the growing bacterial front. Those behind the front were "blocked" and starved of nutrients by their parental lineage. Experiments moving "blocked" compensatory mutants beyond the growing front showed that these compensatory mutants could grow at antibiotic concentrations at which their parental lineage could not. This result highlights the importance of spatial structure and positioning in evolution.

Indeed, a recent experimental evolution study suggests that in dense microbial communities, there is very strong selection for traits such as secretion production to help push bacteria to the growing edge of a colony (7). An exciting avenue for future work

will be to explore how selection on traits that affect positioning during colony growth and selection on traits that affect resistance interact to determine how quickly resistance evolves.

The MEGA plate device could be used to explore several further aspects of drug-resistance evolution. For example, theoretical models predict that variable rates of drug penetration in the human body during combination therapy effectively lead to

monotherapy, facilitating the evolution of multidrug-resistant strains (8). The MEGA plate could be used to test this prediction by setting up different gradients of multiple antibiotics across the plate. Similarly, multiple species could be added to the plate to explore how interspecific interactions may help or hinder the evolution of resistance.

The MEGA plate is much more than a model of antibiotic-resistance evolution. In a clinical context, the MEGA plate could be criticized as merely a caricature of real-world environments, but such a perspective misses its value as a tool to elucidate the fundamental principles of evolution in a spatial environment. The long-term evolution experiment (LTEE), in which *E. coli* have been evolving in flasks containing a simple glucose-based medium since the 1980s, could be similarly criticized for being unrealistic yet has provided key insights into the long-term bounds of evolutionary fitness (9) and the dynamics of evolutionary innovations (10), among many other discoveries.

The MEGA plate holds similar promise as a tool for increasing our understanding of evolution in a spatial context. Spatial microbial ecology is a rapidly expanding field that has explored how defined competitive interactions play out in spatial environments (11). The MEGA plate provides the potential to explore the evolutionary aspects of this field, with mutants arising from population genetic processes and competing in an iterated series of spatial contests. Adapting the modeling techniques from microbial spatial ecology to deal with the spatiotemporal data generated from the MEGA plate will be critical to maximizing its value.

In addition to its scientific value, the MEGA plate is a potentially powerful tool for education and outreach. The principles of population genetics and spatial ecology are abstract and mathematical. By providing a clear visualization of the evolutionary ecology of expanding and diversifying lineages, the MEGA plate makes the abstract concrete; it thus offers, as Baym *et al.* put it, a "seeing is believing" insight into evolution. ■

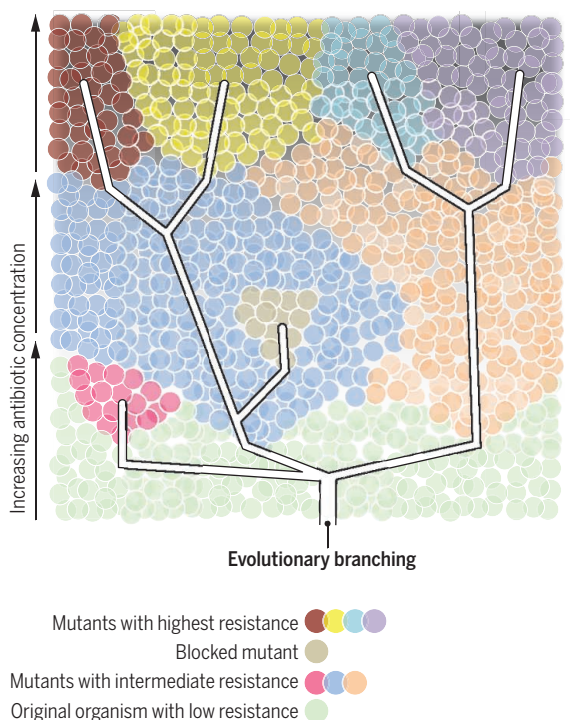
## REFERENCES

1. A. Buckling, R. C. Maclean, M. A. Brockhurst, N. Colegrave, *Nature* **457**, 824 (2009).
2. M. Baym *et al.*, *Science* **353**, 1147 (2016).
3. H. J. Muller, *Am. Nat.* **66**, 118 (1932).
4. G. D. Wright, *BMC Biology* **11**, 51 (2013).
5. Q. Zhang *et al.*, *Science* **333**, 1764 (2011).
6. B. R. Levin, V. Perrot, N. Walker, *Genetics* **154**, 985 (2000).
7. W. Kim, F. Racimo, J. Schluter, S. B. Levy, K. R. Foster, *Proc. Natl. Acad. Sci. U.S.A.* **111**, E1639 (2014).
8. S. Moreno-Gomez *et al.*, *Proc. Natl. Acad. Sci. U.S.A.* **112**, E2874 (2015).
9. M. J. Wiser, N. Ribeck, R. E. Lenski, *Science* **342**, 1364 (2013).
10. Z. D. Blount, J. E. Barrick, C. J. Davidson, R. E. Lenski, *Nature* **489**, 513 (2012).
11. C. D. Nadell, K. Drescher, K. R. Foster, *Nature Rev. Microbiol.* **10**, 1038/nmicro.2016.84 (2016).

10.1126/science.aah5641

## Watching evolution through space

In Baym *et al.*'s experiment, bacterial cells are inoculated in a region of low antibiotic concentration on the MEGA plate. Mutants with greater resistance arise and spread into unoccupied areas with greater antibiotic concentrations, creating fanlike evolutionary branching patterns.



experiments evolved to become 10,000 times more resistant to trimethoprim and 100,000 times more resistant to ciprofloxacin.

In agreement with previous work using antibiotic gradients in microspatial environments on ~2-cm-long chips (5), a shallow antibiotic gradient was necessary for the evolution of resistance; without these gradients, mutants of intermediate resistance could not expand, blocking off evolutionary routes to resistance. However, in experiments in mi-

## NANOMATERIALS

# Asymmetry in supramolecular assembly

Photoresponsive organic nanowires connect to gold nanomesh and silicon electrodes

By **Suzette Slim**<sup>1,2</sup> and **Federico Rosei**<sup>1,2</sup>

Like their inorganic counterparts, the optoelectronic properties of organic semiconductors (OSCs) can be tuned by confining charge carriers in nanoscale dimensions. In particular, one-dimensional (1D) nanowires made of conjugated molecules may be formed through supramolecular interactions based on  $\pi$ -stacking. To fully exploit their properties in devices, Zhang *et al.* (1) report supramolecular control of OSC nanowire growth. A nanoscale scaffold regulates assembly of nanowires across asymmetric electrodes (gold and silicon), creating p-n junctions that bias current flow. This architecture is then used to demonstrate high-performance photovoltaic device characteristics.

Organic photovoltaics (OPVs) are good candidates for third-generation solar cells because organic synthesis that enables tuning of electronic and optical properties, solution processing, and compatibility with flexible substrates helps reduce manufacturing costs (2). Localized excitons (electron-hole pairs) are generated in OPVs when light is absorbed by small molecules or polymers. The power conversion efficiencies of OPVs reached ~11% in laboratory prototypes (3), which is well below the 20% target required for commercial devices. Efficiency limitations and long-term stability are two major drawbacks that hinder deployment. To increase efficiency, it is necessary to improve both the absorption and mobility properties of the absorbing OSCs by optimizing the molecular structure of their building blocks, together with their supramolecular ordering.

The high surface-to-volume ratio of nanowires facilitates exciton separation by minimizing the diffusion length from the bulk to the surface, where exciton dissociation into free carriers typically occurs (4). In addition, the 1D  $\pi$ -stacking in nanowires favors charge transport (5). Thus, the high absorption coefficient and remarkable light sensitivity of supramolecular organic nanowires (SMNWs) compared with that of bulk crystals makes them ideal building blocks for optoelectronic technologies (6). However,

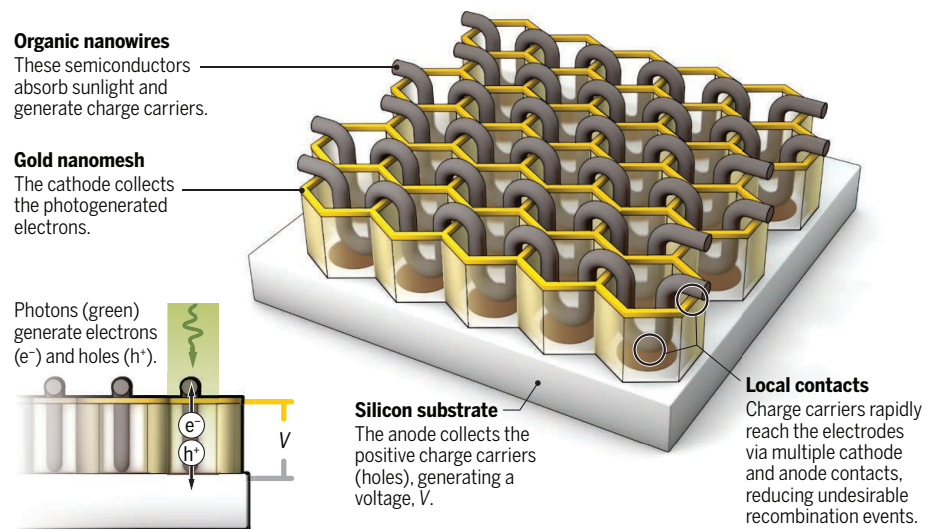
the development of photonic devices based on SMNWs has been hindered by two major challenges. One is the difficulty in wiring them with nanoscale electrodes that have different work functions, which is crucial to harvesting their photogenerated current. The other is the development of approaches that easily and simultaneously connect hundreds of nanowires.

Zhang *et al.* report a general methodology to integrate SMNWs in a hexagonal nanomesh scaffold featuring asymmetric electrodes in order to fabricate a small-molecule OPV cell (see the figure). The nanomesh provides

selective etching, allowing the fabrication of periodic large-area nanoscale patterns. The gold nanomesh acts as the cathode, and the anode is the n-doped silicon substrate. The anode was modified by functionalizing it with a layer of p-type semiconducting polymer (P3HT) so as to enhance hole selectivity and reduce radiative recombination at the silicon/nanowire interface, facilitating PV response. By connecting hundreds of SMNWs, optimized PTCDI-C8 nanowire solar cells exhibit a signal-to-noise ratio approaching  $10^7$ , a photoresponse time as fast as 10 ns, and an external quantum efficiency exceeding 50%.

## Organic nanowire photovoltaics

Illustration showing the high-density array of supramolecular nanowires, assembled by using a vertical channel nanomesh scaffold with asymmetric electrodes fabricated on a silicon substrate.



a periodic array of surface templates that guide the growth of SMNWs horizontally, encapsulating them between asymmetric electrodes with different work functions, hence realizing a vertical channel (7). Specifically, they assembled nanowires of *N,N'*-dioctyl-3,4,9,10-perylenedicarboximide (PTCDI-C8) and showed that controlling supramolecular interactions is crucial to obtaining high-performance optoelectronic devices.

The nanomesh is fabricated by using nanosphere lithography, in which a monolayer of hexagonal close-packed nanoscale spheres of polystyrene acts as a mask (8). This versatile technique adds materials by deposition and subtracts other materials by

Thus, SMNWs have potential applications in high-performance OPVs.

In a broader perspective, the nanomesh scaffold used by Zhang *et al.* is quite versatile and represents a valuable tool for investigating inherent photonic properties of 1D OSCs. By varying geometrical parameters of the mesh, the nanowires, or both, they observed substantial changes in optoelectronic properties. In the vertical direction, the interelectrode distance could be tuned to <100 nm, whereas the device could extend up to a few millimeters laterally. The underlying concept is to optimize charge transport with an ordered array of nanowires that are connected to the same nanoscale electrode.

<sup>1</sup>Institute for Fundamental and Frontier Science, University of Electronic Science and Technology of China, No. 4, Section 2, North Jianshe Road, Chengdu 610051, China. <sup>2</sup>Centre for Energy, Materials and Telecommunications, INRS, Varennes, Québec J3X 1S2, Canada. Email: rosei@emt.inrs.ca



The use of tailored supramolecular structures for PV applications allows the study of the fundamental physics and chemistry of nanostructured materials through unraveling structure-property relations. The vertical-channel device configuration can be exploited for model studies in spintronics and other applications in optoelectronics such as light-emitting diodes and transistors, which require the optimal combination of asymmetric electrodes with ad hoc work function, nanoscale controlled channel length, and maximal density of active nanostructures. Photovoltaic performance could also be optimized by using SMNWs with higher charge mobility or by introducing a dopant to improve conductivity (9, 10). In addition, the gold nanomesh could enhance optical absorption by acting as a plasmonic antenna (11), increasing quantum efficiency. The photoresponse could be used to develop ultrafast nanoscale photodetectors, which would be components of future optical quantum computers. Alternative lithographic methods, such as nanoimprint or nanostencil (12, 13), could access more complex geometries that are required for specific architectures (such as memory storage devices).

Controlling supramolecular interactions holds the promise of growing highly ordered organic films and nanostructures, which is a prerequisite for the fabrication of high-performance devices (14). The device configuration of Zhang *et al.* bridges the gap between bottom-up grown semiconductor nanostructures and macroscopic photonic technologies. We anticipate that it will draw broad interest from the scientific community and affect future developments at the intersection between supramolecular chemistry, nanotechnology, and optoelectronics. ■

#### REFERENCES AND NOTES

1. L. Zhang *et al.*, *Nat. Nanotechnol.* 10.1038/nnano.2016.125 (2016).
2. S. Gunes, H. Neugebauer, N. S. Saricic, *Chem. Rev.* **107**, 1324 (2007).
3. J. You *et al.*, *Nat. Commun.* **4**, 1446 (2013).
4. B. Tian *et al.*, *Nature* **449**, 885 (2007).
5. A. P. H. J. Schenning, E. W. Meijer, *Chem. Commun.* **2005**, 3245 (2005).
6. A. T. Haedler *et al.*, *Nature* **523**, 196 (2015).
7. F. Cicoira, F. Rosei, *Surf. Sci.* **600**, 1 (2006).
8. P. Colson, C. Henrist, R. Cloots, *J. Nanomater.* **2013**, 1 (2013).
9. Y. Che *et al.*, *J. Am. Chem. Soc.* **133**, 1087 (2011).
10. M. F. Calhoun, J. Sanchez, D. Olaya, M. E. Gershenson, V. Podzorov, *Nat. Mater.* **7**, 84 (2008).
11. H. A. Atwater, A. Polman, *Nat. Mater.* **9**, 205 (2010).
12. G. J. Burger *et al.*, *Sensors Actuators A* **54**, 669 (1996).
13. S. Y. Chou, P. R. Krauss, P. J. Renstrom, *Science* **272**, 85 (1996).
14. H. T. Black, D. F. Perepichka, *Angew. Chem. Int. Ed.* **53**, 2138 (2014).

#### ACKNOWLEDGMENTS

F.R. thanks the Canada Research Chairs program for partial salary support and is grateful to the government of China for a Chang Jiang Chair Professorship.

10.1126/science.aah5571

#### ECOLOGY

## How dams can go with the flow

Small changes to water flow regimes from dams can help to restore river ecosystems

By N. LeRoy Poff<sup>1,2</sup> and John C. Schmidt<sup>3</sup>

The world's rivers are regulated by about 58,000 large dams (more than 15 m high) that provide water supplies for municipalities and irrigation, allow downstream navigation, and enable hydropower production (1). New dams are widely seen as sources of green energy. An estimated 75% of the world's potential hydropower capacity is unexploited (2), and some 3700 new dams are currently proposed in developing economies (3, 4).

### ***“Managing...rivers to better meet both human and ecosystem needs is a complex societal challenge.”***

But dams also cause substantial and often unacknowledged environmental damage. Recent research affords insight into how dams might be strategically operated to partially restore some lost ecosystem functions and services.

Dams transform rivers by creating artificial lakes, fragmenting river networks, and greatly distorting natural patterns of sediment transport and of seasonal variation in water temperature and stream flow (5). Impeded upstream-downstream movement of fish and other species and highly altered environmental conditions severely impair downstream ecosystems by modifying productivity and causing species extirpations and replacements (see the figure). Intentional releases of reservoir water can restore some semblance of the predam flow regime. Such environmental flows (6) enable recovery of some lost ecosystem functions but carry an economic cost by a dam's operational efficiency.

Many hydropower dams release more water during daytime when societal demand for electricity is greatest. Such hydropeaking creates a fluctuating daily pattern of

water flows that typically severely impairs productive, downstream shoreline habitats through repeated wetting and drying. River scientists have long struggled with the conundrum of how to diminish these negative ecological effects in a cost-effective manner, given the strong economic incentive of hydropeaking. A recent study of the Colorado River ecosystem downstream from the hydropeaking Glen Canyon Dam by Kennedy *et al.* (7) offers a promising approach (see the figure).

The authors found that the river food web, a fundamental feature of a river's ecological integrity (8), lacks large aquatic insects, key species that are common in sections of the Colorado River not strongly influenced by hydropeaking flows. Although aquatic insects spend most of their lifetimes in the water, adults take flight to mate and lay eggs in shallow water near the shoreline. Large aquatic insects firmly cement their eggs just under the water surface on partially exposed boulders. Sudden drops in water level from hydropeaking expose them to the atmosphere and cause extensive mortality.

Using a model that estimates shoreline water-level fluctuations due to hydropeaking throughout the 400 km of river in the Grand Canyon, the authors evaluated egg desiccation risk based on female egg-laying behavior relative to fluctuating water levels. The model predicted that large insects would not occur anywhere in the Grand Canyon. But it also made a second, unexpected prediction: Native, small-bodied insect species would be much more common in two sections of the river where low water levels from the propagating hydropeaking waves occur predictably in the evening, when adults actively fly and lay eggs. These insect species do not cement all eggs on boulders, so some should remain underwater during the entire hydropeaking cycle and thus survive and hatch.

To test these predictions, the researchers turned to the river rafters who camp everywhere throughout the Grand Canyon from late spring to early fall. Over the course of 3 years, hundreds of these citizen scientists captured and preserved more than 2500 individual insect samples during 1 hour beginning at local sunset by attracting flying insects to ultraviolet lamps. The results were striking: Large-bodied insect species were

<sup>1</sup>Department of Biology, Colorado State University, Fort Collins, CO 80524, USA. <sup>2</sup>Institute of Applied Ecology, University of Canberra, ACT 2617, Australia. <sup>3</sup>Department of Watershed Sciences, Utah State University, Logan, UT 84322, USA. Email: n.poff@colostate.edu

rarely collected, and the small insects were more than three times as abundant in the two places predicted by the model. Comparing their data with that from studies on 15 other dammed rivers in the western United States, Kennedy *et al.* show that aquatic insect diversity is lowest where hydropowering is greatest (7).

Based on their results, Kennedy *et al.* propose an experiment as part of the Long-Term Experimental and Management Plan for Glen Canyon Dam. Eliminating hydropowering on weekends, when energy demand is relatively low, would make reliable egg-laying habitat available. Restricting hydropowering on several weekends each year during the prime reproductive season might suffice to allow the highly fecund aquatic insects to recover in abundance within a few years. Restoring the integrity of the food web with large insects should enhance production of river fishes and also benefit terrestrial predators that eat flying adult insects (birds, bats, and spiders) at minimal cost to foregone hydroelectric production.

The principle of targeted, cost-effective flow restoration is also emerging from research on dams that distort the natural patterns of seasonal, rather than daily, flows. For most large dams, runoff from spring rains or snowmelt is stored in the reservoir to be released later in the year for hydropower, water supply, or irrigation. Environmental flow restoration in these rivers often aims to recreate a large, seasonal flow pulse timed to meet downstream ecosystem needs (such as floodplain inundation for riparian vegetation or stimulation of fish spawning or migration). At least 113 experimental flow releases have been conducted in more than 20 countries around the world with varying success (9). For these seasonally impaired rivers, a fundamental question is how a natural (seasonal) flow regime might be adequately mimicked to restore desired ecosystem functions but still adequately satisfy the utilitarian objectives of river regulation.

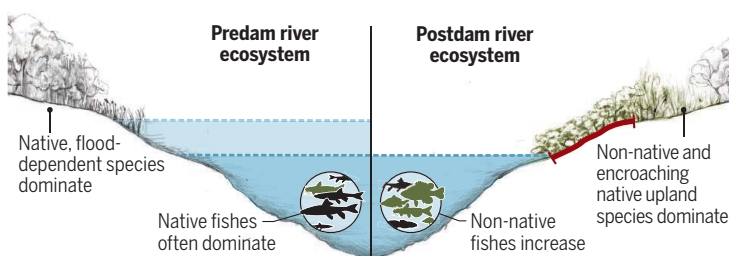
A study by Kiernan *et al.* shows how, as in the case of daily flows, seasonal flow regulation can help to restore ecosystem functions at low cost (10). The authors reported on nearly two decades of research conducted along a 30-km stretch

## How dams affect river ecosystems

Dams alter flow, sediment, and thermal regimes of rivers. Seasonal flow distortions (top) cause shifts in species compositions. Dammed rivers with hydropowering (bottom) cause daily distortions that can eliminate key species from food webs. Small changes to flow releases can counteract these distortions and provide ecological benefit (see text).

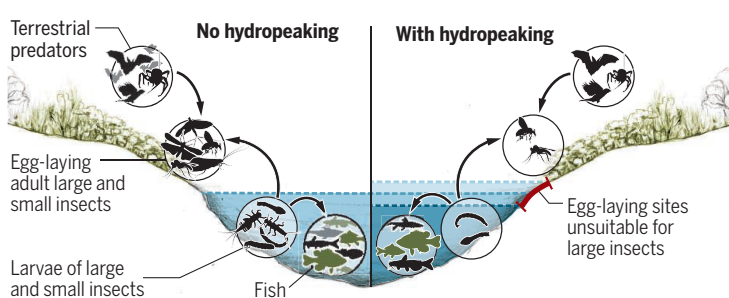
### Free-flowing vs. dam-regulated river

■ Average predam flood ■ Average postdam flood I Lack of seasonal inundation and fish access to floodplain



### Dammed hydropower river

■ Maximum daily flow ■ Average daily flow ■ Minimum daily flow I Fluctuating daily "intertidal zone"



of Putah Creek in California. An upstream dam diverts water for irrigation, reducing in-stream flows and facilitating the displacement of native fish species by exotic fishes. In an effort to reverse this trend, which is common in dammed rivers (see the figure), a court-ordered flow regime designed to benefit native species was implemented. High springtime flow pulses created favorable spawning and rearing conditions, and stable base flow releases maintained favorable flow conditions. After 9 years of flow management, native fishes had regained dominance in two-thirds of the study reach. Only a small annual increase in downstream water releases was needed, making this a cost-effective management strategy.

Managing the world's regulated rivers to better meet both human and ecosystem needs is a complex societal challenge. Opportunities to modify flow release patterns at existing dams are often constrained by original engineering design, but small changes to existing dam operations may be possible through incentives offered by regulatory relicensing requirements (11) and government dictates to incorporate consideration of ecosystem services in infrastructure management where possible (12). The studies by

Kennedy *et al.* (7) and Kiernan *et al.* (10) show that even small operational tweaks have the potential to be ecologically beneficial.

The thousands of proposed new hydropower dams pose a significant global threat to freshwater biodiversity (3, 4) and to the livelihoods of indigenous peoples who rely on ecosystem services of free-flowing rivers and floodplains (13). The conversion of free-flowing rivers to artificial lakes will fragment river corridors and diminish ecosystem services. Strategic planning is needed to decide where these dams can be located to lessen overall environmental and societal harm (4, 14). Ideally, new dams should be designed to minimize distortions in flow and thermal regimes, allow sediment transport to downstream ecosystems, and enable fish migration throughout the river network.

Postdam environmental flow management can only incrementally improve lost ecosystem functions, making

predam environmental planning essential. Making hydropower greener and dams more sustainable generally requires not only better design and management of flow releases but also balancing economic gain against environmental degradation and human dislocations, all in an increasingly uncertain hydrologic future (15). ■

### REFERENCES

1. International Commission on Large Dams: [www.icold-cigb.org/GB/World\\_register/general\\_synthesis.asp](http://www.icold-cigb.org/GB/World_register/general_synthesis.asp) (2016).
2. A. Kumar *et al.*, in *IPCC Special Report on Renewable Energy Sources and Climate Change Mitigation*, O. Edenhofer *et al.*, Eds. (Cambridge Univ. Press, 2011).
3. C. Zarfl *et al.*, *Aquat. Sci.* **77**, 161 (2015).
4. K. O. Winemiller *et al.*, *Science* **351**, 128 (2016).
5. N. L. Poff *et al.*, *BioScience* **47**, 769 (1997).
6. A. H. Arthington, *Environmental Flows: Saving Rivers for the Third Millennium* (Univ. California Press, 2012).
7. T. A. Kennedy *et al.*, *BioScience* **66**, 561 (2016).
8. R. J. Naiman *et al.*, *Proc. Natl. Acad. Sci.* **109**, 21201 (2012).
9. J. D. Olden *et al.*, *Frontiers Ecol. Environ.* **12**, 176 (2014).
10. J. D. Kiernan *et al.*, *Ecol. Appl.* **22**, 1472 (2012).
11. J. Pittock, J. Hartmann, *Mar. Freshwat. Res.* **62**, 312 (2011).
12. Executive Office of the President of the United States, Memorandum; <https://www.whitehouse.gov/sites/default/files/omb/memoranda/2016/m-16-01.pdf> (2015).
13. J. Estrin, Brazil's Dams Submerge Tribal Life. *New York Times*, 2 June 2016; [http://lens.blogs.nytimes.com/2016/06/02/at-look3-brazils-dams-submerging-tribal-life/?\\_r=1](http://lens.blogs.nytimes.com/2016/06/02/at-look3-brazils-dams-submerging-tribal-life/?_r=1).
14. H. I. Jager *et al.*, *Renew. Sust. Energ. Rev.* **45**, 808 (2015).
15. N. L. Poff *et al.*, *Nat. Clim. Change* **6**, 25 (2016).

10.1126/science.aah4926



# Lentiviral vectors, two decades later

A deadly virus became an effective gene delivery tool

By **Luigi Naldini,<sup>1</sup> Didier Trono,<sup>2</sup>**  
**Inder M. Verma<sup>3</sup>**

In the mid-1990s, several years after a variety of viral vectors started being used for gene transfer into cells, tissues, and in some cases humans, it became clear that there were considerable limitations (1). For applications requiring a stable genetic modification that could lead to sustained gene expression in cells and their progeny, a delivery vehicle was needed that could transduce foreign cargo into dividing and nondividing cells, without causing immuno- or genotoxicity. A decade earlier, human immunodeficiency virus (HIV) had been identified as the cause of AIDS, and rapid studies of its biology led to the idea that this genus of retrovirus—lentiviruses—could be optimized for gene therapy.

Lentiviruses, in contrast to other types of retroviruses used to develop vectors, had the ability to infect, replicate, and integrate in some nondividing cells, such as macrophages (2). However, there were substantial challenges in developing gene therapy vectors from HIV. Paramount among them was the pathogenic nature of HIV, which was not fully elucidated and for which no effective treatment was available at that time. In addition, the restricted tropism of HIV to some types of lymphocytes and myeloid cells would limit the usefulness of a vector derived from HIV to the targeting of only a few cell types. The complexity of its genome, comprising many more regulatory genes than simple gammaretroviruses, posed new challenges for vector design.

## THE MILESTONE EXPERIMENT

In 1994, one of us (L.N.) joined the other's (I.M.V.'s) laboratory at the Salk Institute as a visiting scientist to explore the possibility of targeting retroviral vectors to specific cell types. Two floors above, another one of us (D.T.) was working independently on the role of HIV proteins in infection and replication,

with a particular interest in how the provirus was imported into the host cell nucleus. We started a collaboration to see whether specific genomic sequences from HIV could be inserted into a gammaretroviral vector [Moloney mouse leukemia virus (MLV)] to impart the ability of transducing nondividing cells. The quick fix did not work, so we decided to use HIV itself as a vector, even though we anticipated that the idea of using derivatives of a lethal pathogen to deliver genes in people would raise a lot of eyebrows and disbelief.

To broaden the very limited range of cellular targets accessible through the HIV envelope protein, we replaced it with the

***“...the idea of using...a lethal pathogen to deliver genes in people would raise a lot of eyebrows and disbelief.”***

more promiscuous envelope glycoprotein (G) of vesicular stomatitis virus, which afforded an additional advantage. The stability of G protein allowed one to concentrate the viral particles released into the culture media from “producer” cells (or “packaging” cells) by ultracentrifugation. This afforded an infectious titer that was hundred-folds higher than previously achieved. In 1996, these concentrated first generation lentiviral vectors could transduce neurons in the rat brain, a paradigmatic example of nondividing cells (see the image). This milestone experiment was made possible by advanced in vivo imaging developed in the next-door laboratory of Fred “Rusty” Gage (3). Indeed, targeted neurons could be made to carry stably integrated foreign transgenes in their genome.

## RESEARCH ADVANCES

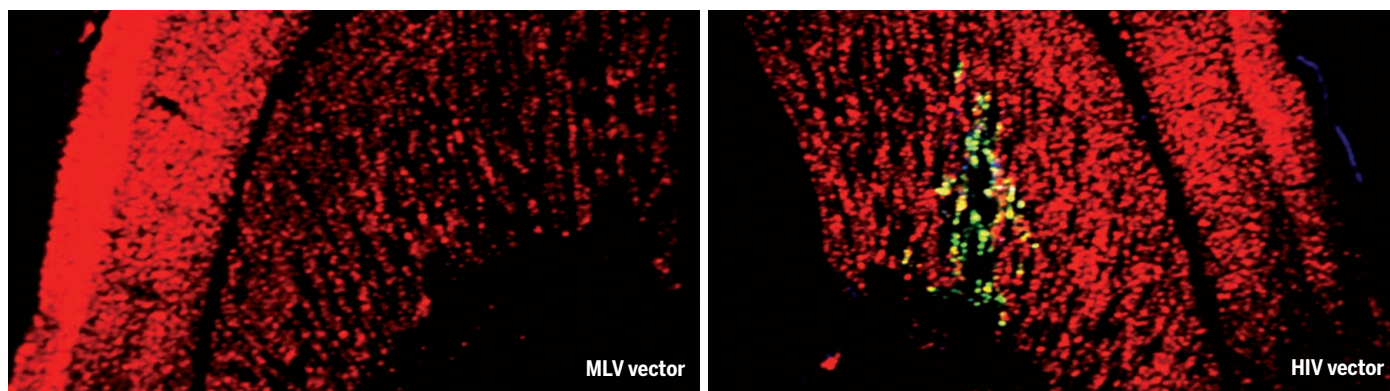
Soon thereafter, hepatocytes, hematopoietic stem cells (HSCs), and a host of nondividing as well as dividing cells were efficiently transduced by these vectors (4). Sequences encoding proteins important for HIV virulence, but with no apparent role in the transduction process per se, were deleted from the packaging construct to generate second ( $\Delta$ Vpr, Vif, Vpu, Nef) (5) and third (also  $\Delta$ Tat) (6) generation vector systems, thus moving away

from the pathogenic features of the parental virus. And to add additional safety features, promoter-enhancer sequences in the long terminal repeats (LTRs) of the integrated transgene (a provirus) were deleted through the so-called self-inactivating (SIN) design, which further minimized the chance of generating replication-competent recombinant lentivirus. This assigned full control of transgene expression to the exogenous promoter inserted in the vector (6).

These tools held great promise for the gene therapy of human disorders, notably those for which manipulating HSCs was likely to do the job. These cells could now be more efficiently transduced ex vivo and then reinjected to repopulate the organism with gene-corrected progeny of all hematopoietic lineages. However, it is in the research arena that the potential of lentiviral vectors was immediately exploited. There was an abundance of knowledge accumulated through the study of HIV, and from the past successes and failures of other gene delivery systems. That HIV was also a retrovirus allowed one to capitalize on much of the experience acquired through MLV-based systems, and to easily design vectors that were highly efficient at transducing most cell types, could be exogenously regulated, or could be made tissue-specific using well-established or new methods, such as by exploiting microRNA regulation (7). Soon, the lentiviral vector system became a favorite gene delivery tool for experimentalists from many fields over a broad range of research applications. These included transgenesis by instillation of a few nanoliters of concentrated vector in the perivitelline zone of fertilized mouse eggs, a procedure soon extended to species that were out of reach by the more conventional intranuclear injection of plasmid DNA, such as the rat, pig, and marmoset (8). Lentiviral vectors could also be used to generate transgenic mice in which the expression of a specific gene was reduced by vector-encoded small-hairpin RNAs (9).

HIV-derived vectors also became workhorses for introducing libraries of complementary DNAs, small-hairpin RNAs, and cis-acting regulators into a wide variety of targets, including embryonic stem cells. As such, they have been routinely used for a broad diversity of functional screens for tumorigenesis, cell growth, and senescence, among other cellular states. Lentiviral vectors are

<sup>1</sup>San Raffaele Telethon Institute for Gene Therapy; Division of Regenerative Medicine, Stem Cells and Gene Therapy, San Raffaele Scientific Institute; Tissue Biology and Gene and Cell Therapy, Vita-Salute San Raffaele University Medical School, Via Olgettina, 58, 20132 Milano, Italy. <sup>2</sup>School of Life Sciences, École Polytechnique Fédérale de Lausanne, SV-LVG Station 19, 1015 Lausanne, Switzerland. <sup>3</sup>Laboratory of Genetics, Salk Institute, 10010 North Torrey Pines Road, La Jolla, CA 92037, USA. Email: naldini.luigi@hsr.it; didier.trono@epfl.ch; verma@salk.edu



Confocal microscope image of a section of an adult rat brain transduced in vivo with either an MLV or HIV vector that expresses  $\beta$ -galactosidase ( $\beta$ -Gal). The protein only appears on the HIV vector side, visualized (green) by staining with antibodies to  $\beta$ -Gal.

also being used to generate models of human cancers and, by altering the viral envelope protein, can be designed to target specific cell types and generate vaccines. Nonintegrating lentiviral vectors have also been used to transduce dendritic cells with tumor antigens for cancer gene therapy (10, 11).

### CLINICAL APPLICATIONS

Clinical testing of lentiviral vectors eventually ensued, initially involving the expression of antiviral transgenes in the lymphocytes of HIV-infected individuals. This was in a setting where the risk of first-in-human administration of HIV-derived vectors was alleviated (12). This paved the way for applications of lentiviral vectors in cancer immunotherapy—notably, to engineer lymphocytes to express tumor-specific T cell receptors or chimeric antigen receptor (CAR) (13). The combination of versatile vector design and robust stable expression in T cells has propelled lentiviral vectors to the forefront of this rapidly growing field.

Efficient transduction of HSCs by lentiviral vectors also has led to successful clinical applications. Indeed, earlier clinical trials using gammaretroviral vectors showed a low extent of gene transfer into HSCs, thus limiting utility to those diseases in which gene correction confers a selective growth advantage to the transduced cell progeny and enables functional reconstitution of one or more hematopoietic lineages, even from few corrected progenitors. Some of these trials using gammaretroviral vectors also reported the delayed occurrence of leukemia, driven by vector insertion near oncogenes, in a fraction of treated patients. This increased skepticism about the overall safety of this strategy (14).

By contrast, substantial levels of stable HSC gene transfer have been obtained in clinical trials of lentiviral-based HSC gene therapy, achieving up to 80% success. Many children suffering from rare fatal disorders such as X-linked adrenoleukodystrophy (ALD) (15), metachromatic leukodystrophy

(16), Wiskott-Aldrich syndrome (17), and a growing number of other severe combined immunodeficiencies have been treated with lentiviral vectors that provide the deficient gene product. These patients are reported to enjoy substantial benefits to this day, 9 years after the first ALD patient was treated. More recently, lentiviral vectors have been used to treat patients with hemoglobinopathies such as thalassemias and sickle cell disease. These later developments were spearheaded by seminal work exploiting the biology of HIV to load the vector with complex regulatory sequences from the hemoglobin locus. This modification ensured robust, erythroid-specific expression of the globin transgene (18, 19). In all of these trials, engraftment of the transduced HSCs required preparative myeloablation, similar to when transplanting HSCs from healthy donors. In HSC gene therapy, however, the infused cells are the patient's own cells; thus, there is no risk of immune complications such as rejection or graft-versus-host disease, which are major causes of morbidity in conventional transplants. Sustained expression of the transgene in the reconstituted hematopoiesis is observed for many years. Because the vector integrates quasi-randomly genome wide, each transduced cell acquires a unique genetic marker (the junction between the vector LTR and the genomic sequence at the insertion site) that can be used to track its progeny in vivo (20). The clonal composition of the hematopoietic graft can thus be monitored in the treated patients. To date, these studies have revealed that lentiviral vectors exhibit far less genotoxicity than observed with gammaretroviral vectors (15–19), consistent with preclinical predictions from experimental models (21). Moreover, these studies now provide the first glimpse of HSC activity in living humans at the clonal level. Whereas long-term follow-up data are still limited, the number of patients treated is rapidly growing given the increasing number of active studies and trial sites.

Lentiviral vectors are also being tried for the gene therapy of various other genetic and acquired diseases, by administration into the eye or brain, or intravenously to reach the liver. However, it is for stem cells, including induced pluripotent stem cells, that they are uniquely attractive, because of their ability to integrate into the host genome. At the dawn of the genome-editing era, lentiviral vectors (whether integrase defective or competent) continue to serve scientists by providing effective delivery of the template for targeted gene repair and for the expression of engineered nucleases (22), including Cas9 and clustered regularly interspaced short palindromic repeat (CRISPR) guide RNAs.

It is immensely rewarding and a testimony to the transformative power of science that 20 years after the original work, and thanks to the contribution of many other scientists and clinicians, a deadly virus that has plagued humankind and claimed millions of lives has been turned into a beneficial tool that now helps to relieve the suffering of people affected by debilitating maladies. ■

### REFERENCES

1. I. M. Verma, *Sci. Am.* **262**, 68 (November 1990).
2. J. B. Weinberg et al., *J. Exp. Med.* **174**, 1477 (1991).
3. L. Naldini et al., *Science* **272**, 263 (1996).
4. R. Zufferey, D. Nagy, R. J. Mandel, L. Naldini, D. Trono, *Nat. Biotechnol.* **15**, 871 (1997).
5. T. Dull et al., *J. Virol.* **72**, 8463 (1998).
6. H. Miyoshi, K. A. Smith, D. E. Mosier, I. M. Verma, B. E. Torbett, *Science* **283**, 682 (1999).
7. B. D. Brown et al., *Nat. Biotechnol.* **25**, 1457 (2007).
8. A. Pfeifer, *Curr. Gene Ther.* **6**, 535 (2006).
9. G. Tiscornia et al., *Proc. Natl. Acad. Sci. U.S.A.* **100**, 1844 (2003).
10. L. Yang et al., *Nat. Biotechnol.* **26**, 326 (2008).
11. K. Wanisch, R. J. Yáñez-Muñoz, *Mol. Ther.* **17**, 1316 (2009).
12. P. Tebas et al., *Blood* **121**, 1524 (2013).
13. M. V. Maus et al., *Annu. Rev. Immunol.* **32**, 189 (2014).
14. L. Naldini et al., *Nat. Rev. Genet.* **12**, 301 (2011).
15. N. Cartier et al., *Science* **326**, 818 (2009).
16. A. Biffi et al., *Science* **341**, 1233158 (2013).
17. A. Aiuti et al., *Science* **341**, 1233151 (2013).
18. C. May et al., *Nature* **406**, 82 (2000).
19. R. Pawliuk et al., *Science* **294**, 2368 (2001).
20. A. R. Schroder et al., *Cell* **110**, 521 (2002).
21. E. Montini et al., *Nat. Biotechnol.* **24**, 687 (2006).
22. A. Lombardo et al., *Nat. Biotechnol.* **25**, 1298 (2007).

10.1126/science.aah6192



# Ahmed H. Zewail (1946–2016)

A Nobel laureate, who pioneered femtochemistry, promoted a scientific renaissance in the Middle East

By Peter B. Dervan

**A**hmed H. Zewail, an Egyptian-American scientist who won the 1999 Nobel Prize in Chemistry for pioneering investigations of fundamental chemical reactions on the femtosecond time scale, died on 2 August 2016. He was 70 years old. Zewail was an academic star at the California Institute of Technology (Caltech) and spent his final years advocating for investment in science education and research in Egypt.

Zewail was born in 1946 in Damanhur, Egypt, and studied at Alexandria University in the city where he grew up. After earning bachelor's and master's degrees, he looked abroad to pursue his Ph.D. in chemistry. Egyptians seeking overseas education in 1969 typically went to the Soviet Union. In a stroke of good fortune, the University of Pennsylvania offered him a scholarship and he came to the United States. After earning his doctorate from Penn, he spent 2 years as a postdoctoral researcher at the University of California, Berkeley, and then joined the faculty at Caltech in Pasadena in 1976. Zewail, the Linus Pauling Professor of Chemistry and professor of physics, set out to make movies of chemical reactions with the world's fastest camera—one with shutter speed measured in femtoseconds, a millionth of a billionth of a second.

Before Zewail's work, chemists could only infer the structures of short-lived intermediates between reactants and products during the breaking and making of bonds in chemical reactions. Transition states are so fleeting that they had never been observed directly. A femtosecond is shorter than the period of a nuclear vibration or rotation in the molecule and Zewail was able to freeze the system in time using ultrafast laser spectroscopy. Zewail's brilliant insight was the demonstration that rotational and vibrational coherence is the key to making femtosecond movies. He was able to choreograph an ensemble of molecules and synchronize their motion. Using two laser pulses—a pump pulse to start the clock and trigger the reaction, followed by

a probe pulse—Zewail photographed snapshots of the evolution of chemical reactions. Zewail's hero and friend, Caltech's Linus Pauling, won the Nobel Prize in 1954 for his research on the nature of the chemical bond. Zewail connected the chemical bond to its dynamics by setting those bonds in motion.

Zewail received honors from around the globe, including 46 honorary degrees, the Grand Collar of the Order of the Nile (Egypt's highest state honor), and the Order of Légion d'Honneur. He was an elected member of academies and learned societies including the U.S. National Academy of Sciences, the Royal Society of London, the American Philosophical Society, the French



Academy, the Russian Academy, the Chinese Academy, and the Swedish Academy. Among his more than 100 international prizes and awards, he was recipient of the Benjamin Franklin Medal, the Leonardo da Vinci Award, the Robert A. Welch Award, the Wolf Prize, the King Faisal Prize, and the Priestley Medal.

After the Nobel in 1999, Zewail became an outspoken leader in global affairs, particularly as they relate to progress in science and education in the developing world. In 2009, he was appointed to Obama's President's Council of Advisors on Science and

Technology and appointed U.S. Science Envoy to the Middle East. He still found time to write some 600 research articles and 14 books. Zewail was passionate about his next discovery in chemical physics—seeing structures with electrons in the four dimensions of time and space. He and his group developed femtosecond electron diffraction for direct imaging of the architecture of biological molecules or materials changing with time.

Ahmed was a brilliant scientist who combined vision, hard work, and optimism in his research. Ahmed and I were colleagues together for 40 years at Caltech, and I was fortunate to hear his thoughts about the importance of fundamental research, the widening gap between the haves and have nots, and his hopes for the Middle East. Although he loved America and was grateful to be at Caltech for 40 years, his commitment to Egypt, the country of his birth, never wavered.

In a 2013 op-ed, Zewail wrote, "A part of the world that pioneered science and mathematics during Europe's dark ages is now lost in a dark age of illiteracy and knowledge deficiency." Ahmed's message to the Arab world was to build a "scientific society." Shortly after receiving the Nobel, he proposed to President Mubarak the creation of a science and technology institute in Egypt. He imagined a private research institute unimpeded by bureaucracy and political instability—a Caltech model in Egypt. During the 2011 Egyptian revolution, he supported the students' goals—democracy, and social and economic change. In 2013, the Zewail City of Science and Technology began enrolling students in biomedicine, solar energy, nanotechnology, and other fields. The question remains whether his dream for an independent Egyptian science and technology institute will live on.

Like his role model Benjamin Franklin, Ahmed Zewail was an intellectual and a statesman who made important contributions to both science and society. He was a charismatic person with an infectious laugh and a sonorous voice. All his colleagues delighted to be in his presence. His personal warmth made everyone feel like they were his best friend. Caltech, the scientific community, and the entire Arab world deeply mourn his loss. He was buried in Egypt with a full military funeral on 7 August 2016. Ahmed Zewail was the first Egyptian and the first Arab to win a Nobel Prize in the sciences.

He is survived by his wife, Dema Faham, and four children: Maha, Amani, Nabeel, and Hani. ■

Division of Chemistry and Chemical Engineering,  
California Institute of Technology, Pasadena, CA, USA.  
Email: dervan@caltech.edu

10.1126/science.aai8466

## RETROSPECTIVE

# Donald A. Henderson (1928–2016)

A pragmatic and tireless epidemiologist led the international eradication of smallpox

By David L. Heymann<sup>1,2</sup>

The smallpox eradication listserv—which contains the names of many who worked in the smallpox eradication program—looks like a page from the *Who's Who* of public health, including many who became public health leaders during the 20th century. The listserv has been particularly active recently in sharing condolences with the family of Donald A. Henderson and reminiscing about the great man that he was.

“D.A.” died on 19 August in Towson, Maryland, at the age of 87. Born in 1928 in Lakewood, Ohio, he graduated from Oberlin College, and earned his medical degree from the University of Rochester, New York. In 1955, he joined the Centers for Disease Control and Prevention and began a program to address smallpox in Africa. In 1966, he left for Geneva to expand the program through the World Health Organization (WHO), galvanizing people, resources, and support to tackle smallpox through vaccination. In 1980, smallpox was certified as eradicated. From 1977 to 1990, D.A. was dean of the Johns Hopkins University School of Hygiene and Public Health. He would go on to serve as an adviser on bioterrorism and, in 2002, was awarded the Presidential Medal of Freedom, the highest U.S. civilian honor.

I first met D.A. in 1974 when he came to the London School of Hygiene and Tropical Medicine to recruit public health workers for the smallpox eradication program in India. He was like the Pied Piper—a charismatic and pragmatic leader who convinced people to follow and fill the urgent needs of stopping the spread of smallpox. Many of us from the London School did indeed follow, embarking on an adventure that led to great personal and professional satisfaction, lifelong friendships, and wisdom from D.A. until his death.

D.A. was a lifelong mentor and source of support. My own career frequently crossed paths with him or his legacy. In Africa, D.A.'s name was still a legend when I began work

there in 1976 during the first Ebola virus outbreak, and through the next 5 years at the Organisation de Coordination pour la lutte contre les Endémies en Afrique Centrale, the Central African agency based in Cameroon that coordinated eradication activities with the WHO in Central Africa. D.A. was remembered as having led them to success.

D.A. and I often spoke after 1996, when I led the newly created WHO Emerging Infections Program that oversaw the regular inspection of laboratories in the United States and Russia where the smallpox virus was maintained. We also conferred when I took the lead in the WHO's polio eradication activities in 2003.

During an early discussion with D.A. about polio eradication in 2003, and of his sometimes vocal concerns about its feasibility, he

described the embarrassed reaction of some of the Asian ministers of health, and how easily the resolution was passed. The Asian programs were revived, and smallpox transmission was rapidly interrupted.

When activities to revive the program in northern Nigeria came to a standstill, it was, in the end, a similar facilitated resolution that was the final contribution to a successful restart of the program. D.A. was always careful to say that rules at the WHO needed to be respected but interpreted liberally and with justification, and that they should not be permitted to become an obstacle to good public health.

D.A. also approved of planning for the polio eradication endgame and its consolidation and destruction of wild and Sabin poliovirus. He described to me how the

last cases of smallpox—caused by a laboratory accident in the United Kingdom—led to the recommendation that countries either destroy or consolidate the remaining smallpox viruses in maximum security laboratories in the United States and Russia. D.A. was convinced that all viruses should be destroyed, and that eradication would not be complete until then. He had scientific and technical support from WHO advisory groups, as well as the political will from many countries throughout the world, but a resolution to destroy the remaining virus remained elusive despite numerous attempts.

In the early 2000s, concern about deliberate use of the smallpox virus to cause harm was raised by D.A. after discussions with scientists from the former Soviet Union. It was, ironically, this threat that provided another reason not to destroy the remaining smallpox virus, and a resolution was passed requiring the WHO to oversee a research program to develop new and safer smallpox vaccines, diagnostics, and drugs. The WHO is to determine when this research program is complete before reviving destruction discussions. The active research program is now rapidly coming to a conclusion. What better tribute to D.A. than to now destroy the smallpox virus in these laboratories and complete the eradication of smallpox for its tireless leader. ■



D.A. Henderson (center) worked to eradicate smallpox in Africa in the 1970s.

promised—and kept his promise until 2009 when I left the WHO—that he would withhold public statements and work with the WHO behind the scenes to overcome obstacles. He remained skeptical, but offered sound advice. From 2003 to 2004, when efforts to restart polio eradication in northern Nigeria faced difficulties, D.A. described how he had facilitated a resolution in the World Health Assembly—not a politically condoned practice—when smallpox eradication efforts flagged in Asia. He had convinced several West and Central African ministers of health to describe how they had stopped smallpox transmission, despite weak infrastructure, in front of other health ministers from the WHO member countries. The ministers clearly stated that they were still at risk from polio that was not yet eliminated in Asia, a region with a strong infrastructure. They then proposed a resolution that countries in Asia increase their efforts toward eradication. D.A.

<sup>1</sup>Centre on Global Health Security at Chatham House, London SW1Y 4LE, UK. <sup>2</sup>Infectious Disease Epidemiology, London School of Hygiene and Tropical Medicine, London WC1E 7HT, UK. Email: david.heyman@phe.gov.uk



Immunotherapy—a Blue Ribbon Panel focus.  
[Cytotoxic T cells (red) killing a cancer cell.]

## POLICY FORUM

### BIOMEDICINE

# A U.S. “Cancer Moonshot” to accelerate cancer research

Patient engagement and data sharing must improve

By **Dinah S. Singer**,<sup>1</sup> **Tyler Jacks**,<sup>2</sup>  
**Elizabeth Jaffee**<sup>3</sup>

In January 2016 President Obama announced a “Cancer Moonshot” to “accelerate our understanding of cancer and its prevention, early detection, treatment, and cure” (1). A Blue Ribbon Panel (BRP) of scientific experts was convened to make recommendations to the National Cancer Advisory Board (NCAB), the adviser to the National Cancer Institute (NCI), on research opportunities uniquely poised for acceleration. These recommendations were presented on 7 September 2016 (2). As co-chairs of the BRP, we describe our approach, what it produced, and our expectations.

The BRP chose to focus on areas well positioned to benefit from additional coordination and support promised by the Cancer Moonshot. The BRP established working groups to focus on research areas that were not already well advanced. Each working group was charged with developing two to three recommendations for research already begun. What sets these recommendations apart from previous efforts and ongoing investigator-initiated research is the opportunity to establish coordinated, multidisciplinary collaborative projects with the impetus of the Cancer Moonshot.

More than 150 people—including scientists, clinicians, patient advocates, and industry representatives—participated in the working groups. To supplement the working

groups, NCI led a campaign to collect input from the wider research community and the public. This included a website where more than 1600 ideas and comments were submitted (3), all of which were reviewed by the BRP co-chairs and the relevant working groups. The majority of the ideas submitted aligned with those discussed by the BRP; all had been considered. Thus, the recommendations of the BRP reflect what the broader community sees as ripe for progress.

## RECOMMENDATIONS AND EMPHASIS

Ten recommendations were generated by the BRP emphasizing the importance of direct patient engagement in cancer research, a deeper understanding of why some therapies work and others do not, the dynamics of tumor evolution, and the need for mechanisms of data sharing, access, and analysis.

One recommendation calls for development of a patient engagement network. The vast majority of Americans do not have easy access to genetic and other molecular testing methods at the core of precision cancer medicine; thus, a broad segment of the cancer patient population is not evaluated for newly approved medicines or is excluded from clinical trials. A national program would allow large numbers of patients to have their tumors profiled and to directly contribute the data (including tumor genomics and information about immune cells and microenvironment) plus information on their clinical status and outcomes to a nationally federated and shared database. This would inform research on therapeutic agents and help identify new, clinically relevant cancer groupings. Such a database could collect and integrate patient-reported

symptom and side-effect data, which could lead to improved symptom control.

Only about 5% of all cancer patients are enrolled in clinical trials. One contributing factor is lack of awareness of eligibility for trials. The network would help by providing a database of eligible patients for clinical trials and “preregistering” them. This effort will link and expand existing efforts and could fundamentally change how patients access and interact with clinical trials. Conducting such an effort at the proposed national scale and scope can be done only with the support of the Cancer Moonshot.

Patient (and public) engagement is also key to the recommendation to implement evidence-based approaches to prevention. The need to extend colorectal screening—which can save many lives—and make it more accessible to a wider population was highlighted. Most individuals with cancer-predisposing inherited mutations or alleles are unaware of it and so are not monitored for early detection of cancer. One recommendation is a pilot project in which all patients with newly diagnosed colorectal or endometrial cancer would be screened for DNA mismatch-repair deficiency; those with such defects would then have targeted genome sequencing for mutations in DNA mismatch-repair genes associated with Lynch syndrome (a hereditary dominant predisposition to a number of cancer types). When such mutations are identified, first-degree relatives of the patient would be offered the opportunity to be screened. Identification of affected individuals would allow early detection and thus reduce morbidity and mortality.

Another cross-cutting theme is the value of cataloging molecular and cellular changes that occur in the course of tumor development—in the tumor but also in the tumor microenvironment and the immune cell milieu. Although researchers know an increasing amount about the state of human tumors at diagnosis, knowledge is needed to be able to predict which cancers will respond to specific therapies, how they become resistant to those therapies, which will develop metastases, and which will recur. Thus, one recommendation calls for development of a “Tumor Atlas” that, like The Cancer Genome Atlas (TCGA), would contain detailed cellular, molecular, and genomic (and other omics) information on the cancer cells in a tumor, linked to patient demographic and clinical data. It would also characterize the noncancerous surrounding cells, including immune components. Unlike TCGA, this atlas would include information representing all stages of tumor evolution, from precancerous lesions to primary can-

<sup>1</sup>National Cancer Institute, Bethesda, MD 20892, USA.

<sup>2</sup>Massachusetts Institute of Technology, Cambridge, MA

02139, USA. <sup>3</sup>Johns Hopkins School of Medicine, Baltimore, MD 21231, USA. Email: singerd@mail.nih.gov

cers, to development of treatment resistance, through metastasis—from the same patient, where possible. Such an atlas would enable development of computational models that could predict progression and treatment response and help reveal new therapeutic targets and biomarkers. Even more than TCGA, a tumor atlas of this complexity requires a coordinated, collaborative national effort.

Another recommendation calls for analysis of samples already available from patients who have received the standard of care. Many thousands of patients have been treated with similar standard-of-care regimens. Some have had outstanding responses with substantial prolongation of life, some responded but eventually relapsed, and others did not respond at all. The underlying molecular, genetic, and cellular mechanisms that may distinguish these groups of patients—even if they initially fall within the same disease classification—remain poorly understood. A detailed genomic analysis of acquired biopsies, as recommended, would lead to better understanding of how to identify patients who are or are not likely to benefit from existing therapies. A catalog of potential immune targets (on the tumor and in the tumor microenvironment) would identify targets for vaccines and other immunotherapies.

A need to better understand unique features of childhood cancers is integral to many of the BRP's recommendations. One recommendation is to enhance understanding of how fusion oncoproteins, which result from recurrent chromosomal translocations and are a hallmark of many childhood cancers, drive cancer development. Because few models of these cancers exist, new experimental models are needed to study the mechanism of action and key vulnerabilities of these oncoproteins, as well as to develop therapies and preventive approaches for childhood cancers. The ability to speed this basic research and to carry it out at the needed scale will require a network of investigators with unique expertise—the kind of collaborative effort that the Cancer Moonshot seeks to foster.

One recommendation proposes a cancer immunotherapy clinical trials network. Despite recent successes in immunotherapy, patients with many types of cancer—including pediatric cancers—do not show long-term responses to these treatments. Differences in the mutational burden between pediatric and adult cancers may result in less susceptibility of pediatric cancers versus adult cancers to immunotherapies, such as checkpoint inhibitors. This network would help define the cell surface landscape of high-risk pediatric cancers to identify key targets (i.e., those that are uniformly and specifically expressed on tumor cells and are required for cell viability) against which to develop specific im-

munotherapies. This recommendation calls for defining the essential elements that help tumors in children evade immune attack.

The recommendation to improve symptom management through accelerated systematic efforts to gather information on patient-reported outcomes is of critical importance to survivors of childhood cancer, many of whom experience disabling long-term side effects.

Several of the recommendations address cancer health disparities. Part of the goal of enabling direct patient engagement is to broaden the spectrum of patients involved in clinical research. Much of the data on the association between genomic changes and clinical outcomes represents patients coming from “privileged” hospitals, and it is essential to have the wider population represented. Similarly, outreach to a more diverse group of patients is essential for the recommendation to increase implementation of evidence-based approaches to prevention.

Finally, an important theme across many

---

### ***“... research [based on] BRP's recommendations will depend on ... funding ... approved by Congress.”***

recommendations is the need for infrastructure to connect existing and future data repositories, analytical tools, and knowledge bases. The BRP recommends the establishment of a Cancer Data Ecosystem, which would consist of research platforms accessible to researchers, clinicians, and patients; they would serve as research resources and provide information that patients and clinicians could use to plan treatment and predict outcomes. Development of this system will be a major undertaking and will require extensive development with the NCI and the extramural community, both the academic and private sectors. New funding models and cooperative efforts anticipated by the Cancer Moonshot Initiative will be key to success.

#### **WHAT HAPPENS NEXT?**

NCI intends to begin to implement the recommendations, with the goal of funding some initiatives in summer 2017. Given the novelty and scope of the recommendations, NCI is considering nontraditional funding mechanisms and research structures, such as those used by the Common Fund and the Precision Medicine Initiative, to complement traditional funding approaches.

The ability to conduct research stemming from the BRP's recommendations will de-

pend on whether, and how much, funding is approved by Congress. Because the BRP focused on research that could be accelerated, in most cases, they could proceed in a limited fashion without new funds. However, they would advance more quickly if funded to a higher level. Many recommendations build on collaborative efforts that leverage the work and funding of multiple partners.

Some approaches or ideas are advanced enough that new research can proceed quickly; others will take longer. For certain recommendations, it will be necessary to first address policy issues, such as medical coverage and reimbursement, patient privacy and consent, and barriers to data sharing. For example, patients identified as genetically at high risk for particular cancers, along with their relatives, may need to receive screening and preventive care that are not covered by insurance. Another example is establishing a national standard for biospecimen collection and storage. Some of these policy issues are already the focus of discussions by the Cancer Moonshot Task Force directed by Vice President Joe Biden. Other recommendations will require additional technology development before they can be fully realized.

Potential for progress will depend on collaborations between NCI, other federal agencies, and the private sector, including those on data sharing, strategic computing, and public-private partnerships around drug development. Although NCI and other government agencies will lead the implementation of many of these recommendations, nobody “owns” them; thus, many may be carried forward by foundations, pharmaceutical companies, advocacy organizations, or other groups.

Although the BRP recommendations clarify what efforts might lead to transformative changes with new funding, these will not come at the expense of traditional funding expectations. Many ideas the BRP received are being and will continue to be pursued through the NCI's standard research funding process. Excitement about the Cancer Moonshot process is balanced by a commitment to the value of basic research, population studies, technology development, and traditional approaches all of which are essential if we are to continue making progress. ■

#### **REFERENCES**

1. White House, Memorandum—White House Cancer Moonshot Task Force, 28 January 2016; <http://bit.ly/WhiteHouseMemoMoonshot>.
2. Cancer Moonshot Blue Ribbon Panel (NCI, 2016); [www.cancer.gov/brp](http://www.cancer.gov/brp).
3. Clinical Trials Ideas (NCI, 2016); <https://cancerresearch-ideas.cancer.gov/a/index>.

Published online 7 September 2016.  
10.1126/science.aai7862



Edited by Jennifer Sills

## Nuclear energy: Improve collaboration

TECHNOLOGICAL collaboration between China and the United States in the field of nuclear energy is important for developing alternative energy and mitigating climate change ("China-U.S. cooperation to advance nuclear power," J. Cao *et al.*, Policy Forum, 5 August, p. 547). However, China should also expand collaboration with developed countries on the regulation and management of nuclear energy and in tackling public concerns (1).

After the Fukushima accident, the percentage of the Chinese population against new nuclear power plants increased from 13 to 54% (2). After a 3-year suspension, China reignited its ambitious nuclear plan. However, numerous industrial accidents occurred, including the deadly 2015 Tianjin explosion (3), and as a result the program has slowed once again because it lacks public trust (4). For example, on 6 August 2016, thousands of people protested against a proposed nuclear waste treatment plant in Lianyungang, east China. Four days later, local government suspended the project (5).

As living standards have improved, the Chinese middle class has woken up to China's many environmental problems (6). The United States and Europe address public concerns through community outreach, education, and advisory boards (7). China needs to develop similar approaches. To address the poor coordination, planning, and management of its nuclear program, China must develop the institutions required for safe nuclear development (8), encourage an independent and transparent regulatory regime, and strictly enforce regulations (9).

These changes will require more social science research and funding to incorporate expertise and information from community leaders and indigenous groups (1, 10). Development of state-of-the-art nuclear energy technology should go hand-in-hand with world-class regulatory infrastructure and public engagement mechanisms.

**Hong Yang,<sup>1,2\*</sup> Jihong Liu Clarke,<sup>2</sup>  
Julian R. Thompson<sup>3</sup>**

<sup>1</sup>Norwegian Institute of Bioeconomy Research (NIBIO), 1431, Ås, Norway. <sup>2</sup>CEES, Department of Biosciences, University of Oslo, Blindern, 0316, Oslo,



A Tokyo Electric Power Co. (TEPCO) employee walks in front of the No. 1 reactor building at TEPCO's tsunami-crippled Fukushima Daiichi nuclear power plant in the town of Okuma, Japan. After the Fukushima disaster, support among Chinese citizens for China's nuclear energy program plummeted.

Norway. <sup>3</sup>UCL Department of Geography, University College London, London, WC1E 6BT, UK.

\*Corresponding author.  
Email: hongyanghy@gmail.com

### REFERENCES

1. B. K. Sovacool, *Nature* **511**, 529 (2014).
2. L. Huang *et al.*, *Proc. Natl. Acad. Sci. U.S.A.* **110**, 19742 (2013).
3. Z. W. Tang, Q. F. Huang, Y. F. Yang, *Nature* **525**, 455 (2015).
4. Lianyungang Government, "Lianyungang Government's decision: Suspend the pilot work of selecting place for the nuclear waste recycling project" (2016); [www.lyg.gov.cn/art/2016/8/10/art\\_1756\\_643365.html](http://www.lyg.gov.cn/art/2016/8/10/art_1756_643365.html) [in Chinese].
5. X. Guo, X. Guo, *Renew. Sust. Energ. Rev.* **57**, 999 (2016).
6. T. Johnson, *Environ. Polit.* **19**, 430 (2010).
7. M. R. Greenberg, *Energy Res. Soc. Sci.* **1**, 152 (2014).
8. Y. C. Xu, *Energy Pol.* **73**, 21 (2014).
9. H. Yang, X. Huang, J. R. Thompson, R. J. Flower, *Science* **347**, 834 (2015).
10. S. Christopher, V. Watts, A. K. H. G. McCormick, S. Young, *Am. J. Public Health* **98**, 1398 (2008).

10.1126/science.aai8681

## Cancel Yulin's annual dog meat festival

ON 21 JUNE, residents of Yulin held this year's notorious dog-meat festival amid intense criticism from animal rights groups (1). It is often wrongly assumed that this festival is an ancient Chinese tradition. In fact, it began in 2009 and is run by private individuals and businesses with no local or state government support (2).

The dogs for the festival are primarily acquired through illegal underground trading in China (2). In addition to animal welfare concerns (2), this illegal trade

puts humans at risk by facilitating the spread of disease (3). Rates of sterilization and rabies vaccinations are both extremely low in rural China (4), and the capture, transport, and marketing of stray dogs are likely to exacerbate existing disease concerns.

We appeal to all Chinese animal lovers to promote a change in legislation to forbid the festival. By doing so, we can both promote animal welfare and protect humans from disease.

**Qinghui Meng,<sup>1,2\*</sup> Ruixia Li,<sup>1</sup> Rowena Hamer,<sup>1,2</sup> Hongmin Dong,<sup>1</sup> Xiuping Tao,<sup>1</sup> Jiade Bai,<sup>2</sup> Yanju Liu,<sup>2</sup> Zhenyu Zhong,<sup>2</sup> Shumiao Zhang,<sup>2</sup> Yuping Meng,<sup>2</sup> Qingyun Guo<sup>2</sup>**

<sup>1</sup>Institute of Environment and Sustainable Development in Agriculture, Chinese Academy of Agricultural Sciences, Beijing, 100081, China.

<sup>2</sup>Beijing Milu Ecological Research Centre, Beijing, 100076, China.

\*Corresponding author.  
Email: mengqinghui2006@hotmail.com

### REFERENCES

1. BBC News, "Yulin dog meat festival begins in China amid widespread criticism" (2016); [www.bbc.com/news/world-asia-china-36583400](http://www.bbc.com/news/world-asia-china-36583400).
2. E. Henderson, "Yulin Dog Meat Festival 2016: 10,000 dogs to be killed and eaten at China's annual food event," *Independent* (2016); [www.independent.co.uk/news/world/asia/yulin-dog-meat-festival-2016-10000-dogs-set-to-be-killed-and-eaten-at-chinese-food-event-a7093321.html](http://www.independent.co.uk/news/world/asia/yulin-dog-meat-festival-2016-10000-dogs-set-to-be-killed-and-eaten-at-chinese-food-event-a7093321.html).
3. K. M. Smith *et al.*, *PLOS ONE* **7**, e29505 (2012).
4. Animals Asia, "An Animals Asia investigation, Report No. 3: China's rural dogs in crisis" (2015); [www.animalsasia.org/assets/pdf/2015\\_FOF\\_reports-report3\\_A4-EN-20150609\\_low.pdf](http://www.animalsasia.org/assets/pdf/2015_FOF_reports-report3_A4-EN-20150609_low.pdf).

10.1126/science.aah4388

## TECHNICAL COMMENT ABSTRACTS

## Comment on “Principles of connectivity among morphologically defined cell types in adult neocortex”

*Alison Barth, Andreas Burkhalter, Edward M. Callaway, Barry W. Connors, Bruno Cauli, Javier DeFelipe, Dirk Feldmeyer, Tamas Freund, Yasuo Kawaguchi, Zoltan Kisvarday, Yoshiyuki Kubota, Chris McBain, Marcel Oberlaender, Jean Rossier, Bernardo Rudy, Jochen F. Staiger, Peter Somogyi, Gabor Tamas, Rafael Yuste*

Jiang *et al.* (Research Article, 27 November 2015, aac9462) describe detailed experiments that substantially add to the knowledge of cortical microcircuitry and are unique in the number of connections reported and the quality of interneuron reconstruction. The work appeals to experts and laypersons because of the notion that it unveils new principles and provides a complete description of cortical circuits. We provide a counterbalance to the authors' claims to give those less familiar with the minutiae

of cortical circuits a better sense of the contributions and the limitations of this study. Full text at <http://dx.doi.org/10.1126/science.aaf5663>

## Response to Comment on “Principles of connectivity among morphologically defined cell types in adult neocortex”

*Xiaolong Jiang, Shan Shen, Fabian Sinz, Jacob Reimer, Cathryn R. Cadwell, Philipp Berens, Alexander S. Ecker, Saumil Patel, George H. Denfield, Emmanouil Froudarakis, Shuang Li, Edgar Walker, Andreas S. Tolias*

The critique of Barth *et al.* centers on three points: (i) the completeness of our study is overstated; (ii) the connectivity matrix we describe is biased by technical limitations of our brain-slicing and multipatching methods; and (iii) our cell classification scheme is arbitrary and we have simply renamed previously identified interneuron types. We address these criticisms in our Response.

Full text at <http://dx.doi.org/10.1126/science.aaf6102>

## ONLINE BUZZ

## Biodiversity boundaries

In their Report “Has land use pushed terrestrial biodiversity beyond the planetary boundary? A global assessment” (15 July, p. 288), T. Newbold *et al.* determined that 58.1% of Earth's surface has lost more than 10% of its biodiversity, putting it below the “safe” planetary boundary. In response, readers questioned whether accepting a certain amount of loss as “safe” is constructive. Excerpts of their comments are below. To read all the eLetters, and post your own, go to <http://science.sciencemag.org/content/353/6296/288.e-letters>.

...[Setting] an arbitrary, planetary, “safe” level or threshold...ignores the inherent ecological complexity of biodiversity, its wide variation across spatial and temporal scales..., and the very real need for locally appropriate solutions. The policy implications of an arbitrary safe level are manifold. For example, [in] North America's grasslands,...biodiversity has been drastically reduced. Restoring a “safe level” of biodiversity in this region, one of the most agriculturally productive in the world, would almost certainly lead to undesirable trade-offs, including displacement of food production to lower productivity regions,... more land use overall, [and] hardships caused by increasing food prices....

**Erle Ellis et al.**

...[D]efining a threshold for biodiversity needed to safeguard human well-being...implies there is a safe level of biodiversity loss that will not [affect] the long-term functioning of ecosystems and...our future welfare....[I]t may salve people's conscience, justify continuing environmental destruction in regions currently deemed “safe,” and lead to subsequent establishment of ever-diminishing “safe” levels....[S]hort-term economic benefits from achieving a “safe level” of environmental destruction across spatial scales could easily pervert conservation....[S]uch a threshold would be better communicated...as the minimum target for restoring a functional natural environment that has the potential to sustain human well-being, where extensive biodiversity loss has already occurred.

**Richard J. Smithers et al.**

10.1126/science.aai9171



## TECHNICAL COMMENT

## NEUROSCIENCE

# Comment on “Principles of connectivity among morphologically defined cell types in adult neocortex”

Alison Barth,<sup>1</sup> Andreas Burkhalter,<sup>2</sup> Edward M. Callaway,<sup>3\*</sup> Barry W. Connors,<sup>4</sup> Bruno Cauli,<sup>5</sup> Javier DeFelipe,<sup>6,7</sup> Dirk Feldmeyer,<sup>8</sup> Tamas Freund,<sup>9</sup> Yasuo Kawaguchi,<sup>10</sup> Zoltan Kisvarday,<sup>11</sup> Yoshiyuki Kubota,<sup>10</sup> Chris McBain,<sup>12</sup> Marcel Oberlaender,<sup>13</sup> Jean Rossier,<sup>14</sup> Bernardo Rudy,<sup>15\*</sup> Jochen F. Staiger,<sup>16\*</sup> Peter Somogyi,<sup>17</sup> Gabor Tamas,<sup>18</sup> Rafael Yuste<sup>19</sup>

Jiang *et al.* (Research Article, 27 November 2015, aac9462) describe detailed experiments that substantially add to the knowledge of cortical microcircuitry and are unique in the number of connections reported and the quality of interneuron reconstruction. The work appeals to experts and laypersons because of the notion that it unveils new principles and provides a complete description of cortical circuits. We provide a counterbalance to the authors' claims to give those less familiar with the minutiae of cortical circuits a better sense of the contributions and the limitations of this study.

There is no doubt that the data described in Jiang *et al.* (1) will be a valuable source for descriptions of connectivity between defined neurons.

Some of the authors' observations are new, some confirm previous observations, and some are at odds with previous studies. Because no single method used to identify cortical connections (such as paired recordings used by Jiang *et al.*) can provide a definitive description of the connectivity between specific identified cell types, the observations that conflict with previous results must be further explored. The limitations of this study must be recognized, and further experiments must be conducted to unambiguously resolve these issues.

Because Jiang *et al.* present a large and complex data set and the literature on cortical circuits is very extensive, it is beyond the scope of this Comment to delve into all of the issues that are raised. We highlight some key limitations of the study, as well as limitations of other studies, to exemplify what challenges lie ahead. The primary method used was to simultaneously record intracellularly from up to eight neurons in cortical brain slices. Each cell is sequentially activated while recording from others to test for possible connections. By recording from many neurons at once, there is a combinatorial explosion in the numbers of cell pairs that can be sampled, allowing for the generation of a very large sample (more than 11,000 pairs in Jiang *et al.*). However, many connections are cut during the preparation of brain slices. The effects can be enormous and depend on slice thickness, the distance of recorded cells from the slice surface, and the distances between recorded cells (2). All of these parameters were biased toward connec-

tion loss—slices were thin, cells were close to the surface (within 15 to 60  $\mu\text{m}$ ), and to fit eight electrodes in the recording space, sampled cells were far apart. These factors result in a failure to detect connections and, accordingly, the paper detected no connections whatsoever between layer 5 excitatory neurons and extremely few between layer 2/3 excitatory neurons (only 1.8% connectivity rate). These numbers contrast with numerous published studies, and the authors suggest that other studies used slices from immature animals and that connections are eliminated as animals mature. The authors fail to cite or address previous studies from adult animals [e.g., (3)] in which connections were assessed using sharp electrode recordings (which sample deeper cells) and thicker slices that revealed connection rates comparable to those in younger animals (typically at least 10 to 20% connected pairs).

Moreover, not all connections are cut equally, and the loss of connectivity depends on the trajectory of the axon of different cell types and the plane of sectioning, as well as laminar location and distance (2). Therefore, the connectivity matrix reported by Jiang *et al.* is likely scaled down and distorted.

This is just one example of a discrepancy with published studies and a single example of a limitation of the methods used; not all discrepancies can be so easily resolved based on the published literature. Other limitations include the use of current clamp to measure synaptic responses, which will bias conclusions of connectivity depending on the input resistance of the postsynaptic cells and will favor large connections, and the exclusive usage of potassium gluconate-based intracellular solution, which is associated with severe space-clamp problems (4). Further experi-

ments using complementary approaches and direct comparisons across ages will be necessary to resolve discrepancies between this study and the published literature.

Concerning the identification and classification of cell types, community efforts to arrive at a unified nomenclature (5) have not resulted in complete agreement. However, there is consensus that multiple parameters must be measured and used. Jiang *et al.* defined their cells primarily based on morphological reconstructions. The computational methods for classification were not confirmed with external validators provided by different methods. This is necessary because, by definition, any classification algorithm used will generate a classification, regardless of whether it is real.

Using these methods, the authors claim to have discovered several “new cell classes,” but it is not clear that their groupings really represent distinct groups or are new. They imply, for instance, that, other than Martinotti cells, no other interneuron types were previously described in layer 5. This is at odds with publications reporting vasointestinal peptide (VIP) bipolar interneurons in layer 5 [e.g., (6) and earlier references therein]

<sup>1</sup>159C Mellon Institute, Department of Biological Sciences, Carnegie Mellon University, 4400 Fifth Avenue, Pittsburgh, PA 15213, USA. <sup>2</sup>Department of Anatomy and Neurobiology, Washington University School of Medicine, St. Louis, MO 63110, USA. <sup>3</sup>Systems Neurobiology Laboratories, The Salk Institute for Biological Studies, 10010 North Torrey Pines Road, La Jolla, CA 92037, USA. <sup>4</sup>Department of Neuroscience, Division of Biology and Medicine, Brown University, Providence, RI 02912, USA. <sup>5</sup>Neuroscience Paris Seine (NPS), Cortical Network and Neurovascular Coupling (CNVC), CNRS UMR 8246, Inserm U 1130, UPMC UM 119, Université Pierre et Marie Curie, 9 Quai Saint Bernard, 75005 Paris, France. <sup>6</sup>Laboratorio Cajal de Circuitos Corticales, Centro de Tecnología Biomédica, Universidad Politécnica de Madrid, Campus Montegancedo S/N, Pozuelo de Alarcón, 28223 Madrid, Spain. <sup>7</sup>Instituto Cajal (CSIC), Avenida Doctor Arce 37, 28002 Madrid, Spain. <sup>8</sup>Institut für Neurowissenschaften und Medizin (INM-2), Forschungszentrum Jülich, 52425 Jülich, Germany. <sup>9</sup>Department of Cellular and Network Neurobiology, Laboratory of Cerebral Cortex Research, Institute of Experimental Medicine, Hungarian Academy of Sciences, H-1450 Budapest, POB 67, Hungary. <sup>10</sup>Division of Cerebral Circuitry, National Institute for Physiological Sciences, 5-1 Myodaiji-Higashiyama, Okazaki, Aichi 444-8787, Japan. <sup>11</sup>University of Debrecen, Department of Anatomy, Histology, Embryology, Laboratory for Cortical Systems Neuroscience, Nagyerdei krt. 98, 4012 Debrecen, Hungary. <sup>12</sup>Laboratory of Cellular and Synaptic Neurophysiology, National Institute of Child Health and Human Development, 35 Convent Drive MSC3715, Bethesda, MD 20892, USA. <sup>13</sup>Max Planck Institute for Biological Cybernetics, Computational Neuroanatomy Group, D-72076 Tübingen, Germany. <sup>14</sup>Neuroscience Paris Seine, Université Pierre et Marie Curie (UPMC) Paris VI, 7-9 Quai Saint Bernard, 75005 Paris, France. <sup>15</sup>Neuroscience Institute, Department of Anesthesiology, Perioperative Care, and Pain Medicine, New York University School of Medicine, Smilow Research Center, 522 First Avenue, New York, NY 10016, USA. <sup>16</sup>University Medicine Goettingen, Center for Anatomy, Institute for Neuroanatomy, Kreuzberggring 36, D-37075 Goettingen, Germany. <sup>17</sup>Medical Research Council Brain Network Dynamics Unit, Department of Pharmacology, University of Oxford, Mansfield Road, Oxford, OX1 3TH, UK. <sup>18</sup>Research Group for Cortical Microcircuits of the Hungarian Academy of Sciences, Department of Physiology, Anatomy and Neuroscience, University of Szeged, Közép Fásor 52, Szeged, H-6726 Hungary. <sup>19</sup>Kavli Institute of Brain Science, Columbia University, Department of Biological Sciences, West 120 Street, New York, NY 10027, USA.

\*Corresponding author. Email: jochen.staiger@med.uni-goettingen.de (J.S.); rudyb01@med.nyu.edu (B.R.); callaway@salk.edu (E.C.)

and the studies on fast-spiking parvalbumin (PV) basket cells in this layer [recently reviewed by (7)]. The authors redefine and rename interneuron types resulting in claims of novel cell classes and improper acknowledgment of much of the literature. For instance, their new cell types in layer 5—including the shrunken cell (SC), the horizontally elongated cell (HEC), and the VIP-expressing bitufted cell (BTC)—appear to correspond to previously described interneurons: (i) SCs resemble small and nest basket cells (8); (ii) HECs resemble layer 5a fast-spiking basket cells that have an axonal arbor that is horizontally focused in the narrow layer 5a [e.g., (9, 10)]; and (iii) the VIP-expressing BTCs likely correspond to the VIP bipolar interneurons previously described in layers 2 to 6 (6). A more careful comparison to the cell types described in the literature and analysis should be performed before it is concluded that a new cell type has been discovered. Last, given the large sample presented by Jiang *et al.*, it is surprising that several well-documented interneuron types, such as cholecystokinin (CCK) basket cells

and  $\gamma$ -aminobutyric acid-releasing (GABAergic) projection cells (11, 12), were missed, although their representation is likely much higher than 1 in 1000. This suggests that the selection of types to categorize and illustrate might have been biased.

Contrary to the authors' claim that they have provided "the most complete wiring diagram of neocortical microcircuits to date," their description is incomplete, partly arbitrary, and also not definitive. The completeness of their description does not rival the accumulated knowledge from decades of studies on cortical connectivity using a diverse range of complementary and powerful techniques. It ignores cortical layers 4 and 6 and focuses largely on the diversity of inhibitory neurons in layers 2/3 and 5, with little consideration for the diversity of excitatory neuron types, and there is no consideration of gap-junction coupling, a major feature of the connectivity between interneurons. We hope that our colleagues will recognize that this study adds to a growing body of knowledge about the cell types and connec-

tivity of the cerebral cortex, but we are far from finished.

## REFERENCES

1. X. Jiang *et al.*, *Science* **350**, aac9462 (2015).
2. A. Stepanyants, L. M. Martinez, A. S. Ferecskó, Z. F. Kisvárdy, *Proc. Natl. Acad. Sci. U.S.A.* **106**, 3555–3560 (2009).
3. A. M. Thomson, D. C. West, Y. Wang, A. P. Bannister, *Cereb. Cortex* **12**, 936–953 (2002).
4. S. R. Williams, S. J. Mitchell, *Nat. Neurosci.* **11**, 790–798 (2008).
5. G. A. Ascoli *et al.*, *Nat. Rev. Neurosci.* **9**, 557–568 (2008).
6. A. Prönnke *et al.*, *Cereb. Cortex* **25**, 4854–4868 (2015).
7. A. Naka, H. Adesnik, *Front. Neural Circuits* **10**, 35 (2016).
8. Y. Wang, A. Gupta, M. Toledo-Rodriguez, C. Z. Wu, H. Markram, *Cereb. Cortex* **12**, 395–410 (2002).
9. G. Doron, M. von Heimendahl, P. Schlattmann, A. R. Houweling, M. Brecht, *Neuron* **81**, 653–663 (2014).
10. W. Muñoz, R. Tremblay, B. Rudy, *Cell Reports* **9**, 2304–2316 (2014).
11. A. Caputi, S. Melzer, M. Michael, H. Monyer, *Curr. Opin. Neurobiol.* **23**, 179–186 (2013).
12. R. Tomioka *et al.*, *Eur. J. Neurosci.* **21**, 1587–1600 (2005).

29 February 2016; accepted 3 August 2016  
10.1126/science.aaf5663



## TECHNICAL RESPONSE

## NEUROSCIENCE

# Response to Comment on “Principles of connectivity among morphologically defined cell types in adult neocortex”

Xiaolong Jiang,<sup>1\*</sup> Shan Shen,<sup>1</sup> Fabian Sinz,<sup>1</sup> Jacob Reimer,<sup>1</sup> Cathryn R. Cadwell,<sup>1</sup> Philipp Berens,<sup>1,2,3,4</sup> Alexander S. Ecker,<sup>1,2,4</sup> Saumil Patel,<sup>1</sup> George H. Denfield,<sup>1</sup> Emmanouil Froudarakis,<sup>1</sup> Shuang Li,<sup>1</sup> Edgar Walker,<sup>1</sup> Andreas S. Tolias<sup>1,2\*</sup>

The critique of Barth *et al.* centers on three points: (i) the completeness of our study is overstated; (ii) the connectivity matrix we describe is biased by technical limitations of our brain-slicing and multipatching methods; and (iii) our cell classification scheme is arbitrary and we have simply renamed previously identified interneuron types. We address these criticisms in our Response.

**W**e will address Barth *et al.*'s (1) three critiques of our Research Article (2) in turn. (i) The strength of our study is the number of connections tested (>11,000) in one species, cortical area, and age range, using the same experimental protocol. We agree that our study is not exhaustive, because it is focused on synaptic connectivity between interneurons in layers 1, 2/3, and 5, and we point this out in the abstract of the original paper. However, we do believe that no single study to date has presented a more complete wiring diagram of the adult neocortical microcircuit.

(ii) Severed connections are a well-known limitation of slice recordings, which we discussed explicitly on p. 3 of the supplementary materials (SM) for (2). However, we do not agree that our study is substantially more susceptible to connection loss than previous patching studies, most of which also used 300- to 350- $\mu$ m slices [we found fewer than half a dozen multipatching studies using 450- to 500- $\mu$ m slices (3–5)]. Although cell depth is not reported in many of these studies, the depths at which we recorded (15 to 60  $\mu$ m) seem typical (6). We patched cells at a wide range of intersomatic distances [see fig. S13A in (2)]; this range reflects the sparsity of labeled interneurons and is not a limitation of octupole patching.

Like many previous studies, we used current-clamp mode to measure connectivity, which suffers less distance-dependent voltage attenuation compared with voltage clamp (7). Using potassium internal solution allowed us to characterize spiking

properties and test bidirectional connectivity, whereas cesium-based internal solutions would prevent the patched neuron from firing. We discussed potential problems of voltage attenuation [SM for (2), p. 9], such as the underestimation of synaptic event amplitudes and potential non-detection of small synaptic events on the distal dendrites [e.g., connections from Martinotti cells onto layer 5 (L5) pyramidal neurons].

To directly address Barth *et al.*'s concern that the connectivity matrix may be distorted due to slice cutting, we simulated the effect of slicing based on interneuron morphology (8) (Fig. 1A) [see also (6)] for the worst-case scenario where two neurons (pre- and postsynaptic) are both located 15- $\mu$ m deep from the cutting surface. The resulting correction factor was similar across pairs of cell types (Fig. 1B), more or less scaling the entire connectivity matrix by a factor of  $1.36 \pm 0.10$  (mean  $\pm$  SD) (Fig. 1, C and D). Given these results and the fact that our connectivity principles mostly rely on the presence or absence of connectivity between specific types regardless of its magnitude, we believe that our connectivity principles are valid rules of cortical organization.

A key concern of Barth *et al.* is our finding of much lower connectivity between excitatory cells compared with previous studies, which we believe could reflect true differences in connectivity between adult and juvenile animals. Ours is the first large-scale slice electrophysiology study on adult mice ( $\geq 2$  months). Most others were typically done on rodents 14 to 21 days postnatal (P14 to P21). [Based on the weight range, the study that Barth *et al.* cite (9) appears to use juveniles as well.] When we tested connectivity among layer 5 pyramidal neurons in juvenile (P15 to P20) slices, we found it to be around 10% for nearby neurons (18 of 186 pairs in  $< 50$   $\mu$ m radius), comparable to previous reports (10, 11) and significantly higher than the connectivity we measured in adult slices using the same technique (0 of 44 pairs in  $< 50$   $\mu$ m

radius;  $P < 0.02$ , Mann-Whitney U test). However, synaptic weights in adult pyramidal cells could be smaller in amplitude, or synapses could be electrotonically further from the soma, both of which might put them below the detection limit. Slicing could also affect adult tissue differently than juvenile tissue. For example, pyramidal cells may be more likely to survive in juvenile slices. Therefore, we generally agree with Barth *et al.* that a detailed comparison of connectivity in juvenile and adult animals is needed. Improved in vivo approaches, such as rabies virus circuit mapping or large-scale electron microscopy reconstruction (12–14), will be crucial to resolve the issues mentioned above, including the rare occurrence of gap junctions in our adult slices.

(iii) The lack of a unified taxonomy of cell types has been a major challenge in neuroscience (15, 16). Our interneuron classification was based on morphological features (17–19) and was validated by an automated method using cross-validated logistic regression. With random class labels, the classification accuracy dropped to  $\sim 48\%$  on average (from  $\sim 97\%$ ), suggesting that our morphological classification scheme is robust. When we projected the morphological features on the weight vector of the classifier, we found a clear clustering of cell types, further corroborating our method. Finally, our classification was confirmed independently for L1 interneurons by a recent single-cell transcriptomics study (20). Some of the morphological types we found might be further subdivided, but more data are needed. All fully reconstructed neurons from our study ( $n = 298$ ) have been submitted to NeuroMorpho.org and will soon be publicly available.

Barth *et al.* are correct that we are not the first to study L5 interneurons. For example, previous studies (21, 22) recovered a few L5 parvalbumin-expressing (PV) neurons that resemble horizontally elongated cells (HECs). However, the validation of a morphological cell type requires a much larger amount of data. By recovering the morphology of many L5 neurons, we found that L5 PV neurons have three distinct morphologies (axon confined locally, axon extending horizontally, and axon projecting to both L5 and L2/3) with distinct connectivity profiles, suggesting that L5 PV neurons form a heterogeneous group. The L5 basket cells (BCs) were similar to L2/3 BCs, whereas shrub cells (SCs) and HECs were different in every respect. It is unlikely that the fast-spiking SCs reported in our study are identical to the small and nest basket cells reported in (23), because small and nest basket cells often display an adapting regular-spiking firing pattern (unlike SCs) and were observed in neocortical L2/3 and L4 (unlike SCs) (23). In adult visual cortex, we found that L5 vaso-intestinal peptide (VIP-cre/Ai9 mice) (24) cells were very sparse, and the few we studied did not exhibit obvious bipolar morphology as previously reported in somatosensory cortex (25). Therefore, more work is needed to study the L5 VIP types.

Barth *et al.* point out that we did not find certain previously described interneuron subtypes [namely, cholecystokinin-expressing (CCK<sup>+</sup>) BCs and long-range  $\gamma$ -aminobutyric acid-releasing

<sup>1</sup>Department of Neuroscience, Baylor College of Medicine, Houston, TX, USA. <sup>2</sup>Bernstein Centre for Computational Neuroscience, Tübingen, Germany. <sup>3</sup>Institute for Ophthalmic Research, University of Tübingen, Tübingen, Germany. <sup>4</sup>Werner Reichardt Center for Integrative Neuroscience and Institute of Theoretical Physics, University of Tübingen, Tübingen, Germany.

\*Corresponding author. Email: astolias@bcm.edu (A.S.T.); xiaolongj@bcm.edu (X.J.)

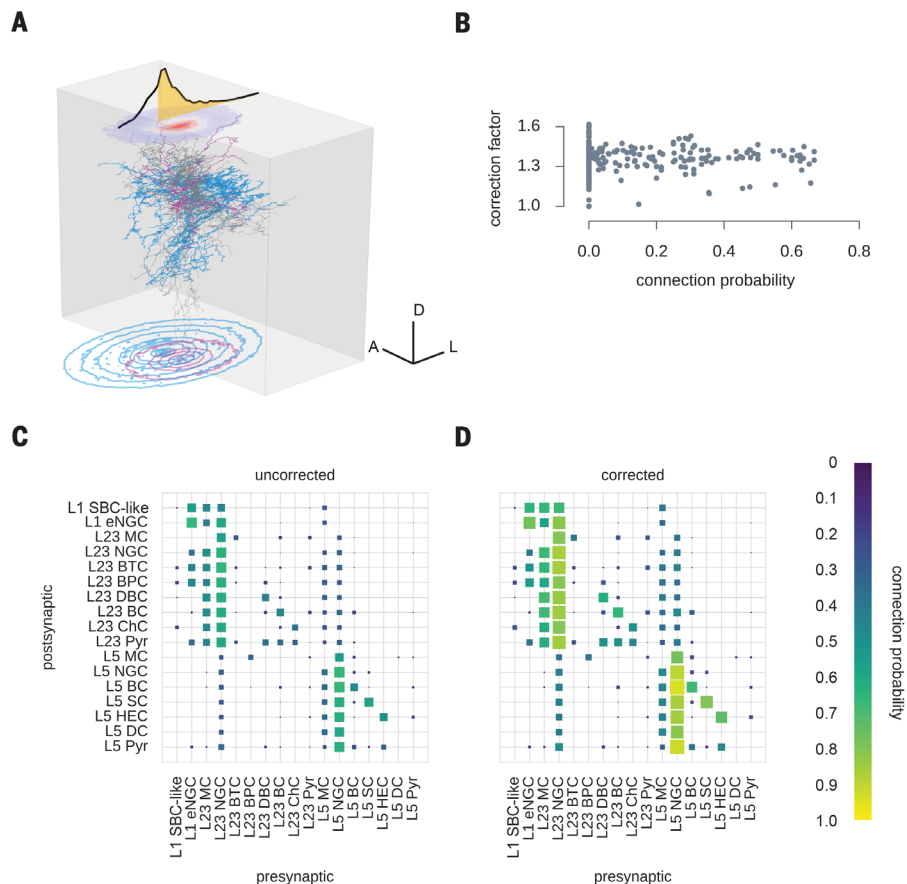


**Fig. 1. Slice cutting does not distort the connectivity matrix.** (A) Schematic of the correction factor estimation. For each pair of cell types (here, L23 Martinotti cells and L23 BCs), we compute pre-synaptic axonal densities (blue; here, L23 Martinotti cell) and postsynaptic dendritic densities (violet; here, L23 BC) by rasterizing all neurons of those particular types, randomly rotating the single points around an axis orthogonal to the pial surface, and binning the result in a three-dimensional histogram. Only one neuron per type is shown here for clarity. The bottom contour plots depict the marginal densities for the dendrites (blue) and the axons (violet) of the example cell type pair after radial symmetrization. The neurons of each type were centered on their cell bodies, and the different types were offset by different amounts measured in our experiments. For each offset, we computed the product of the two densities (overlap density, top contour plot) and the relative volume that remains after slice cutting (yellow area under the black marginal density,  $1 - q$ ). The inverse of this value is used as a correction factor for the connection probabilities  $1/(1 - q)$ . The gray rectangular solid represents a single 300- $\mu\text{m}$  slice. A, D, and L represent the anterior, dorsal and lateral axes, respectively. To mimic the worst-case scenario, the neuron somata were placed 15  $\mu\text{m}$  away from the cutting surface (somata not shown for clarity). (B) Correction factor was weakly correlated with the connection probability. The resulting correction factors had a mean and SD of  $1.36 \pm 0.10$ . Pearson correlation between connection probability and the correction factor is 0.02. (C) Original connection probability ( $p$ ) matrix as shown in (2). (D) Corrected connection probability  $p/(1 - q)$  matrix. The structure of the connection probability matrix is very similar to the original one shown in (C). Although cutting does change the connection probabilities, our analysis indicates that it does not affect our connectivity principles because the entire matrix is scaled globally instead of overemphasizing single-connection probabilities.

(GABAergic) interneurons] in our study.  $\text{CCK}^+$  BCs have been well documented in the hippocampus (26) but are less well characterized in neocortex.  $\text{CCK}^+$  BCs in the neocortex have been reported in rats (27, 28) and  $\text{CCK}^+$  cells are thought to be rare [only 5% of all GABAergic interneurons in adult mouse visual cortex (29)] and heterogeneous. None of the BCs in our data set appear to fit the electrophysiological profile of  $\text{CCK}^+$  BCs. If they exist in adult visual cortex, they might have been missed in our study because of their low prevalence. Long-range GABAergic cells in the neocortex are also rare (<0.5% of all interneurons), and 60 to 90% of them are located in L6 and the white matter (30–32), neither of which were targeted in our study. If they do exist in L1 to L5, they could be easily missed in our study because their main axon may be cut during slicing.

In summary, we believe that many of the potential confounds raised by Barth *et al.* apply quite generally to in vitro patching experiments and do not especially bias our study. Beyond their specific technical concerns, the main message of the Barth *et al.* Comment seems to be that more work is needed to validate and extend the cortical connectivity matrix. On this point, we respond with enthusiastic agreement. By continued application of the multipatching approach and the

addition of complementary approaches in the intact brain (12–14, 33–36), we hope to asymptotically approach the true underlying average connectivity matrix and to identify variations linked to species, ages, and cortical areas. These are exciting times, and we look forward to participating in this common concerted effort.

#### REFERENCES

1. A. Barth *et al.*, *Science* **353**, 1108 (2016).
2. X. Jiang *et al.*, *Science* **350**, aac9462 (2015).
3. M. Beierlein, J. R. Gibson, B. W. Connors, *Nat. Neurosci.* **3**, 904–910 (2000).
4. J. R. Gibson, M. Beierlein, B. W. Connors, *Nature* **402**, 75–79 (1999).
5. Y. H. Tanaka *et al.*, *Front. Neural Circuits* **5**, 12 (2011).
6. R. B. Levy, A. D. Reyes, *J. Neurosci.* **32**, 5609–5619 (2012).
7. S. R. Williams, S. J. Mitchell, *Nat. Neurosci.* **11**, 790–798 (2008).
8. A. Stepanyants, L. M. Martinez, A. S. Ferecskó, Z. F. Kisvárdy, *Proc. Natl. Acad. Sci. U.S.A.* **106**, 3555–3560 (2009).
9. A. M. Thomson, D. C. West, Y. Wang, A. P. Bannister, *Cereb. Cortex* **12**, 936–953 (2002).
10. H. Markram, J. Lübke, M. Frotscher, A. Roth, B. Sakmann, *J. Physiol.* **500**, 409–440 (1997).
11. S. Song, P. J. Sjöström, M. Reigl, S. Nelson, D. B. Chklovskii, *PLOS Biol.* **3**, e68 (2005).
12. E. A. Rancz *et al.*, *Nat. Neurosci.* **14**, 527–532 (2011).
13. J. H. Marshel, T. Mori, K. J. Nielsen, E. M. Callaway, *Neuron* **67**, 562–574 (2010).
14. W. C. Lee *et al.*, *Nature* **532**, 370–374 (2016).
15. J. DeFelipe *et al.*, *Nat. Rev. Neurosci.* **14**, 202–216 (2013).
16. L. A. Jorgenson *et al.*, *Philos. Trans. R. Soc. Lond. B Biol. Sci.* **370**, 20140164 (2015).

17. G. A. Ascoli *et al.*, *Nat. Rev. Neurosci.* **9**, 557–568 (2008).
18. X. Jiang, G. Wang, A. J. Lee, R. L. Stormetta, J. J. Zhu, *Nat. Neurosci.* **16**, 210–218 (2013).
19. H. Markram *et al.*, *Nat. Rev. Neurosci.* **5**, 793–807 (2004).
20. C. R. Cadwell *et al.*, *Nat. Biotechnol.* **34**, 199–203 (2016).
21. G. Doron, M. von Heimendahl, P. Schlattmann, A. R. Houweling, M. Brecht, *Neuron* **81**, 653–663 (2014).
22. W. Muñoz, R. Tremblay, B. Rudy, *Cell Reports* **9**, 2304–2316 (2014).
23. Y. Wang, A. Gupta, M. Toledo-Rodriguez, C. Z. Wu, H. Markram, *Cereb. Cortex* **12**, 395–410 (2002).
24. H. Taniguchi *et al.*, *Neuron* **71**, 995–1013 (2011).
25. A. Prönnke *et al.*, *Cereb. Cortex* **25**, 4854–4868 (2015).
26. T. F. Freund, I. Katona, *Neuron* **56**, 33–42 (2007).
27. A. L. Bodor *et al.*, *J. Neurosci.* **25**, 6845–6856 (2005).
28. Y. Kawaguchi, S. Kondo, *J. Neurocytol.* **31**, 277–287 (2002).
29. Y. Gonchar, Q. Wang, A. H. Burkhalter, *Front. Neuroanat.* **1**, 3 (2007).
30. N. Tamamaki, R. Tomioka, *Front. Neurosci.* **4**, 202 (2010).
31. R. Tomioka *et al.*, *Eur. J. Neurosci.* **21**, 1587–1600 (2005).
32. C. Rock, H. Zurita, C. Wilson, A. J. Apicella, *eLife* **5**, e15890 (2016).
33. K. L. Briggman, M. Helmstaedter, W. Denk, *Nature* **471**, 183–188 (2011).
34. H. K. Ouyibo, P. Znamenskiy, H. V. Oviedo, L. W. Enquist, A. M. Zador, *Front. Neuroanat.* **8**, 86 (2014).
35. J. L. Morgan, D. R. Berger, A. W. Wetzel, J. W. Lichtman, *Cell* **165**, 192–206 (2016).
36. M. N. Economo *et al.*, *eLife* **5**, e10566 (2016).

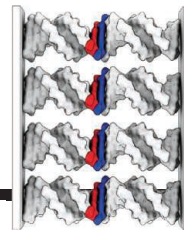
7 April 2016; accepted 3 August 2016  
10.1126/science.aaf6102



# RESEARCH

## Origami structures for DNA stacking forces

Kilchherr et al., p. 1116



## IN SCIENCE JOURNALS

Edited by **Caroline Ash**



### GEOPHYSICS

## Filling in the aftershock gap

**T**he aftershocks after an earthquake provide important data for future hazard assessments in seismically active regions. Fan and Shearer tackle the challenge of identifying aftershocks that occur within seconds of the main earthquake. It turns out that large dynamically triggered aftershocks—earthquakes caused by the mainshock—are more common than previously recognized. —BG

*Science*, this issue p. 1133

**Data from large aftershocks help with regional hazard assessment.**

### MEMORY

## Assessing the brain's memory storage capacity

A hallmark property of the neuronal network in the hippocampus of the brain is its ability to retrieve patterns from partial or noisy cues. This process is called pattern completion. Despite the importance of pattern completion for memory retrieval, its underlying synaptic mechanisms are poorly understood. By simultaneously recording from up to eight neurons, Guzman *et al.* found sparse connections between CA3 pyramidal cells in the hippocampus and few synaptic contacts. Computational modeling revealed that such concise macroscopic and microscopic connectivity combine to ensure efficient memory storage and retrieval in this brain region. —PRS

*Science*, this issue p. 1117

### ANIMAL BEHAVIOR

## Counting up or eyeing the sky?

Ants have remarkable navigation abilities. The accurate measurement of distance by ants is thought to be based on counting strides. Previous work indicates that ants can also measure distance by the movement of the landscape past the eyes (optic flow). Pfeffer and Wittlinger capitalized on the distinctive



*Cataglyphis bicolor* with blindfolded eyes

behavior of *Cataglyphis* ants, which carry their nest mates, to distinguish the relative importance of these strategies. They found that both approaches are used but operate independently, and that carried ants exclusively use optic flow. —SNV

*Science*, this issue p. 1155

### INHIBITORY SYNAPSES

## Identifying synapse-specific proteins

Recently, we have seen enormous progress in our understanding of the protein complexes at excitatory synapses. Much less is known about the molecules at inhibitory synapses. Uezu *et al.* have discovered that many molecules cluster at postsynaptic inhibitory structures to form a network of proteins with, as

yet, mostly unknown functions. However, one novel component, called InSyn1, has been found to colocalize with key scaffolding proteins and regulate inhibitory synaptic transmission in hippocampal neurons. —PRS

*Science*, this issue p. 1123

### ORGANIC CHEMISTRY

## A rhodium route from C–H to C–N bonds

Linking nitrogen to the carbons in aryl rings is a common need in pharmaceutical chemistry. To do so, the carbon usually has to be adorned ahead of time with a reactive group, such as bromide. Paudyal *et al.* report a rhodium-catalyzed reaction that substitutes aryl C–H bonds with nitrogen groups directly to produce a wide variety of aromatic amines. Cleavage of a N–O bond

in the nitrogen-bearing precursor drives the reaction with no need for an external oxidant. All of this can be done for both intermolecular and intramolecular couplings. —JSY

*Science*, this issue p. 1144

## MATERIALS SCIENCE

### Flexible and lightweight shielding

Electromagnetic shielding can be used to isolate devices from outside interference or to protect people from the radiation generated by a device. Shielding usually takes the form of metal sheets, screens, or foams, but often a flexible and lightweight material is preferable. To fulfill this goal, Shahzad *et al.* have constructed a shielding material from flakes of transition metal carbides embedded in a polymer matrix. A multilayered material improves shielding effectiveness owing to the greater absorption resulting from multiple internal reflections of the electromagnetic waves. —MSL

*Science*, this issue p. 1137

## INTERNET ACCESS

### Persistent political bias in Internet allocation

Many groups are using the Internet as a way to share information, organize, and increase their influence. However, there is a digital divide that impedes such efforts that cannot be explained by socioeconomic or geographic factors. Weidmann *et al.* show that ethnic groups who are excluded from political power within countries also have less access to the Internet. —BJ

*Science*, this issue p. 1151

## CELL MIGRATION

### Dissecting collective cell migration

During development or wound healing, cells frequently move in concert. Sunyer *et al.* describe a mechanism by which clusters of cells respond to a

gradient in the stiffness of the extracellular matrix. The same machinery that senses stiffness, the actomyosin cytoskeleton, is responsible for propulsion toward it. This so-called collective durotaxis appears to be a simple and primitive, but nonetheless efficient, mechanism by which clusters of cells migrate. —SMH

*Science*, this issue p. 1157

## ALZHEIMER'S DISEASE

### Losing memory by protein cleavage

Learning and remembering changes the shape of neurons. In mouse models of Alzheimer's disease, neurons do not undergo the morphological changes induced by learning and remembering and they also have defects in calcium signaling. Tong *et al.* found that forms of presenilin-1 (PS1) with familial Alzheimer's disease-associated mutations excessively cleaved and inactivated the calcium sensor STIM1. The cleavage of STIM1 by PS1 may contribute to the memory loss that is characteristic of Alzheimer's disease. —WW

*Sci. Signal.* **9**, ra89 (2016).

## CANCER

### Standardizing the CAR assembly line

Chimeric antigen receptor–modified T (CAR-T) cells are engineered to recognize specific tumor antigens. They have shown promising results in clinical trials for leukemia, but it has been difficult to predict therapeutic efficacy and toxicity for individual patients. To address this issue, Turtle *et al.* treated non-Hodgkin's lymphoma patients with CAR-T cells prepared from strictly defined subsets. By carefully controlling the ratio of CD4 to CD8 T cells, treatment conditions can be characterized that correlate with therapeutic response and toxicity, including the drug regimen before CAR-T treatment. —YN

*Sci. Transl. Med.* **8**, 355ra116 (2016).

## IN OTHER JOURNALS

Edited by **Kristen Mueller**  
and **Jesse Smith**

## MICROBIOLOGY

### Sexual development in schistosomes

Schistosomiasis is a severe parasitic disease that affects ~200 million people globally. The flatworms that cause the disease have a complex life cycle in which, unusually, male and female worms must pair to produce eggs. Eggs trapped in host body tissues are the main cause of pathology. Lu *et al.* used RNA-sequencing analysis to show that gonad development in females requires pairing and occurs when the juvenile worms pass through the host's liver. They also found that neuropeptidergic signaling stimulates female gonad development. At present, there is only one safe treatment for schistosomiasis, and thus elucidating the details of sexual development in schistosomes may offer valuable targets for drugs and vaccines. —CA

*Sci. Rep.* **6**, 31150 (2016).



Gonad development in female schistosome worms relies on pairing with males.

## FISHERIES

### Modeling the distribution of tuna fleets

The purse-seine tuna fishery in the eastern Pacific Ocean, off the west coast of the Americas, is fished by vessels with thousand-ton capacities that range over an area the size of Canada. The large size of the fishery means

that vessel distribution is patchy. Sun *et al.* developed a model to predict vessel distribution on the basis of decisions that skippers make before and after going to sea. The model accounts for environmental factors such as chlorophyll content and dissolved oxygen concentration, as well as weather conditions. Modeling the far-flung fishery can inform



ALSO IN *SCIENCE* JOURNALSEdited by **Caroline Ash**

## SOCIAL SCIENCES

**The many human impacts of climate**

It is now possible to link specific human outcomes to weather events that are drawn from the probability distribution of climate, thanks to high-dimensional data sets and longitudinal analysis. Carleton and Hsiang review recent findings in the areas of human health, economics, social conflict, and demographics, all of which show marks of changes in climate. —GJC

*Science*, this issue p. 1112

## CLIMATE CHANGE

**Improving predictions**

Climate change is here, and understanding how we might mitigate its effects is a priority. Despite the urgency, attaining an understanding of the responses of complex natural systems to climate is an incredibly challenging venture. In a Review, Urban *et al.* find that the biggest obstacle to making accurate predictions is a lack of basic data across species. Improved acquisition of such data, in conjunction with improved theoretical models, is vital to understand what may happen to ecosystems under changing climate conditions. —SNV

*Science*, this issue p. 1113

## MACROPHAGES

**How tissue macrophages differentiate**

Immune cells called macrophages reside in nearly every organ of the body, where they play roles in pathogen resistance

and tissue homeostasis and repair. Although the tissue microenvironment strongly shapes macrophage phenotype and function, all tissue macrophages arise during embryonic development and originate, at least in part, from a common progenitor. Using a variety of techniques, including population-level and single-cell RNA sequencing, Mass *et al.* find that tissue macrophages in mice stem from a common precursor called a premacrophage, which colonizes the whole embryo 9 to 10 days after conception. Once seeded in tissues, macrophages acquire diverse gene expression profiles. —KLM

*Science*, this issue p. 1114

## BIOENGINEERING

**Building better cellular memories**

A challenge for bioengineering is to build cellular recording devices that can monitor and store information about the timing and magnitude of events in a living organism. Perli *et al.* describe an ingenious strategy to adapt CRISPR-Cas-mediated genome editing for this task. They modified the editing mechanism so that small guide RNAs act on the same locus in DNA from which the guide RNAs themselves were transcribed. This causes mutagenesis that increases over time and in proportion to the intensity of a signal and leaves a molecular record of the activity of a specific promoter. Such a system could, for example, provide better insight into the location and timing of events that regulate tumor cells as they grow *in vivo*. —LBR

*Science*, this issue p. 1115

## BIOPHYSICS

**How base pairs stack up**

The interactions between nucleic acid bases include not only the hydrogen bonding between bases but also the  $\pi$ -orbital interactions between base pairs. To probe these interactions, Kilchherr *et al.* constructed an ensemble of DNA origami structures of blunt-end DNA strands. The forces in the structures between two particles held together only by stacking interactions were determined with optical tweezers. The derived free energy for stacking interactions varied from  $-0.7$  to  $-3$  kcal/mol, depending on base sequences. —PDS

*Science*, this issue p. 1116

## VACCINES

**Zika vaccines protect monkeys**

The best way to halt the current Zika virus epidemic would be a protective vaccine. Abbink *et al.* tested the immunogenicity and protective efficacy of inactivated virus, gene-based, and vector-based vaccines in rhesus monkeys. All three platforms completely protected the animals from infectious Zika virus challenge (see the Perspective by Lipsitch and Cowling). Antibodies isolated from vaccinated animals conferred protection when passively transferred into unvaccinated mice or monkeys, demonstrating the important role that antibodies play in mediating protection. These studies set the stage for the development and testing of Zika virus vaccines for humans. —KLM

*Science*, this issue p. 1129;

see also p. 1094

## GEOCHEMISTRY

**Iron sulfide sails through the Grand Tack**

A long-standing problem in geochemistry is the sequestration of iron-loving elements into the core of early Earth. Rather than causing the observed depletion of these elements in the mantle, Rubie *et al.* contend that metal segregation during the formation of Earth's core should have increased mantle concentrations. This is because of the high-pressure conditions of core formation that prevailed for Earth when Jupiter was executing its "Grand Tack" through the solar system. The sulfur concentrations in the magma oceans of early Earth became very high during accretion and, as Earth cooled, liquid iron sulfide stripped the mantle of the iron-loving elements, explaining the observed depletion. —BG

*Science*, this issue p. 1141

## ANTIBIOTIC RESISTANCE

**Visualizing evolution in real time**

Microbial antibiotic resistance arises in large, complex natural environments over time. Baym *et al.* developed a large culturing device in which they studied the emergence of resistance over space, time, and increasing antibiotic concentrations (see the Perspective by McNally and Brown). Diverse patterns of mutations always resulted in resistance. Sometimes resistance came with a cost to growth, requiring compensatory mutations to regain fitness. Sometimes mutator phenotypes arose. Unexpectedly, the most fit mutants were not necessarily

the lineages that emerged to invade regions with higher antibiotic concentrations. Often, outgrowths trapped even more resistant lineages behind them. This observatory allows regular sampling to monitor rates and sequences of mutation and can be modified for a range of model organisms and evolutionary questions. —CA

*Science*, this issue p. 1147;  
see also p. 1096

## TUMOR METABOLISM

### Putting precision medicine in tissue context

Cancer patients are often matched to targeted therapies on the basis of the specific driver mutations present in their tumors. For an emerging group of therapies, Mayers *et al.* find that the metabolism of a target tumor may be a key determinant of its response and may be determined by the tumor's tissue of origin, not mutation status alone (see the Perspective by Vousden and Yang). They traced the fate of branched-chain amino acids (BCAAs) in mouse models of lung and pancreatic cancer that were initiated with identical driver mutations. Lung tumors showed increased uptake and utilization of BCAA nitrogen for amino acid and nucleotide biosynthesis. In contrast, pancreatic tumors showed decreased uptake of free BCAAs. These differences indicate that the tissue of origin shapes tumor metabolism and should be considered when matching patients with therapies. —PAK

*Science*, this issue p. 1161;  
see also p. 1095

## ECOLOGY

### Reducing the ecosystem impacts of dams

Around the world, tens of thousands of dams regulate river flow and provide electrical power. By altering water and sediment flows, dams influence downstream ecosystems. In a Perspective, Poff and Schmidt explain that negative downstream effects can be ameliorated at low cost by managing either daily or seasonal water releases to make allowances for local ecosystem requirements. For example, avoiding water releases from a dam on the Colorado River for a few weekends each year could help large insects to recover, thereby also providing food for local fishes. —JFU

*Science*, this issue p. 1099



regulatory decisions aimed at ensuring a sustainable tuna fishery while minimizing dolphin mortality. —PJH

PLOS ONE 10.1371/journal.pone.0159626 (2016).

## SUPERCONDUCTIVITY Lightly doping a Mott insulator

Cuprates usually acquire their superconductivity when charged carriers, typically holes, are chemically introduced into a “parent” state called a Mott insulator. However, this part of the cuprate phase diagram is rich in phases, including a pseudogap and a charge-order phase, whose relationship to each other and to superconductivity is under debate. Cai *et al.* used scanning tunneling spectroscopy of a very lightly doped  $\text{Bi}_2\text{Sr}_{2-x}\text{La}_x\text{CuO}_{6+\delta}$  to unravel the phase conundrum. As the hole dopants were introduced, a pseudogap-like density of states started to emerge, followed by a checkerboard pattern characteristic of the charge order. When further doping caused the material to become superconductive, the charge-order pattern became less prominent, indicating a competition between the two phases. —JS

Nat. Phys. 10.1038/PHYS3840 (2016).

## HOST RESPONSES Inflammation blocks recovery

Although antibiotics can clear the pathogen, doctors typically do not prescribe them to treat nontyphoidal *Salmonella* infections, which are a major cause of gastroenteritis worldwide. This is because antibiotics actually extend the course of disease. Now, Dolowschiak *et al.* provide some insight into why. Using a mouse model of *Salmonella* infection treated with ciprofloxacin, they found that the cytokine interferon- $\gamma$  (IFN $\gamma$ ) promotes intestinal pathology even after the majority of the bacteria are cleared.



Shipping routes across the Arctic Ocean will multiply as climate warms.

## CLIMATE CHANGE IMPACTS

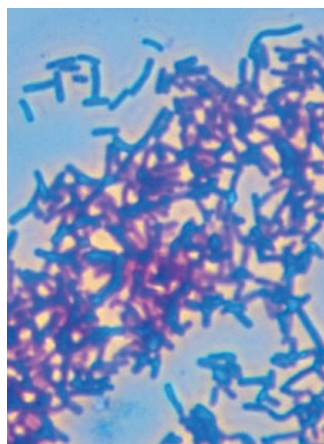
### A sea-route change in the Arctic

Arctic sea ice is rapidly disappearing as climate warms, ushering in an entirely novel era in marine transportation with important economic implications, because more frequent open seas will allow increasing volumes of trans-Arctic shipping. Melia *et al.* used an ensemble of climate models from the Fifth Coupled Model Intercomparison Project to project how sea ice loss might increase opportunities for ocean-going vessels to cross the Arctic. They find that standard open-water vessels will have twice as many navigable periods by the middle of the 21st century as they do now, including some across the central Arctic. The shipping season length could reach 4 to 8 months by late century, when moderately ice-strengthened vessels could be able to complete Arctic transits during 10 to 12 months of the year. —HJS

Geophys. Res. Lett. 10.1002/2016GL069315 (2016).

T cells and natural killer cells make IFN $\gamma$ , which drives pro-inflammatory myeloid cells to accumulate, spewing forth pathology-causing soluble mediators that prevent tissue repair. Targeting this pathway therapeutically may help alleviate the debilitating symptoms that *Salmonella* can cause. —KLM

Cell Host Microbe 20, 238 (2016).



Nontyphoidal *Salmonella* infections are not typically treated with antibiotics.

## INORGANIC CHEMISTRY A pair of tablemates for aromatic benzene

Chemists do not designate a compound as aromatic because it smells nice. Rather, the term refers to the stability conferred by a particular delocalized arrangement of electrons first characterized in benzene and related carbon rings. Is the concept exclusive to carbon? Over the years, inorganic chemists have extended it to a range of analogs composed of other elements, and now Seitz *et al.* introduce two more. Specifically, they prepared hexagonal benzene analogs in which three silicon centers alternate with either three phosphorus or three arsenic centers. Structural and computational characterization supported aromaticity. The reactions fortuitously also produced tetragonal cyclobutadiene analogs that were weakly antiaromatic. —JSY

J. Am. Chem. Soc. 10.1021/jacs.6b07389 (2016).

## STRUCTURAL BIOLOGY Bacteriophage fights back

Bacteria and archaea have CRISPR-Cas systems that target and destroy invading DNA from phages and plasmids. However, invaders can fight back. Wang *et al.* report a structure that shows how the bacteriophage protein AcrF3 inhibits *Pseudomonas aeruginosa* Cas3 (PaCas3). The Cascade protein complex recruits Cas3 to target DNA. In addition to binding to a protein in Cascade, Cas3 also binds the nontarget DNA strand. There, Cas3 uses its ATP-driven helicase domain to open up the DNA and its nuclease domain to degrade it. The structure showed an AcrF3 dimer complexed to ADP-bound PaCas3, thus locking it in an inactive conformation. Moreover, AcrF3 blocked both the DNA and the protein binding sites involved in recruiting Cas3 to target DNA. —VV

Nat. Struct. Mol. Biol. 10.1038/nsmb.3269 (2016).

## REVIEW SUMMARY

## SOCIAL SCIENCES

## Social and economic impacts of climate

Tamma A. Carleton\* and Solomon M. Hsiang\*†

**BACKGROUND:** For centuries, thinkers have considered whether and how climatic conditions influence the nature of societies and the performance of economies. A multidisciplinary renaissance of quantitative empirical research has begun to illuminate key linkages in the coupling of these complex natural and human systems, uncovering notable effects of climate on health, agriculture, economics, conflict, migration, and demographics.

and violence while lowering human productivity. High temperatures also damage crops, inflate electricity demand, and may trigger population movements within and across national borders. Tropical cyclones cause mortality, damage assets, and reduce economic output for long periods. Precipitation extremes harm economies and populations predominately in agriculturally dependent settings. These effects are often quantitatively substantial; for example,

stance, we calculate that current temperature climatologies slow global economic growth roughly 0.25 percentage points year<sup>-1</sup>, comparable to the additional slowing of 0.28 percentage points year<sup>-1</sup> projected from future warming.

Both current and future losses can theoretically be avoided if populations adapt to fully insulate themselves from the climate—why

## ON OUR WEBSITE

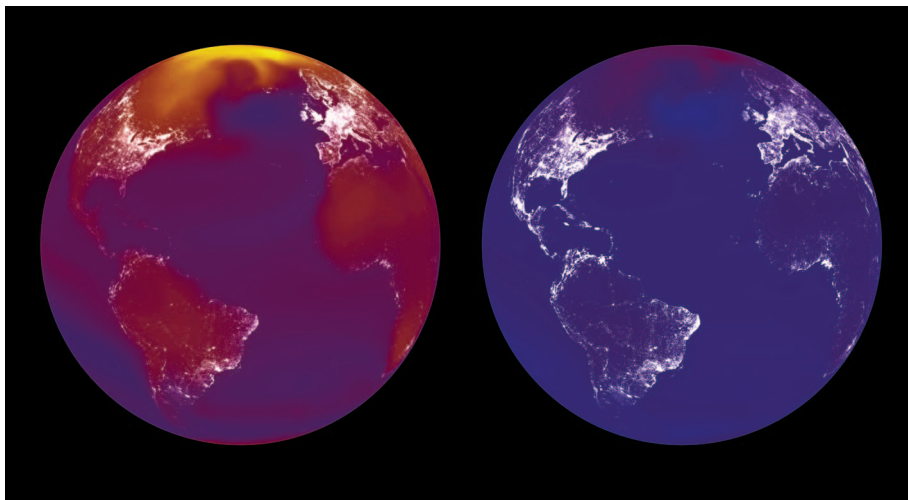
Read the full article at <http://dx.doi.org/10.1126/science.aad9837>

this has not already occurred everywhere remains a critical open question. For example, clear patterns of adaptation in health impacts and in response to tropical cyclones contrast

strongly with limited adaptation in agricultural and macroeconomic responses to temperature. Although some theories suggest these various levels of adaptation ought to be economically optimal, in the sense that costs of additional adaptive actions should exactly balance the benefits of avoided climate-related losses, there is no evidence that allows us to determine how closely observed “adaptation gaps” reflect optimal investments or constrained suboptimal adaptation that should be addressed through policy.

**OUTLOOK:** Recent findings provide insight into the historical evolution of the global economy; they should inform how we respond to modern climatic conditions, and they can guide how we understand the consequences of future climate changes. Although climate is clearly not the only factor that affects social and economic outcomes, new quantitative measurements reveal that it is a major factor, often with first-order consequences. Research over the coming decade will seek to understand the numerous mechanisms that drive these effects, with the hope that policy may interfere with the most damaging pathways of influence.

Both current and future generations will benefit from near-term investigations. “Cracking the code” on when, where, and why adaptation is or is not successful will generate major social benefits today and in the future. In addition, calculations used to design global climate change policies require as input “damage functions” that describe how social and economic losses accrue under different climatic conditions, essential elements that now can (and should) be calibrated to real-world relationships. Designing effective, efficient, and fair policies to manage anthropogenic climate change requires that we possess a quantitative grasp of how different investments today may affect economic and social possibilities in the future. ■



**Two globes depict two possible futures for how the climate might change and how those changes are likely to affect humanity, based on recent empirical findings.** Base colors are temperature change under “Business as usual” (left, RCP 8.5) and “stringent emissions mitigation” (right, RCP 2.6). Overlaid are composite satellite images of nighttime lights with rescaled intensity reflecting changes in economic productivity in each climate scenario.

**ADVANCES:** Past scholars of climate-society interactions were limited to theorizing on the basis of anecdotal evidence; advances in computing, data availability, and study design now allow researchers to draw generalizable causal inferences tying climatic events to social outcomes. This endeavor has demonstrated that a range of climate factors have substantial influence on societies and economies, both past and present, with important implications for the future.

Temperature, in particular, exerts remarkable influence over human systems at many social scales; heat induces mortality, has lasting impact on fetuses and infants, and incites aggression

we compute that temperature depresses current U.S. maize yields roughly 48%, warming trends since 1980 elevated conflict risk in Africa by 11%, and future warming may slow global economic growth rates by 0.28 percentage points year<sup>-1</sup>.

Much research aims to forecast impacts of future climate change, but we point out that society may also benefit from attending to ongoing impacts of climate in the present, because current climatic conditions impose economic and social burdens on populations today that rival in magnitude the projected end-of-century impacts of climate change. For in-

The list of author affiliations is available in the full article online.

\*These authors contributed equally to this work.

†Corresponding author. Email: [shsiang@berkeley.edu](mailto:shsiang@berkeley.edu)

Cite this article as T. A. Carleton and S. M. Hsiang, *Science* 353, aad9837 (2016). DOI: 10.1126/science.aad9837



## REVIEW

## SOCIAL SCIENCES

# Social and economic impacts of climate

Tamma A. Carleton<sup>1,2\*</sup> and Solomon M. Hsiang<sup>2,3,\*†</sup>

For centuries, thinkers have considered whether and how climatic conditions—such as temperature, rainfall, and violent storms—influence the nature of societies and the performance of economies. A multidisciplinary renaissance of quantitative empirical research is illuminating important linkages in the coupled climate-human system. We highlight key methodological innovations and results describing effects of climate on health, economics, conflict, migration, and demographics. Because of persistent “adaptation gaps,” current climate conditions continue to play a substantial role in shaping modern society, and future climate changes will likely have additional impact. For example, we compute that temperature depresses current U.S. maize yields by ~48%, warming since 1980 elevated conflict risk in Africa by ~11%, and future warming may slow global economic growth rates by ~0.28 percentage points per year. In general, we estimate that the economic and social burden of current climates tends to be comparable in magnitude to the additional projected impact caused by future anthropogenic climate changes. Overall, findings from this literature point to climate as an important influence on the historical evolution of the global economy, they should inform how we respond to modern climatic conditions, and they can guide how we predict the consequences of future climate changes.

Does climate affect our society? Or do human willpower and ingenuity render climate largely irrelevant to our affairs, as we overcome environmental challenges with resilience and innovation? If climate affects our lives, how much does it matter and why? Thinkers have asked these questions for generations, wondering whether climatic differences between regions could be partially responsible for differences in politics, economics, and culture, and whether large-scale social transformations, such as the rise of golden ages and the fall of empires, could be triggered by climatic changes. Over the last decade, an innovative community of researchers has taken a rigorous quantitative approach to these questions—mixing data and methods from the climate, social, and statistical sciences—making unprecedented and exciting progress. In this article, we review recent advances, findings, and open questions in this emerging interdisciplinary field.

Our focus is recent progress, but consideration of the social impact of climate is as old as the academy. Aristotle developed a climate classification system in which the tropics were described as an uninhabitable “torrid zone” (1), and Montesquieu argued that climate played a fundamental causal role in determining the structure and prosperity of different societies (2). In the late 19th

century, theories on the impact of climate and other geographical factors led to a collection of ideas known as “environmental determinism,” the notion that environmental conditions played the primary role in shaping social, economic and political outcomes, with little scope for leadership, innovation, institutions, or social will to alter societal trajectories. Some of these hypotheses were invoked to justify European colonialism as responsible paternalism—colonial advocates argued that climatically caused “morally inferior” character traits could be remedied through oversight by “advanced” societies that had already matured in more conducive climes (3).

The association of environmental determinism with colonial ambition had a chilling effect on this line of research in much of the social sciences during the late 20th century. Nonetheless, research continued among engineers and ergonomists interested in optimizing military and industrial performance using laboratory experiments to test the effects of environmental conditions on human performance (4, 5).

Beginning in the 1970s, concern over booming populations led to a blossoming of theoretical work in resource economics. A key realization was that environmental conditions might influence economic performance and could be modeled as “natural capital,” analogous to physical capital (e.g., machines) or human capital (e.g., education), and could be similarly developed or degraded (6).

At the turn of the 21st century, this economic approach, supported by advances in computing, led to the development of theoretical-numerical “integrated assessment models” that provide insights into how the global climate might be

managed to maximize future “global welfare” under different assumptions (7–9). At the core of these models are theoretical “damage functions” that describe how global mean temperature translates into economic and social costs (10). Because these models are now used to design global policies (11, 12), much of the current empirical research summarized here is framed as providing an empirical basis for global climate policy calculations (13, 14).

A research agenda running parallel to climate change policy design is aimed at understanding how current climatic events, such as droughts or tropical cyclones, shape social outcomes today, irrespective of possible future climatic changes. This strand of work aims to minimize current social costs of climate events and promote economic development (15, 16), either by identifying cost-effective risk-management strategies or minimizing harm through reactive instruments or policies, such as weather index insurance (17). As with climate change management, success in this arena depends critically on our quantitative understanding of the causal effect that climatic conditions have on populations.

## Quantifying climatic influence on societies and economies

Recent advances in empirically measuring the effect of climate on society have been rapid, catalyzed by growth in computing power, access to data, and advances in the statistical theory of causal inference for non-experimental studies (18). Progress has been particularly explosive over the last decade, with exponential growth in publication volume due to innovations specific to studying the climate-human system, such as new methods to map climatic data onto social data and the development of spatiotemporal statistical models. For an in-depth treatment of the following techniques and innovations, we refer readers to reference (19).

## Breaking down the problem

Climate is the joint probability distribution over several weather parameters, such as temperature or wind speed, that can be expected to occur at a given location during a specific interval of time (Fig. 1, A and B). To understand how alterations in this distribution affect populations, modern approaches separate the influence of climate into two pathways: through information regarding what environmental conditions might occur and through directly altering what actually happens (19). The “informational” pathway operates because individuals’ expectations about their climate (Fig. 1A) may change how they act; for example, individuals who believe they live in a rainy climate may purchase umbrellas. The “direct” pathway operates because any change in the probability distribution of weather events must generate a change in the distribution of events that individuals actually experience (Fig. 1B); for example, individuals who live in a rainy climate will face rain more often. Informational effects result from individuals preparing for a distribution of weather events and corresponding

<sup>1</sup>Department of Agricultural and Resource Economics, University of California, Berkeley, Berkeley, CA 94720, USA.

<sup>2</sup>Global Policy Lab, Goldman School of Public Policy, University of California, Berkeley, Berkeley, CA 94720, USA.

<sup>3</sup>National Bureau of Economic Research Cambridge, MA 02138, USA.

\*These authors contributed equally to this work. †Corresponding author. Email: shsiang@berkeley.edu

direct effects that they expect. These adaptations may alter the overall direct effect of specific weather events (Fig. 1C)—for example, individuals who own umbrellas may use them to stay drier when an actual rainstorm occurs—a distinction that can be accounted for when examining these relationships empirically.

Figure 1 depicts these two ways that climate and social outcomes are linked. Weather events (Fig. 1B) are drawn from the probability distribution that defines the climate (Fig. 1A). Each event generates some direct effect on a population, where these direct effects can be described by a dose-response function  $f(X)$  where specific “doses” of a weather parameter  $X$  (e.g., rain) generate “responses” within the population (e.g., getting wet; see arrow from Fig. 1, B to D). This sequence of direct effects combine with nonclimatic influences on the social outcome to produce the distribution of observed social data (Fig. 1D and E). If the climate shifts (pink in Fig. 1A), this will alter the distribution of weather (Fig. 1B) and its corresponding social impacts. A direct effect (e.g., experiencing more rainfall) occurs, but the information effect (e.g., buying umbrellas) may also cause populations to adapt such that the structure of the dose-response function changes (Fig. 1C), leading to a shift in the distribution of outcomes that is a combination and interaction of these two effects (Fig. 1E). The core of the empirical challenge is to credibly reconstruct the dose-response function for pairings of weather variables and social outcomes, while simultaneously accounting for the possibility that adaptations alter this relationship.

### Mapping climate data onto societies and economies

The first step in analysis is to collapse large quantities of high-dimensional climate data into measures that efficiently summarize the dimensions of climate that are influential on specific aspects of populations. This procedure is challenging because most weather data are collected by physical scientists with the goal of answering physical science questions, so existing structures used to organize these spatially and temporally varying data do not map directly onto social systems. Often, devising a suitable approach for “translating” physical data into a socially meaningful measure  $X$  is the critical innovation that allows researchers to study an entire class of phenomena (19). For example, the construction of data describing extreme heat-hours, measured in units of “degree days” and properly aggregated across space, led to strikingly consistent measurement of the effect of temperature on crop yields (20–23) and electricity demand (24, 25). In another example, tropical cyclone track data were converted into surface wind-exposure of populations to understand the human and economic damage of these storms (26). In other work, researchers gain insight from developing new measures of human exposure to the El Niño–Southern Oscillation (ENSO) (27), drought indices (28–30), daily temperature distributions (31, 32), rainfall variability (33), crop exposure

to vapor pressure deficits (34), and trade or neighbor network exposure to multiple variables (35–37).

### Using research design to identify causal effects

Once societally relevant measures of climate exposure  $X$  are constructed, measuring the causal effect of a weather event on a societal outcome requires that we compare what actually occurred to a counterfactual outcome that would have occurred had the weather been different (18, 19). For example, simply observing that 10 individuals are admitted to a hospital on a hot day does not imply all 10 admissions were caused by the heat; it might be the case that nine of those individuals would have gone to the hospital anyway, regardless of the temperature.

In an ideal experiment designed to measure the effect of climate on a social outcome, we would take two populations that are identical in every way and expose one to a “control” climate while exposing the other to a “treatment” climate. The

control population serves as the counterfactual for the treatment population, and the difference in outcomes would be the effect of the climate treatment. In general, this experiment is infeasible, forcing researchers to rely on “natural experiments” or quasi-experiments.

Early researchers, stretching back to Montequieu, tried to approximate this ideal experiment, implementing cross-sectional analyses in which different populations inhabiting different climates are compared to one another and their differences are attributed to their climates. For example, a researcher might observe that Nigeria has higher crime rates and is hotter than Norway, concluding that higher temperatures lead to crime. This comparison and conclusion are flawed as there are numerous dimensions along which Norway and Nigeria differ—such as geography, history, culture, politics, social institutions—which make Nigeria an unsuitable “treatment” comparison for a Norwegian “control.” Some researchers have tried to adjust their analyses to account for important factors known to influence their outcome

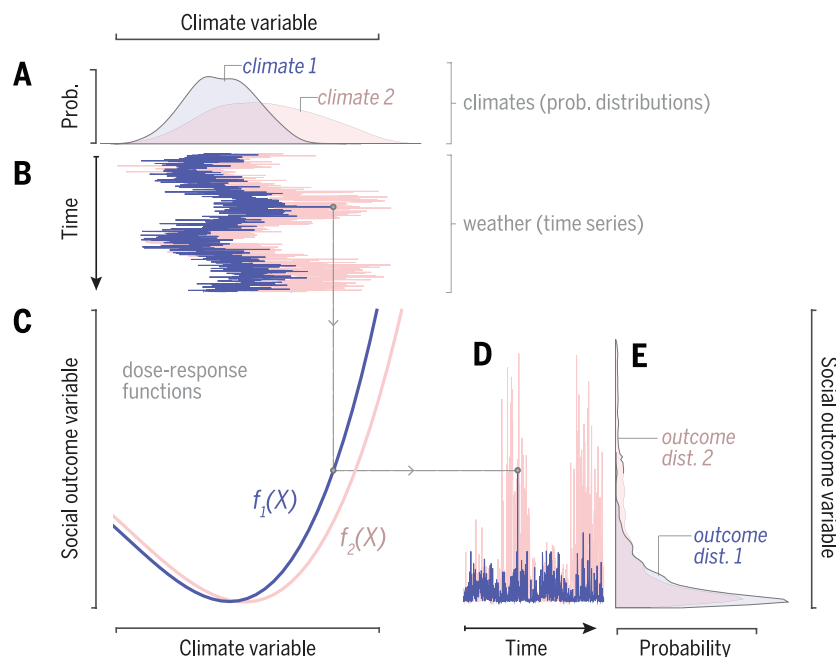


**Fig. 1. Breaking down the influence of climate into analytical components.** Climate affects the distribution of social outcomes by altering the distribution of weather events and how populations prepare and respond to these events. (A) Climate is defined as a probability distribution over weather events, such as the distribution *climate 1* (blue) characterizing the probability of the event *climate variable* =  $X$ , e.g., the likelihood of a rainy day. *climate 2* (pink) characterizes a climate distribution that is shifted to the right and more variable. (B) Weather events over time are realized from each climate, experienced by individuals on the ground, and observed as time series. (C) Statistical analysis recovers “dose-response” functions  $f(X)$  that describe social outcomes as a response to each weather “dosage.” If populations adapt to their climates (*climate 1* and *climate 2*), then they may respond differently to physically similar weather events, producing dose-response functions that differ [blue =  $f_1(X)$ , pink =  $f_2(X)$ ]; e.g., if individuals in rainy climates own umbrellas, they may get less wet than populations in normally dry climates (who own few umbrellas) when both populations experience a day with *rainfall* =  $X$ . (D) Mapping a sequence of weather events through dose-response functions (gray dashed line) generates time series of social outcomes attributable to climatological conditions, accounting both for different distributions of weather events and corresponding adaptations. Signals in an outcome resulting from political, economic, cultural, and other drivers of outcomes might be superimposed on these time series (not shown). (E) Different distributions of expected social outcomes can then be attributable to the two climates (*outcome distribution 1* and *outcome distribution 2*), e.g., how much individuals in each climate were soaked by rain over the course of a year.



of interest, but for many complex social outcomes, such as economic growth or civil conflict, it is impossible to know if all relevant factors have been accounted for, and thus unknowable whether a result is plausibly causal.

Recent work recognizes this weakness of cross-sectional analysis and does not compare different populations to one another. Instead, it leverages the insight that the most comparable group for a certain population is itself, at a moment earlier or later in time. Thus, these longitudinal studies follow individual populations over time and ex-

amine how they respond to changes in the climatic conditions that they face. When using this approach, researchers have confidence that fundamental factors that influence societies, such as geography and political institutions, are “held fixed” because the population is not changing. In essence, a population just before an event serves as the “control” for that same population right after the event “treatment.” Comparing outcomes before and after the climatic event, while accounting for secular trends, provides insight into its effect.

In practice, this approach is complicated by the multiplicity of states that exist for weather and climate, and because societies experience constant variation in both (as suggested by Fig. 1), it is sometimes difficult to determine if an observed social outcome is the result of current conditions or of climatic events in the past. This challenge is solved by deconvolution of the outcome as a series of responses to continuous climatic conditions. Having observed time series of climatic events or “impulses” (Fig. 2A) and resulting outcomes (Fig. 2, B to D), one can search for the characteristic impulse-response function that best fits how a single climatic event of unit “dosage” (Fig. 2E) generates a response in the outcome (formally, the impulse-response function describes intertemporal structure of the dose-response function). Figure 2, F to H, displays the characteristic responses that would have been recovered from the different types of outcome data in Fig. 2, B to D (these simulated responses have been constructed to illustrate three types of real behavior recovered by previous studies).

Considering the different structures of these responses is important for understanding the response of social systems to different types of climatic factors. For example, it has been shown that extreme heat reduces the number of children born exactly 9 months later but elevates births 11 to 13 months later, as some of the successful conceptions that would have occurred during the hot period, but did not, end up occurring in the near future (38). In these cases, where climatic events simply displace the timing of societal outcomes (a pattern illustrated in Fig. 2G), changes in the distribution of climatic events may have a smaller net effect than one would predict if this dynamic response were not accounted for. Although we do not illustrate it here, it is worth noting that different locations in the dose-response function (Fig. 1C) may have different dynamics over time (Fig. 2)—for example, cold days cause delayed excess mortality by causing individuals to become ill (analogous to Fig. 2F), whereas hot days generate essentially all excess mortality immediately (39).

### Using statistical results to translate climate into outcomes

Once the full structure of a dose-response function, along with its dynamic properties, is identified for a specific population across different weather and climate conditions, researchers can simulate how a population might respond to distributions of weather events that differ slightly from historically experienced distributions (Fig. 2, I and J)—with repeated simulations enabling probabilistic assessment (Fig. 2, K to M). Gradually distorting the climatological distribution of weather events in such calculations, while adjusting response functions to account for measured patterns of adaptation, allows us to estimate how a shift in the climate may translate into a shift in the distribution of expected social outcomes (19).

### Effects of climate on societies

Recent application of the tools described above demonstrate that societies are influenced by the

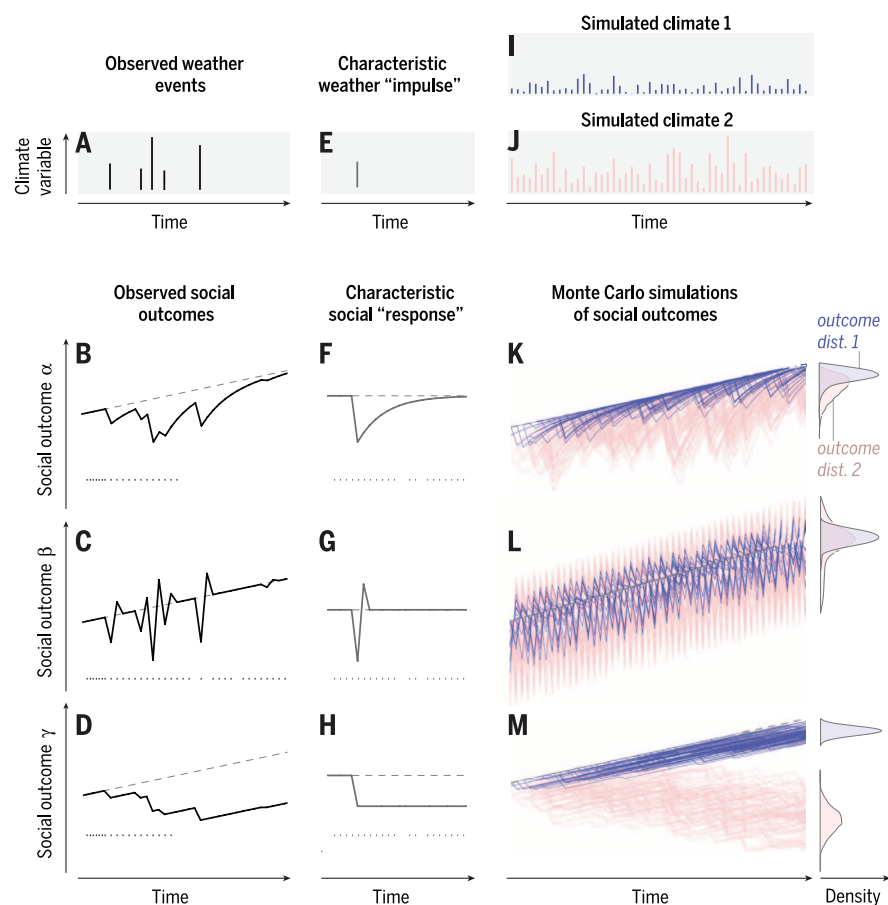


**Fig. 2. The dynamics of societal responses to climate determine how alterations to a climate influence social outcomes.** Modern approaches “hold nonclimatic factors fixed” by studying a single population over time and identifying social responses to sequential climatic events. Because societal responses may persist (or reverse) after a climatic event ends, continuing through another event that generates another overlapping response, a characteristic impulse-response function can only be recovered from the original data by deconvolution. (A) Time series of a single population’s exposure to weather events each period of magnitude  $X$ , indicated as the height of bars (analogous to Fig. 1B). (B to D) Example time series of three different social outcomes (solid line) that vary relative to baseline trends (dashed line) in response to weather events in (A). (E) A characteristic single weather “impulse” of normalized magnitude. (F to H) Characteristic impulse-response functions describing how each social outcome responds to the weather impulse in (E), recovered from deconvolving data in (A) to (D). Impulse-responses illustrate different classes of behavior: (F) persistent but decaying effects (e.g., cold-related mortality; see Fig. 4A); (G) “temporal displacement” or “harvesting,” where delayed responses partially compensate for initial responses (e.g., heat effect on births; see Fig. 4C); and (H) permanent effects (e.g., cyclone effects on GDP; see Fig. 4D). (I and J) Simulations of weather drawn from two distinct climate distributions. (K to M) Monte-Carlo simulations of social outcomes based on sampling weather from climate distribution 1 [blue, from (I)] and climate distribution 2 [pink, from (J)] and convolving these impulses with the characteristic impulse-response of each social outcome from (F) to (H). Distributions of social outcomes under each simulated climate are shown to the right of each panel (analogous to Fig. 1E).

climate in numerous dimensions and at many scales. Individuals face conditions that compromise personal health, while entire trade networks or countries can be weakened under adverse climate variation. The linkages between individuals within societal groups can themselves even be fractured by climatic conditions, triggering violence or migrant flows, for example. We review major findings at all these scales, examining effects on human health, economic conditions, social inter-

actions (including violence), and demographic responses (including migration).

### Health impacts: Mortality

As individuals, each of us is constantly exposed to temperature, and under extreme heat or cold, our bodies struggle to successfully thermoregulate, sometimes leading to severe cardiovascular, respiratory, and cerebrovascular effects that can result in death (40, 41). Both hot and cold environmental

temperatures increase death rates (Fig. 3, A and B): In Delhi, deaths increase by 3.2% per °C above 20°C (42), and in the United States, days above 90°F (32.2°C) and below 20°F (−6.7°C) increase male mortality rates by 2 and 1.4%, respectively (39). Effects of high temperature are rapid and acute but decay quickly, sometimes depressing mortality in following days, as some of the same individuals would have died in subsequent days had an extreme heat event not occurred (39) (red line in Fig. 4A).

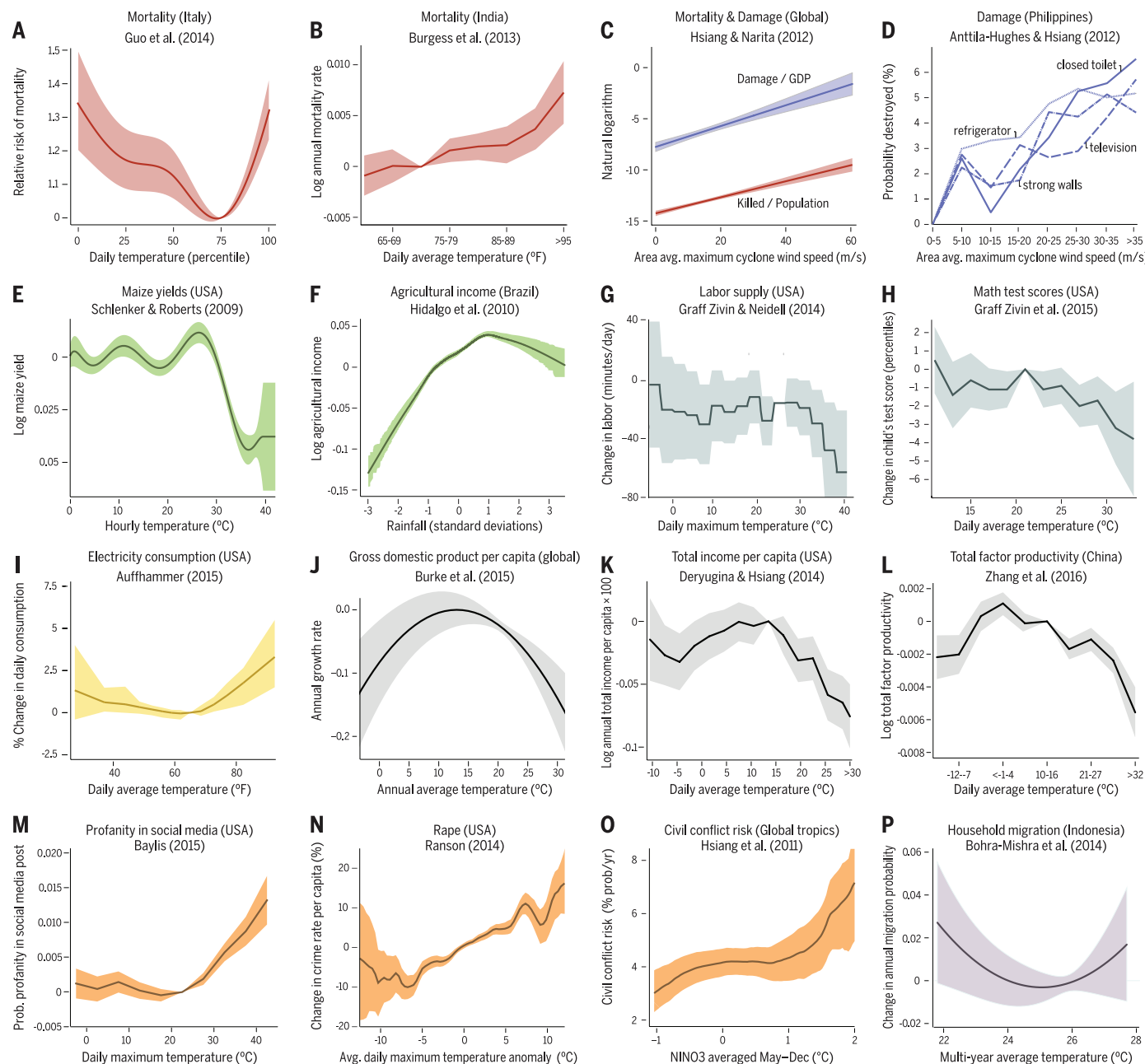


**Fig. 3. Empirical studies demonstrate that climate variables influence social and economic outcomes in many sectors and contexts.** (A to P) Examples of dose-response functions estimating the causal effect of climatological events on various social outcomes. Reproduced from authors' original estimation; titles list the outcome variable and location studied. Colors indicate categories of outcome variables: red, mortality (44, 46); blue, cyclone damage to assets (48, 116); green, agriculture (21, 153); teal, labor productivity (96, 97); yellow,

electricity (25); gray, aggregate economic indicators (32, 100, 125); orange, aggression, violence, and conflict (27, 130, 134, 136); purple, migration (171). Climate variables differ by study but include temperature, cyclone wind speed, rainfall anomalies, and ENSO measures. Response functions only identify relative changes and are either normalized to "zero effect" at a designated climatic event, such as a minimum valued outcome, or the sample mean of an outcome. Shaded areas are confidence intervals, as computed by original authors.



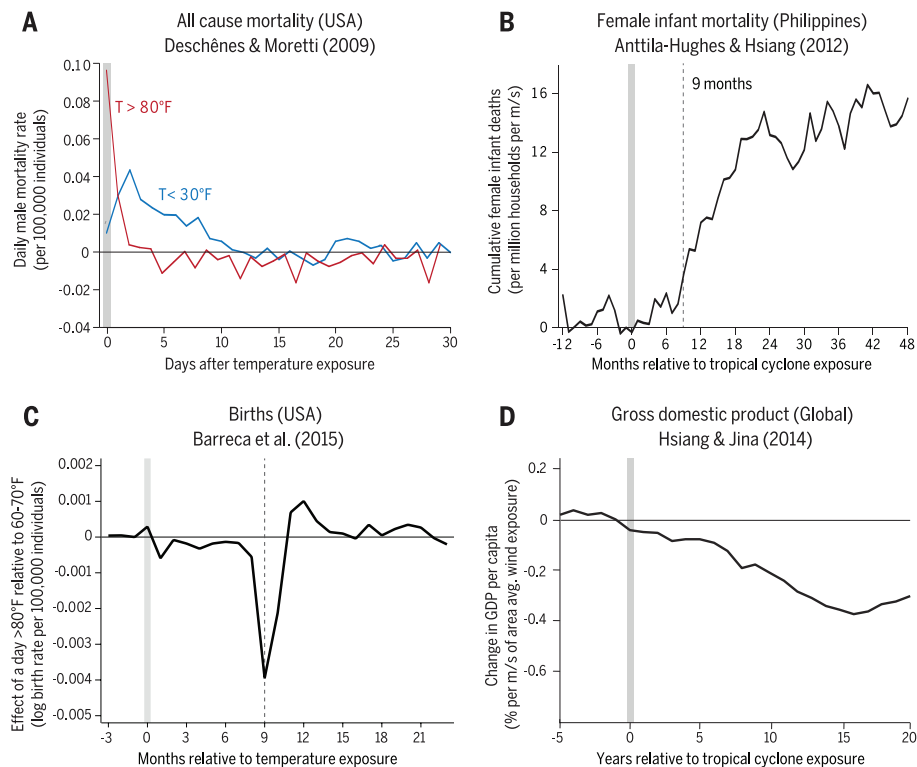


**Fig. 4. Distinct dynamic characteristics of impulse-response functions uncovered in empirical studies.** Examples of impulse-response functions from studies identifying dynamic relationships between climate variables and social outcomes, as illustrated schematically in Fig. 2, F to H. Vertical gray shaded bars indicates the timing of a unit climate “impulse.” (A) Male mortality rates in the United States increase on both hot and cold days, but hot-day responses rapidly decay and tend to be small and negative for multiple weeks—indicating temporal displacement—whereas cold days generate a more gradual and enduring mortality effect (39). (B) Tropical cyclones increase female infant deaths but with a delayed effect that grows rapidly roughly a year after exposure (49). (C) Birth rates in the United States fall 8 to 10 months after a hot day, but this decline is partially compensated for by an increase during months 11 to 13 (38). (D) GDP in countries exposed to tropical cyclones falls gradually but persistently during the 15 years following exposure (116).

In contrast, cold days have delayed and smaller—albeit enduring—effects lasting up to a month as some individuals become ill, such as contracting influenza, and fail to recover (blue line in Fig. 4A).

Evidence suggests that adaptations moderate these direct mortality effects. For example, in the United States, mortality from extreme heat declined 80% over the course of the 20th century as air conditioner adoption soared (43) (Fig. 5D). Remarkably, mortality responses are highly consistent across contexts, when “hot” and “cold” conditions are defined relative to what populations are accustomed to (44), suggesting that populations cope with regional climates in a consistent way. Anthropogenic climate change is projected to increase heat-related mortality but decrease cold-related mortality, redistributing mortality rates across locations (45), but with an overall net increase in total mortality rates (31, 46). In a cost-analysis of climate change in the United States, these deaths accounted for the largest share of losses across all impacts (45). Effects of humidity exacerbate these patterns (45, 47), and mortality impacts in poor agricultural contexts are more extreme (46).

Climatic factors other than temperature also influence mortality. Tropical cyclones directly

cause mortality—for example, through trauma or drowning—with immediate deaths in storms increasing exponentially with wind-speed exposure (48) (Fig. 3C). Populations regularly exposed to storms appear to adapt somewhat, as their mortality rates are lower than those of more naïve populations when both experience physically comparable events (48) (Fig. 5A). However, these immediate deaths may be minor in magnitude compared to “economic” deaths that occur in the wake of a cyclone (48, 49). For example, in the Philippines, changing economic conditions in the years after a cyclone lowers incomes and corresponding spending on food and health care, causing mortality among female infants roughly 15 times as high as direct mortality across all age groups (49) (Fig. 4B). Extreme rainfall events outside tropical storms also influence mortality—in agriculturally dependent contexts, infants born in arid areas face elevated risk of death when exposed to droughts (46, 50), while flooding has been linked to death throughout Europe (51).

#### Health impacts: Morbidity

Many injuries to human health caused by climate are nonfatal. One means of detecting these effects

is to measure the impact of climatic events on hospital admissions. Admissions for respiratory and cardiovascular diseases respond to temperature similarly to mortality, with impacts at both high and low daily temperatures (52, 53). The precise spatial and temporal resolution of these hospital- or city-level studies allows authors to account for key temperature correlates, such as air pollution and humidity, which also influence hospitalizations. This adjustment is important, as failing to account for particulate matter and ozone may exaggerate the effect of temperature by up to a factor of 2 (52, 54). Even without hospital-level data, evidence using cause-of-death records can illuminate key morbidity effects; for example, humidity is an important driver of influenza, a notable cause of hospitalization and mortality in temperate climates (55).

A major component of morbidity affected by the climate is vector-borne disease. For example, malaria and dengue fever infect about 200 million and 50 million people globally each year (56), respectively, and the life-cycles of mosquito vectors transmitting these illnesses are strongly influenced by climate. Temperature nonlinearly influences the reproduction of parasites, extreme temperatures lower mosquito survival rates, and open water critical for mosquito breeding is constrained by rainfall (57, 58). These climatic factors affect the intensity of infection in areas where malaria and dengue are already endemic (59), as well as affect where the disease may spread to (60). These dynamics make measurement of climate-disease interaction challenging: Some studies aim to recover incidence as nonlinear functions of temperature and rainfall (61, 62), while others parameterize ecological models of vector transmission, using model output as indices to predict cases with data (63) or simulation (64). Anthropogenic climate change is likely to shift disease ranges and increase exposure globally, but changing temperatures, rainfall, and intervention strategies complicate projections (60, 65); more research in this area is needed to link climate, ecological models, and social data.

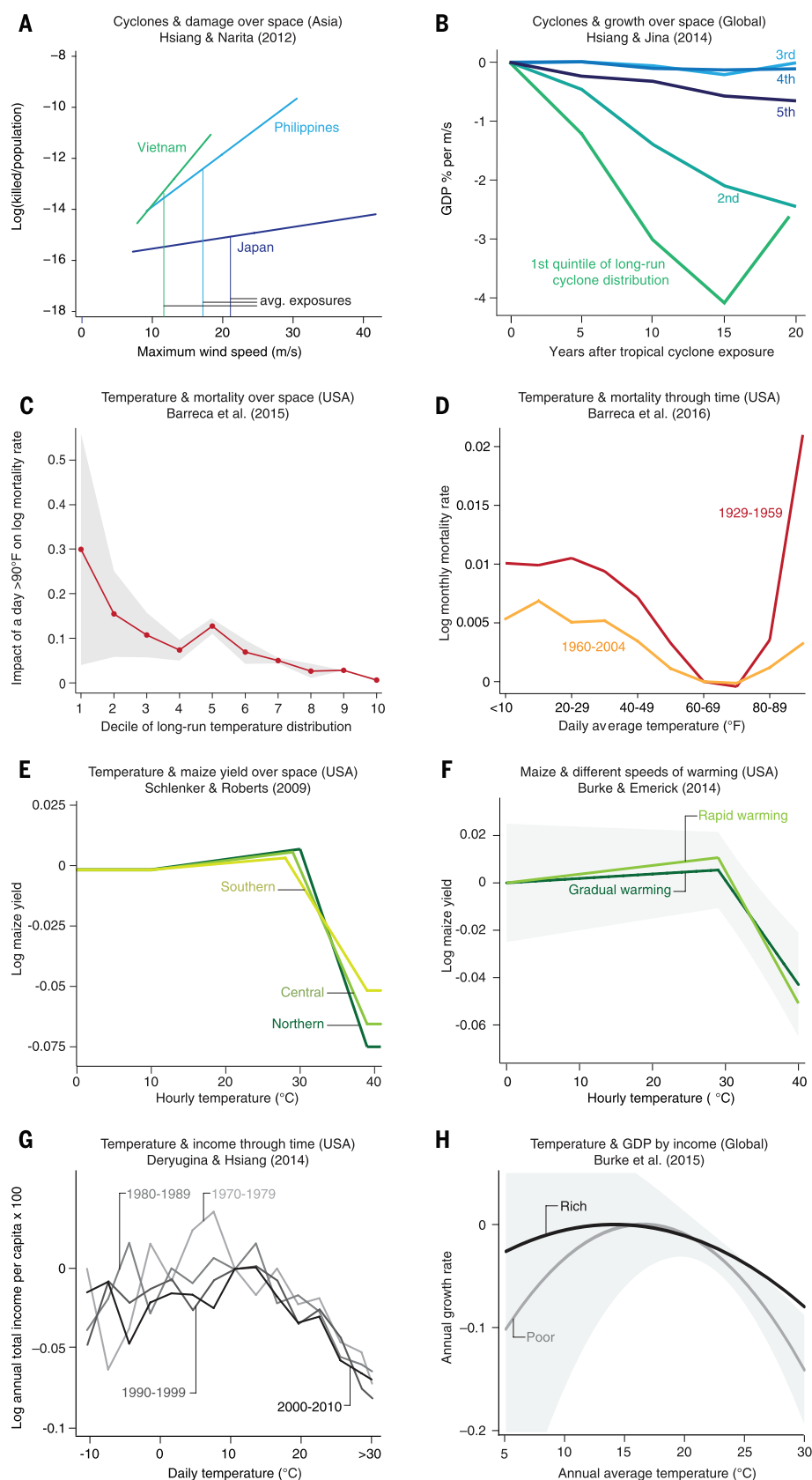
#### Health impacts: Early life

Climatic conditions experienced during early stages of life can have outsized impact because altered early development affects long-run health and well-being (66). For example, in-utero exposure to high temperatures can lower birth weight (67), and exposure to tropical cyclones leads to a variety of birth complications (68). Mechanisms explaining these in-utero effects remain elusive, as it is challenging to separate effects on gestational length and nutrient accumulation (67), and because climate shocks occurring at different points in the gestational period likely operate through distinct channels. For example, high temperatures at conception lead to fetal losses that, through selection, improve outcomes for babies who do survive (69), whereas high temperatures in the third trimester have unambiguously negative impacts (70).

Regardless of mechanism, in-utero health insults have later-life economic consequences, such as lowered income (33, 70). In developing-country

**Fig. 5. Responses to physically similar events in different contexts may indicate the presence or absence of effective adaptations.** Comparison

of response functions over time and across space can indicate where populations have been successful in adaptation and where an “adaptation gap” might persist. Global cyclone losses indicate adaptation: (A) mortality rates increase with cyclone intensity more in countries where average exposure (thin vertical line) is lower (48) and (B) effects of cyclones on GDP over time are most negative in countries with the lowest levels of historical experience—rank indicates quintile of exposure (116). Temperature-induced mortality in the United States exhibits adaptation: (C) locations that have hotter long-run climates tend to have smaller effects (185) and (D) sensitivities have declined over time (43). Maize yields in the United States indicate limited adaptation: (E) Hot and cool climates exhibit similar effects of heat (21), and (F) yields are equally affected by rapid and slow changes in temperature (23). Aggregate income exhibits limited adaptation: (G) County-level losses from high temperatures have not changed over time in the United States (32), and (H) country-level GDP reductions are slightly less severe in rich nations than in poor countries but are not statistically different (100). Shaded areas are confidence intervals, as computed by original authors.





contexts, adverse rainfall in the year of birth lowers adult female health outcomes and educational attainment (71), and droughts experienced by toddlers lower childhood growth and education (30, 72). These rainfall-related impacts likely operate through agricultural income loss and lowered nutrition; however, our understanding of these channels is generally weak, and work is needed to parse out direct physiological impacts from economic factors and behavioral responses.

### **Economic impacts: Agricultural yields**

Study of the direct effect of climate on economic outcomes began in agriculture, where the importance of climatic factors is clearest (73). Despite centuries of agricultural experience, a surprising recent finding is the importance of temperature, often dominating rainfall, in the production of staple crops (21, 74–76). Highly nonlinear yield losses on the hottest days drive much of this effect (21) (Fig. 3E), a relationship recovered in the United States (21), Africa (20), Europe (77), Southeast Asia (78), and India (46, 79). Crops are most sensitive to temperatures during specific phases of the growth cycle (76, 78). Although temperature impacts generally outweigh those of rainfall, low and very high total seasonal rainfall levels do damage yields in many contexts (21, 33) (Fig. 3F), an effect that is partially attenuated when water storage and irrigation are widely available (76, 78, 80, 81). Similarly, within a single growing season, farms that experience a small number of extremely rainy days suffer damaged yields, relative to the same quantity of rain distributed evenly across growing days (33). These various dose-response functions have been recovered and replicated for major global crops like maize, rice, soy, and wheat, but less is known about effects on regional crops like millet and cassava—which can be critical in poor rural regions—and specialty crops like fruits and vegetables, with some notable exceptions (20, 82, 83). A body of research in dairy science suggests that both temperature and humidity nonlinearly affect milk yields (84–86) while linearly lowering cattle pregnancy rates (87), but little is known outside of highly managed livestock operations in industrialized countries.

Effective adaptation to climate in agriculture appears modest, as dose-response functions change little across time and space (21, 88) (Fig. 5E), even when warming effects are gradual (23) (Fig. 5F). Furthermore, large but temporary climate events, like the U.S. Dust Bowl, have had persistent multi-decadal impacts on farm values (89). These findings contrast with historical narratives of farmer adaptability, such as the 200-year-long spread of agriculture into previously nonarable land (90, 91) and adjustment of cultivars in response to drought (92). These two views of agriculture adaptability remain unreconciled, and identifying obstacles to adaptation, such as poor incentives (93) or high adaptation costs (88), are a critical area for future research.

### **Economic impacts: Labor supply and productivity**

Agricultural effects cannot explain many patterns in the overall economic response to climate, leading

to the hypothesis that effects on labor are another important channel of influence (26). A growing body of evidence now supports this theory (94). Heat stress can lower work intensity (95), reduce cognitive performance (96), and voluntarily shorten work hours in sectors of the economy most exposed to outdoor temperature, such as construction and agriculture (97) (Fig. 3, G and H). Impacts on manufacturing production have been identified in both high- and low-income contexts (98, 99), although understanding the full impact of this effect is made challenging by reallocation of labor within an economy (35). Patterns in the overall macroeconomic responses to temperature (discussed below) are consistent with labor effects playing an important role (26, 32, 100) (Fig. 3, J to L), where individuals are each affected modestly but a large number of affected individuals might generate substantive aggregate impacts on output, and possibly on growth (100). Theory suggests that labor productivity losses might be exacerbated by market reactions that reduce the intensity of labor used in economic activities (101) and slow downstream production (102). Investments in climate control for work environments can offset some of these labor productivity effects (98), but at substantial cost, such as expenditures on energy.

### **Economic impacts: Energy supply and demand**

The relationship between climate and energy is unique. Energy systems are directly affected by climate—high temperatures provoke demand surges while straining supply and transmission—and they also serve a critical role supporting adaptation by enabling cooling, heating, irrigation, trade, and so forth. Simultaneously, energy use is the largest contributor to anthropogenic climate change.

The effect of temperature on energy demand is highly nonlinear. Households and firms use energy heavily for indoor climate, based on the weather and available infrastructure (103, 104). Almost universally, energy demands fall with rising cool temperatures and increase steeply at high temperatures, leading to a U-shaped relationship (Fig. 3I) (24, 31, 105). Investments in new energy-intensive infrastructure, such as heaters, may respond to climate more slowly as households and industry adopt expensive technology based on their beliefs about their climates. Evidence from the United States (106), Mexico (105), and China (107) indicates that electricity demands on hot days rise fastest in locations that tend to be hot, presumably because more buildings in these locations have air conditioners that are all used simultaneously on hot days.

Engineering models and simple thermodynamics suggest that electricity supply and transmission systems should suffer efficiency losses at high temperatures (108), but these effects are empirically challenging to measure in the presence of fluctuating demand. Evidence indicates that river-water temperatures can influence electricity prices (109), nuclear power capacity utilization may fall with high temperature (110), and

droughts can shift generation away from hydropower and toward carbon-intensive fuel sources (111, 112), but it is unclear whether these findings generalize.

Projections under climate change generally indicate that energy demand will grow on net, even though fewer days will require energy for heating. Sensitivity to high temperatures will likely grow as air conditioner use expands owing to improvements in technology, rising incomes, and investments specifically motivated by warming (105, 107). These investments may affect energy prices by substantially elevating peak demand (45), but better understanding of these issues is required to support long-term energy planning.

### **Economic impacts: Trade**

The current structure of the global economy represents a spatial equilibrium in which the location of populations and sites of economic production are all determined by the functioning and friction of markets through which individuals trade with one another and the factors that make locations more or less productive. Analyses of climatic influence on migration can be interpreted as a reallocation of labor across these locations, perhaps in response to changing economic conditions, which we discuss below. Yet, given an approximately fixed distribution of populations across locations, climate may also affect how populations decide to trade with one another. For example, global wind patterns and ocean currents have strongly influenced patterns of trade historically because of the role these factors play in the cost of shipping along different routes (113, 114). High temperatures that reduce productivity lower the quantity of goods exported from a country, both in agriculture (36) and manufacturing (115), and cyclone strikes that lower national incomes tend to reduce imports (116). In large integrated trade networks, the spatial distribution of climatic conditions can affect market prices (45, 117), presumably through effects on both supply costs and demand, and should theoretically determine the location of different economic activities (118, 119).

These reallocations across space and time can, in some contexts, mitigate the direct damages of climate. For example, outdoor labor supply shifts to cooler hours of the day during heat waves (97), water storage weakens the link between rainfall and agricultural productivity (81), unskilled labor moves from agriculture to manufacturing when crops are hit by high temperatures (35), and grain inventories adjust to smooth weather impacts on farm profits (36). However, these adjustments may be limited—historical evidence of intertemporal substitution is minimal for aggregate incomes (32, 100) and cyclone damages (116), and in the future, sequential periods of similar extreme conditions may make such reallocations over time more difficult. Reallocation across space may also be constrained in the future—current simulations disagree as to whether adjustment of trade patterns under climate change will dampen or amplify its overall social costs (45, 119, 120). Investigation of

substitution patterns across both space and time is a key area for future work.

### **Economic impacts: Economy-wide effects**

Rather than examining individual or sectoral responses to climate, an alternative “top down” approach examines how the macro-economy as a whole responds to climatic conditions. This approach is usually implemented by examining total income or gross domestic product (GDP) per capita as the outcome of interest. Recent work has shown that low rainfall slows national incomes greatly in Africa (*121, 122*), ENSO modulates a see-saw-like oscillation in total agricultural income between tropical and temperate countries (*123*), tropical cyclone strikes slow GDP growth for roughly 15 years in proportion to the intensity of the storm (*116*) (Fig. 4D), and temperatures have a nonlinear effect on economic production, such that output is maximized around 13°C (*100*) (Fig. 3, J to L). The roughly linear effects of cyclones and nonlinear effects of temperature at the macro level are fully consistent with the structure of effects measured in micro-level analyses (*32, 49, 124, 125*). Determining the persistence of these GDP losses is important because enduring losses may accumulate and compound, leading to larger long-run losses (*100, 116*)—this could occur if climatic events alter investment behavior (*100*) or capital depreciation (*45, 126*). However, existing data and approaches have had difficulty constraining the overall persistence of these effects (*100, 127*).

Perhaps remarkably, effects of temperature and cyclones are globally generalizable in the sense that they have been recovered using subsamples of data from around the world, including both rich and poor countries (*32, 100, 116, 125*). Early analyses focused on large negative effects of temperature on GDP in poor countries (*26, 128*), although later studies demonstrated that almost identical responses appeared in rich countries as well (*32, 100*) (Fig. 5H). This finding—in conjunction with the result that the effects of temperature on income in the United States remained essentially unchanged from 1960 to 2010 (*32, 100*) (Fig. 5G) and gradual warming has effects identical to those of short-lived warming (*128*)—leads naturally to the conclusion that effective adaptation to temperature, at the macro level, is limited. Across a variety of contexts, once temperatures are higher than the optimum, each increase in temperatures by 1°C lowers economic production by roughly 1 to 1.7%. The single finding that suggests some effective adaptation at the macro level is that cyclone-prone countries experience GDP losses (per cyclone) much smaller than countries where storms are infrequent (*116*) (Fig. 5B).

### **Social interactions: Women and girls**

Under economic pressure from climate, the terms and bargaining positions in personal relationships may change. These bargaining interactions are often gender-based, causing women and girls to experience these changes differently. For example, in sub-Saharan Africa, evidence suggests some women suffering income shortfalls during

drought engage in “transactional” intercourse, leading to increased probability of HIV infection (*129*); in the Philippines, female infants conceived after a tropical cyclone have elevated risk of mortality (Fig. 4B), particularly if they have older brothers (*49*); and in Indonesia, girls born in drought years exhibit lower long-run health and education, as diminished family resources are more often allocated toward investment in boys (*71*).

### **Social interactions: Interpersonal violence and aggression**

Evidence from numerous contexts repeatedly finds that interpersonal violence increases with temperatures and sometimes low rainfall (*130, 131*). This response manifests in low-level aggression, such as horn honking (*132*), antisocial behavior toward service employees (*133*), and the use of profanity in social media (*134*) (Fig. 3M), as well as in outright violence, such as retaliation in sports (*135*) and violent crimes: rape, murder, robbery, and assault (*136–138*) (Fig. 3N). The effect of temperature is strikingly linear with almost no delay, suggesting it might be driven by a physiological mechanism (*139–141*). Effects of rainfall on interpersonal violence appear primarily in some poor agricultural contexts, such as rural India (*138, 142, 143*) and Tanzania (*144*), suggesting that damage to agricultural yields may be a mediating factor.

### **Social interactions: Intergroup violence**

Climatic conditions also influence relationships between groups, changing the risk of large-scale conflict (*130, 131*). Cold events during cold epochs, such as feudal Europe and dynastic China (*145–148*), or periods of low rainfall (*149–151*), produced instability and upheaval—probably related to crop failures. During the modern warm period, hotter conditions increase collective violence in settings as diverse as insurgency in India (*152*), land invasions in Brazil (*153*), and civil war intensity in Somalia (*154*). This relationship is linear, with violence rising roughly 11% per standard deviation in temperature, exhibits some evidence of adaptation through rising incomes (*155*), and has an unknown mechanism (*131*). Rainfall extremes also increase intergroup conflict in agricultural contexts (*28, 121, 153, 156*), as does El Niño (*27*) (Fig. 3O).

### **Social interactions: Institutional breakdown and state failure**

Governing institutions may falter under sufficiently strong climatological stress. Patterns such as the forcible removal of rulers (*157–160*) can be tied to fluctuations in climate, but attributing societal collapse to climate is more difficult because there are fewer events. Nonetheless, several historical cases are compelling, such as the collapse of the Akkadian (*161*), Mayan (*162*), and Angkor (*163*) empires, dynastic changes in China (*164*), and major transitions in Europe (*165*).

### **Demographic effects: Migration**

Human mobility is likely an important strategy to cope with climatic changes, but it is challenging

to characterize as climate appears to have two opposing influences: Deteriorating economic conditions and safety motivate migration while simultaneously undercutting household resources needed to migrate (*166, 167*). Net effects are mixed; for example, urbanization and outmigration from agriculturally dependent areas may increase as temperatures hit crop-damaging levels and moisture declines (*89, 168–172*) (Fig. 3P), but nonagricultural workers in Mexico move in response to temperature more rapidly than farm laborers (*173*), and some of the poorest countries show no emigration response (*167*). In Africa, flows from urban to foreign locations appear responsive to weather (*174*), but U.S.-bound migration from urban Mexico is unaffected by heat waves (*175*). Climatological natural disasters that influence incomes, such as hurricanes and flooding, appear to have limited impact on total migration in low-income contexts (*171, 176, 177*) and cause simultaneous inflow and outflow of migrants in the United States (*178, 179*). Overall, the wide-ranging climatic effects on migration are not well understood and remain an area of active investigation.

### **Demographic effects: Population structure and growth**

Because climatic events affect subgroups within a population differently, such as women or the poor, it is thought that repeated exposure of the population may gradually distort its demographic structure. For example, recent findings suggest that male fetuses are less likely to survive challenging climatic events, such as extreme heat, leading to disproportionately female cohorts of surviving infants born just after hot years (*69, 180*). Demographic distortions may also occur through nonfatal mechanisms, such as the disproportionate migration of wealthy older individuals away from U.S. counties struck by cyclones simultaneous with the movement of young and low-income individuals into these same counties (*178, 179*). These seemingly small individual effects might grow to be substantial after repeated exposure, but the full scale and scope of climatological influence on equilibrium demographic structure remain unknown.

New findings also suggest that overall population growth may be directly influenced by the climate through altering sexual behavior or fertility rates. Birth rates are abnormally lower 9 months after extreme heat events in both sub-Saharan Africa (*69*) and the United States (*38*) (Fig. 4C), although identifying the mechanism driving this effect is challenging. Remarkably, these results appear to explain a large fraction of birth seasonality across climates, and projections for the United States suggest that warming will reduce birth rates 3% (*38*).

### **Attributing current and future effects of climate**

The results above describe the structure of the dose-response functions that govern how populations respond to individual climatic events, where these relationships were isolated from data containing overlapping signals of numerous



**Table 1. Attribution of climate impacts.**

Study	Social impact	Sample region	Sample period	Effects of current climate distribution	Effects of climate trends to date	Future impacts of climate change
<b>Agriculture</b>						
Auffhammer <i>et al.</i> 2012 (76)	Rice yield	India	1966–2002		Between 1966 and 2002, trends in temperature, monsoon characteristics, and rainfall lowered yields by 5.7% on average	
Lobell and Field 2007 (197)	Major crop yields	Global	1961–2002		By 2002, trends in temperature since 1981 caused annual losses of 40 megatons or \$5 billion	
Lobell <i>et al.</i> 2011 (184)	Major crop yields	Global	1960–2008		Between 1980 and 2002, trends in temperature and precipitation lowered maize and wheat yields by 3.8 and 5.5%; rice and soy were unaffected	
Schlenker and Lobell 2010 (20)	Major crop yields	Sub-Saharan Africa	1961–2007			Predicted climate change <sup>‡</sup> by 2050 lowers annual yields by 22% for maize, 17% for sorghum and millet, 18% for groundnut, and 17% for cassava
Schlenker and Roberts 2009 (21)	Maize yield	Eastern USA	1950–2008	Relative to an optimal season at 29°C, realized temperatures lower annual yields by 48% on average*		Predicted climate change <sup>‡</sup> by 2100 lowers annual yields by 63 to 82%
Welch <i>et al.</i> 2010 (78)	Rice yield	South Asia	1979–2004		Between 1979 and 2004, trends in temperature and solar radiation lowered yield growth by 0 to 0.76%	
<b>Income</b>						
Burke <i>et al.</i> 2015 (100)	Income	Global	1960–2010	Relative to each country's optimal annual temperature, realized temperatures lower the annual global growth rate by 0.25 percentage points on average*	Between 1980 and 2010, trends in temperature lowered the annual global growth rate by 0.002 percentage points on average*	Predicted climate change <sup>§</sup> by 2100 lowers global GDP by 23% and between 2010 and 2100 lowers the global annual growth rate by 0.28 percentage points on average
Deryugina and Hsiang 2015 (32)	Income	USA	1969–2011	Relative to each county's optimal annual temperature, realized county temperatures lowered the U.S. growth rate between 1970 and 2011 by 1.69 percentage points on average		Predicted climate change <sup>§</sup> by 2100 lowers the U.S. annual growth rate by 0.06 to 0.16 percentage points
Hsiang and Jina 2014 (116)	GDP growth	Global	1950–2008	Relative to a world without cyclones, realized cyclones lowered the global annual growth rate between 1970 and 2008 by 1.27 percentage points		Predicted climate change <sup>‡</sup> by 2090 induces damages valued at \$9.7 trillion in net present value
Zhang <i>et al.</i> 2016 (125)	Total factor productivity (TFP)	China	1998–2007	Relative to a full year at 50° to 60°F, realized temperatures lower TFP by 31% on average*		Predicted climate change <sup>‡</sup> by 2050 lowers annual TFP by 4.18%

Continued on the next page

Study	Social impact	Sample region	Sample period	Effects of current climate distribution	Effects of climate trends to date	Future impacts of climate change
<b>Health</b>						
Anttila-Hughes and Hsiang 2012 (49)	Mortality rate, total deaths	Philippines	1950–2008	Realized typhoon-induced “economic” deaths account for 13% of the overall infant mortality rate		
Burke et al. 2015 (129)	HIV rate	Sub-Saharan Africa	2003–2009	Rainfall shocks account for 14 to 21% of cross-country variation in HIV prevalence		
Deschênes and Greenstone 2011 (31)	Mortality rate, energy use	USA	1968–2002	Relative to a full year at 50° to 60°F, realized temperatures increase mortality rates by 11.2% and energy use by 29% on average*		Predicted climate change† by 2100 increases annual mortality rates by 3% and energy use by 11%
<b>Conflict</b>						
Burke et al. 2009 (183)	Civil conflict	Sub-Saharan Africa	1981–2002	Relative to each country’s optimal annual temperature, realized temperatures increase annual incidence of war by 29.3% on average*	Between 1981 and 2006, trends in temperature increased the annual incidence of war by 11.1% on average*	Predicted climate change‡ by 2030 increases annual incidence of war by 54%
Hsiang et al. 2011 (27)	Civil conflict	Global	1950–2004	Relative to the optimal state, realized ENSO conditions had a role in 21% of all civil conflicts between 1950 and 2004		
Ranson 2014 (136)	Violent crime	USA	1980–2009	Relative to each county’s optimal monthly temperature, realized temperatures increase crime rates by 6.1% for rape, 2.4% for murder, and 3.6% for aggravated assault on average*		Predicted climate change‡ between 2010 and 2099 increases total crime cases by 180,000 for rape, 22,000 for murder, and 2.3 million for aggravated assault
*New calculation generated either from reanalysis of the authors’ data, or from analysis of statistics provided in the authors’ paper. See supplementary materials for detailed descriptions of each calculation. †‡Climate change impacts are predicted using the Intergovernmental Panel on Climate Change A1F1†, A1B‡, or RCP 8.5§ future climate change scenarios.						

sequential climatic events. By mapping distributions of multiple climatic events back onto these empirically recovered dose-response functions, we can reconstruct distributions of predicted outcomes attributable to these weather distributions (as illustrated in Figs. 1 and 2). Comparison of outcome distributions resulting from different climatologies allows us to estimate the first-order effects of any arbitrary change in the climate (19). In principle, with sufficient information on patterns of adaptation to climate (i.e., the “informational” channel that caused the dose-response function in Fig. 1C to change), these comparisons can account for the full range of adaptations observed in the real world; although in practice, such adjustments tend to be relatively minor (45, 48, 88, 181), in part because they are mathematically second-order (19, 48), a notion that is consistent with observation that the informational effect tends to be modest in magnitude across numerous contexts (23, 32, 136, 182), especially once the costs of adaptive adjustments are accounted for (19, 88).

By using this approach to “reconstitute” distributions of impacts from climate, researchers are

now beginning to provide first-order answers to three questions that originally motivated this research agenda: How much does the current climate affect outcomes that we observe in the current world? How much has recent warming affected outcomes? And how are projected changes in the climate expected to alter social outcomes?

**The current climate**

Most analyses do not explicitly report how much the distribution of a social outcome examined is driven by climatic factors, but such results are implicitly computed and relied upon in every deconvolution or regression analysis, and estimating the total effect of current climate distributions provides perspective on the magnitude of contemporary impacts. In column 5 of Table 1 we tabulate estimates from studies that do report such results, as well as compute some new estimates based on reported values and available data. To compute the total effect of the current climate, one can use the sample of data analyzed and the empirical relationship recovered by the analysis to (i) compute the dis-

tribution of outcomes predicted by the current distribution of climatic events; and (ii) compare this to the distribution of outcomes obtained if the same population were exposed to their best possible environmental conditions continuously, where “best possible” is based on the nature of the estimated empirical relationship (see supplementary materials for details). Essentially, to create this benchmark we imagine a world in which climate could be managed as other aspects of societies and economies are, such as the allocation of law enforcement or capital investments. For example, in their analysis of the effect of ENSO on civil conflict, Hsiang et al. (27) estimate average conflict rates predicted by historical ENSO conditions and compare them to conflict rates that would be predicted if the world were to experience La Niña-like conditions, the climate state with least conflict, continuously. This thought experiment is clearly impossible to confirm, as societies cannot uniformly be exposed to an optimal climate; however, it is a useful and precisely defined benchmark for considering the overall magnitude of effects resulting from observed climates.



In general, modern climates have substantial influence on social and economic outcomes. For example, historical temperatures in the United States are estimated to currently suppress maize yields by roughly 48% relative to ideal growing conditions (21); raise average murder rates by 2% and assault rates by 4% relative to the coolest conditions experienced in each county and month (136); increase residential energy consumption by 29% and elevate mortality rates by 11% on net (31); and reduce GDP growth by roughly 1.7 percentage points year<sup>-1</sup> (32). Temperatures contribute to 29% of civil conflicts in sub-Saharan Africa (183), and 13% of infant mortality in the Philippines is attributable to tropical cyclones (49). Globally, ENSO has elevated civil conflict rates by 21% relative to constant low-conflict conditions (27), while temperature and tropical cyclones reduce global economic growth by roughly 0.25 and 1.3 percentage points year<sup>-1</sup>, respectively (100, 116).

### Climate change to date

Only a few agricultural studies estimate the social effect of recent already-observed anthropogenic climate trends. In Table 1, column 6, we show that, relative to an unchanged climate, trends in various climatic variables that occurred at the end of the 20th century have lowered rice yield growth rates in South Asia by up to 0.76% annually (78) and reduced global maize and wheat production 3.8% and 5.5%, respectively, whereas global gains and losses for soy and rice roughly balance one another out (184). Based on calculations using data from (100) and (183), we estimate that warming trends since 1980 have slowed global average GDP growth by 0.002 percentage points per year and increased the incidence of civil conflict in Sub-Saharan Africa by ~11% (see supplementary materials for details).

### Future climate change

Projected impacts of future “business-as-usual” climate changes, relative to a counterfactual of no climate change, are generally much larger than impacts of warming that have already occurred and tend to be comparable to the baseline impact of climate on social and economic outcomes today (Table 1, column 7). For example, crop yields in Africa are likely to decline 17 to 22% for maize, sorghum, millet, and groundnuts by 2050 (20); yields for major crops in the United States are likely to decline 15 to 20% by 2050 (21, 23, 45) and 63 to 82% by 2100 (21, 45), although accounting for estimated effects of CO<sub>2</sub> fertilization may keep expected losses nearer to 15% (45). Projected estimates suggest that armed conflict in Africa may rise roughly 50% by 2030 (183), while violent and property crimes in the United States may increase roughly 3 and 1%, respectively (45, 136). Warming by end of century is projected to increase U.S. mortality rates 3 to 9% and electricity consumption 11% (31, 45). The growth rate of overall economic production is projected to fall roughly 0.12 percentage points year<sup>-1</sup> in the United States (32) and 0.28 percentage points year<sup>-1</sup> globally (100) during the next century owing to the effects of rising

temperature, with additional projected losses due to cyclones costing roughly \$9.7 trillion dollars in present discounted value (116). Notably, these impact projections are all constructed on the basis of historically observed responses to environmental conditions, and the actual impact of future changes might be less disruptive if, for example, adaptive technologies improve dramatically in the future. Alternatively, future impacts could be worse than described here if current adaptive strategies, such as irrigation using fossil aquifers, are unsustainable or societal responses become highly nonlinear once the environment shifts to conditions beyond recent experience.

### Critical challenge: Understanding “adaptation gaps”

Overall, new empirical measurements suggest that current climatic conditions impose substantial economic and social burdens on modern populations and that future climate change will further increase these ongoing costs considerably. These losses could be avoided, in theory, if populations could costlessly and fully adapt to these dimensions of their climate—why this has not occurred to date remains an important open question, with potentially large gains for both present and future populations should it be solved.

Given information on the climatically determined probability distribution of potential weather events, populations may take actions or make investments that will reduce the influence of these events when they actually occur. As depicted in Fig. 1, this adaptation can be detected implicitly by observing how the dose-response function linking climate variables to outcomes changes. More highly adapted populations will have flatter responses (48), such that changes in climatic variables have less influence on an outcome. An alternative approach to detecting adaptation is explicit measurement of outcomes that are themselves thought to be adaptations, such as investing in crop switching after a drought (89). Notably, measurement of adaptation using either approach is made possible by the use of intertemporal changes in climatic variables, whether over short time scales (e.g., days) or long time scales (23) (e.g., decades)—and we note that in contrast to widely cited heuristics, short-term weather variation can be used to exactly measure the influence of long-term climate changes under the right conditions, even when populations adapt to knowledge of their climate (19).

Comparison of adaptation results across different sectors reveals striking dissimilarities: In some cases, adaptation appears remarkably effective at minimizing damages, whereas in other cases, we observe essentially no adaptation, leading to seemingly costly “adaptation gaps.” For example, populations regularly exposed to cyclones experience substantially smaller losses than naïve populations when exposed to physically similar events (48, 49, 116) (Fig. 5, A and B). Similarly, mortality on hot days in hot climates is lower than in similar populations in cooler climates (44, 185) (Fig. 5C),

and heat-related mortality has declined over time with rising availability of air-conditioning and other technologies (43) (Fig. 5D). In sharp contrast, violence and crop yields in hot and cool locations respond almost identically to temperature in the United States (21, 136) (Fig. 5E), and the temperature sensitivity of agriculture (23), crime (136), and economic productivity (32, 100) has changed little over multiple decades, even though populations are presumably innovating and adjusting to climate over this time period (Fig. 5, F and G). At a global scale, it has been widely hypothesized that wealthy populations will adapt effectively to future climate changes because they have greater resources, have access to wider arrays of technology, and tend to have stronger governments (8, 186, 187), but data from the present largely suggest that overall economic activity in wealthy countries actually responds to temperature (in percentage terms) similarly to economic activity in poor countries (Fig. 5, G and H)—although there is suggestive but statistically insignificant evidence that wealthy countries might be adapting slightly more effectively. In puzzling incongruity, wealthy countries appear substantially more adapted than poor countries, in terms of some outcomes, to tropical cyclones (48) and ENSO (27).

To date, it is not well understood why populations adapt so effectively in some dimensions with respect to certain aspects of the climate while entirely failing to adapt in other contexts. Existing evidence suggests that high costs of adaptation (48, 88, 105), incentives to adapt (48, 93), limited access to credit for financing adaptations (46), limited rationality when planning for future risks (16, 188), incorrect or limited information about the benefits of adaptation (89, 189), perverse political incentives (190, 191) or weak government institutions (187, 192), constraints to sharing risk among individuals and groups (193), and access to technologies (90, 185) might play substantial roles, although existing evidence is primarily suggestive as it relies on cross-sectional associations. To better understand what constrains adaptation, future work will likely need to exploit natural experiments where specific potential constraints (or costs) are exogenously eliminated; if the link between an outcome and climate disappears, it can be more confidently inferred that the altered constraint was playing a critical role in limiting adaptation (43, 152).

It is theoretically possible that existing adaptation gaps are “economically optimal” in the sense that the costs of additional adaptive actions and investments exactly balance their benefits, which are avoided climate-related social losses (48). Many patterns of adaptation described above seem qualitatively consistent with this notion of optimality; for example, cyclone-prone locations benefit more from investments in cyclone shelters because they are used more often, so cost-benefit analyses would predict more shelters in locations that are more cyclone-prone. However, many patterns seem inconsistent with optimality, such as the persistent sensitivity of crop yields to temperature (23, 182), but could be reconciled as optimal if

adaptation technologies are extraordinarily costly. In general, there is no quantitative evidence that allows us to determine how closely current adaptation gaps reflect optimal investments or are bound at suboptimal levels by the market failures and other constraints described above.

Because the persistence of adaptation gaps has such large impacts on current and future well-being around the globe, understanding its cause is likely the most pressing current research question. Identifying the causes of these gaps and determining whether they are optimal is critical for designing policies that can support and accelerate adaptation in the numerous contexts where it lags. For example, if current adaptation gaps are optimal, then policy should focus on improving the cost-effectiveness of adaptation technologies (48) rather than on correcting market failures. Such policies, if carefully designed and effectively implemented, could both substantially benefit current generations that presently suffer large economic and social burdens from the modern climate, and also benefit future generations that would otherwise continue bearing these burdens along with all additional costs of climate change.

## Discussion

The endeavor to understand the impact of climate on society is unlocking promise. Climate has imposed varied environmental constraints on humanity for millennia, and new understanding provides insight into the role of climate in global historical development. More urgently, current climatic conditions and variations are constantly shaping and reshaping human well-being today, thus understanding these processes allow us to better prepare for and respond to the climate that we experience now. Finally, designing effective, efficient, and fair policies to manage anthropogenic climate change requires, critically, that we develop a quantitative grasp of how different investments today may affect economic and social possibilities in the future.

Advances in data, computing, and methods have triggered rapid progress in our ability to empirically measure how climatic conditions affect human well-being and productivity around the world. Although climate is clearly not the only factor that affects social and economic outcomes, quantitative measurements reveal that it is a major factor, often with first-order consequences. Notably, these results suggest that the magnitude of influence that current climatic conditions have on social outcomes is generally comparable to (and sometimes larger than) the projected effects of future warming. Collectively, these findings suggest that both local climatic conditions and the state of the global climate can be thought of as forms of “natural capital” that play an important role in supporting human welfare and are inputs to economic production.

An insight that emerges from these findings is the notion that current climate patterns may be an important source of inequality. Populations endowed with different distributions of climatic conditions face different environmental constraints that may lead to different distributions of out-

comes. In a thought experiment where we hold all other factors constant, these recent findings directly suggest that hotter locations with more extreme rainfall patterns and more major disturbances, such as ENSO and tropical cyclones, will generally face additional health costs, lower productivity, and additional economic costs, greater population movement, and higher rates of violence. To first order, this idea is broadly consistent with cross-sectional patterns (194); however, as described earlier, it is not yet possible to ensure that the “all other factors constant” assumption holds when comparing outcomes across different populations, so we cannot directly test these cross-sectional predictions empirically. Nonetheless, such inferences, with important repercussions for present and future inequality, would follow logically from these results.

Projections of climate changes based on these empirical results also inform questions of inequality, as predicted future impacts are highly unevenly distributed across locations, often because the effects of climate are nonlinear and different populations have different baseline climates, such that incremental warming has heterogeneous effects. For example, warming is expected to increase productivity in cool locations while decreasing productivity in warm locations, leading to projections where current patterns of inequality increase, sometimes dramatically (32, 45, 100).

Recent advances in this literature point toward two areas of future work with important policy consequences. First, “cracking the code” on when, where, and why adaptation is or is not successful promises major social benefits. New evidence suggests that (i) there are some cases where populations are able to adapt such that they partially neutralize the effects of climate; (ii) there are many cases where adaptation does not occur; and (iii) the social and economic benefits of successful, low-cost, and widespread adaptation are potentially very large for both current and future populations, especially in many low-income countries. Understanding what causes this “adaptation gap” can help policy address it; for example, if adaptation technologies are expensive (48, 88), then policy should focus on their research and development. Second, models used to understand the costs and benefits of different global climate change policies take as inputs various “damage functions” that describe how social and economic losses accrue under different future climate change scenarios (11). Historically, these damage functions were theoretical constructs whose structures were based on modeling intuition informed by some data (10, 195), but the recent explosion of empirical work suggests that these global policy models can now be calibrated to real-world relationships that characterize the many social impacts of climate (45, 196).

## REFERENCES AND NOTES

1. Aristotle, *Meteorologica*, transl. H. D. P. Lee (Loeb Classical Library, 1952), vol. 397.
2. C. B. De Montesquieu, *The Spirit of Laws* (Cosimo, 2011).
3. S. Howe, *Empire: A Very Short Introduction* (Oxford Paperbacks, 2002).

4. N. H. MacKworth, Effects of heat on wireless telegraphy operators hearing and recording Morse messages. *Br. J. Ind. Med.* **3**, 143–158 (1946). pmid: 20991172
5. P. Froom, Y. Caine, I. Shochat, J. Ribak, Heat stress and helicopter pilot errors. *J. Occup. Med.* **35**, 720–724 (1993). doi: 10.1097/00043764-199307000-00016; pmid: 8366397
6. R. M. Solow, *Sustainability: An Economist's Perspective* (1991).
7. W. D. Nordhaus, Optimal greenhouse-gas reductions and tax policy in the “DICE” model. *Am. Econ. Rev.* **83**, 313–317 (1993).
8. S. T. Waldhoff, D. Anthoff, S. Rose, R. S. Tol, The marginal damage costs of different greenhouse gases: An application of FUND. *Economics* **8**, 1–33 (2011). doi: 10.5018/economics-ejournal.ja.2014-31
9. N. Stern, *Stern Review: The Economics of Climate Change* (Cambridge Univ. Press, 2006).
10. R. L. Revesz et al., Global warming: Improve economic models of climate change. *Nature* **508**, 173–175 (2014). doi: 10.1038/508173a; pmid: 24724186
11. Interagency Working Group on Social Cost of Carbon, Social cost of carbon for regulatory impact analysis—under executive order 12866, Tech. Rep., United States Government (2010).
12. Department for Environment, Food and Rural Affairs, The social cost of carbon review, Tech. Rep., UK Department for Environment, Food and Rural Affairs (2005).
13. R. E. Kopp, S. M. Hsiang, M. Oppenheimer, Empirically calibrating damage functions and considering stochasticity when integrated assessment models are used as decision tools. *Impacts World 2013*, International Conference on Climate Change Effects (2013).
14. M. Burke et al., Opportunities for advances in climate change economics. *Science* **352**, 292–293 (2016). doi: 10.1126/science.aad9634; pmid: 27081055
15. P. Peduzzi, A. De Bono, C. Herold, Making development sustainable: The future of disaster risk management. Global assessment report on disaster risk reduction (2015). [www.preventionweb.net/english/hyogo/gar/2015/en/gar-pdf/GAR2015\\_EN.pdf](http://www.preventionweb.net/english/hyogo/gar/2015/en/gar-pdf/GAR2015_EN.pdf).
16. H. C. Kunreuther, E. O. Michel-Kerjan, *At War with the Weather: Managing Large-Scale Risks in a New Era of Catastrophes* (MIT Press, 2009).
17. D. Bryla-Tressler et al., Weather index insurance for agriculture: Guidance for development practitioners, Tech. Rep., World Bank (2011).
18. P. W. Holland, Statistics and causal inference. *J. Am. Stat. Assoc.* **81**, 945–960 (1986). doi: 10.1080/01621459.1986.10478354
19. S. M. Hsiang, Climate econometrics. *Annu. Rev. Res. Econ.* (2016). doi: 10.1146/annurev-resource-100815-095343
20. W. Schlenker, D. Lobell, Robust negative impacts of climate change on African agriculture. *Environ. Res. Lett.* **5**, 014010 (2010). doi: 10.1088/1748-9326/5/1/014010
21. W. Schlenker, M. J. Roberts, Nonlinear temperature effects indicate severe damages to U.S. crop yields under climate change. *Proc. Natl. Acad. Sci. U.S.A.* **106**, 15594–15598 (2009). doi: 10.1073/pnas.0906865106; pmid: 19717432
22. W. Schlenker, W. M. Hanemann, S. C. Fisher, Water availability, degree days and the potential impact of climate change on irrigated agriculture in California. *Clim. Change* **81**, 19–38 (2007). doi: 10.1007/s10584-005-9008-z
23. M. Burke, K. Emerick, Adaptation to climate change: Evidence from US agriculture. *Am. Econ. J.: Econ. Pol.* **8**, 106–140 (2016). doi: 10.1257/pol.20130025; <http://ssrn.com/abstract=2144928>
24. M. Auffhammer, A. Aroonruengsawat, Simulating the impacts of climate change, prices and population on California's residential electricity consumption. *Clim. Change* **109**, 191–210 (2011). doi: 10.1007/s10584-011-0299-y
25. M. Auffhammer, Estimating extensive and intensive margin adaptation to climate change from consumption data. Working paper (2015). [https://business.illinois.edu/finance/wp-content/uploads/sites/46/2015/08/15\\_10\\_13\\_Auffhammer\\_Adaptation.pdf](https://business.illinois.edu/finance/wp-content/uploads/sites/46/2015/08/15_10_13_Auffhammer_Adaptation.pdf).
26. S. M. Hsiang, Temperatures and cyclones strongly associated with economic production in the Caribbean and Central America. *Proc. Natl. Acad. Sci. U.S.A.* **107**, 15367–15372 (2010). doi: 10.1073/pnas.1009510107; pmid: 20713696
27. S. M. Hsiang, K. C. Meng, M. A. Cane, Civil conflicts are associated with the global climate. *Nature* **476**, 438–441 (2011). doi: 10.1038/nature10311; pmid: 21866157
28. M. Harari, E. La Ferrara, Conflict, climate and cells: A disaggregated analysis, Working paper (2013). <http://economics.mit.edu/files/10058>.
29. P. Bastos, M. Busso, S. Miller, Adapting to climate change: Long-term effects of drought on local labor markets. Working paper (2013). <http://idbdocs.iadb.org/wsdocs/getdocument.aspx?docnum=38335273>.



30. J. Hoddinott, B. Kinsey, Child growth in the time of drought. *Oxf. Bull. Econ. Stat.* **63**, 409–436 (2001). doi: [10.1111/1468-0084.t01-1-00227](https://doi.org/10.1111/1468-0084.t01-1-00227)
31. O. Deschênes, M. Greenstone, Climate change, mortality, and adaptation: Evidence from annual fluctuations in weather in the US. *Am. Econ. J. Appl. Econ.* **3**, 152–185 (2011). doi: [10.1257/app.3.4.152](https://doi.org/10.1257/app.3.4.152)
32. T. Deryugina, S. M. Hsiang, Does the environment still matter? Daily temperature and income in the United States, NBER working paper 20750 (2014). [www.nber.org/papers/w20750.pdf](http://www.nber.org/papers/w20750.pdf)
33. R. M. Fishman, More uneven distributions overturn benefits of higher precipitation for crop yields. *Environ. Res. Lett.* **11.2**, 024004 (2016).
34. D. B. Lobell et al., The critical role of extreme heat for maize production in the United States. *Nat. Clim. Chang.* **3**, 497–501 (2013). doi: [10.1038/nclimate1832](https://doi.org/10.1038/nclimate1832)
35. J. Colmer, Weather, labour reallocation, and industrial production: Evidence from India, Working paper (2016). <https://drive.google.com/file/d/0B-BakBtoHwF8UjNTU3Z0NmJOTA/view>
36. M. J. Roberts, W. Schlenker, Identifying supply and demand elasticities of agricultural commodities: Implications for the US ethanol mandate. *Am. Econ. Rev.* **103**, 2265–2295 (2013). doi: [10.1257/aer.103.6.2265](https://doi.org/10.1257/aer.103.6.2265)
37. K. Munshi, Networks in the modern economy: Mexican migrants in the US labor market. *Q. J. Econ.* **118**, 549–599 (2003). doi: [10.1162/00335503321675455](https://doi.org/10.1162/00335503321675455)
38. A. Barreca, O. Deschênes, M. Guld, Maybe next month? Temperature shocks, climate change, and dynamic adjustments in birth rates, Working paper, National Bureau of Economic Research (2015).
39. O. Deschênes, E. Moretti, Extreme weather events, mortality and migration. *Rev. Econ. Stat.* **91**, 659–681 (2009). doi: [10.1162/rest.91.4.659](https://doi.org/10.1162/rest.91.4.659)
40. R. Basu, J. M. Samet, Relation between elevated ambient temperature and mortality: A review of the epidemiologic evidence. *Epidemiol. Rev.* **24**, 190–202 (2002). doi: [10.1093/epirev/mxf007](https://doi.org/10.1093/epirev/mxf007); pmid: [12762092](https://pubmed.ncbi.nlm.nih.gov/12762092/)
41. O. Deschênes, Temperature, human health, and adaptation: A review of the empirical literature. *Energy Econ.* **46**, 606–619 (2014). doi: [10.1016/j.eneco.2013.10.013](https://doi.org/10.1016/j.eneco.2013.10.013)
42. S. Hajat, B. G. Armstrong, N. Gouveia, P. Wilkinson, Mortality displacement of heat-related deaths: A comparison of Delhi, São Paulo, and London. *Epidemiology* **16**, 613–620 (2005). doi: [10.1097/01.ede.0000164559.41092.2a](https://doi.org/10.1097/01.ede.0000164559.41092.2a); pmid: [16135936](https://pubmed.ncbi.nlm.nih.gov/16135936/)
43. A. Barreca, K. Clay, O. Deschênes, M. Greenstone, J. S. Shapiro, Adapting to climate change: The remarkable decline in the US temperature-mortality relationship over the 20th century. *J. Polit. Econ.* **124**, 105–159 (2016). doi: [10.1086/684582](https://doi.org/10.1086/684582)
44. Y. Guo et al., Global variation in the effects of ambient temperature on mortality: A systematic evaluation. *Epidemiology* **25**, 781–789 (2014). doi: [10.1097/EDE.0000000000000165](https://doi.org/10.1097/EDE.0000000000000165); pmid: [25166878](https://pubmed.ncbi.nlm.nih.gov/25166878/)
45. T. Houser et al., American Climate Prospectus: Economic Risks in the United States (2015).
46. R. Burgess, O. Deschênes, D. Donaldson, M. Greenstone, The unequal effects of weather and climate change: Evidence from mortality in India. Working paper (2014). [www.lse.ac.uk/economics/people/facultyPersonalPages/facultyFiles/RobinBurgess/UnequalEffectsOfWeatherAndClimateChange140514.pdf](http://www.lse.ac.uk/economics/people/facultyPersonalPages/facultyFiles/RobinBurgess/UnequalEffectsOfWeatherAndClimateChange140514.pdf)
47. A. I. Barreca, Climate change, humidity, and mortality in the United States. *J. Environ. Econ. Manage.* **63**, 19–34 (2012). doi: [10.1016/j.jeem.2011.07.004](https://doi.org/10.1016/j.jeem.2011.07.004); pmid: [25328254](https://pubmed.ncbi.nlm.nih.gov/25328254/)
48. S. M. Hsiang, D. Narita, Adaptation to cyclone risk: Evidence from the global cross-section. *Climate Change Econ.* **3**, 1250011 (2012). doi: [10.1142/S201000781250011X](https://doi.org/10.1142/S201000781250011X)
49. J. K. Anttila-Hughes, S. M. Hsiang, Destruction, disinvestment, and death: Economic and human losses following environmental disaster, Working paper (2012). [http://papers.ssrn.com/abstract\\_id=2220501](http://papers.ssrn.com/abstract_id=2220501)
50. M. Kudamatsu, T. Persson, D. Strömberg, *Weather and Infant Mortality in Africa*. Working paper (2012).
51. S. Hajat et al., Extreme Weather Events and Public Health Responses. *Epidemiology* **16**, 613–620 (2005). doi: [10.1097/01.ede.0000164559.41092.2a](https://doi.org/10.1097/01.ede.0000164559.41092.2a)
52. N. R. Ziebarth, M. Schmitt, M. Karlsson, The short-term population health effects of weather and pollution, Working paper (2014). [http://papers.ssrn.com/sol3/papers.cfm?abstract\\_id=2377611](http://papers.ssrn.com/sol3/papers.cfm?abstract_id=2377611)
53. R. S. Kovats, S. Hajat, P. Wilkinson, Contrasting patterns of mortality and hospital admissions during hot weather and heat waves in Greater London, UK. *Occup. Environ. Med.* **61**, 893–898 (2004). doi: [10.1136/oem.2003.012047](https://doi.org/10.1136/oem.2003.012047); pmid: [15477282](https://pubmed.ncbi.nlm.nih.gov/15477282/)
54. M. S. O'Neill, S. Hajat, A. Zanobetti, M. Ramirez-Aguilar, J. Schwartz, Impact of control for air pollution and respiratory epidemics on the estimated associations of temperature and daily mortality. *Int. J. Biometeorol.* **50**, 121–129 (2005). doi: [10.1007/s00484-005-0269-z](https://doi.org/10.1007/s00484-005-0269-z); pmid: [15912362](https://pubmed.ncbi.nlm.nih.gov/15912362/)
55. A. I. Barreca, J. P. Shimshack, Absolute humidity, temperature, and influenza mortality: 30 years of county-level evidence from the United States. *Am. J. Epidemiol.* **176** (suppl. 7), S114–S122 (2012). doi: [10.1093/aje/kws259](https://doi.org/10.1093/aje/kws259); pmid: [23035135](https://pubmed.ncbi.nlm.nih.gov/23035135/)
56. World Health Organization, A global brief on vector-borne diseases. Tech. Rep., World Health Organization (2014).
57. M. H. Craig, R. W. Snow, D. Le Sueur, A climate-based distribution model of malaria transmission in sub-Saharan Africa. *Parasitol. Today* **15**, 105–111 (1999). doi: [10.1016/S0169-4758\(99\)001396-4](https://doi.org/10.1016/S0169-4758(99)001396-4); pmid: [10322323](https://pubmed.ncbi.nlm.nih.gov/10322323/)
58. P. W. Gething et al., Modelling the global constraints of temperature on transmission of *Plasmodium falciparum* and *P. vivax*. *Parasit. Vectors* **4**, 92 (2011). doi: [10.1186/1756-3305-4-92](https://doi.org/10.1186/1756-3305-4-92); pmid: [21615906](https://pubmed.ncbi.nlm.nih.gov/21615906/)
59. G. Zhou, N. Minakawa, A. K. Githeko, G. Yan, Association between climate variability and malaria epidemics in the East African highlands. *Proc. Natl. Acad. Sci. U.S.A.* **101**, 2375–2380 (2004). doi: [10.1073/pnas.0308714100](https://doi.org/10.1073/pnas.0308714100); pmid: [14983017](https://pubmed.ncbi.nlm.nih.gov/14983017/)
60. S. Bhatt et al., The global distribution and burden of dengue. *Nature* **496**, 504–507 (2013). doi: [10.1038/nature12060](https://doi.org/10.1038/nature12060); pmid: [23563266](https://pubmed.ncbi.nlm.nih.gov/23563266/)
61. A. I. Barreca, The long-term economic impact of in utero and postnatal exposure to malaria. *J. Hum. Resour.* **45**, 865–892 (2010). doi: [10.3368/jhr.45.4.865](https://doi.org/10.3368/jhr.45.4.865)
62. F. J. Colón-González, C. Fezzi, I. R. Lake, P. R. Hunter, The effects of weather and climate change on dengue. *PLOS Negl. Trop. Dis.* **7**, e2503 (2013). pmid: [24244765](https://pubmed.ncbi.nlm.nih.gov/24244765/)
63. G. C. McCord, Malaria ecology and climate change. *Eur. Phys. J. Spec. Top.* **225.3**, 459–470 (2016).
64. J. Small, S. J. Goetz, S. I. Hay, Climatic suitability for malaria transmission in Africa, 1911–1995. *Proc. Natl. Acad. Sci. U.S.A.* **100**, 15341–15345 (2003). doi: [10.1073/pnas.2236969100](https://doi.org/10.1073/pnas.2236969100); pmid: [14663146](https://pubmed.ncbi.nlm.nih.gov/14663146/)
65. P. W. Gething et al., Climate change and the global malaria recession. *Nature* **465**, 342–345 (2010). doi: [10.1038/nature09098](https://doi.org/10.1038/nature09098); pmid: [20485434](https://pubmed.ncbi.nlm.nih.gov/20485434/)
66. D. Almond, J. Currie, Killing me softly: The fetal origins hypothesis. *J. Econ. Perspect.* **25**, 153–172 (2011). doi: [10.1257/jep.25.3.153](https://doi.org/10.1257/jep.25.3.153); pmid: [25152565](https://pubmed.ncbi.nlm.nih.gov/25152565/)
67. O. Deschênes, M. Greenstone, J. Guryan, Climate change and birth weight. *Am. Econ. Rev.* **99**, 211–217 (2009). doi: [10.1257/aer.99.2.211](https://doi.org/10.1257/aer.99.2.211)
68. J. Currie, M. Rossin-Slater, Weathering the storm: Hurricanes and birth outcomes. *J. Health Econ.* **32**, 487–503 (2013). doi: [10.1016/j.jhealeco.2013.01.004](https://doi.org/10.1016/j.jhealeco.2013.01.004); pmid: [23500506](https://pubmed.ncbi.nlm.nih.gov/23500506/)
69. J. Wilde, B. Apouey, T. Jung, Heat waves at conception and later life outcomes, Working paper (2014). [http://economics.usf.edu/PDF/Wilde\\_Apouey\\_Jung\\_HeatWavesConception.pdf](http://economics.usf.edu/PDF/Wilde_Apouey_Jung_HeatWavesConception.pdf)
70. A. Isen, M. Rossin-Slater, R. Walker, Heat and long-run human capital formation, Working paper (2015). [www.iza.org/conference\\_files/environ/2015/rossin-slater\\_m7513.pdf](http://www.iza.org/conference_files/environ/2015/rossin-slater_m7513.pdf)
71. S. Maccini, D. Yang, Under the weather: Health, schooling, and economic consequences of early-life rainfall. *Am. Econ. Rev.* **99**, 1006–1026 (2009). doi: [10.1257/aer.99.3.1006](https://doi.org/10.1257/aer.99.3.1006)
72. H. Alderman, J. Hoddinott, B. Kinsey, Long term consequences of early childhood malnutrition. *Oxf. Econ. Pap.* **58**, 450–474 (2006). doi: [10.1093/oxep/gpl008](https://doi.org/10.1093/oxep/gpl008)
73. M. Auffhammer, W. Schlenker, Empirical studies on agricultural impacts and adaptation. *Energy Econ.* **46**, 555–561 (2014). doi: [10.1016/j.eneco.2014.09.010](https://doi.org/10.1016/j.eneco.2014.09.010)
74. D. B. Lobell, M. B. Burke, Why are agricultural impacts of climate change so uncertain? The importance of temperature relative to precipitation. *Environ. Res. Lett.* **3**, 034007 (2008). doi: [10.1088/1748-9326/3/3/034007](https://doi.org/10.1088/1748-9326/3/3/034007)
75. W. Schlenker, W. M. Hanemann, A. C. Fisher, Will US agriculture really benefit from global warming? Accounting for irrigation in the hedonic approach. *Am. Econ. Rev.* **95**, 395–406 (2005). doi: [10.1257/0002828053828455](https://doi.org/10.1257/0002828053828455)
76. M. Auffhammer, V. Ramanathan, J. R. Vincent, Climate change, the monsoon, and rice yield in India. *Clim. Change* **111**, 411–424 (2012). doi: [10.1007/s10584-011-0208-4](https://doi.org/10.1007/s10584-011-0208-4)
77. F. C. Moore, D. B. Lobell, The fingerprint of climate trends on European crop yields. *Proc. Natl. Acad. Sci. U.S.A.* **112**, 2670–2675 (2015). doi: [10.1073/pnas.1409606112](https://doi.org/10.1073/pnas.1409606112); pmid: [25691735](https://pubmed.ncbi.nlm.nih.gov/25691735/)
78. J. R. Welch et al., Rice yields in tropical/subtropical Asia exhibit large but opposing sensitivities to minimum and maximum temperatures. *Proc. Natl. Acad. Sci. U.S.A.* **107**, 14562–14567 (2010). doi: [10.1073/pnas.1001222107](https://doi.org/10.1073/pnas.1001222107); pmid: [20696908](https://pubmed.ncbi.nlm.nih.gov/20696908/)
79. R. Guiteras, The impact of climate change on Indian agriculture, University of Maryland, College Park, Working paper (2009).
80. R. M. Fishman, Climate change, rainfall variability, and adaptation through irrigation: Evidence from Indian agriculture, Working paper (2011).
81. E. Duflo, R. Pande, Dams. *Q. J. Econ.* **122**, 601–646 (2007). doi: [10.1162/qjec.122.2.601](https://doi.org/10.1162/qjec.122.2.601)
82. A. Wineman, B. Mulenga, Sensitivity of field crops to climate shocks in Zambia, Working paper 18 (2014). [http://fsg.afre.msu.edu/climate\\_change/Crop\\_yield\\_and\\_weather\\_in\\_Zambia\\_August\\_16\\_2014.pdf](http://fsg.afre.msu.edu/climate_change/Crop_yield_and_weather_in_Zambia_August_16_2014.pdf)
83. D. B. Lobell et al., Prioritizing climate change adaptation needs for food security in 2030. *Science* **319**, 607–610 (2008). doi: [10.1126/science.1152339](https://doi.org/10.1126/science.1152339); pmid: [18239122](https://pubmed.ncbi.nlm.nih.gov/18239122/)
84. G. André, B. Engel, P. B. Berentsen, T. V. Vellinga, A. G. J. M. Oude Lansink, Quantifying the effect of heat stress on daily milk yield and monitoring dynamic changes using an adaptive dynamic model. *J. Dairy Sci.* **94**, 4502–4513 (2011). doi: [10.3168/jds.2010-4139](https://doi.org/10.3168/jds.2010-4139); pmid: [21854922](https://pubmed.ncbi.nlm.nih.gov/21854922/)
85. J. Bryant, N. López-Villalobos, J. E. Pryce, C. W. Holmes, D. L. Johnson, N. Lo'pez-Villalobos, J. Pryce, C. Holmes, D. Johnson, Quantifying the effect of thermal environment on production traits in three breeds of dairy cattle in New Zealand. *N. Z. J. Agric. Res.* **50**, 327–338 (2007). doi: [10.1080/00288230709510301](https://doi.org/10.1080/00288230709510301)
86. N. Key, S. Sneeringer, D. Marquardt, Climate change, heat stress, and US dairy production. USDA-ERS Economic Research Report (2014).
87. J. Amundson, T. Mader, R. Rasby, Q. Hu, Environmental effects on pregnancy rate in beef cattle. *J. Anim. Sci.* **84.12**, 3415–3420 (2006).
88. W. Schlenker, M. J. Roberts, D. B. Lobell, US maize adaptability. *Nat. Clim. Chang.* **3**, 690–691 (2013). doi: [10.1038/nclimate1959](https://doi.org/10.1038/nclimate1959)
89. R. Hornbeck, The enduring impact of the American Dust Bowl: Short and long-run adjustments to environmental catastrophe. *Am. Econ. Rev.* **102**, 1477–1507 (2012). doi: [10.1257/aer.102.4.1477](https://doi.org/10.1257/aer.102.4.1477)
90. A. L. Olmstead, P. W. Rhode, Adapting North American wheat production to climatic challenges, 1839–2009. *Proc. Natl. Acad. Sci. U.S.A.* **108**, 480–485 (2011). doi: [10.1073/pnas.1008279108](https://doi.org/10.1073/pnas.1008279108); pmid: [2187376](https://pubmed.ncbi.nlm.nih.gov/2187376/)
91. A. L. Olmstead, P. W. Rhode, in *The Economics of Climate Change: Adaptations Past and Present* (Univ. of Chicago Press, 2011), pp. 169–194.
92. R. Sutch, in *The Economics of Climate Change: Adaptations Past and Present* (Univ. of Chicago Press, 2011), pp. 195–223.
93. F. Annan, W. Schlenker, Federal crop insurance and the disincentive to adapt to extreme heat. *Am. Econ. Rev.* **105**, 262–266 (2015). doi: [10.1257/aer.p20151031](https://doi.org/10.1257/aer.p20151031)
94. G. Heal, J. Park, Goldlocks economies? Temperature stress and the direct impacts of climate change, NBER Working Paper 21119, (2015).
95. O. Seppanen, W. J. Fisk, Q. Lei, Room temperature and productivity in office work. Lawrence Berkeley National Laboratory (2006).
96. J. S. Graff Zivin, S. M. Hsiang, M. J. Neidell, Temperature and human capital in the short and long-run. NBER Working Paper 21157 (2015).
97. J. Graff Zivin, M. Neidell, Temperature and the allocation of time: Implications for climate change. *J. Labor Econ.* **32**, 1–26 (2014). doi: [10.1086/671766](https://doi.org/10.1086/671766)
98. E. Somanathan, R. Somanathan, A. Sudarshan, M. Tewari, The impact of temperature on productivity and labor supply: Evidence from Indian manufacturing, Working paper (2015). [www.isid.ac.in/~pu/disapers/dp14-10.pdf](http://www.isid.ac.in/~pu/disapers/dp14-10.pdf)
99. A. Advharyu, N. Kala, A. Nyshadham, The light and the heat: Productivity co-benefits of energy-saving technology, Working paper (2014). <http://economics.yale.edu/sites/default/files/advharyu.pdf>

100. M. Burke, S. M. Hsiang, E. Miguel, Global non-linear effect of temperature on economic production. *Nature* **527**, 235–239 (2015). doi: [10.1038/nature15725](https://doi.org/10.1038/nature15725); pmid: 26503051
101. G. Heal, J. Park, Feeling the heat: Temperature, physiology and the wealth of nations. NBER Working Paper 19725 (2013).
102. L. Wenz, A. Levermann, Enhanced economic connectivity to foster heat stress-related losses. *Sci. Adv.* **2**, e1501026 (2016). pmid: 27386555
103. M. Auffhammer, E. T. Mansur, Measuring climatic impacts on energy consumption: A review of the empirical literature. *Energy Econ.* **46**, 522–530 (2014). doi: [10.1016/j.eneco.2014.04.017](https://doi.org/10.1016/j.eneco.2014.04.017)
104. E. d. Cian et al., Climate change impacts on energy demand, CMCC Research Paper (2014). [www.cmcc.it/wp-content/uploads/2015/02/rp0240-cip-12-20141.pdf](http://www.cmcc.it/wp-content/uploads/2015/02/rp0240-cip-12-20141.pdf).
105. L. W. Davis, P. J. Gertler, Contribution of air conditioning adoption to future energy use under global warming. *Proc. Natl. Acad. Sci. U.S.A.* **112**, 5962–5967 (2015). doi: [10.1073/pnas.1423558112](https://doi.org/10.1073/pnas.1423558112); pmid: 25918391
106. D. J. Sailor, A. Pavlova, Air conditioning market saturation and long-term response of residential cooling energy demand to climate change. *Energy* **28**, 941–951 (2003). doi: [10.1016/S0360-5442\(03\)00033-1](https://doi.org/10.1016/S0360-5442(03)00033-1)
107. M. Auffhammer, Cooling China: The weather dependence of air conditioner adoption. *Front. Econ. China* **9**, 70–84 (2014).
108. W. S. Jaglom et al., Assessment of projected temperature impacts from climate change on the US electric power sector using the integrated planning model. *Energy Policy* **73**, 524–539 (2014). doi: [10.1016/j.enpol.2014.04.032](https://doi.org/10.1016/j.enpol.2014.04.032)
109. G. R. McDermott, Ø. A. Nilsen, Electricity prices, river temperatures, and cooling water scarcity. *Land Econ.* **90**, 131–148 (2014). doi: [10.3368/le.90.1.131](https://doi.org/10.3368/le.90.1.131)
110. K. Linnerud, T. K. Mideksa, G. S. Eskeland, The impact of climate change on nuclear power supply. *Energy J.* **32**, 1 (2011). doi: [10.5547/ISSN0195-6574-EJ-Vol32-No1-6](https://doi.org/10.5547/ISSN0195-6574-EJ-Vol32-No1-6)
111. J. R. Muñoz, D. J. Sailor, J. R. Muñoz, D. J. Sailor, A modelling methodology for assessing the impact of climate variability and climatic change on hydroelectric generation. *Energy Convers. Manage.* **39**, 1459–1469 (1998). doi: [10.1016/S0196-8904\(98\)00017-X](https://doi.org/10.1016/S0196-8904(98)00017-X)
112. J. Eyer, C. Wichman, The effect of water supply shocks on the electricity generation mix: Implications for climate change. Working paper, pp. 1459–1469 (2014).
113. J. Feyrer, B. Sacerdote, Colonialism and modern income: Islands as natural experiments. *Rev. Econ. Stat.* **91**, 245–262 (2009). doi: [10.1162/rest.91.2.245](https://doi.org/10.1162/rest.91.2.245)
114. P. Kaluza, A. Kölsch, M. T. Gastner, B. Blasius, The complex network of global cargo ship movements. *J. R. Soc. Interface* **7**, 1093 (2010). doi: [10.1098/rsif.2009.0495](https://doi.org/10.1098/rsif.2009.0495); pmid: 20086053
115. B. Jones, B. Olken, Climate shocks and exports. *Am. Econ. Rev. Pap. Proc.* **100**, 454–459 (2010). doi: [10.1257/aer.100.2.454](https://doi.org/10.1257/aer.100.2.454)
116. S. M. Hsiang, A. S. Jina, The causal effect of environmental catastrophe on long-run economic growth: Evidence from 6,700 cyclones. NBER Working Paper 20352 (2014).
117. H. Kazianga, C. Udry, Consumption smoothing? Livestock, insurance and drought in rural Burkina Faso. *J. Dev. Econ.* **79**, 413–446 (2006). doi: [10.1016/j.jdevco.2006.01.011](https://doi.org/10.1016/j.jdevco.2006.01.011)
118. K. Desmet, E. Rossi-Hansberg, On the spatial economic impact of global warming. *J. Urban Econ.* **88**, 16–37 (2015). doi: [10.1016/j.jue.2015.04.004](https://doi.org/10.1016/j.jue.2015.04.004)
119. A. Costinot, D. Donaldson, C. Smith, Evolving comparative advantage and the impact of climate change in agricultural markets: Evidence from 1.7 million fields around the world. *J. Pol. Econ.* (2016).
120. C. B. d'Amour, L. Wenz, M. Kalkuhl, J. C. Steckel, F. Creutzig, Teleconnected food supply shocks. *Environ. Res. Lett.* **11**, 035007 (2016). doi: [10.1088/1748-9326/11/3/035007](https://doi.org/10.1088/1748-9326/11/3/035007)
121. E. Miguel, S. Satyanath, E. Sergenti, Economic shocks and civil conflict: An instrumental variables approach. *J. Polit. Econ.* **112**, 725–753 (2004). doi: [10.1086/421174](https://doi.org/10.1086/421174)
122. S. Barrios, L. Bertinelli, E. Strobl, Trends in rainfall and economic growth in Africa: A neglected cause of the African growth tragedy. *Rev. Econ. Stat.* **92**, 350–366 (2010). doi: [10.1162/rest.2010.11212](https://doi.org/10.1162/rest.2010.11212)
123. S. M. Hsiang, K. C. Meng, Tropical economics. *Am. Econ. Rev.* **105**, 257–261 (2015). doi: [10.1257/aer.p20151030](https://doi.org/10.1257/aer.p20151030)
124. R. Colacito, B. Hoffmann, T. Phan, Temperatures and growth: A panel analysis of the United States. Working paper (2014). [http://papers.ssrn.com/sol3/papers.cfm?abstract\\_id=2546456](http://papers.ssrn.com/sol3/papers.cfm?abstract_id=2546456).
125. P. Zhang, J. Zhang, O. Deschênes, K. Meng, Temperature effects on productivity and factor reallocation: Evidence from a half million chinese manufacturing plants. Working paper (2016). [http://papers.ssrn.com/sol3/papers.cfm?abstract\\_id=2654406](http://papers.ssrn.com/sol3/papers.cfm?abstract_id=2654406)
126. S. M. Hsiang, A. S. Jina, Geography, depreciation, and growth. *Am. Econ. Rev.* **105**, 252–256 (2015). doi: [10.1257/aer.p20151029](https://doi.org/10.1257/aer.p20151029)
127. M. Dell, B. F. Jones, B. A. Olken, Climate change and economic growth: Evidence from the last half century. *Am. Econ. J. Macroecon.* **4**, 66–95 (2012). doi: [10.1257/mac.4.3.66](https://doi.org/10.1257/mac.4.3.66)
128. M. Dell, B. F. Jones, B. A. Olken, Temperature shocks and economic growth: Evidence from the last half century. *Am. Econ. J. Macroecon.* **4**, 66–95 (2012). doi: [10.1257/mac.4.3.66](https://doi.org/10.1257/mac.4.3.66)
129. M. Burke, E. Gong, K. Jones, Income shocks and HIV in Africa. *Econ. J.* **125**, 1157–1189 (2015). doi: [10.1111/ecoj.12149](https://doi.org/10.1111/ecoj.12149)
130. S. M. Hsiang, M. Burke, E. Miguel, Quantifying the influence of climate on human conflict. *Science* **341**, 1235367 (2013). doi: [10.1126/science.1235367](https://doi.org/10.1126/science.1235367); pmid: 24031020
131. M. Burke, S. M. Hsiang, E. Miguel, Climate and conflict. *Annu. Rev. Econ.* **7**, 577–617 (2015). doi: [10.1146/annurev-economics-080614-115430](https://doi.org/10.1146/annurev-economics-080614-115430)
132. D. T. Kenrick, S. W. Macfarlane, Ambient temperature and horn kicking: A field study of the heat/aggression relationship. *Environ. Behav.* **18**, 179–191 (1986). doi: [10.1177/0013916586182002](https://doi.org/10.1177/0013916586182002)
133. P. Kolb, C. Gockel, L. Werth, The effects of temperature on service employees' customer orientation: An experimental approach. *Ergonomics* **55**, 621–635 (2012). doi: [10.1080/00140139.2012.659763](https://doi.org/10.1080/00140139.2012.659763); pmid: 22455315
134. P. Baylis, Temperature and temperament: Evidence from a billion tweets. Working paper (2015). <https://doi.org/10.1177/0013916586182002>
135. R. P. Larrick, T. A. Timmerman, A. M. Carton, J. Abrevaya, Temper, temperature, and temptation: Heat-related retaliation in baseball. *Psychol. Sci.* **22**, 423–428 (2011). doi: [10.1177/0956797611399292](https://doi.org/10.1177/0956797611399292); pmid: 21350182
136. M. Ranson, Crime, weather, and climate change. *J. Environ. Econ. Manage.* **67**, 274–302 (2014). doi: [10.1016/j.jeem.2013.11.008](https://doi.org/10.1016/j.jeem.2013.11.008)
137. B. Jacob, L. Lefgren, E. Moretti, The dynamics of criminal behavior: Evidence from weather shocks. *J. Hum. Resour.* **XLII**, 489–527 (2007). doi: [10.3368/jhr.XLII.3.489](https://doi.org/10.3368/jhr.XLII.3.489)
138. D. Blakeslee, R. Fishman, Rainfall shocks and property crimes in agrarian societies: Evidence from India. Working paper (2015).
139. S. F. Morrison, K. Nakamura, C. J. Madden, Central control of thermogenesis in mammals. *Exp. Physiol.* **93**, 773–797 (2008). doi: [10.1113/expphysiol.2007.041848](https://doi.org/10.1113/expphysiol.2007.041848); pmid: 18469069
140. R. S. Ray et al., Impaired respiratory and body temperature control upon acute serotonergic neuron inhibition. *Science* **333**, 637–642 (2011). doi: [10.1126/science.1205295](https://doi.org/10.1126/science.1205295); pmid: 21798952
141. D. Seo, C. J. Patrick, P. J. Kennealy, Christopher Patrick, Role of serotonin and dopamine system interactions in the neurobiology of impulsive aggression and its comorbidity with other clinical disorders. *Aggress. Violent. Behav.* **13**, 383–395 (2008). doi: [10.1016/j.avb.2008.06.003](https://doi.org/10.1016/j.avb.2008.06.003); pmid: 19802333
142. L. Iyer, P. Topalova, Poverty and crime: Evidence from rainfall and trade shocks in India. Working paper (2014). [www.hbs.edu/faculty/Publication%20Files/14-067\\_45092fee-b164-4662-894b-5d28471fa69b.pdf](http://www.hbs.edu/faculty/Publication%20Files/14-067_45092fee-b164-4662-894b-5d28471fa69b.pdf).
143. S. Sekhri, A. Storeygard, Dowry deaths: Consumption smoothing in response to climate variability in India. Working paper (2012). [www.virginia.edu/economics/RePEc/vir/virpap/papers/virpap407.pdf](http://www.virginia.edu/economics/RePEc/vir/virpap/papers/virpap407.pdf).
144. E. Miguel, Poverty and witch killing. *Rev. Econ. Stud.* **72**, 1153–1172 (2005). doi: [10.1111/0034-6527.00365](https://doi.org/10.1111/0034-6527.00365)
145. D. Zhang et al., Clim. change, wars and dynastic cycles in China over the last millennium. *Clim. Chang.* (2006).
146. D. D. Zhang, P. Brecke, H. F. Lee, Y.-Q. He, J. Zhang, Global climate change, war, and population decline in recent human history. *Proc. Natl. Acad. Sci. U.S.A.* **104**, 19214–19219 (2007). doi: [10.1073/pnas.0703073104](https://doi.org/10.1073/pnas.0703073104); pmid: 18048343
147. R. Tol, S. Wagner, Climate change and violent conflict in Europe over the last millennium. *Clim. Change* **99**, 65–79 (2010).
148. R. W. Anderson, N. D. Johnson, M. Koyama, From the persecuting to the protective state? Jewish expulsions and weather shocks: 1100 to 1800. Working paper (2013). <http://ssrn.com/abstract=2212323>.
149. R. Jia, Weather shocks, sweet potatoes and peasant revolts in historical China. *Econ. J.* **124**, 92–118 (2013). doi: [10.1111/ecoj.12037](https://doi.org/10.1111/ecoj.12037)
150. J. K. Kung, C. Ma, Can cultural norms reduce conflicts? Confucianism and peasant rebellions in Qing China. Working paper (2012). [http://ahc2012.org/papers/S6B-2\\_Kai-singKung\\_Ma.pdf](http://ahc2012.org/papers/S6B-2_Kai-singKung_Ma.pdf).
151. Y. Bai, J. Kung, Climate shocks and Sino-nomadic conflict. *Rev. Econ. Stat.* **93**, 970–981 (2010). doi: [10.1162/REST\\_a.00106](https://doi.org/10.1162/REST_a.00106)
152. T. Fetzter, Can warfare programs moderate violence? Evidence from India. Working paper (2014). <http://sticder.lse.ac.uk/dps/eopp/eopp53.pdf>.
153. F. Hidalgo, S. Naidu, S. Nichter, N. Richardson, Economic determinants of land invasions. *Rev. Econ. Stat.* **92**, 505–523 (2010). doi: [10.1162/REST\\_a.00007](https://doi.org/10.1162/REST_a.00007)
154. J. Maystadt, O. Ecker, Extreme weather and civil war in Somalia: Does drought fuel conflict in Somalia through livestock price shocks? *Am. J. Agric. Econ.* **96**, 1157–1182 (2014). doi: [10.1093/ajae/auo010](https://doi.org/10.1093/ajae/auo010)
155. T. A. Carleton, S. M. Hsiang, M. B. Burke, Conflict in a changing climate. *Eur. Phys. J. Spec. Top.* **225**, 489–511 (2016). doi: [10.1140/epjst/e2015-50100-5](https://doi.org/10.1140/epjst/e2015-50100-5)
156. L. Ralston, Conflict and climate: A micro-level analysis. CEQA Working paper pp. 1–59 (2015). [http://ceqa.berkeley.edu/assets/miscellaneous\\_files/19\\_ABCA-Conflict\\_and\\_Climate\\_Ralston.pdf](http://ceqa.berkeley.edu/assets/miscellaneous_files/19_ABCA-Conflict_and_Climate_Ralston.pdf).
157. N. K. Kim, Revisiting economic shocks and coups. *J. Conflict Resolut.* **60**, 3–31 (2014). doi: [10.1177/0022002713520531](https://doi.org/10.1177/0022002713520531)
158. P. J. Burke, A. Leigh, Do output contractions trigger democratic change? *Am. Econ. J. Macroecon.* **2**, 124–157 (2010). doi: [10.1257/mac.2.4.124](https://doi.org/10.1257/mac.2.4.124)
159. P. J. Burke, Economic growth and political survival. *B.E. J. Macroecon.* **12**, 1935–1690 (2012). doi: [10.1515/1935-1690.2398](https://doi.org/10.1515/1935-1690.2398)
160. E. Chaney, Revolt on the Nile: Economic shocks, religion, and political power. *Econometrica* **81**, 2033–2053 (2013). doi: [10.3982/ECTA10233](https://doi.org/10.3982/ECTA10233)
161. H. Cullen et al., Climate change and the collapse of the Akkadian empire: Evidence from the deep sea. *Geology* **28**, 379 (2000). doi: [10.1130/0091-7613\(2000\)28<379:CCATCo>2.0.CO;2](https://doi.org/10.1130/0091-7613(2000)28<379:CCATCo>2.0.CO;2)
162. G. H. Haug et al., Climate and the collapse of Maya civilization. *Science* **299**, 1731–1735 (2003). doi: [10.1126/science.1080444](https://doi.org/10.1126/science.1080444); pmid: 12637744
163. B. M. Buckley et al., Climate as a contributing factor in the demise of Angkor, Cambodia. *Proc. Natl. Acad. Sci. U.S.A.* **107**, 6748–6752 (2010). doi: [10.1073/pnas.0910827107](https://doi.org/10.1073/pnas.0910827107); pmid: 20351244
164. G. Yancheva et al., Influence of the intertropical convergence zone on the East Asian monsoon. *Nature* **445**, 74–77 (2007). doi: [10.1038/nature05431](https://doi.org/10.1038/nature05431); pmid: 17203059
165. U. Büntgen et al., 2500 years of European climate variability and human susceptibility. *Science* **331**, 578–582 (2011). doi: [10.1126/science.1197175](https://doi.org/10.1126/science.1197175); pmid: 21233349
166. M. Kleemann, Migration choice under risk and liquidity constraints. Working paper (2014). [www.economics.illinois.edu/seminars/documents/Kleemann.pdf](http://www.economics.illinois.edu/seminars/documents/Kleemann.pdf).
167. C. Cattaneo, G. Peri, The migration response to increasing temperatures. *J. Dev. Econ.* (2016).
168. S. Feng, A. B. Krueger, M. Oppenheimer, Linkages among climate change, crop yields and Mexico-US cross-border migration. *Proc. Natl. Acad. Sci. U.S.A.* **107**, 14257–14262 (2010). doi: [10.1073/pnas.1002632107](https://doi.org/10.1073/pnas.1002632107); pmid: 20660749
169. S. Feng, M. Oppenheimer, W. Schlenker, Climate Change, Crop Yields, and Internal Migration in the United States (NBER Work. Pap. 17734, 2012).
170. J. V. Henderson, A. Storeygard, U. Deichmann, 50 years of urbanization in Africa: Examining the role of climate change. World Bank Policy Research Working Paper (2014). [www.wds.worldbank.org/external/default/WDSContentServer/WDS/IB/2014/06/16/000158349\\_20140616110124/Rendered/PDF/WPS6925.pdf](http://www.wds.worldbank.org/external/default/WDSContentServer/WDS/IB/2014/06/16/000158349_20140616110124/Rendered/PDF/WPS6925.pdf).
171. P. Bohra-Mishra, M. Oppenheimer, S. M. Hsiang, Nonlinear permanent migration response to climatic variations but minimal response to disasters. *Proc. Natl. Acad. Sci. U.S.A.* **111**, 9780–9785 (2014). doi: [10.1073/pnas.1317166111](https://doi.org/10.1073/pnas.1317166111); pmid: 24958887
172. R. Cai, S. Feng, M. Pytkikova, M. Oppenheimer, Climate variability and international migration: The importance of the agricultural linkage. IZA Discussion Paper (2014). <http://ftp.iza.org/dp8183.pdf>.
173. K. Jessoe et al., Climate change and labor markets in rural Mexico: Evidence from annual fluctuations in weather. Working paper (2014). [http://ageconsearch.umn.edu/bitstream/170556/2/WeatherLaborMexico\\_AEA.pdf](http://ageconsearch.umn.edu/bitstream/170556/2/WeatherLaborMexico_AEA.pdf).



174. L. Marchiori, J.-F. Maystadt, I. Schumacher, The impact of weather anomalies on migration in sub-Saharan Africa. *J. Environ. Econ. Manage.* **63**, 355–374 (2012). doi: [10.1016/j.jeem.2012.02.001](https://doi.org/10.1016/j.jeem.2012.02.001)
175. R. J. Nawrotzki, L. M. Hunter, D. M. Runfola, F. Riosmena, Climate change as a migration driver from rural to urban Mexico. *Environ. Res. Lett.* **10**, 114023 (2015). doi: [10.1088/1748-9326/10/11/114023](https://doi.org/10.1088/1748-9326/10/11/114023); pmid: 26692890
176. A. Drabo, L. Mbaye, Climate change, natural disasters and migration: An empirical analysis in developing countries, IZA Discussion Paper (2011). <http://ftp.iza.org/dp5927.pdf>.
177. C. L. Gray, V. Mueller, Natural disasters and population mobility in Bangladesh. *Proc. Natl. Acad. Sci. U.S.A.* **109**, 6000–6005 (2012). doi: [10.1073/pnas.1115944109](https://doi.org/10.1073/pnas.1115944109); pmid: 22474361
178. E. Strobl, The economic growth impact of hurricanes: Evidence from US coastal counties. *Rev. Econ. Stat.* **93**, 575–589 (2011). doi: [10.1162/REST\\_a\\_00082](https://doi.org/10.1162/REST_a_00082)
179. T. Deryugina, The role of transfer payments in mitigating shocks: Evidence from the impact of hurricanes (2013). [http://papers.ssrn.com/sol3/papers.cfm?abstract\\_id=2314663](http://papers.ssrn.com/sol3/papers.cfm?abstract_id=2314663).
180. R. Fishman, J. Russ, P. Carrillo, Long-term impacts of high temperatures on economic productivity, Working paper (2015). [www.gwu.edu/~iiep/assets/docs/papers/2015WP/FishmanRussCarrillo\\_October2015.pdf](http://www.gwu.edu/~iiep/assets/docs/papers/2015WP/FishmanRussCarrillo_October2015.pdf).
181. M. Auffhammer, Quantifying intensive and extensive margin adaptation responses to climate change: A study of California's residential electricity consumption, Working paper (2013). [www.arec.umd.edu/sites/default/files/\\_docs/events/Maximilian%20Auffhammer-Quantifying%20Intensive%20and%20extensive%20margin%20adaptation%20responses%20to%20climate%20change-A%20study%20of%20California's%20residential%20electricity%20consumption.pdf](http://www.arec.umd.edu/sites/default/files/_docs/events/Maximilian%20Auffhammer-Quantifying%20Intensive%20and%20extensive%20margin%20adaptation%20responses%20to%20climate%20change-A%20study%20of%20California's%20residential%20electricity%20consumption.pdf).
182. D. B. Lobell *et al.*, Greater sensitivity to drought accompanies maize yield increase in the U.S. Midwest. *Science* **344**, 516–519 (2014). doi: [10.1126/science.1251423](https://doi.org/10.1126/science.1251423); pmid: 24786079
183. M. B. Burke, E. Miguel, S. Satyanath, J. A. Dykema, D. B. Lobell, Warming increases the risk of civil war in Africa. *Proc. Natl. Acad. Sci. U.S.A.* **106**, 20670–20674 (2009). doi: [10.1073/pnas.0907998106](https://doi.org/10.1073/pnas.0907998106); pmid: 19934048
184. D. B. Lobell, W. Schlenker, J. Costa-Roberts, Climate trends and global crop production since 1980. *Science* **333**, 616–620 (2011). doi: [10.1126/science.1204531](https://doi.org/10.1126/science.1204531); pmid: 21551030
185. A. I. Barreca, K. Clay, O. Deschênes, M. Greenstone, J. S. Shapiro, Convergence in adaptation to climate change: Evidence from high temperatures and mortality, 1900–2004. *Am. Econ. Rev.* **105**, 247–251 (2015). doi: [10.1257/aer.p20151028](https://doi.org/10.1257/aer.p20151028)
186. B. Lomborg, *Global crises, global solutions* (Cambridge University Press, 2004).
187. M. E. Kahn, The death toll from natural disasters: The role of income, geography, and institutions. *Rev. Econ. Stat.* **87**, 271–284 (2005). doi: [10.1162/0034653053970339](https://doi.org/10.1162/0034653053970339)
188. T. Deryugina, How do people update? The effects of local weather fluctuations on beliefs about global warming. *Clim. Change* **118**, 397–416 (2013). doi: [10.1007/s10584-012-0615-1](https://doi.org/10.1007/s10584-012-0615-1)
189. J. Shrader, Expectations and adaptation to environmental risks, Working paper (2016). [http://acsweb.ucsd.edu/~jgshrader/papers/forecasts\\_and\\_adaptation.pdf](http://acsweb.ucsd.edu/~jgshrader/papers/forecasts_and_adaptation.pdf).
190. T. A. Garrett, R. S. Sobel, The political economy of FEMA disaster payments. *Econ. Inq.* **41**, 496–509 (2003). doi: [10.1093/ei/cbg023](https://doi.org/10.1093/ei/cbg023)
191. A. Healy, N. Malhotra, Myopic voters and natural disaster policy. *Am. Polit. Sci. Rev.* **103**, 387–406 (2009). doi: [10.1017/S0003055409990104](https://doi.org/10.1017/S0003055409990104)
192. T. Besley, R. Burgess, The political economy of government responsiveness: Theory and evidence from India. *Q. J. Econ.* **117**, 1415–1451 (2002). doi: [10.1162/0033555302320935061](https://doi.org/10.1162/0033555302320935061)
193. R. M. Townsend, Consumption insurance: An evaluation of risk-bearing systems in low-income economies. *J. Econ. Perspect.* **9**, 83–102 (1995). doi: [10.1257/jep.9.3.83](https://doi.org/10.1257/jep.9.3.83)
194. W. D. Nordhaus, Geography and macroeconomics: New data and new findings. *Proc. Natl. Acad. Sci. U.S.A.* **103**, 3510–3517 (2006). pmid: 16473945
195. R. S. Pindyck, Climate change policy: What do the models tell us? NBER Working paper 19244 (2013). [www.nber.org/papers/w19244](http://www.nber.org/papers/w19244).
196. F. C. Moore, D. B. Diaz, Temperature impacts on economic growth warrant stringent mitigation policy. *Nat. Clim. Chang.* **5**, 127–131 (2015). doi: [10.1038/nclimate2481](https://doi.org/10.1038/nclimate2481)
197. D. B. Lobell, C. B. Field, Global scale climate–crop yield relationships and the impacts of recent warming. *Environ. Res. Lett.* **2**, 014002 (2007). doi: [10.1088/1748-9326/2/1/014002](https://doi.org/10.1088/1748-9326/2/1/014002)

## ACKNOWLEDGMENTS

We thank P. Lau, A. Hultgren, and M. Landin for research assistance and R. Burgess for comments. T.A.C. received support from the STAR Fellowship No. FP91780401 awarded by the U.S. Environmental Protection Agency (EPA). This article has not been formally reviewed by EPA and the views expressed herein are solely those of the authors.

## SUPPLEMENTARY MATERIALS

[www.sciencemag.org/content/353/6304/aad9837/suppl/DC1](http://www.sciencemag.org/content/353/6304/aad9837/suppl/DC1)  
Materials and Methods  
Figs. S1 and S2  
References

10.1126/science.aad9837

## REVIEW SUMMARY

## CLIMATE CHANGE

# Improving the forecast for biodiversity under climate change

M. C. Urban,\* G. Bocedi, A. P. Hendry, J.-B. Mihoub, G. Pe'er, A. Singer, J. R. Bridle, L. G. Crozier, L. De Meester, W. Godsoe, A. Gonzalez, J. J. Hellmann, R. D. Holt, A. Huth, K. Johst, C. B. Krug, P. W. Leadley, S. C. F. Palmer, J. H. Pantel, A. Schmitz, P. A. Zollner, J. M. J. Travis

**BACKGROUND:** As global climate change accelerates, one of the most urgent tasks for the coming decades is to develop accurate predictions about biological responses to guide the effective protection of biodiversity. Predictive models in biology provide a means for scientists to project changes to species and ecosystems in response to disturbances such as climate change. Most current predictive models, however, exclude important biological mechanisms such as demography, dispersal, evolution, and species interactions. These biological mechanisms have been shown to be important in mediating past and present responses to climate change. Thus, current modeling efforts do not provide sufficiently accurate predic-

tions. Despite the many complexities involved, biologists are rapidly developing tools that include the key biological processes needed to improve predictive accuracy. The biggest obstacle to applying these more realistic models is that the data needed to inform them are almost always missing. We suggest ways to fill this growing gap between model sophistication and information to predict and prevent the most damaging aspects of climate change for life on Earth.

**ADVANCES:** On the basis of empirical and theoretical evidence, we identify six biological mechanisms that commonly shape responses to climate change yet are too often missing

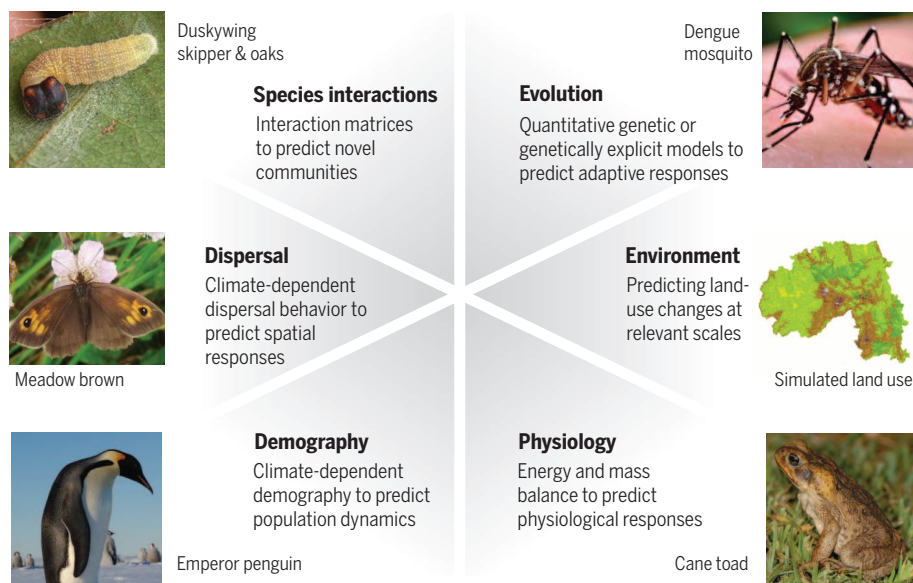
from current predictive models: physiology; demography, life history, and phenology; species interactions; evolutionary potential and population differentiation; dispersal, colonization, and range dynamics; and responses to environmental variation. We prioritize the types of information needed to inform each of these mechanisms and suggest proxies for data that are missing or difficult to collect. We show that even for well-studied species, we often lack critical information that would be necessary to apply more realistic, mechanistic models. Consequently, data limitations likely override the potential gains in accuracy of more realistic models. Given the

## ON OUR WEBSITE

Read the full article at <http://dx.doi.org/10.1126/science.aad8466>

enormous challenge of collecting this detailed information on millions of species around the world, we highlight practical methods that promote the greatest gains in predictive accuracy. Trait-based approaches leverage sparse data to make more general inferences about unstudied species. Targeting species with high climate sensitivity and disproportionate ecological impact can yield important insights about future ecosystem change. Adaptive modeling schemes provide a means to target the most important data while simultaneously improving predictive accuracy.

**OUTLOOK:** Strategic collections of essential biological information will allow us to build generalizable insights that inform our broader ability to anticipate species' responses to climate change and other human-caused disturbances. By increasing accuracy and making uncertainties explicit, scientists can deliver improved projections for biodiversity under climate change together with characterizations of uncertainty to support more informed decisions by policymakers and land managers. Toward this end, a globally coordinated effort to fill data gaps in advance of the growing climate-fueled biodiversity crisis offers substantial advantages in efficiency, coverage, and accuracy. Biologists can take advantage of the lessons learned from the Intergovernmental Panel on Climate Change's development, coordination, and integration of climate change projections. Climate and weather projections were greatly improved by incorporating important mechanisms and testing predictions against global weather station data. Biology can do the same. We need to adopt this meteorological approach to predicting biological responses to climate change to enhance our ability to mitigate future changes to global biodiversity and the services it provides to humans. ■



**Emerging models are beginning to incorporate six key biological mechanisms that can improve predictions of biological responses to climate change.** Models that include biological mechanisms have been used to project (clockwise from top) the evolution of disease-harboring mosquitoes, future environments and land use, physiological responses of invasive species such as cane toads, demographic responses of penguins to future climates, climate-dependent dispersal behavior in butterflies, and mismatched interactions between butterflies and their host plants. Despite these modeling advances, we seldom have the detailed data needed to build these models, necessitating new efforts to collect the relevant data to parameterize more biologically realistic predictive models.

The list of author affiliations is available in the full article online.

\*Corresponding author. Email: [mark.urban@uconn.edu](mailto:mark.urban@uconn.edu)

Cite this article as M. C. Urban et al., *Science* 353, aad8466 (2016). DOI: 10.1126/science.aad8466



## REVIEW

## CLIMATE CHANGE

# Improving the forecast for biodiversity under climate change

M. C. Urban,<sup>1\*</sup> G. Bocedi,<sup>2</sup> A. P. Hendry,<sup>3</sup> J.-B. Mihoub,<sup>4,5</sup> G. Pe'er,<sup>5,6</sup> A. Singer,<sup>6,7,8</sup> J. R. Bridle,<sup>9</sup> L. G. Crozier,<sup>10</sup> L. De Meester,<sup>11</sup> W. Godsoe,<sup>12</sup> A. Gonzalez,<sup>13</sup> J. J. Hellmann,<sup>14</sup> R. D. Holt,<sup>15</sup> A. Huth,<sup>7,6,16</sup> K. Johst,<sup>7</sup> C. B. Krug,<sup>17,18</sup> P. W. Leadley,<sup>17,18</sup> S. C. F. Palmer,<sup>2</sup> J. H. Pantel,<sup>19</sup> A. Schmitz,<sup>5</sup> P. A. Zollner,<sup>20</sup> J. M. J. Travis<sup>2</sup>

New biological models are incorporating the realistic processes underlying biological responses to climate change and other human-caused disturbances. However, these more realistic models require detailed information, which is lacking for most species on Earth. Current monitoring efforts mainly document changes in biodiversity, rather than collecting the mechanistic data needed to predict future changes. We describe and prioritize the biological information needed to inform more realistic projections of species' responses to climate change. We also highlight how trait-based approaches and adaptive modeling can leverage sparse data to make broader predictions. We outline a global effort to collect the data necessary to better understand, anticipate, and reduce the damaging effects of climate change on biodiversity.

We need to predict how climate change will alter biodiversity if we are to prevent serious damage to the biosphere (1). Biologists develop predictive models to anticipate how environmental changes might affect the future properties of species and ecosystems (2, 3). Many models have been developed to understand climate change impacts (fig. S1) (4), but biological responses remain difficult to predict (5, 6). One reason is that most models forecasting biodiversity change ignore underlying mechanisms, such as demographic shifts, species interactions,

and evolution, and instead extrapolate correlations between current species' ranges and climate (Fig. 1) (4). These omissions are troubling because we know that these missing biological mechanisms played key roles in mediating past and present biotic responses to climate change (7–9). Moreover, models ignoring biological mechanisms often become unreliable when extrapolated to novel conditions (10–13). As climates and ecological communities without historical precedent become more common and correlations between current species distributions and climate become uncoupled (10, 14, 15), we cannot rely on tools based on statistical descriptions of the past. Given the essential role of biological processes in mediating species' responses to climate change, accurate forecasts of future biodiversity likely will require more realistic models.

Emerging models incorporate fundamental biological mechanisms rather than relying solely on statistical correlations (16–19). Unlike correlative approaches, mechanistic models do not assume that a species' range reflects its niche perfectly, has reached equilibrium with the environment, or is independent of species interactions—all commonly violated assumptions (7, 13, 20, 21). Mechanistic models can also integrate multiple, interacting biological processes, as well as non-linear and stochastic dynamics (Fig. 2) (17, 18, 22), and can better characterize uncertainty by directly modeling error sources (2, 21, 23).

By incorporating realistic features such as demography and dispersal, mechanistic models commonly outperform correlative approaches in projecting climate change responses (13, 20). For example, mechanistic models consistently predicted simulated species' range dynamics over a period of 75 years, whereas correlative models became increasingly inaccurate over this same time frame (20). Mechanistic models improve predictive accu-

racy, especially when species face strong biotic interactions, experience novel climates, or cannot disperse far (13, 20, 24). Moreover, mechanistic models can inform predictive efforts by indicating processes (e.g., biotic limits on ranges) hidden by current associations between environments and species distributions (24). Although more work is needed to craft more sophisticated and accurate mechanistic models that are customizable for individual species and ecosystems, the tools are already mature enough to improve projections (2, 16, 19).

Mechanistic models, however, require high-quality data about how a species' unique biology governs its responses to climate. Parameters provide this information. For example, a parameter such as population growth rate determines how population abundances change through time. In contrast, a model variable such as population abundance describes emergent properties. Differentiating between parameters and variables is important given the recent focus on harmonizing efforts to collect variables that monitor the state of global biodiversity (25). We believe that such endeavors should focus not solely on collecting variables that indicate the state of biodiversity, but also on measuring mechanistic parameters critical for predicting future responses.

Here, we identify the mechanistic data needed to make substantial gains in predictive modeling. Rather than focusing on one particular mechanism (15, 18, 22, 26, 27), we take a comprehensive approach, assess data availability for each mechanism, prioritize data needs, demonstrate how to leverage sparse data to make general predictions, and suggest how global coordination could facilitate these efforts. By synthesizing this information in one framework, we aim to inspire the future research agenda needed to develop the full predictive potential of mechanistic models. Consistent with the Intergovernmental Panel on Climate

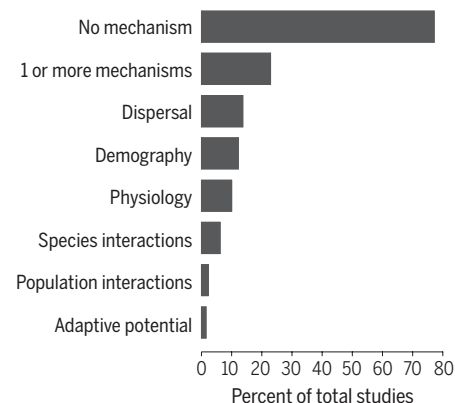


**Fig. 1. Most models of biological responses to climate change omit important biological mechanisms.** Only 23% of reviewed studies (4) included a biological mechanism. Models that included one mechanism usually incorporated others, but no model included all six mechanisms. All models included environmental variation, generally via correlations, but usually did not explicitly incorporate species' sensitivities to environmental variation at relevant spatiotemporal scales.

<sup>1</sup>Institute of Biological Risk, Ecology and Evolutionary Biology, University of Connecticut, Storrs, CT, USA. <sup>2</sup>Institute of Biological and Environmental Sciences, University of Aberdeen, Aberdeen, UK. <sup>3</sup>Redpath Museum, Department of Biology, McGill University, Montreal, Canada. <sup>4</sup>Sorbonne Universités, UPMC Université Paris 06, Muséum National d'Histoire Naturelle, CNRS, CESCO, UMR 7204, Paris, France. <sup>5</sup>Conservation Biology, UFZ-Helmholtz Centre for Environmental Research, Leipzig, Germany. <sup>6</sup>German Centre for Integrative Biodiversity Research (iDiv) Halle-Jena-Leipzig, Leipzig, Germany. <sup>7</sup>Ecological Modelling, UFZ-Helmholtz Centre for Environmental Research, Leipzig, Germany. <sup>8</sup>Swedish University of Agricultural Sciences, Swedish Species Information Centre, Uppsala, Sweden. <sup>9</sup>School of Biological Sciences, University of Bristol, Bristol, UK. <sup>10</sup>NOAA Fisheries Northwest Fisheries Science Center, Seattle, WA, USA. <sup>11</sup>Laboratory of Aquatic Ecology, Evolution and Conservation, KU Leuven, Leuven, Belgium. <sup>12</sup>Bio-Protection Research Centre, Lincoln University, Lincoln, New Zealand. <sup>13</sup>Biology, McGill University, Montreal, Canada. <sup>14</sup>Institute on the Environment; Ecology, Evolution, and Behavior, University of Minnesota, St. Paul, MN, USA. <sup>15</sup>Biology, University of Florida, Gainesville, FL, USA. <sup>16</sup>Institute for Environmental Systems Research, Department of Mathematics/Computer Science, University of Osnabrück, Osnabrück, Germany. <sup>17</sup>Ecologie Systématique Evolution, University Paris-Sud, CNRS, AgroParisTech, Université Paris-Saclay, Orsay, France. <sup>18</sup>DIVERSITAS, Paris, France. <sup>19</sup>Centre d'Ecologie fonctionnelle et Evolutive, UMR 5175 CNRS-Université de Montpellier-EPHE, Montpellier Cedex, France. <sup>20</sup>Forestry and Natural Resources, Purdue University, West Lafayette, IN, USA.

\*Corresponding author. Email: mark.urban@uconn.edu

Change (IPCC), we use “projection” to define all descriptions of the future and reserve “forecast” for the most likely projections.

### Crucial biological information

In Table 1, we identify six mechanisms that determine biological responses to climate change. On the basis of these mechanisms, we assess data availability for four well-studied species (Fig. 3). We find that although information on the six key mechanisms partly exists for species with high economic value, it is incomplete for even the best-studied species and absent for the vast majority of Earth's species. Consequently, the most realistic models usually rely on sparse data or data extrapolated from nonrepresentative populations, environments, or species.

We next describe each mechanism in further detail, highlighting key parameters and discussing challenges of measurement, uncertainty, and sen-

sitivity. Here, uncertainty encompasses both limited knowledge and random outcomes; sensitivity denotes how changes in a parameter value influence model outcomes. After describing these mechanisms, we recommend how to collect data efficiently and leverage imperfect data.

### Physiology

Physiology mediates how climate conditions such as temperature, growing degree-days, water availability, and potential evapotranspiration influence survival, growth, development, movement, and reproduction (18, 28–30). Physiological parameters include critical thermal minima or maxima (the low and high temperatures at which organisms cease organized movement), evaporative water loss, photosynthetic rate, and metabolic rate. These individual physiological responses often are used to inform higher-level processes such as population persistence and range shifts (29, 31). For example,

knowledge of the proportion of time a lizard remains active outside its burrow, where it is thermally neutral, can help in predicting its extinction risk under future climates (32).

Physiologists measure parameters from natural observations or experiments in climate-controlled chambers (28). However, using natural observations risks confounding responses to climate with other environmental factors (28). High-priority traits include responses to extreme heat or dryness, where survival often declines steeply. Uncertainty about physiological responses increases when we lack information on habitat heterogeneity, local adaptation, and physiological impacts on overall fitness.

### Demography, life history, and phenology

Demographic (birth, death, migration), life history (schedule of life cycle events), and phenological (timing of life history events) traits play critical

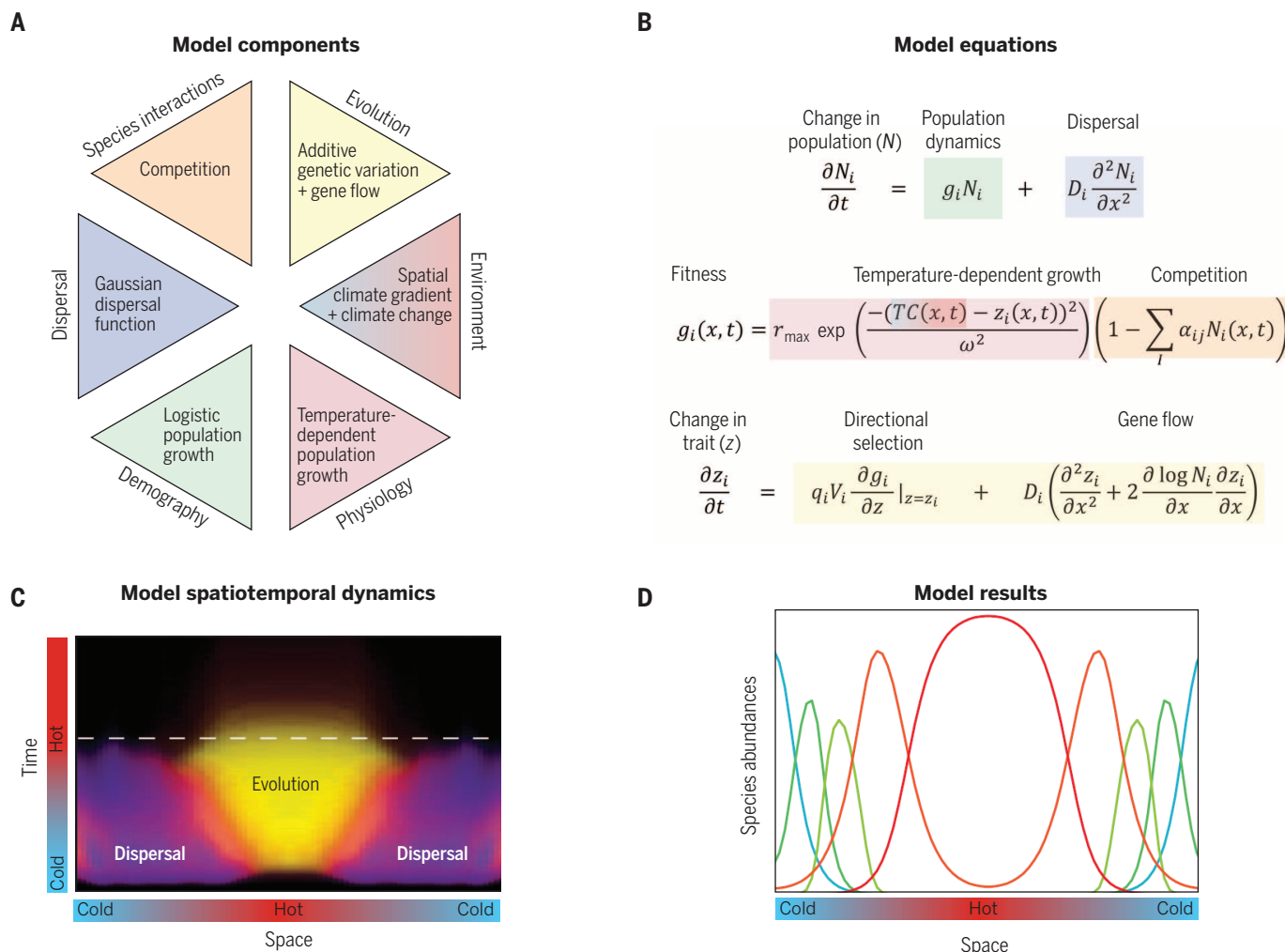


**Fig. 2. A generic model integrates six biological mechanisms to predict climate change responses.** (A to C) The six mechanisms (A) are matched by color to their representation in equations (B) simplified from (11) (see table S1 for symbol descriptions). Results suggest how dispersal (blue-purple), adaptive evolution (yellow), and their combination (red-orange) determine the match between community-wide thermal traits and changing local temper-

atures (C). Temperatures increase before stabilizing at the white dashed line. Black indicates no trait change. In cold regions, warm-adapted species disperse into newly suitable, warmer habitats. In warm regions, evolution dominates because no species with higher thermal tolerances exist. (D) Equilibrium abundances of five hypothetical species (each indicated by differently colored lines) after climate change.



roles in climate change responses (29, 33, 34). Important parameters include birth and death rates, age at maturity, development rate, and reproductive investment. Parameters are best collected on marked individuals across representative populations spanning different densities and climates.

However, these efforts require long-term, costly commitments. Changes in population abundances from short-term weather variation can provide proxies, but these become unreliable over time. Long-term vegetation plots can provide detailed demographic information for plants. Citizen sci-

tists can collect data over large regions, on traits such as flowering time or breeding date, but concerns about data quality likely limit their usefulness for less easily measured traits such as genetic variation.

Certain demographic parameters are especially important. For example, adult survival often affects population growth rate more than fecundity does in long-lived species (35). Density dependence and generation length also strongly affect extinction risk from climate change (22). Additional uncertainty stems from local adaptation, responses to novel environments, mismatched phenology, community shifts, and interactions with nonclimate stressors (15, 36, 37).

### Evolutionary potential and local adaptation

Assaying genetic variation is crucial for predicting future responses (27, 38) because it could allow populations to adapt to climate change in situ. Unfortunately, scientists seldom know if, or how quickly, populations can evolve climate-sensitive traits (36). Moreover, species usually comprise many locally adapted populations that each respond differently to climate change (39). Species might not shift their ranges with climate change if locally adapted populations become isolated and cannot colonize new habitats (39). Alternatively, individuals dispersing from locally adapted populations might track optimal climates across landscapes, and thus might not need to adapt locally (Fig. 2) (11).

The breeder's and Price equations can be used to predict responses to natural selection based on selection strength and genetic (co)variances (40). Genetic (co)variances are commonly measured through controlled breeding experiments or pedigrees. However, these estimates can become unreliable over long time scales or in novel environments if selection regimes or adaptive potential change (41). Also, genetic (co)variances often vary among populations and environments, thus requiring broad sampling and careful sensitivity analyses. Other approaches involve tracking evolution using long-term observations, reconstructing evolution from layered propagule banks, or applying experimental evolution (42, 43). For instance, comparing *Brassica rapa* plants grown from seeds collected before and after a drought revealed rapid evolution of flowering time (43). Past local adaptations to spatial climatic gradients are easier to assess. However, these patterns suggest past adaptive potential, not future evolutionary rates (36). By scanning entire genomes, next-generation sequencing offers a promising tool to uncover fine-scale evolutionary diversification (44), and declining cost for genomics could rapidly expand our limited knowledge of adaptive potential. Other frequently applied approaches include common garden experiments, natural transplants, and observations of phenotypic variation (Table 1).

Adaptive potential and population differentiation represent high-priority parameters because ignoring them contributes high levels of uncertainty (12, 27, 36, 43). For example, the Quino

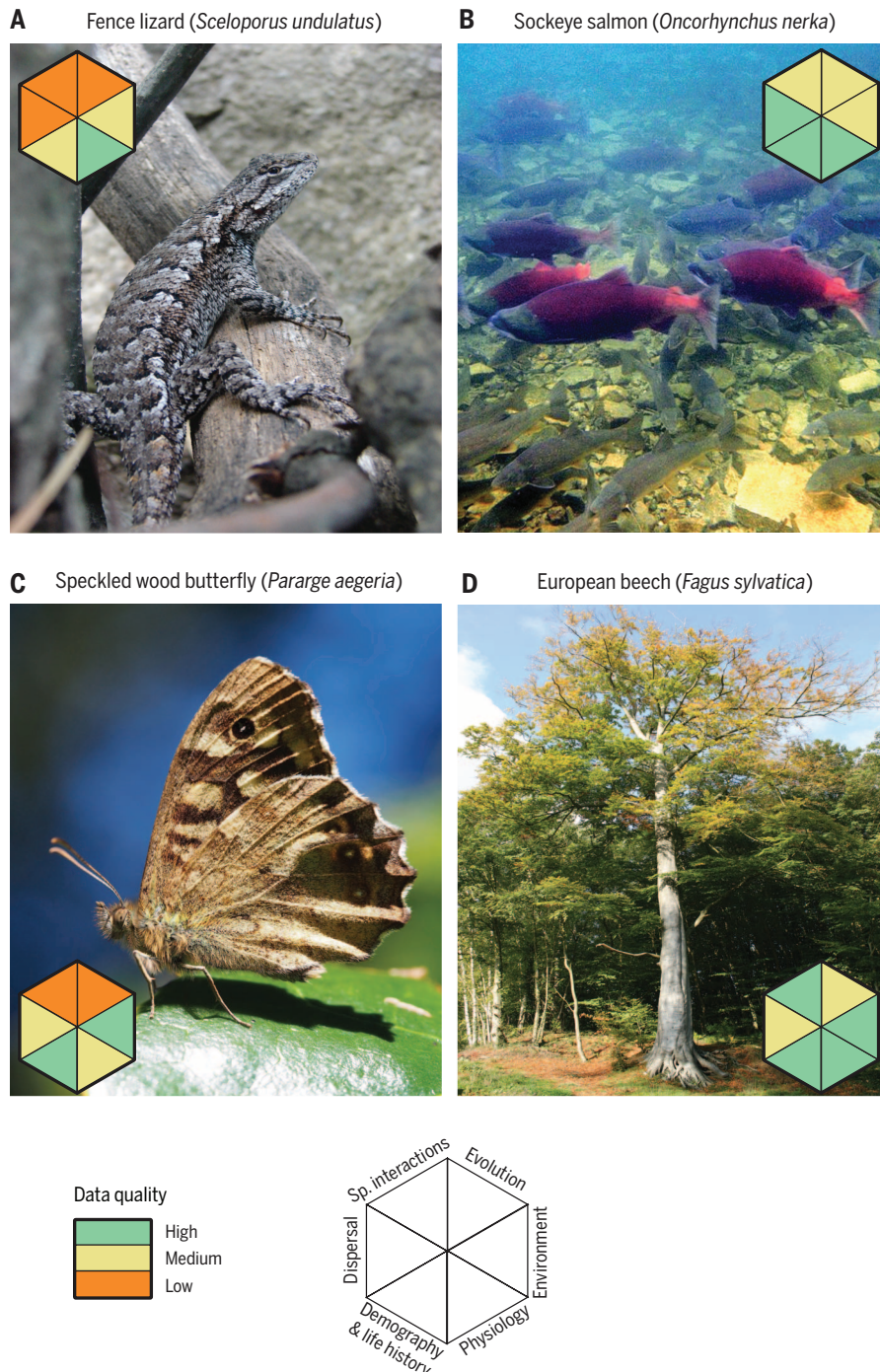


**Fig. 3. Data gaps exist even for well-studied species.** We rated data quality for some of the best-studied species in climate change research: (A) fence lizard, (B) sockeye salmon, (C) speckled wood butterfly, and (D) European beech. Data quality: high = near-complete information; medium = information available but missing critical components; low = information mostly absent. We evaluated data availability by examining models of climate responses, reviewing species-specific literature, and contacting experts.

checkerspot butterfly was expected to become extinct from climate change, but it persists after adapting to live on a new host plant (45). Given limited genetic and evolutionary information, we will often need to generalize adaptive rates across species based on characteristics such as generation time, genetic isolation, phenotypic variation, and phylogenetic position. Fortunately, even coarse estimates of maximum adaptive rate compared to climate change suggest tipping points, where minor changes in climate initiate major biological disruptions and thus represent targets for facilitating adaptation in threatened populations (46).

### Species interactions

Species interactions often underlie unexpected responses to climate change (10, 15), and most extinctions attributed to climate change to date have involved altered species interactions (47). Surprises occur when specialist interactions such as mutualism constrain species' responses (48), phenological mismatches alter species interactions (37), or top consumers propagate climate change effects throughout food webs (8). For instance, high temperatures along the Pacific Coast exacerbated predation by sea stars on mussels, which caused local extirpations (49). Yet few models account for species interactions explicitly, instead assuming that each species responds independently to climate change (6, 15) (Fig. 1).

High-quality information on species interactions requires well-resolved information about interacting species, interaction types and strengths, spatiotemporal variation, and phenology. Unfortunately, such detailed information is usually missing. One approach to overcome this deficit is to analyze important subsets of strongly interacting species (15). Less robust alternatives include estimating trophic position using isotopes, understanding competition via diet breadth or species co-occurrence patterns, extrapolating from correlations between body size and trophic level, or discerning species co-occurrence patterns from metagenomics. High-priority parameters include those characterizing specialist interactions, top-down food web interactions, and timing mismatches among interacting species. High uncertainty arises from changes in species interactions themselves (e.g., shifts from competition to facilitation) and complex indirect effects that propagate through food webs (9). Additional uncertainties arise from species' differential abilities to track climate change in space, creating previously unseen communities as coevolved interactions disappear and novel interactions form (10).

### Dispersal, colonization, and range dynamics

To persist, species often must track suitable climates into new regions through dispersal, colonization, and subsequent range shifts (50, 51). Most models unrealistically assume that all organisms disperse comparably and across any landscape (Fig. 1) (26). In reality, dispersal depends on the interplay among individual behavior, fitness, habitat quality, and landscape configuration

(52). Range shifts are particularly sensitive to dynamics at range boundaries where low abundances challenge accurate estimation (53).

Global positioning system units can record fine-scaled individual movement but are costly and unsuitable for many small organisms. Passive integrated transponders, acoustic tags, and telemetry devices track smaller individuals at lower cost, but these require strategically placed recorders.

Neutral genetic variation across landscapes can indicate movement patterns, but demographic history can confound these estimates. Citizen science sometimes enables cost-effective, coordinated, and large-scale data collection, assuming adequate quality control. Dispersal distances also can be inferred from proxies [e.g., body size–dispersal relationships in animals (51) and growth form, seed mass, and vegetation type in plants (54)] until

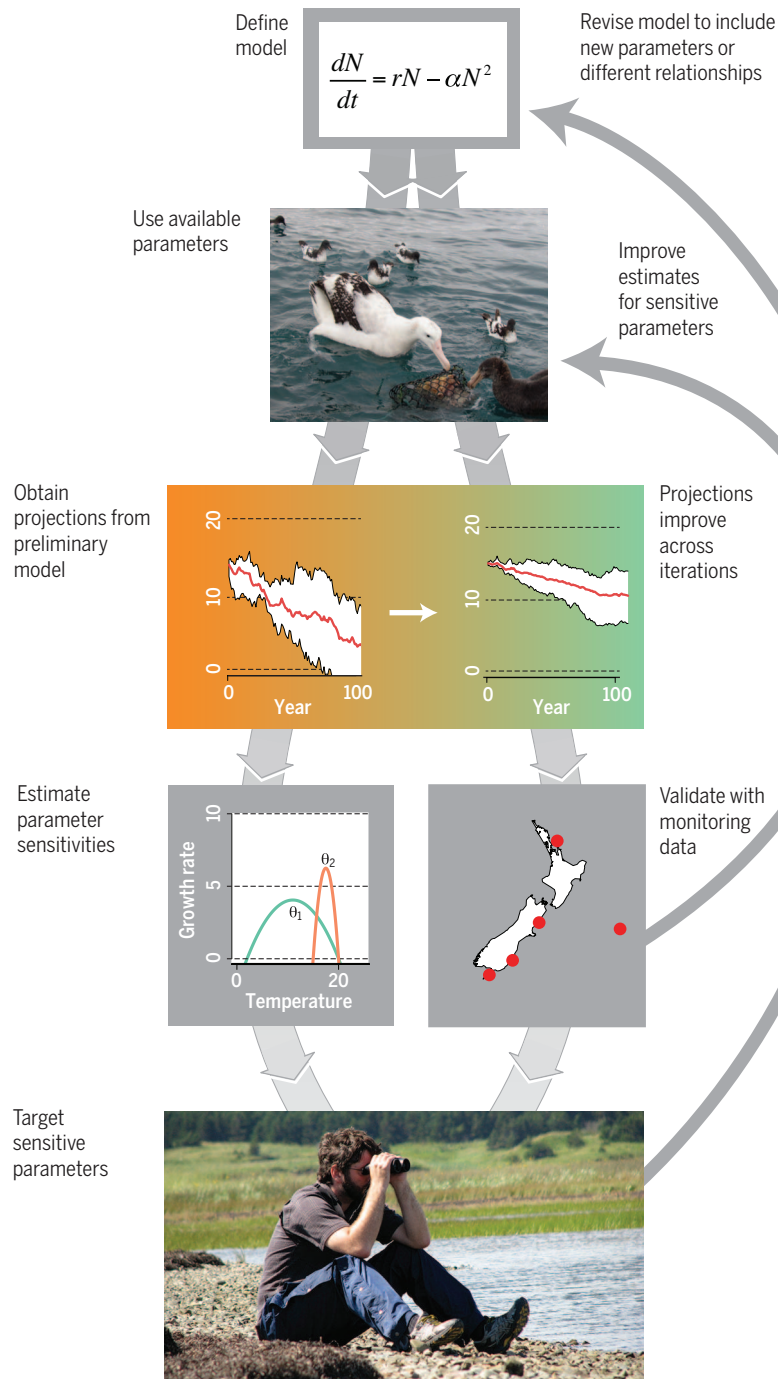


**Fig. 4. Biological models improve iteratively through time by applying an adaptive modeling scheme.** Steps include parameterizing models using available data, estimating parameter sensitivities, targeting better measurements for sensitive parameters, validating projections with observations, and iteratively refining and updating the model to improve predictive accuracy and precision through time.



**Table 1. Biological parameters, collection methods, proxies, priorities, and key uncertainties.** We list six classes of biological mechanisms, example parameters, methods to collect them, possible proxy relationships that could fill in gaps for poorly studied taxa, priority parameters, and key remaining uncertainties. We list methods in an illustrative descending order of data accuracy. The ordering of collection methods is illustrative only and will clearly change depending on the particular attributes of species and systems. The best methods, however, might not be easily implemented for some taxa, necessitating more practical methods followed by sensitivity analysis. They will also change through time—for example, as emerging methods become less costly. In reality, the ideal

approach for collecting data on a key process will involve joint use of more than one method. For example, for dispersal we might currently want to collect high-quality telemetry data for the movement of a relatively small number of dispersers because of cost constraints while also obtaining population-level estimates of dispersal through either landscape genetics or mark-release-recapture methods (or both). We encourage readers to tailor costs and benefits of the alternative and complementary approaches to their own system and adjust decisions for investment of resources appropriately. Note that each of these mechanisms likely interacts with other mechanisms.

Biological mechanisms	Example parameters	Alternative and complementary methods	Proxy relationships	Priority parameters	Key uncertainties
Physiology	Thermal, desiccation, and chemical tolerances; environment-dependent performance and metabolic rate; photosynthesis	<ul style="list-style-type: none"> <li>Experimental understanding of physiological responses to environmental conditions in nature or the laboratory</li> <li>Observed correlations between physiological responses and environmental conditions in time or space</li> <li>Trait-based proxies (e.g., body mass for metabolism)</li> </ul>	<ul style="list-style-type: none"> <li>Body mass correlates strongly with energy requirements</li> <li>Water and light requirements in vegetation models</li> </ul>	Physiological responses in extreme environments (e.g., performance under hot or dry conditions)	<ul style="list-style-type: none"> <li>How does behavior modify physiology?</li> <li>To what degree do organisms evolve different physiological responses across a range?</li> <li>How do physiological sensitivities of different performance traits scale to whole-organism fitness?</li> </ul>
Demography, life history, and phenology	Birth and death rates, including age or stage structure, age of maturity, development and growth rates, environmental dependence, timing, and individual variability	<ul style="list-style-type: none"> <li>Long-term mark recapture parentage studies or long-term demographic data from vegetation plots</li> <li>Experimental studies of environment-dependent birth and death rates in nature (best) or the laboratory</li> <li>Population growth rates from observed abundance data</li> </ul>	<ul style="list-style-type: none"> <li>Demographic parameters correlate with life history traits (e.g., slow-fast continuum) and niche specialization</li> </ul>	<ul style="list-style-type: none"> <li>Vital rates that most influence population growth rates (e.g., adult survival for long-lived organisms, generation length, mismatches in timing of life history events)</li> </ul>	<ul style="list-style-type: none"> <li>To what degree do organisms evolve different life histories across a range?</li> <li>Does rapid adaptation to climate change play a role?</li> <li>When does phenology depend on climate versus nondimate triggers (e.g., day length)?</li> <li>How do other environmental changes (e.g., habitat degradation) interact with climate responses?</li> <li>To what degree is trait change determined by genetics versus environment?</li> <li>How well do short-term measurements of adaptive mechanisms perform in the long run?</li> <li>How does local adaptation within a range alter species-level responses to climate change?</li> </ul>
Evolutionary potential and local adaptation	Additive genetic trait (co)variance/heritability and additive genetic covariance between traits and fitness	<ul style="list-style-type: none"> <li>Quantitative genetic variation in key traits estimated from controlled breeding designs, from populations with pedigrees, or from individuals raised under common conditions</li> <li>Experimental or correlational estimation of selection gradients</li> <li>Gene expression patterns for understanding functional trait variation under different environmental conditions</li> </ul>	<ul style="list-style-type: none"> <li>Evolutionary rates correlate negatively with generation length</li> <li>Genetic variation within populations positively correlates with population size</li> <li>Space-for-time substitutions</li> </ul>	<ul style="list-style-type: none"> <li>Adaptive potential, local adaptation of climate-sensitive parameters across species range</li> </ul>	
	Fitness differences among populations and environments; genetic variation among populations; phenotypic variation, including plasticity among populations	<ul style="list-style-type: none"> <li>Phenotypic variation within populations</li> <li>Reciprocal transplant and common garden experiments that reveal fitness and trait differences among populations in response to relevant environmental gradients</li> <li>Statistical search for variation in loci under selection</li> </ul>	<ul style="list-style-type: none"> <li>Genetic variation among populations positively correlates with range size</li> </ul>		

Continued on the next page

Biological mechanisms	Example parameters	Alternative and complementary methods	Proxy relationships	Priority parameters	Key uncertainties
Species interactions	Interaction webs with spatiotemporal variation and phenology, interaction types and strengths, community module, diet or resource overlap, trophic position	<ul style="list-style-type: none"> <li>Gene expression patterns for understanding functional trait variation under different environmental conditions</li> <li>Population genetics with neutral loci to understand population differentiation through barriers to gene flow</li> <li>Observation of phenotypic variation within and among populations</li> <li>Experimental evaluation of species interaction strength and direction in nature (best) or the laboratory</li> <li>Natural history observations of interactions</li> <li>Isotope analysis to reveal trophic levels and food web links</li> <li>Statistical co-occurrence patterns (e.g., checkerboard patterns for competition)</li> <li>Satellite telemetry of moving organisms to reveal landscape movement tracks</li> <li>Mark-recapture and relocations to evaluate absolute movement</li> <li>Experiments (e.g., linked mesocosms) to understand movement</li> <li>Landscape genetics to reveal landscape connectivity among populations</li> <li>Historical reconstruction of movement patterns during expansion</li> <li>Incidence functions in metapopulations to determine population connectivity</li> <li>Citizen science to track organisms (e.g., tagged birds)</li> </ul>	<ul style="list-style-type: none"> <li>Trophic level increases with body size</li> <li>Similar trophic levels are shared by phylogenetically similar species</li> </ul>	<ul style="list-style-type: none"> <li>Specialist interactions, sensitivity of top consumers, phenological mismatches between interacting species</li> </ul>	<ul style="list-style-type: none"> <li>What happens as coevolved interactions disappear and new species interactions form?</li> <li>How sensitive are food webs to top-down versus bottom-up climate disturbances?</li> <li>To what degree can species adapt to novel species interactions?</li> </ul>
		<ul style="list-style-type: none"> <li>Dispersal behaviors; movement and settlement rules; interindividual variability; environment-, density-, and condition-dependent dispersal; landscape permeability (e.g., least-cost path analysis)</li> </ul>	<ul style="list-style-type: none"> <li>Larger-bodied animals disperse farther</li> <li>Smaller seeds travel farther</li> <li>Animal-dispersed seeds travel farther</li> <li>Larger-winged organisms disperse farther</li> <li>Pelagic animals disperse farther than benthic ones</li> </ul>	<ul style="list-style-type: none"> <li>Long-distance dispersal, fitness at range boundaries</li> </ul>	<ul style="list-style-type: none"> <li>How important is long-range dispersal for range dynamics?</li> <li>How does fitness vary across a range?</li> </ul>
Responses to environmental variation	Functional relationships between traits and environments; identification and quantification of key environmental gradients across species-relevant scales of space and time	<ul style="list-style-type: none"> <li>Experimental manipulation of key environments to understand functional responses</li> <li>Statistical analysis of environmental gradients and responses</li> <li>Characterization of environmental gradients at biologically relevant scales</li> <li>Surveys of environmental parameters conducted at relevant spatial and temporal scales</li> <li>Ground-truthed maps to be used in environmental gradient analyses</li> <li>Statistical interpolation of coarse map data</li> </ul>	<ul style="list-style-type: none"> <li>Determining networks of co-acting environmental variables</li> <li>Correlating easily collected remotely sensed data to other factors such as resources</li> </ul>	<ul style="list-style-type: none"> <li>Identifying key gradients, spatial scale dependence of environmental responses, dynamic change in gradients</li> </ul>	<ul style="list-style-type: none"> <li>Are there general ways to predict the relevant scales at which different species will respond to environmental variation?</li> <li>What biological parameters are linked with the environmental factors and how?</li> <li>How are important environmental gradients changing through time?</li> </ul>



better estimates become available. Long-distance dispersal and fitness at range edges are high-priority parameters because they introduce high uncertainty in model outcomes (26), yet are difficult to measure.

### Responses to environmental variation

Responses to climate change depend on species-specific sensitivities and exposures to climate and habitat variation at relevant spatiotemporal scales. For instance, birds respond idiosyncratically to different climate variables, depending on their individual sensitivities to temperature and precipitation change (55). Researchers must carefully identify which specific climate components actually affect species. Many organisms respond not to average annual temperature or precipitation, but rather to temperature thresholds, season length, humidity, potential evapotranspiration, or extreme events such as droughts. Species also differ in the relevant spatiotemporal scales of environmental variation. Researchers should evaluate the environment through the eyes of the organism. The scales relevant to focal organisms often are meters and minutes rather than the measurements in kilometers and months typically available. Despite the increasing availability of fine-scaled information, most predictions are still made at coarse scales, which can substantially reduce predictive accuracy (56). Hierarchical sampling can maximize information content by combining large-scale sampling with targeted fine-scale measurements that capture relevant gradients. Species characteristics such as body size or generation length also can provide proxies for missing data on species' environmental responses.

In addition, we need to integrate predictions of climate change with other human disturbances, including land use, pollution, invasive species, and harvesting, to gauge the full extent of future environmental change. Improving predictions of these disturbances [e.g., (57)] and downscaling data to relevant ecological resolutions are critical for reducing future uncertainty.

### Interacting mechanisms

Each mechanism potentially interacts with many others. Specifically, climate responses depend proximately on dispersal and demography; demography in turn depends on physiology, species interactions, and environments; and each trait can evolve. For example, great tit birds in the Netherlands do not lay eggs earlier in warmer springs (involving demography, phenology, and environmental responses), whereas their caterpillar prey (species interaction) emerge earlier. This phenological mismatch between birds and their prey decreases nestling fitness (demography) (37). Yet great tits from the United Kingdom do breed earlier in warmer springs, suggesting population genetic differentiation (58). A challenge is to integrate multiple interacting mechanisms without unnecessarily increasing model complexity (Fig. 2).

### A practical way forward

We recognize that the complexity of natural systems will add uncertainty to even the best-

parameterized and most realistic models (59). Collecting the relevant information and developing realistic biological models will require substantial investment in time and resources. Despite these challenges, we believe that collecting mechanistic data will both enhance our fundamental understanding of the biological processes that underlie climate responses and contribute to more accurate, longer-term projections that facilitate more effective conservation. Mechanistic models might not make accurate predictions initially, but learning from those failures provides the insights that ultimately improve projections. Predictive science advances most quickly via iterative prediction-failure-improvement cycles, and mechanistically grounded models often quicken the pace of these advances (2, 3, 19). Even small gains in understanding can improve future models by indicating critical missing information, highlighting key uncertainties, suggesting general trait-based predictions for nonmodeled organisms, and delimiting the best options for retaining biodiversity under a range of future policy scenarios.

Given limited time and resources, however, we need to develop strategies that leverage existing data and target essential information. Toward this end, we advocate for an adaptive modeling scheme that facilitates cost-effective model development and data collection (Fig. 4). The process of model testing and revision—steps rarely taken today, but facilitated by a more systematic approach—can reveal data of particular importance for improving predictions. Researchers first parameterize models with available data. In Table 1, we demonstrate how to tailor data collection efforts to system-specific constraints by listing ideal methods along with more easily collected proxies. Researchers then use independently collected variables from monitoring efforts to test outcomes and fit uncertain relationships. Sensitivity analyses identify the most important parameters to collect, ensuring that resources go toward producing the greatest gains in accuracy. On the basis of these analyses, researchers can collect improved or new parameter estimates and revise the model through successive iterations of the approach. Crucially, results from multiple independent models should be combined because ensemble forecasts often prove more accurate (3, 60). Researchers also need to articulate clearly how uncertainty in parameter estimates and model choice propagates at each modeling step. We recommend adopting the IPCC's standards (1) for classifying model confidence and probabilistic uncertainty.

Several approaches are available to extend projections from a few carefully studied species to many unstudied ones. We often possess extensive information that is spread across many species but is incomplete for any particular species. Emerging phylogenetic and trait-based approaches could fill these data gaps. Trait-based approaches use trait correlations (e.g., between adult survival and fecundity) to predict missing parameters for species (50). Researchers also can simulate the climate responses of virtual species with realistic combinations of traits. For example, this virtual approach predicted that 30% of terrestrial mam-

mals might not keep pace with climate change (61). Minimally, these efforts provide qualitative insights about which types of species are most vulnerable to climate change and therefore should be targeted for future, in-depth study (22). Another cost-effective strategy is to prioritize research on species with both high climate sensitivity and disproportionately large impacts on ecosystems. These so-called biotic multipliers—often, top predators and other keystone species—amplify small changes in climate to produce large ecological effects (8) such that their future dynamics drive overall ecosystem changes (9).

Conservation sometimes focuses on overall biodiversity rather than focal species. Estimates from subsets of species might be cautiously extrapolated to overall biodiversity, assuming suitable representation across taxonomic and phylogenetic diversity. However, trait-based approaches might more efficiently suggest species that have vulnerable trait combinations or amplify community-wide impacts of climate change. For example, focusing on top consumers and other keystone species can indicate how their responses reverberate through entire food webs (8), thus further extending the value of single-species forecasts.

Lastly, hybrid correlative-mechanistic approaches offer a pragmatic initial approach to improving predictions by adding key mechanisms to simple models. For example, adjusting predicted ranges from correlative models with species-specific dispersal abilities (62) or interacting species' ranges (48) can add realism and improve predictions. Given the simplicity of most current approaches (Fig. 1), even minimally more realistic models might improve projections until more complicated models can be developed (13, 19).

### Global coordination

Global coordination will be critical at all stages, including defining projection goals, developing better models, collating and incorporating existing data, determining which additional data might improve forecasts, collecting new data, monitoring biodiversity changes, and organizing and maintaining data. Researchers and policymakers first must agree on the nature of the projection itself, including the accuracy, coverage, and time horizon of forecasts. A global clearinghouse would be useful to organize trait data, standardize terminology (e.g., dispersal versus migration), and monitor climate responses.

It would also be useful to form regional working groups with local experts. Regional working groups would define representative ecosystems and climatic and environmental gradients in their region, while taking advantage of existing data and long-term monitoring sites. Groups would select species representing a broad range of regional trait diversity and build initial models with available data to estimate parameter sensitivity. To address immediate extinction threats, regional working groups might also characterize the climate change risk for threatened species on the International Union for Conservation of Nature Red List. Groups should then develop plans to refine sensitive parameters through targeted funding opportunities and citizen

science. Collected biological information must be accessible, quality-checked, standardized, and maintained in databases such as Encyclopedia of Life's TraitBank (traits) and Global Biodiversity Information Facility (species occurrences).

The IPCC's development of climate change predictions provides a template for how to achieve comparable progress in biodiversity projections. The IPCC's biodiversity analog, the Intergovernmental Platform on Biodiversity and Ecosystem Services, can also help to coordinate this effort. Already, the Group on Earth Observations–Biodiversity Observation Network is developing a list of essential biodiversity variables (EBVs) for monitoring global biodiversity (25) and is working to address monitoring gaps (19). Despite some overlap between the modeling parameters outlined here and EBVs, the two collection schemes have divergent objectives. The EBVs monitor changes in biodiversity and provide variables for initializing and testing mechanistic predictions. Mechanistic models, however, also require parameters governing key processes, which often mandate more detailed observations or experiments than monitoring programs currently entail.

### Combining predictive modeling with robust scenario analysis

Collecting the data necessary to inform mechanistic biological models presents an enormous challenge given the vast diversity of life, its complexity, and our inadequate knowledge about it. This inherent complexity and stochasticity limits the accuracy of biological predictions for policy and management (59, 63), especially over long forecast horizons (3). We must accept that even the best-informed predictions could fail for a variety of unanticipated reasons.

An alternative approach to planning for climate change develops conservation strategies robust to a broad range of future scenarios (64), thus insuring against inevitable surprises. For example, applying this “robust scenario” approach might include maintaining dispersal corridors, preserving existing natural habitat and genetic diversity, and facilitating monitoring and flexible, adaptive management (59, 65). This strategy broadly protects biodiversity and depends less on accurate predictions. However, practical considerations will often limit the number of options that are feasible, especially when management options for one species trade off against another.

The two approaches are not mutually exclusive, and we believe that they work best in tandem. Mechanistic approaches likely will improve predictions at intermediate time horizons (e.g., 25 to 50 years), when current environmental correlations break down and correlative approaches become less accurate (3). Beyond this time frame, even the best mechanistic models become uncertain as key parameters can shift and uncertainty propagates. Yet predictive models are still needed to delimit plausible expectations, place bounds on uncertainty, and direct limited resources toward strategies that target the most threatened regions and species (23, 59). Hence, a tandem approach builds general insights from key representative

species while preserving flexible options that work when models fail.

### Conclusions

Climate scientists in 1975 acknowledged their inability to predict climate accurately and highlighted the many challenges to reaching this objective (66). Despite these challenges, they outlined an ambitious long-term research program aimed at understanding key mechanisms governing climate change and collecting key pieces of missing information. This program ultimately produced the improvements in forecasting weather and climate change that society benefits from today. We believe that biology can and must do the same.

We advocate for a renewed global focus on targeting the natural history information needed to predict the future of biodiversity. Such efforts would more than compensate for their cost by improving our ability to understand, anticipate, and thereby prevent biodiversity loss and damage to ecosystems from climate change as well as other disturbances. Ultimately, understanding how nature works will provide innumerable benefits for long-term sustainability and human well-being.

### REFERENCES AND NOTES

1. J. Settele *et al.*, in *Climate Change 2014: Impacts, Adaptation, and Vulnerability. Fifth Assessment Report of the Intergovernmental Panel on Climate Change*, C. B. Field *et al.*, Eds. (Cambridge Univ. Press, 2014), pp. 1–153.
2. N. Mouquet *et al.*, Predictive ecology in a changing world. *J. Appl. Ecol.* **52**, 1293–1310 (2015). doi: [10.1111/1365-2664.12482](https://doi.org/10.1111/1365-2664.12482)
3. O. L. Petchey *et al.*, The ecological forecast horizon, and examples of its uses and determinants. *Ecol. Lett.* **18**, 597–611 (2015). doi: [10.1111/ele.12443](https://doi.org/10.1111/ele.12443); pmid: [25960188](https://pubmed.ncbi.nlm.nih.gov/25960188/)
4. M. C. Urban, Accelerating extinction risk from climate change. *Science* **348**, 571–573 (2015). doi: [10.1126/science.aaa4984](https://doi.org/10.1126/science.aaa4984); pmid: [25931559](https://pubmed.ncbi.nlm.nih.gov/25931559/)
5. A. L. Angert *et al.*, Do species' traits predict recent shifts at expanding range edges? *Ecol. Lett.* **14**, 677–689 (2011). doi: [10.1111/j.1461-0248.2011.01620.x](https://doi.org/10.1111/j.1461-0248.2011.01620.x); pmid: [21535340](https://pubmed.ncbi.nlm.nih.gov/21535340/)
6. A. J. Davis, L. S. Jenkinson, J. H. Lawton, B. Shorrocks, S. Wood, Making mistakes when predicting shifts in species range in response to global warming. *Nature* **391**, 783–786 (1998). doi: [10.1038/35842](https://doi.org/10.1038/35842); pmid: [9486646](https://pubmed.ncbi.nlm.nih.gov/9486646/)
7. S. D. Veloz *et al.*, No-analog climates and shifting realized niches during the late quaternary: Implications for 21st-century predictions by species distribution models. *Global Change Biol.* **18**, 1698–1713 (2012). doi: [10.1111/j.1365-2486.2011.02635.x](https://doi.org/10.1111/j.1365-2486.2011.02635.x)
8. P. L. Zarnetske, D. K. Skelly, M. C. Urban, Biotic multipliers of climate change. *Science* **336**, 1516–1518 (2012). doi: [10.1126/science.1222732](https://doi.org/10.1126/science.1222732); pmid: [22723403](https://pubmed.ncbi.nlm.nih.gov/22723403/)
9. E. Post, *Ecology of Climate Change: The Importance of Biotic Interactions* (Princeton Univ. Press, 2013).
10. M. C. Urban, J. J. Tewksbury, K. S. Sheldon, On a collision course: Competition and dispersal differences create no-analog communities and cause extinctions during climate change. *Proc. R. Soc. B* **279**, 2072–2080 (2012). doi: [10.1098/rspb.2011.2367](https://doi.org/10.1098/rspb.2011.2367); pmid: [22217718](https://pubmed.ncbi.nlm.nih.gov/22217718/)
11. J. Norberg, M. C. Urban, M. Vellend, C. A. Klausmeier, N. Loeuille, Eco-evolutionary responses of biodiversity to climate change. *Nat. Clim. Change* **2**, 747–751 (2012). doi: [10.1038/nclimate1588](https://doi.org/10.1038/nclimate1588)
12. G. Bodei *et al.*, Effects of local adaptation and interspecific competition on species' responses to climate change. *Ann. N.Y. Acad. Sci.* **1297**, 83–97 (2013). pmid: [23905876](https://pubmed.ncbi.nlm.nih.gov/23905876/)
13. D. Zurell *et al.*, Benchmarking novel approaches for modelling species range dynamics. *Global Change Biol.* **22**, 2651–2664 (2016). doi: [10.1111/gcb.13251](https://doi.org/10.1111/gcb.13251); pmid: [26872305](https://pubmed.ncbi.nlm.nih.gov/26872305/)
14. J. W. Williams, S. T. Jackson, J. E. Kutzbach, Projected distributions of novel and disappearing climates by 2100 AD. *Proc. Natl. Acad. Sci. U.S.A.* **104**, 5738–5742 (2007). doi: [10.1073/pnas.0606292104](https://doi.org/10.1073/pnas.0606292104); pmid: [17389402](https://pubmed.ncbi.nlm.nih.gov/17389402/)
15. S. E. Gilman, M. C. Urban, J. Tewksbury, G. W. Gilchrist, R. D. Holt, A framework for community interactions under climate change. *Trends Ecol. Evol.* **25**, 325–331 (2010). doi: [10.1016/j.tree.2010.03.002](https://doi.org/10.1016/j.tree.2010.03.002); pmid: [20392517](https://pubmed.ncbi.nlm.nih.gov/20392517/)
16. D. Purves *et al.*, Ecosystems: Time to model all life on Earth. *Nature* **493**, 295–297 (2013). pmid: [23325192](https://pubmed.ncbi.nlm.nih.gov/23325192/)
17. G. Bodei *et al.*, RangeShifter: A platform for modelling spatial eco-evolutionary dynamics and species' responses to environmental changes. *Methods Ecol. Evol.* **5**, 388–396 (2014). doi: [10.1111/2041-210X.12162](https://doi.org/10.1111/2041-210X.12162)
18. M. Kearney, W. Porter, Mechanistic niche modelling: Combining physiological and spatial data to predict species' ranges. *Ecol. Lett.* **12**, 334–350 (2009). doi: [10.1111/j.1461-0248.2008.01277.x](https://doi.org/10.1111/j.1461-0248.2008.01277.x); pmid: [19292794](https://pubmed.ncbi.nlm.nih.gov/19292794/)
19. S. M. McMahon *et al.*, Improving assessment and modelling of climate change impacts on global terrestrial biodiversity. *Trends Ecol. Evol.* **26**, 249–259 (2011). doi: [10.1016/j.tree.2011.02.012](https://doi.org/10.1016/j.tree.2011.02.012); pmid: [21474198](https://pubmed.ncbi.nlm.nih.gov/21474198/)
20. J. Págel, F. M. Schurr, Forecasting species ranges by statistical estimation of ecological niches and spatial population dynamics. *Glob. Ecol. Biogeogr.* **21**, 293–304 (2012). doi: [10.1111/j.1466-8238.2011.00663.x](https://doi.org/10.1111/j.1466-8238.2011.00663.x)
21. H. R. Pulliam, On the relationship between niche and distribution. *Ecol. Lett.* **3**, 349–361 (2000). doi: [10.1046/j.1461-0248.2000.00143.x](https://doi.org/10.1046/j.1461-0248.2000.00143.x)
22. R. G. Pearson *et al.*, Life history and spatial traits predict extinction risk due to climate change. *Nat. Clim. Change* **4**, 217–221 (2014). doi: [10.1038/nclimate2113](https://doi.org/10.1038/nclimate2113)
23. A. Singer *et al.*, Community dynamics under environmental change: How can next generation mechanistic models improve projections of species distributions? *Ecol. Model.* **326**, 63–74 (2016). doi: [10.1016/j.ecolmodel.2015.11.007](https://doi.org/10.1016/j.ecolmodel.2015.11.007)
24. L. B. Buckley *et al.*, Can mechanism inform species' distribution models? *Ecol. Lett.* **13**, 1041–1054 (2010). pmid: [20482574](https://pubmed.ncbi.nlm.nih.gov/20482574/)
25. H. M. Pereira *et al.*, Essential biodiversity variables. *Science* **339**, 277–278 (2013). doi: [10.1126/science.1229931](https://doi.org/10.1126/science.1229931); pmid: [23329036](https://pubmed.ncbi.nlm.nih.gov/23329036/)
26. M. C. Urban, P. L. Zarnetske, D. K. Skelly, Moving forward: Dispersal and species interactions determine biotic responses to climate change. *Ann. N.Y. Acad. Sci.* **1297**, 44–60 (2013). pmid: [23819864](https://pubmed.ncbi.nlm.nih.gov/23819864/)
27. A. A. Hoffmann, C. M. Sgrò, Climate change and evolutionary adaptation. *Nature* **470**, 479–485 (2011). doi: [10.1038/nature09670](https://doi.org/10.1038/nature09670); pmid: [21350480](https://pubmed.ncbi.nlm.nih.gov/21350480/)
28. M. J. Angilletta, *Thermal Adaptation: A Theoretical and Empirical Synthesis* (Oxford Univ. Press, Oxford, 2009).
29. L. Crozier, G. Dwyer, Combining population-dynamic and ecophysiological models to predict climate-induced insect range shifts. *Am. Nat.* **167**, 853–866 (2006). doi: [10.1086/504848](https://doi.org/10.1086/504848); pmid: [16685639](https://pubmed.ncbi.nlm.nih.gov/16685639/)
30. M. Kearney *et al.*, Modelling species distributions without using species distributions: The cane toad in Australia under current and future climates. *Ecography* **31**, 423–434 (2008). doi: [10.1111/j.0906-7590.2008.05457.x](https://doi.org/10.1111/j.0906-7590.2008.05457.x)
31. M. Kearney, W. P. Porter, C. Williams, S. Ritchie, A. A. Hoffmann, Integrating biophysical models and evolutionary theory to predict climatic impacts on species' ranges: The dengue mosquito *Aedes aegypti* in Australia. *Funct. Ecol.* **23**, 528–538 (2009). doi: [10.1111/j.1365-2435.2008.01538.x](https://doi.org/10.1111/j.1365-2435.2008.01538.x)
32. B. Sinervo *et al.*, Erosion of lizard diversity by climate change and altered thermal niches. *Science* **328**, 894–899 (2010). doi: [10.1126/science.1184695](https://doi.org/10.1126/science.1184695)
33. D. A. Keith *et al.*, Predicting extinction risks under climate change: Coupling stochastic population models with dynamic bioclimatic habitat models. *Biol. Lett.* **4**, 560–563 (2008). doi: [10.1098/rsbl.2008.0049](https://doi.org/10.1098/rsbl.2008.0049); pmid: [18664424](https://pubmed.ncbi.nlm.nih.gov/18664424/)
34. S. Jenouvrier *et al.*, Demographic models and IPCC climate projections predict the decline of an emperor penguin population. *Proc. Natl. Acad. Sci. U.S.A.* **106**, 1844–1847 (2009). doi: [10.1073/pnas.0806638106](https://doi.org/10.1073/pnas.0806638106); pmid: [19171908](https://pubmed.ncbi.nlm.nih.gov/19171908/)
35. B.-E. Sæther, Ø. Bakke, Avian life history variation and contribution of demographic traits to the population growth rate. *Ecology* **81**, 642 (2000). doi: [10.2307/177366](https://doi.org/10.2307/177366)
36. J. Merilä, A. P. Hendry, Climate change, adaptation, and phenotypic plasticity: The problem and the evidence. *Evol. Appl.* **7**, 1–14 (2014). doi: [10.1111/eva.12137](https://doi.org/10.1111/eva.12137)
37. M. E. Visser, A. J. van Noordwijk, J. M. Tinbergen, C. M. Lessells, Warmer springs lead to mistimed reproduction in great tits (*Parus major*). *Proc. R. Soc. B* **265**, 1867–1870 (1998). doi: [10.1098/rspb.1998.0514](https://doi.org/10.1098/rspb.1998.0514)



38. S. P. Carroll *et al.*, Applying evolutionary biology to address global challenges. *Science* **346**, 1245993 (2014). doi: [10.1126/science.1245993](https://doi.org/10.1126/science.1245993); pmid: [25213376](https://pubmed.ncbi.nlm.nih.gov/25213376/)
39. S. L. Pelini, J. A. Keppel, A. E. Kelley, J. J. Hellmann, Adaptation to host plants may prevent rapid insect responses to climate change. *Global Change Biol.* **16**, 2923 (2010). doi: [10.1111/j.1365-2486.2010.02177.x](https://doi.org/10.1111/j.1365-2486.2010.02177.x)
40. M. B. Morrissey *et al.*, The prediction of adaptive evolution: Empirical application of the secondary theorem of selection and comparison to the breeder's equation. *Evolution* **66**, 2399–2410 (2012). doi: [10.1111/j.1558-5646.2012.01632.x](https://doi.org/10.1111/j.1558-5646.2012.01632.x); pmid: [22834740](https://pubmed.ncbi.nlm.nih.gov/22834740/)
41. J. P. Reeve, Predicting long-term response to selection. *Genet. Res.* **75**, 83–94 (2000). doi: [10.1017/S0016672399004140](https://doi.org/10.1017/S0016672399004140); pmid: [10740924](https://pubmed.ncbi.nlm.nih.gov/10740924/)
42. W. E. Bradshaw, C. M. Holzapfel, Evolutionary response to rapid climate change. *Science* **312**, 1477–1478 (2006). doi: [10.1126/science.1127000](https://doi.org/10.1126/science.1127000); pmid: [16763134](https://pubmed.ncbi.nlm.nih.gov/16763134/)
43. S. J. Franks, S. Sim, A. E. Weis, Rapid evolution of flowering time by an annual plant in response to a climate fluctuation. *Proc. Natl. Acad. Sci. U.S.A.* **104**, 1278–1282 (2007). doi: [10.1073/pnas.0608379104](https://doi.org/10.1073/pnas.0608379104); pmid: [17220273](https://pubmed.ncbi.nlm.nih.gov/17220273/)
44. J. Buckley, R. K. Butlin, J. R. Bridle, Evidence for evolutionary change associated with the recent range expansion of the British butterfly, *Aricia agestis*, in response to climate change. *Mol. Ecol.* **21**, 267–280 (2012). doi: [10.1111/j.1365-294X.2011.05388.x](https://doi.org/10.1111/j.1365-294X.2011.05388.x); pmid: [22118243](https://pubmed.ncbi.nlm.nih.gov/22118243/)
45. C. Parmesan, A. Williams-Anderson, M. Moskwik, A. S. Mikheyev, M. C. Singer, Endangered Quino checkerspot butterfly and climate change: Short-term success but long-term vulnerability? *J. Insect Conserv.* **19**, 185–204 (2015). doi: [10.1007/s10841-014-9743-4](https://doi.org/10.1007/s10841-014-9743-4)
46. C. A. Botero, F. J. Weissing, J. Wright, D. R. Rubenstein, Evolutionary tipping points in the capacity to adapt to environmental change. *Proc. Natl. Acad. Sci. U.S.A.* **112**, 184–189 (2015). doi: [10.1073/pnas.1408589111](https://doi.org/10.1073/pnas.1408589111); pmid: [25422451](https://pubmed.ncbi.nlm.nih.gov/25422451/)
47. A. E. Cahill *et al.*, How does climate change cause extinction? *Proc. R. Soc. B* **280**, 20121890 (2013). doi: [10.1098/rspb.2012.1890](https://doi.org/10.1098/rspb.2012.1890); pmid: [23075836](https://pubmed.ncbi.nlm.nih.gov/23075836/)
48. O. Schweiger, J. Settele, O. Kudrna, S. Klotz, I. Kühn, Climate change can cause spatial mismatch of trophically interacting species. *Ecology* **89**, 3472–3479 (2008). doi: [10.1890/07-1748.1](https://doi.org/10.1890/07-1748.1); pmid: [19137952](https://pubmed.ncbi.nlm.nih.gov/19137952/)
49. C. D. G. Harley, Climate change, keystone predation, and biodiversity loss. *Science* **334**, 1124–1127 (2011). doi: [10.1126/science.1210199](https://doi.org/10.1126/science.1210199); pmid: [22116885](https://pubmed.ncbi.nlm.nih.gov/22116885/)
50. C. A. Schloss, T. A. Nuñez, J. J. Lawler, Dispersal will limit ability of mammals to track climate change in the Western Hemisphere. *Proc. Natl. Acad. Sci. U.S.A.* **109**, 8606–8611 (2012). doi: [10.1073/pnas.1116791109](https://doi.org/10.1073/pnas.1116791109); pmid: [22586104](https://pubmed.ncbi.nlm.nih.gov/22586104/)
51. B. J. Anderson *et al.*, Dynamics of range margins for metapopulations under climate change. *Proc. R. Soc. B* **276**, 1415–1420 (2009). doi: [10.1098/rspb.2008.1681](https://doi.org/10.1098/rspb.2008.1681); pmid: [19324811](https://pubmed.ncbi.nlm.nih.gov/19324811/)
52. T. Delattre *et al.*, Interactive effects of landscape and weather on dispersal. *Oikos* **122**, 1576–1585 (2013). doi: [10.1111/j.1600-0706.2013.00123.x](https://doi.org/10.1111/j.1600-0706.2013.00123.x); pmid: [19324811](https://pubmed.ncbi.nlm.nih.gov/19324811/)
53. J. P. Sexton, P. J. McIntyre, A. L. Angert, K. J. Rice, Evolution and ecology of species range limits. *Annu. Rev. Ecol. Syst.* **40**, 415–436 (2009). doi: [10.1146/annurev.ecolsys.110308.120317](https://doi.org/10.1146/annurev.ecolsys.110308.120317)
54. F. J. Thomson *et al.*, Chasing the unknown: Predicting seed dispersal mechanisms from plant traits. *J. Ecol.* **98**, 1310–1318 (2010). doi: [10.1111/j.1365-2745.2010.01724.x](https://doi.org/10.1111/j.1365-2745.2010.01724.x)
55. M. W. Tingley, M. S. Koo, C. Moritz, A. C. Rush, S. R. Beissinger, The push and pull of climate change causes heterogeneous shifts in avian elevational ranges. *Global Change Biol.* **18**, 3279–3290 (2012). doi: [10.1111/j.1365-2486.2012.02784.x](https://doi.org/10.1111/j.1365-2486.2012.02784.x)
56. R. Early, D. F. Sax, Analysis of climate paths reveals potential limitations on species range shifts. *Ecol. Lett.* **14**, 1125–1133 (2011). doi: [10.1111/j.1461-0248.2011.01681.x](https://doi.org/10.1111/j.1461-0248.2011.01681.x); pmid: [21955643](https://pubmed.ncbi.nlm.nih.gov/21955643/)
57. D. Murray-Rust *et al.*, Combining agent functional types, capitals and services to model land use dynamics. *Environ. Model. Softw.* **59**, 187–201 (2014). doi: [10.1016/j.envsoft.2014.05.019](https://doi.org/10.1016/j.envsoft.2014.05.019)
58. A. Charmanier *et al.*, Adaptive phenotypic plasticity in response to climate change in a wild bird population. *Science* **320**, 800–803 (2008). doi: [10.1126/science.1157174](https://doi.org/10.1126/science.1157174); pmid: [18467590](https://pubmed.ncbi.nlm.nih.gov/18467590/)
59. D. E. Schindler, R. Hilborn, Prediction, precaution, and policy under global change. *Science* **347**, 953–954 (2015). doi: [10.1126/science.1261824](https://doi.org/10.1126/science.1261824); pmid: [25722401](https://pubmed.ncbi.nlm.nih.gov/25722401/)
60. M. B. Araújo, M. New, Ensemble forecasting of species distributions. *Trends Ecol. Evol.* **22**, 42–47 (2007). doi: [10.1016/j.tree.2006.09.010](https://doi.org/10.1016/j.tree.2006.09.010); pmid: [17011070](https://pubmed.ncbi.nlm.nih.gov/17011070/)
61. L. Santini *et al.*, A trait-based approach for predicting species responses to environmental change from sparse data: How well might terrestrial mammals track climate change? *Global Change Biol.* **22**, 2415–2424 (2016). doi: [10.1111/gcb.13271](https://doi.org/10.1111/gcb.13271); pmid: [27073017](https://pubmed.ncbi.nlm.nih.gov/27073017/)
62. S. Dullinger *et al.*, Extinction debt of high-mountain plants under twenty-first-century climate change. *Nat. Clim. Change* **2**, 619–622 (2012). doi: [10.1038/nclimate1514](https://doi.org/10.1038/nclimate1514)
63. B. Beckage, L. J. Gross, S. Kauffman, The limits to prediction in ecological systems. *Ecosphere* **2**, 125 (2011). doi: [10.1890/ES11-00211](https://doi.org/10.1890/ES11-00211)
64. R. J. Lempert, M. E. Schlesinger, Robust strategies for abating climate change. *Clim. Change* **45**, 387–401 (2000). doi: [10.1023/A:1005698407365](https://doi.org/10.1023/A:1005698407365)
65. B. Rayfield, D. Pelletier, M. Dumitru, J. A. Cardille, A. Gonzalez, Multipurpose habitat networks for short-range and long-range connectivity: A new method combining graph and circuit connectivity. *Methods Ecol. Evol.* **7**, 222–231 (2016). doi: [10.1111/2041-210X.12470](https://doi.org/10.1111/2041-210X.12470)
66. U.S. Committee for the Global Atmospheric Research Program, National Research Council, *Understanding Climatic Change* (National Academy of Sciences, Washington, DC, 1975).

## ACKNOWLEDGMENTS

This paper originates from the “Ecological Interactions and Range Evolution Under Environmental Change” and “RangeShifter” working groups, supported by the Synthesis Centre of the German Centre for Integrative Biodiversity Research (DFG-FZT-118), DIVERSITAS, and its core projects bioDISCOVERY and bioGENESIS. Supported by the Canada Research Chair, Natural Sciences and Engineering Research Council of Canada, and Quebec Centre for Biodiversity Science (A.G.); the University of Florida Foundation (R.D.H.); KU Leuven Research Fund grant PF/2010/07, ERA-Net BiodivERsA TIPPINGPOND, and Belspo IAP SPEEDY (L.D.M.); European Union Biodiversity Observation Network grant EU-BON-FP7-308454 (J.-B.M. and G.P.); KU Leuven Research Fund (J.P.); and NSF grants DEB-1119877 and PLR-1417754 and the McDonnell Foundation (M.C.U.).

## SUPPLEMENTARY MATERIALS

[www.sciencemag.org/content/353/6304/aad8466/suppl/DC1](http://www.sciencemag.org/content/353/6304/aad8466/suppl/DC1)  
Fig. S1  
Table S1

10.1126/science.aad8466

## RESEARCH ARTICLE SUMMARY

## MACROPHAGES

# Specification of tissue-resident macrophages during organogenesis

Elvira Mass,\* Ivan Ballesteros,\* Matthias Farlik,\* Florian Halbritter,\* Patrick Günther,\* Lucile Crozet, Christian E. Jacome-Galarza, Kristian Händler, Johanna Klughammer, Yasuhiro Kobayashi, Elisa Gomez-Perdiguero, Joachim L. Schultze, Marc Beyer,† Christoph Bock,‡ Frederic Geissmann†‡

**INTRODUCTION:** Embryonic development and tissue homeostasis depend on cooperation between specialized cell types. Resident macrophages are professional phagocytes that survey their surroundings; eliminate unfit cells, microorganisms, and metabolic waste; and produce a large range of bioactive molecules and growth factors. Resident macrophages also serve tissue-specific purposes: For example, microglia in the central nervous system support neuronal circuit development, Kupffer cells scavenge blood particles and dying red blood cells in the liver, and alveolar macrophages uptake surfactant and remove airborne pollutants and microbes from the airways. Resident macrophage diversity in adult mice is reflected in tissue-specific gene expression profiles, which may be due to responses to specific cues from their micro-

environment, different developmental processes, and the contribution of distinct progenitors cell types. Altogether, the mechanisms responsible for the generation of tissue-resident macrophage diversity remain unclear.

**RATIONALE:** Tissue-resident macrophages originate, at least in part, from mesodermal erythro-myeloid progenitors (EMPs) from the yolk sac, which invade the embryo proper at the onset of organogenesis. These tissue-resident macrophages are also self-maintained in postnatal tissues, independently of definitive hematopoietic stem cells (HSCs) in a steady state. We therefore hypothesized that resident macrophages represent a founding cell type within most organ anlagen. In this model, the generation of macrophage diversity, as observed in

the tissues of postnatal mice, may be integral to organogenesis.

**RESULTS:** To test this hypothesis and explore the molecular basis of macrophage diversity in mammals, we performed a spatiotemporal analysis of macrophage development in mice, from embryonic day 9 (E9) to 3 weeks after birth. Unbiased single-cell RNA sequencing (RNA-seq) analysis of CD45<sup>+</sup> cells, combined with RNA-seq analyses of sorted cell populations, genetic fate mapping, and in situ analyses, revealed that EMPs give rise to a population of pre-macrophages (pMac) that colonize the whole embryo from E9.5, as they acquire a core macrophage differentiation program that includes

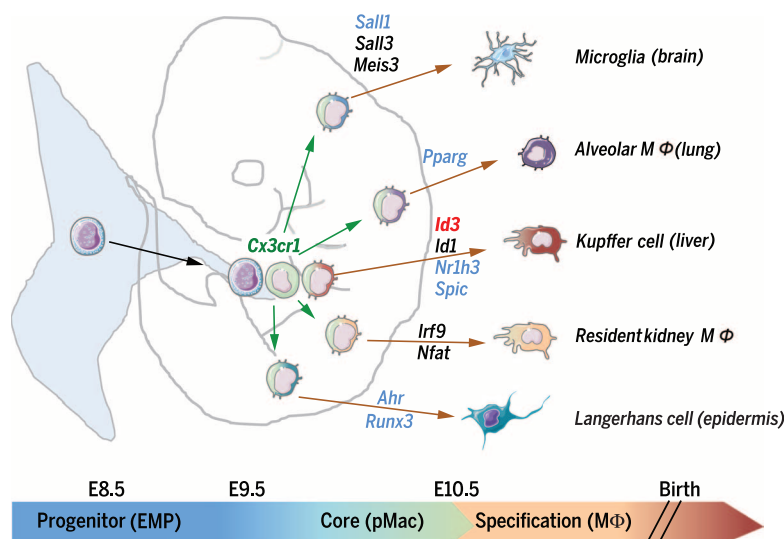
## ON OUR WEBSITE

Read the full article at <http://dx.doi.org/10.1126/science.aaf4238>

pattern recognition, scavengers, and cytokine receptors. The chemokine receptor *Cx3cr1* is up-regulated in pMac and is important for embryo

colonization, which is delayed in *Cx3cr1*-deficient embryos. Fate mapping of pMac using a *Tnfrsf11a*-Cre reporter labels homogeneously fetal and adult tissue-resident macrophages but not HSCs and their progeny. Transcriptional regulators that identify postnatal tissue-resident macrophages in the brain, liver, kidney, skin, and lung were specifically up-regulated immediately after colonization. These dynamic changes mark the onset of diversification into adult macrophages. We identified *Id3* as a Kupffer cell-specific transcriptional regulator. Deletion of *Id3* in pMac resulted in Kupffer cell deficiency but did not affect development of microglia and kidney macrophages.

**CONCLUSION:** Our study shows that EMP-derived precursors colonize embryonic tissues and simultaneously acquire a full core macrophage program. This is followed by their diversification into tissue-specific macrophages during organogenesis, likely via the expression of distinct sets of transcriptional regulators. These results indicate that differentiation of tissue-resident macrophages is an integral part of organogenesis and identify a spatiotemporal molecular road map for the generation of macrophage diversity in vivo. Our findings provide a conceptual framework to analyze and understand the consequence(s) of genetic variation for macrophage contribution to development, homeostasis, and disease pathogenesis in different tissues and will support efforts to differentiate specialized macrophages in vitro. ■



**Specification of tissue-resident macrophages.** Erythro-myeloid progenitors (EMPs) from the yolk sac colonize the fetal liver and give rise to macrophage precursors (pMac) that acquire a core macrophage transcriptional program and colonize the embryo from E9.5 in a *Cx3cr1*-dependent manner (green arrows). Specification of F4/80<sup>+</sup> resident macrophages (brown arrows), starting from E10.25, is initiated by the expression of tissue-specific transcriptional regulators. *Id3* (red) is important for Kupffer cell development. Transcription factors noted in blue have been shown to be important for the differentiation or the maintenance of the corresponding macrophage subsets. MΦ, macrophage.

The list of author affiliations is available in the full article online.

\*These authors contributed equally to this work.

†These authors contributed equally to this work.

‡Corresponding author. Email: [geissma@mskcc.org](mailto:geissma@mskcc.org)

Cite this article as E. Mass et al., *Science* 353, aaf4238 (2016). DOI: 10.1126/science.aaf4238



## RESEARCH ARTICLE

## MACROPHAGES

## Specification of tissue-resident macrophages during organogenesis

Elvira Mass,<sup>1\*</sup> Ivan Ballesteros,<sup>1\*</sup> Matthias Farlik,<sup>2\*</sup> Florian Halbritter,<sup>2\*</sup> Patrick Günther,<sup>3\*</sup> Lucile Crozet,<sup>1,4</sup> Christian E. Jacome-Galarza,<sup>1</sup> Kristian Händler,<sup>3</sup> Johanna Klughammer,<sup>2</sup> Yasuhiro Kobayashi,<sup>5</sup> Elisa Gomez-Perdiguero,<sup>6†</sup> Joachim L. Schultze,<sup>3,7</sup> Marc Beyer,<sup>3,7,†</sup> Christoph Bock,<sup>2,8,9,†</sup> Frederic Geissmann<sup>1,4,6,†,§</sup>

Tissue-resident macrophages support embryonic development and tissue homeostasis and repair. The mechanisms that control their differentiation remain unclear. We report here that erythro-myeloid progenitors in mice generate premacrophages (pMacs) that simultaneously colonize the whole embryo from embryonic day 9.5 in a chemokine-receptor-dependent manner. The core macrophage program initiated in pMacs is rapidly diversified as expression of transcriptional regulators becomes tissue-specific in early macrophages. This process appears essential for macrophage specification and maintenance, as inactivation of *Id3* impairs the development of liver macrophages and results in selective Kupffer cell deficiency in adults. We propose that macrophage differentiation is an integral part of organogenesis, as colonization of organ anlagen by pMacs is followed by their specification into tissue macrophages, hereby generating the macrophage diversity observed in postnatal tissues.

**T**issue-resident macrophages are a diverse family of cells found in most organs. They include brain microglia, liver Kupffer cells, lung alveolar macrophages, and epidermal Langerhans cells. In mice, tissue-resident macrophages share an embryonic origin and differentiate, at least in part, from yolk sac (YS) erythro-myeloid progenitors (EMPs) (1, 2). Tissue-resident macrophages are also self-maintained in adult tissues, independently of hematopoietic stem cells (HSCs) under steady-state conditions (3–6). However, the mechanisms responsible for the generation of macrophage diversity observed in adult mice remain unclear. It has been proposed that resident macrophage diversity reflects their exposure to specialized tissue environments (7–10) or the contribution of distinct embryonic or fetal progenitors to distinct subsets (2, 11–13).

The preferential expression of transcription factors in macrophage subsets was also noted (7) and appears functionally important. Several such cases—including *Gata6* for large peritoneal macrophages (9, 10, 14), *Runx3* for Langerhans cells (15), *Nr1h3* for splenic marginal zone macrophages (16), *SpiC* for splenic red pulp macrophages (17), and *Pparg* for alveolar macrophages (18)—have been functionally validated by knockout mice. To better understand how macrophage diversity is generated, we performed a molecular and spatiotemporal analysis of macrophage development in mice.

## Colonization of developing tissues by EMP-derived macrophage precursors

Erythro-myeloid progenitors (Csflr<sup>+</sup> Kit<sup>+</sup> CD45<sup>low</sup> AA4.1<sup>+</sup>) are first detected in the YS at embryonic day 8.5 (E8.5) (2, 19) and subsequently colonize the fetal liver (1, 2). Previous fate-mapping analysis of EMP differentiation indicated that their progeny lose Kit expression and increase CD45 expression as they invade the embryo before acquiring F4/80 expression to give rise to fetal and postnatal tissue-resident macrophages (2) (Fig. 1A). To explore the spatiotemporal and molecular determinants of macrophage differentiation and diversification, we first performed whole-transcriptome sequencing of sorted CD45<sup>low</sup> Kit<sup>+</sup> EMPs, CD45<sup>+</sup> Kit<sup>+</sup> Lin<sup>−</sup> (Ter119, Gr1, F4/80) cells and F4/80<sup>+</sup> macrophages from embryonic and postnatal tissues up to 3 weeks after birth (Fig. 1A and fig. S1, A and B). We identified genes that were significantly up-regulated between EMPs and CD45<sup>+</sup> Kit<sup>+</sup> Lin<sup>−</sup> cells [adjusted *P* ≤ 0.05, DESeq2 (20), Benjamini Hochberg (BH) correction, table S1]. Subsequent summariza-

tion and visualization of these genes via scorecard analysis (21) (Fig. 1B) indicated that the signature of CD45<sup>+</sup> Kit<sup>+</sup> Lin<sup>−</sup> cells was also present in F4/80<sup>+</sup> macrophages across tissues and over the entire time-course analysis in the embryo and postnatal mice in the kidney, liver, and brain. Epidermal Langerhans cell and lung alveolar macrophage signatures were modified after birth (Fig. 1B). A second scorecard analysis of genes up-regulated between EMPs and early (E10.25 to E10.5) F4/80<sup>+</sup> macrophages identified a signature that was already detectable in CD45<sup>+</sup> Kit<sup>+</sup> Lin<sup>−</sup> cells and conserved in later macrophages across tissues (fig. S1C and table S1). Unsupervised principal component analysis (PCA) showed a distinct grouping of EMPs, CD45<sup>+</sup> Kit<sup>+</sup> Lin<sup>−</sup> cells, and macrophages, regardless of their tissue of origin—i.e., YS, liver, head, or caudal region (fig. S1D). Morphologically, CD45<sup>+</sup> Kit<sup>+</sup> Lin<sup>−</sup> cells from the YS, fetal liver, head, and caudal embryo displayed a similar morphology, as did macrophages from the same tissues (Fig. 1C). CD45<sup>+</sup> Kit<sup>+</sup> Lin<sup>−</sup> cells resembled EMPs, albeit with the presence of occasional phagocytic vacuoles, whereas phagocytic features become prominent in F4/80<sup>+</sup> cells (Fig. 1C).

These data suggest that a macrophage differentiation program was initiated simultaneously in the whole embryo in CD45<sup>+</sup> Kit<sup>+</sup> Lin<sup>−</sup> cells; these macrophage precursors will subsequently be referred to as premacrophages (pMacs). To further test this hypothesis, we performed independent, unbiased whole-transcriptome single-cell RNA sequencing (scRNA-seq) of CD45<sup>low/+</sup> cells purified from the whole embryo at E10.25 [30 to 34 somite pairs (sp)]. Nonlinear dimensionality reduction in combination with unsupervised clustering of cells indicated that these cells are best described by three major clusters (Fig. 1D and fig. S2). Overlay of EMP, pMac, and macrophage signatures from differentially expressed genes in bulk RNA-seq analysis (table S2) indicated superimposition on clusters 1, 2, and 3, respectively (Fig. 1E). Intermediate differentiation states in EMPs, pMacs, and macrophages were clearly apparent, which suggests a gradual differentiation path from EMPs to macrophages via pMacs (Fig. 1E), consistent with the scorecard analysis.

## Core macrophage transcriptional program

Analysis of genes differentially expressed in EMPs, pMacs, and early macrophages by scRNA-seq (Figs. 1F and 2A and table S2) and bulk RNA-seq (Fig. 2B and table S1) confirmed that a core macrophage transcriptional program was initiated in pMacs. As *Kit*, *Gata1*, and *Gata2* expression was lost, pMacs up-regulated expression of *Csflr*; the transcription factors *Maf*, *Batf3*, *Pparg*, *Irf8*, and *Zeb2*; the chemokine receptor *Cx3cr1*; cytokine receptors; complement and complement receptors; pattern-recognition receptors; phagocytic receptors; Fc gamma receptors; the inhibitory receptor *Slrp*; *MerTK*; cathepsins; *Aif1* (Iba1); *Emr1* (F4/80); and *Grn* (Granulin). Expression of selected genes was confirmed at the protein

<sup>1</sup>Immunology Program, Memorial Sloan Kettering Cancer Center (MSKCC), New York, NY 10065, USA. <sup>2</sup>CeMM Research Center for Molecular Medicine of the Austrian Academy of Sciences, 1090 Vienna, Austria. <sup>3</sup>Genomics and Immunoregulation, Life and Medical Sciences Institute, University of Bonn, Bonn, Germany. <sup>4</sup>Weill Cornell Graduate School of Medical Sciences, New York, NY 10065, USA. <sup>5</sup>Institute for Oral Science, Matsumoto Dental University, 1780 Hiro-Oka Gobara Shiojiri, Nagano 390-0781, Japan. <sup>6</sup>Centre for Molecular and Cellular Biology of Inflammation, King's College London, London SE1 1UL, UK. <sup>7</sup>Single Cell Genomics and Epigenomics Unit at the German Center for Neurodegenerative Diseases and the University of Bonn, Bonn, Germany. <sup>8</sup>Department of Laboratory Medicine, Medical University of Vienna, 1090 Vienna, Austria. <sup>9</sup>Max Planck Institute for Informatics, 66123 Saarbrücken, Germany.

\*These authors contributed equally to this work. †Present address: Macrophages and Endothelial Cells Group, Department of Developmental and Stem Cell Biology, CNRS UMR 3738, Institut Pasteur, Paris, France. ‡These authors contributed equally to this work. §Corresponding author. Email: geissma@mskcc.org

level by fate mapping in EMP-derived cells. Fate-mapping of EMPs was performed by pulse labeling of *Csf1r*<sup>MerCreMer</sup>; *Rosa26*<sup>LSL-YFP</sup> E8.5 embryos, with 4-hydroxy-tamoxifen (OH-TAM) (2, 5). Short-lived OH-TAM allows transient nuclear translocation of the estrogen receptor–Cre recombinase fusion protein (MerCreMer) in cells expressing the *Csf1r*<sup>MerCreMer</sup> transgene and deletion of a floxed stop cassette (LSL) in the *Rosa26*<sup>LSL-YFP</sup> allele, resulting in stable yellow fluorescent protein (YFP) expression in targeted cells and their progeny (2, 5). Expression of cytokine receptors for interleukin (IL)–4, IL–13, interferon-γ, and tumor necrosis factor-α; phagocytic and activating receptors Mrc1 (CD206), Trem2, and Dectin-1 (*Clec7a*); Fc-gamma receptors (Fcgr1, Fcgr2/3, Fcgr4); and Iba1 and Grn was confirmed by flow cytometry and immunofluorescence in situ on EMP-derived pMacs and early macrophages from the YS, as well as from the head, caudal region, limbs, and liver of the embryo proper; fetal macrophages; and adult tissue macrophages

(Figs. 3, A and B; 4A; and 5A and figs. S3 and S4). Protein expression was first detected in pMacs and increased as pMacs differentiated into F4/80<sup>+</sup> macrophages (Fig. 3, A and B, and fig. S3). Of note, pMacs and macrophages represented 70 to 90% of EMP-derived cells in the head and caudal embryo, whereas 80 to 90% of YFP<sup>+</sup> cells in the E10.25 fetal liver represented progenitors (Fig. 3B and fig. S4). Detection of the early expression of the cytokine receptor *Tnfrsf11a* in pMacs by RNA-seq and scRNA-seq analyses (Figs. 2B and 3C) predicted that pMacs and their progeny can be genetically labeled in *Tnfrsf11a*<sup>Cre</sup> (22); *Rosa26*<sup>LSL-YFP</sup> mice. The *Tnfrsf11a*<sup>Cre</sup> transgene allows expression of the Cre recombinase in cells expressing *Tnfrsf11a* and deletion of the floxed stop cassette from the *Rosa26*<sup>LSL-YFP</sup> allele. We observed YFP labeling by flow cytometry in ~80% of pMacs and early macrophages from the YS and embryo of *Tnfrsf11a*<sup>Cre</sup>; *Rosa26*<sup>LSL-YFP</sup> mice (Fig. 3D and fig. S5). Fetal macrophages in

all tissues also expressed YFP at comparable levels at E10.25 and E14.5 (Fig. 3D). In addition, ~80% of brain, lung, epidermis, kidney, and liver macrophages from 6-week-old mice expressed YFP (Fig. 3D). Therefore, the whole resident macrophage lineage is labeled in *Tnfrsf11a*<sup>Cre</sup>; *Rosa26*<sup>LSL-YFP</sup> mice, although *Tnfrsf11a* expression itself is lost in postnatal Langerhans cells and alveolar macrophages (Fig. 2B). Moreover, we noted that YFP expression was observed in only ~15% of fetal HSCs, adult HSCs, and HSC-derived cells in the blood and tissues of adult mice (Fig. 3D and fig. S5). *Tnfrsf11a*<sup>Cre</sup>; *Rosa26*<sup>LSL-YFP</sup> mice thus represent an efficient and relatively specific model for genetic labeling of tissue-resident macrophages in fetuses and adult mice. Early *Cx3cr1* expression by pMacs (Figs. 2B and 3C) is consistent with previous reports showing *Cx3cr1* expression in macrophage precursors (23) and suggests that this chemokine receptor may be involved in colonization of embryo tissues

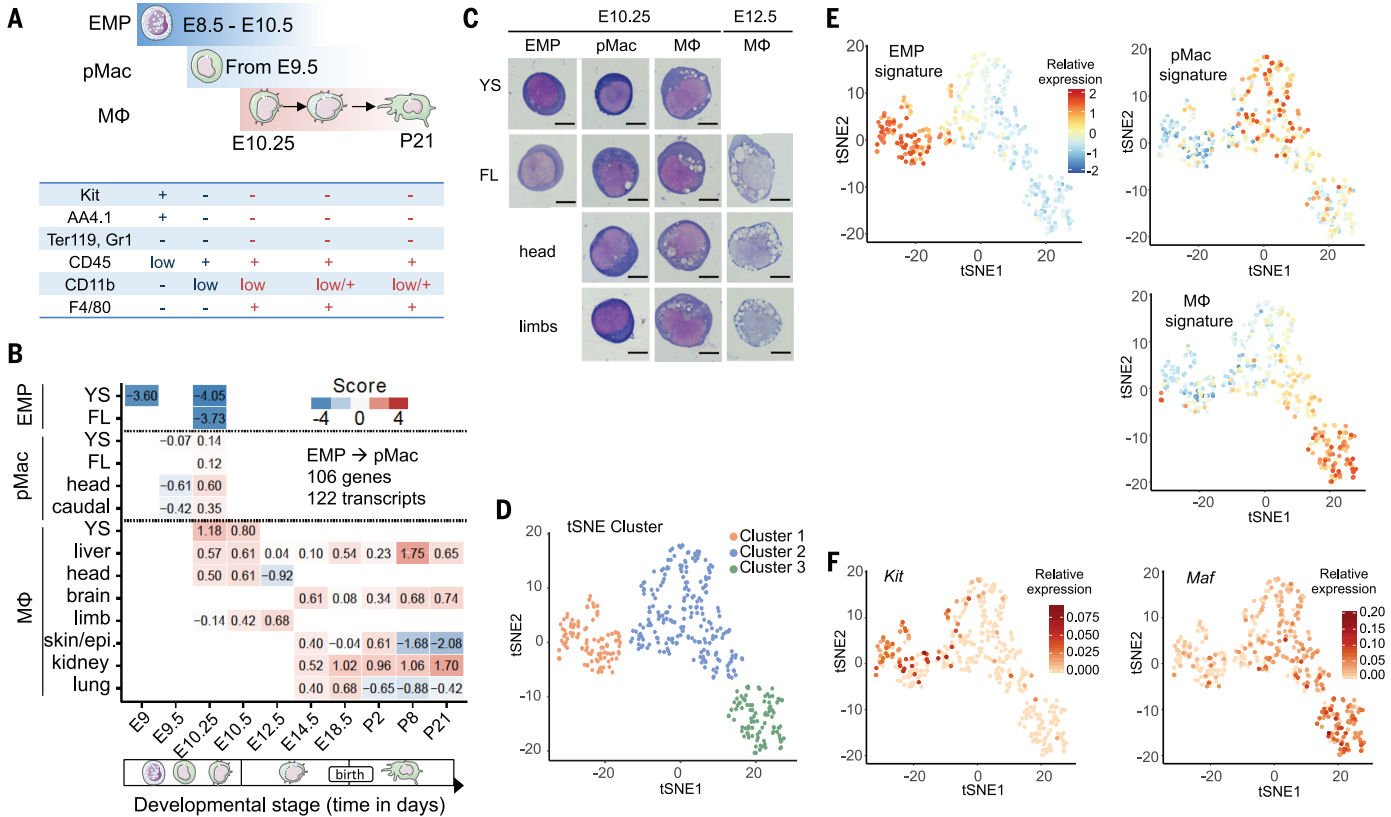


**Fig. 1. A core macrophage program is initiated simultaneously in pMacs in all tissues.** (A) Summary of surface phenotype used for EMPs, pMacs, and macrophages (MΦ). (B) Scorecard visualization of differentially up-regulated genes (DESeq2 Wald test, adjusted  $P < 0.05$ , BH correction) in pMacs (E9.5 and E10.25) compared with EMPs, on the basis of whole-transcriptome sequencing of indicated populations. The table shows the relative enrichment of differentially up-regulated genes in pMacs across cell types and tissues (y axis) and developmental time points (x axis, from E9 to P21). Each sample represents the mean of at least two biological replicates and two technical replicates, except for E14.5 liver macrophages and P8 and P21 lung macrophages, which consist of one biological replicate and two technical replicates. See table S1, fig. S1, and methods for details of

the scorecard. YS, yolk sac; FL, fetal liver; epi., epidermis. (C) May-Grünwald-Giemsa-stained cytospin preparations of sorted EMPs, pMacs, and early macrophages from YS, head, limbs, and fetal liver at E10.25 and E12.5. Images are representative of  $n = 3$  independent experiments. Scale bars, 10  $\mu\text{m}$ . (D) t-Distributed stochastic neighbor embedding (tSNE) plot of single-cell RNA-seq data showing distribution of CD45<sup>low/+</sup> cells from E10.25 embryos into three clusters (see also fig. S2). Cluster distribution based on DBScan is overlaid onto the graph. In total, we analyzed 408 single cells from  $n = 2$  independent experiments with four to six embryos per experiment. (E) Superimposition of EMP-, pMac-, or macrophage-specific signatures defined by the bulk RNA-seq on the tSNE plot shown in (D). (F) tSNE plot as in (D), overlaid with the relative expression values for *Kit* and *Maf*.



by pMac. Time-course analysis of green fluorescent protein (GFP) expression in *Cx3cr1<sup>EGFP/+</sup>* mice (where GFP expression denotes transcription of *Cx3cr1*) from E8.5 (19 to 21 sp) to E10.5 (38 to 39 sp) indicated that GFP expression, and therefore *Cx3cr1* expression, is not detected in Kit<sup>+</sup> progenitors but is up-regulated in Kit<sup>low</sup> Dectin-1<sup>+</sup> pMac and is highest in F4/80<sup>+</sup> macrophages that appear at E10.25 (Fig. 4A). Next, we found that colonization of the head and caudal tissues is delayed in *Cx3cr1*-deficient embryos, as pMac and macrophage numbers are decreased in the head, caudal region, and limbs of E9.5 and E10.5 embryos in comparison with *Cx3cr1*<sup>-/-</sup> littermates while they accumulate in the YS and fetal liver (Fig. 4B). Nevertheless, tissue macrophage numbers even out in the consecutive days of embryonic development in most tissues, with the exception of the kidney, where a 50% lower number in resident macrophages is still observed in adult mice, in line with previous research (24) (fig. S6).

A progressive enrichment of pMac- and macrophage-specific gene expression signatures was observed in gene set enrichment analysis (GSEA) of bulk RNA-seq data (fig. S7, A and B). Moreover, the core macrophage signature identified in adult mice by the Immunological Genome Consortium (25) was already enriched in the genes up-regulated in pMac and early macrophages compared with EMPs (fig. S7, C and D). In silico investigation of transcription factor binding sites identified using chromatin immunoprecipitation sequencing (ChIP-seq) in the proximity of up-regulated genes [transcription start site (TSS)  $\pm$  20 kb] in pMac and macrophages further supports the proposition that pMac undergo a coordinated macrophage differentiation program: A Locus Overlap Analysis (LOLA) (26) yielded a statistically significant association (adjusted  $P \leq 0.001$ , Benjamini Yekutieli correction) with binding sites for *Sp1*, *Egr1*, *Irf1*, *Irf8*, *Maf*, *Jun*, *Stat1*, *Stat3*, *Stat5b*, *Stat6*, *Rela*, and *Relb* (fig. S8A). These factors are expressed in our data set (fig. S8B and tables

S1 and S5), and their binding sites align at the same loci in enhancers and superenhancers associated with differentially regulated genes such as thrombospondin1 (*Thbs1*) (27), *Cx3cr1* (8), F4/80 (*Emr1*), and *Mrc1* but not with control genes such as *Gata1* and *MyoD* (fig. S8C). Comparable results, with a higher statistical significance, were found for genes differentially up-regulated in early macrophages when compared with EMPs (fig. S8A).

Together, these results characterize, at the cellular and molecular level, the EMP-derived macrophage precursors (pMac) that acquire a core macrophage transcriptional program as they colonize the head and caudal embryo from E9.5 in a *Cx3cr1*-dependent manner to give rise to tissue-resident macrophages. These data are consistent with our previous demonstration that the vast majority of resident macrophages in these tissues originate from a progenitor that does not express the stem cell and endothelial marker *Tie2* after E10.5 (2). However, our results do not exclude the possibility

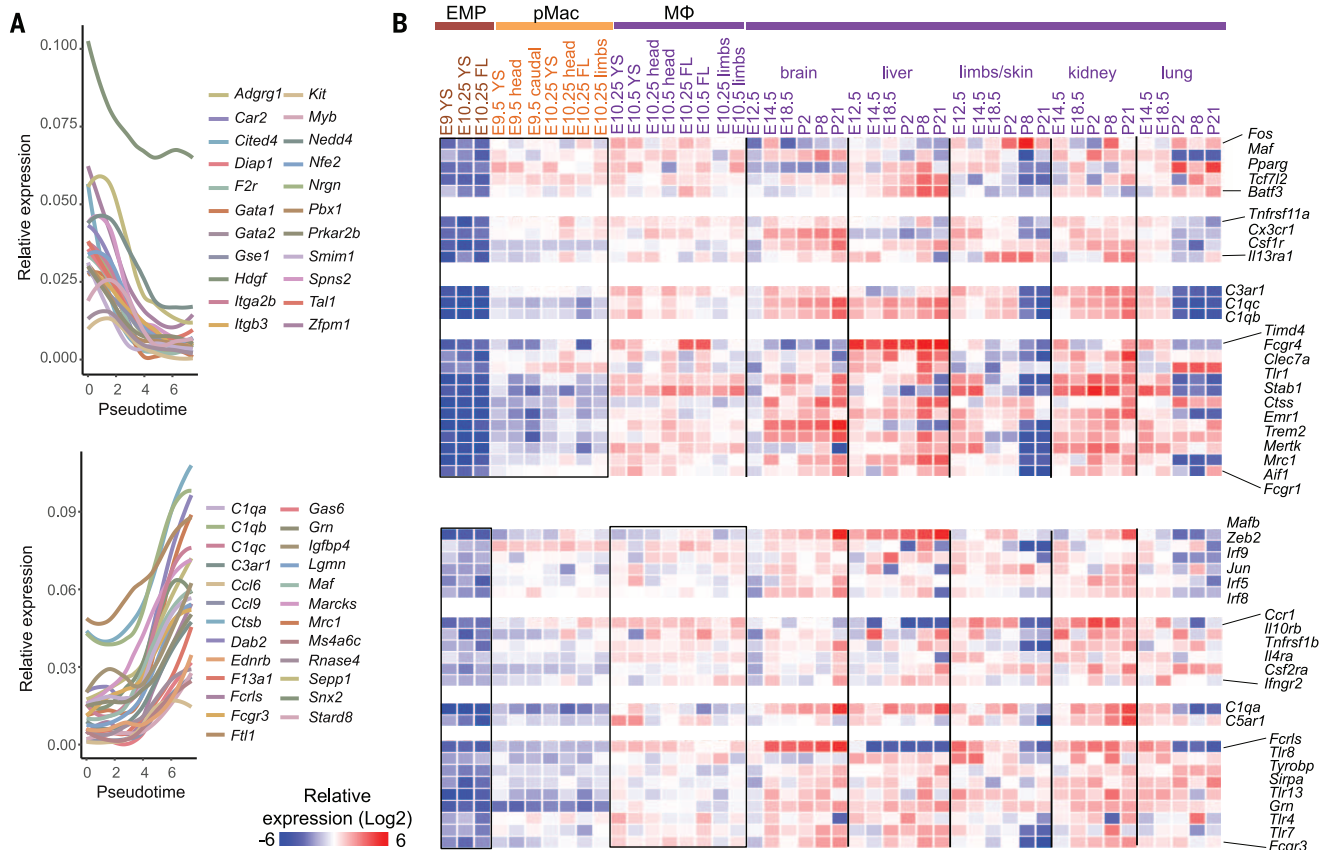


**Fig. 2. Differentially expressed genes during differentiation from EMP to macrophage.** (A) Kinetic diagrams show the pseudotemporal behavioral of 408 single CD45<sup>low/+</sup> cells from scRNA-seq at E10.25, as aligned by Monocle 2, a tool used to analyze differentially expressed genes during an ongoing biological process such as differentiation. See fig. S2G for progression of single cells over developmental pseudotime. Cells within cluster 1 (Fig. 1D) are found farther left on the pseudotime scale, cluster 2 cells are in the middle, and cells within cluster 3 are farther to the right. (Upper panel) Developmental pseudotime diagram ( $q < 0.05$ ) showing down-regulation of EMP-specific

genes [differentially expressed compared with the macrophage and pMac cluster,  $P < 0.05$ , fold change (FC)  $> 1.4$ ] over the differentiation path from EMP to pMac and macrophages. (Lower panel) Similar plot depicting macrophage-specific genes significantly regulated over pseudotime ( $q < 0.05$ ) and differentially expressed compared with the EMP and pMac cluster ( $P < 0.05$ , FC  $> 1.4$ ). (B) Heat-map representation of selected genes differentially regulated between EMPs versus pMac and EMPs versus early macrophages in bulk RNA-seq analysis. Black boxes were drawn around those samples used for differential expression analysis. See also tables S1 and S2.

that later precursors may also contribute to the resident macrophage pool.

### Early specification of tissue-resident macrophages

Following the acquisition of this core program, F4/80<sup>+</sup> macrophages soon display heterogeneity between different tissues (Figs. 2B and 5A). For example, expression of *Timd4* is lost at the transcriptional and protein level in microglia, alveolar macrophages, and Langerhans cells but is maintained in Kupffer cells throughout development and postnatally. Expression of the mannose receptor (CD206) is lost in microglia and Langerhans cells. Dectin-1 and CD64 expression is maintained in all subsets except Langerhans cells (Figs. 2B and 5A and fig. S3). To systematically investigate the kinetics and molecular determinants of macrophage diversification, we first characterized tissue-specific signatures of genes differentially up-regulated in postnatal microglia, kidney macrophages, Langerhans cells, alveolar macrophages, and Kupffer cells in the bulk RNA-seq data set. Unsupervised clustering analysis suggested that macrophages in different tissues undergo characteristic differentiation trajectories (fig. S9A).

Supervised analyses identified lists of genes differentially up-regulated in each cell population (table S3 and fig. S9, B and C). The signatures of adult tissue-resident macrophages of the brain, lung, and liver previously defined by independent research (7, 25, 28) were progressively enriched in our developing resident macrophage populations (fig. S10, A to D). Finally, scorecard (21) and GSEA analysis of differentially up-regulated genes for each postnatal macrophage population in all tissues and over time from E9 to P21 (Fig. 5, B and C, and fig. S10C) revealed that the tissue-specific signature of postnatal microglia, Kupffer cells, and kidney macrophages could be traced back to fetal macrophages as early as E12.5 (Fig. 5B). The signatures of Langerhans cells and alveolar macrophages reflected important postnatal changes in gene expression (Fig. 5C), noted in previous studies (29), which may reflect their anatomical location at epithelial barriers.

### Tissue-specific sets of transcriptional regulators define macrophage diversity

A heat-map visualization of all transcriptional regulators present in the postnatal tissue-specific

signatures (twofold change, adj.  $P < 0.05$ , BH correction, Fig. 5D) confirmed the tissue-specific expression of the transcription factors *Sall1* and *Sall3* in microglia (7), *Nr1h3* (*Lxra*) in Kupffer cells (30), *Pparg* in lung alveolar macrophages (18, 31), and *Runx3* and *Ahr* in Langerhans cells (15, 32) (Fig. 5D) and identified additional tissue-specific transcriptional regulators such as *Id1* and *Id3* in Kupffer cells (Fig. 5D). In addition, this analysis showed that many of these transcriptional regulators start to be differentially expressed in tissue macrophages as early as E10.25—for example, in *Sall1* and *Sall3* in head macrophages; *Nr1h3*, *Id1*, and *Id3* in the liver; and *Ahr* in limb macrophages (Fig. 5D). Some genes, like *Id1* and *Sall3*, are expressed by progenitors and pMac before their expression becomes restricted to macrophages in the liver and the head, respectively (fig. S10E), whereas expression of other genes, such as *Id3* and *Sall1*, is low in progenitors and up-regulated in pMac (fig. S10E). In situ immunofluorescence confirmed expression of *Id3* by E10.25 macrophages in the liver and head and of *Id1* in liver macrophages (Fig. 6A). Together these data suggest that the transcriptional programs of tissue-specific

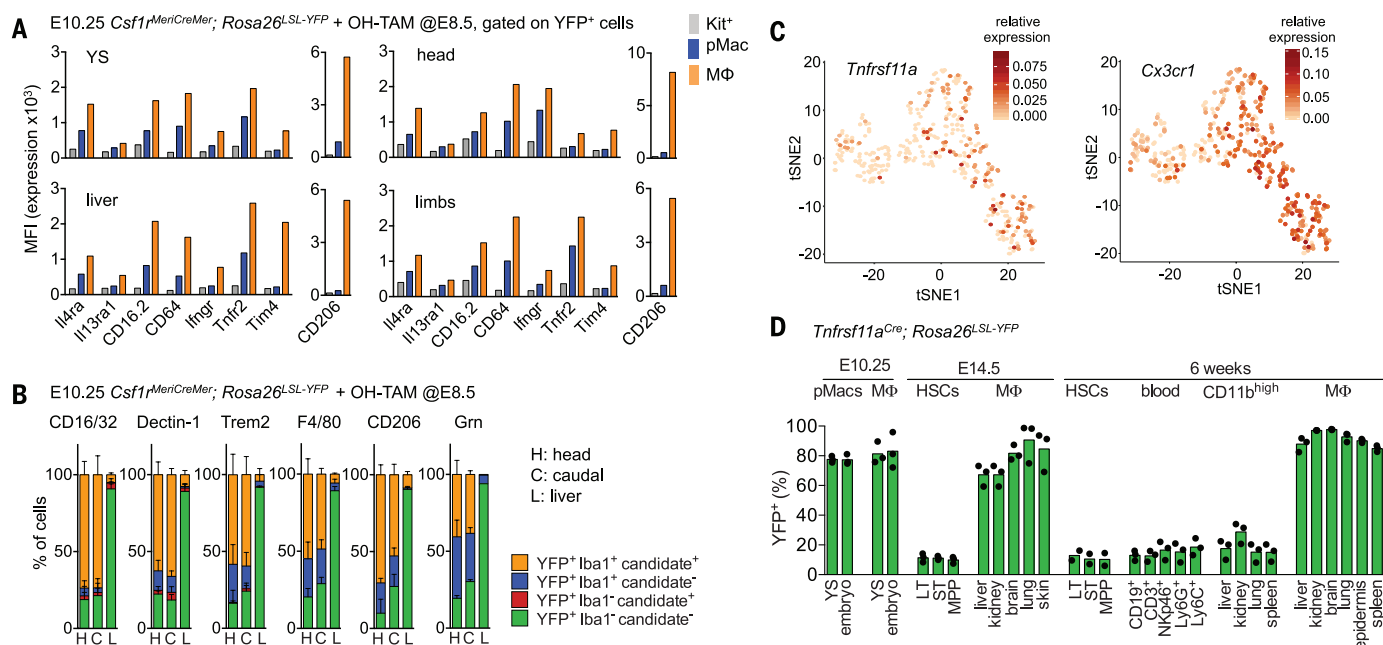


**Fig. 3. EMP-derived pMacS colonize the embryo to generate macrophages.** (A) Flow cytometry analysis of E10.25 *Csf1r<sup>MeriCreMer</sup>; Rosa26<sup>LSL-YFP</sup>* (OH-TAM at E8.5) tissues showing expression of *Il4ra*, *Il13ra1*, *CD16.2*, *CD64*, *Ifngr*, *Tnfr2*, *Tim4*, and *CD206* on YFP<sup>+</sup> Kit<sup>+</sup> progenitors, pMacS, and macrophages. MFI, mean fluorescence intensity. Data are representative of  $n = 4$  independent experiments with four to six embryos per marker. See also fig. S3A. (B) Quantification of immunostainings on cryosections from E10.25 *Csf1r<sup>MeriCreMer</sup>; Rosa26<sup>LSL-YFP</sup>* embryos, pulse-labeled with OH-TAM at E8.5 with antibodies against YFP, Iba1, and additional candidate genes (*CD16/32*, *Dectin-1*, *Trem2*, *F4/80*, *CD206* or *Granulin*). Orange bars represent the percentage of YFP<sup>+</sup> cells expressing Iba1 and the indicated candidate; blue bars denote the percentage of YFP<sup>+</sup> cells expressing only Iba1. Red and green bars represent the percentage of YFP<sup>+</sup> cells negative for Iba1 and expressing (red) or negative for (green) the indicated candidate gene.  $n = 2$  to 4 embryos and two sections per

embryo per marker. See also fig. S4. (C) tSNE plot (as in Fig. 1D) overlaid with the relative expression values for *Tnfrsf11a* and *Cx3cr1*. (D) Genetic labeling efficiency in *Tnfrsf11a<sup>Cre</sup>; Rosa26<sup>LSL-YFP</sup>* mice measures efficiency of Cre-mediated recombination of the floxed stop sequence at the *Rosa26<sup>LSL-YFP</sup>* locus and, therefore, transcription of *Tnfrsf11a* in the indicated cell types and their progenitors. Cells analyzed were pMacS and F4/80<sup>+</sup> macrophages in the YS and whole embryo at E10.25; fetal liver HSCs [long-term (LT) (Lin<sup>+</sup>Kit<sup>+</sup>Sca1<sup>+</sup>CD150<sup>+</sup>CD48<sup>-</sup>), short-term (ST) (Lin<sup>+</sup>Kit<sup>+</sup>Sca1<sup>+</sup>CD150<sup>+</sup>CD48<sup>-</sup>) and multipotent progenitor (MPP) (Lin<sup>+</sup>Kit<sup>+</sup>Sca1<sup>+</sup>CD150<sup>+</sup>CD48<sup>-</sup>)] and tissue macrophages at E14.5 and 6 weeks; and blood leukocytes [B cells (CD19<sup>+</sup>), T cells (CD19<sup>+</sup>Ly6G<sup>+</sup>CD115<sup>+</sup>CD3<sup>+</sup>), natural killer (NK) cells (CD19<sup>+</sup>Ly6G<sup>+</sup>CD115<sup>+</sup>CD3<sup>+</sup>NKp46<sup>+</sup>), neutrophils (CD19<sup>+</sup>Ly6G<sup>+</sup>) and Ly6C<sup>hi</sup> monocytes (CD19<sup>+</sup>CD115<sup>+</sup>Ly6G<sup>+</sup>Ly6C<sup>hi</sup>), and tissue CD11b<sup>high</sup> myeloid cells from 6-week-old mice. Circles represent individual mice from  $n = 4$  independent experiments. See also fig. S5.



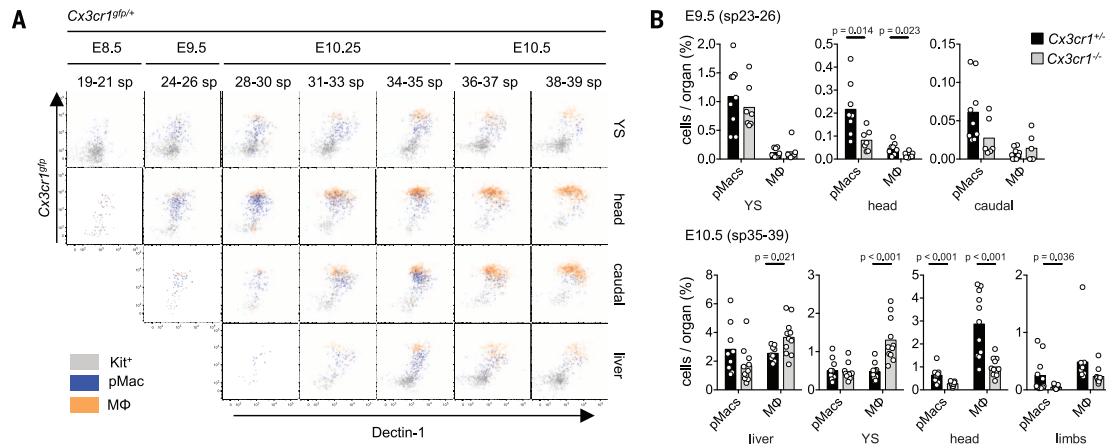


**Fig. 4. Tissue colonization by pMacs is dependent on *Cx3cr1*.** (A) Expression of GFP and Dectin-1 in *Cx3cr1<sup>GFP/+</sup>* mice during development (E8.5 to E10.5) in Kit<sup>+</sup> cells (CD45<sup>low</sup>, Kit<sup>+</sup>), pMacs, and macrophages. sp, somite pairs. Data are representative of *n* = 9 independent experiments. Biological replicates have been aggregated per cell type, time point, and tissue. (B) Flow cytometry analysis in *Cx3cr1<sup>+/+</sup>* and *Cx3cr1<sup>-/-</sup>* pMacs and macrophages from the YS, head, and caudal region at E9.5 (upper panel) and the liver, YS, head, and limbs at E10.5 (lower panel). Circles represent individual mice. Data are pooled from *n* = 6 independent experiments. *P* were calculated using Student's *t* test.

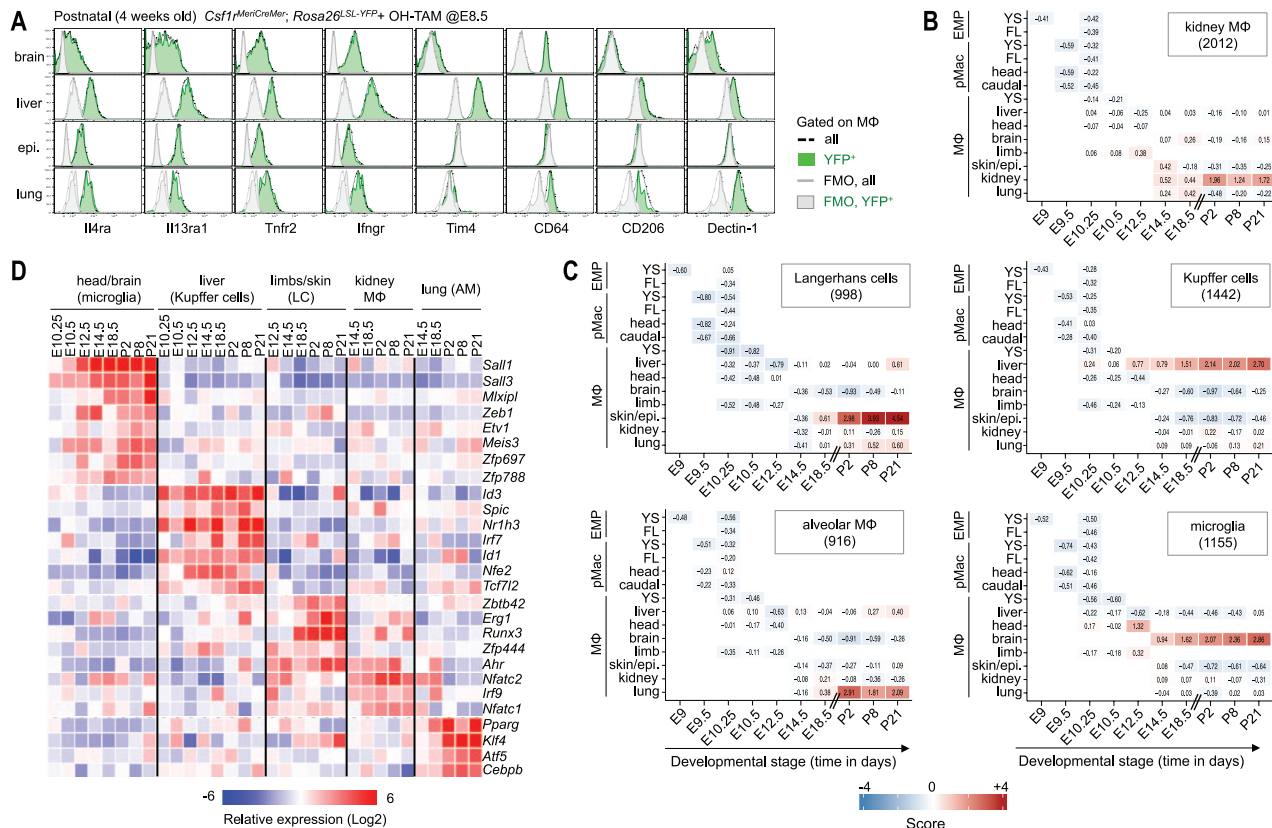


**Fig. 5. Early specification of tissue-resident macrophages.** (A) Flow cytometry analysis of *Csfl<sup>MerCreMer</sup>; Rosa26<sup>LSL-YFP</sup>* (OH-TAM at E8.5) liver, brain, lung, and skin F4/80<sup>+</sup> cells from postnatal mice (4 weeks old) showing expression of Il4ra, Il13ra1, Tnfr2, Ifngr, Dectin-1, CD64, Tim4, and CD206. Black dashed lines depict expression by all macrophages (CD45<sup>+</sup>CD11b<sup>low</sup>F4/80<sup>high</sup>); green tinted lines show expression by the subsets of YFP<sup>+</sup> macrophages. Gray histograms show the fluorescence intensity of the FMO (fluorescence minus one) controls for all macrophages (gray lines) and YFP<sup>+</sup> macrophages (gray tinted lines). Histograms are representative of five mice and *n* = 2 independent experiments. (B and C) Scorecard analysis of all differentially up-regulated genes in postnatal macrophages from bulk RNA-seq. The scorecards show

the relative enrichment of each set of up-regulated genes across each cell type (y axis) and developmental time point (x axis). See Materials and methods for details of the score card. Numbers for each population indicate differentially up-regulated transcripts in postnatal (P2 to P21) brain, liver, kidney, epidermis, or lung macrophages when comparing one population versus the others. See also table S3. (D) Heat map representing all differentially up-regulated transcriptional regulators from bulk RNA-seq (twofold change, adj. *P* < 0.05, BH correction) between postnatal macrophages from the brain, liver, kidney, skin, and lung, as well as their relative expression in tissue macrophages from E10.25 to P21. LC, Langerhans cells; AM, alveolar macrophages.

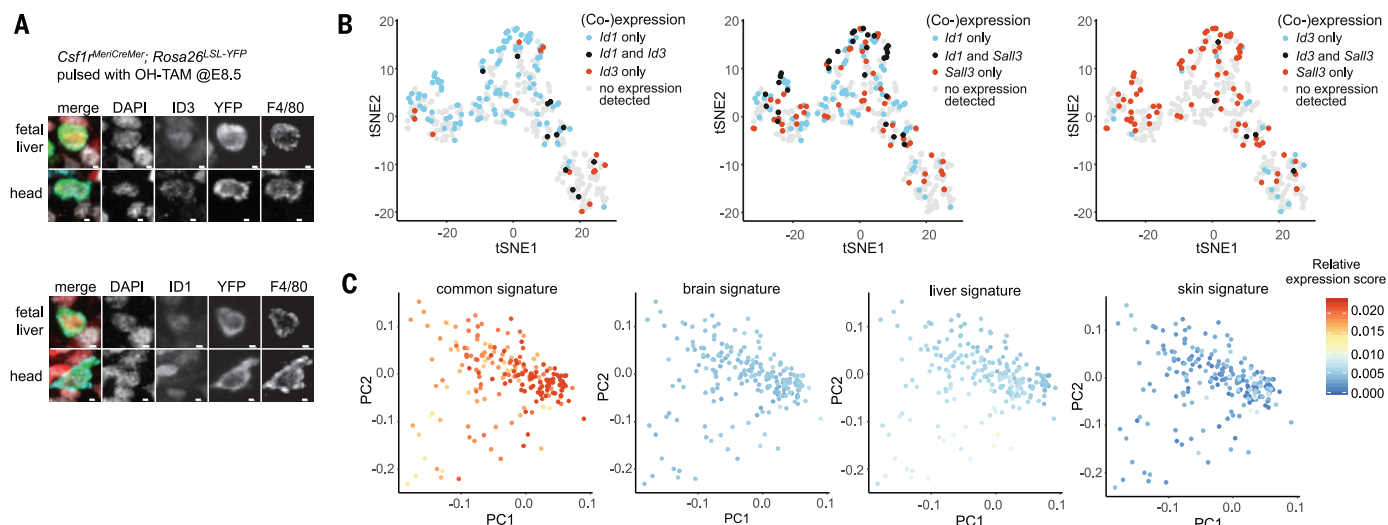


**Fig. 6. Tissue-specific macrophage signatures are not detected in pMacs.** (A) Immunostaining with antibodies against Id3 (red, upper panel) or Id1 (red, lower panel), F4/80 (cyan), and YFP (green) on cryosections from E10.25 *Csf1r<sup>MerCreMer</sup>; Rosa26<sup>LSL-YFP</sup>* embryos (OH-TAM at E8.5), analyzed by confocal microscopy. Nuclei are counterstained with 4',6-diamidino-2-phenylindole (DAPI) (white). Scale bars, 2  $\mu$ m. Images are representative of  $n = 3$  independent experiments. (B) tSNE plots of scRNA-seq data from CD45<sup>low/+</sup> cells from E10.25 embryos (as in Fig. 1), showing coexpression of *Id1*, *Id3*, and *Sall3*. See also fig. S11. (C) PCA plots of scRNA-seq data of cells from cluster 2 (pMacs, defined in Fig. 1D) with superimposed fetal tissue macrophage-specific signatures. See also fig. S11, table S2, and Materials and methods.

resident macrophages start to be established early on, as soon as macrophages or pMacs are present in tissues, and identify a number of “candidate” tissue-specific transcriptional regulators.

We thus investigated whether specification of tissue macrophages takes place in F4/80<sup>+</sup> macrophages or at the level of their pMac or EMP precursors. We plotted transcriptional coexpression of *Id1*, *Id3*, and *Sall3* onto the t-distributed stochastic neighbor embedding (tSNE) representation of single CD45<sup>low/+</sup> cells from our scRNA-seq data set (Figs. 1D and 6B and fig. S11). Coexpression of *Id1* and *Id3* was found in pMacs and macrophages. However, *Id1* and *Sall3* were coexpressed in EMPs and pMacs, and *Id3* and *Sall3* were coexpressed in pMacs, suggesting that cells at the pMac state are not completely committed to exclusive expression of tissue-specific transcription factors. These data confirmed that *Id1* and *Sall3* are expressed by progenitors and pMacs (fig. S10E), although their expression is ultimately lost by tissue macrophages outside the liver and the brain, respectively (Figs. 5D and 6B and fig. S10E). When common and tissue-specific E14.5 to E18.5 macrophage signatures (table S2) were superimposed on the pMac population, we found that the common macrophage signature was expressed in pMacs with a gradual enrichment within this population (Fig. 6C). However, we did not observe pMac subsets expressing tissue-specific signatures (Fig. 6C). The lack of tissue specificity within pMacs was confirmed using an alternative bioinformatic approach based on analysis of multimodal expression followed by hierarchical clustering of genes with subsequent analysis of enrichment of tissue signatures within these clusters in pMacs (fig. S11E).

Taken together, these data suggest that expression of *Id1* and *Id3* or *Sall3* does not specify

pMac subsets precommitted to give rise to either Kupffer cells or microglia. More generally, diversification of tissue macrophages appears to take place after pMacs have colonized tissues and differentiated into F4/80<sup>+</sup> macrophages.

### The transcriptional regulator *Id3* is essential for Kupffer cell development

To functionally validate the role of early tissue-specific transcriptional regulators on the development and specification of tissue macrophages—and, thereby, to validate the importance of our findings—we studied the role of *Id3* expression in Kupffer cell differentiation. E10.25 *Id3*-deficient embryos had normal or increased numbers of pMacs and early macrophages in the YS, but macrophages were reduced in numbers in the embryo proper (liver and head) in comparison with littermate controls (Fig. 7A). The further development of liver macrophages was severely impaired in E14.5 and E18.5 *Id3*-deficient embryos, as determined by flow cytometry and histology, and 4-week-old *Id3*-deficient mice still presented with a marked Kupffer cell deficiency, whereas development of microglia and kidney macrophages appeared normal (Fig. 7, B, C, and E, and fig. S12C). The role of *Id3* in Kupffer cells appears to be cell-autonomous, as targeted deletion of an *Id3* floxed allele in pMacs (*Tnfrsf11a<sup>Cre/+</sup>; Id3<sup>f/f</sup>*) recapitulated the phenotype of the *Id3*-deficient mice in embryo and postnatal mice (Fig. 7, C and D). Expression of *Id3* in postnatal Kupffer cells was confirmed by quantitative reverse transcription polymerase chain reaction (qRT-PCR) (fig. S12A) and by immunofluorescence in Kupffer cells from *Csf1r<sup>MerCreMer</sup>; Rosa26<sup>LSL-YFP</sup>* mice pulse-labeled with OH-TAM at E8.5 (Fig. 7F and fig. S12B). In contrast, fate-mapped microglia do not express *Id3* (fig. S12B), in line with our

RNA-seq data (Fig. 5D). Of note, the partial Kupffer cell deficiency observed in *Id3*-deficient and *Tnfrsf11a<sup>Cre/+</sup>; Id3<sup>f/f</sup>* embryos and adults was not associated with an abnormal liver lobular architecture or vasculature (Fig. 7, C and D, and fig. S12D). Kupffer cell proliferation in the steady state was not affected by *Id3* deficiency (Fig. 7G), but RNA-seq analysis of *Id3<sup>-/-</sup>* and *Id3<sup>+/-</sup>* adult Kupffer cells indicated the up-regulation (>threefold) of *Id1* expression, and gene ontology (GO)-term analysis evidenced that *Id3<sup>-/-</sup>* cells overexpressed genes involved in the control of cell death and cytokine responses and down-regulated genes involved in metabolic processes (Fig. 7H; fig. S12, E and F; and table S6). These data suggest that *Id3* is important for the development and maintenance of Kupffer cells in the liver but is dispensable for other macrophage subsets. As *Id1* and *Id3* are coexpressed, it will be interesting to investigate whether up-regulation of *Id1* partially compensates for *Id3* deficiency (33, 34).

### Conclusions

We show here that EMPs rapidly differentiate into a population of cells that we call pMacs, because they simultaneously colonize the whole embryo from E9.5 in a *Cx3cr1*-dependent manner while differentiating into macrophages. pMacs do not yet have macrophage morphology but are in the process of establishing a full core macrophage differentiation program that includes cytokine receptors, phagocytic and pattern recognition receptors, and complement. Starting from E10.5, almost immediately after colonization of embryonic tissues, tissue-specific expression of transcriptional regulators in F4/80<sup>+</sup> macrophages initiates their specification into adult-type resident macrophages (Fig. 8). Our



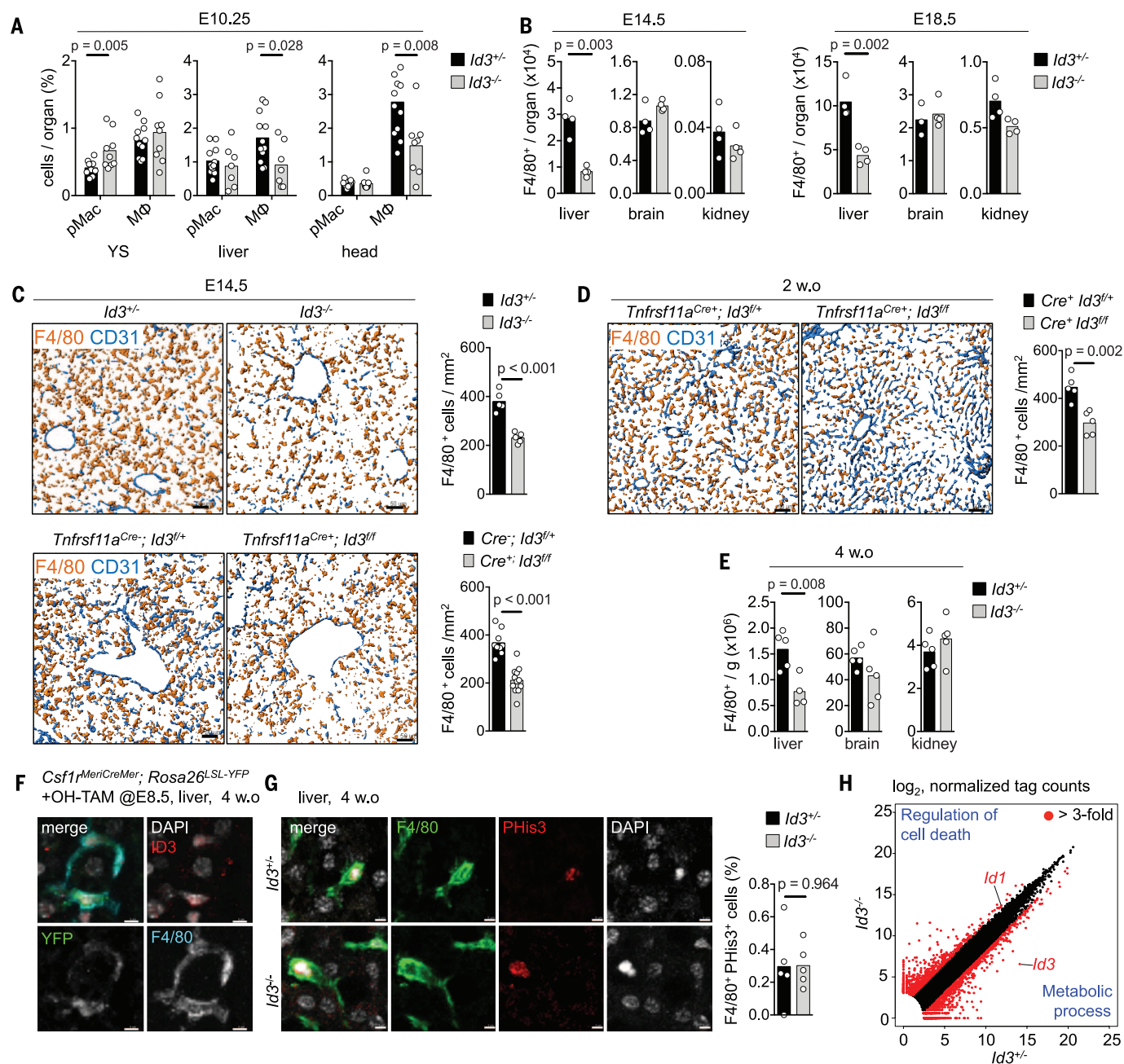
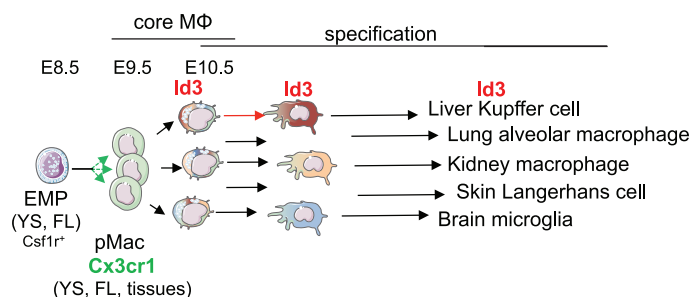


**Fig. 7. *Id3* is important for Kupffer cell development.** (A) Flow cytometry analysis of the percentage of pMac and macrophages in the YS and liver from E10.25 *Id3*<sup>-/-</sup> and *Id3*<sup>+/+</sup> embryos. Circles represent individual mice from *n* = 3 independent experiments. (B) Flow cytometry analysis of F4/80<sup>+</sup> macrophages in the liver, brain, and kidney from E14.5 and E18.5 *Id3*<sup>-/-</sup> and *Id3*<sup>+/+</sup> mice. Cell suspensions were prepared, stained, and acquired from whole organs, and the number of live cells per tissue was directly obtained from flow cytometry standard (FCS) files (see Materials and methods). Circles represent individual mice from *n* = 4 independent experiments. (C and D) Immunostaining with antibodies against CD31, which labels endothelial cells, and F4/80 on liver cryosections from E14.5 and 2-week-old (2 w.o.) *Id3*<sup>-/-</sup>, *Id3*<sup>+/+</sup>, *Tnfrsf11a*<sup>Cre/+</sup>; *Id3*<sup>+/+</sup>, *Tnfrsf11a*<sup>Cre/+</sup>; *Id3*<sup>fl/fl</sup>, and *Tnfrsf11a*<sup>Cre/+</sup>; *Id3*<sup>fl/fl</sup> littermates. The figures display is representative of isovolume-rendered images from *n* = 4 independent experiments. Circles in bar graphs represent quantification of F4/80<sup>+</sup> cells per square millimeter in individual fields of view. See also fig. S12. (E) Flow cytometry analysis of F4/80<sup>+</sup> macrophages in the liver, brain, and

kidney from 4-week-old *Id3*<sup>-/-</sup> and *Id3*<sup>+/+</sup> mice. Circles represent individual mice from *n* = 2 independent experiments. (F) Immunostaining with antibodies against ID3 (red), F4/80 (cyan) and YFP (green) on cryosections from the livers of 4-week-old *Csf1*<sup>MerCreMer</sup>; *Rosa26*<sup>LSL-YFP</sup> (OH-TAM at E8.5) mice. Nuclei are counterstained with DAPI (white). Scale bars, 5  $\mu$ m. Images are representative of three independent experiments. (G) Immunostaining with antibodies against F4/80 (green) phospho-histone 3 (PHis3, red) and DAPI (gray) on liver cryosections from 4-week-old *Id3*<sup>-/-</sup> and *Id3*<sup>+/+</sup> mice. Scale bars, 10  $\mu$ m. Individual dots in the bar graph represent mean percentages of F4/80<sup>+</sup> cells labeled with PHis3 from five sampling areas (830  $\mu$ m<sup>2</sup>) per liver from *n* = 5 mice per genotype. (H) Scatter-plot comparison of gene expression of 3-week-old *Id3*<sup>-/-</sup> and *Id3*<sup>+/+</sup> Kupffer cells performed on bulk RNA-seq data. Both axes (in  $\log_2$  scale) represent normalized gene expression values (average value from three *Id3*<sup>+/+</sup> and two *Id3*<sup>-/-</sup> replicates). Red circles mark the threefold cut-off in both directions in gene expression level. Top GO terms for genes enriched in either *Id3*<sup>+/+</sup> or *Id3*<sup>-/-</sup> are indicated. *P* values were calculated using Student's *t* test. See also fig. S12.

**Fig. 8. Graphic summary of the establishment of the core macrophage program and subsequent specification.** *Cx3cr1* is expressed in pMac and is important for colonization of the embryo. *Id3* is a liver macrophage-specific gene, which is essential for Kupffer cell development.



data, therefore, suggest that a broad or core macrophage program is progressively restricted or refined to a tissue-specific one in response to the absence and presence of tissue-specific cues, rather than the alternative possibility that committed subsets of early macrophages, pMac, or even EMPs choose their future tissue of residence. The present results are consistent with an EMP origin of tissue-resident macrophages (2), although they do not exclude the additional contribution of primitive precursors (23), fetal HSCs, or a second wave of EMPs (11, 12), which would adopt a similar differentiation program when entering tissues. However, the transcriptional data set described here may lead to reinterpretation of fate-mapping models used to characterize the contribution of such later waves. For example, the progressive YFP expression by fetal macrophages in *S100a4<sup>Cre</sup>*; *Rosa26<sup>LSL-YFP</sup>* mice (12) is compatible with our present findings and does not require the existence of a second wave of precursors because expression of *S100a4* and several other *S100a* family members was found to be part of the pMac transcriptional profile (fig. S13).

We propose that establishment of a core macrophage differentiation program in EMP-derived pMac, as they colonize the embryo, is followed by the initiation of macrophage specification via the acquisition of tissue-specific transcriptional regulators, such as *Id3* in Kupffer cells. This process is initiated simultaneously in the whole embryo during the first 2 days of organogenesis, from E8.5 to E10.5. Differentiation of resident macrophages is thus a developmental process and an integral part of organogenesis, independent of postnatal changes in the environment in the kidney, liver, and brain but not in the skin or lung. These results also identify a developmental window where the molecular mechanisms of macrophage specification can best be studied, tools to selectively label resident macrophages, and sets of tissue-specific transcriptional regulators expressed by developing and adult macrophages that may control their differentiation, maintenance, and function. Additionally, our results elucidate a molecular road map that will support efforts to differentiate specialized macrophages—microglia, Kupffer cells, kidney macrophages, alveolar macrophages, and Langerhans cells—in vitro from multipotent progenitors. Finally, our work provides a framework to analyze

and understand the consequence(s) of genetic variation for macrophage contribution to disease pathogenesis in different tissues.

## Materials and methods

### Mice

*Csf1r<sup>MerCreMer</sup>*, *Csf1r<sup>iCre</sup>*, *Rosa26<sup>YFP-LSL</sup>*, *Cx3cr1<sup>sf/p/+</sup>* and *Tnfrsf11a<sup>Cre</sup>* mice (2, 5, 22, 35) and *Id3<sup>-/-</sup>*; *Id1<sup>fl/fl</sup>* and *Id3<sup>fl/fl</sup>* mice—kindly provided by R. Benezra (34, 36, 37)—were maintained under SPF conditions. Animal procedures were performed in adherence to our project license issued by the United Kingdom Home Office under the Animals (Scientific Procedures) Act 1986 and by the Institutional Review Board (IACUC 15-04-006) from MSKCC. Genotyping was performed according to protocols described previously for *Csf1r<sup>iCre</sup>* (38), *Csf1r<sup>MerCreMer</sup>* (5), *Id3<sup>-/-</sup>*; *Id1<sup>fl/fl</sup>* (36), and *Tnfrsf11a<sup>Cre</sup>* (22) mice. Genotyping of *Cx3cr1<sup>sf/p/+</sup>* was performed as recommended by Jackson Laboratory, Bar Harbor, Maine with the following primers: *Cx3cr1* F 5'-CCC AGA CAC TCG TTG TCC TT-3', *Cx3cr1* R 5'-GTC TTC ACG TTC GGT CTG GT and *Cx3cr1* R mut 5'-CTC CCC CTG AAC CTG AAA C-3'. Cre recombination in *Csf1r<sup>MerCreMer</sup>*; *Rosa26<sup>LSL-YFP</sup>* embryos was induced by single injection at E8.5 of 75 mg per g (body weight) of 4-hydroxytamoxifen (OH-TAM, Sigma) into pregnant females as described (2). The OH-TAM was supplemented with 37.5 mg per gram (body weight) progesterone (Sigma) to counteract the mixed estrogen agonist effects of tamoxifen, which can result in fetal abortions. Embryonic development was estimated as previously considering the day of vaginal plug formation as 0.5 days post-coitum (dpc), and staged by developmental criteria. E9: 20 to 25 sp, E9.5: 26 to 29 sp, E10.25: 30 to 35 sp, E10.5: 36 to 44 sp.

## Preparation of cell suspensions and cell sorting

Pregnant females were killed by cervical dislocation or by exposure to CO<sub>2</sub>. Embryos ranging from E9 to E18.5 were removed from the uterus, washed in 4°C phosphate-buffered saline (PBS, Invitrogen) and dissected under a Leica M80 microscope. Yolk sacs (YS) were harvested from embryos between E9 and E10.5. To obtain single-cell suspensions for FACS sorting, tissues were included in cold PBS and mechanically disrupted under a 100µm filter. Postnatal tissues were collected following the same procedure. For collec-

tion of Langerhans cells, epidermal sheets (from E18.5 to P21) were separated from the dermis after incubation for 45 min at RT in 4.8 mg/ml of dispase (Invitrogen), 3% fetal calf serum (FCS, Invitrogen) and 1 µM of flavopiridol (Sigma). The epidermis was further digested for 30 min at RT in PBS containing 2 mg/ml of collagenase D (Roche), 200 U/ml DNase I (Sigma), 4.8 mg/ml of dispase (Invitrogen), 3% FCS (Invitrogen) and 1µM of flavopiridol (Sigma) followed by mechanical disruption under a 100µm filter. For blood phenotyping, mice were anaesthetized and blood was collected by cardiac puncture. For flow cytometry experiments, organs were incubated in PBS containing 1 mg/ml collagenase D (Roche), 100 U/ml DNase I (Sigma), 2.4 mg/ml of dispase (Invitrogen) and 3% FCS (Invitrogen) at 37°C for 30 min prior to mechanical disruption. Epidermal sheets were obtained as previously described (2). For embryonic tissue incubation time at 37°C was reduced to 20 min. Cell suspensions were centrifuged at 320g for 7 min, resuspended in FACS buffer (PBS, 0.5% BSA and 2 mM EDTA) containing purified anti-CD16/32 (FcγRIII/II) (1:100 dilution) and incubated for 15 min at 4°C. Samples were immunostained with antibodies mixes for 30 min at 4°C, and analyzed by flow cytometry using a LSR Fortessa X-20 (BD-Bioscience). Single live cells were gated on the basis of dead cell exclusion (Hoechst 33258), side (SSC-A) and forward scatter (FSC-A) gating, and doublet exclusion using forward scatter width (FSC-W) against FSC-A. The full list of antibodies used can be found in table S4. Cell numbers per organ or per gram of tissue were calculated as follow. In E9.5 to E12.5 embryonic tissue cell suspensions were prepared, stained, and acquired from whole organs, and the number of live cells per tissue was directly obtained from FCS files. In E14.5 to E18.5 embryos, cells suspensions were prepared as above, but half were stained and acquired. In adult mice, organs were weighted, cell suspensions were prepared from 100 to 500 mg of tissues, and the number of live single F4/80<sup>+</sup> cells per gram of tissue was determined using a cell counter (GUAVA easyCyte HT).

Cell sorting was performed using an Aria II BD cell sorter. Cell suspensions were prepared as above, except for the gating of single live cells which was performed using dead cell exclusion with DAPI. For bulk sequencing, EMPs were identified after gating on Kit<sup>+</sup>CD45<sup>lo</sup> cells based on AA4.1 expression. pMac were identified after gating on Kit<sup>+</sup>CD45<sup>+</sup> based on CD11b expression and no expression of F4/80. Additionally, Gr1<sup>+</sup> or Ter119<sup>+</sup> cells were excluded from the F4/80<sup>+</sup>CD11b<sup>+</sup> gate. Macrophage populations were identified after gating on CD45 based on expression of F4/80 and CD11b. 100 cells for each sample were directly sorted into a 96 well plate (Biorad) in 4 µl of H<sub>2</sub>O containing 0.2% of triton TXT (Sigma) and 0.8 U/µl of RNase inhibitor (Clontech), and processed as indicated below (*Generation and analysis of "bulk" transcriptomes from candidate EMP, pMac, and macrophage populations from E9 to P21*). For single-cell sequencing, all CD45<sup>low/+</sup> single cells from a E10.25 (30 to 34 sp) embryo



proper were sorted into 384-well plates filled with 2  $\mu$ l lysis buffer (Triton-X 0.2%) (Sigma) in molecular biology grade H<sub>2</sub>O (Sigma) supplemented with 0.4 U/ $\mu$ l protein-based RNase inhibitor (Takara) and barcoded poly-T primers, and processed as described below (*Generation and analysis of single-cell transcriptomes*).

### Cytology

Cells were collected into FCS and centrifuged (800 rpm, 10 min, low acceleration) onto Superfrost slides (Thermo Scientific) using a Cytospin 3 (Thermo Shandon). Slides were air-dried for at least 30 min, and fixed for 5 min in methanol, stained in 50% May-Grünwald solution for 5 min, 14% Giemsa for 15 min, washed with Sorensens buffered distilled water (pH 6.8) for 5 min and rinsed with Sorensens buffered distilled water (pH 6.8). Slides were air-dried and mounted with Entellan New (Merck) and representative pictures were taken using an Axio Lab.A1 microscope (Zeiss) under a N-Achroplan 100x/01.25 objective.

### Immunofluorescence, imaging, analysis, and illustrations

E10.25 Embryos were fixed for 4 hours in 4% formaldehyde (Sigma) under agitation and >E10.25 embryos were fixed overnight. After fixation, embryos were incubated overnight in 30% sucrose and embedded in OCT compound (Sakura Finetek). Cryoblocks were cut at a thickness of 10-12  $\mu$ m and then blocked with PBS containing 5% normal goat serum (Invitrogen); 1% BSA (w/v); 0.3% Triton X-100 for 1 hour at room temperature. Samples were incubated overnight at 4°C with rat anti-mouse F4/80 (1:200, Biorad), rabbit anti-mouse Iba1 (1:200; Wako), chicken anti-GFP for YFP detection (1:500, Invitrogen), rat anti-mouse Dectin-1 (1:200, Biorad), anti-Granulin (1:200, abcam), rat anti-mouse CD206 (1:200, Biorad), Armenian hamster anti-mouse PECAM-1 (1:300, Thermo Scientific), rabbit anti-mouse/human ID3 (1:500, Biocheck), rabbit anti-mouse ID1 (1:500, Biocheck), rat anti-mouse CD16/CD32 (BD Biosciences), goat anti-mouse Trem2 (1:200, Abcam), armenian hamster anti-mouse CD119 (1:200, Clone 2E2, eBioscience), armenian hamster anti-mouse CD120b (1:200, clone 55R-286, Biolegend). Secondary antibodies used were anti-rabbit Cy3 (1:500; Invitrogen), anti-chicken Alexa Fluor 488 (1:500; Invitrogen), anti-rat Alexa Fluor 555 (1:500; Invitrogen), anti-rat Alexa Fluor 488 (1:500; Invitrogen), anti-rat Alexa Fluor 647 (1:500; Invitrogen), anti-goat Alexa Fluor 568 and anti-armenian hamster Dylight 649 (Jackson ImmunoResearch Laboratories). Samples were then mounted with Fluoromount mounting medium with DAPI (eBiosciences) and visualized using a LSM880 Zeiss microscope with 20x/0.5 (dry), performing a tile scan and Z-stack on whole embryos or tissues. Image analysis and cell quantification was performed using Imaris (Bitplane) software. To determine the CD31<sup>+</sup> area in *Id3*<sup>-/-</sup> and *Id3*<sup>+/-</sup> liver sections, maximum intensity Z-projections pictures were converted into binary images and the CD31<sup>+</sup> area was measured using Image J (NIH, Bethesda, MD, USA) (39).

Results were normalized per mm<sup>2</sup> of tissue. Illustrations were created by adapting templates from Servier Medical Arts ([www.servier.com/Powerpoint-image-bank](http://www.servier.com/Powerpoint-image-bank)), licensed under a Creative Commons Attribution 3.0 Unported License).

### Generation and analysis of Kupffer cell transcriptome in *Id3*<sup>-/-</sup> and littermate controls

For qRT-PCR experiments, cells were sorted as described above. Hepatocytes were enriched by centrifugation of the whole liver cell suspension at 50 g for 3 min (Sorvall Legend XTR centrifuge). Supernatant was taken for further staining of macrophages (CD45<sup>+</sup>, CD11b<sup>lo</sup>, F4/80<sup>+</sup>). Hepatocytes were sorted using the FSC-A and SSC-A gate with subsequent exclusion of doublets and CD45<sup>+</sup> cells. Cells were sorted into RNA lysis buffer and RNA extraction was performed as per manufacturers protocol (Macherey-Nagel). cDNA was synthesized using the QuantiTect Reverse Transcription Kit (Qiagen) as per manufacturers protocol. qRT-PCR was performed on a QuantStudio 6 Flex using TaqMan Fast Advanced Master Mix (Applied Biosystems) and TaqMan probes for *Id3* (Mm00492575\_m1), *Nrlh3* (Mm00443451\_m1), and *GAPDH* (Mm99999915\_g1) (Life Technology). For RNA-seq analysis of *Id3*<sup>+/-</sup> and *Id3*<sup>-/-</sup> Kupffer cells, cells were sorted into Trizol as described above. RNA from sorted cells was extracted using RNeasy mini kit (Qiagen) according to instructions provided by the manufacturer. After ribogreen quantification and quality control of Agilent BioAnalyzer, 400 pg of total RNA underwent amplification (12 cycles) using the SMART-seq V4 (Clontech) ultra low input RNA kit for sequencing. 10 ng of amplified cDNA was used to prepare Illumina HiSeq libraries with the Kapa DNA library preparation chemistry (Kapa Biosystems) using 8 cycles of PCR. Samples were bar-coded and run on a HiSeq 2500 IT in a 50 bp/50 bp Paired end run, using the TruSeq SBS Kit v3 (Illumina). An average of 54 million paired reads were generated per sample and the percent of mRNA bases was closed to 77% on average. The output data (FASTQ files) were mapped to the target genome using the rnaStar aligner (40) that maps reads genomically and resolves reads across splice junctions. 2 pass mapping method was used, outlined in Engstrom *et al.* (41) in which the reads are mapped twice. The first mapping pass uses a list of known annotated junctions from Ensemble. Novel junctions found in the first pass are then added to the known junctions and a second mapping pass is done (on the second pass the RemoveNoncanonical flag is used). After mapping we post process the output SAM files using the PICARD tools to: add read groups, AddOrReplaceReadGroups which in additional sorts the file and converts it to the compressed BAM format. We then compute the expression count matrix from the mapped reads using HTSeq and one of several possible gene model databases. The raw count matrix generated by HTSeq are then processed using the R/Bioconductor package DESeq, which was used to both normalize the full

data set and analyze differential expression between sample groups. Gene Ontology analysis was performed using the GO analysis function in GeneSpring GX 13.0 (Agilent), with the *P* value calculated using a hypergeometric test with Benjamini-Yekutieli correction. For that, genes with a fold change difference of  $\pm 2$  between *Id3*<sup>+/-</sup> and *Id3*<sup>-/-</sup> Kupffer cells were selected. Significantly regulated genes (*t* test *P* < 0.05; FDR < 0.05) from this selection were grouped into GO terms.

### Generation and analysis of “bulk” transcriptomes from candidate EMP, pMac, and macrophage populations from E9 to P21

#### RNA isolation and library construction

cDNA synthesis and enrichment was performed following the Smart-seq2 protocol as described (42, 43). ERCC spike-in RNA (Ambion) was added to the lysis buffer in a final dilution of 1:1,000,000. After the cDNA was synthesized and amplified from single cells using 18 cycles, quantitative PCR was performed with GoTaq-PCR master mix (Promega) on a C1000 Touch Thermal Cycler qPCR instrument (Bio-Rad) to test for house keeping gene expression. Library preparation was conducted on lng of cDNA using the Nextera XT library preparation kit (Illumina) as described (43). Sequencing was performed by the Biomedical Sequencing Facility at CeMM using a 50 bp single-read setup on the Illumina HiSeq 2500 platform.

#### RNA-seq analysis

We first trimmed off sequencing adapter from the reads generated, and then aligned the reads using Bowtie v 1.1.1 (44) (parameters: -q -p 6 -a -m 100 -minins 0 -maxins 5000 -fr -sam -chunkmbs 200) to the cDNA reference transcriptome (mm10 cDNA sequences from Ensembl). For genome browser track visualization, we generated a second alignment with Tophat2 (45) (v 2.0.13, parameters: -b2-L 15 -library-type fr-unstranded -mate-inner-dist 150 -max-multihits 100 -no-coverage-search -GTF) against the reference genome (mm10). Next, we removed duplicate reads before quantifying transcript levels with BitSeq (46) (v 1.12.0). The raw transcript counts were loaded into R and processed further. At this stage, we removed samples with a substandard quality, that is, all samples that had less than 2 million reads, less than 33% of reads aligned, or less than 5,000 transcripts detected (with  $\geq 25$  reads). 20 out of 178 data sets failed these criteria (11.2%). Of the remaining data sets, we merged technical replicates creating 93 unique biological samples. We took forward only transcripts that were detected reliably ( $\geq 50$  reads) in at least four samples (*n* = 37,521). For statistical analysis, we used raw read counts as input for DESeq2 (20), factoring in the flowcell identifier as a covariate to reduce the effect of technical variation. To identify genes of particular interest to the development of tissue-resident macrophages over time and in different tissues, we performed two types of comparisons: (a) Cell type-specific: Pairwise comparisons (Wald test) between EMPs, pMacs, and macrophages (up to E10.5) independent of their tissue of

origin (treating time and tissue as covariates). (b) Tissue-specific: Pairwise comparisons (Wald test) between macrophages from all tissues stratified and stage (post-natal). We considered genes with an FDR-corrected  $P \leq 0.05$  as differentially expressed. For visualization and illustration purposes (PCA, supplementary tables, heatmaps), we used values adjusted by variance stabilizing transformation from DESeq2 in which batch-effects had been corrected for with ComBat (47).

#### Evaluation of lists of differentially expressed genes from the RNA-seq data

We bioinformatically investigated the differentially expressed transcripts (table S5) from our statistical comparisons in several ways: To identify transcription factors specifically regulating each set of transcripts, we used LOLA (26) (v 0.99.4) together with its core database of ChIP-seq binding peaks from CODEX (48) to identify enrichment of experimentally-derived transcription factor binding locations in a window around the promoter regions (TSS  $\pm$  20 kb) of differentially expressed transcripts. We corrected for multiple testing using the Benjamini and Yekutieli method. To visualize and summarize the expression patterns of many genes (lists of differentially expressed genes) in many different conditions (different tissues at different time points) and across replicates, we sought to use an adaptation of lineage scorecards (21). Briefly, we considered each list of differentially up-regulated genes as a set of marker genes and determined the relative enrichment of these marker sets in each individual condition (tissue by cell type by time) in comparison to all other data sets using a modified version of parametric gene set enrichment analysis in R (package: *PGSEA*). We also used GSEA to test for the relative overrepresentation of gene signatures in sorted gene lists. To this end, we extracted lists of genes sorted by logarithmic fold change between the mean expression levels in any one tissue Mac, pMac, or EMP sample stratified by stage (early = E9 to E10.5, fetal = E12.5 to E18.5, postnatal = P2 to P21) compared to all other samples at the same stage. Additionally, we extracted lists of all genes we found differentially up-regulated in any tissue-specific signature, cell type-specific signature, or in lists of genes extracted from (7, 25, 28). External gene lists were translated to Ensembl Transcript IDs using g:profiler (49). Both sets of data were loaded into and analyzed using the GSEA tool (50) and the results read and summarized using the *metaGSEA* R library. We also incorporated ChIP-seq binding profiles (bigWig) for factors identified in the LOLA analysis from the CODEX database. Heatmaps were generated using GeneSpring GX 13.0 (Agilent). All other analyses and plotting was performed in R.

#### Generation and analysis of single-cell transcriptomes

For single-cell RNA sequencing the MARS-seq approach described by Jaitin *et al.* (51) was applied using the Biomek FXP system (Beckman Coulter). In brief, single cells were sorted into

each well of 384-well plates filled with 2  $\mu$ l lysis buffer [Triton-X 0.2% (Sigma) in molecular biology grade H<sub>2</sub>O (Sigma) supplemented with 0.4 U/ $\mu$ l protein-based RNase inhibitor (Takara)] and barcoded poly-T primers [400 nM (IDT); for barcode details see (51)]. Samples were pre-incubated (3 min at 80°), reverse transcriptase mix (10 mM DTT (Invitrogen), 4 mM dNTPs (NEB), 2.5 U/ $\mu$ l Superscript III RT enzyme (Invitrogen) in 50 mM Tris-HCl (pH 8.3; Sigma), 75 mM KCl (Sigma), 3 mM MgCl<sub>2</sub> (Sigma), ERCC RNA Spike-In mix (Life Technologies) at 1:80  $\times$  10<sup>7</sup> dilution per cell) was added to each well and mRNA was reverse transcribed to cDNA (2 min at 42°C, 50 min at 50°C, 5 min at 85°C). Excess primers were digested [Exo I (NEB); 37°C for 30 min then 10 min at 80°C] followed by a 1.2 x SPRI bead (Beckman Coulter) cleanup, samples were pooled and second strands synthesized (second strand synthesis kit (NEB); 2.5 hours at 16°C) followed by a 1.4 x SPRI bead (Beckman Coulter) cleanup. Samples were linearly amplified by T7-promoter guided in vitro transcription (T7 High Yield RNA polymerase IVT kit (NEB); 37°C for 12 hours). DNA templates were digested [Turbo DNase I (Ambion); 15 min at 37°C] followed by a 1.2 x SPRI bead (Beckman Coulter) cleanup and the RNA was fragmented [Zn<sup>2+</sup> RNA fragmentation solution (Ambion); 1.5 min at 70°C] followed by a 2 x SPRI bead (Beckman Coulter) cleanup. Barcoded ssDNA adapters [IDT; for barcode details see (51)] were ligated to the fragmented RNA (9.5% DMSO (Sigma), 1 mM ATP, 20% PEG8000 and 1 U/ $\mu$ l T4 RNA ligase I (NEB) in 50 mM Tris HCl pH 7.5 (Sigma), 10 mM MgCl<sub>2</sub> and 1 mM DTT; 22°C for 2 hours) and a second RT reaction (Affinity Script RT buffer, 10 mM DTT, 4 mM dNTP, 2.5 U/ $\mu$ l Affinity Script RT enzyme (Agilent); 2 min at 42°C, 45 min at 50°C, 5 min at 85°C) was performed followed by a 1.5 x SPRI bead (Beckman Coulter) cleanup. Final libraries were generated by subsequent nested PCR reaction (0.5  $\mu$ M of each Illumina primer [IDT; for primers details see (51)] and KAPA HiFi HotStart ready mix (Kapa Biosystems) for 15 cycles according to manufacturer's protocol followed by a 0.7 x SPRI bead (Beckman Coulter) cleanup. Library quantity and quality were assessed using the Agilent 2200 TapeStation system and libraries were subjected to next generation sequencing using an Illumina HiSeq1500 instrument (PE with no index; read 1: 61 bases (3 bases random nucleotides, 4 bases pool barcode, 53 bases specific sequence), read 2: 13 bases [6 bases cell barcode, 6 bases unique molecular identifier]).

#### Preprocessing, quality assessment, and control of single-cell transcriptome data

From sequenced data, pool barcodes, cell specific tags and Unique molecular identifiers (UMI) were extracted (576 cells sequenced). Subsequently, sequencing reads with ambiguous plate/cell-specific tags or UMI sequence with low quality (Phred < 27) and reads which map to *E. coli* were eliminated using Bowtie with parameters “-M 1 -t -best -chunkmbs 64 -strata.” Next, fastq files were

demultiplexed using the *fastx\_barcode\_splitter* from the *fastx* toolkit and R1 reads (after trimming of pool barcode sequences) were mapped to the mouse mm10 and ERCC pseudo genome assembly using Bowtie “-m 1 -t -best -chunkmbs 64 -strata.”

Valid reads were then counted using unique molecular identifiers if they mapped to the exon based gene model derived from Ensembl's bio-mart, mm10. Following this, a gene expression matrix was generated containing the number of unique UMIs associated with valid reads for every cell and every gene. Additionally, UMI sequencing errors were corrected for and filtered as described in (51).

#### Filtering single-cell transcriptome data

In order to avoid biases introduced by low quality data we performed the following filtering of single-cell data. Removal of cells with a ratio of mitochondrial versus endogenous genes exceeding 0.15 and cells with less than 320 molecule counts or less than 150 unique genes were removed from the analysis. Prior to analysis expression tables were filtered for mitochondrial, ribosomal and predicted genes to reduce noise.

#### Analysis of MARS-seq single-cell transcriptome data

Analysis of the normalized and filtered single-cell gene expression data (8657 genes across 408 single-cell transcriptomes used in the final expression table) was done using several functions of the SEURAT single-cell analysis package (52) and Monocle 2 (53). First, highly variable genes were determined as genes exceeding the dispersion threshold of 0.75. To infer the structure of the gene expression data a PCA was performed on the basis of highly variable genes. Following tSNE DBScan clustering was performed to identify clusters of cells. The optimal number of clusters was identified by calculating several cluster indices by the NbClust R package (54). Relative expression for a cell was calculated as gene expression of a gene/gene set in relation to the total molecule counts in this cell. To identify clusters within the MARS-seq data the relative gene expression profiles of cell type specific gene signatures were overlaid to the tSNE plots. Pseudotime analysis was performed by the Monocle 2 algorithm by genes exceeding the average expression cutoff of 1 while having an empirical dispersion higher than 1. To analyze expression of single genes, relative expression was overlaid onto the tSNE plots or visualized as dot plots.

#### Generation of cell signatures for analysis of single-cell data

In order to unambiguously identify cell state specific genes for EMPs, pMacs and early macrophages we generated exclusive gene signatures. Here, differentially expressed (DE) genes were identified by a one-way ANOVA model [||FC| > 1.4, FDR-adjusted  $P < 0.05$  (55)] between EMPs (E10.25 YS and fetal liver), pMacs (E10.25 YS, fetal liver, head, and limbs) and early macrophages (E10.25 and E10.5 YS, fetal liver, head,



and limbs). The nonoverlapping DE genes between these three contrasts were chosen as exclusive gene signatures for further analysis.

### Generation of tissue signatures for analysis of single-cell data

To identify genes that are up-regulated in tissue macrophages in relation to early macrophages a one-way ANOVA model [ $|\text{FC}| > 1.5$ , FDR-adjusted  $P < 0.05$  (37)] was calculated. Up-regulated non-overlapping DE genes between early macrophages (E10.25 and E10.5, fetal liver, head, and limbs/skin) versus brain macrophages (E14.5 and E18.5 brain), liver macrophages (E14.5 and E18.5 liver) or limb/skin macrophages (E14.5 and E18.5 limb/skin) were used as tissue macrophage specific gene signatures. Furthermore, a common early macrophage signature was defined as being up-regulated in early macrophages (E10.25 and E10.5 fetal liver, head, and limbs) versus all other late tissue macrophages (E14.5 and E18.5 liver, head, and limbs/skin). We assessed enrichment of these signatures in scRNA-seq data from pMacs by calculating an relative enrichment score for each signature in pMacs (molecule count of signature genes/(total molecule count  $\times$  number of signature genes).

### Enrichment of tissue signatures in scRNA-seq data

To assess enrichment of tissue macrophage-specific signatures or differentiation signatures in scRNA-seq data from pMacs, we identified genes with multimodal expression using Hartigan's Dip test statistic for unimodality. Next, multimodal genes were grouped by hierarchical clustering and enrichment of signatures within the clusters tested using hypergeometric testing with FDR correction (Benjamini-Hochberg).

### REFERENCES AND NOTES

1. K. E. McGrath *et al.*, Distinct sources of hematopoietic progenitors emerge before HSCs and provide functional blood cells in the mammalian embryo. *Cell Reports* **11**, 1892–1904 (2015). doi: [10.1016/j.celrep.2015.05.036](https://doi.org/10.1016/j.celrep.2015.05.036); pmid: 26095363
2. E. Gomez Perdiguero *et al.*, Tissue-resident macrophages originate from yolk-sac-derived erythro-myeloid progenitors. *Nature* **518**, 547–551 (2015). doi: [10.1038/nature13989](https://doi.org/10.1038/nature13989); pmid: 25470051
3. D. Hashimoto *et al.*, Tissue-resident macrophages self-maintain locally throughout adult life with minimal contribution from circulating monocytes. *Immunity* **38**, 792–804 (2013). doi: [10.1016/j.immuni.2013.04.004](https://doi.org/10.1016/j.immuni.2013.04.004); pmid: 23601688
4. S. Yona *et al.*, Fate mapping reveals origins and dynamics of monocytes and tissue macrophages under homeostasis. *Immunity* **38**, 79–91 (2013). doi: [10.1016/j.immuni.2012.12.001](https://doi.org/10.1016/j.immuni.2012.12.001); pmid: 23273845
5. C. Schulz *et al.*, A lineage of myeloid cells independent of Myb and hematopoietic stem cells. *Science* **336**, 86–90 (2012). doi: [10.1126/science.1219179](https://doi.org/10.1126/science.1219179); pmid: 22442384
6. L. C. Davies *et al.*, A quantifiable proliferative burst of tissue macrophages restores homeostatic macrophage populations after acute inflammation. *Eur. J. Immunol.* **41**, 2155–2164 (2011). doi: [10.1002/eji.201141817](https://doi.org/10.1002/eji.201141817); pmid: 21710478
7. Y. Lavin *et al.*, Tissue-resident macrophage enhancer landscapes are shaped by the local microenvironment. *Cell* **159**, 1312–1326 (2014). doi: [10.1016/j.cell.2014.11.018](https://doi.org/10.1016/j.cell.2014.11.018); pmid: 25480296
8. D. Gosselin *et al.*, Environment drives selection and function of enhancers controlling tissue-specific macrophage identities. *Cell* **159**, 1327–1340 (2014). doi: [10.1016/j.cell.2014.11.023](https://doi.org/10.1016/j.cell.2014.11.023); pmid: 25480297
9. Y. Okabe, R. Medzhitov, Tissue-specific signals control reversible program of localization and functional polarization of macrophages. *Cell* **157**, 832–844 (2014). doi: [10.1016/j.cell.2014.04.016](https://doi.org/10.1016/j.cell.2014.04.016); pmid: 24792964
10. M. Rosas *et al.*, The transcription factor Gata6 links tissue macrophage phenotype and proliferative renewal. *Science* **344**, 645–648 (2014). doi: [10.1126/science.1251414](https://doi.org/10.1126/science.1251414); pmid: 24762537
11. J. Sheng, C. Ruedl, K. Karjalainen, Most tissue-resident macrophages except microglia are derived from fetal hematopoietic stem cells. *Immunity* **43**, 382–393 (2015). doi: [10.1016/j.immuni.2015.07.016](https://doi.org/10.1016/j.immuni.2015.07.016); pmid: 26287683
12. G. Hoeffel *et al.*, C-Myb<sup>+</sup> erythro-myeloid progenitor-derived fetal monocytes give rise to adult tissue-resident macrophages. *Immunity* **42**, 665–678 (2015). doi: [10.1016/j.immuni.2015.03.011](https://doi.org/10.1016/j.immuni.2015.03.011); pmid: 25902481
13. F. Ginhoux *et al.*, Fate mapping analysis reveals that adult microglia derive from primitive macrophages. *Science* **330**, 841–845 (2010). doi: [10.1126/science.1194637](https://doi.org/10.1126/science.1194637); pmid: 20966214
14. E. L. Gautier *et al.*, Gata6 regulates aspartoacylase expression in resident peritoneal macrophages and controls their survival. *J. Exp. Med.* **211**, 1525–1531 (2014). doi: [10.1084/jem.20140570](https://doi.org/10.1084/jem.20140570); pmid: 25024137
15. O. Fainaru *et al.*, Runx3 regulates mouse TGF- $\beta$ -mediated dendritic cell function and its absence results in airway inflammation. *EMBO J.* **23**, 969–979 (2004). doi: [10.1038/sj.emboj.7600085](https://doi.org/10.1038/sj.emboj.7600085); pmid: 14765120
16. N. A-Gonzalez *et al.*, The nuclear receptor LXR $\alpha$  controls the functional specialization of splenic macrophages. *Nat. Immunol.* **14**, 831–839 (2013). doi: [10.1038/ni.2622](https://doi.org/10.1038/ni.2622); pmid: 23770640
17. M. Kohyama *et al.*, Role for Spi-C in the development of red pulp macrophages and splenic iron homeostasis. *Nature* **457**, 318–321 (2009). doi: [10.1038/nature07472](https://doi.org/10.1038/nature07472); pmid: 19037245
18. E. L. Gautier *et al.*, Systemic analysis of PPAR $\gamma$  in mouse macrophage populations reveals marked diversity in expression with critical roles in resolution of inflammation and airway immunity. *J. Immunol.* **189**, 2614–2624 (2012). doi: [10.4049/jimmunol.1200495](https://doi.org/10.4049/jimmunol.1200495); pmid: 22855714
19. J. Y. Bertrand *et al.*, Characterization of purified intraembryonic hematopoietic stem cells as a tool to define their site of origin. *Proc. Natl. Acad. Sci. U.S.A.* **102**, 134–139 (2005). doi: [10.1073/pnas.0402270102](https://doi.org/10.1073/pnas.0402270102); pmid: 15623562
20. M. I. Love, W. Huber, S. Anders, Moderated estimation of fold change and dispersion for RNA-seq data with DESeq2. *Genome Biol.* **15**, 550 (2014). doi: [10.1186/s13059-014-0550-8](https://doi.org/10.1186/s13059-014-0550-8); pmid: 25516281
21. C. Bock *et al.*, Reference Maps of human ES and iPS cell variation enable high-throughput characterization of pluripotent cell lines. *Cell* **144**, 439–452 (2011). doi: [10.1016/j.cell.2010.12.032](https://doi.org/10.1016/j.cell.2010.12.032); pmid: 21295703
22. K. Maeda *et al.*, Wnt5a-Ror2 signaling between osteoblast-lineage cells and osteoclast precursors enhances osteoclastogenesis. *Nat. Med.* **18**, 405–412 (2012). doi: [10.1038/nm.2653](https://doi.org/10.1038/nm.2653); pmid: 22344299
23. J. Y. Bertrand *et al.*, Three pathways to mature macrophages in the early mouse yolk sac. *Blood* **106**, 3004–3011 (2005). doi: [10.1182/blood-2005-02-0461](https://doi.org/10.1182/blood-2005-02-0461); pmid: 16020514
24. M. S. Lionakis *et al.*, CX $_{3}$ CR1-dependent renal macrophage survival promotes *Candida* control and host survival. *J. Clin. Invest.* **123**, 5035–5051 (2013). doi: [10.1172/JCI17307](https://doi.org/10.1172/JCI17307); pmid: 24177428
25. E. L. Gautier *et al.*, Gene-expression profiles and transcriptional regulatory pathways that underlie the identity and diversity of mouse tissue macrophages. *Nat. Immunol.* **13**, 1118–1128 (2012). doi: [10.1038/ni.2419](https://doi.org/10.1038/ni.2419); pmid: 23023392
26. N. C. Sheffield, C. Bock, LOLA: Enrichment analysis for genomic region sets and regulatory elements in R and Bioconductor. *Bioinformatics* **32**, 587–589 (2016). pmid: 26508757
27. W. A. Whyte *et al.*, Master transcription factors and mediators establish super-enhancers at key cell identity genes. *Cell* **153**, 307–319 (2013). doi: [10.1016/j.cell.2013.03.035](https://doi.org/10.1016/j.cell.2013.03.035); pmid: 23582322
28. N. N. Gorgani, Y. Ma, H. F. Clark, Gene signatures reflect the marked heterogeneity of tissue-resident macrophages. *Immunol. Cell Biol.* **86**, 246–254 (2008). doi: [10.1038/sj.icb.7100131](https://doi.org/10.1038/sj.icb.7100131); pmid: 17998916
29. L. Chorro *et al.*, Langerhans cell (LC) proliferation mediates neonatal development, homeostasis, and inflammation-associated expansion of the epidermal LC network. *J. Exp. Med.* **206**, 3089–3100 (2009). doi: [10.1084/jem.20091586](https://doi.org/10.1084/jem.20091586); pmid: 19995948
30. M. Hoekstra, J. K. Kruijt, M. Van Eck, T. J. Van Berkel, Specific gene expression of ATP-binding cassette transporters and nuclear hormone receptors in rat liver parenchymal, endothelial, and Kupffer cells. *J. Biol. Chem.* **278**, 25448–25453 (2003). doi: [10.1074/jbc.M301189200](https://doi.org/10.1074/jbc.M301189200); pmid: 12704191
31. C. Schneider *et al.*, Induction of the nuclear receptor PPAR- $\gamma$  by the cytokine GM-CSF is critical for the differentiation of fetal monocytes into alveolar macrophages. *Nat. Immunol.* **15**, 1026–1037 (2014). doi: [10.1038/ni.3005](https://doi.org/10.1038/ni.3005); pmid: 25263125
32. B. Jux, S. Kadow, C. Esser, Langerhans cell maturation and contact hypersensitivity are impaired in aryl hydrocarbon receptor-null mice. *J. Immunol.* **182**, 6709–6717 (2009). doi: [10.4049/jimmunol.0713344](https://doi.org/10.4049/jimmunol.0713344); pmid: 19454665
33. Y. Jen, K. Manova, R. Benezra, Expression patterns of *Id1*, *Id2*, and *Id3* are highly related but distinct from that of *Id4* during mouse embryogenesis. *Dev. Dyn.* **207**, 235–252 (1996). doi: [10.1002/\(SICI\)1097-0177\(199611\)207:3<235::AID-AJAI-3.0.CO;2-I](https://doi.org/10.1002/(SICI)1097-0177(199611)207:3<235::AID-AJAI-3.0.CO;2-I); pmid: 8922523
34. D. Lyden *et al.*, *Id1* and *Id3* are required for neurogenesis, angiogenesis and vascularization of tumour xenografts. *Nature* **401**, 670–677 (1999). doi: [10.1038/44334](https://doi.org/10.1038/44334); pmid: 10537105
35. B. Z. Qian *et al.*, CCL2 recruits inflammatory monocytes to facilitate breast-tumour metastasis. *Nature* **475**, 222–225 (2011). doi: [10.1038/nature10138](https://doi.org/10.1038/nature10138); pmid: 21654748
36. Q. Zhao *et al.*, Developmental ablation of *Id1* and *Id3* genes in the vasculature leads to postnatal cardiac phenotypes. *Dev. Biol.* **349**, 53–64 (2011). doi: [10.1016/j.ydbio.2010.10.004](https://doi.org/10.1016/j.ydbio.2010.10.004); pmid: 20937270
37. Z. Guo *et al.*, Modeling Sjögren's syndrome with *Id3* conditional knockout mice. *Immunol. Lett.* **135**, 34–42 (2011). doi: [10.1016/j.imlet.2010.09.009](https://doi.org/10.1016/j.imlet.2010.09.009); pmid: 20932862
38. L. Deng *et al.*, A novel mouse model of inflammatory bowel disease links mammalian target of rapamycin-dependent hyperproliferation of colonic epithelium to inflammation-associated tumorigenesis. *Am. J. Pathol.* **176**, 952–967 (2010). doi: [10.2353/ajpath.2010.090622](https://doi.org/10.2353/ajpath.2010.090622); pmid: 20042677
39. V. Sreeramkumar *et al.*, Neutrophils scan for activated platelets to initiate inflammation. *Science* **346**, 1234–1238 (2014). doi: [10.1126/science.1256478](https://doi.org/10.1126/science.1256478); pmid: 25477463
40. A. Dobin *et al.*, STAR: Ultrafast universal RNA-seq aligner. *Bioinformatics* **29**, 15–21 (2013). doi: [10.1093/bioinformatics/bts635](https://doi.org/10.1093/bioinformatics/bts635); pmid: 23104886
41. P. G. Engström *et al.*, Systematic evaluation of spliced alignment programs for RNA-seq data. *Nat. Methods* **10**, 1185–1191 (2013). doi: [10.1038/nmeth.2722](https://doi.org/10.1038/nmeth.2722); pmid: 24185836
42. J. Li *et al.*, Single-cell transcriptomes reveal characteristic features of human pancreatic islet cell types. *EMBO Rep.* **17**, 178–187 (2016). pmid: 26691212
43. S. Picelli *et al.*, Full-length RNA-seq from single cells using Smart-seq2. *Nat. Protoc.* **9**, 171–181 (2014). doi: [10.1038/nprot.2014.006](https://doi.org/10.1038/nprot.2014.006); pmid: 24385147
44. B. Langmead, C. Trapnell, M. Pop, S. L. Salzberg, Ultrafast and memory-efficient alignment of short DNA sequences to the human genome. *Genome Biol.* **10**, R25 (2009). doi: [10.1186/gb-2009-10-3-r25](https://doi.org/10.1186/gb-2009-10-3-r25); pmid: 19261174
45. D. Kim *et al.*, TopHat2: Accurate alignment of transcriptomes in the presence of insertions, deletions and gene fusions. *Genome Biol.* **14**, R36 (2013). doi: [10.1186/gb-2013-14-4-r36](https://doi.org/10.1186/gb-2013-14-4-r36); pmid: 23618408
46. P. Glaus, A. Honkela, M. Rattray, Identifying differentially expressed transcripts from RNA-seq data with biological variation. *Bioinformatics* **28**, 1721–1728 (2012). doi: [10.1093/bioinformatics/bts260](https://doi.org/10.1093/bioinformatics/bts260); pmid: 22563066
47. W. E. Johnson, C. Li, A. Rabinovic, Adjusting batch effects in microarray expression data using empirical Bayes methods. *Biostatistics* **8**, 118–127 (2007). doi: [10.1093/biostatistics/kjx037](https://doi.org/10.1093/biostatistics/kjx037); pmid: 16632515
48. M. Sánchez-Castillo *et al.*, CODEX: A next-generation sequencing experiment database for the haematopoietic and embryonic stem cell communities. *Nucleic Acids Res.* **43**, D1117–D1123 (2015). doi: [10.1093/nar/gku895](https://doi.org/10.1093/nar/gku895); pmid: 25270877
49. J. Reimand, T. Arak, J. Vilo, g:Profiler—A web server for functional interpretation of gene lists (2011 update). *Nucleic Acids Res.* **39** (suppl. 2), W307–W315 (2011). doi: [10.1093/nar/gkr378](https://doi.org/10.1093/nar/gkr378); pmid: 21646343
50. A. Subramanian *et al.*, Gene set enrichment analysis: A knowledge-based approach for interpreting genome-wide expression profiles. *Proc. Natl. Acad. Sci. U.S.A.* **102**, 15545–15550 (2005). doi: [10.1073/pnas.0506580102](https://doi.org/10.1073/pnas.0506580102); pmid: 16199517

51. D. A. Jaitin et al., Massively parallel single-cell RNA-seq for marker-free decomposition of tissues into cell types. *Science* **343**, 776–779 (2014). PMID: [24531970](#)
52. R. Satija, J. A. Farrell, D. Gennert, A. F. Schier, A. Regev, Spatial reconstruction of single-cell gene expression data. *Nat. Biotechnol.* **33**, 495–502 (2015). doi: [10.1038/nbt.3192](#); PMID: [25867923](#)
53. C. Trapnell et al., The dynamics and regulators of cell fate decisions are revealed by pseudotemporal ordering of single cells. *Nat. Biotechnol.* **32**, 381–386 (2014). doi: [10.1038/nbt.2859](#); PMID: [24658644](#)
54. M. Charrad, N. Ghazzali, V. Boiteau, A. Niknafs, NbClust: An R package for determining the relevant number of clusters in a data set. *J. Stat. Softw.* **61**, 1–36 (2014). doi: [10.18637/jss.v061.i06](#)
55. Y. Benjamini, Y. Hochberg, Controlling the false discovery rate: A practical and powerful approach to multiple testing. *J. R. Stat. Soc. B* **57**, 289–300 (1995).

## ACKNOWLEDGMENTS

We thank R. Benezra (MSKCC, New York) for the *Id3<sup>-/-</sup>* and *Id3<sup>+/+</sup>* strains. We thank the Biomedical Sequencing Facility at CeMM and the MSKCC Integrated Genomics and Bioinformatics Cores for assistance with next-generation sequencing. The data presented in this manuscript are tabulated in the main paper and the supplementary materials. Sequencing data sets described in this work have been submitted to the Gene Expression Omnibus (GEO) repository (GEO accession number GSE81774). Additionally, a genome browser track hub and additional supplementary data are available at <http://macrophage-development.computational-epigenetics.org/>. This work was supported by the National Cancer Institute of the U.S. NIH (grant P30CA008748) and by investigator awards from the Wellcome Trust (WT101853MA) and the European Research Council (2010-StG-261299) to F.G. E.M. is supported by a European Molecular Biology Organization long-term fellowship (ALTF 530-2015). F.H. is supported by a Deutsche Forschungsgemeinschaft (DFG) postdoctoral fellowship

(HA 7723/1-1). J.K. is supported by a Doktorand/inn/enprogramm der Österreichischen Akademie der Wissenschaften (DOC) Fellowship of the Austrian Academy of Sciences. C.B. is supported by a New Frontiers Group award from the Austrian Academy of Sciences. M.B. and J.L.S. are members of the Excellence Cluster ImmunoSensation. M.B. is supported by a DFG grant (BE 4427/3-1). J.L.S. is supported by DFG grants SFB 704, SFB 645, INST 217/575-1, INST 217/576-1, and INST 217/577-1.

## SUPPLEMENTARY MATERIALS

[www.sciencemag.org/content/353/6304/aaf4238/suppl/DC1](http://www.sciencemag.org/content/353/6304/aaf4238/suppl/DC1)  
Supplementary Text  
Figs. S1 to S13  
Tables S1 to S6

4 February 2016; accepted 20 July 2016  
Published online 4 August 2016  
[10.1126/science.aaf4238](http://10.1126/science.aaf4238)



## RESEARCH ARTICLE SUMMARY

## BIOENGINEERING

# Continuous genetic recording with self-targeting CRISPR-Cas in human cells

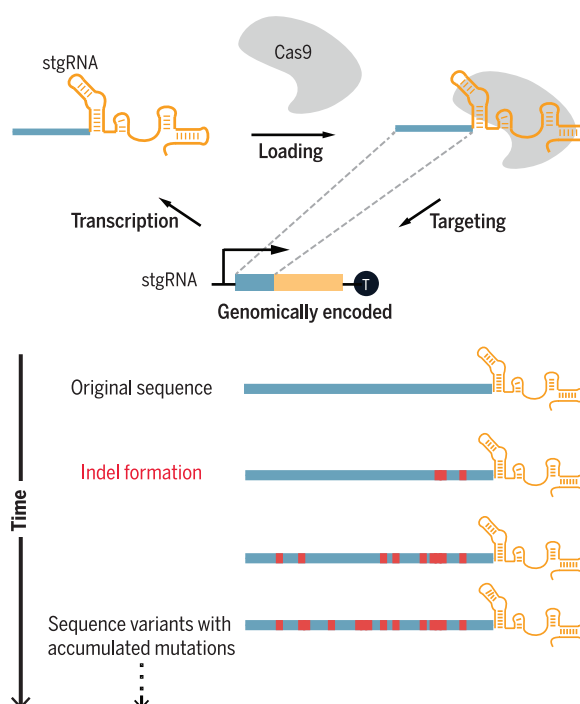
Samuel D. Perli,\* Cheryl H. Cui,\* Timothy K. Lu†

**INTRODUCTION:** Technologies that enable the longitudinal tracking and recording of molecular events into genomic DNA would be useful for the detailed monitoring of cellular state in artificial and native contexts. Although previous systems have been used to memorize digital information such as the presence or absence of biological signals, tools for recording analog information such as the duration or magnitude of biological activity in human cells are needed. Here, we present Mammalian Synthetic Cellular Recorders Integrating Biological Events (mSCRIBE), a memory system for storing analog biological information in the form of accumulating DNA mutations in human cells. mSCRIBE leverages self-targeting guide RNAs (stgRNAs) that are engineered to direct *Streptococcus pyogenes* Cas9 cleavage against DNA loci that encode the stgRNAs, thus accumulating mutations at stgRNA loci as a record of stgRNA or Cas9 expression.

**RATIONALE:** The RNA-guided DNA endonuclease Cas9 introduces a double-stranded break in target DNA containing a 5'-NGG-3' protospacer-adjacent motif (PAM) and homology to the specificity-determining sequence (SDS) of a small guide RNA (sgRNA). Once a double-strand break is introduced, the targeted DNA can be repaired via error-prone DNA repair mechanisms in human cells. We hypothesized that if a PAM sequence were introduced in the DNA locus encoding the sgRNA, the transcribed sgRNA would direct Cas9 to cleave its own encoding DNA, thus acting as a stgRNA. After error-prone repair, the mutagenized stgRNA locus should continue to be transcribed and enact additional rounds of continuous, self-targeted mutagenesis. Thus, the stgRNA locus should acquire mutations corresponding to the level of activity of the Cas9-stgRNA complex. We hypothesized that by linking the

expression of stgRNA or Cas9 to biological events of interest, one could then record the duration and/or intensity of such events in the form of accumulated mutations at the stgRNA locus. The recorded information could be read by sequencing the stgRNA locus or by other related strategies.

**RESULTS:** We first built a stgRNA by engineering a sgRNA-encoding DNA locus to contain a 5'-NGG-3' PAM immediately downstream of the SDS-encoding region. We then validated that the stgRNA could undergo multi-



**Continuously evolving stgRNAs.** The Cas9-stgRNA complex cleaves the DNA locus from which the stgRNA is transcribed, leading to error-prone DNA repair. Multiple rounds of transcription and DNA cleavage can occur, resulting in progressive mutagenesis of the DNA encoding the stgRNA. The accumulation of mutations in the stgRNA locus provides a molecular record of cellular events that regulate stgRNA or Cas9 expression.

ple rounds of self-targeted mutagenesis by building a mutation-based toggling reporter system in which the progressive accumulation of mutations at the stgRNA locus is reported by individual cells toggling between

## ON OUR WEBSITE

Read the full article at <http://dx.doi.org/10.1126/science.aag0511>

green and red fluorescent protein expression. Next, we analyzed the sequence-evolution properties of stgRNAs in order to devise a sequence-based recording metric that con-

veys information on the duration and/or magnitude of stgRNA activity. We showed that computationally designed stgRNAs that contain longer SDSs of length 30, 40, and 70 nucleotides are able to accumulate mutations over longer durations of time. We demonstrated the analog nature of mSCRIBE by building a tumor necrosis factor- $\alpha$  (TNF $\alpha$ )-inducible Cas9 expression system and observing graded increases in the recording metric as a function of increasing TNF $\alpha$  concentration and/or duration of exposure in vitro. By designing doxycycline and isopropyl- $\beta$ -D-thiogalactoside-inducible stgRNA expression systems, we also showed inducible, multiplexed recording at two independent DNA loci. Last, we confirmed that human cells containing TNF $\alpha$ -responsive mSCRIBE units can record lipopolysaccharide (LPS)-induced acute inflammation events over time in mice.

**CONCLUSION:** We demonstrate that sgRNAs can be engineered to function as stgRNAs. By linking stgRNA or Cas9 expression to specific biological events of interest—such as the presence of small molecules, exposure to TNF $\alpha$ , or LPS-induced inflammation—we validated mSCRIBE as an analog memory device that records information about the duration and/or magnitude of biological events. Moreover, we demonstrated that multiple biological events can be simultaneously monitored by using independent stgRNA loci. We envision that this platform for genomically encoded memory in human cells should be broadly useful for studying biological systems and longitudinal and dynamic events in vitro and in situ, such as signaling pathways, gene regulatory networks, and tissue heterogeneity involved in development, healthy cell function, and disease pathogenesis. ■

The list of author affiliations is available in the full article online.

\*These authors contributed equally to this work.  
†Corresponding author. Email: [timlu@mit.edu](mailto:timlu@mit.edu)  
Cite this article as S. D. Perli et al., *Science* 353, aag0511 (2016). DOI: 10.1126/science.aag0511

## RESEARCH ARTICLE

## BIOENGINEERING

# Continuous genetic recording with self-targeting CRISPR-Cas in human cells

Samuel D. Perli,<sup>1,2,3,\*</sup> Cheryl H. Cui,<sup>1,2,4,\*</sup> Timothy K. Lu<sup>1,2,3,5,†</sup>

The ability to record molecular events in vivo would enable monitoring of signaling dynamics within cellular niches and critical factors that orchestrate cellular behavior. We present a self-contained analog memory device for longitudinal recording of molecular stimuli into DNA mutations in human cells. This device consists of a self-targeting guide RNA (stgRNA) that repeatedly directs *Streptococcus pyogenes* Cas9 nuclease activity toward the DNA that encodes the stgRNA, enabling localized, continuous DNA mutagenesis as a function of stgRNA expression. We demonstrate programmable and multiplexed memory storage in human cells triggered by exogenous inducers or inflammation, both in vitro and in vivo. This tool, Mammalian Synthetic Cellular Recorder Integrating Biological Events (mSCRIBE), provides a distinct strategy for investigating cell biology in vivo and enables continuous evolution of targeted DNA sequences.

Cellular behavior is dynamic, responsive, and regulated by the integration of multiple molecular signals. Biological memory devices that can record regulatory events would be useful tools for investigating cellular behavior over the course of a biological process and furthering our understanding of signaling dynamics within cellular niches. Earlier generations of biological memory devices relied on digital switching between two or multiple quasi-stable states based on active transcription and translation of proteins (1–3). However, such systems do not maintain their memory after the cells are disruptively harvested. Encoding transient cellular events into genomic DNA memory by using DNA recombinases enables the storage of heritable biological information even after gene regulation is disrupted (4, 5). The capacity and scalability of these memory devices are limited by the number of orthogonal regulatory elements (such as transcription factors and recombinases) that can reliably function together. Furthermore, because they are restricted to a small number of digital states, they cannot record dynamic (analog) biological information, such as the magnitude or duration of a cellular event. We recently demonstrated a population-based technology for genomically encoded analog memory in *Escherichia coli* based on dynamic genome editing with retrons (6). Here, we present Mammalian Synthetic

Cellular Recorders Integrating Biological Events (mSCRIBE), an analog memory system that enables the recording of cellular events within human cell populations in the form of DNA mutations. mSCRIBE uses self-targeting guide RNAs (stgRNAs) that direct clustered regularly interspaced short palindromic repeats–associated (CRISPR-Cas) activity to repeatedly mutagenize the DNA loci that encodes the stgRNAs (7). During the course of review of this work, systems with similar principles have been proposed (8, 9). Although these systems use Cas9 to record information in DNA, they pursue different applications, such as lineage tracing and generating barcodes, to specifically tag multiple cells simultaneously. In contrast, we use our platform to build memory devices capable of recording analog biological activity into mammalian cells both in vitro and in vivo.

The *Streptococcus pyogenes* Cas9 system from the CRISPR-Cas family is an effective genome-engineering enzyme that catalyzes double-strand breaks and generates mutations at DNA loci targeted by a small guide RNA (sgRNA) (11–13). Normal sgRNAs are composed of a 20-nucleotide (nt) specificity determining sequence (SDS), which specifies the DNA sequence to be targeted and is immediately followed by an 80-nt scaffold sequence, which associates the sgRNA with Cas9. In addition to sequence homology with the SDS, targeted DNA sequences must possess a protospacer-adjacent motif (PAM) (5'-NGG-3') immediately adjacent to their 3'-end in order to be bound by the Cas9-sgRNA complex and cleaved (14). When a double-strand break is introduced in the target DNA locus in the genome, the break is repaired through either homologous recombination (when a repair template is provided) or error-prone nonhomologous end joining (NHEJ) DNA repair mechanisms, resulting

in mutagenesis of the targeted locus (11, 12). Even though the DNA locus encoding a normal sgRNA sequence is perfectly homologous to the sgRNA, it is not targeted by the standard Cas9-sgRNA complex because it does not contain a PAM.

To enable continuous encoding of population-level memory in human cells, we sought to build a modular memory unit that can be repeatedly written to generate new sequences and encode additional information over time. With the standard CRISPR-Cas system, once a genomic DNA target is repaired, resulting in a different DNA sequence, it is unlikely to be targeted again by the original sgRNA because the resulting DNA sequence and the sgRNA would lack the necessary sequence homology. We hypothesized that if the standard sgRNA architecture could be engineered so that it acted on the same DNA locus from which the sgRNA is transcribed, rather than a separate sequence elsewhere in the genome, this would yield a stgRNA that should repeatedly target and mutagenize the DNA that encodes it. To achieve this, we modified the DNA sequence from which the sgRNA is transcribed to include a 5'-NGG-3' PAM immediately downstream of the region encoding the SDS so that the resulting PAM-modified stgRNA would direct Cas9 endonuclease activity toward the stgRNA's own DNA locus. After a double-strand DNA break is introduced in the SDS-encoding region and repaired via the NHEJ repair pathway, the resulting de novo mutated stgRNA locus should continue to be transcribed as a mutated version of the original stgRNA and participate in another cycle of self-targeting mutagenesis. Multiple cycles of transcription followed by cleavage and error-prone repair should occur, resulting in a continuous, self-evolving Cas9-stgRNA system (Fig. 1A). We hypothesized that by biologically linking the activity of this system with regulatory events of interest, mSCRIBE can serve as a memory device that records information in the form of DNA mutations. We analyzed the sequence evolution dynamics of stgRNAs containing 20-, 30-, and 40-nucleotide SDSs and created a population-based recording metric that conveys information about the duration and/or intensity of stgRNA activity.

## Modifying a sgRNA-expressing DNA locus to include a PAM renders it self-targeting

We built multiple variants of a *S. pyogenes* sgRNA-encoding DNA sequence with a 5'-GGG-3' PAM located immediately downstream of the region encoding the 20-nt SDS and tested them for their ability to generate mutations at their own DNA locus. Human embryonic kidney (HEK) 293T-derived stable cell lines were built to express either the wild-type (WT) or each of the variant sgRNAs shown in Fig. 1B (table S2, constructs 1 to 6, and Materials and methods). Plasmids encoding either spCas9 (table S2, construct 7) or monomeric yellow fluorescent protein (mYFP) (negative control) driven by the cytomegalovirus promoter (CMVp) were transfected into cells stably expressing the depicted sgRNAs, and the sgRNA

<sup>1</sup>Synthetic Biology Group, MIT Synthetic Biology Center, Massachusetts Institute of Technology (MIT), Cambridge, MA 02139, USA. <sup>2</sup>Research Laboratory of Electronics, MIT, Cambridge, MA 02139, USA. <sup>3</sup>Department of Electrical Engineering and Computer Science, MIT, Cambridge, MA 02139, USA. <sup>4</sup>Harvard-MIT Division of Health Sciences and Technology, Cambridge, MA 02139, USA. <sup>5</sup>Department of Biological Engineering, MIT, Cambridge, MA 02139, USA.

\*These authors contributed equally to this work. †Corresponding author. Email: timlu@mit.edu



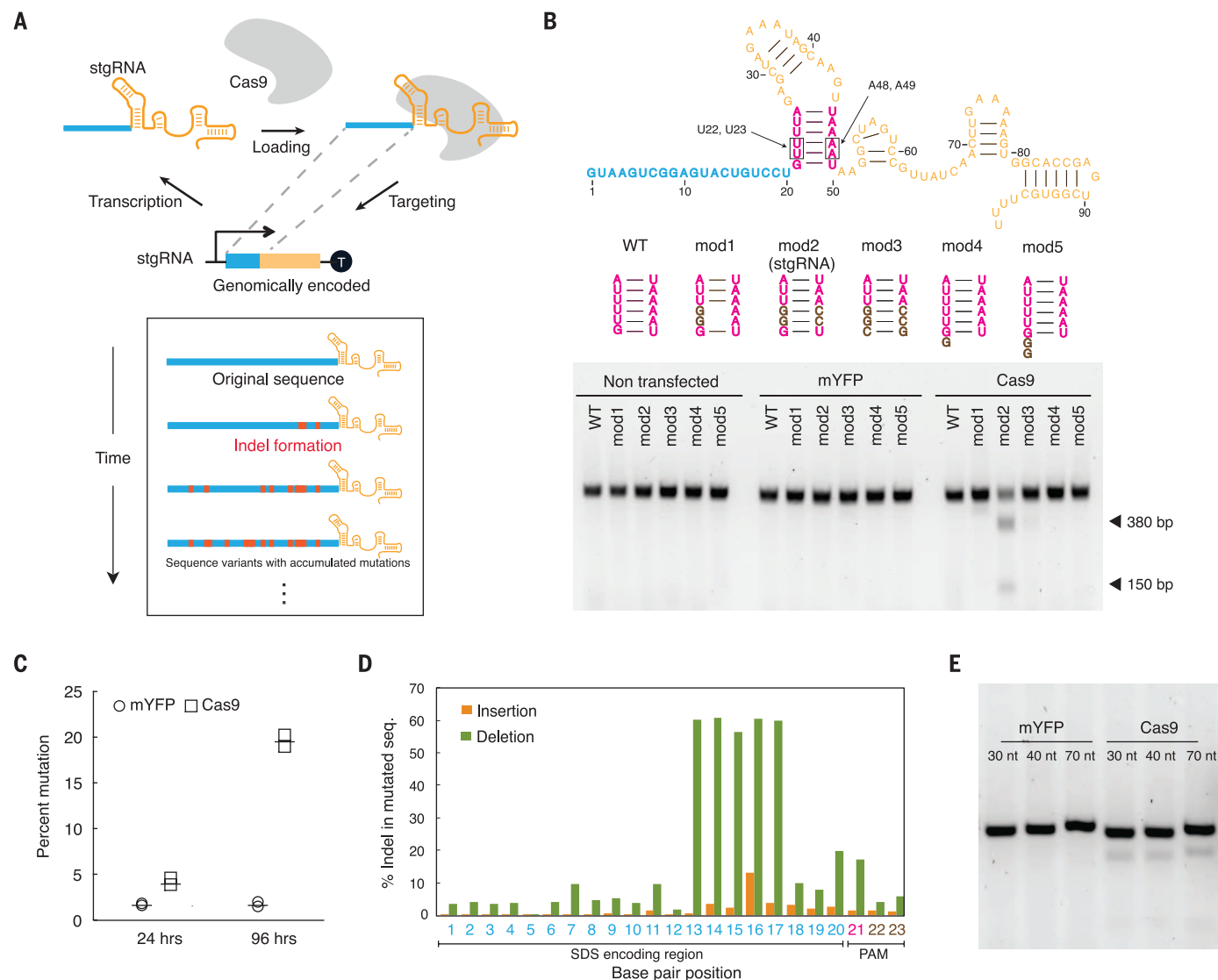


**Fig. 1. Continuously evolving stgRNAs.** (A) Schematic of the self-targeting CRISPR-Cas9 system. The Cas9-stgRNA complex cleaves the DNA from which the stgRNA is transcribed, leading to error-prone DNA repair. Multiple rounds of transcription and DNA cleavage can occur, resulting in continuous mutagenesis of the DNA encoding the stgRNA. The blue line in the stgRNA schematic represents the SDS, and mutations in the stgRNAs are illustrated as red marks. The accumulation of mutations in the stgRNA provides a molecular record of cellular events that regulate stgRNA or Cas9 expression. (B) Multiple variants of sgRNAs were built and tested for inducing mutations at the DNA loci that encoded them by using T7 E1 assays. Introducing a PAM into the DNA encoding the *S. pyogenes* sgRNA (black arrows) renders the sgRNA self-targeting, as evidenced by Cas9-dependent cleavage of PCR amplicons into two frag-

ments (380 and 150 bp) in the mod2 sgRNA variant (referred to as stgRNA), based on T7 E1 assays. (C) Further analysis of the percentage of mutated sequences via Illumina MiSeq sequencing confirmed that stgRNA can effectively generate mutations at its own DNA locus (two biological replicates were performed). (D) The percentage of sequences containing specific mutation types (insertion or deletion) at individual base pair positions out of all mutated sequences. By aligning each of the Illumina MiSeq reads with the original unmutated stgRNA sequence, the base pair positions of insertions and deletions acquired by the stgRNA locus was calculated. (E) Computationally designed stgRNAs with longer SDS (30nt-1, 40nt-1, and 70nt-1) demonstrate self-targeting activity based on T7 E1 assays (fig. S1 and table S2, constructs 1 to 11).

loci were inspected for mutagenesis by using T7 endonuclease I (T7 E1) assays 4 days after transfection. A straightforward variant sgRNA (mod1) with guanine substitutions at the U23 and U24 positions did not exhibit any noticeable self-targeting activity. We speculated that this was due to the presence of bulky guanine and adenine residues facing each other in the stem region, resulting in a destabilized secondary structure. Thus, we encoded compensatory adenine-to-cytosine mutations within the stem region (A48,

A49 position) of the mod2 sgRNA variant and observed robust mutagenesis at the modified sgRNA locus (Fig. 1B). Additional variant sgRNAs (mod3, mod4, and mod5) did not exhibit noticeable self-targeting activity. Thus, the mod2 sgRNA was hereafter referred to and used as the stgRNA architecture.

We further characterized the mutagenesis pattern of the stgRNA by sequencing the DNA locus encoding it. A HEK 293T cell line expressing the stgRNA was transfected with a plasmid express-

ing either Cas9 (table S2, construct 7) or mYFP driven by the CMV promoter. Genomic DNA was harvested from the cells at either 24 or 96 hours after transfection and subjected to targeted polymerase chain reaction (PCR) amplification of the region encoding the stgRNAs. The PCR amplicons were either sequenced with MiSeq or cloned into *E. coli* for Sanger sequencing of individual bacterial colonies (fig. S1). We found that cells transfected with the Cas9-expressing plasmid exhibited enhanced mutation frequencies in the

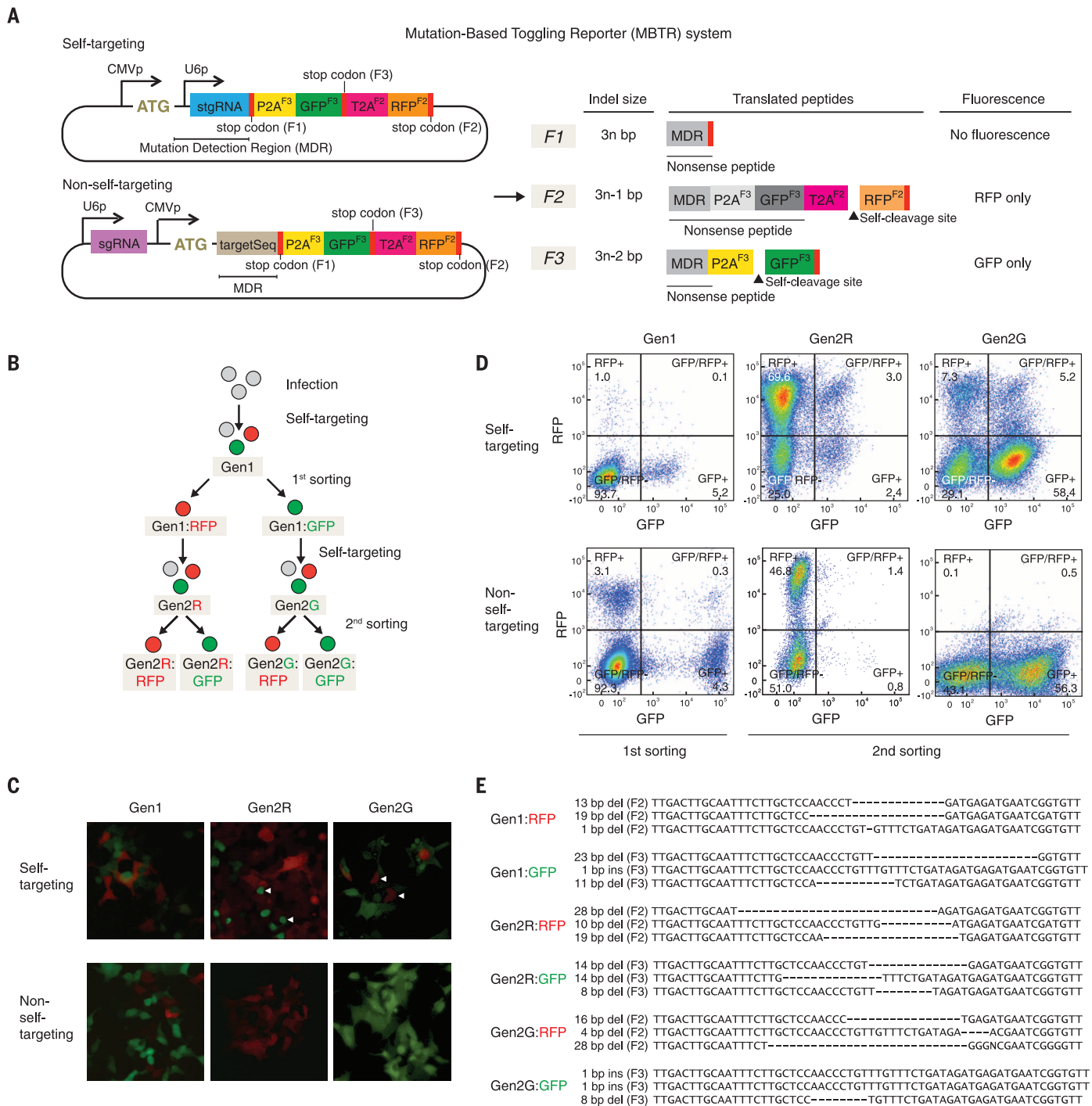


**Fig. 2. Tracking repetitive and continuous self-targeting activity at the stgRNA locus. (A)** Schematic of MBTR system consisting of a stgRNA in the MDR or a regular sgRNA target sequence in the MDR. We illustrate the expected fluorescent readouts of the MBTR system based on different indel sizes in the MDR. Correct reading frames of each protein relative to the start codon are indicated in the superscript as F1, F2, and F3. **(B)** An outline illustrating the double-sorting experiment that tracks repetitive self-targeting activity by using the MBTR system (Materials and methods). **(C)** Microscopy analysis and **(D)** flow cytometry data before the first and second sorting of UBCp-Cas9 cells con-

taining the self-targeting or nonself-targeting MBTR constructs. The white arrows in the microscope images indicate cells that expressed a fluorescent protein different from the one they were sorted for 7 days earlier. **(E)** The genomic DNA collected from sorted cells was amplified and cloned into *E. coli*; the resulting bacterial colonies were then Sanger sequenced (Materials and methods). A sample of Sanger sequences for the different sorted populations is presented along with their mutation type, and the correct reading frame annotated. We observed a high correspondence between the mutated genotype and the observed fluorescent protein expression phenotype (figs. S2 and S3).

stgRNA loci, and those frequencies increased over time, compared with cells transfected with the control mYFP-expressing plasmid (Fig. 1C). By

using high-throughput sequencing, we inspected the mutated sequences generated by stgRNAs to determine the probability of insertions or dele-

tions occurring at specific base pair positions. We calculated the percentage of those that contained insertions or deletions at each base pair position



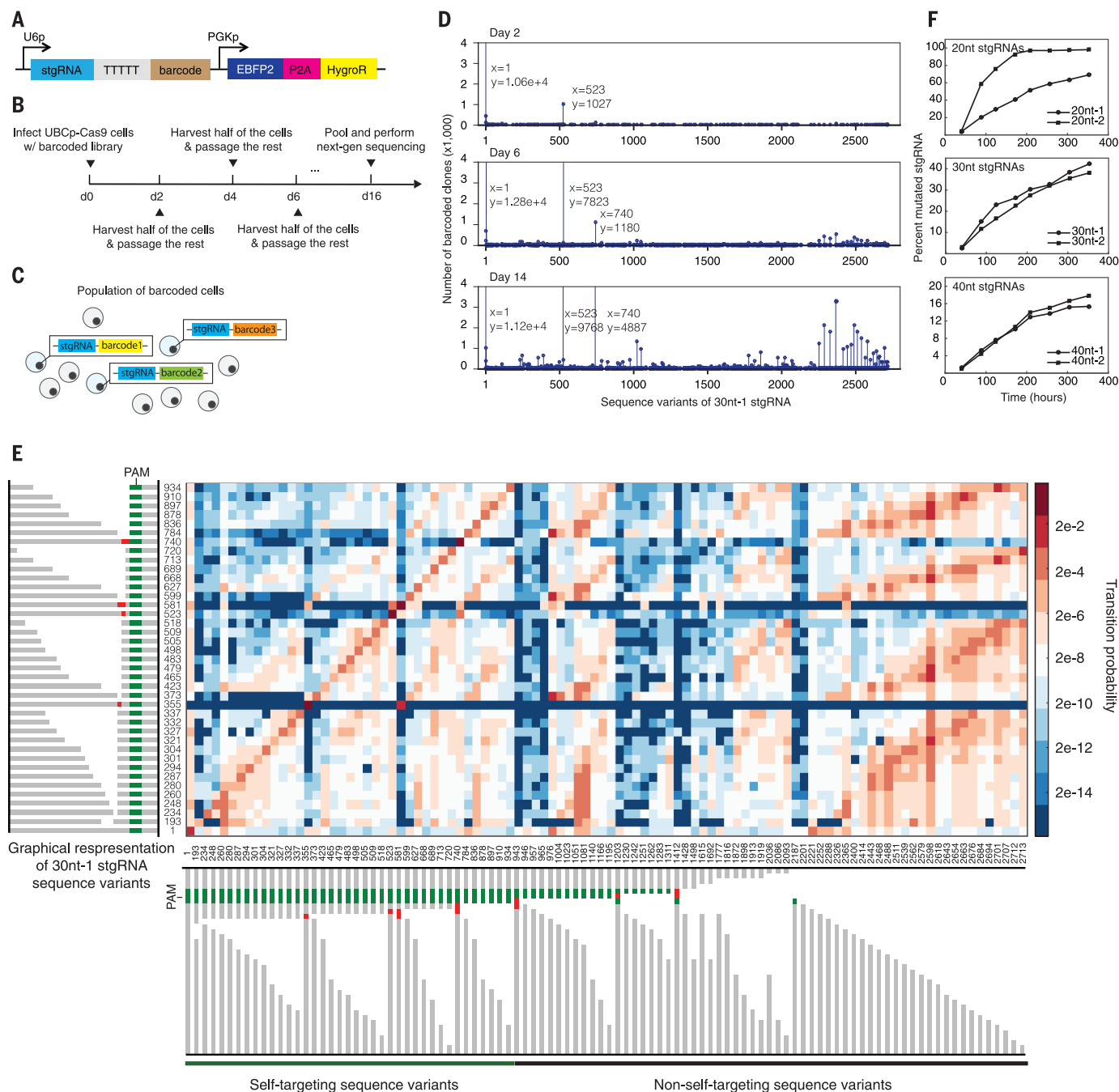


**Fig. 3. stgRNA sequence evolution analysis.** (A) Schematic of the DNA construct used in building barcoded libraries encoding stgRNA loci. A randomized 16-bp barcode was placed immediately downstream of the stgRNA expression cassette in order to individually tag UBCp-Cas9 cells that contained integrated stgRNA loci. (B) The 16-day time course involved repeated sampling and passaging of cells in order to study sequence-evolution characteristics of stgRNA loci. (C) We lentivirally infected UBCp-Cas9 cells at a MOI ~0.3 so that the dominant population in infected cells contained single genomic copies of 16-bp-barcode-tagged stgRNA loci, which should be independently evolving. (D) The raw number of 16-bp barcodes that were associated with any particular 30nt-1 stgRNA sequence variant was plotted on the y axis for three different time points (day 2, day 6, and day 14). Each discrete, aligned sequence is identified by an integer index along the x axis. The starting stgRNA sequence is shown as index 1. (E) A transition probability matrix for the top 100 most frequent sequence variants of the 30nt-1 stgRNA. The color intensity at each (x, y) position in the matrix indicates the likelihood of the stgRNA sequence variant in each

row (y) transitioning to a stgRNA sequence variant in each column (x) within the defined time scale (2 days). Because the non-self-targeting sequence variants (which contain mutations in the PAM) do not participate in self-targeting action, the y axis only consists of self-targeting stgRNA variants. The integer index of a stgRNA sequence variant, in which a deletion is illustrated with a blank space, an insertion with a red box, and an unmutated base pair with a gray box. The PAM is shown in green. From left to right on the x axis and bottom to top on the y axis, the sequence variants are arranged in order of decreasing distance between the mutated region and the PAM. When the distances are the same, the sequence variants are arranged in order of increasing number of deletions. (F) The percent mutated stgRNA metric is plotted for each of the stgRNAs as a function of time. We observed a reasonably linear range of performance metric for stgRNAs, especially for the longer SDS containing 30nt-1, 30nt-2, 40nt-1, and 40nt-2 stgRNAs (figs. S4 to S7).

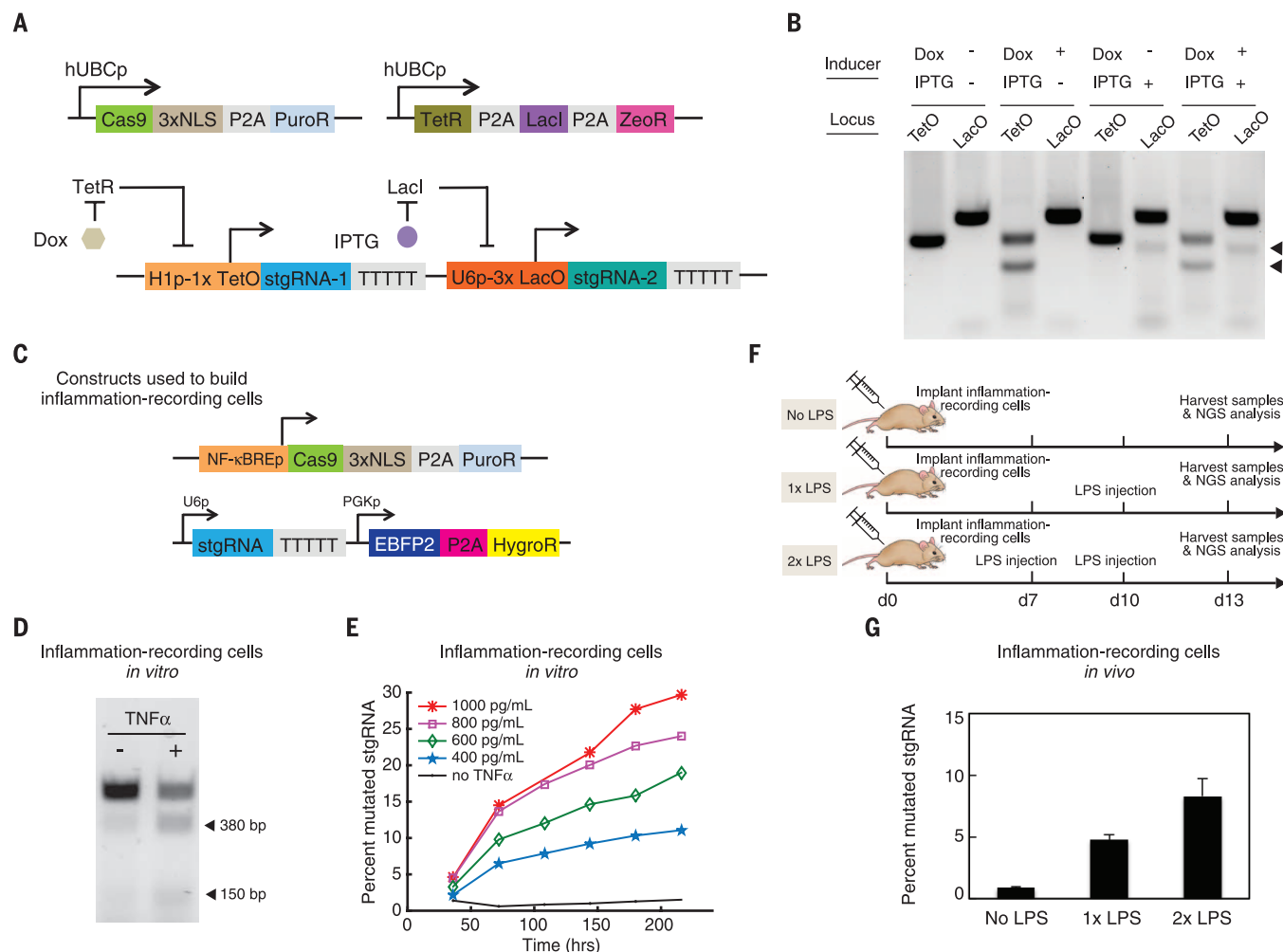


**Fig. 4. mSCRIBE as an analog memory device in vitro and in vivo.** (A) Schematic of multiplexed doxycycline and IPTG-inducible stgRNA cassettes within human cell populations. By introducing small-molecule-inducible stgRNA expression constructs into UBCp-Cas9 cells that also express TetR and LacI, the expression and self-targeting activity of each stgRNA can be independently regulated by doxycycline and IPTG, respectively. (B) mSCRIBE implements independently programmable, multiplexed genomic recording in human cells. Cleavage fragments observed from the T7 E1 assay of mSCRIBE units under independent regulation by doxycycline (Dox; 500 ng/mL) and IPTG (2 mM) are presented. (C) Constructs used to build a HEK 293T-derived clonal NF- $\kappa$ B-Cas9 cell line that expresses Cas9 in response to NF- $\kappa$ B activation. The 30nt-1 stgRNA construct was placed on a lentiviral backbone that expresses EBFP2 constitutively and was introduced into NF- $\kappa$ B-Cas9 cells via lentiviral infections at 0.3 MOI so as to build inflammation-recording cells. (D) T7 E1 assay testing for TNF $\alpha$ -inducible stgRNA activity in inflammation-recording cells in vitro. Inflammation-recording cells were grown either in the absence or presence of 1 ng/mL TNF $\alpha$  for 96 hours. (E) Graded increases in recording

activity as a function of time and concentrations of TNF $\alpha$  demonstrate the analog nature of mSCRIBE. Inflammation-recording cells were grown in media containing different amounts of TNF $\alpha$  or no TNF $\alpha$ . Cell samples were collected at 36-hour-time point intervals for each of the concentrations. Genomic DNA from the samples was PCR-amplified and sequenced via next-generation sequencing, and the percent mutated stgRNA metric was calculated. (F) Experimental outline for testing mSCRIBE in living mice. Inflammation-recording cells were implanted in the flank of three cohorts of four mice each. Three different cohorts of mice were treated with either no LPS, or with one or two doses of LPS on days 7 and 10. After harvesting the samples on day 13 and PCR-amplifying the genomic DNA followed by next-generation sequencing, the percent mutated stgRNA metric was calculated. (G) The percent mutated stgRNA metric calculated for the three cohorts of four mice is presented. The solid bars indicate the mean for each cohort ( $n = 4$  mice in each condition), and the error bars indicate the SEM. mSCRIBE demonstrates increasing genomic recording activity with increasing doses of LPS in mice (figs. S8 to 10).

among all mutated sequences (Fig. 1D). We observed higher rates of deletions as compared with insertions at each nucleotide position. Moreover, an elevated percentage of mutated sequences exhibited deletions consecutively spanning nucleotide positions 13 to 17 for this specific stgRNA (20nt-1). We later carried out a more thorough analysis into the sequence evolution patterns of stgRNAs.

Given our observation that deletions are preferred over insertions, we suspected that stgRNAs

would be shortened over time with repeated self-targeting activity, ultimately rendering them ineffective because of loss of the PAM or shortened SDS. To enable multiple cycles of self-targeting activity, we designed stgRNAs that are made up of longer SDSs. We initially built a cell line expressing a stgRNA containing a randomly chosen 30-nt SDS (table S2, construct 8) but did not detect noticeable self-targeting activity when the cell line was transfected with a plasmid expressing Cas9. We speculated that stgRNAs with longer than

20-nt SDSs might contain undesirable secondary structures that result in loss of activity. Therefore, we computationally designed stgRNAs that were predicted to maintain the scaffold fold of sgRNAs without undesirable secondary structures, such as stem loops and pseudoknots within the SDS (Materials and methods). Stable cell lines encoding stgRNAs containing these computationally designed 30-, 40-, and 70-nt SDS (table S2, constructs 9 to 11) were transfected with a plasmid expressing Cas9 driven by the CMV promoter. T7



E1 assays of PCR-amplified genomic DNA demonstrated robust indel formation in the respective stgRNA loci (Fig. 1E).

### stgRNA-encoding loci undergo multiple rounds of self-targeted mutagenesis

We sought to demonstrate that the stgRNA-encoding DNA locus in individual cells undergoes multiple rounds of self-targeted mutagenesis. To track genomic mutations in single cells over time, we developed a mutation-based toggling reporter (MBTR) system that generates distinct fluorescence outputs based on indel sizes at the stgRNA-encoding locus, which was inspired by a design previously described for tracking DNA mutagenesis outcomes (15). Downstream of a CMV promoter and a canonical ATG start codon, we embedded the mutation detection region (MDR), which consists of a modified U6 promoter followed by a stgRNA locus. The MDR was immediately followed by out-of-frame green (GFP) and red (RFP) fluorescent proteins, which were separated by correspondingly out-of-frame "2A self-cleaving peptides" (P2A and T2A) (Fig. 2A and table S2, construct 13). Different reading frames are expected to be in-frame with the start codon, depending on the size of indels in the MDR. In the starting state (reading frame 1, F1), no fluorescence is expected. In reading frame 2 (F2), which corresponds to any -1 base pair (bp) frameshift mutation, an in-frame RFP is translated along with the T2A self-cleaving peptide, which enables release of the functional RFP from the upstream nonsense peptide. In reading frame 3 (F3), which corresponds to any -2 bp frameshift mutation, GFP is properly expressed downstream of an in-frame P2A and followed by a stop codon. We confirmed the functionality of this design by manually building constructs with stgRNA loci containing indels of various sizes (0 bp, -1 bp, and -2 bp corresponding to constructs 13, 14, and 15 in table S2, respectively) and introducing them into cells without Cas9. We observed the expected correspondence between indel sizes and fluorescence output (fig. S2).

We subsequently used the MBTR system to assess changes in fluorescent gene expression within cells constitutively expressing Cas9 in order to track repeated mutagenesis at the stgRNA locus over time. We built a self-targeting MBTR construct containing a computationally designed 27-nt stgRNA driven by a modified U6 promoter embedded in the MDR (Fig. 2A and table S2, construct 13). As a control, we built a non-self-targeting MBTR construct with a regular sgRNA that targets an identical 27-bp DNA sequence embedded in the MDR (Fig. 2A and table S2, construct 16). We integrated the self-targeting or the non-self-targeting construct [via lentiviral transduction at multiplicity of infection (MOI) ~0.3 to ensure that most infected cells contained single copies] into the genome of clonally derived Cas9-expressing HEK 293T cells (hereafter called UBCp-Cas9 cells) and analyzed the cells by means of two rounds of fluorescence-activated cell sorting (FACS) based on RFP and GFP levels (Fig. 2B). In both cases, we found ~1 to 5% of

the cells were RFP<sup>+</sup>/GFP<sup>-</sup> or RFP<sup>-</sup>/GFP<sup>+</sup>, which were sorted into Gen1:RFP and Gen1:GFP populations, respectively (Fig. 2, C and D), and <0.3% cells expressed both GFP and RFP. We cultured the Gen1:RFP and Gen1:GFP cells for 7 days, resulting in Gen2R and Gen2G populations, respectively. We then subjected the Gen2R and Gen2G populations to a second round of FACS. For cells with the stgRNA MBTR, a subpopulation of Gen2R cells toggled into being GFP-positive, and similarly, a subpopulation of Gen2G cells toggled into being RFP-positive. In contrast, cells containing the non-self-targeting MBTR with a regular sgRNA maintained their original fluorescence signals with no appreciable toggling behavior observed with FACS analysis (Fig. 2, C and D). The toggling of fluorescence output observed in UBCp-Cas9 cells transduced with the stgRNA MBTR suggests that repeated mutagenesis, resulting in multiple frameshifts in the MDR, occurred at the stgRNA locus within single cells. We also observed a double-positive cell population in the self-targeting group, which we believe is mostly likely due to residual fluorescence from one fluorophore not being completely lost before the expression of the other fluorophore. To further corroborate this finding, we sequenced the stgRNA locus in individual cells from post-sorted populations in both rounds of sorting by cloning PCR amplicons into *E. coli* and performing Sanger sequencing on individual bacterial colonies (Fig. 2E and fig. S3A). We found strong correlations (77 to 100% accuracy) between the sequenced genotype and observed fluorescence phenotype in all of the sorted cell populations (fig. S3B). Together, these results confirmed that repetitive mutagenesis can occur at the stgRNA locus within single cells.

### stgRNAs exhibit characteristic sequence evolution patterns

Having established that stgRNA loci are capable of undergoing multiple rounds of targeted mutagenesis, we set out to delineate their sequence evolution patterns over time. We hypothesized that we could infer characteristic properties associated with stgRNA sequence evolution by simultaneously investigating many independently evolving cell clones, all of which contain an exactly identical stgRNA sequence to start with (Fig. 3C). We synthesized barcoded plasmid DNA libraries in which the stgRNA sequence was maintained constant while a chemically randomized 16-bp barcode was placed immediately downstream of the stgRNA (Fig. 3A). Six separate DNA libraries were synthesized that encode stgRNAs containing six distinct SDs of different lengths: 20nt-1, 20nt-2, 30nt-1, 30nt-2, 40nt-1, or 40nt-2 (table S2, constructs 19 to 24). We used a constitutively expressed blue fluorescent protein, EBFP2, to confirm a MOI of ~0.3 so that most of the infected cells should contain single-copy integrants.

On day 0, lentiviral particles encoding each of the six stgRNA libraries were used to infect 200,000 UBCp-Cas9 cells in six separate wells of a 24-well plate. At a target MOI of 0.3, the

infections resulted in ~60,000 successfully transduced cells per well. For each stgRNA library, eight cell samples were collected at time points spaced ~48 hours apart until day 16 (Fig. 3B). All samples from eight different time points across the six different libraries were pooled together and sequenced via NextSeq (Illumina, San Diego, CA). After aligning the next-generation sequencing reads to reference DNA sequences (Materials and methods), 16-bp barcodes that were observed across all the time points and the corresponding upstream stgRNA sequences were identified (fig. S4A). For each of the stgRNA libraries, we found >10<sup>4</sup> distinct 16-bp barcoded loci that were observed across all of the eight time points (fig. S4B). The aligned stgRNA sequence variants were represented with words composed of a four-letter alphabet: At each base pair position, the stgRNA sequence was represented by either M, I, X, or D, which stand for match, insertion, mismatch, or deletion, respectively (fig. S4, C and D, and Materials and methods). We identified >1000 distinct sequence variants that were observed in any of the time points and any of the barcoded loci for each stgRNA (fig. S5A and table S1, stgRNA sequences). Although some sequence variants are found in common across the stgRNAs, the majority of the sequence variants are specific to each stgRNA.

We plotted the number of barcoded loci associated with each sequence variant derived from the original 30nt-1 stgRNA for three different time points (Fig. 3D). Although the majority of the barcoded loci contained the original unmutated stgRNA sequence (index 1) for all three time points, we observed that a sequence variant containing an insertion at base pair 29 (index 523) and another sequence variant containing insertions at base pairs 29 and 30 (index 740) gained major representation by day 14. We noticed that most of the barcoded stgRNA loci evolved into just a few major sequence variants and thus sought to determine whether these specific sequences would dominate across different experimental conditions. In fig. S5B, we present the top seven most abundant sequence variants of the 30nt-1 stgRNA observed in three different experiments discussed in this work. The three experiments were performed with the 30nt-1 stgRNA encoded and (i) tested in vitro in a HEK 293T-derived cell line (UBCp-Cas9), (ii) tested in vitro in a HEK 293T-derived cell line in which Cas9 was regulated by the nuclear factor- $\kappa$ B (NF- $\kappa$ B)-responsive promoter (inflammation-recording cells), or (iii) tested in vivo in inflammation-recording cells (Figs. 3F and 4, E and G, respectively). We found that six sequence variants (including indices 523 and 740) were represented in the top seven sequence variants for all three different experiments we performed with the 30nt-1 stgRNA. Moreover, even though we observed >1000 distinct sequence variants for 30nt-1 stgRNA (fig. S5A and table S1, stgRNA sequences), these top seven most abundant sequence variants constituted >85% of the total sequences represented in each of these experiments. Thus, we speculate that stgRNA

activity can result in specific and consistent mutations. We also analyzed whether any of stgRNA variants might contain direct homology to human genomic DNA. In fig. S5C, we present homology analysis for the top 100 most frequent 30nt-1 stgRNA variants. We found that only one of the top 100 stgRNA variants (35th most frequent variant) had perfect homology to genomic DNA (an intronic region), whereas most of the variants differed from the DNA by at least 2 bp in their SDS. Hence, the DNA locus encoding each stgRNA variant was the most likely targeted sequence for the majority of the 30nt-1 stgRNA variants.

Given our observation that stgRNAs may have characteristic sequence evolution patterns, we sought to infer the likelihood of a stgRNA locus transitioning from any given sequence variant to another variant owing to self-targeted mutagenesis. We computed such likelihoods in the form of a transition probability matrix, which captures the probability of a sequence variant transitioning to any sequence variant within a given time frame (Fig. 3E, fig. S4, and Materials and methods). We found that self-targeting sequence variants were generally more likely to remain unchanged than be mutagenized across the 2-day time period, as indicated by high probabilities along the main diagonal (matrix elements where  $x = y$ ), as annotated in fig. S6. In addition, transition probability values were found to be typically higher for sequence transitions below the main diagonal versus for those above the main diagonal, implying that sequence variants tend to progressively gain deletions (fig. S6). Moreover, when compared with deletion-containing sequence variants, insertion-containing sequence variants tended to have a very narrow set of sequence variants into which they were likely to mutagenize. Last, we noticed that the predominant way in which mutated self-targeting sequence variants mutagenize into non-self-targeting sequence variants is by losing the PAM and downstream region encoding the stgRNA handle while keeping the SDS-encoding region intact.

Having analyzed the sequence evolution characteristics of stgRNAs, we envisioned that a metric could be computed on the basis of the relative abundance of stgRNA sequence variants as a measure of stgRNA activity. Such a metric would enable the use of stgRNAs as intracellular recording devices in a population to store biologically relevant, time-dependent information that could be reliably interpreted after the events were recorded. From our analysis of stgRNA sequence evolution, we reasoned that novel self-targeting sequence variants at a given time point should have arisen from prior self-targeting sequence variants and not from non-self-targeting sequence variants. Thus, we calculated the percentage of sequences that contain mutations only in the SDS-encoding region among all the sequences that contain an intact PAM, which we call the percent mutated stgRNA, to serve as an indicator of stgRNA activity. In Fig. 3F, we plot the percent mutated stgRNA as a function of time for the six different stgRNAs. Except for

the 20nt-2 stgRNA, which saturated to ~100% by 10 days, we observed nonsaturating and steadily increasing responses of the metric for all stgRNAs over the entire 16-day experimentation period. On the basis of the rate of increase of the percent mutated stgRNA (percent mutated stgRNA/time), stgRNAs encoding SDSs of longer length should have a greater capacity to maintain a steady increase in the recording metric for longer durations of time and thus should be more suitable for longer-term recording applications.

We also conducted a time course experiment with regular sgRNAs targeting a DNA target sequence so as to test their ability to serve as memory registers (fig. S7). We used sgRNAs encoding the same 20nt-1, 30nt-2, and 40nt-1 SDSs tested in Fig. 3F (table S2, constructs 25 to 27) and found that unlike stgRNA loci, sgRNA target loci quickly saturate the percent mutated sequence metric and exhibit restricted linear ranges.

### Small-molecule inducible and multiplexed memory storage using mSCRIBE

We placed stgRNA loci under the control of small-molecule inducers in order to record chemical inputs into genomic memory registers. We designed doxycycline-inducible and isopropyl- $\beta$ -D-thiogalactoside (IPTG)-inducible RNA polymerase III (RNAP III) promoters to express stgRNAs, similar to prior work with short hairpin RNAs (Fig. 4A) (16, 17). We engineered the RNAP III H1 promoter to contain a Tet-operator, allowing for tight repression of promoter activity in the presence of the TetR protein, which can be rapidly and efficiently relieved by the addition of doxycycline (table S2, construct 29). Similarly, we built an IPTG-inducible stgRNA locus by introducing three LacO sites into the RNAP III U6 promoter so that LacI can repress transcription of the stgRNA, which is relieved by the addition of IPTG (table S2, construct 30). We first verified that doxycycline and IPTG-inducible stgRNAs worked independently when integrated into the genome of UBCp-Cas9 cells that also express TetR and LacI (table S2, construct 28) (fig. S8). Next, we placed the doxycycline and IPTG-inducible stgRNA loci on to a single lentiviral backbone (Fig. 4A and table S2, construct 31) and integrated them into the genome of UBCp-Cas9 cells that also expressed TetR and LacI. The induction of stgRNA expression by exposure to doxycycline or IPTG led to efficient self-targeting mutagenesis at the cognate loci as detected with the T7 E1 assay, whereas lack of exposure to doxycycline or IPTG did not (Fig. 4B and Materials and methods). Moreover, when cells were exposed to both doxycycline and IPTG, we detected simultaneous mutation acquisition at both loci, thus demonstrating inducible and multiplexed molecular recording across the cell populations.

### Recording the activation of the NF- $\kappa$ B pathway via mSCRIBE

We next sought to build stgRNA memory units that record signaling events in cells within live

animals. We adapted a well-established acute inflammation model involving repetitive intraperitoneal injection of lipopolysaccharide (LPS) in mice (18). Immune cells that sense LPS release tumor necrosis factor  $\alpha$  (TNF $\alpha$ ), which is a potent activator of the NF- $\kappa$ B pathway (19). The activation of the NF- $\kappa$ B pathway plays an important role in coordinating responses to inflammation (20). To sense the activation of the NF- $\kappa$ B pathway, we built a construct containing a NF- $\kappa$ B-responsive promoter driving the expression of the RFP mKate2 (table S2, construct 32) and stably integrated it into HEK 293T cells. We observed a >50-fold increase in expression levels when these cells were exposed to TNF $\alpha$  in vitro (fig. S9, A, B, and C). Next, we implanted these cells into the flanks of athymic nude mice (female nu/nu). After implanted cells reached a palpable volume, we performed intraperitoneal injection of LPS and observed robust mKate2 expression (fig. S9D) and elevated TNF $\alpha$  concentrations in the serum after LPS injection (fig. S9E).

We then built a clonal HEK 293T cell line containing an NF- $\kappa$ B-induced Cas9 expression cassette (NF- $\kappa$ Bp-Cas9 cells) and infected the cells with lentiviral particles encoding the 30nt-1 stgRNA at MOI ~0.3. These cells (hereafter referred to as inflammation-recording cells) accumulated stgRNA mutations, as detected with the T7 E1 assay, when induced with TNF $\alpha$  (Fig. 4D). We characterized the stgRNA memory unit in inflammation-recording cells by varying the concentration [within physiologically relevant concentrations (fig. S9E) (21)] and duration of exposure to TNF $\alpha$  in vitro and determining the percent mutated stgRNA metric (Fig. 4E). We observed graded increases in the percent mutated stgRNA metric as a function of time, thus demonstrating that stgRNA-based memory can record temporal information on signaling events in human cells. Furthermore, higher TNF $\alpha$  concentrations resulted in cells that had higher values for the percent mutated stgRNA metric, indicating that signal magnitude can modulate the mSCRIBE memory register in an analog fashion.

### Recording LPS-inducible inflammation in vivo via mSCRIBE

After characterizing the in vitro time and dosage sensitivity of our inflammation-recording cells, we implanted them into mice. The implanted mice were split into three cohorts: no LPS injection over 13 days, an LPS injection on day 7, and an LPS injection on day 7 followed by another LPS injection on day 10 (Fig. 4F). The genomic DNA of implanted cells was extracted from all cohorts on day 13. The stgRNA locus was PCR-amplified and sequenced via next-generation sequencing. We observed a direct correlation between the LPS dosage and the percent mutated stgRNA metric, with increasing numbers of LPS injections resulting in increased percent mutated stgRNA metric (fig. S5B). Our results indicate that stgRNA memory registers can be used in vivo to record physiologically relevant biological signals in an analog fashion.



While generating data for Figs. 3F and 4E, we used PCR to amplify the stgRNA loci from ~30,000 cells and then calculated the percent mutated stgRNA metric as a readout of genomic memory. However, access to tissues or biological samples could be limited in certain *in vivo* contexts. To investigate the sensitivity of our stgRNA-encoded memory when the input biological material is restricted, we sampled 1:100 dilutions of the genomic DNA extracted from the TNF $\alpha$ -treated inflammation-recording cells in Fig. 4E (which corresponds to ~300 cells) in triplicate followed by PCR amplification, sequencing, and calculation of the percent mutated stgRNA metric (fig. S10). We found very little deviation between the percent mutated sgRNA metric between samples with ~300 cells versus those from ~30,000 cells. We hypothesize that this tight correspondence is due to stgRNA evolution toward very few, dominating sequence variants, as was observed in Fig. 3D and fig. S5B.

## Discussion and conclusions

In this Research Article, we describe an architecture for stgRNAs that can repeatedly direct Cas9 activity against the DNA loci that encode the stgRNAs. This technology enables the creation of self-contained genomic analog memory units in human cell populations. We show that stgRNAs can be engineered by introducing a PAM into the sgRNA sequence and with our MBTR system validate that mutations accumulate repeatedly in stgRNA-encoding loci over time. After characterizing the sequence evolution dynamics of stgRNAs, we derived a computational metric that can be used to map the extent of stgRNA mutagenesis in a cell population to the duration or magnitude of the recorded input signal. Our results demonstrate that the percent mutated stgRNA metric increases with the magnitude and duration of input signals, thus resulting in long-lasting analog memory stored in the genomic DNA of human cell populations.

Because the stgRNA loci can be multiplexed for memory storage and function *in vivo*, this approach for analog memory in human cells could be used to map dynamic and combinatorial sets of gene regulatory events without the need for continuous cell imaging or destructive sampling. For example, cellular recorders could be used to monitor the spatiotemporal heterogeneity of molecular stimuli that cancer cells are exposed to within tumor microenvironments (22), such as exposure to hypoxia, pro-inflammatory cytokines, and other soluble factors. One could also track the extent to which specific signaling pathways are activated during disease progression or development, such as the mitogen-activated protein kinase (MAPK), Wnt, Sonic Hedgehog (SHH), and TGF- $\beta$ -regulated signaling pathways (23–26).

One limitation of our approach is that the NHEJ DNA repair mechanism is error-prone, so it is not easy to precisely control how each stgRNA cleavage event translates into a defined mutation, which could result in errors and noise in interpreting a given memory register. Ideally,

each stgRNA cleavage event would result in a defined mutation, rather than a range of mutations. Among NHEJ repair mechanisms, recent studies have identified a more error-prone repair pathway, termed alternative NHEJ (aNHEJ). To enhance the controllability of mutations that arise over time, small-molecule inhibitors of aNHEJ components, including ligase III and PARP1, could be used (27, 28). The systematic engineering and characterization of a larger library of stgRNA sequences could also help to identify memory registers that are more efficient than the ones tested here.

Moreover, because our system generates a diverse set of stgRNA variants during the self-mutagenesis process, it is difficult to predict and eliminate potential off-target effects that may arise even if the original stgRNA can be designed for minimal off-target effects. As an alternative, we could fuse deactivated Cas9 (dCas9) to DNA cleavage domains such as single-chain FokI nucleases (29) so that dCas9 could be targeted to a specific DNA locus, with cleavage occurring away from the dCas9 binding site. This way, one can avoid generating variants of stgRNAs that might target other sites in the genome while repeated targeting of the DNA locus can occur at locations distal to the dCas9 binding site, hence serving as a continuous memory register. Alternatively, adopting the recently described “base-editing” strategy that uses cytidine deaminase (30) activity could help to avoid issues with using mutagenesis via DNA double-strand breaks for memory storage. Epigenetic strategies—for example, by fusing methyltransferases (31) or demethylases (32) to dCas9—could also be leveraged for continuous memory storage. Last, in addition to recording information, this technology could be used for lineage tracing in the context of organogenesis. Embryonic stem cells containing stgRNAs could be allowed to develop into a whole organism, and the resulting lineage relationships between multiple cell types could be delineated via *in situ* RNA sequencing (33). We show that mSCRIBE, enabled by self-targeting CRISPR-Cas, is useful for analog memory in mammalian cells. We anticipate that mSCRIBE will be applicable to a broad range of biological settings and should provide insights into signaling dynamics and regulatory events in cell populations within living animals.

## Materials and methods

### Vector construction

The vectors used in this study (table S2, construct 12) were constructed using standard molecular cloning techniques, including restriction enzyme digestion, ligation, PCR, and Gibson assembly. Custom oligonucleotides were purchased from Integrated DNA Technologies. The vector constructs were transformed into *E. coli* strain DH5 $\alpha$ , and 50  $\mu$ g/ml of carbenicillin (Teknova) was used to isolate colonies harboring the constructs. DNA was extracted and purified using Plasmid Mini or Midi Kits (Qiagen). Sequences of the vector constructs were verified with Genewiz and Quintara Bio’s DNA sequencing service. Sequences of all of

the DNA constructs used in this work are listed in Table S2 and their plasmid maps are available at [www.rle.mit.edu/sbg/resources/stgRNA](http://www.rle.mit.edu/sbg/resources/stgRNA).

### T7 Endonuclease I (T7 E1) assay and Sanger sequencing

Unless otherwise stated, cells used for T7 E1 assays were grown in 24-well plates with 200,000 cells per well. Genomic DNA from respective cell lines containing stgRNA or the sgRNA loci was extracted using the QuickExtract DNA extraction solution (Epicentre). Genomic PCR was performed using the KAPA-Hifi polymerase (KAPA biosystems) using the primers:

JP1710 – GCAGAGATCCAGTTTGGGGGGTTC-CGCGCAC and JP1711 – CCCGGTAGAATTCCTC-GACGTCTAATGCCAAC at 65°C for 30s and 25s/cycle extension at 72°C for 29 cycles. Purified PCR DNA was then used in the T7 Endonuclease I (T7 E1) assays. Specifically, 400 ng of PCR DNA was used per 20  $\mu$ l T7 E1 reaction mixture (NEB Protocols, M0302). For Sanger sequencing, PCR amplicons from mutated genomic DNA were cloned in to KpnI/NheI sites of Construct 13 from previous work (34) and transformed into *E. coli* (DH5 $\alpha$ , NEB). Single colonies of bacteria were Sanger sequenced using the Rolling Circle Amplification method (Genewiz, Inc).

### Cell culture, transfections and lentiviral infections

Cell culture and transfections were performed as described earlier (34). HEK 293T cells (ATCC CRL-11268) were purchased from and authenticated by ATCC. Our cell lines were tested negative for mycoplasma contamination by the Diagnostic Laboratory of the Division of Comparative Medicine at MIT. Lentiviruses were packaged using the FUGW backbone (2) (Addgene #25870) in HEK 293T cells. Filtered lentiviruses were used to infect respective cell lines in the presence of polybrene (8  $\mu$ g/mL). Successful lentiviral integration was confirmed by using lentiviral plasmid constructs constitutively expressing fluorescent proteins or antibiotic resistance genes to serve as infection markers.

### Clonal cell lines and DNA constructs

A lentiviral plasmid construct expressing spCas9, codon optimized for expression in human cells fused to the puromycin resistance gene with a P2A linker was built from the taCas9 plasmid (34) (table S2, construct 12). The UB Cp-Cas9 cell line was constructed by infecting early passage HEK 293T cells with high titer lentiviral particles encoding Construct 12 and selecting for clonal populations grown in the presence of puromycin (7  $\mu$ g/mL). The NF- $\kappa$ B-Cas9 cell line was built by infecting HEK 293T cells with high titer lentiviral particles encoding a NF- $\kappa$ B-responsive Cas9 expressing construct (table S2, construct 33). Transduced cells were induced with 1 ng/mL TNF $\alpha$  for three days followed by selection with 3  $\mu$ g/mL puromycin. NF- $\kappa$ B-Cas9 cells were then clonally isolated in the absence of TNF $\alpha$ . NF- $\kappa$ B-Cas9 cells were infected with lentivirus

particles encoding the 30nt-1 stgRNA locus at 0.3 multiplicity of infection (MOI) to build inflammation-recording cells. Cell lines used to test stgRNA activity were built by infecting HEK 293T cells with lentiviral particles encoding constructs 1 through 6 (table S2) and selecting for successfully transduced cells with 300 µg/mL hygromycin. The cell line used to test inducible and multiplexed recording with doxycycline and IPTG was built by infecting UBCp-Cas9 cells with lentiviral particles encoding a DNA construct that expresses TetR and LacI constitutively (table S2, construct 28) followed by selection with 200 mg/mL zeocin for seven days.

### Design of longer stgRNAs

Longer stgRNAs were designed using the ViennaRNA package (36). Specifically, the RNAfold software was used to generate SDSs that retain the native structure of the guide RNA handle and no secondary structures in the SDS encoding region in the minimum free energy structure.

### FACS and microscopy

Before analysis and sorting, cells were suspended in PBS with 2% fetal bovine serum. Cells were sorted using Beckmann Coulter MoFlo cell sorter. Flow cytometry analysis was performed with Becton Dickinson LSRFortessa and FlowJo. Fluorescence microscopy images of cells were obtained by using Thermo Scientific's EVOS cell imager. The cells were directly imaged from tissue culture plates.

### Mutation-based toggling reporter (MBTR)-based cell sorting experiment

HEK 293T cells stably expressing Cas9 (UBCp-Cas9 cells) were infected with MBTR constructs at low titer (MOI = 0.3) so that most of the infected cells had a single copy of the construct. In the self-targeting scenario, a U6 promoter driven stgRNA with a 27 nt SDS is embedded between a constitutive human CMV promoter and modified GFP and RFP reporters. RNAP II mediated transcription starts upstream of the U6 promoter. Different sizes of indel formation at the stgRNA locus should result in different peptide sequences being translated. When translated in-frame, two "self-cleaving" 2A peptides, P2A and T2A, are designed to cause co-translational "cleavage" of the peptides and release functional fluorescent protein from the nonsense peptides, thus resulting in the appropriate fluorescent signal. The non-self-targeting construct consists of a U6 promoter driving expression of a regular sgRNA, which targets a sequence corresponding to the sgRNA embedded in the MBTR system as the MDR. Five days after the initial infection, generation 1 (Gen1) cells were sorted into RFP or GFP positive populations (Gen1:RFP and Gen1:GFP). The genomic DNA was extracted from a portion of the sorted cells. The rest of the sorted cells were allowed to grow to acquire further mutations at the stgRNA loci. The cells initially sorted for RFP or GFP fluorescence (Gen2R and Gen2G) were sorted again seven days after the first sort. The genomic DNA of the sorted cells

(Gen2R:RFP, Gen2R:GFP, Gen2G:RFP and Gen2G:GFP) was collected, PCR amplified and Sanger sequenced after bacterial cloning. See Fig. 2 and fig. S3.

### Next-generation sequencing and alignment

Genomic DNA from respective cell lines was extracted using QuickExtract (Epicenter) and amplified using sequence specific primers containing Illumina adapter sequences P5 – AATGATACGG-CGACCACCGAGATCTACAC and P7 – CAAGCA-GAAGACGGCATAACGAGAT as primer overhangs. Multiple PCR samples were multiplexed together and sequenced on a single flow cell using 8 bp multiplexing barcodes incorporated via reverse primers. The barcode library stgRNA samples in Fig. 3 were split into two groups and sequenced on the NextSeq platform (resulting in 154 and 178 million reads) while the 20nt-1 stgRNA samples in Fig. 1, the regular sgRNA samples in fig. S7, TNFa dosage and time course characterization samples in Fig. 4E and the mouse tumor PCR samples in Fig. 4G were sequenced on the MiSeq platform (resulting in ~13 million reads per experiment). Paired end reads were assembled using the PEAR package (37). Optimal sequence alignment was performed by a custom written C++ code implementing the SS-2 algorithm (38) using affine gap costs with a gap opening penalty of 2.5 and a gap continuation penalty of 0.5 (see Code availability). The aligned sequences were represented using a four-letter alphabet in the "MIXD" format where M represents a match, I represents an insertion, X represents a mismatch and D represents a deletion. At each base-pair position, the sequence aligned base pair is represented by one of the following letters: 'M', 'I', 'X' or 'D' (fig. S4). 27 letter words were used to represent the 20nt stgRNA sequence variants wherein the 27 letters correspond to the first 20 bp of the SDS encoding region, followed by 3 bp of PAM and 4 bp representing the immediately adjacent 4 bp region encoding the stgRNA handle. Similarly, 37 and 47 letter words were used to represent the 30nt and 40nt stgRNA sequence variants.

### Barcoded stgRNA sequence evolution and transition probabilities

After sequence alignment, 16 bp barcodes and the stgRNA sequence variants (in the MIXD format) were extracted. Only the 16 bp barcodes that were represented in all of the time points were considered for further analysis. We employ the well-established Discrete Time Markov Chain (DTMC) analysis to model stgRNA sequence evolution. Each unique stgRNA sequence variant is considered to represent a "state" and the list of stgRNA sequence variants belonging to the same 16 bp barcode and consecutive time points to comprise a DTMC. A maximum likelihood estimation of the transition probabilities is then computed. Specifically, all possible two-wise combinations of sequence variants associated with the same barcode but consecutive time points were evaluated for a "parent-daughter" association. For every sequence variant in a future time point (a daughter), a sequence variant with the same bar-

code in the immediately preceding time point that had the minimum Hamming distance to the daughter sequence variant was assigned as the parent. Since the presence of an intact PAM is an absolute requirement for self-targeting capability of stgRNAs, only the sequence variants that contained an intact PAM were considered as potential parents. Many parent-daughter associations were computed across all the barcodes and time points, resulting in an overall count for each specific parent-daughter association. Finally, the counts were normalized such that the total likelihood of transitioning from each parent to all possible daughters would sum to one. The Hamming distance metric between two sequence variants in the MIXD format was calculated by assigning a distance score for each base pair position. Specifically, if only one of the sequence variants being compared had an insertion at a particular base pair position, then the score for that position is assigned 2. In all other cases, the score at a base pair position was assigned 0 if the sequence variant letters were identical and 1 if they were not identical. The scores for each base pair position were summed up and used as the Hamming distance metric between the two sequence variants. Finally, while assigning parent-daughter associations, unless the parent and the daughter sequence variants were exactly identical, sequence variants that contain mutations in the PAM were not considered as potential parents. The implementation of the above algorithm using a specific barcoded locus is presented in fig. S4. See Fig. 3E.

While designing an mSCRIBE memory device, it is important to keep in mind that stgRNA sequence evolution in its current implementation relies on an undirected phenomenon that can involve potential sources of bias. Over time, the newly generated stgRNAs could become inactive due to severe shortening of their SDS, acquisition of mutations that modify the downstream *S. pyogenes* scaffold required for recognition by Cas9, introduction of runs of 'T' residues could inactivate the stgRNA due to RNA Pol III termination, and homologous repair from the sister chromatid that might result in complete loss of the stgRNA locus. There could also be unanticipated off-target effects because of newly formed stgRNAs targeting sites elsewhere in the genome. However, as we have observed with the stgRNA sequences used in this work, stgRNAs tend to progressively gain deletions and hence, we believe one can minimize such unanticipated affects by designing stgRNAs that are maximally orthogonal to genomic DNA.

### Small-molecule-inducible and multiplexed memory storage

We first built a cell line expressing TetR and LacI by infecting UBCp-Cas9 cells with construct 28, table S2. This cell line was then infected with lentiviral particles encoding the inducible stgRNA cassette from table S2, constructs 29 to 31, and the cells were grown either in the presence or absence of 500 ng/mL doxycycline and/or 2mM IPTG. The cells were harvested 96 hours post



induction and PCR amplified genomic DNA was subject to T7 E1 assays. See Fig. 4, A and B.

### In vivo inflammation model

Four to six weeks old female athymic nude mice (strain nu/nu) were obtained from the rodent breeding colony at Charles River Laboratory. They were specific pathogen free and maintained on sterilized water and animal food. All animals were maintained and used in accordance with the guidelines of the Institutional Animal Care and Use Committee. Sample sizes of the study were estimated based according to in vivo pilot studies and in vitro studies on the expected variance between animals and assay sensitivity (32). Inflammation-recording cells were suspended in matrigel (Corning, NY) in 1:1 ratio with cell growth media.  $2 \times 10^6$  cells were implanted subcutaneously in the flank regions of mice. Animals were randomly assigned into experimental groups after tumor implantation with matched tumor sizes. Where indicated, mice were injected intraperitoneally with lipopolysaccharide (LPS) (from *Escherichia coli* serotype O111:B4, prepared by from sterile ready-made solution from Sigma Chemical Co., St. Louis, MO) dissolved in 0.1 ml saline solution. Animal studies were conducted without blinding. The exclusion and inclusion criteria of the animal study were pre-established. Animals with tumors that grew more than 10 mm in its largest diameter during the experimental period were sacrificed and excluded from the study. See Fig. 4, F and G.

### Code availability

Relevant C++ routines used for data analysis can be found at [www.rle.mit.edu/sbg/resources/stgRNA](http://www.rle.mit.edu/sbg/resources/stgRNA).

### REFERENCES AND NOTES

1. T. S. Gardner, C. R. Cantor, J. J. Collins, Construction of a genetic toggle switch in *Escherichia coli*. *Nature* **403**, 339–342 (2000). doi: [10.1038/35002131](https://doi.org/10.1038/35002131); pmid: 10659857
2. J. W. Kotula et al., Programmable bacteria detect and record an environmental signal in the mammalian gut. *Proc. Natl. Acad. Sci. U.S.A.* **111**, 4838–4843 (2014). doi: [10.1073/pnas.1321321111](https://doi.org/10.1073/pnas.1321321111); pmid: 24639514
3. C. M. Ajo-Franklin et al., Rational design of memory in eukaryotic cells. *Genes Dev.* **21**, 2271–2276 (2007). doi: [10.1101/gad.1586107](https://doi.org/10.1101/gad.1586107); pmid: 17875664
4. A. E. Friedland et al., Synthetic gene networks that count. *Science* **324**, 1199–1202 (2009). doi: [10.1126/science.1172005](https://doi.org/10.1126/science.1172005); pmid: 19478183
5. P. Siuti, J. Yazbek, T. K. Lu, Synthetic circuits integrating logic and memory in living cells. *Nat. Biotechnol.* **31**, 448–452 (2013). doi: [10.1038/nbt.2510](https://doi.org/10.1038/nbt.2510); pmid: 23396014
6. F. Farzadfar, T. K. Lu, Synthetic biology. Genomically encoded analog memory with precise in vivo DNA writing in living cell populations. *Science* **346**, 1256272 (2014).; pmid: 25395541
7. S. Perli, C. Cui, T. K. Lu, Continuous Genetic Recording with Self-Targeting CRISPR-Cas in Human Cells. *bioRxiv*. doi: [10.1101/053058](https://doi.org/10.1101/053058) (2016).
8. A. McKenna et al., Whole organism lineage tracing by combinatorial and cumulative genome editing. *Science* **353**, aaf7907 (2016).

9. R. Kalthor, P. Mali, G. M. Church, Rapidly evolving homing CRISPR barcodes. *bioRxiv* 10.1101/055863 (2016); available at <http://biorxiv.org/content/early/2016/05/27/055863.abstract>.
10. M. Jinek et al., RNA-programmed genome editing in human cells. *eLife* **2**, e00471–e00471 (2013). doi: [10.7554/eLife.00471](https://doi.org/10.7554/eLife.00471); pmid: 23386978
11. L. Cong et al., Multiplex genome engineering using CRISPR/Cas systems. *Science* **339**, 819–823 (2013). doi: [10.1126/science.1231143](https://doi.org/10.1126/science.1231143); pmid: 23287718
12. P. Mali et al., RNA-guided human genome engineering via Cas9. *Science* **339**, 823–826 (2013). doi: [10.1126/science.1232033](https://doi.org/10.1126/science.1232033); pmid: 23287722
13. L. Nissim, S. D. Perli, A. Fridkin, P. Perez-Pinera, T. K. Lu, Multiplexed and programmable regulation of gene networks with an integrated RNA and CRISPR/Cas toolkit in human cells. *Mol. Cell* **54**, 698–710 (2014) doi: [10.1016/j.molcel.2014.04.022](https://doi.org/10.1016/j.molcel.2014.04.022); pmid: 24837679
14. C. Anders, O. Niewoehner, A. Duerst, M. Jinek, Structural basis of PAM-dependent target DNA recognition by the Cas9 endonuclease. *Nature* **513**, 569–573 (2014). doi: [10.1038/nature13579](https://doi.org/10.1038/nature13579); pmid: 25079318
15. M. T. Certo et al., Tracking genome engineering outcome at individual DNA breakpoints. *Nat. Methods* **8**, 671–676 (2011). doi: [10.1038/nmeth.1648](https://doi.org/10.1038/nmeth.1648); pmid: 21743461
16. M. J. Herold, J. van den Brandt, J. Seibler, H. M. Reichardt, Inducible and reversible gene silencing by stable integration of an shRNA-encoding lentivirus in transgenic rats. *Proc. Natl. Acad. Sci. U.S.A.* **105**, 18507–18512 (2008). doi: [10.1073/pnas.0806213105](https://doi.org/10.1073/pnas.0806213105); pmid: 19017805
17. K. Kiss et al., Shifting the paradigm: The putative mitochondrial protein ABCB6 resides in the lysosomes of cells and in the plasma membrane of erythrocytes. *PLOS ONE* **7**, e37378–e37378 (2012). doi: [10.1371/journal.pone.0037378](https://doi.org/10.1371/journal.pone.0037378); pmid: 22655043
18. S. Copeland, H. S. Warren, S. F. Lowry, S. E. Calvano, D. RemickInflammation and the Host Response to Injury Investigators, Acute inflammatory response to endotoxin in mice and humans. *Clin. Diagn. Lab. Immunol.* **12**, 60–67 (2005). pmid: 15642986
19. M. H. Bemelmans, D. J. Gouma, W. A. Buurman, LPS-induced sTNF-receptor release in vivo in a murine model. Investigation of the role of tumor necrosis factor, IL-1, leukemia inhibiting factor, and IFN-gamma. *J. Immunol.* **151**, 5554–5562 (1993). pmid: 8228246
20. D. J. Van Antwerp, S. J. Martin, T. Kafri, D. R. Green, I. M. Verma, Suppression of TNF- $\alpha$ -induced apoptosis by NF- $\kappa$ B. *Science* **274**, 787–789 (1996). doi: [10.1126/science.274.5288.787](https://doi.org/10.1126/science.274.5288.787); pmid: 8864120
21. B. Bozkurt et al., Pathophysiologically relevant concentrations of tumor necrosis factor- $\alpha$  promote progressive left ventricular dysfunction and remodeling in rats. *Circulation* **97**, 1382–1391 (1998). doi: [10.1161/01.CIR.97.14.1382](https://doi.org/10.1161/01.CIR.97.14.1382); pmid: 9577950
22. T. L. Whiteside, The tumor microenvironment and its role in promoting tumor growth. *Oncogene* **27**, 5904–5912 (2008). doi: [10.1038/onc.2008.271](https://doi.org/10.1038/onc.2008.271); pmid: 18836471
23. A. S. Dhillion, S. Hagan, O. Rath, W. Kolch, MAP kinase signalling pathways in cancer. *Oncogene* **26**, 3279–3290 (2007). doi: [10.1038/sj.onc.1210421](https://doi.org/10.1038/sj.onc.1210421); pmid: 17496922
24. A. Wodarz, R. Nüsse, Mechanisms of Wnt signaling in development. *Annu. Rev. Cell Dev. Biol.* **14**, 59–88 (1998). doi: [10.1146/annurev.cellbio.14.1.59](https://doi.org/10.1146/annurev.cellbio.14.1.59); pmid: 9891778
25. L. L. Rubin, F. J. de Sauvage, Targeting the Hedgehog pathway in cancer. *Nat. Rev. Drug Discov.* **5**, 1026–1033 (2006). doi: [10.1038/nrd2086](https://doi.org/10.1038/nrd2086); pmid: 17139287
26. R. Derynck, R. J. Akhurst, A. Balmain, TGF- $\beta$  signaling in tumor suppression and cancer progression. *Nat. Genet.* **29**, 117–129 (2001). doi: [10.1038/ng1001-117](https://doi.org/10.1038/ng1001-117); pmid: 11586292
27. L. Deriano, D. B. Roth, Modernizing the nonhomologous end-joining repertoire: Alternative and classical NHEJ share the stage. *Annu. Rev. Genet.* **47**, 433–455 (2013). doi: [10.1146/annurev-genet-110711-155540](https://doi.org/10.1146/annurev-genet-110711-155540); pmid: 24050180
28. M. Rouleau, A. Patel, M. J. Hendzel, S. H. Kaufmann, G. G. Poirier, PARP inhibition: PARP1 and beyond. *Nat. Rev. Cancer* **10**, 293–301 (2010). doi: [10.1038/nrc2812](https://doi.org/10.1038/nrc2812); pmid: 20200537
29. M. Minczuk, M. A. Papworth, J. C. Miller, M. P. Murphy, A. Klug, Development of a single-chain, quasi-dimeric zinc-finger nuclease for the selective degradation of mutated human mitochondrial DNA. *Nucleic Acids Res.* **36**, 3926–3938 (2008). doi: [10.1093/nar/gkn313](https://doi.org/10.1093/nar/gkn313); pmid: 18511461
30. A. C. Komor, Y. B. Kim, M. S. Packer, J. A. Zuris, D. R. Liu, Programmable editing of a target base in genomic DNA without double-stranded DNA cleavage. *Nature* **533**, 420–424 (2016). doi: [10.1038/nature17946](https://doi.org/10.1038/nature17946); pmid: 27096365
31. R. J. Klose, A. P. Bird, Genomic DNA methylation: The mark and its mediators. *Trends Biochem. Sci.* **31**, 89–97 (2006). doi: [10.1016/j.tibs.2005.12.008](https://doi.org/10.1016/j.tibs.2005.12.008); pmid: 16403636
32. M. L. Maeder et al., Targeted DNA demethylation and activation of endogenous genes using programmable TALE-TET1 fusion proteins. *Nat. Biotechnol.* **31**, 1137–1142 (2013). doi: [10.1038/nbt.2726](https://doi.org/10.1038/nbt.2726); pmid: 24108092
33. J. H. Lee et al., Highly multiplexed subcellular RNA sequencing in situ. *Science* **343**, 1360–1363 (2014). doi: [10.1126/science.1250212](https://doi.org/10.1126/science.1250212); pmid: 24578530
34. C. Lois, E. J. Hong, S. Pease, E. J. Brown, D. Baltimore, Germline transmission and tissue-specific expression of transgenes delivered by lentiviral vectors. *Science* **295**, 868–872 (2002). doi: [10.1126/science.1067081](https://doi.org/10.1126/science.1067081); pmid: 11786607
35. R. Lorenz et al., ViennaRNA Package 2.0. *Algorithms Mol. Biol.* **6**, 26 (2011). doi: [10.1186/1748-7188-6-26](https://doi.org/10.1186/1748-7188-6-26); pmid: 22115189
36. J. Zhang, K. Kobert, T. Flouri, A. Stamatakis, PEAR: A fast and accurate Illumina Paired-End reAd mergeR. *Bioinformatics* **30**, 614–620 (2014). doi: [10.1093/bioinformatics/btt593](https://doi.org/10.1093/bioinformatics/btt593); pmid: 24142950
37. S. F. Altschul, B. W. Erickson, Optimal sequence alignment using affine gap costs. *Bull. Math. Biol.* **48**, 603–616 (1986). doi: [10.1007/BF02462326](https://doi.org/10.1007/BF02462326); pmid: 3580642
38. S. Bae, J. Park, J.-S. Kim, Cas-OFFinder: A fast and versatile algorithm that searches for potential off-target sites of Cas9 RNA-guided endonucleases. *Bioinformatics* **30**, 1473–1475 (2014). doi: [10.1093/bioinformatics/btu048](https://doi.org/10.1093/bioinformatics/btu048); pmid: 24463181

### ACKNOWLEDGMENTS

The plasmid constructs mentioned in table S2 are available from Addgene via their standard materials transfer agreement. T.K.L., S.D.P., and C.H.C. are inventors on a U.S. patent application (PCT/US2016/032348) submitted by MIT that covers the self-targeting genome editing system. We thank members of the Lu laboratory for helpful discussions. We thank the MIT MicroBioCenter for technical support by the National Institutes of Health (grants DP2 OD008435 and P50 GM098792), the Office of Naval Research (grant N00014-13-1-0424), the National Science Foundation (grant MCB-1350625), the Defense Advanced Research Projects Agency, The Center for Microbiome Informatics and Therapeutics, and NSF Expeditions in Computing Program Award 1522074. C.H.C. was supported by a *Natural Sciences and Engineering Research Council of Canada* postgraduate fellowship. S.P., C.H.C., and T.K.L. conceived the work. S.D.P. and C.H.C. designed and performed experiments. S.D.P. performed computational analyses on next-generation sequencing data. C.H.C. conducted in vivo animal studies. S.D.P., C.H.C., and T.K.L. designed the experiments and interpreted and analyzed the data. S.D.P., C.H.C., and T.K.L. wrote the paper. Sequences of all of the DNA constructs used in this work are listed in table S2, and their plasmid maps and C++ routines are available at [www.rle.mit.edu/sbg/resources/stgRNA](http://www.rle.mit.edu/sbg/resources/stgRNA).

### SUPPLEMENTARY MATERIALS

[www.sciencemag.org/content/353/6304/aag0511/suppl/DC1](http://www.sciencemag.org/content/353/6304/aag0511/suppl/DC1)  
Figs. S1 to S10  
Tables S1 and S2  
References

5 May 2016; accepted 27 July 2016  
Published online 18 August 2016  
[10.1126/science.aag0511](https://doi.org/10.1126/science.aag0511)

## RESEARCH ARTICLE SUMMARY

## BIOPHYSICS

## Single-molecule dissection of stacking forces in DNA

Fabian Kilchherr, Christian Wachauf, Benjamin Pelz, Matthias Rief, Martin Zacharias, Hendrik Dietz\*

**INTRODUCTION:** In DNA double helices, hydrogen bonds connect the base pairs across the two strands, and stacking bonds act along the helical axis between neighboring base pairs. Our understanding of DNA and the way it is processed in biology would profit from improved knowledge about the elementary bonds in DNA. Detailed knowledge of the time scales for breaking and forming individual base pairs and base-pair stacks would also help to make more informed decisions in the design of dynamic DNA-based nanoscale devices.

**RATIONALE:** The goal of this work is to measure the dynamics of DNA base-pair stacking at the level of individual base-pair steps. Because stacking interactions act perpendicularly to the hydrogen bonds, it should be possible to use mechanical forces to break stacking while leaving hydrogen bonds intact. To realize such measurements, we combine the positioning capabilities of DNA origami with single-molecule manipulation, as enabled by dual-beam optical traps. To make the weak single-base-pair stacking interactions experimentally accessible, we prepared parallel arrays of blunt-end DNA dou-

ble helices to take advantage of avidity effects when these arrays form stacking interactions (see the figure). Our design allowed controlling the number and the sequences of the base-pair stacks. Noise-suppressing by stiff DNA origami beams connected by a flexible polymer tether enabled the repeated detection of unbinding and rebinding of stacking contacts at low forces (down to 2 piconewtons) with high time resolution (up to 1 kHz).

**RESULTS:** We sampled all 16 sequence combinations of installing a particular interfacial base pair on the array on the left beam and another base pair in the array on the right beam, and we created arrays with two, four, and six blunt ends. We could measure the force-dependent lifetimes for all base-pair step sequence combinations in the presence of 20 mM  $\text{MgCl}_2$ , which is a condition typically used in DNA nanotechnology. For a subset of base-pair step combinations, we also obtained data in the presence of 500 mM NaCl, which mimics the conditions in the cell nucleus. The base-pair stack arrays spontaneously dissociated at average rates ranging from 0.02 to 500 per second, where the dissociation time

scale strongly depended on the sequence combination and the stack array size. For a given sequence combination, larger array sizes always had larger lifetimes, as expected from avidity. Another key feature revealed in the lifetime data was the low sensitivity of the stacking interactions on the extent of pulling force. This phenomenon reflects short-ranged interaction potentials. Concerning rebinding of the stack arrays, we found that the rebinding kinetics depended much more strongly on the applied force, which may be understood by considering that rebinding of the stacks requires a thermally

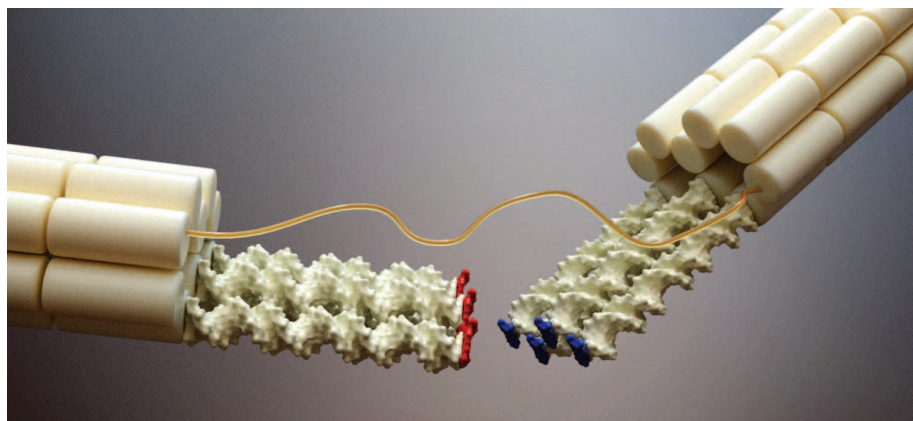
## ON OUR WEBSITE

Read the full article at <http://dx.doi.org/10.1126/science.aaf5508>

activated contraction of the flexible tether—which was the same for all variants—against an opposing force tether contraction. However, the rebinding kinetics was independent, within

experimental error, of the base-pair step sequence combination and the size of the array under study. We used a model to estimate the free-energy increments per single base-pair stack from the kinetic rates that we measured with stack arrays. The free-energy increments per stack ranged from  $-0.8$  to  $-3.4$  kilocalories per mole. Our data reveals a trend in the stacking-strength hierarchy that may be associated with the extent of geometrical atomic overlap between the bases within a base-pair step.

**CONCLUSION:** Our data provides a quantitative basis for the rational design of dynamic DNA-based nanoscale machines and assemblies. Nanoengineers can directly read off the expected lifetimes of stack arrays for all sequence combinations and for various array sizes and at salt conditions that are commonly used in the field. With this data, design solutions for transition kinetics may be generated that cover several orders of magnitudes in lifetime, from milliseconds to several seconds. The sequence-resolved information obtained in our experiments may inform kinetic models of DNA hybridization and may help in adjusting force fields to perform more realistic molecular dynamics simulations. More generally, our experimental methods advance the capabilities of single-molecule mechanical experiments. Using the tethered-beam system, target molecules may be placed and exposed in controlled orientations and stoichiometry so as to study the weak forces occurring between them in solution. A variety of interactions between various kinds of molecules may be studied in the future due to the modularity and the addressability of the DNA origami-based tethered-beam system. ■



**How strong is DNA base-pair stacking?** Schematic illustration of the experimental system to measure the strength of base-pair stacking on the level of single particles. The system consists of two tethered DNA origami beams that feature parallel arrays of blunt-end DNA double helices. The beams may be attached to two micrometer-sized beads for manipulation in a dual-beam optical trap. With this system, we could measure lifetimes at which DNA base-pair stacks spontaneously dissociate as a function of force applied in the helical direction.

The list of author affiliations is available in the full article online.

\*Corresponding author. Email: [dietz@tum.de](mailto:dietz@tum.de)

Cite this article as F. Kilchherr et al., *Science* 353, aaf5508 (2016). DOI: 10.1126/science.aaf5508



## RESEARCH ARTICLE

## BIOPHYSICS

## Single-molecule dissection of stacking forces in DNA

Fabian Kilchherr,<sup>1</sup> Christian Wachauf,<sup>1</sup> Benjamin Pelz,<sup>2</sup> Matthias Rief,<sup>2,4</sup> Martin Zacharias,<sup>3,4</sup> Hendrik Dietz<sup>1,4,5,\*</sup>

We directly measured at the single-molecule level the forces and lifetimes of DNA base-pair stacking interactions for all stack sequence combinations. Our experimental approach combined dual-beam optical tweezers with DNA origami components to allow positioning of blunt-end DNA helices so that the weak stacking force could be isolated. Base-pair stack arrays that lacked a covalent backbone connection spontaneously dissociated at average rates ranging from 0.02 to 500 per second, depending on the sequence combination and stack array size. Forces in the range from 2 to 8 piconewtons that act along the helical direction only mildly accelerated the stochastic unstacking process. The free-energy increments per stack that we estimate from the measured forward and backward kinetic rates ranged from  $-0.8$  to  $-3.4$  kilocalories per mole, depending on the sequence combination. Our data contributes to understanding the mechanics of DNA processing in biology, and it is helpful for designing the kinetics of DNA-based nanoscale devices according to user specifications.

The processing of genetic information relies on the forces and energies underlying base-pair interactions in DNA. Hydrogen bonds connect the two Watson-Crick base pairs AT and GC across the two strands (1), and stacking forces act along the helical axis between neighboring base pairs (2) (Fig. 1A). Various spectroscopic techniques have been used to study the dynamics of DNA molecules, including the opening and flipping of mismatched bases (3, 4). The local and global dynamics of DNA is, however, determined by many contributions of base-pairing, stacking, and backbone interactions. In particular, the force-dependent time scales of breaking and reforming single base pairs and single base-pair stacks remain experimentally unexplored. At present, we do not know to which extent enzymes such as polymerases have to use actual force to break base pairs and base-pair stacks to process DNA. Furthermore, the time scales of these elementary bond-breaking and bond-forming steps ultimately determine the kinetics of nanotechnological devices and machines currently being developed from DNA (5–7). The goal of this work is to measure the dynamics of DNA base-pair stacking at the level of individual base-pair steps.

Because stacking interactions act perpendicularly to the hydrogen bonds, it should be possible to use mechanical forces to break stacking while leaving hydrogen bonds intact. We thus combine the capabilities of DNA nanotechnology, which allow positioning of molecules with atomic precision (8), with single-molecule force spectroscopy to manipulate molecular interactions in controlled spatial directions. Previous single-molecule mechanical assays based on atomic force microscopy (9, 10), optical traps (11–14), and magnetic tweezers (15–17) have provided important insight into the mechanics of DNA and into the folding energy landscapes of DNA secondary structures (18–20). However, the previous experiments measured the total contribution of all interactions stabilizing long DNA duplexes and lacked the control to break or form individual DNA base-pair steps.

## Results

## Experimental design

To enable a direct mechanical investigation of base-pair stacking forces on the level of individual DNA base pairs (Fig. 1A), without breaking hydrogen bonds, we have combined the molecular-level positioning capabilities of DNA origami-based nanotechnology (21–23) with the single-molecule manipulation capabilities of a dual-beam optical trap (24) (Fig. 1). Our experimental design integrates three components: (i) parallel arrays of base-pair stacks to rationally exploit avidity effects (Fig. 1B) for moving the weak individual stacking interactions into the force regimes and time scales that are experimentally accessible for the optical trap; (ii) stiff DNA beams to link the stack arrays to the optically trapped beads (Fig. 1C), where the beams have noise-suppressing

capabilities (20) to support the detection of unbinding and rebinding events occurring at extremely low forces (down to 2 pN) with fast kinetics (up to 1 kHz); (iii) a user-defined flexible tether linking the two beams (Fig. 1C), which enables the repeated observation and classification of unbinding and rebinding events, as seen previously with peptide linkers (25, 26) and long duplex DNA loops (27).

## Design details of blunt-end arrays

The 10-helix DNA origami beams that we used in our experiments had persistence lengths  $p$  well above  $3.5\ \mu\text{m}$  (20) at a total length  $L$  of 250 nm per beam. Based on the high tangent angle correlation according to  $\exp(-L/p)$ , the beams were thus firmly in the rigid rod regime. The cantilevered blunt-end duplex DNA segments typically had a length of around three to four helical turns. Within the arrays of cantilevered, blunt-end DNA double helices (Fig. 1C, insets), the protruding helices were also coupled via lateral strand linkages to minimize translations and rotations of the interfacial blunt ends (fig. S1) (28). Given the persistence length of single-duplex DNA, which is on the order of 15 helical turns, and ignoring the fact that the cantilevered segments were further stabilized by lateral coupling, the protruding blunt-end arrays were also in the rigid rod regime. The cantilevered helices on the two opposing beam interfaces were also designed to be in helical register. Our design thus templates the formation of backbone-interrupted but geometrically continuous B-form DNA helices through base-pair stacking interactions that engage when the two opposing and cantilevered blunt-end arrays come into contact (Fig. 1C, bottom inset). The design also allows controlling the number and the sequences of the interfacial base pairs (fig. S2). In total, we prepared 50 distinct variants (figs. S3 to S8) that sampled all 16 possible combinations of installing a particular interfacial base-pair type on the array on the left beam and another type in the array on the right beam. Some of those variants were identical at the interface (dyad pairs with point-mirrored sequences), which we considered a desirable redundancy. For each particular sequence combination, we created arrays with two, four, and six blunt ends on either beam interface. Each blunt end in an array had the same terminal base-pair sequence. For the sequence combinations (TA:GC) and (GC:TA) we also created arrays with eight interfacial blunt-end contacts.

## TEM imaging

To illustrate the function of the tethered-beam variants, we imaged exemplarily several variants (figs. S9 and S10) using negative-staining transmission electron microscopy (TEM). One control variant (“open”); (fig. S10C) lacked interfacial blunt ends (Fig. 2A). The TEM data of the open variant shows flexibly tethered particles where the orientation of one beam correlates poorly with the orientation of the other beam of the construct. Another control variant (“hybridized”) (fig. S10B) had stable double-helical connections

<sup>1</sup>Labor für Biomolekulare Nanotechnologie, Physik Department and Walter Schottky Institute, Technische Universität München, Am Coulombwall 4a, Garching near Munich, Germany. <sup>2</sup>Lehrstuhl für Molekulare Biophysik, Physik Department, Technische Universität München, James-Frank-Strasse 1, Garching near Munich, Germany. <sup>3</sup>Lehrstuhl für Theoretische Biophysik, Physik Department, Technische Universität München, James-Frank-Strasse 1, Garching near Munich, Germany. <sup>4</sup>Munich Center for Integrated Protein Science, 81377 Munich, Germany. <sup>5</sup>Institute for Advanced Study, TUM, Germany.

\*Corresponding author. Email: dietz@tum.de

between the two beams, as realized via four complementary sticky ends that bridge the two beams (Fig. 2B). TEM data of the hybridized variant revealed particles with a rigid-beam-like appearance in which the orientation of one beam correlates strongly with that of the other beam. Finally, we also imaged several of our stacking variants (Fig. 2C) [see also figs. S11 and S12 for images of other variants with the longer beams used in the single-molecule mechanical experiments (28)]. In the TEM data obtained with stacking variants, we observed both open particles and particles with a rigid-beam-like appearance resembling those of the hybridized variant. The appearance of the linkage between the beams agreed well with the expected appearance based on the design of the variant (see arrows in Fig. 2, B and C). The TEM data therefore supports that our tethered-beam particles featuring arrays of blunt ends function as desired: When the stacking bonds between the beam interfaces are engaged, a rigid-beam-like state is adopted in which the stacking mediates geometrical and mechanical properties that are similar to those mediated by continuous double-helical DNA domains. If the stacking bonds are broken, the particles extend and become much more flexible.

### Electrophoretic mobility analysis

The difference in effective size of the particles with engaged versus open stacking bonds affects their electrophoretic mobility (fig. S13), which

allowed us to analyze the conformational equilibrium of the full 500-nm-long stacking variants on the ensemble level in a gel shift assay (Fig. 2D). Twenty-seven variants migrated in a sharp band with the high mobility that is associated with the closed, rigid-beam-like conformation [e.g., 4x (AT:CG) and 6x (AT:CG)]. Thirteen variants migrated in a band with the low mobility that corresponds to the open, flexible conformation [e.g., 2x (CG:AT) and 4x (CG:AT)]. Ten variants migrated in a less-well-defined band, with mobility in between those of the open and the closed conformation. The gel data reflects a strong dependency of the conformational equilibrium on the particular stack sequence combination, as previously seen for individual nicked DNA duplexes (29) and on the array size in a variant. When sorting the gel lanes according to the mobility of the leading band (Fig. 2E), going from low mobility (open states, weak stacking) to high mobility (closed states, strong stacking), it becomes apparent that the greater the number of stacking bonds in a variant, the more sequence combinations firmly populate the closed state, reflecting the desired avidity effects.

### Mechanics of stack arrays and lifetime measurements

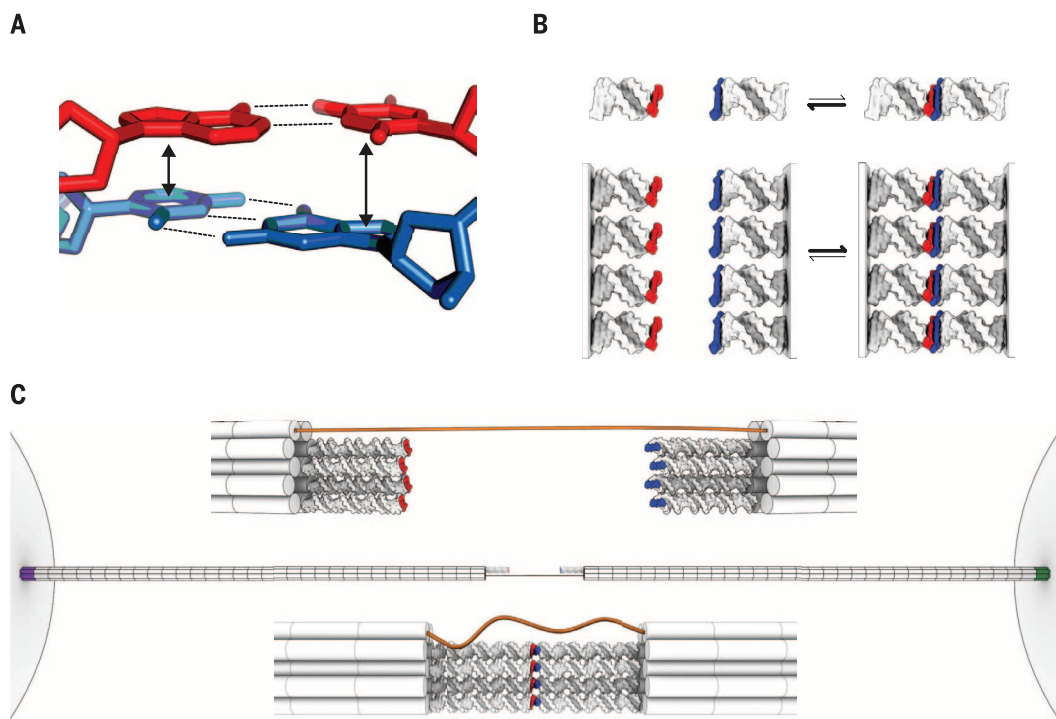
We used a dual-beam optical trap to study the force-extension response and the force-dependent transition kinetics of our stacking variants on the single-particle level. Consistent with their design, the stacking variants exhibited the nonlinear force-

extension response of multihelix bundles (20) and reversible transitions between a short and noise-reduced state and a longer, noise-enhanced state (Fig. 3A). The change in extension was consistent with the properties of the designed tether (figs. S14 and S15). The difference in noise amplitude at the same forces (Fig. 3A, red arrows) reflects the reversible change in the mechanics of the particles between the shorter, rigid-beam-like state with closed stacks and low noise and the extended, more flexible state with broken stacks and increased noise. Exemplary force-extension data obtained for the four base-pair stacking configurations that may be created with the two bases A and T, namely (AT:TA), (TA:AT), (AT:AT), and (TA:TA) illustrate the broad spectrum of mechanical stability and transition kinetics that we observed among the variants studied, including saw-tooth-like out-of-equilibrium unstacking at high forces and restacking at low forces (Fig. 3A) over close-to-equilibrium flips at intermediate forces (Fig. 3, B and C) to plateau-like rapid equilibrium transitions at low forces (Fig. 3D). The force versus extension data verified the integrity of our stacking variants but was not evaluated to extract bond lifetimes.

Instead, to focus on the particular force regime at which transitions occur as seen in the force versus extension data (Fig. 3, B and C, insets), we studied the stacking variants at different, but constant, trap distances. At each constant trap distance, we observed transitions between the open and closed states and measured the time

### Fig. 1. Exploring base-stacking forces on the single-molecule level.

(A) Schematic depiction of two consecutive base pairs within a B-form double-helical domain. Helix axis is oriented vertically. Arrows, stacking interactions; dashed lines, hydrogen bonds. (B) (Top) Schematic illustration of the interaction of blunt-end double-helical DNA through stacking. Red, blue: terminal base pairs that form the stacking contact. The interaction is weak; it takes ~150 mM duplex concentration to effectively populate the bound state (55). (Bottom) Avidity effects in arrays of parallel blunt ends will shift the equilibrium. (C) Schematic illustration of the tethered-beam platform attached to two micrometer-sized beads via biotin-streptavidin (purple) and digoxigenin-antidigoxigenin (green) linkages (see fig. S3 for details) (28). Beads are drawn at  $\sim 1/5$  of the actual radius. Beams are formed from 10 parallel DNA double



helices arranged in honeycomb packing (22). The tether (orange) is a [T]68 single strand. (Top inset) Zoom-in showing the system in the open state with stretched tether. The interfaces are functionalized; the configuration shown has four cantilevered blunt-end DNA double helices. Terminal base pairs are in helical register within an array. The change in helical twist between red and blue corresponds to those in B-Form DNA. (Bottom inset) Zoom-in showing the closed, bound state with geometrically continuous B-form double helices that are stabilized via stacking interactions between the blunt ends.



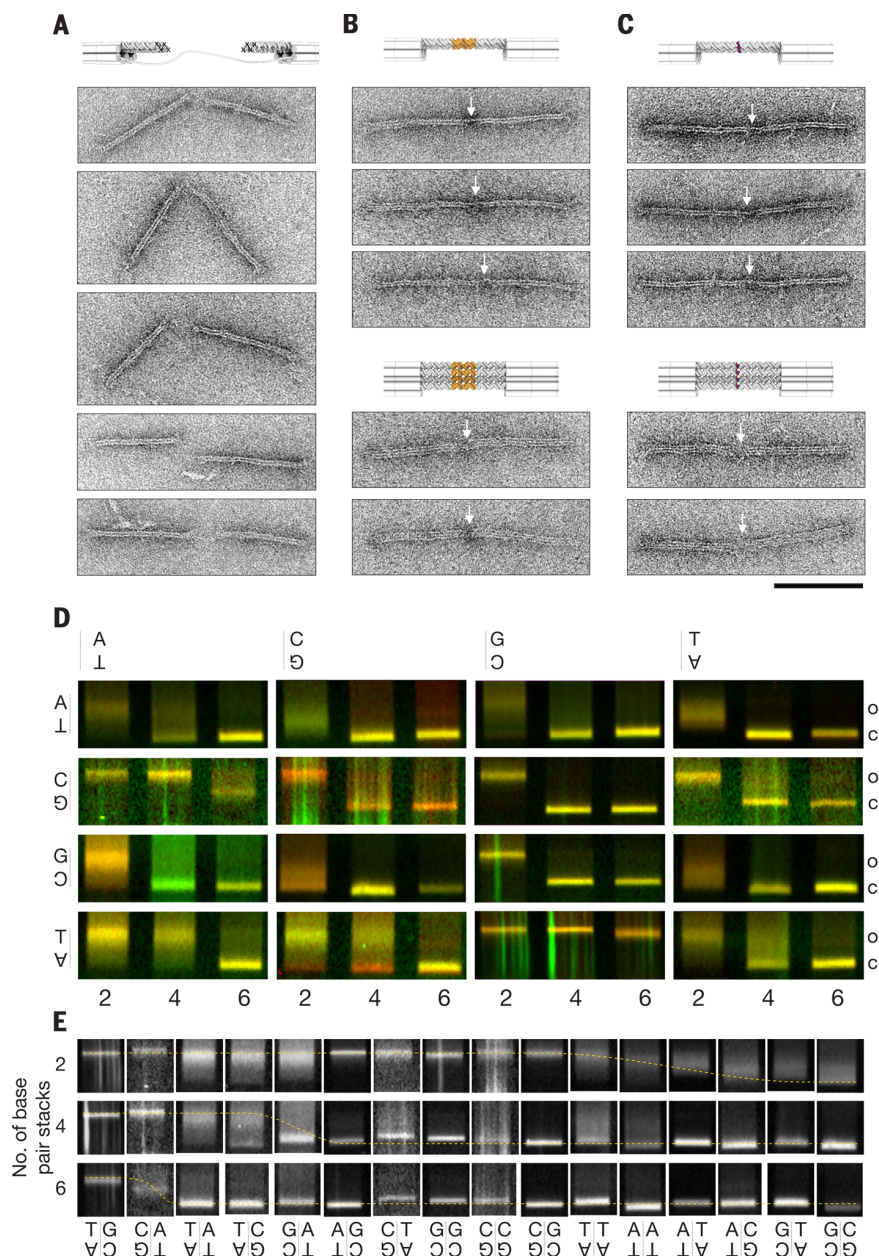


**Fig. 2. TEM images and gel electrophoretic mobility.** Typical negative-staining TEM micrographs. (A) A control variant with passivated interfaces. (B) A control variant with four cantilevered DNA domains on each beam stably connected by 3-base-pair-long sticky end interactions. (C) A dynamic stacking variant with four blunt-end stacking contacts (GC:CG) in the closed, bound state. Arrows indicate the interfacial helix sheet. Scale bar, 100 nm. The variants used in optical trapping experiments were twice as long and were produced by dimerization of two separate DNA origami beams (see materials and methods and figs. S4 to S10) (28). (D) Laser-scanned, channel-merged, false-colored images of agarose gels on which tethered-beam platform variants with stacking contacts were electrophoresed. One beam was labeled with Cy5 (red), the other with Cy3 (green). The data shown were collected from three different gels. Sequence combinations are given such that rows and columns give the identities of the left versus right base pair in our nomenclature. Numbers indicate array size. For example, the top left triple denotes samples with 2, 4, and 6 (AT:AT) stacks. "o" versus "c" indicates mobility of open versus closed states. (E) Individual gel lanes were cropped from the gel images and sorted according to the electrophoretic mobility of the leading band. Dashed line: guide to the eye that interpolates the position of the leading band, highlighting the shift in the equilibrium from open to closed states. Variants with (AT:GC), (CG:TA), (GC:GC), (CG:CG), and (CG:GC) had comparable mobilities within the same array size class and cannot be unambiguously sorted.

the system dwells in each of the two states (Fig. 3, E and F). The equilibrium between the two states, as well as the force exerted on the particles in each conformational state, depends on the particular value of the constant trap distance. This type of experiment is suited particularly for measuring rapid transitions without limitations from the finite delay time of a force-feedback system (30). It enabled us to determine stacking lifetimes over four orders of magnitude, ranging from milliseconds to several seconds (Fig. 3G), where the system became limited by drift and other disturbances. Altogether, 31 out of 50 variants gave measurable transitions in the presence of 20 mM magnesium chloride, where the remaining variants either were too stable or too fragile to collect transitions with our assay. Among those variants were all 16 possible stacking sequence combinations (when taking into account identity of left versus right beam). Fifteen sequence combinations occur in two different array sizes, either two and four, four and six, or six and eight stacks. For another subset of nine variants, we also collected lifetime versus force data in the presence of 500 mM sodium chloride, which is a model for the physiological concentration of monovalent cations in the cell nucleus (31). To extract the lifetimes of the stacked and unstacked states as a function of force, we analyzed in total more than two million dwells. The transition statistics varies among the dynamic stacking variants because of fast versus slow kinetics.

### Force-dependent transition kinetics of stack arrays

The average lifetimes of the unbound states with extended tether and broken stacks were comparable (within experimental error) across all variants that we tested (figs. S16 to S18). This observation indicates sequence-independent rebinding rates. The rebinding of the stack arrays also had a pronounced dependency on force, which may be understood by considering that rebinding of the stacks requires a thermally activated contraction of the flexible tether—which was the same for all variants—against an opposing force.

The average lifetimes of the stacked states, however, provided a much more diverse picture (Fig. 4, A and B). The total range of lifetimes of the stacked states covers almost five orders of magnitude, from milliseconds to tens of seconds. Larger array sizes always have substantially longer lifetimes than smaller array sizes for a given base-pair step sequence combination, consistent with the expectation based on avidity. We note that in the case of larger array sizes, partial restacking with lateral shifts in the stacking contacts may occur occasionally. The lifetime data also reflect a strong dependency of unstacking on the particular sequence combination of the base-pair steps (Fig. 4A). Consider the stark contrast in the kinetics of unstacking (TA:GC) versus (GC:CG) base-pair steps: Six (TA:GC) steps in parallel together still make only quite transient bonds that last on average less than 10 ms. By contrast, two (GC:CG) steps were already much more stable and lasted nearly 1 s. In fact, (GC:CG) base-pair

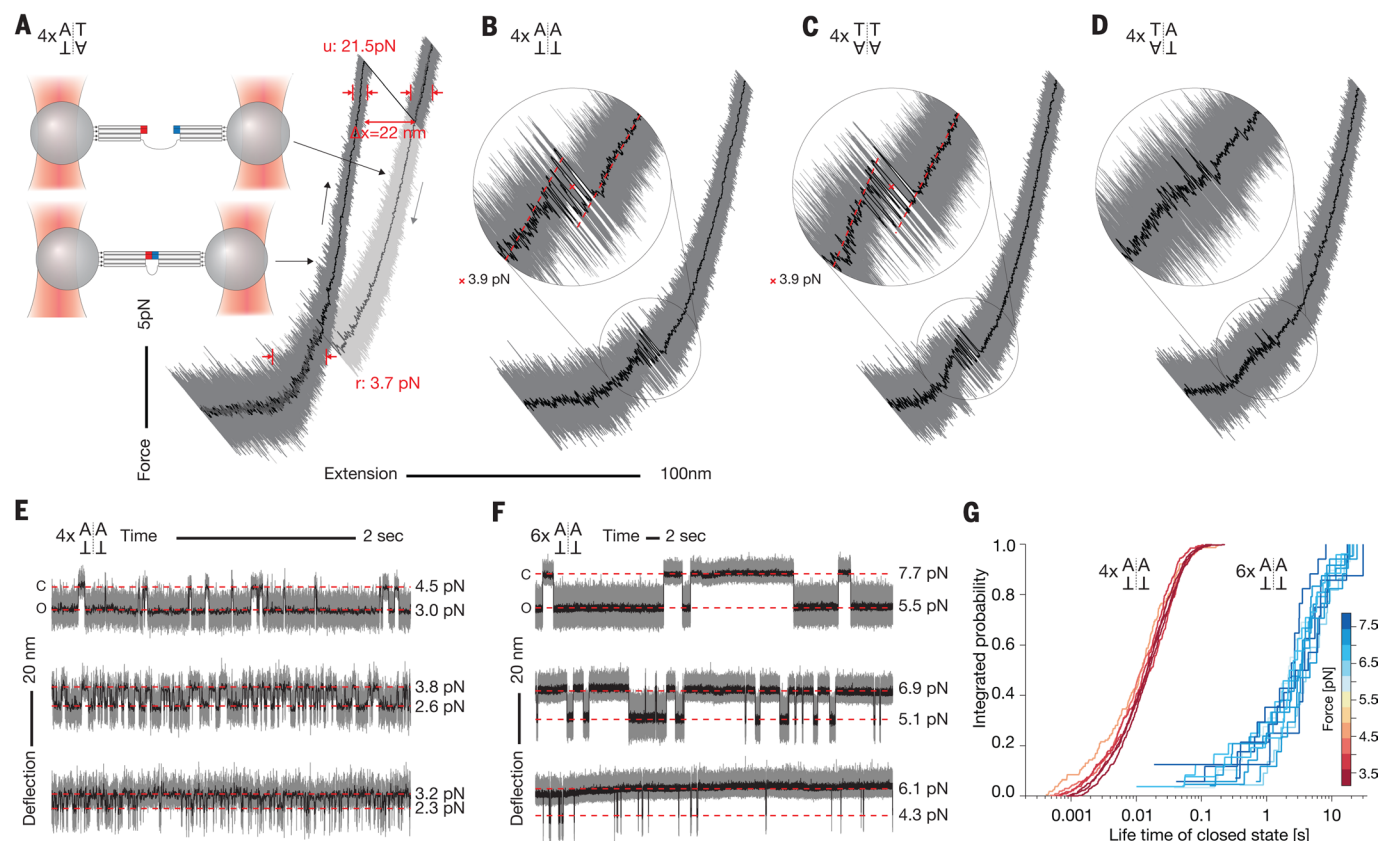


**Fig. 3. Force-extension and constant-distance data of single tethered-beam particles featuring stacking contacts.** (A) Exemplary force-extension data of a single tethered-beam particle with four (AT:TA) stacking contacts, as measured in a dumbbell assay with a dual-beam optical trap (inset). Dark gray, stretching; light gray, consecutive relaxing. Upon stretching, a rupture transition (marked with “u”) occurs at 21.5 pN, leading to an extension gain  $\Delta x$  that is consistent with wormlike chain lengthening of the [T]68 tether. Upon relaxing, a snap (marked with “r”) back to the shorter state with closed stacks occurs at 3.7 pN. The noise amplitudes are smaller in the shorter, closed state than in the longer, open state (see red arrows) due to greater stiffness of the closed state. (B to D) Exemplary force-extension data of single particles featuring the other three possible stacking combinations of A and T in arrays with four stacks. Insets show the transition

regime. The point-mirrored combinations (AT:AT) versus (TA:TA) [(B) versus (C)] have comparable mechanics featuring multiple close-to-equilibrium transitions (see insets) occurring at 4 pN. The least stable variant (TA:AT) unstacks and restacks in apparent equilibrium as reflected in a plateau-like transition. (TA:AT) is sequence-swapped compared with the (AT:TA) variant [see (A)]. (E and F) Constant trap-to-trap distance data of single particles with four versus six (AT:AT) stacking contacts. The particles transition reversibly between two states. “c” and “o” denote the shorter, closed state with intact stacking bonds versus the longer, open state, respectively. Increasing the force reduces the frequency of occurrence and the duration of the stacked states (bottom to top). The increase in array size from four to six stacks has a drastic effect on the overall transition kinetics. (G) Cumulative dwell time histogram of the closed states with intact stacking bonds.

steps had such long lifetimes that we had to change the salt concentration to study transitions with variants that had more than two (GC:CG) contacts (Fig. 4B). Together, the kinetic data now allows ranking base-pair steps according to their force-dependent lifetime. Because we did not detect appreciable differences in the rebinding rates, this kinetic ranking also reflects a ranking according to thermodynamic stability. From the lifetime data in Fig. 4, designers of DNA-based nanoscale devices (7, 32) can directly read off the expected lifetimes of stack arrays for all sequence combinations and for various array sizes and at salt conditions that are commonly used in the field. The data thus provides design solutions that cover orders of magnitude from milliseconds to several seconds.

### Dyads and swapped base pairs

Among the sequence combinations that we tested were six pairs having point-mirrored sequence combinations (“dyads”) such as (AT:CG) versus

(GC:TA) (see fig. S19A for a scheme). The type and the relative orientation of molecular surfaces that interact in the point-mirrored pairs are identical. The dyad pairs had comparable force-dependent lifetimes within one order of magnitude in the single-particle measurements (Fig. 4 and fig. S19), and they also had comparable electrophoretic mobility patterns in ensemble (Fig. 2). The similar behavior of dyad pairs points against significant influences from phenomena such as fraying on the association and dissociation, because fraying is expected to depend on the type of neighboring base pairs located next to the terminal base pairs within the cantilevered stack arrays, but the neighbors were different within the dyad pair designs. There were also six swapped-sequence pairs such as (AT:CG) versus (CG:AT) (see fig. S19A for a scheme). Even though the base-pair composition was the same, buried versus exposed molecular surfaces were interchanged in swapped-sequence pairs. Our data revealed that swapping the sequence led to strong differences in the lifetime

of the stacking interaction, because five out of six swapped sequence pairs had lifetime differences that spanned several orders of magnitude (fig. S20). The data on swapped sequence pairs underlines the sensitivity of our assay for the details of the interfacial stacking interactions.

### Low force sensitivity

Another feature revealed in our lifetime data is the overall low sensitivity of stacking contacts on the extent of pulling force in the helical direction. Increasing the force by 2 pN on the most force-sensitive of our stacking variants (TA:CG) leads to a lifetime reduction by merely a factor of 3. The most insensitive variant was the one with four (CG:CG) stacks whose lifetime was essentially independent of the applied force. Therefore, pulling on DNA base-pair stacks along the helical direction with biologically relevant forces in the <10-pN range hardly accelerated stack dissociation. The low force dependence indicates short-range interactions with transition states in subnanometer



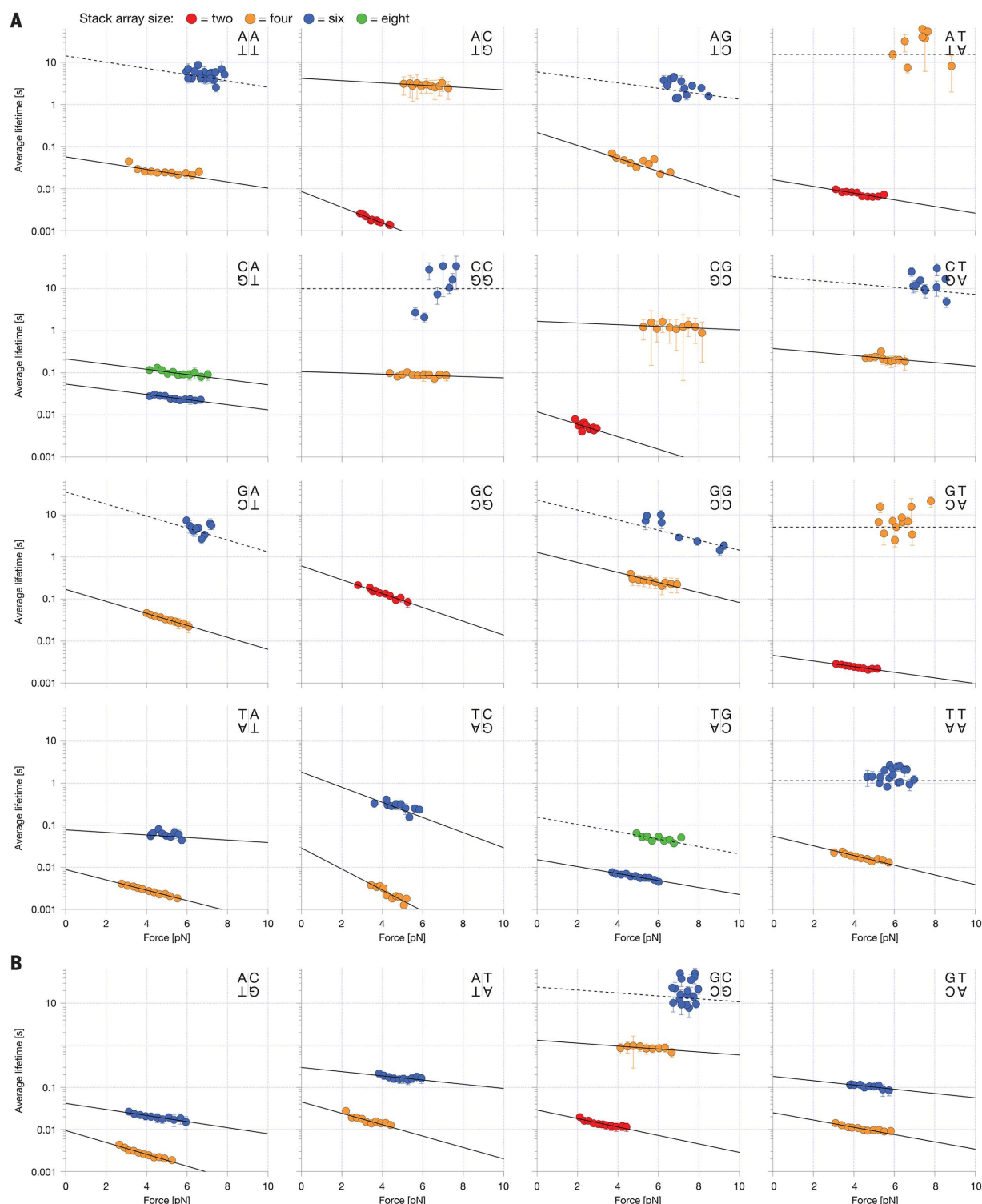


**Fig. 4. Average lifetime of base-pair stack arrays as a function of force.**

(A and B) Average stack array bound-state lifetime versus applied force data branches as determined from single particle data obtained in the presence of 20 mM  $\text{MgCl}_2$  (A) versus 500 mM  $\text{NaCl}$  (B) for all possible stack sequence combinations and for various array sizes (red circles, two stacks; orange circles, four stacks; blue circles, six stacks; green circles, eight stacks). Solid lines are exponential fits. For the variants with particularly long lifetimes in the  $>1$  s regime, drift and optical trap contamination limited the overall measurement time, which in turn resulted in low transition statistics per force value. In these cases, no force-resolved lifetime averages were calculated. Instead, given the generally

weak dependency on force, we used the overall mean. Dashed lines give a guide to the eye. Note the effect of salt concentration on the average lifetime: e.g., the variant with four AT.TA stacks has the overall longest lifetime in 20 mM  $\text{MgCl}_2$  but ranks among the variants with the shortest lifetime in the presence of 500 mM  $\text{NaCl}$ . The rebinding lifetime versus force data are given in figs. S16 and S17. See supplementary materials section 1.6.1 for details, figs. S29 to S31, and tables S1 to S5 for a list of parameters from individual fits and global fits (28). At a stacking contact, our constructs feature the phosphates contributed by the scaffold strand. Blunt-end forming DNA oligonucleotides did not contain terminal phosphates.

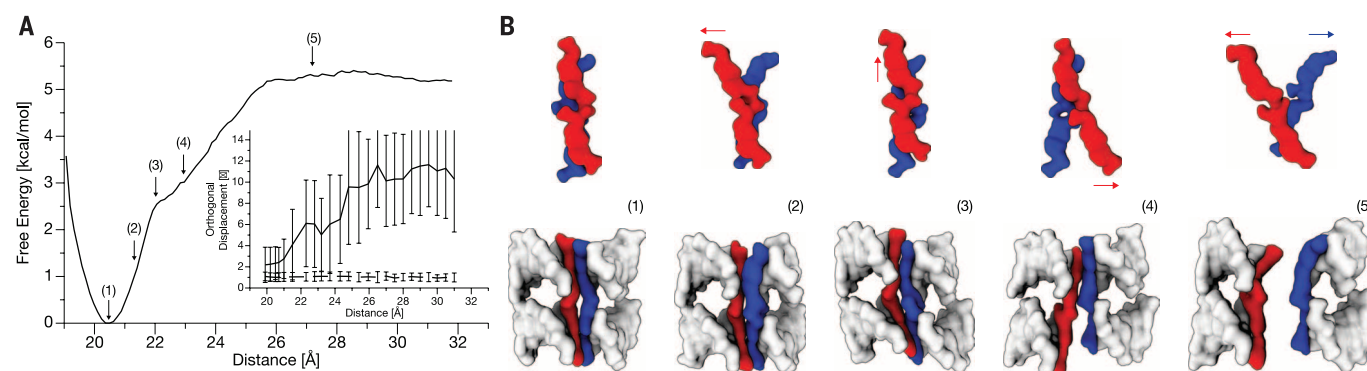


**Fig. 5. Molecular mechanism of stack disruption.** (A) The change in free energy was calculated for the disruption/formation of two (GC:CG) stacks along the axis perpendicular to the base-pair plane (helical axis) using umbrella sampling with molecular dynamics simulations (see supplementary materials section 1.5). The free energy approaches a minimum at a distance corresponding to the fully stacked configuration (~20.4 Å between centers of the two DNAs) and reaches a plateau upon complete dissociation (>26 Å). (Inset) Calculated average displacement in Angstroms (orthogonal to the helical axis) of the two terminal base pairs on one beam interface relative to the two terminal base

pairs on the other beam interface [illustrated in red and blue in (B)]. Disruption of stacking results in a steep rise of displacements orthogonal to the pulling direction (bold line) compared to mean base-pair displacement within an intact helix (shown for comparison as a dashed line; error bars indicate standard deviations of the mean). (B) Snapshots of the dynamics of the two interacting base pairs (indicated in red and blue, respectively) corresponding to the labeled positions in the free-energy plot shown in (A). The top row is the view along the helical axis, showing only the interfacial base pairs. Arrows indicate displacement directions (orthogonal to the direction of stacking disruption/formation).

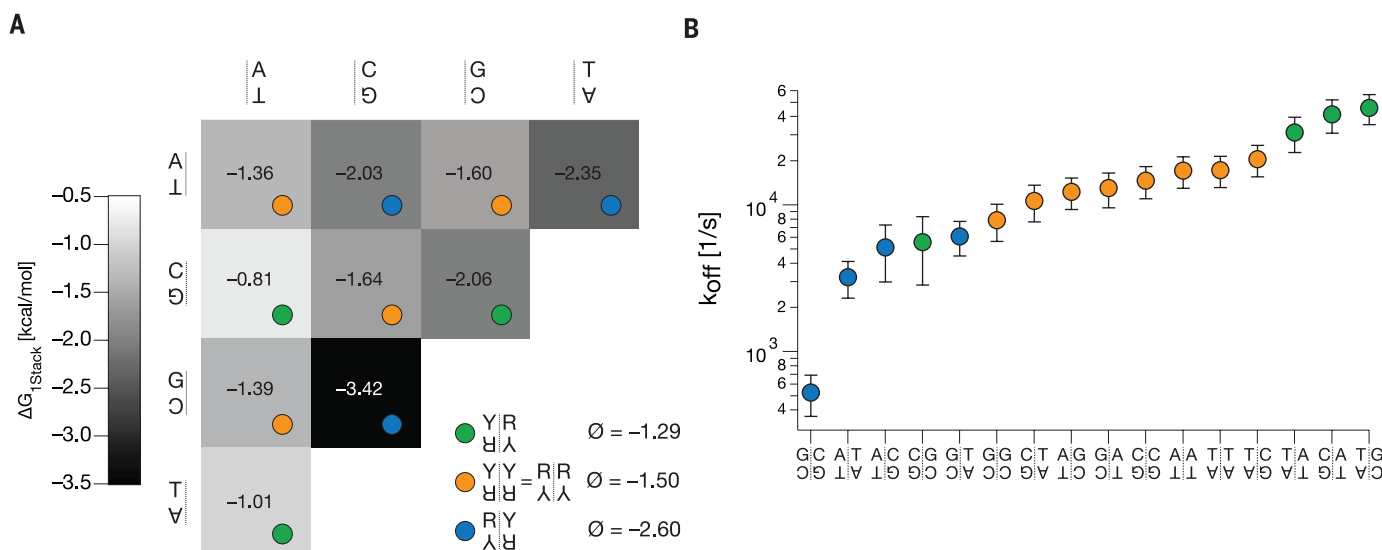


**Fig. 6. Energetics and kinetics of base-pair stacking.** (A) Single-stack free-energy increments for closing the 10 unique base-pair steps, as derived from single-molecule two-state association and dissociation rates in equilibrium (see supplementary materials section 1.6.2). The estimate uses  $1.7 \times 10^5 \text{ s}^{-1}$  as the global association rate, which was obtained through trap-stiffness-corrected extrapolation of rebinding data to zero force (30, 50). Colored dots give stack classification according to underlying chemical backbone. We estimate the error per value to about  $\pm 0.2 \text{ kcal/mol}$ ; see fig. S22. (B) Symbols: single-stack dissociation rates at zero force. See supplementary materials section 1.6.2 and table S6. Bars give propagated statistical error of the extrapolation to zero force in Fig. 4, A and B.

distances to the bound states (33). The low force sensitivity of stacking bonds observed herein may be contrasted with the much larger force sensitivity for unzipping of nucleic acid hairpins (19), where transition state distances depend on the sequences and stem lengths of the hairpins and can be several nanometers long, as expected for transitions that involve the breaking of several base pairs and base-pair stacks in series.

### Molecular mechanics of stack disruption

To study the molecular details associated with the disruption of a blunt-end stack and to address the origin of the insensitivity of unstacking base-

pair steps through axial pulling forces, we investigated exemplarily (CG:GC) base-pair step disruption using molecular dynamics umbrella sampling (Fig. 5). Two (CG:GC) base-pair step stacking units were disrupted along a helical axis pulling direction, allowing calculation of a potential of mean force (PMF) (free energy change) along the direction of separation (Fig. 5A). The PMF was comparable to those computed previously for the end-to-end attraction between individual DNA duplexes (34). The free-energy change reached a plateau upon separation by ~0.6 nm relative to the free-energy minimum (unstacking completed). The magnitude of the calculated PMF depends on

the restraints to align the DNA molecules with respect to the pulling direction [see methods for details (28)]. A sequential disruption of the two blunt-end stacks was observed (disruption of the first base-pair stack at ~0.3 nm separation). Interestingly, during the onset of the dissociation of the first blunt-end stacking contact, a dramatic increase in the base-pair motion orthogonal to the pulling direction was already observed (Fig. 5A, inset), with amplitudes much larger than the shift-and-slide motion of a regular base-pair stacking contact. The orthogonal motions increased even further during disruption of the second blunt-end stack (see snapshots in Fig. 5B). We



conclude that the motions orthogonal to the pulling direction promote onset of dissociation caused by stack overlap reduction, similar to that seen previously for the end-to-end dissociation of individual DNA duplexes (34). Because the motions occur orthogonally to the direction of the applied force, they are hardly influenced by the actual magnitude of the force, which concurs with our experimental observation of force-insensitive unstacking kinetics (Fig. 4, A and B).

## Discussion

Because we have measured forward and backward rates of arrays of base-pair stacks in equilibrium, we can attempt an estimate of the equilibrium free-energy differences for unstacking a single base-pair step. To this end, we use a constant rebinding rate informed by our experimental observation of comparable rebinding kinetics independent of sequence and array size (figs. S16 to S18), and we use average bound-state lifetimes extrapolated to zero force (Fig. 4). For our estimate, we further assume additive free energies per stacking bond within an array, and we ignore a potential penalty for forming the bound state. Based on the rates and these assumptions, we computed the free-energy increments per single stack for all stack arrays that we measured (supplementary materials section 1.6.2). The free energy increments per stack were largely independent of the total number of stacks, and there is no clear trend visible that argues against our simplifying assumptions (fig. S21). The free-energy differences obtained from different array sizes were averaged, and the energies from dyad sequences were also averaged. The free-energy increments that we thus obtained (Fig. 6A) from our single-molecule transition rates in equilibrium and under native solution conditions correlate well with those obtained previously from ensemble experiments with nicked DNA duplexes under denaturing conditions at low ionic strength (see figs. S22 and S23) (28, 35). We consider the agreement between the two parameter sets as remarkably good, given the strongly differing experimental approaches. However, aside from our simplifying assumptions, our estimates are also affected by force-calibration uncertainties (36). We use the deviations from an ideal linear relationship between our parameters and those obtained previously (35) as a measure of the joint error from both measurements (see caption of Fig. 6 and fig. S22).

The single-stack free-energy increments show a trend with respect to the chemical backbone of the nucleobases: 3' pyrimidine interfaces stacked on 5' purines [as in (CG:AT) steps] form the weakest bonds. Combinations having purines on purines and pyrimidines on pyrimidines [as in (AT:AT) base-pair steps] have intermediate stability, while 3' purine interfaces stacked on 5' pyrimidines [as in (GC:CG) or (AT:TA)] form the strongest bonds. This hierarchy is not visible in the next-neighbor base-pairing free-energy parameters derived previously from ensemble duplex melting (37), presumably because these parameters give the joint contribution from stacking and hydrogen-

bonding forces (figs. S22 and S23) (28). The trend in the stacking-strength hierarchy may be associated with the extent of geometrical atomic overlap between the bases within a base-pair step (see, for illustration, fig. S24) (28), which also holds for the outlier from the chemical backbone hierarchy trend [(CG:GC) in Fig. 6A].

The data obtained experimentally with multiple base-pair stacks in parallel enable estimating the average dissociation rates for a single stack (Fig. 6B). For the estimate, we considered the stack arrays as a two-state system with additive energies per stack, as above. The statistical treatment as a two-state system is supported by the observation that the lifetimes of many of the variants that we studied were distributed in a single exponential fashion. In particular, for arrays with six and eight stacks, deviations from a two-state-like behavior could have been expected due to large bond numbers, which was not the case. According to our estimate, the bonds between individual base-pair stacks break stochastically with average rates that vary between  $500\text{ s}^{-1}$  for the most stable (GC:CG) combination and up to  $50,000\text{ s}^{-1}$  for the most transient combinations (TA:AT), (CG:AT), and (TA:GC). The average dissociation rate per base-pair stack is on the order of 15 thousand events per second at our conditions. The dissociation and association rates are salt dependent (figs. S25 and S26). We note that the estimated single-stack dissociation rates are consistent with the high speeds at which DNA replication occurs in vivo (e.g., several thousand base pairs per second in *Escherichia coli*). Given also our finding that forces below 10 pN in the helical direction do not substantially accelerate the breaking of base-pair stacks, we speculate whether stepwise strand separation during the replication could be considered as a Brownian-ratchet-like process with forward bias, in which the enzymes involved exploit spontaneous DNA base-pair-stack opening, rather than actively breaking DNA base pairs in the helical direction. However, forces orthogonal to the helical direction could potentially have a strong influence on destacking kinetics.

Assuming that the sequence dependence of DNA double-strand formation is determined by differences in stacking and base pairing (mainly hydrogen bonding), one can use next-neighbor DNA stability parameters (37) and our stacking parameters to estimate the hydrogen bonding contribution. However, the analysis involves a salt correction (38), and the calculated hydrogen bonding contribution can only be interpreted as an extracted trend (fig. S27) (28). According to this trend, the hydrogen bonding contribution is more favorable for GC than for AT base pairs.

## Outlook

Our experimental methods that use molecularly precise DNA origami components expand the capabilities of single-molecule mechanical experiments. Target molecular surfaces may be placed and exposed in controlled orientations and stoichiometry to study the weak forces occurring between them in solution. A variety of interactions

between various kinds of molecules may be studied in the future, due to the modularity and the addressability of the DNA origami-based tethered-beam system. The sequence-resolved kinetic information obtained in our experiments may inform models of DNA hybridization that are currently being developed (39). The insights obtained about stacking forces may help adjusting force fields to perform more realistic molecular dynamics simulations (40). Our data also provides a quantitative basis for the rational design of dynamic DNA-based nanoscale machines and assemblies (7, 32, 41), because the stacking free energies and the kinetic parameters can inform the design of conformational equilibria and the timing of transition kinetics according to user specifications.

## Materials and methods Design and preparation of tethered-beam platforms

The tethered-beam platforms were designed with caDNAno v0.1 (23). The two beams were folded individually, then agarose-gel purified, dimerized, and the dimers were again agarose-gel purified. Staple oligonucleotides (each at 200 nM) and the scaffold DNA (50 nM) were mixed in folding buffer containing 1 mM EDTA, 5 mM NaCl, 5 mM TRIS-Base, and 20 mM  $\text{MgCl}_2$  at pH 8. Before the dimerization incubation, the concentration of the constructs was increased about five-fold using a PEG-precipitation step (42).

## Electrophoretic ensemble analysis

The variants were electrophoresed on agarose gels after the dimerization reaction. The gels were laser-scanned in two channels (excitation at 635 nm, emission >665 nm, and excitation at 532 nm, emission between 520 nm and 540 nm) to measure the fluorescence of the dye labels included on each of the two beams of the tethered-beam platform.

## TEM

5  $\mu\text{l}$  of sample solution was applied to the carbon side of formvar-supported plasma-cleaned Cu400 copper grids (Science services) and incubated for 0.5 to 3 min. The samples were stained with a 2% uranyl formate solution containing 25 mM sodium hydroxide. The structures were imaged with a Philips CM100 electron microscope operated at 100 kV equipped with an AMT 4 Megapixel CCD camera.

## Single-molecule measurements

Experiments were performed with a custom-built optical tweezers setup with back focal plane detection. The setup is described in detail elsewhere (24, 43). The calibration was performed as described previously (44). The measurements were conducted in a dumbbell assay (45, 46). The measurements were carried out in the presence of an oxygen scavenger system (47). State assignment was performed using either threshold analysis or using hidden Markov modeling (48). Force-dependent lifetimes of open and closed states of all measured variants were fitted with the Bell

Model (49). A previously described trap-stiffness correction was applied (30, 50).

### Molecular dynamics free-energy simulations

For the generation of the starting structure, two B-DNA duplex molecules aligned along the  $z$  axis were placed in close vicinity with respect to the backbone segment of the central nucleotides (fig. S28). The generated new strand arrangement was energy minimized and solvated [TIP3P water (51)]. Neutralization of the system by addition of counter- and coions was done using the Amber14 package (52). The motion along the dissociation direction ( $z$  direction) was controlled by a quadratic center-of-mass distance restraint between the two segments. The free-energy change along the coordinate was calculated using the weighted histogram analysis method (53). The Curves+ program (54) was used for the analysis of helical fluctuations of the construct by treating the two stacked duplexes as two continuous helices in the Curves setup.

### REFERENCES AND NOTES

- J. D. Watson, F. H. Crick, Molecular structure of nucleic acids: A structure for deoxyribose nucleic acid. *Nature* **171**, 737–738 (1953). doi: [10.1038/171737a0](https://doi.org/10.1038/171737a0); pmid: [13054692](https://pubmed.ncbi.nlm.nih.gov/13054692/)
- E. T. Kool, Hydrogen bonding, base stacking, and steric effects in DNA replication. *Annu. Rev. Biophys. Biomol. Struct.* **30**, 1–22 (2001). doi: [10.1146/annurev.biophys.30.1.1](https://doi.org/10.1146/annurev.biophys.30.1.1); pmid: [11340050](https://pubmed.ncbi.nlm.nih.gov/11340050/)
- B. H. Robinson, C. Mailer, G. Drobny, Site-specific dynamics in DNA: Experiments. *Annu. Rev. Biophys. Biomol. Struct.* **26**, 629–658 (1997). doi: [10.1146/annurev.biophys.26.1.629](https://doi.org/10.1146/annurev.biophys.26.1.629); pmid: [9241432](https://pubmed.ncbi.nlm.nih.gov/9241432/)
- Y. Yin *et al.*, Dynamics of spontaneous flipping of a mismatched base in DNA duplex. *Proc. Natl. Acad. Sci. U.S.A.* **111**, 8043–8048 (2014). doi: [10.1073/pnas.1400667111](https://doi.org/10.1073/pnas.1400667111); pmid: [24843124](https://pubmed.ncbi.nlm.nih.gov/24843124/)
- S. F. Wickham *et al.*, A DNA-based molecular motor that can navigate a network of tracks. *Nat. Nanotechnol.* **7**, 169–173 (2012). doi: [10.1038/nnano.2011.253](https://doi.org/10.1038/nnano.2011.253); pmid: [22266636](https://pubmed.ncbi.nlm.nih.gov/22266636/)
- B. Yurke, A. J. Turberfield, A. P. Mills Jr., F. C. Simmel, J. L. Neumann, A DNA-fuelled molecular machine made of DNA. *Nature* **406**, 605–608 (2000). doi: [10.1038/35020524](https://doi.org/10.1038/35020524); pmid: [10949296](https://pubmed.ncbi.nlm.nih.gov/10949296/)
- T. Gerling, K. F. Wagenbauer, A. M. Neuner, H. Dietz, Dynamic DNA devices and assemblies formed by shape-complementary, non-base pairing 3D components. *Science* **347**, 1446–1452 (2015). doi: [10.1126/science.1253372](https://doi.org/10.1126/science.1253372); pmid: [25814577](https://pubmed.ncbi.nlm.nih.gov/25814577/)
- J. J. Funke, H. Dietz, Placing molecules with Bohr radius resolution using DNA origami. *Nat. Nanotechnol.* **11**, 47–52 (2016). doi: [10.1038/nnano.2015.240](https://doi.org/10.1038/nnano.2015.240); pmid: [26479026](https://pubmed.ncbi.nlm.nih.gov/26479026/)
- H. Clausen-Schaumann, M. Rief, C. Tolksdorf, H. E. Gaub, Mechanical stability of single DNA molecules. *Biophys. J.* **78**, 1997–2007 (2000). doi: [10.1016/S0006-3495\(00\)76747-6](https://doi.org/10.1016/S0006-3495(00)76747-6); pmid: [10733978](https://pubmed.ncbi.nlm.nih.gov/10733978/)
- M. Rief, H. Clausen-Schaumann, H. E. Gaub, Sequence-dependent mechanics of single DNA molecules. *Nat. Struct. Biol.* **6**, 346–349 (1999). doi: [10.1038/7582](https://doi.org/10.1038/7582); pmid: [10201403](https://pubmed.ncbi.nlm.nih.gov/10201403/)
- S. B. Smith, Y. Cui, C. Bustamante, Overstretching B-DNA: The elastic response of individual double-stranded and single-stranded DNA molecules. *Science* **271**, 795–799 (1996). doi: [10.1126/science.271.5250.795](https://doi.org/10.1126/science.271.5250.795); pmid: [8628994](https://pubmed.ncbi.nlm.nih.gov/8628994/)
- Z. Bryant *et al.*, Structural transitions and elasticity from torque measurements on DNA. *Nature* **424**, 338–341 (2003). doi: [10.1038/nature01810](https://doi.org/10.1038/nature01810); pmid: [12867987](https://pubmed.ncbi.nlm.nih.gov/12867987/)
- J. Gore *et al.*, DNA overwinds when stretched. *Nature* **442**, 836–839 (2006). doi: [10.1038/nature04974](https://doi.org/10.1038/nature04974); pmid: [16862122](https://pubmed.ncbi.nlm.nih.gov/16862122/)
- J. M. Huguet *et al.*, Single-molecule derivation of salt dependent base-pair free energies in DNA. *Proc. Natl. Acad. Sci. U.S.A.* **107**, 15431–15436 (2010). doi: [10.1073/pnas.1001454107](https://doi.org/10.1073/pnas.1001454107); pmid: [20716688](https://pubmed.ncbi.nlm.nih.gov/20716688/)
- S. B. Smith, L. Finzi, C. Bustamante, Direct mechanical measurements of the elasticity of single DNA molecules by using magnetic beads. *Science* **258**, 1122–1126 (1992). doi: [10.1126/science.1439819](https://doi.org/10.1126/science.1439819); pmid: [1439819](https://pubmed.ncbi.nlm.nih.gov/1439819/)
- T. R. Strick, J. F. Allemand, D. Bensimon, A. Bensimon, V. Croquette, The elasticity of a single supercoiled DNA molecule. *Science* **271**, 1835–1837 (1996). doi: [10.1126/science.271.5257.1835](https://doi.org/10.1126/science.271.5257.1835); pmid: [8596951](https://pubmed.ncbi.nlm.nih.gov/8596951/)
- J. Lipfert *et al.*, Double-stranded RNA under force and torque: Similarities to and striking differences from double-stranded DNA. *Proc. Natl. Acad. Sci. U.S.A.* **111**, 15408–15413 (2014). doi: [10.1073/pnas.1407197111](https://doi.org/10.1073/pnas.1407197111); pmid: [25313077](https://pubmed.ncbi.nlm.nih.gov/25313077/)
- M. T. Woodside *et al.*, Direct measurement of the full, sequence-dependent folding landscape of a nucleic acid. *Science* **314**, 1001–1004 (2006). doi: [10.1126/science.1133601](https://doi.org/10.1126/science.1133601); pmid: [17095702](https://pubmed.ncbi.nlm.nih.gov/17095702/)
- M. T. Woodside *et al.*, Nanomechanical measurements of the sequence-dependent folding landscapes of single nucleic acid hairpins. *Proc. Natl. Acad. Sci. U.S.A.* **103**, 6190–6195 (2006). doi: [10.1073/pnas.0511048103](https://doi.org/10.1073/pnas.0511048103); pmid: [16606839](https://pubmed.ncbi.nlm.nih.gov/16606839/)
- E. Pfitzner *et al.*, Rigid DNA beams for high-resolution single-molecule mechanics. *Angew. Chem.* **52**, 7766–7771 (2013). doi: [10.1002/ange.201302727](https://doi.org/10.1002/ange.201302727); pmid: [23794413](https://pubmed.ncbi.nlm.nih.gov/23794413/)
- P. W. Rothmund, Folding DNA to create nanoscale shapes and patterns. *Nature* **440**, 297–302 (2006). doi: [10.1038/nature04586](https://doi.org/10.1038/nature04586); pmid: [16541064](https://pubmed.ncbi.nlm.nih.gov/16541064/)
- S. M. Douglas *et al.*, Self-assembly of DNA into nanoscale three-dimensional shapes. *Nature* **459**, 414–418 (2009). doi: [10.1038/nature08016](https://doi.org/10.1038/nature08016); pmid: [19458720](https://pubmed.ncbi.nlm.nih.gov/19458720/)
- S. M. Douglas *et al.*, Rapid prototyping of 3D DNA-origami shapes with caDNAno. *Nucleic Acids Res.* **37**, 5001–5006 (2009). doi: [10.1093/nar/gkp436](https://doi.org/10.1093/nar/gkp436); pmid: [19531737](https://pubmed.ncbi.nlm.nih.gov/19531737/)
- Y. von Hansen, A. Mehlich, B. Pelz, M. Rief, R. Netz, Auto- and cross-power spectral analysis of dual trap optical tweezer experiments using Bayesian inference. *Rev. Sci. Instrum.* **83**, 095116 (2012). doi: [10.1063/1.4753917](https://doi.org/10.1063/1.4753917); pmid: [23020428](https://pubmed.ncbi.nlm.nih.gov/23020428/)
- J. P. Junker, F. Ziegler, M. Rief, Ligand-dependent equilibrium fluctuations of single calmodulin molecules. *Science* **323**, 633–637 (2009). pmid: [19179531](https://pubmed.ncbi.nlm.nih.gov/19179531/)
- J. Kim, C. Z. Zhang, X. Zhang, T. A. Springer, A mechanically stabilized receptor-ligand flex-bond important in the vasculature. *Nature* **466**, 992–995 (2010). doi: [10.1038/nature09295](https://doi.org/10.1038/nature09295); pmid: [20725043](https://pubmed.ncbi.nlm.nih.gov/20725043/)
- K. Halvorsen, D. Schaak, W. P. Wong, Nanoengineering a single-molecule mechanical switch using DNA self-assembly. *Nanotechnology* **22**, 494005 (2011). doi: [10.1088/0957-4484/22/49/494005](https://doi.org/10.1088/0957-4484/22/49/494005); pmid: [22101354](https://pubmed.ncbi.nlm.nih.gov/22101354/)
- Materials and methods are available as supplementary materials on Science Online.
- E. Protopanova, P. Yakovchuk, M. D. Frank-Kamenetskii, Stacked-unstacked equilibrium at the nick site of DNA. *J. Mol. Biol.* **342**, 775–785 (2004). doi: [10.1016/j.jmb.2004.07.075](https://doi.org/10.1016/j.jmb.2004.07.075); pmid: [15342236](https://pubmed.ncbi.nlm.nih.gov/15342236/)
- P. J. Elms, J. D. Chodera, C. J. Bustamante, S. Marqusee, Limitations of constant-force-feedback experiments. *Biophys. J.* **103**, 1490–1499 (2012). doi: [10.1016/j.bpj.2012.06.051](https://doi.org/10.1016/j.bpj.2012.06.051); pmid: [23062341](https://pubmed.ncbi.nlm.nih.gov/23062341/)
- R. D. Moore, G. A. Morrill, A possible mechanism for concentrating sodium and potassium in the cell nucleus. *Biophys. J.* **16**, 527–533 (1976). doi: [10.1016/S0006-3495\(76\)85707-4](https://doi.org/10.1016/S0006-3495(76)85707-4); pmid: [1276381](https://pubmed.ncbi.nlm.nih.gov/1276381/)
- P. Ketterer, E. M. Willner, H. Dietz, Nanoscale rotary apparatus from tight-fitting 3D DNA components. *Science Advances* **2**, e1501209 (2016). doi: [10.1126/sciadv.1501209](https://doi.org/10.1126/sciadv.1501209); pmid: [26989778](https://pubmed.ncbi.nlm.nih.gov/26989778/)
- E. Evans, K. Ritchie, Dynamic strength of molecular adhesion bonds. *Biophys. J.* **72**, 1541–1555 (1997). doi: [10.1016/S0006-3495\(97\)78802-7](https://doi.org/10.1016/S0006-3495(97)78802-7); pmid: [9083660](https://pubmed.ncbi.nlm.nih.gov/9083660/)
- C. Maffeo, B. Luan, A. Aksimentiev, End-to-end attraction of duplex DNA. *Nucleic Acids Res.* **40**, 3812–3821 (2012). doi: [10.1093/nar/gkr1220](https://doi.org/10.1093/nar/gkr1220); pmid: [22241779](https://pubmed.ncbi.nlm.nih.gov/22241779/)
- A. Krueger, E. Protopanova, M. D. Frank-Kamenetskii, Sequence-dependent base pair opening in DNA double helix. *Biophys. J.* **90**, 3091–3099 (2006). doi: [10.1529/biophysj.105.078774](https://doi.org/10.1529/biophysj.105.078774); pmid: [16500982](https://pubmed.ncbi.nlm.nih.gov/16500982/)
- J. Stigler, F. Ziegler, A. Gieseke, J. C. Gebhardt, M. Rief, The complex folding network of single calmodulin molecules. *Science* **334**, 512–516 (2011). doi: [10.1126/science.1207598](https://doi.org/10.1126/science.1207598); pmid: [22034433](https://pubmed.ncbi.nlm.nih.gov/22034433/)
- J. SantaLucia Jr., D. Hicks, The thermodynamics of DNA structural motifs. *Annu. Rev. Biophys. Biomol. Struct.* **33**, 415–440 (2004). doi: [10.1146/annurev.biophys.32.110601.141800](https://doi.org/10.1146/annurev.biophys.32.110601.141800); pmid: [15139820](https://pubmed.ncbi.nlm.nih.gov/15139820/)
- R. Owczarzy, B. G. Moreira, Y. You, M. A. Behlke, J. A. Walder, Predicting stability of DNA duplexes in solutions containing magnesium and monovalent cations. *Biochemistry* **47**, 5336–5353 (2008). doi: [10.1021/bi702363u](https://doi.org/10.1021/bi702363u); pmid: [18422348](https://pubmed.ncbi.nlm.nih.gov/18422348/)
- N. Srinivas *et al.*, On the biophysics and kinetics of toehold-mediated DNA strand displacement. *Nucleic Acids Res.* **41**, 10641–10658 (2013). doi: [10.1093/nar/gkt801](https://doi.org/10.1093/nar/gkt801); pmid: [24019238](https://pubmed.ncbi.nlm.nih.gov/24019238/)
- C. Maffeo *et al.*, Close encounters with DNA. *J. Phys. Condens. Matter* **26**, 413101 (2014). doi: [10.1088/0953-8984/26/41/413101](https://doi.org/10.1088/0953-8984/26/41/413101); pmid: [25238560](https://pubmed.ncbi.nlm.nih.gov/25238560/)
- S. Woo, P. W. Rothmund, Programmable molecular recognition based on the geometry of DNA nanostructures. *Nat. Chem.* **3**, 620–627 (2011). doi: [10.1038/nchem.1070](https://doi.org/10.1038/nchem.1070); pmid: [21778982](https://pubmed.ncbi.nlm.nih.gov/21778982/)
- E. Stahl, T. G. Martin, F. Praetorius, H. Dietz, Facile and scalable preparation of pure and dense DNA origami solutions. *Angew. Chem.* **53**, 12735–12740 (2014). doi: [10.1002/anie.201405991](https://doi.org/10.1002/anie.201405991); pmid: [25346175](https://pubmed.ncbi.nlm.nih.gov/25346175/)
- G. Žoldák, J. Stigler, B. Pelz, H. Li, M. Rief, Ultrafast folding kinetics and cooperativity of villin headpiece in single-molecule force spectroscopy. *Proc. Natl. Acad. Sci. U.S.A.* **110**, 18156–18161 (2013). doi: [10.1073/pnas.1311495110](https://doi.org/10.1073/pnas.1311495110); pmid: [24145407](https://pubmed.ncbi.nlm.nih.gov/24145407/)
- S. F. Tolić-Norreykke *et al.*, Calibration of optical tweezers with positional detection in the back focal plane. *Rev. Sci. Instrum.* **77**, 103101 (2006). doi: [10.1063/1.2356852](https://doi.org/10.1063/1.2356852)
- J. W. Shaevitz, E. A. Abbondanzieri, R. Landick, S. M. Block, Backtracking by single RNA polymerase molecules observed at near-base-pair resolution. *Nature* **426**, 684–687 (2003). doi: [10.1038/nature02191](https://doi.org/10.1038/nature02191); pmid: [14634670](https://pubmed.ncbi.nlm.nih.gov/14634670/)
- S. C. Blanchard, H. D. Kim, R. L. Gonzalez Jr., J. D. Puglisi, S. Chu, tRNA dynamics on the ribosome during translation. *Proc. Natl. Acad. Sci. U.S.A.* **101**, 12893–12898 (2004). doi: [10.1073/pnas.0403884101](https://doi.org/10.1073/pnas.0403884101); pmid: [15317937](https://pubmed.ncbi.nlm.nih.gov/15317937/)
- M. P. Landry, P. M. McCall, Z. Qi, Y. R. Chemla, Characterization of photoactivated singlet oxygen damage in single-molecule optical trap experiments. *Biophys. J.* **97**, 2128–2136 (2009). doi: [10.1016/j.bpj.2009.07.048](https://doi.org/10.1016/j.bpj.2009.07.048); pmid: [19843445](https://pubmed.ncbi.nlm.nih.gov/19843445/)
- J. Stigler, M. Rief, Hidden Markov analysis of trajectories in single-molecule experiments and the effects of missed events. *ChemPhysChem* **13**, 1079–1086 (2012). doi: [10.1002/cphc.201100814](https://doi.org/10.1002/cphc.201100814); pmid: [22392881](https://pubmed.ncbi.nlm.nih.gov/22392881/)
- G. I. Bell, Models for the specific adhesion of cells to cells. *Science* **200**, 618–627 (1978). doi: [10.1126/science.347575](https://doi.org/10.1126/science.347575); pmid: [347575](https://pubmed.ncbi.nlm.nih.gov/347575/)
- W. J. Greenleaf, M. T. Woodside, E. A. Abbondanzieri, S. M. Block, Passive all-optical force clamp for high-resolution laser trapping. *Phys. Rev. Lett.* **95**, 208102 (2005). doi: [10.1103/PhysRevLett.95.208102](https://doi.org/10.1103/PhysRevLett.95.208102); pmid: [16384102](https://pubmed.ncbi.nlm.nih.gov/16384102/)
- W. L. Jorgensen, J. Chandrasekhar, J. D. Madura, R. W. Impey, M. L. Klein, Comparison of simple potential functions for simulating liquid water. *J. Chem. Phys.* **79**, 926–935 (1983). doi: [10.1063/1.445869](https://doi.org/10.1063/1.445869)
- D. A. Case *et al.*, Amber14, University of California, San Francisco, CA (2014).
- S. Kumar, J. M. Rosenberg, D. Bouzida, R. H. Swendsen, P. A. Kollman, The weighted histogram analysis method for free-energy calculations on biomolecules. 1. The method. *J. Comput. Chem.* **13**, 1011–1021 (1992). doi: [10.1002/jcc.540130812](https://doi.org/10.1002/jcc.540130812)
- R. Lavery, M. Moakher, J. H. Maddocks, D. Petkeviciute, K. Zakrzewska, Conformational analysis of nucleic acids revisited: Curves+. *Nucleic Acids Res.* **37**, 5917–5929 (2009). doi: [10.1093/nar/gkp068](https://doi.org/10.1093/nar/gkp068); pmid: [19625494](https://pubmed.ncbi.nlm.nih.gov/19625494/)
- M. Nakata *et al.*, End-to-end stacking and liquid crystal condensation of 6 to 20 base pair DNA duplexes. *Science* **318**, 1276–1279 (2007). doi: [10.1126/science.1143826](https://doi.org/10.1126/science.1143826); pmid: [18033877](https://pubmed.ncbi.nlm.nih.gov/18033877/)

### ACKNOWLEDGMENTS

We thank J. Stigler for technical assistance with data processing tools, P. Ketterer for help with illustrations, and J. P. Sobczak and J. Funke for discussions. F. Praetorius is acknowledged for scaffold DNA preparations. This work was supported by a European Research Council Starting Grant to H.D. (GA no. 256270) and by the Deutsche Forschungsgemeinschaft through grants provided within the Sonderforschungsbereich SFB863 [H.D. (project A9), M.R. (project A2), and M.Z. (project A10)] and the Gottfried-Wilhelm-Leibniz Program (to H.D.). Additional support came from the Nano Initiative Munich. F.K. was in part supported by a stipend from the Complit



program of Elitenetzwerk Bayern. Raw data that are not already included in the supplementary materials will be made available upon request. Author contributions: F.K. performed research; H.D. designed research. F.K., C.W., and H.D. analyzed and discussed data. B.P. and M.R. provided analytical tools and materials. M.Z. performed and analyzed molecular dynamics

simulations. F.K. and H.D. prepared figures and wrote the manuscript. F.K. and C.W. prepared the supplementary materials.

#### SUPPLEMENTARY MATERIALS

[www.sciencemag.org/content/353/6304/aaf5508/suppl/DC1](http://www.sciencemag.org/content/353/6304/aaf5508/suppl/DC1)  
Materials and Methods

Figs. S1 to S31  
Tables S1 to S6  
References

26 February 2016; accepted 1 July 2016  
10.1126/science.aaf5508

## RESEARCH ARTICLES

## MEMORY

# Synaptic mechanisms of pattern completion in the hippocampal CA3 network

Segundo Jose Guzman,<sup>1</sup> Alois Schlögl,<sup>1</sup> Michael Frotscher,<sup>2</sup> Peter Jonas<sup>1\*</sup>

The hippocampal CA3 region plays a key role in learning and memory. Recurrent CA3–CA3 synapses are thought to be the subcellular substrate of pattern completion. However, the synaptic mechanisms of this network computation remain enigmatic. To investigate these mechanisms, we combined functional connectivity analysis with network modeling. Simultaneous recording from up to eight CA3 pyramidal neurons revealed that connectivity was sparse, spatially uniform, and highly enriched in disynaptic motifs (reciprocal, convergence, divergence, and chain motifs). Unitary connections were composed of one or two synaptic contacts, suggesting efficient use of postsynaptic space. Real-size modeling indicated that CA3 networks with sparse connectivity, disynaptic motifs, and single-contact connections robustly generated pattern completion. Thus, macro- and microconnectivity contribute to efficient memory storage and retrieval in hippocampal networks.

The hippocampal CA3 region plays a key role in learning and memory (1–5). A hallmark property of the network is its ability to retrieve patterns from partial or noisy cues, a process referred to as autoassociative recall, attractor dynamics, or pattern completion (3–7). However, the synaptic mechanisms underlying pattern completion have remained enigmatic. Previous neuronal network models suggested that recurrent CA3–CA3 pyramidal cell synapses play a key role in this process (8–14). In the storage phase, a stimulus pattern will activate an ensemble of interconnected neurons and induce synaptic potentiation in the corresponding recurrent synapses. In the recall phase, a partial pattern will initially activate only a fraction of the ensemble, but subsequently recruit the remaining cells via potentiated synapses. Successful pattern completion requires sufficient synaptic efficacy and network connectivity (12, 14). Whether the biological properties of the CA3 network are consistent with these assumptions remains unclear.

## Analysis of functional connectivity in the CA3 network

The CA3 network is often envisaged as a network of highly interconnected neurons (3–5, 8, 11). To test this hypothesis, we analyzed functional connectivity by simultaneous recordings from up to eight CA3 pyramidal neurons in rat brain *in vitro*, followed by selective biocytin labeling (Fig. 1, A to D, and fig. S1). In comparison to recording from sequential pairs, simultaneous recording from the same number of neurons allowed us to test a

much larger number of potential synaptic connections (56 in an octuple configuration versus 8 in four sequential pairs; Fig. 1A). In total, we found 146 synaptic connections in 15,930 pairs tested (in 72 octuple, 66 septuple, 118 sextuple, 120 quintuple, 135 quadruple, 96 triple, and 495 double recordings; 4164 CA3 pyramidal neurons in 1102 slices). The huge majority of interactions were chemical, as demonstrated by block by the AMPA-type glutamate receptor antagonist CNQX; evidence for electrical coupling was found in only 1 out of 15,930 potential connections (fig. S2). Unitary excitatory postsynaptic potentials (EPSPs) had a mean latency of  $2.3 \pm 0.1$  ms, a peak amplitude of  $0.56 \pm 0.01$  mV, and a decay time constant of  $80.1 \pm 6.2$  ms (40 connections; Fig. 1, E and F, and table S1). Unitary excitatory postsynaptic currents (EPSCs) had a mean latency of  $2.2 \pm 0.1$  ms, a peak amplitude of  $17.3 \pm 2.0$  pA, and a decay time constant of  $9.5 \pm 0.6$  ms (39 connections; Fig. 1, G and H, and table S1). These results confirm and extend previous results in guinea-pig slices (15, 16).

## Macroconnectivity in the CA3 network

Our results suggested that connectivity in the CA3 cell network was sparse, with a mean connection probability of 0.92%. Both experimental data and simulations using fully reconstructed CA3 neurons labeled *in vivo* indicated that connectivity was only moderately dependent on slice orientation (materials and methods; fig. S3). However, connectivity may decline with distance (17). Furthermore, connectivity might be nonrandom, with ensembles of highly connected cells embedded in a sparsely connected population (18, 19). To test these hypotheses, we first examined whether the connection probability was dependent on intersomatic distance (Fig. 2A). The average con-

nection probability did not significantly change with distance, for intersomatic distances of up to 400  $\mu$ m (Fig. 2A). Furthermore, both EPSP and EPSC peak amplitudes were not significantly dependent on distance (fig. S4, A and B).

Next, we examined whether synaptic connectivity was random. To test this, we counted all disynaptic connectivity motifs (reciprocal connections, convergent triples, divergent triples, and disynaptic chains) in our experimental data set and compared motif numbers to those of a simulated data set assuming random connectivity and a connection probability of 0.92% (i.e., the experimental value; Fig. 2, B and C). All disynaptic connectivity motifs occurred significantly more frequently than expected by chance. The frequency of reciprocal connections, convergent triples, divergent triples, and disynaptic chains was 6.5-, 2.9-, 6.3-, and 3.4-fold higher, respectively, than the corresponding chance level (Fig. 2C;  $P \leq 0.002$  in all cases). Furthermore, we found several superconnectivity motifs (7 connections in one octuple, 10 and 3 connections in two septuples, and 3 connections in two quintuples), which were highly unlikely in random networks (Fig. 2D). As connection probability was not significantly dependent on intersomatic distance (Fig. 2A), the overabundance of motifs was not an epiphenomenon of distance dependence. Thus, connectivity in the CA3 cell network was not random, but highly enriched in connectivity motifs (17–19), reminiscent of a small-world network architecture (20). Both connection probability and abundance of motifs were similar in the range of ages tested (fig. S4, C and D). Comparison of properties of connections embedded in disynaptic motifs with those of isolated connections revealed that the EPSC peak amplitude was smaller and the proportion of failures was higher for embedded connections, whereas kinetic parameters were not significantly different (fig. S4E).

## Microconnectivity of unitary CA3–CA3 connections

Next, we analyzed the microconnectivity between pairs of synaptically connected neurons (Fig. 3). Functionally connected cells were completely reconstructed, and putative synaptic contacts between presynaptic axons and postsynaptic dendrites were identified by light microscopy (Fig. 3A). In hippocampal CA3–CA3 cell synapses, connections were formed by only one or two putative synaptic contacts. One putative contact per connection was observed in 58% of functionally connected cells (7 out of 12 connections), and two synaptic contacts were observed in the remaining 42% of cases (5 out of 12 connections; Fig. 3C). Synapses were formed at equal proportions on the hilar (proximal) and the fimbrial (distal) side of the presynaptic neuron, suggesting uniformity along the CA3a–c axis (70 and 70 out of 140 connections; Fig. 3C). Putative synaptic contacts were located on basal dendrites in 53% of connections (9 out of 17 contacts) and on apical dendrites of postsynaptic target cells in the remaining 47% of cases (8 out of 17 contacts; Fig. 3C). On average, the dendritic distance of the putative contacts

<sup>1</sup>IST Austria (Institute of Science and Technology Austria), Am Campus 1, A-3400 Klosterneuburg, Austria. <sup>2</sup>Center for Molecular Neurobiology Hamburg, Falkenberg 94, D-20251 Hamburg, Germany. \*Corresponding author. Email: peter.jonas@ist.ac.at



from the center of the soma of the postsynaptic target cell was  $141 \pm 15 \mu\text{m}$  (12 reconstructed pairs; Fig. 3D). Thus, in contrast to the neocortex (21–23), synaptically interconnected CA3 pyramidal neurons showed only one or two morphological contacts per connection.

To determine the number of functional release sites and the corresponding release probability, we recorded EPSPs and EPSCs in physiological extracellular solution containing  $2 \text{ mM Ca}^{2+}$ , and in either reduced ( $1 \text{ mM}$ ) or elevated ( $4 \text{ mM}$ ) extracellular  $\text{Ca}^{2+}$  concentration (Fig. 3, E and

F). The entire peak amplitude data set was fit with a binomial release model in which quantal size and number of functional release sites were assumed to be the same for the two conditions, whereas release probability was specified separately (see materials and methods). Multiple probability binomial analysis revealed that the mean number of functional release sites was  $3.2 \pm 0.8$  and that the corresponding release probability with a physiological extracellular  $\text{Ca}^{2+}$  concentration was  $0.37 \pm 0.04$  (15 connections total; Fig. 3, E and F, and table S2). Thus, synaptic

transmission at CA3–CA3 synapses was mediated by few functional release sites with a relatively high release probability (24, 25). Hence, in contrast to the neocortex (21–23, 26), hippocampal CA3 pyramidal cells often communicated with each other via a small number of functional release sites.

### Efficacy and summation of unitary synaptic events

The sparse connectivity in the CA3 cell network raises the question of how few CA3 pyramidal cells efficiently recruit their postsynaptic targets,

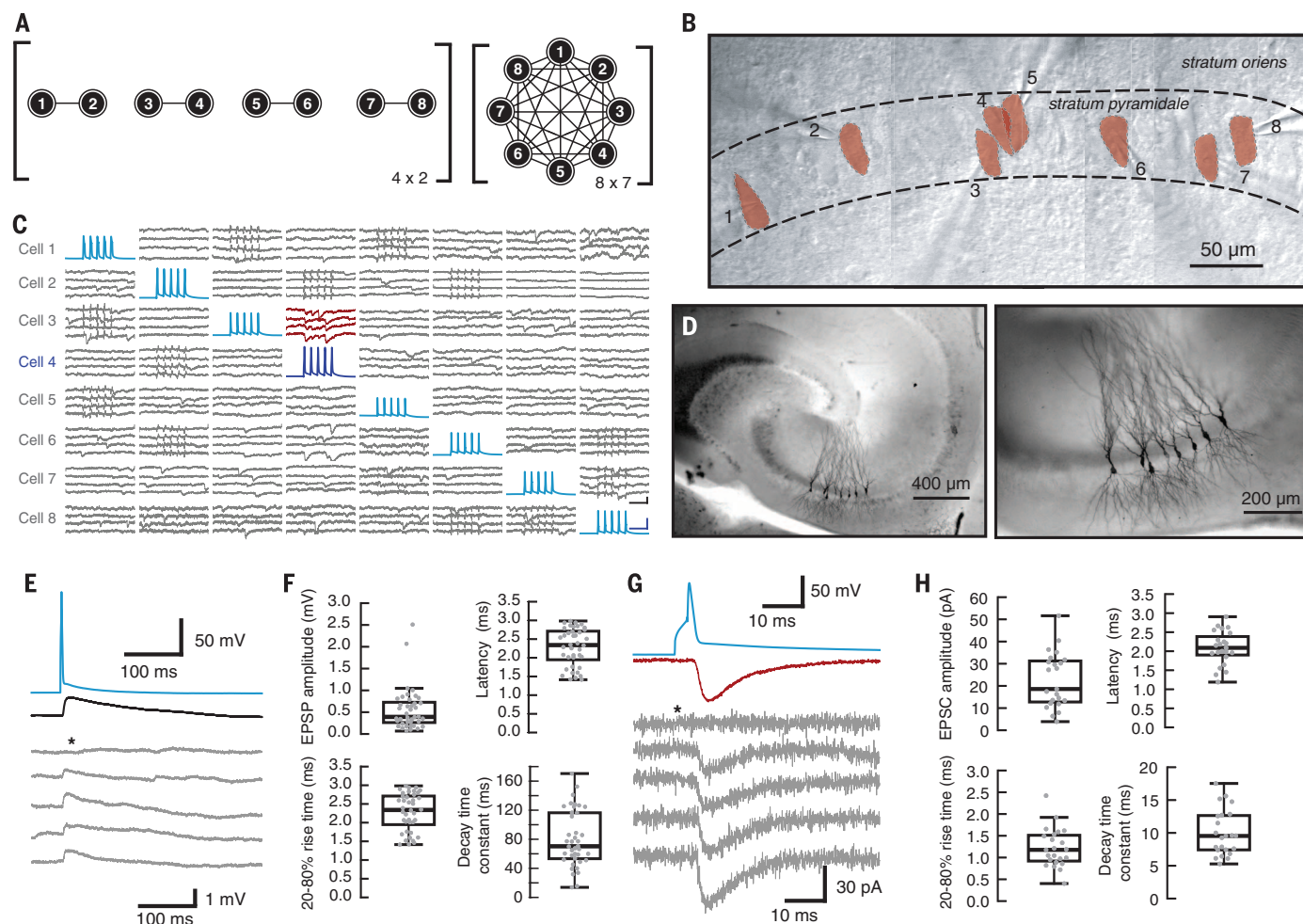


**Fig. 1. Octupole recording in the CA3 cell network.** (A) Advantage of the octupole recording configuration. In sequential paired recordings from eight cells (left),  $4 \times 2 = 8$  potential connections can be examined. In a simultaneous octupole recording (right),  $8 \times 7 = 56$  potential connections can be tested. (B) Infrared differential interference contrast videomicrograph of the hippocampal CA3b region in a thick-slice preparation, with eight recording electrodes attached to the somata of putative pyramidal neurons. Red areas represent the two-dimensional (2D) projections of cell bodies. (C) Functional connectomics in the CA3 pyramidal neuron network. Each column represents single traces from eight cells; number code as shown in (B). In each of the eight columns, a different cell was stimulated by a series of five current pulses in current-clamp (blue traces), while the other cells were recorded in the voltage-clamp configuration (gray traces). In this octupole recording, cell 4 (dark blue trace) was connected to cell 3 (red traces). Scale bars, 50 mV or 10 pA, 10 ms (bottom, right). Brief transients in a subset of traces represent capacitive coupling artifacts, as reported in previous publications [e.g., (47)]. (D) Light micrograph

of a biocytin-labeled octupole (maximal intensity projection stack; left panel, low magnification; right panel, high magnification). Eight CA3 pyramidal neurons in area CA3b were filled with biocytin during whole-cell recording and labeled with 3,3'-diaminobenzidine as chromogen. Data in (B) to (D) were obtained from different octupoles. For the octupole shown in (D), all eight cells were labeled with biocytin for illustration purposes, i.e., selective labeling (fig. S1) was not performed. (E and F) Properties of unitary EPSPs at CA3–CA3 synapses. (E) Representative traces. Top, presynaptic action potential; center, average EPSP; bottom, individual EPSPs. (F) Summary graphs of EPSP peak amplitude, latency, 20 to 80% rise time, and decay time constant. (G and H) Similar graphs to those in (E) and (F), but for EPSCs. Asterisks in (E) and (G) indicate failures. In box plots, horizontal lines represent median; boxes, quartiles; whiskers, most extreme data points  $\leq 1.5$  interquartile range from box edges; and single points, data from individual experiments. Throughout this Article, presynaptic action potentials are shown in blue, EPSPs in black, and EPSCs in red.

as required for pattern completion. To address this question, we explored the properties of unitary postsynaptic conductance (Fig. 4). To estimate peak amplitude and time course of the postsynaptic conductance in the dendrite, we first determined the location of putative synaptic contacts in post-hoc labeled pairs. We then reconstructed the somatodendritic morphology of the postsynaptic CA3 pyramidal neuron and converted it into a detailed cable model (Fig. 4A). Finally, we simulated EPSCs, varying latency, rise time constant, peak amplitude, and decay time constant of the postsynaptic conductance until the best fit of the experimentally recorded average somatic EPSCs was obtained. Experimentally constrained modeling revealed a rise time constant of  $0.26 \pm 0.07$  ms, a peak conductance of  $0.54 \pm 0.12$  nS, and a decay time constant of  $6.71 \pm 1.46$  ms (10 connections; Fig. 4, B and C). Considering the single-channel conductance of dendritic AMPARs in CA3 pyramidal neurons (10 pS) (27) and a mean number of 3.2 functional release sites (Fig. 3F), this peak conductance corresponded to 17 AMPARs per site open at the peak of an EPSC (28). Thus, a large number of postsynaptic

AMPA receptors contributed to synaptic efficacy at recurrent CA3–CA3 synapses.

Because a single unitary EPSP could not fire a postsynaptic CA3 cell (Fig. 1, E and F), we next examined the rules of temporal and spatial summation. To quantify temporal summation, we measured EPSPs evoked by repetitive stimulation of the presynaptic cell, using high-frequency trains of five or ten stimuli (Fig. 4D), which mimics burst activity of CA3 pyramidal cells in vivo (29). EPSPs showed substantial summation during repetitive stimulation. For 20-, 50-, and 100-Hz trains of five presynaptic action potentials, the ratio of  $\text{EPSP}_{\text{max}}/\text{EPSP}_1$  was  $1.58 \pm 0.28$ ,  $2.25 \pm 0.49$ , and  $5.17 \pm 2.50$ , respectively (3, 10, and 4 connections). Thus, for high-frequency stimulation, temporal summation was nearly linear, with a maximal depolarization proportional to the number of spikes in the presynaptic neuron. Both the slow decay time constant of EPSPs (Fig. 1, E and F, and table S1) and the minimal synaptic depression during repetitive stimulation (fig. S5) contributed to efficient temporal summation.

To probe spatial summation, we stimulated two presynaptic cells converging on the same

postsynaptic neuron. Costimulation of the presynaptic cells with 50-Hz trains of stimuli led to compound EPSPs almost indistinguishable from the arithmetic sum of individual unitary EPSPs (Fig. 4D). Thus, spatial summation had approximately linear characteristics (30, 31). To determine the number of convergent presynaptic inputs necessary to drive the cell to firing threshold, we plotted the depolarization evoked by train stimulation against the number of stimulated inputs, and determined the number of inputs required for spiking from the intersection of a regression line with the action potential threshold (Fig. 4, E and F, and table S1). With a mean resting potential of  $-68.2 \pm 1.0$  mV and a mean action potential voltage threshold of  $-36.1 \pm 1.6$  mV, we estimated that  $7.3 \pm 1.9$  coactive convergent inputs were required to initiate action potentials in a postsynaptic CA3 cell for 50-Hz stimulation. In the presence of ongoing synaptic activity in vivo, we estimated that 3.3 inputs would be required (29). Thus, the large number of postsynaptic AMPARs and the efficient temporal and spatial summation underlie the efficacy of synaptic signaling at CA3–CA3 pyramidal neuron synapses.

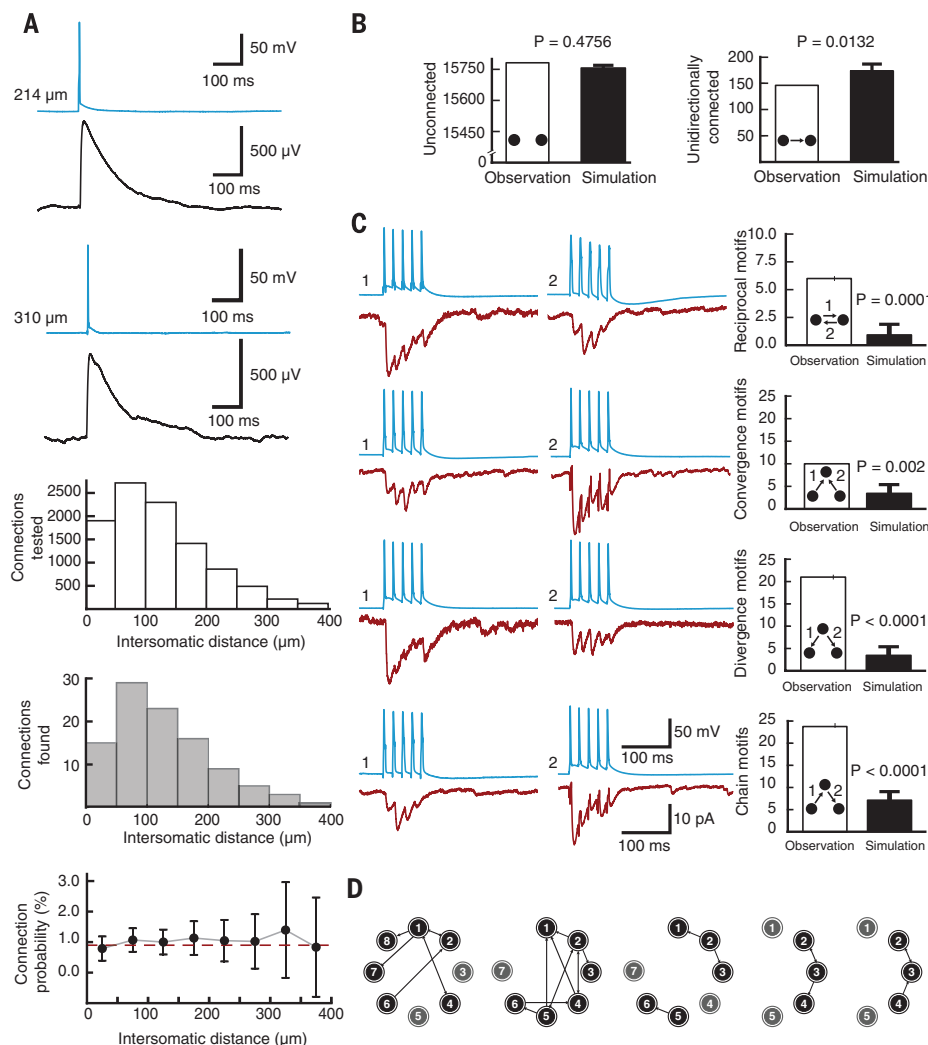


**Fig. 2. Macroconnectivity of the CA3 cell network: Sparse and spatially uniform connectivity with overabundance of connectivity motifs.**

(A) Analysis of dependence of connection probability on intersomatic distance. Top, traces of action potentials and average unitary EPSCs at two different distances (214 and 310  $\mu\text{m}$ ). Center, histogram of number of connections tested (white bars) and functional connections detected (gray bars). Bottom, connection probability, determined as the ratio of connections detected to connections tested, plotted versus distance. Error bars represent 95% confidence intervals estimated from a binomial distribution. Red dashed line indicates the mean connection probability (0.92%). (B) Number of unconnected and unidirectionally connected pairs. Bar graphs show the number of a given motif in the experimental sample (open bars) and the predicted number in a network with random connectivity and mean connection probability of 0.92% (filled bars). Data from 10,000 simulations; error bars indicate SD. (C) Overabundance of disynaptic connectivity motifs: reciprocally connected pairs, convergence motifs, divergence motifs, and chains (from top to bottom). Left, traces of action potentials and average unitary EPSCs. Right, summary bar graphs.  $P$  values are indicated above the simulation bar. The probability of experimentally observed connectivity motifs was significantly higher than expected by chance. (D) Detailed maps of super-connectivity motifs in our data set (7 connections in one octuple; 10 and 3 connections in two septuples; 3 connections in two quintuples). The probability that such connectivity motifs occur by chance is negligibly small.

### Biologically constrained network models of pattern completion

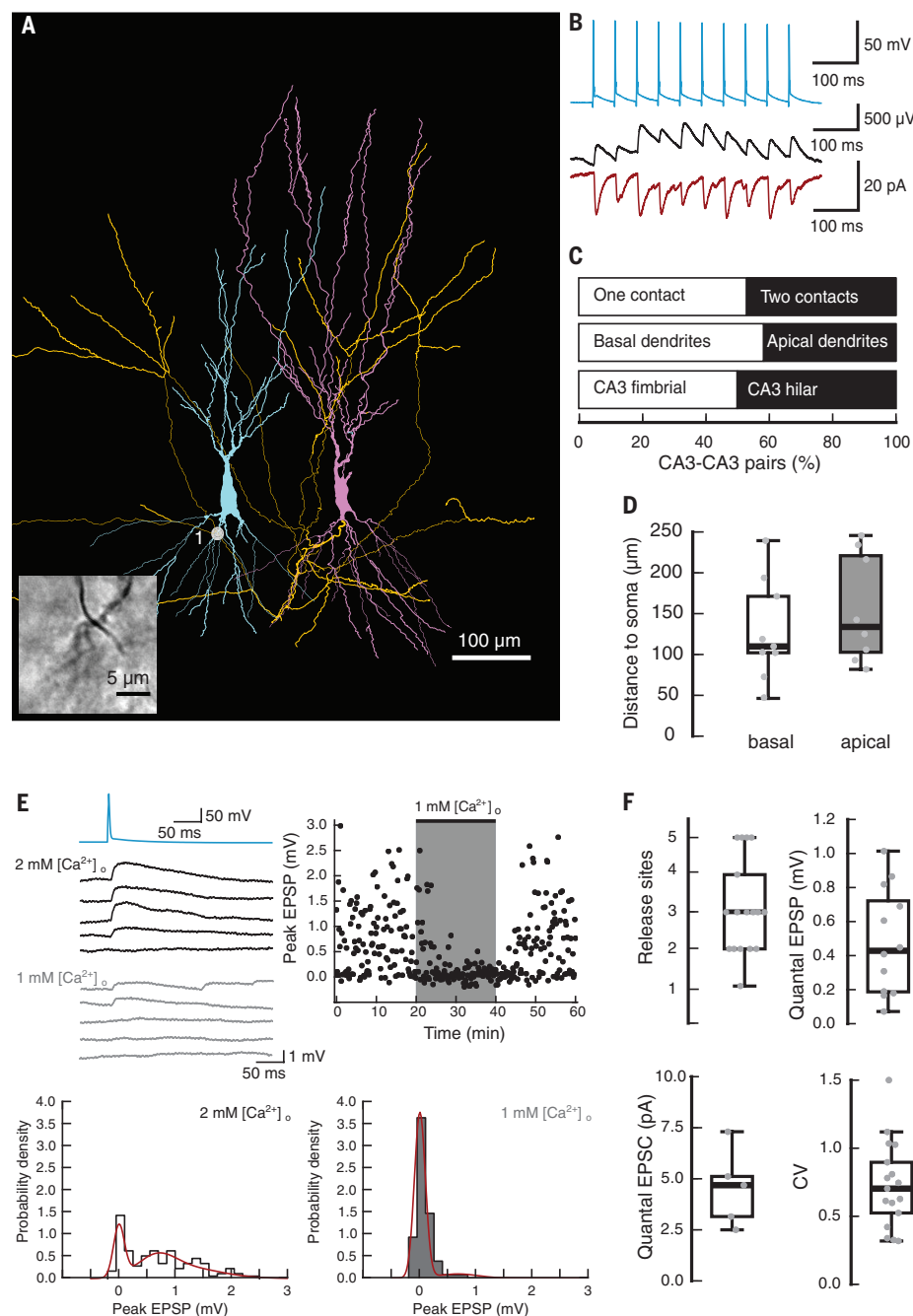
The present experimental findings challenged several assumptions of previous pattern completion models (3–5, 9, 14). First, the low average connectivity may compromise pattern completion. Second, the small number of synaptic contacts per connection will introduce synaptic noise, which may impair pattern completion (14). To examine how the experimentally determined properties of CA3–CA3 cell synapses affect pattern completion, we developed a real-size model of the hippocampal CA3 cell network (Fig. 5). The total number of neurons was 330,000, representing the

CA3 network of one hemisphere (32). Synaptic plasticity was implemented according to a clipped Hebbian rule (8), in agreement with recent experimental results at CA3–CA3 synapses (33). The firing threshold was set according to the observation that  $\geq 3$  synaptic inputs were necessary to activate a postsynaptic neuron (Fig. 4F) (29). An increasing number of random patterns was stored in the network, and recall was tested with degraded patterns (see materials and methods, fig. S6, and table S3). We first examined a network with a connection probability ( $p$ ) of 3% and an activity level ( $f$ ) of 0.001 (i.e., 330 active neurons per pattern). Such a network model produced

robust pattern completion (capacity  $\sim 45,000$  patterns; Fig. 5B, left). Variation of the activity level confirmed that  $f = 0.001$  provided favorable conditions for recall (fig. S7), as previously suggested (14).

Next, we examined how macroconnectivity affected pattern completion. When the connection probability in a random network was reduced, pattern completion was impaired ( $p = 1.5\%$ ; Fig. 5B, center) or completely abolished ( $p = 1\%$ ; Fig. 5B, right). Increasing the activity level ( $f = 0.002$ ) partially rescued pattern completion (capacity  $\sim 8200$  patterns; Fig. 5C, left), although recall was only possible in a narrow range of

**Fig. 3. Microconnectivity of the CA3 cell network: A small number of morphological contacts and functional release sites per unitary connection.** (A) Digital reconstruction of a functionally connected CA3–CA3 pair based on the post-hoc biocytin labeling. Soma and dendrites of presynaptic cell are shown in magenta, axon of presynaptic cell is in yellow, soma and dendrites of postsynaptic cell are in cyan. Gray dot indicates putative synaptic contact; inset shows light micrograph of the contact. (B) Unitary EPSPs and EPSCs from the same morphologically reconstructed neuron. Upper traces represent presynaptic action potentials, center traces average unitary EPSPs, and bottom traces average unitary EPSCs. (C) Summary bar graphs of number of putative contacts per connection (top), number of contacts on basal versus apical dendrites (center), and number of contacts on the fimbrial = distal versus hilar = proximal regions (from the perspective of the presynaptic neuron). (D) Dendritic distance of putative contacts on the basal (left) and the apical (right) dendrites of the postsynaptic cell. (E) A small number of functional release sites revealed by changing the extracellular  $\text{Ca}^{2+}$  concentration. Top left, single EPSP traces during standard (2 mM  $\text{Ca}^{2+}$ , black) and low-release probability conditions (1 mM  $\text{Ca}^{2+}$ , gray). Top right, plot of EPSP peak amplitude against experimental time at CA3–CA3 synapses during reduction of the extracellular  $\text{Ca}^{2+}$  concentration (gray area). Bottom, histogram of EPSP peak amplitude under standard (2 mM  $\text{Ca}^{2+}$ ; left) and low-release probability conditions (1 mM  $\text{Ca}^{2+}$ ; right). Red curve shows the results of multiple probability binomial analysis. Changing the extracellular  $\text{Ca}^{2+}$  concentration markedly altered the proportion of failures and successes, but had relatively small effects on the amplitude of successes, suggesting a small number of functional release sites. (F) Summary graph of number of release sites (top, left), quantal EPSP amplitude (top, right), quantal EPSC amplitude (bottom, left), and coefficient of variation (bottom, right). In box plots, horizontal lines represent median; boxes, quartiles; whiskers, most extreme data points  $\leq 1.5$  interquartile range from box edges; and single points, data from individual experiments.





inhibition. Incorporation of reciprocal, convergence, divergence, and chain motifs (34) also rescued pattern completion (capacity ~3600 patterns; Fig. 5C, center); recall was possible over a wide range of inhibition. Addition of reciprocal, convergence, and divergence motifs (i.e., all except chain motifs) failed to rescue pattern completion, showing that chain motifs played a critical role (Fig. 5C, right; fig. S8). Incorporation of all motifs also rescued pattern completion for  $p = 1.5\%$ , but reduced capacity for  $p = 3\%$  (fig. S9), showing that motifs selectively enhanced network performance in combination with sparse connectivity. Similar conclusions were reached in network models with limited projection along the longitudinal axis (35, 36) (fig. S10) and in network models with  $2 \times 330,000$  neurons and contralateral projections (fig. S11, A and B). In contrast, pattern completion was impaired in network models with  $1/3 \times 330,000$  neurons, suggesting that isolated CA3b subnetworks were insufficient for pattern completion (fig. S11, C and D).

Finally, we tested how microconnectivity affected pattern completion. Two opposite predictions can be made. First, increasing the number of synaptic contacts per connection will reduce the coefficient of variation (CV) of synaptic transmission, which may enhance pattern completion (14). Second, increasing the number of contacts per connection would reduce the effective connectivity, because presynaptic terminals have to compete for space on dendritic spines of postsynaptic target cells. This may decrease network capacity (Fig. 5B). To assess the relative importance of these effects, we introduced synaptic variability in our simulations. With a connection probability of 3% and a CV of 1, pattern completion worked reliably (capacity ~7000 patterns; Fig. 5D, center). Reducing the CV improved pattern completion (capacity ~22,000 patterns; Fig. 5D, left). However, reducing CV and connectivity in combination abolished pattern completion (capacity close to 0; Fig. 5D, right). Therefore, single-contact synapses with high variability were

better suited for pattern completion than multi-contact synapses with low variability.

## Discussion

Previous theories of the hippocampal formation often depicted the CA3 region as a network of highly interconnected cells, in which connectivity is all-to-all, random, or distance dependent (3–5, 8, 9, 11, 14, 37). Our experimental results challenge this view in multiple ways. First, the macroconnectivity in the CA3 cell network is sparse, spatially uniform, and highly enriched in disynaptic connectivity motifs. This is different from the neocortex, where connection probability is higher (~10%), more distance dependent, and less enriched in disynaptic motifs (17, 18, 22, 38). Second, the microconnectivity in individual CA3–CA3 connections is characterized by a small number of synaptic contacts and functional release sites per connection. Again, this is different from the neocortex, where unitary synaptic interactions involve a large number of contacts (up to eight in

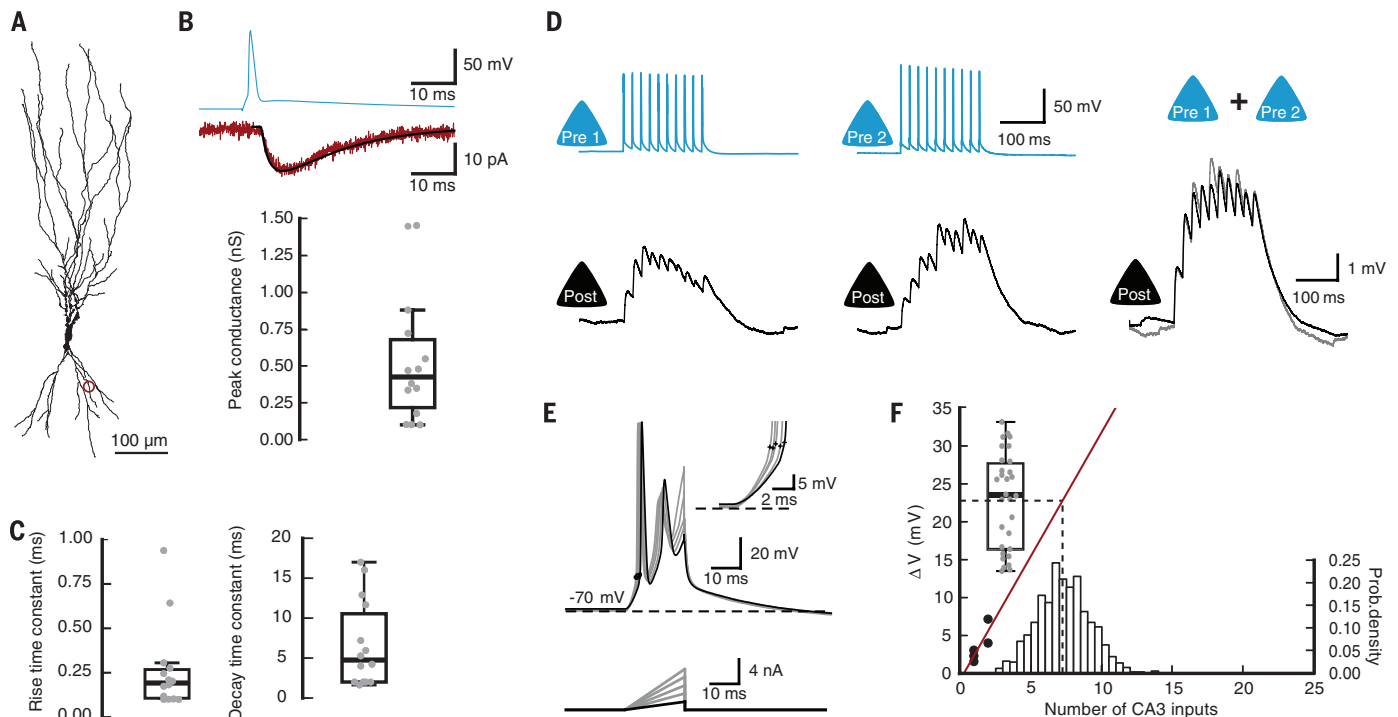
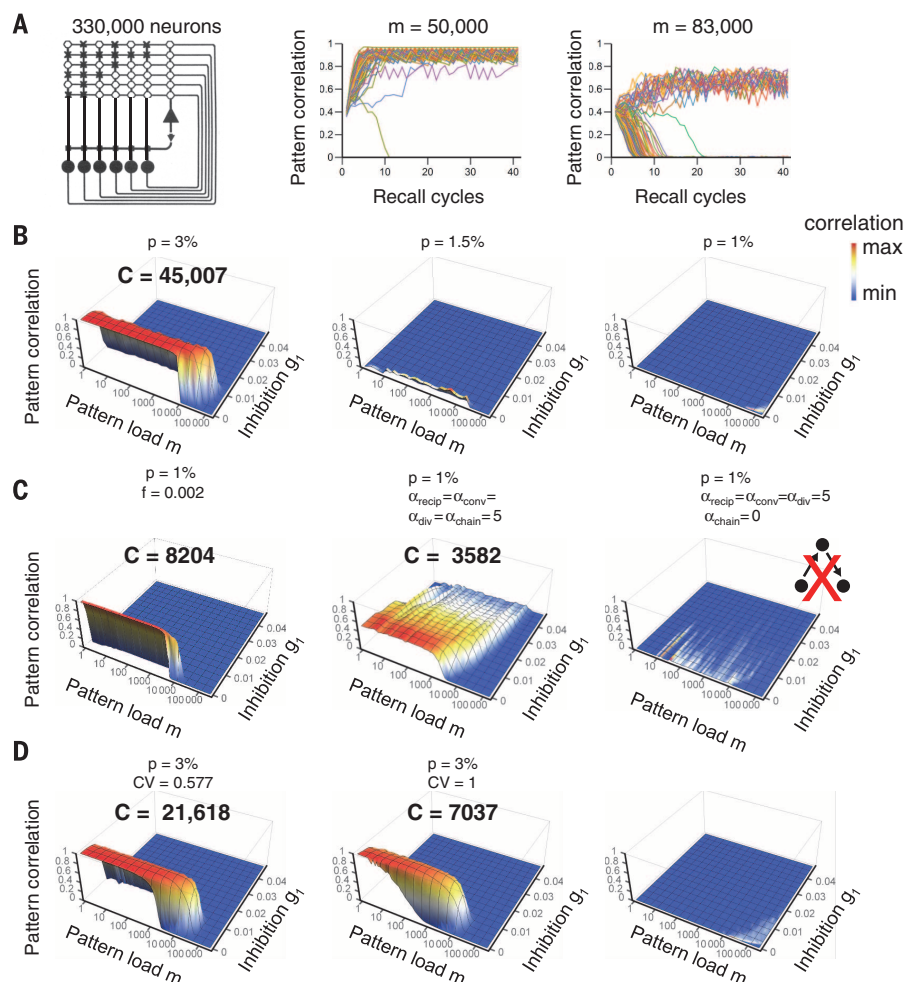


**Fig. 4. Synaptic efficacy at recurrent CA3–CA3 synapses: Large post-synaptic conductance and efficient summation.** (A) Analysis of postsynaptic conductance. Digital reconstruction of soma and dendrites of the postsynaptic cell in a synaptically connected CA3–CA3 pair based on the post-hoc biocytin labeling. Red circle indicates the putative synaptic contact. (B) Unitary EPSCs and estimated peak conductance. Latency, rise time constant, peak amplitude, and decay time constant were fit as free parameters. Top, presynaptic action potential and average EPSC (red trace), superimposed with the results of the postsynaptic conductance fit (black curve). Bottom, summary graph of peak conductance. (C) Rise time and decay time constant of the postsynaptic conductance. (D) Efficient temporal and spatial summation at CA3–CA3 synapses. Left, EPSPs evoked by repetitive stimulation of the presynaptic neuron (10 stimuli applied at a frequency of 50 Hz). Center, EPSPs evoked by repetitive stimulation of another presynaptic neuron converging on the same postsynaptic cell. Right, EPSPs evoked by simultaneous repetitive stimulation of both presynaptic neurons

(black), superimposed with the arithmetic sum of the individual responses (gray). The two curves superimpose, indicating linear summation. In left and center subpanels, the top trace shows the presynaptic action potential, and the bottom trace represents the average EPSP. (E) Analysis of voltage threshold of action potential initiation. A ramp protocol was used to determine the action potential voltage threshold (criterion  $20 \text{ V s}^{-1}$ , small crosses). (F) Plot of summated EPSP amplitude (50 Hz stimulation) against number of stimulated inputs (black circles). Voltage threshold values are shown for comparison (gray circles). Continuous red line indicates the results of linear regression of summation data. Dashed lines indicate mean number of inputs required to fire a postsynaptic CA3 pyramidal cell and the corresponding mean action potential threshold value. Histogram depicts the distribution of the estimated number of inputs required to fire the postsynaptic cell under in vitro conditions. In box plots, horizontal lines represent median; boxes, quartiles; whiskers, most extreme data points  $\leq 1.5$  interquartile range from box edges; and single points, data from individual experiments.

**Fig. 5. Pattern completion in a CA3 network model with sparse connectivity, disynaptic connectivity motifs, and single-contact synapses.** (A) Left, schematic illustration of network topology. Large filled circles, principal neurons; large filled triangle, inhibitory interneuron; small open circles, potentiated synapses; small crosses, unpotentiated synapses. Center, correlation between actual and stored patterns, plotted against the number of the recall cycle. Pattern load was  $m = 50,000$  (center) and  $83,000$  (right), respectively; connection probability  $p = 3\%$ ; inhibition factor  $g_1 = 0.0072$ ; random connectivity in both cases. Lines with different colors represent trajectories for 100 random patterns. (B) Dependence of pattern completion in an autoassociative memory network model on network connectivity. Connection probability was  $p = 3\%$  [left; corresponding plot of pattern correlation against recall cycle shown in (A)],  $1.5\%$  (center), and  $1\%$  (right); random connectivity in all cases; average activity level  $f = 0.001$ . The 3D plots indicate average correlation between original patterns and retrieved patterns, plotted against pattern load ( $m$ ) and inhibition factor ( $g_1$ ). Height of the correlation plot is color coded, with red representing maximal and blue minimal correlation (see pseudocolor scale bar on top right). Performance of the pattern completion network was high for a connection probability of  $3\%$ , but declined as connectivity was reduced. (C) Increasing activity and introducing connectivity motifs rescued pattern completion in sparsely connected networks. A 3D plot of correlation against pattern load ( $m$ ) and inhibition factor ( $g_1$ ). Left,  $p = 1\%$  combined with increased activity ( $f = 0.002$ ). Center,  $p = 1\%$  combined with high abundance of motifs ( $\alpha_{\text{recip}} = \alpha_{\text{conv}} = \alpha_{\text{div}} = \alpha_{\text{chain}} = 5$ ). Right,  $p = 1\%$  combined with selective elimination of chain motifs ( $\alpha_{\text{recip}} = \alpha_{\text{conv}} = \alpha_{\text{div}} = 5$ ;  $\alpha_{\text{chain}} = 0$ ).  $\alpha$  quantifies how much the frequency of a motif exceeds the corresponding value for a random network. (D) Reducing the CV and connection probability, as may occur during the transition from single-contact to multicontact synapses, alters network performance. Center, synaptic CV = 1, connection probability  $p = 3\%$ . Left, effects of reducing CV without change in effective connectivity ( $CV = 1/\sqrt{3} = 0.577$ ;  $p = 3\%$ ). Right, effects of correlated changes of CV and effective connectivity, with the total number of synapses kept constant ( $CV = 1/\sqrt{3} = 0.577$ ;  $p = 1\%$ ). Random connectivity in all cases; average activity level  $f = 0.001$ . The effects of connectivity dominated over those of CV. All simulations were performed with the real-size network (330,000 neurons with standard parameters). Sparse activity ( $f = 0.001$ ) in all cases except panel C, left. For details, see materials and methods and table S3.



layer 5–layer 5 pyramidal neuron pairs) (21–23, 26). Finally, despite the small number of synaptic contacts, the efficacy of unitary connections is high. Therefore, coincident firing of a small number of presynaptic cells is sufficient to initiate action potentials in a postsynaptic cell. Thus, the properties of recurrent CA3–CA3 synapses allow efficient encoding of information by small neuronal ensembles.

Our results give important insights into the synaptic mechanisms of pattern completion. First, they provide a proof of principle that real-size networks with a realistic connection probability of  $1\%$  can perform pattern completion. Second, they demonstrate that connectivity motifs increase the efficacy and robustness of recall under conditions of sparse connectivity and sparse activity. Intuitively, incorporation of motifs will increase the variance in the number of inputs and outputs of each cell, which will facilitate the spread of activity in the network and thereby enhance the robustness of recall (14). Finally, they

suggest that the design of CA3–CA3 synapses with few synaptic contacts per connection is favorable, because it enables maximally efficient use of postsynaptic space. Thus, both macro- and microconnectivity facilitate pattern completion in the CA3 cell network. Similar conclusions were independently reached in a theoretical study, which deduced sparse connectivity and high motif abundance from the assumption of maximal storage capacity (39).

The mechanisms generating the motif structure are currently unknown. Anisotropy of axonal connections may contribute, but it is unlikely to be the only factor. One possibility is that connectivity motifs are formed during development, connecting clonally related groups of sister cells (40, 41). Alternatively, the motifs may arise from structural plasticity in synchronously active neuronal ensembles (33, 42). Because mossy fiber synapses may “detonate” postsynaptic CA3 pyramidal neurons (43, 44), CA3 neurons innervated by the same mossy fiber axon might become preferen-

tially connected through activity-dependent synaptic plasticity. This would provide a structured connection between pattern separation circuits of the dentate gyrus and pattern completion networks of the CA3 region (37). Similarly, CA3 neurons targeted by the same entorhinal inputs could become connected. Finally, the CA3 connectome may be altered during chronic inactivity (45) or brain diseases (46). How this would affect pattern completion in the network remains to be determined.

## REFERENCES AND NOTES

1. H. Eichenbaum, *Neuron* **44**, 109–120 (2004).
2. R. P. Kesner, *Learn. Mem.* **14**, 771–781 (2007).
3. B. L. McNaughton, R. G. M. Morris, *Trends Neurosci.* **10**, 408–415 (1987).
4. A. Treves, E. T. Rolls, *Hippocampus* **4**, 374–391 (1994).
5. J. E. Lisman, *Neuron* **22**, 233–242 (1999).
6. K. Nakazawa, T. J. McHugh, M. A. Wilson, S. Tonegawa, *Nat. Rev. Neurosci.* **5**, 361–372 (2004).
7. J. P. Neunuebel, J. J. Knierim, *Neuron* **81**, 416–427 (2014).

8. D. J. Willshaw, O. P. Buneman, H. C. Longuet-Higgins, *Nature* **222**, 960–962 (1969).
9. D. Marr, *Philos. Trans. R. Soc. Lond. B Biol. Sci.* **262**, 23–81 (1971).
10. G. Palm, *Biol. Cybern.* **36**, 19–31 (1980).
11. J. J. Hopfield, *Proc. Natl. Acad. Sci. U.S.A.* **79**, 2554–2558 (1982).
12. H. Sompolinsky, *Phys. Rev. A Gen. Phys.* **34**, 2571–2574 (1986).
13. D. J. Amit, H. Gutfreund, H. Sompolinsky, *Phys. Rev. A* **35**, 2293–2303 (1987).
14. M. R. Bennett, W. G. Gibson, J. Robinson, *Philos. Trans. R. Soc. Lond. B Biol. Sci.* **343**, 167–187 (1994).
15. R. Miles, R. K. S. Wong, *J. Physiol.* **373**, 397–418 (1986).
16. R. D. Traub, R. Miles, *Neuronal Networks of the Hippocampus*. (Cambridge Univ. Press, Cambridge, 1991).
17. R. Perin, T. K. Berger, H. Markram, *Proc. Natl. Acad. Sci. U.S.A.* **108**, 5419–5424 (2011).
18. S. Song, P. J. Sjöström, M. Reigl, S. Nelson, D. B. Chklovskii, *PLOS Biol.* **3**, e68 (2005).
19. S. Rieubland, A. Roth, M. Häusser, *Neuron* **81**, 913–929 (2014).
20. D. J. Watts, S. H. Strogatz, *Nature* **393**, 440–442 (1998).
21. J. Lübke, H. Markram, M. Frotscher, B. Sakmann, *J. Neurosci.* **16**, 3209–3218 (1996).
22. H. Markram, J. Lübke, M. Frotscher, A. Roth, B. Sakmann, *J. Physiol.* **500**, 409–440 (1997).
23. T. Branco, K. Staras, *Nat. Rev. Neurosci.* **10**, 373–383 (2009).
24. A. I. Gulyás et al., *Nature* **366**, 683–687 (1993).
25. N. Holderith et al., *Nat. Neurosci.* **15**, 988–997 (2012).
26. R. A. Silver, J. Lübke, B. Sakmann, D. Feldmeyer, *Science* **302**, 1981–1984 (2003).
27. N. Spruston, P. Jonas, B. Sakmann, *J. Physiol.* **482**, 325–352 (1995).
28. Z. Nusser et al., *Neuron* **21**, 545–559 (1998).
29. J. Kowalski, J. Gan, P. Jonas, A. J. Pernia-Andrade, *Hippocampus* **26**, 668–682 (2016).
30. S. Cash, R. Yuste, *Neuron* **22**, 383–394 (1999).
31. S. Kim, S. J. Guzman, H. Hu, P. Jonas, *Nat. Neurosci.* **15**, 600–606 (2012).
32. D. G. Amaral, N. Ishizuka, B. Claiborne, *Prog. Brain Res.* **83**, 1–11 (1990).
33. R. K. Mishra, S. Kim, S. J. Guzman, P. Jonas, *Nat. Commun.* **7**, 11552 (2016).
34. L. Zhao, B. Beverlin 2nd, T. Netoff, D. Q. Nykamp, *Front. Comput. Neurosci.* **5**, 28 (2011).
35. X. G. Li, P. Somogyi, A. Ylinen, G. Buzsáki, *J. Comp. Neurol.* **339**, 181–208 (1994).
36. M. P. Witter, *Learn. Mem.* **14**, 705–713 (2007).
37. E. T. Rolls, *Front. Syst. Neurosci.* **7**, 74 (2013).
38. S. Lefort, C. Tómm, J. C. Floyd Sarria, C. C. Petersen, *Neuron* **61**, 301–316 (2009).
39. N. Brunel, *Nat. Neurosci.* **19**, 749–755 (2016).
40. Y. Deguchi, F. Donato, I. Galimberti, E. Cabuy, P. Caroni, *Nat. Neurosci.* **14**, 495–504 (2011).
41. Y. C. Yu, R. S. Bultje, X. Wang, S. H. Shi, *Nature* **458**, 501–504 (2009).
42. F. Engert, T. Bonhoeffer, *Nature* **399**, 66–70 (1999).
43. D. A. Henze, L. Wittner, G. Buzsáki, *Nat. Neurosci.* **5**, 790–795 (2002).
44. N. P. Vyleta, P. Jonas, *Science* **343**, 665–670 (2014).
45. A. Mitra, S. S. Mitra, R. W. Tsien, *Nat. Neurosci.* **15**, 250–257 (2011).
46. J. E. Hanson, M. Blank, R. A. Valenzuela, C. C. Garner, D. V. Madison, *J. Physiol.* **579**, 53–67 (2007).
47. J. J. Couey et al., *Nat. Neurosci.* **16**, 318–324 (2013).

## ACKNOWLEDGMENTS

We thank A. Aertsen, J. Csicsvari, A. Roth, C. Savin, R. Shigemoto, and two anonymous reviewers for critically reading the manuscript, as well as J. Szabadics and S. Rotter for useful discussions. We are grateful to F. Marr for excellent technical assistance, B. Joch for help with morphological analysis, E. Kramberger for manuscript editing, T. Asenov (Miba machine shop) for technical support, and M. Schunn (preclinical facility) for animal maintenance. We also thank the scientific computing facilities, University of Innsbruck, for help with the MACH computer cluster. Finally, we thank D. Nykamp for providing programs and G. Buzsáki,

L. Wittner, G. Ascoli, and D. Ropireddy for sharing CA3 pyramidal neuron models. Supported by the Fond zur Förderung der Wissenschaftlichen Forschung (P 24909-B24 to P.J.), the European Union (European Research Council Advanced Grant 268548 to P.J.), and the Deutsche Forschungsgemeinschaft (FR 620/14-1 to M.F.). M.F. is Senior Research Professor of the Hertie Foundation. The authors declare no conflicts of interest. Original data and programs were stored in the scientific repository of the Institute of Science and Technology Austria and are available on request.

## SUPPLEMENTARY MATERIALS

www.sciencemag.org/content/353/6304/1117/suppl/DC1  
Materials and Methods  
Figs. S1 to S11  
Tables S1 to S4  
References (48–68)

3 January 2016; accepted 15 July 2016  
10.1126/science.aaf1836

## INHIBITORY SYNAPSES

# Identification of an elaborate complex mediating postsynaptic inhibition

Akiyoshi Uezu,<sup>1</sup> Daniel J. Kanak,<sup>1\*</sup> Tyler W. A. Bradshaw,<sup>1\*</sup> Erik J. Soderblom,<sup>1,2</sup> Christina M. Catavero,<sup>1</sup> Alain C. Burette,<sup>3,4</sup> Richard J. Weinberg,<sup>3,4</sup> Scott H. Soderling<sup>1,5,†</sup>

Inhibitory synapses dampen neuronal activity through postsynaptic hyperpolarization. The composition of the inhibitory postsynapse and the mechanistic basis of its regulation, however, remain poorly understood. We used an in vivo chemico-genetic proximity-labeling approach to discover inhibitory postsynaptic proteins. Quantitative mass spectrometry not only recapitulated known inhibitory postsynaptic proteins but also revealed a large network of new proteins, many of which are either implicated in neurodevelopmental disorders or are of unknown function. Clustered regularly interspaced short palindromic repeats (CRISPR) depletion of one of these previously uncharacterized proteins, InSyn1, led to decreased postsynaptic inhibitory sites, reduced the frequency of miniature inhibitory currents, and increased excitability in the hippocampus. Our findings uncover a rich and functionally diverse assemblage of previously unknown proteins that regulate postsynaptic inhibition and might contribute to developmental brain disorders.

Two anatomically distinct classes of synapses are present in the central nervous system: excitatory synapses, predominantly localized to postsynaptic spines, and inhibitory synapses, in which the postsynapse is typically embedded in the soma and dendritic shaft (1). Purification and analysis of the protein complexes of the excitatory postsynapse have led to fundamental insights in neurobiology. These insights include how receptor trafficking, synaptic adhesion, cytoskeletal remodeling, and protein phosphorylation contribute to the synaptic plasticity underlying learning and memory (2, 3). Moreover, genetic perturbations of excitatory postsynaptic proteins are strongly implicated in developmental brain disorders and psychiatric conditions (4, 5).

In contrast, the biochemical purification and analysis of the inhibitory postsynaptic density (iPSD) has remained largely intractable. Accordingly, the molecular basis of postsynaptic inhibitory synapse regulation and its contribution to neurodevelopmental disorders is poorly understood. Recently, an affinity purification approach,

BioID, has been developed that utilizes a promiscuous *Escherichia coli* biotinylation enzyme BirA<sup>R118G</sup> (here termed BirA, with Gly replacing Arg<sup>118</sup>) fused to a bait protein expressed in cells (6). BirA-dependent covalent biotinylation occurs within 10 to 50 nm of the bait protein and allows for efficient isolation and analysis of proximal proteins by streptavidin-based affinity purification and mass spectrometry (MS) (7). Compared with affinity purification methods, the BioID reaction is executed in situ and thus enables the capture of protein complexes, including transient interactions and insoluble proteins from subcellular compartments refractory to biochemical isolation (8).

We adapted the proximity-dependent biotin identification (BioID) approach to enable in vivo BioID (iBioID) of synaptic complexes in mouse brain. We virally expressed inhibitory or excitatory PSD proteins fused to BirA to capture and purify their associated proteins. The method labels the corresponding postsynaptic structures in vivo, and that enabled the identification of virtually all of the known proteins of the iPSD. It also revealed a large number of previously unknown proteins, including a rich diversity of transmembrane and signaling proteins. These results provide a molecular prospectus for the deeper understanding of synaptic physiology that was, until now, largely confined to the excitatory PSD.

## In vivo capture of synaptic protein complexes

Gephyrin is the major scaffolding protein organizing the iPSD structure, interacting directly with

<sup>1</sup>The Department of Cell Biology, Duke University Medical School, Durham, NC 27703, USA. <sup>2</sup>Duke Proteomics and Metabolomics Shared Resource and Duke Center for Genomic and Computational Biology, Duke University Medical School, Durham, NC 27703, USA. <sup>3</sup>Department of Cell Biology and Physiology, University of North Carolina, Chapel Hill, NC 27599, USA. <sup>4</sup>Neuroscience Center, University of North Carolina, Chapel Hill, NC 27599, USA. <sup>5</sup>The Department of Neurobiology, Duke University Medical School, Durham, NC 27703, USA.

\*These authors contributed equally to this work. †Corresponding author. Email: scott.soderling@duke.edu



glycine receptors (GlyRs) or  $\gamma$ -aminobutyric acid type A receptors (GABA<sub>A</sub>Rs) and other molecules such as neuroligin-2 (NL2) and collybistin (Arhgef9) (9–11). To label proteins associated with synaptic proteins in the context of native tissue in vivo, we created adeno-associated viral (AAV) constructs for the expression of gephyrin- and the membrane-associated guanylate kinase, PSD protein 95 (PSD-95), fused with BirA, targeting the proteomes of inhibitory and excitatory postsynapses, respectively (Fig. 1A). To control for synapse specificity of biotinylation, we also expressed soluble BirA, which nonspecifically biotinylates proteins throughout the neuron. Each construct was validated by immunocytochemistry to determine its localization and synaptic site of biotinylation (Fig. 1B). To label synaptic structures in vivo, we developed a protocol that maximizes the number of synapses labeled by injection of AAV into the cortex of postnatal day 0 (P0) mouse pups, followed by 7 days of daily doses of exogenous biotin (Fig. 1C). Immunohistochemical analysis validates the approach for in vivo biotinylation (Fig. 1D), which yields punctate labeling of synaptic sites in brain tissue (Fig. 1E). Immuno-electron micro-

scopy verified that biotinylation occurred at symmetric (i.e., inhibitory) synapses for BirA-gephyrin, and at asymmetric (i.e., excitatory) postsynaptic sites for PSD-95–BirA (Fig. 1, F and G). Subcellular sites of background staining (perhaps due to overexpression or detection of endogenous biotinylated carboxylases) were also noted to guide the final proteomic analysis (fig. S1A and table S1). Purification of biotinylated proteins from neurons expressing each BirA fusion protein and subsequent immunoblotting for known components of inhibitory (collybistin) and excitatory (NR2B and GluA1) synapses verified that each bait specifically labeled components of these synaptic sites, versus the nonspecific labeling of our negative control, soluble BirA (Fig. 1H).

### Discovery of the inhibitory postsynaptic proteome

To pilot the identification of proteins labeled by iBioID, we prepared four cohorts each for BirA, PSD-95–BirA, and BirA-gephyrin using the labeling protocol outlined in Fig. 1C. Biotinylated proteins purified by streptavidin affinity purification were identified by liquid chromatography–tandem

mass spectrometry (LC-MS/MS). In total, 928 unique proteins were identified from 12 separate LC-MS/MS runs, with unique compliments of proteins enriched over BirA in each synaptic fraction (fig. S1, B to E, and table S2). Analysis of the gephyrin–BirA fraction confirmed the presence of several proteins reported to reside at the iPSD (10, 12), including Arhgef9/collybistin, VASP family proteins Mena and Evl, and IQSEC3, and two proteins of unknown function, which we termed “inhibitory synaptic proteins 1 and 2” or InSyn1 (UPF0583 protein C15orf59 homolog) and InSyn2 (protein family 196a). This pilot study suggested that, although the BirA-gephyrin is highly specific, increased coverage of the iPSD would be desirable. We therefore expanded the analysis of the iPSD by performing the MS/MS analysis using more sensitive instrumentation and by including additional BirA-fusion proteins to further label the iPSD (collybistin–BirA and InSyn1–BirA) (fig. S1, F and G). InSyn1 was included because functional studies (described below) verified that it was an important component of the iPSD. Quantitative high-resolution LC-MS/MS was then performed for each sample (PSD data set: BirA versus PSD-95;

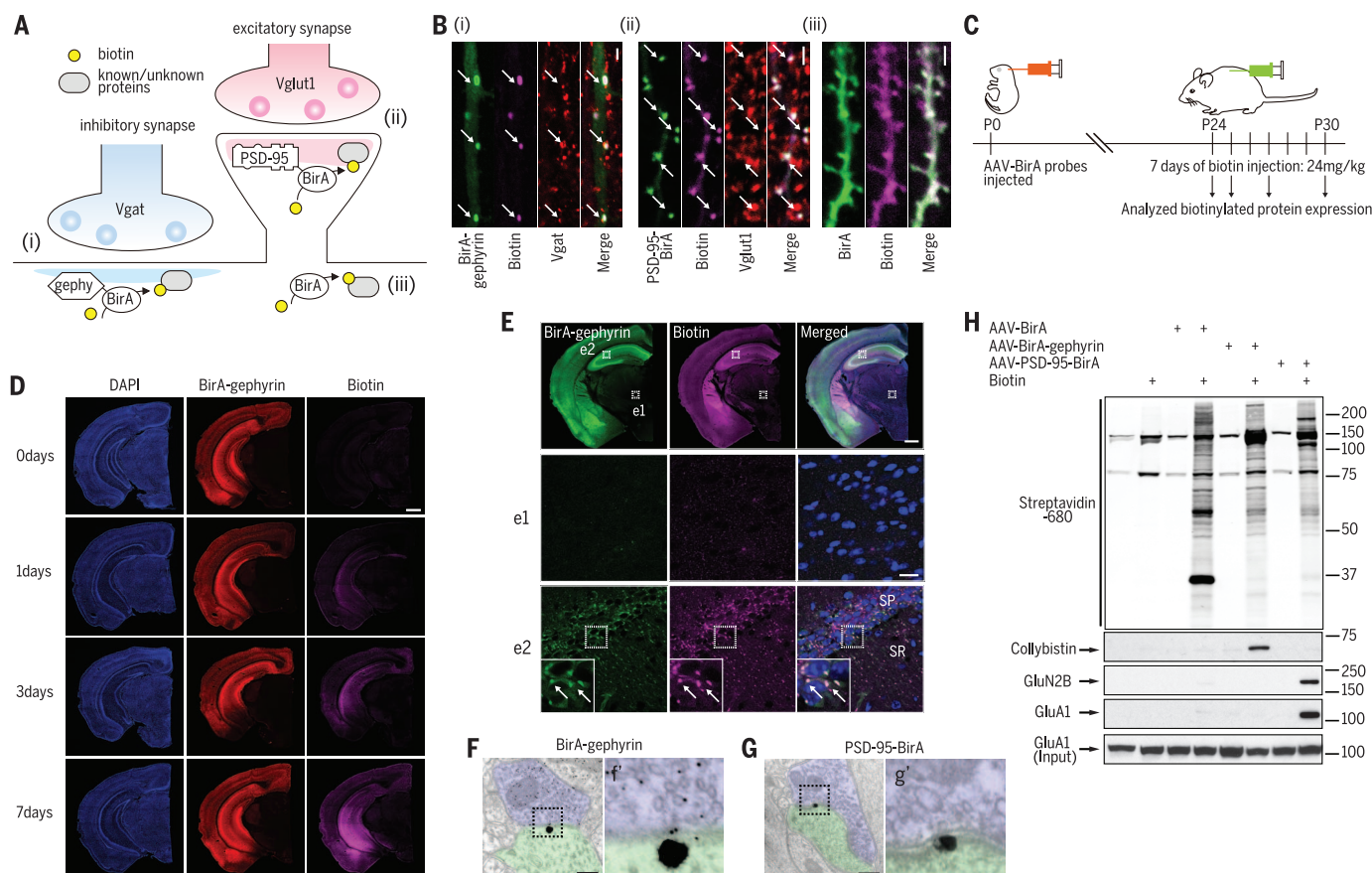


**Fig. 1. Development of iBioID for synaptic proteomics.** (A) Schematic of the iBioID approach for synapses. Vglut, vesicular glutamate transporter; Vgat, vesicular GABA transporter. (B) Validation of BirA constructs in hippocampal slice using markers labeled in (A): (i) BirA-gephyrin and (ii) PSD-95–BirA (white arrows point to colocalized puncta); and (iii) BirA alone nonspecifically labels proteins. Scale bar, 2  $\mu$ m. (C) Outline of iBioID method in mice. (D) Successful biotinylation of proteins in vivo following intraperitoneal biotin administration. Scale bar, 0.5 mm. (E) Biotinylation is specific to regions expressing BirA-gephyrin (coronal section). (Insets) From thalamus (e1) and hippocampus (e2) and insets of e2 are shown. Scale bars: top right, 0.5 mm; e1 and e2, 20  $\mu$ m. Electron micrographs verify enrichment of biotinylation at (F and f) inhibitory or (G and g') excitatory PSD substructures. Large gold beads, streptavidin labeling; small gold beads, immunolabel for GABA. Scale bar, 250 nm. (H) Specific purification of known PSD proteins for each BirA fusion protein.

tion. Scale bar, 0.5 mm. (E) Biotinylation is specific to regions expressing BirA-gephyrin (coronal section). (Insets) From thalamus (e1) and hippocampus (e2) and insets of e2 are shown. Scale bars: top right, 0.5 mm; e1 and e2, 20  $\mu$ m. Electron micrographs verify enrichment of biotinylation at (F and f) inhibitory or (G and g') excitatory PSD substructures. Large gold beads, streptavidin labeling; small gold beads, immunolabel for GABA. Scale bar, 250 nm. (H) Specific purification of known PSD proteins for each BirA fusion protein.

iPSD data set: BirA versus gephyrin, collybistin, InSyn1) in biological triplicates (seven to eight mice per biological fraction). For the excitatory PSD-95 data set, 18,207 peptides corresponding to 2533 unique proteins were quantified, whereas 17,024 peptides corresponding to 2183 proteins were quantified from the iPSD data sets. Proteins were considered enriched in the bait fraction if their average BirA-fusion protein amounts were

at least two times the amount of BirA-alone fractions with  $P < 0.05$ . On the basis of these criteria, 121 excitatory PSD (ePSD) proteins (fig. S2) were specifically labeled by PSD-95–BirA (table S3). More than 95% of the ePSD proteins identified by iBioID were previously known ePSD components, as identified by traditional PSD biochemical fractionation and MS (116 of 121 proteins), demonstrating the specificity of the method.

These proteins included glutamate receptors, scaffolding proteins, and signaling proteins of excitatory synaptic complexes. The iPSD data set identified a combined 181 proteins (table S4), including nearly all previously reported proteins of the iPSD (13); this data set suggested that coverage of the iPSD had approached saturation (Fig. 2). We also identified a large number of proteins not previously known to reside at the iPSD,

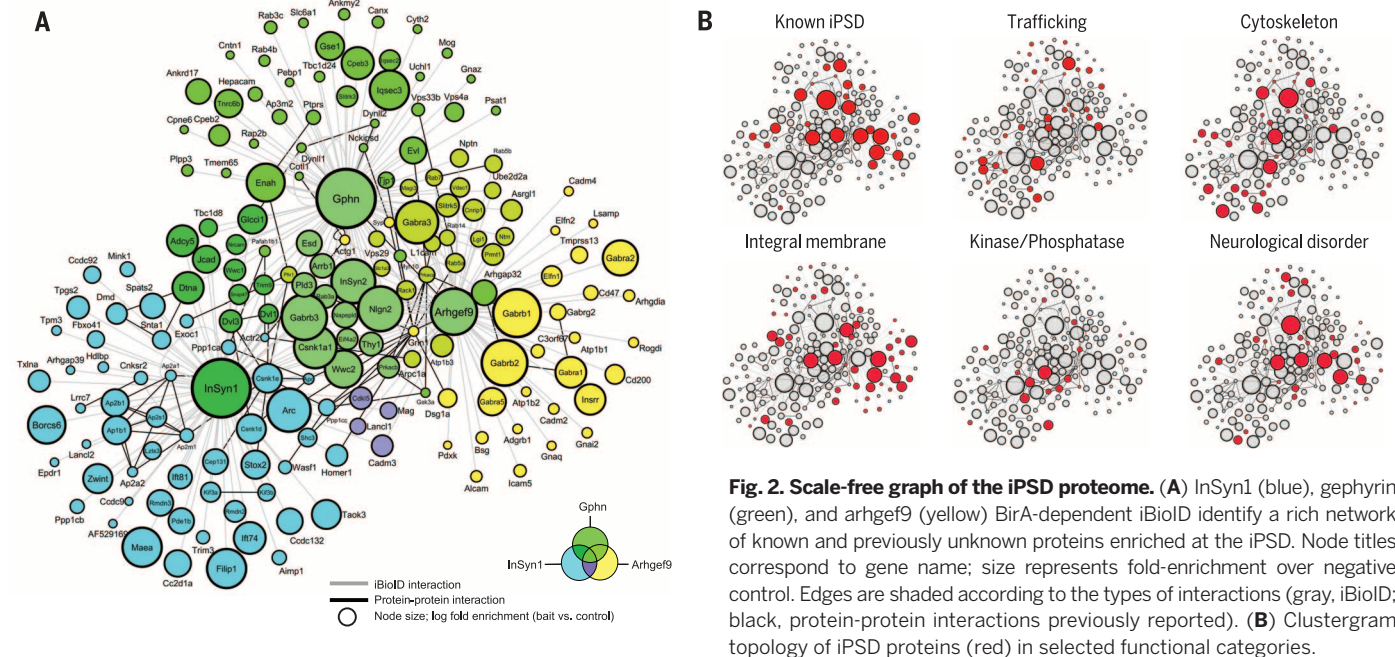


**Fig. 2. Scale-free graph of the iPSD proteome.** (A) InSyn1 (blue), gephyrin (green), and arhgef9 (yellow) BirA-dependent iBioID identify a rich network of known and previously unknown proteins enriched at the iPSD. Node titles correspond to gene name; size represents fold-enrichment over negative control. Edges are shaded according to the types of interactions (gray, iBioID; black, protein-protein interactions previously reported). (B) Clustergram topology of iPSD proteins (red) in selected functional categories.

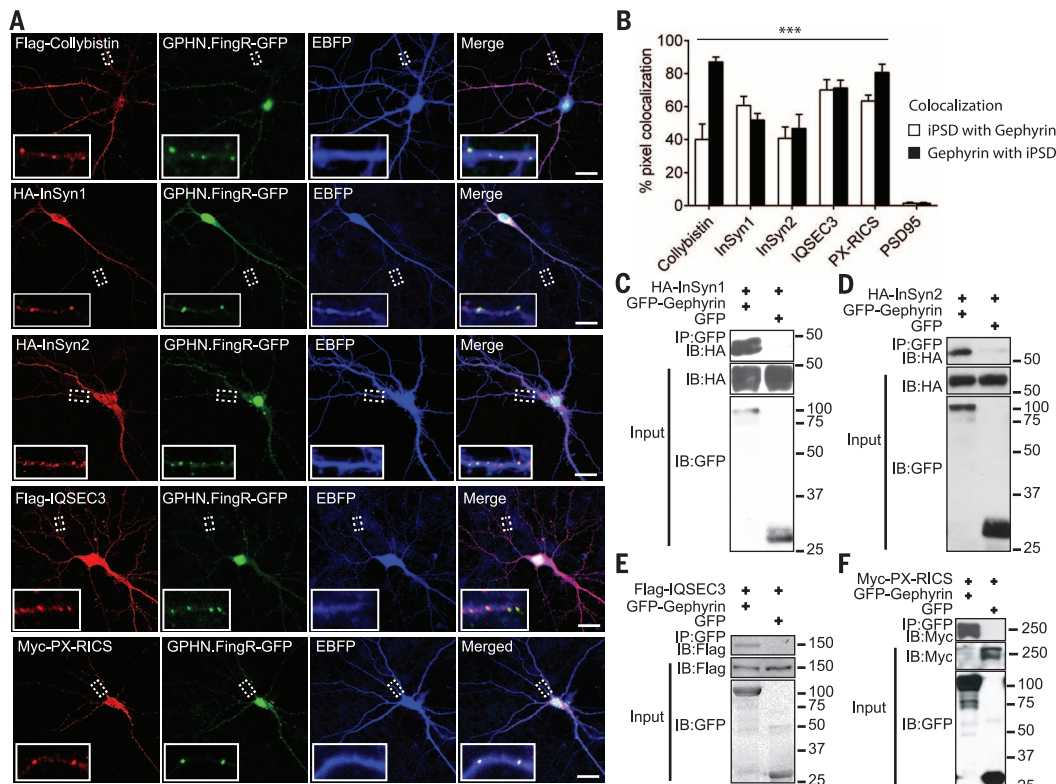


**Fig. 3. Validation of selected iPSD proteins.** (A) Colocalization of iPSD proteins (column 1), some Flag-tagged, some hemagglutinin tagged, and Myc–PX-RICS (Myc epitope-tagged Phox domain-containing isoform of RhoGAP involved in  $\beta$ -catenin–N-cadherin and N-methyl-D-aspartate receptor signaling) with endogenous gephyrin (column 2) in hippocampal neurons. EBFP, enhanced blue fluorescent protein. Scale bar, 10  $\mu$ m. (B) Each iPSD protein significantly colocalizes with gephyrin in dendrites compared with PSD-95 ( $n > 9$  dendritic regions of interest). (C to F) iPSD proteins coimmunoprecipitate with gephyrin when coexpressed in human embryonic kidney 293 (HEK293) cells. \*\*\* $P < 0.001$  one-way analysis of variance (ANOVA) followed by Dunnett's multiple comparisons test (B). Error bars  $\pm$  SEM.



including trafficking proteins, cytoskeletal regulatory proteins, integral membrane proteins, and several protein kinases and phosphatases (Fig. 2B). Many of these proteins (27/181) are encoded by genes implicated in either seizure susceptibility in humans or mice or other brain disorders such as intellectual disability (table S4). Comparison of iPSD and PSD-95 identified 17 proteins shared by the two data sets, 50% of which are signaling proteins (table S5).

### Candidate iPSD proteins colocalize and coimmunoprecipitate with gephyrin

To validate our iBioID results, select iPSD proteins [InSyn1, InSyn2, IQSEC3, collybistin (Arhgeg9), and PX-RICS (Arhgap32)] were cloned and co-expressed in primary neuronal cells with GPHN. FingR-GFP, a recombinant protein sensor of endogenous gephyrin fused to green fluorescent protein (GFP) (14) (Fig. 3A). Collybistin served as a posi-

tive control, and PSD-95 colocalization served as a negative control. Quantification of colocalizing pixels (Fig. 3B) demonstrated that each iPSD protein extensively overlapped with endogenous gephyrin. Each candidate protein was also tested in coimmunoprecipitation experiments. Epitope-tagged iPSD proteins specifically coprecipitated with GFP-gephyrin, including InSyn1 and InSyn2 (Fig. 3, C to F).

### InSyn1 and InSyn2 are iPSD proteins functionally important for GABAergic inhibition

InSyn1 is a previously uncharacterized protein that lacks protein domains of known function, but whose extensive iBioID interactions with core components of the iPSD (gephyrin, neuroligin-2, collybistin, and GABA<sub>A</sub> subunit  $\beta$ -3) suggested a central role in GABA<sub>A</sub>-dependent synaptic inhibition. To test whether InSyn1 is functionally im-

portant for synaptic inhibition, we used depletion of the endogenous protein mediated by single-cell clustered regularly interspaced short palindromic repeats (CRISPRs) (15) (Fig. 4A). GABA<sub>A</sub>-mediated miniature inhibitory postsynaptic currents (mIPSCs) were recorded from CA1 pyramidal cells in hippocampal slices that were biolistically transfected with GFP, spCas9, and validated InSyn1 guide RNA (gRNA) (Fig. 4B). Untransfected (GFP-negative) cells located within a 400- $\mu$ m radius from GFP-positive cells served as controls, and gRNA specificity was tested by reexpression of Cas9-resistant cDNAs (Fig. 4B). Inhibitory currents were confirmed to be GABAergic because they were reversibly abolished in the presence of bicuculline (1  $\mu$ M) (fig. S3A). To verify the efficacy of the CRISPR strategy for functional testing of iPSD synaptic proteins, we targeted the obligatory  $\gamma$ 2 subunit of the GABA<sub>A</sub>R and found a complete abolition of mIPSCs (fig. S3B). We also verified

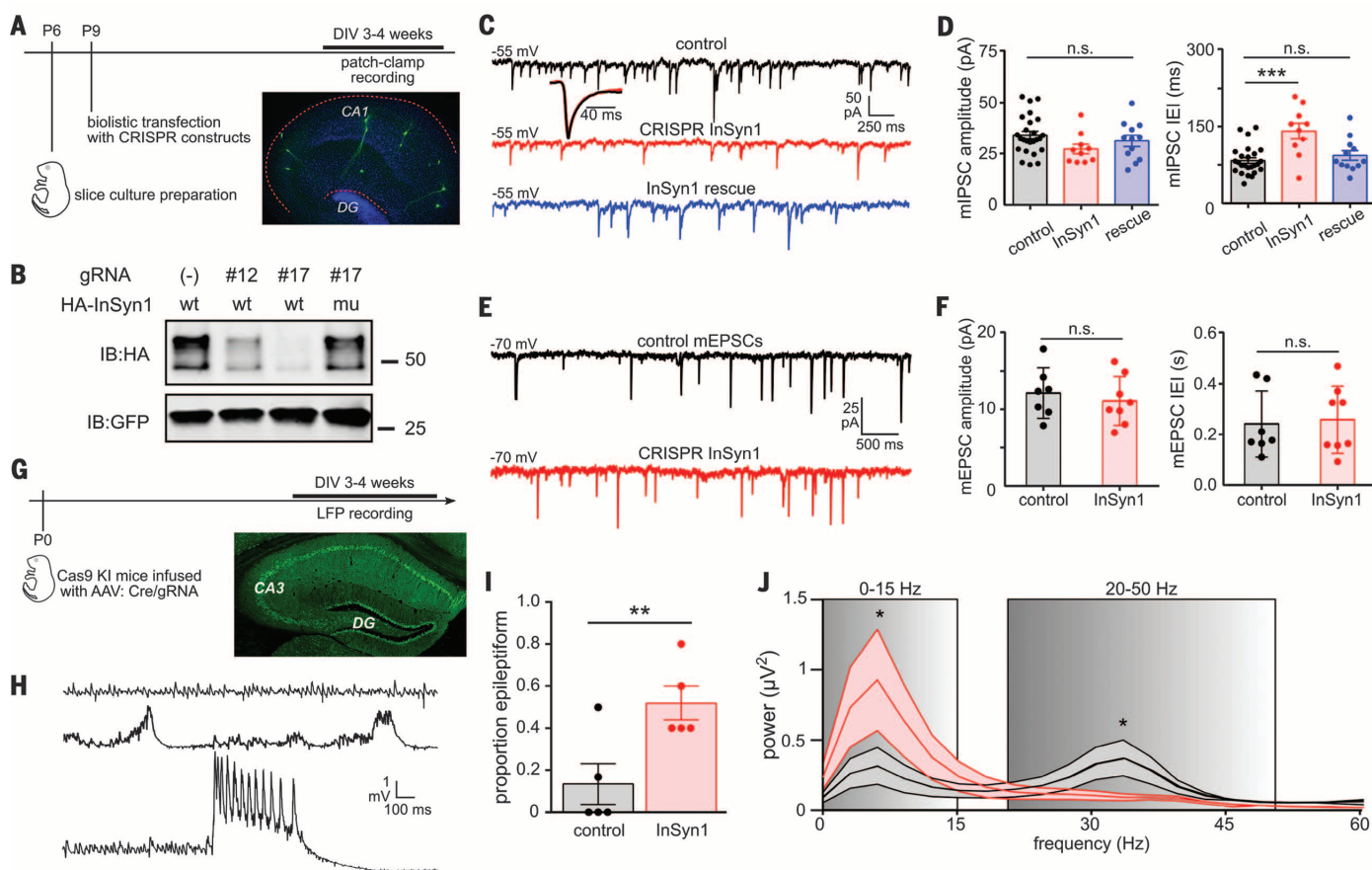


**Fig. 4. Abnormal synaptic inhibition follows loss of the iPSD protein InSyn1.** (A) Experimental schematic for (C) to (F). DIV, days in vitro. (B) Validation of InSyn1 gRNAs (#12 and #17) and rescue constructs by cotransfection of 293T cells and immunoblotting. (C and D) GABA<sub>A</sub>-dependent miniature inhibitory postsynaptic currents (mIPSCs) recorded from CA1 pyramidal cells. (Inset) GABA<sub>A</sub> mIPSC waveform averages. InSyn1 depletion did not alter mIPSC kinetics (rise: controls,  $3.6 \pm 0.6$  ms; InSyn1,  $3.4 \pm 0.6$  ms;  $P = 0.51$ ; decay: controls,  $9.7 \pm 2.1$  ms; InSyn1,  $10.3 \pm 1.8$  ms;  $P = 0.42$ ). IELs of InSyn1-depleted GABA<sub>A</sub> mIPSCs (red) are specifically increased compared with control (black) and rescue (blue) neurons. (E and F) AMPAR-dependent mEPSCs are not altered in InSyn1-depleted neurons. (G) Time-line schematic for local field

potential (LFP) recordings in acute slices from Cas9 knock-in (KI) mice infected with AAV:Cre/InSyn1 gRNA. Representative extent of AAV infection in hippocampus. (H) Representative LFP activities recorded in hippocampal area CA3 in the presence of 10  $\mu$ M carbachol to model “awake state” gamma rhythm. Top trace, Pure 30 to 40 Hz gamma oscillation; middle trace, 3 to 5 Hz spike-wave discharges; bottom trace, ictal-like burst—the latter two indicative of hyperexcitable or epileptiform activity. (I) InSyn1 gRNA-expressing slices exhibit increased-epileptiform activity. (J) Averaged power spectra showing signal energy in the InSyn1 gRNA-expressing slices is increased in the 0 to 15 Hz frequency band and decreased in the 20 to 50 Hz frequency bands. \* $P < 0.05$ , \*\* $P < 0.01$ ; \*\*\* $P < 0.001$ ; n.s., not statistically significant. Error bars  $\pm$  SEM.



that biolistic transfection of GFP alone did not alter mIPSC characteristics (fig. S3, C to E). Using sgRNA targeting *InSyn1* with and without an

*InSyn1* rescue construct, we found a significant and reversible 69% increase in mIPSC interevent intervals (IEI); the difference in amplitude was not

statistically significant (Fig. 4, C and D). The effect of *InSyn1* gRNA was specific to inhibitory currents, as  $\alpha$ -amino-3-hydroxy-5-methyl-4-isoxazolepropionic

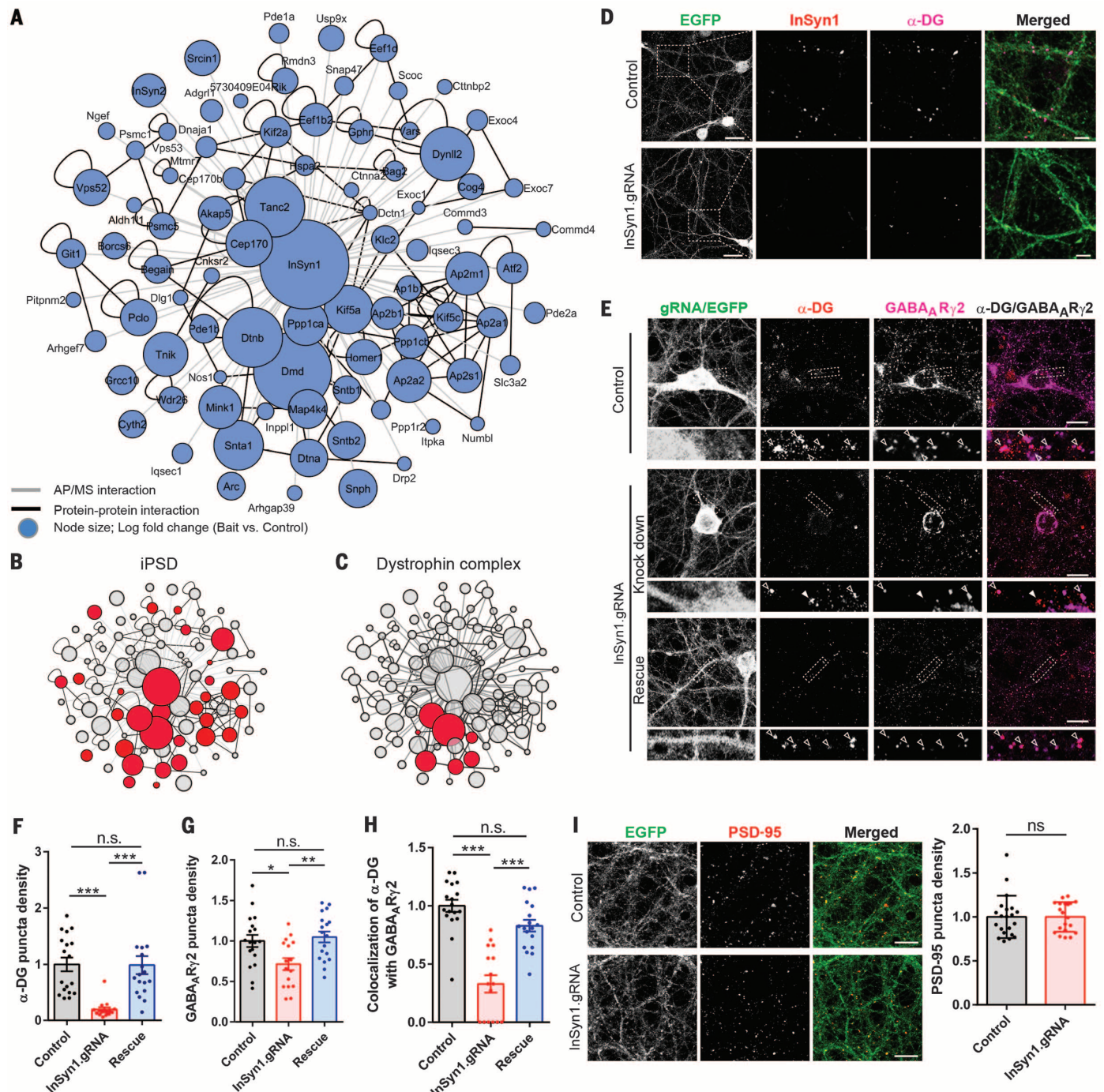


**Fig. 5. *InSyn1* functionally associates with the dystrophin complex at the iPSD.** (A) Network analysis of affinity-purified *InSyn1*-GFP proteome from mouse brain. Affinity purification–mass spectrometry (AP/MS) interaction. (B and C) Clustergram topologies of *InSyn1*-associated proteins in selected functional categories. (D) Colocalization of *InSyn1* with  $\alpha$ -dystroglycan ( $\alpha$ -DG) is diminished after depleting *InSyn1* with Cas9 conditional knock-in mouse hippocampal neurons infected with AAV:Cre/*InSyn1* gRNA. EGFP, enhanced GFP. Scale bar, 10  $\mu$ m. (E) *InSyn1* is essential for GABA<sub>A</sub>R and  $\alpha$ -DG cluster density. Hippocampal neurons from Cas9 KI mice were stained for GABA<sub>A</sub> subunit Ry2 and  $\alpha$ -DG following infection with control AAV:Cre/(-)gRNA (top panel, control); AAV:Cre/*InSyn1*gRNA

(middle panel, knockdown), or AAV:Cre/*InSyn1* gRNA, and transfected with *InSyn1* gRNA-resistant plasmid (bottom panels, Rescue). (Insets) Higher magnification regions with open (colocalized puncta) and closed (noncolocalized puncta) arrows. (F to H) Quantification of  $\alpha$ -DG and GABA<sub>A</sub>Ry2 puncta colocalization or density ( $n = 16$  to  $18$ ). \* $P < 0.05$ , \*\* $P < 0.01$ , \*\*\* $P < 0.001$  one-way ANOVA followed by Tukey's multiple comparisons test (F) to (H). Error bars  $\pm$  SEM. Scale bar, 10  $\mu$ m. (I) Loss of *InSyn1* does not alter PSD-95 puncta density. Cas9 knock-in mouse hippocampal neurons infected with AAV:Cre/*InSyn1* gRNA were stained with PSD-95 and quantified ( $n = 18$  to  $20$  neurons); n.s., not significant, by two-tailed  $t$  test (I).

acid receptor (AMPA)-mediated miniature excitatory postsynaptic current (mEPSC) characteristics were unaltered (Fig. 5, E and F). To further test the predictive value of the iPSD data set, we performed analogous experiments targeting InSyn2. Depletion of InSyn2 resulted in a specific and reversible 62% increase of mIPSC IEI (fig. S4).

Given the large effect of InSyn1 depletion on mIPSC frequency, we next asked whether the inhibitory deficits evident at the single-cell level manifest at the network level. We used a carbachol (CCH)-induced model of the “awake-state” gamma rhythm, which is critically dependent on GABAergic inhibition (16). PO *Rosa26-LSL-Cas9* (17) pups were bilaterally infused with AAV:Cre/*InSyn1*:gRNA virus or AAV:Cre/(-):gRNA control virus in the hippocampus (Fig. 4G). In the majority of hippocampal slices prepared from control mice and kept vital in vitro, CCH induced a pure gamma rhythm with peak frequencies of ~30 to 40 Hz (Fig. 4H, top trace). In contrast, the majority of InSyn1 gRNA-infected slices exhibited a mixture of gamma oscillations with hyperexcitable events including interictal epileptiform discharges (IEDs) (Fig. 4H, middle trace) and prolonged (2- to 5-s) bursts resembling ictal discharges (Fig. 4H, lower trace). Overall, we found a fourfold increase in the proportion of slices with IEDs (Fig. 4I). Power spectral analysis revealed a 2.2-fold increase in low-frequency (0 to 15 Hz) power corresponding to epileptiform activity, and a 42% reduction in gamma-band (20 to 50 Hz) power (Fig. 4J). These effects likely reflect loss of GABAergic inhibition, as bath application of low concentrations of bicuculline (0.5- $\mu$ M steps) abolished the gamma rhythm in control slices and induced epileptiform activity similar to that seen in InSyn1 gRNA slices (fig. S3F).

### InSyn1 functions via the dystrophin complex at inhibitory synaptic sites

We next analyzed how InSyn1 functions at inhibitory synapses by further examining its interacting proteins and how its loss alters the iPSD. InSyn1-GFP expressed in hippocampal neurons colocalized with gephyrin in dendritic shafts (fig. S5A). InSyn1-GFP protein or GFP protein alone was virally expressed in the frontal cortex and hippocampus of C57BL/6 mice with AAV and precipitated with GFP-trap resin. InSyn1-GFP and GFP alone coprecipitating proteins were analyzed by LC-MS/MS and compared. InSyn1, pull-down fractions were enriched with 86 proteins (Fig. 5A and table S6) and formed a highly interconnected protein-protein interaction network that included many proteins in the iBioID iPSD (including InSyn2, gephyrin, and Iqsec3) (Fig. 5B).

Among the most enriched proteins were seven components of the dystrophin complex, including dystrophin (DMD), dystrobrevin alpha and beta (Dtna and Dtnb), and alpha-1-, beta-1-, and beta-2-syntrophins (Snta1, Sntb1, and Sntb2) (Fig. 5C). In brain, the dystrophin complex is a component of the iPSD, and its loss in muscular dystrophies contributes to cognitive impairments and epilepsy (18). InSyn1-BirA also captured multiple components of the dystrophin complex (Fig. 2, A

and B), which suggests that InSyn1-BirA forms a physical complex with both gephyrin and the dystrophin complex. Affinity-purified antibody against InSyn1 (anti-InSyn1) recognized a band of about 50 to 52 kD from cells transfected with hemagglutinin epitope-tagged (HA)-InSyn1 or from mouse brain extract (fig. S5B). Immunofluorescence demonstrated that InSyn1 colocalizes with endogenous  $\alpha$ -dystroglycan ( $\alpha$ -DG); this punctate staining was lost in neurons cultured from *Rosa26-LSL-Cas9* mice and infected with AAV:Cre/*InSyn1*:gRNA virus (Fig. 5D). Quantitative analysis demonstrated that InSyn1 gRNA-infected neurons had significant reductions in densities of both  $\alpha$ -DG and GABA<sub>A</sub>R puncta and a significant reduction in their colocalization (Fig. 5, E to H). In contrast, the density of PSD-95 puncta was unaffected (Fig. 5I). These results are consistent with the reduced mIPSC frequencies we observed in single-neuron CRISPR-mediated InSyn1 depletion and support the notion that the loss of postsynaptic sites of inhibition occurs in the absence of InSyn1.

### Discussion

We report here the in vivo application of the BioID approach to analyze the local proteome of the postsynaptic compartment of inhibitory synapses by quantitative mass spectrometry. Comparing this approach with prior reports of the iPSD using affinity purification (19–21), iBioID offers important advantages. Nearly all proteins previously reported to exist at the iPSD were identified. iBioID also identified 140 proteins not previously associated with the iPSD, including a wide range of signaling, transmembrane, structural, and uncharacterized proteins. Although we included multiple controls (BirA alone and electron microscopy analysis of nonspecific label) for the overexpression strategy, we anticipate future studies with endogenous proteins fused to BirA will likely further refine the iBioID approach.

To validate our results and to determine how the iPSD is regulated, we focused on two proteins of unknown function, InSyn1 and InSyn2, that associate with several core components of the iPSD. When expressed in neurons, both colocalized with endogenous gephyrin, and their loss resulted in a significant reduction in mIPSC frequency, confirming the validity of the iBioID approach. The mechanism of reduced mIPSC frequency for InSyn1 is likely through the disruption of the ability of InSyn1 to form complexes with both gephyrin and the dystrophin complex at the iPSD. Loss of dystrophin might also lead to a secondary trans-synaptic effect on presynaptic release probability through its ability to bind neurexins (22, 23).

Twenty-seven of the proteins of the iPSD, including several proteins first identified here, are implicated by either human or mouse genetics in seizure susceptibility and/or familial epilepsy, intellectual disability, or autism (Fig. 2G). Of the newly identified iPSD proteins implicated in developmental disorders, many are signaling proteins or are proteins of unknown functions (discussion in supplementary text). It is also interesting to note

that 17 proteins overlapped between the inhibitory and excitatory PSD fractions. These could reflect dual synapses [spines containing gephyrin (24)] or might represent signaling proteins that transit between synapse types to facilitate synaptic crosstalk.

Our results indicate that the composition of the iPSD is far more complex than previously appreciated. This concept is in line both with emerging evidence of inhibitory synaptic plasticity at the postsynaptic specialization (25–32), and with our molecular evidence that the iPSD is associated with a variety of signaling proteins, analogous to that of excitatory synapses. The identification of the iPSD proteome provides a rational basis for investigating fundamental mechanisms that regulate synaptic inhibition. It also establishes a new reference frame to ascertain how perturbations of this protein complex may contribute to developmental brain disorders.

### REFERENCES AND NOTES

1. E. G. Gray, *J. Anat.* **93**, 420–433 (1959).
2. R. C. Malenka, M. F. Bear, *Neuron* **44**, 5–21 (2004).
3. M. B. Kennedy, H. C. Beale, H. J. Carlisle, L. R. Washburn, *Nat. Rev. Neurosci.* **6**, 423–434 (2005).
4. S. G. Grant, *Curr. Opin. Neurobiol.* **22**, 522–529 (2012).
5. L. Volk, S. L. Chiu, K. Sharma, R. L. Huganir, *Annu. Rev. Neurosci.* **38**, 127–149 (2015).
6. K. J. Roux, D. I. Kim, M. Raida, B. Burke, *J. Cell Biol.* **196**, 801–810 (2012).
7. D. I. Kim et al., *Proc. Natl. Acad. Sci. U.S.A.* **111**, E2453–E2461 (2014).
8. Z. Yao, J. Petschnigg, R. Ketteler, I. Stagljar, *Nat. Chem. Biol.* **11**, 387–397 (2015).
9. A. Pouloupoulos et al., *Neuron* **63**, 628–642 (2009).
10. S. K. Tyagarajan, J. M. Fritschy, *Nat. Rev. Neurosci.* **15**, 141–156 (2014).
11. P. Prior et al., *Neuron* **8**, 1161–1170 (1992).
12. J. W. Um et al., *J. Biol. Chem.* **291**, 10119–10130 (2016).
13. Known iPSD proteins included eight GABA<sub>A</sub> receptor subunits, inhibitory transmembrane adhesion proteins [e.g., neuroligin-2 (33–35), Slitrk3 (36)], and neuroligin-1 (37, 38)], as well as signaling- and actin-associated proteins, such as Trim3 (39), Enah (40), profilin (41); and dystrophin complex proteins (including alpha-1-syntrophin, dystrobrevin alpha, and dystrophin) (42).
14. G. G. Gross et al., *Neuron* **78**, 971–985 (2013).
15. S. Incontro, C. S. Asensio, R. H. Edwards, R. A. Nicoll, *Neuron* **83**, 1051–1057 (2014).
16. E. O. Mann, J. M. Suckling, N. Hajos, S. A. Greenfield, O. Paulsen, *Neuron* **45**, 105–117 (2005).
17. R. J. Platt et al., *Cell* **159**, 440–455 (2014).
18. M. Pane et al., *Neuromuscul. Disord.* **23**, 313–315 (2013).
19. E. A. Heller et al., *PLOS ONE* **7**, e39572 (2012).
20. Y. Kang et al., *J. Biol. Chem.* **289**, 29350–29364 (2014).
21. Y. Nakamura et al., *J. Biol. Chem.* **291**, 12394–12407 (2016).
22. S. Sugita et al., *J. Cell Biol.* **154**, 435–446 (2001).
23. D. E. Michele et al., *Nature* **418**, 417–421 (2002).
24. K. L. Villa et al., *Neuron* **89**, 756–769 (2016).
25. J. N. Bourne, K. M. Harris, *Hippocampus* **21**, 354–373 (2011).
26. I. Lushnikova, G. Skibo, D. Muller, I. Nikonenko, *Neuropharmacology* **60**, 757–764 (2011).
27. F. Niwa et al., *PLOS ONE* **7**, e36148 (2012).
28. B. Dejanovic et al., *PLOS Biol.* **12**, e1001908 (2014).
29. E. M. Petriani et al., *Nat. Commun.* **5**, 3921 (2014).
30. C. E. Flores et al., *Proc. Natl. Acad. Sci. U.S.A.* **112**, E65–E72 (2015).
31. J. L. Chen et al., *Neuron* **74**, 361–373 (2012).
32. D. van Versendaal et al., *Neuron* **74**, 374–383 (2012).
33. F. Varoqueaux, S. Jamin, N. Brose, *Eur. J. Cell Biol.* **83**, 449–456 (2004).
34. E. R. Graf, X. Zhang, S. X. Jin, M. W. Linhoff, A. M. Craig, *Cell* **119**, 1013–1026 (2004).
35. B. Chih, H. Engelman, P. Scheiffele, *Science* **307**, 1324–1328 (2005).
36. H. Takahashi et al., *Nat. Neurosci.* **15**, 389–398, S1–S2 (2012).



37. P. W. Beesley, R. Herrera-Molina, K. H. Smalla, C. Seidenbecher, *J. Neurochem.* **131**, 268–283 (2014).  
 38. R. Herrera-Molina et al., *J. Biol. Chem.* **289**, 8973–8988 (2014).  
 39. C. C. Cheung et al., *Proc. Natl. Acad. Sci. U.S.A.* **107**, 11883–11888 (2010).  
 40. T. Giesemann et al., *J. Neurosci.* **23**, 8330–8339 (2003).  
 41. K. Murk et al., *PLOS ONE* **7**, e34167 (2012).  
 42. G. S. Pilgram, S. Potikanond, R. A. Baines, L. G. Fradkin, J. N. Noordermeer, *Mol. Neurobiol.* **41**, 1–21 (2010).

## ACKNOWLEDGMENTS

This work was supported by NIH grants MH104736 (S.H.S.) and NS039444 (R.J.W.). We thank J. Ding for animal perfusions, B. Carlson for advice on image analysis, A. Swartz for cloning, and K. Sakurai and J. Takatoh for advice on AAV production and injection protocols. Raw data relating to all mass spectrometry-based experiments can be viewed or downloaded from [www.ChorusProject.org](http://www.ChorusProject.org) under the project title "Uezu\_Soderling\_RawData\_July2016."

## SUPPLEMENTARY MATERIALS

[www.sciencemag.org/content/353/6304/1123/suppl/DC1](http://www.sciencemag.org/content/353/6304/1123/suppl/DC1)  
 Materials and Methods  
 Supplementary Text  
 Figs. S1 to S5  
 Tables S1 to S6  
 References (43–61)

6 May 2016; accepted 25 July 2016  
 10.1126/science.aag0821

## VACCINES

# Protective efficacy of multiple vaccine platforms against Zika virus challenge in rhesus monkeys

Peter Abbink,<sup>1,\*</sup> Rafael A. Larocca,<sup>1,\*</sup> Rafael A. De La Barrera,<sup>2</sup> Christine A. Bricault,<sup>1</sup> Edward T. Moseley,<sup>1</sup> Michael Boyd,<sup>1</sup> Marinela Kirilova,<sup>1</sup> Zhenfeng Li,<sup>1</sup> David Ng'ang'a,<sup>1</sup> Ovin Nanayakkara,<sup>1</sup> Ramya Nityanandam,<sup>1</sup> Noe B. Mercado,<sup>1</sup> Erica N. Borduechi,<sup>1</sup> Arshi Agarwal,<sup>1</sup> Amanda L. Brinkman,<sup>1</sup> Crystal Cabral,<sup>1</sup> Abishek Chandrashekar,<sup>1</sup> Patricia B. Giglio,<sup>1</sup> David Jetton,<sup>1</sup> Jessica Jimenez,<sup>1</sup> Benjamin C. Lee,<sup>1</sup> Shanell Mojta,<sup>1</sup> Katherine Molloy,<sup>1</sup> Mayuri Shetty,<sup>1</sup> George H. Neubauer,<sup>1</sup> Kathryn E. Stephenson,<sup>1</sup> Jean Pierre S. Peron,<sup>3</sup> Paolo M. de A. Zanotto,<sup>3</sup> Johnathan Misamore,<sup>4</sup> Brad Finneyfrock,<sup>4</sup> Mark G. Lewis,<sup>4</sup> Galit Alter,<sup>5</sup> Kayvon Modjarrad,<sup>2,6</sup> Richard G. Jarman,<sup>2</sup> Kenneth H. Eckels,<sup>2</sup> Nelson L. Michael,<sup>2</sup> Stephen J. Thomas,<sup>2,†</sup> Dan H. Barouch<sup>1,5,†,‡</sup>

Zika virus (ZIKV) is responsible for a major ongoing epidemic in the Americas and has been causally associated with fetal microcephaly. The development of a safe and effective ZIKV vaccine is therefore an urgent global health priority. Here we demonstrate that three different vaccine platforms protect against ZIKV challenge in rhesus monkeys. A purified inactivated virus vaccine induced ZIKV-specific neutralizing antibodies and completely protected monkeys against ZIKV strains from both Brazil and Puerto Rico. Purified immunoglobulin from vaccinated monkeys also conferred passive protection in adoptive transfer studies. A plasmid DNA vaccine and a single-shot recombinant rhesus adenovirus serotype 52 vector vaccine, both expressing ZIKV premembrane and envelope, also elicited neutralizing antibodies and completely protected monkeys against ZIKV challenge. These data support the rapid clinical development of ZIKV vaccines for humans.

The explosive and unprecedented ZIKV outbreak in the Americas (1, 2) prompted the World Health Organization to declare this epidemic a public health emergency of international concern. ZIKV has been causally associated with fetal microcephaly, intrauterine growth retardation, and other congenital malformations in both humans (3–6) and mice (7–9), and it has also been linked with neurologic disorders such as Guillain-Barre syndrome (10). Several reports have shown that ZIKV can infect placental and fetal tissues, leading to prolonged viremia in pregnant women (11) and nonhuman primates (12). ZIKV also appears to target cortical neural progenitor cells (7–9, 13, 14), which likely contributes to neuropathology.

We recently reported the protective efficacy of two vaccines against ZIKV challenges in mice: a purified inactivated virus (PIV) vaccine from ZIKV strain PRVABC59 and a DNA vaccine expressing an optimized premembrane and envelope (prM-Env) immunogen from ZIKV strain BeH815744 (15). These studies used ZIKV challenge strains from Brazil (ZIKV-BR; Brazil/ZK/2015) (9) and Puerto Rico (ZIKV-PR; PRVABC59). ZIKV replication in

mice was dependent on the mouse strain (15) and may be less extensive than in nonhuman primates (12). We therefore evaluated the immunogenicity and protective efficacy of inactivated virus, DNA-based, and vector-based vaccines against ZIKV challenge in rhesus monkeys.

## ZIKV PIV vaccine study

We first immunized 16 rhesus monkeys by the subcutaneous route with 5  $\mu$ g of ZIKV PIV vaccine plus alum ( $n = 8$ ) or sham vaccine (alum only) ( $n = 8$ ) at weeks 0 and 4 (fig. S1). All PIV-vaccinated animals developed ZIKV Env-specific binding antibodies, as measured by enzyme-linked immunosorbent assays (ELISAs), and ZIKV-specific neutralizing antibodies, as measured by micro-neutralization (MN50) assays, at week 2 after initial immunization. Median log antibody titers at week 2 were 1.87 (Fig. 1A) and 2.27 (Fig. 1B) in ELISAs and MN50 assays, respectively. After the week 4 boost immunization, median log antibody titers increased substantially to 3.54 (Fig. 1A) and 3.66 (Fig. 1B), respectively, at week 6. In contrast, sham control monkeys did not develop detectable ZIKV-specific antibody responses (fig. S2).

Binding antibody titers correlated with neutralizing antibody titers in the PIV-vaccinated animals ( $P < 0.0001$ , coefficient of correlation  $R = 0.88$ , Spearman rank correlation test; fig. S3). Only minimal antibody-dependent cellular phagocytosis responses were observed. The majority of PIV-vaccinated monkeys (Fig. 1, C and D), but not sham control animals (fig. S4), also developed modest cellular immune responses, primarily to Env, as measured by interferon (IFN)- $\gamma$  enzyme-linked immunospot (ELISPOT) assays.

To assess the protective efficacy of the PIV vaccine against ZIKV challenge, we infected PIV-immunized and sham control monkeys by the subcutaneous route with  $10^6$  viral particles [vp;  $10^3$  plaque-forming units (PFU)] of ZIKV-BR or ZIKV-PR ( $n = 4$  per group) (15). Viral loads after ZIKV challenge were quantitated by reverse transcription polymerase chain reaction (15), and viral infectivity was confirmed by growth in Vero cells. ZIKV-specific MN50 titers increased after challenge, particularly in the sham controls (fig. S5). Sham control monkeys exhibited 6 to 7 days of detectable viremia, with median peak viral loads of 5.82 log copies/ml (range, 5.21 to 6.29 log copies/ml;  $n = 8$ ) on day 3 to 5 after challenge (Fig. 2A). Virus was also detected in the majority of sham control animals in urine and cerebrospinal fluid (CSF) on day 3, as well as in colorectal secretions and cervicovaginal secretions on day 7 (Fig. 2, B to E). In contrast, PIV-vaccinated monkeys showed complete protection against ZIKV challenge, as evidenced by no detectable virus ( $<100$  copies/ml) in the blood, urine, CSF, colorectal secretions, or cervicovaginal secretions in any animal after challenge ( $n = 8$ ;  $P = 0.0002$ , Fisher's exact test comparing PIV-vaccinated animals with sham controls). We were unable to assess ZIKV in semen in the male animals in this study because of inadequate sample volumes. No major differences in plasma viral loads were observed between the sham controls that received ZIKV-BR versus those that received ZIKV-PR (fig. S6).

## Adoptive transfer studies

We next explored the mechanism of the observed protection through adoptive transfer studies.

<sup>1</sup>Center for Virology and Vaccine Research, Beth Israel Deaconess Medical Center, Harvard Medical School, Boston, MA 02215, USA. <sup>2</sup>Walter Reed Army Institute of Research, Silver Spring, MD 20910, USA. <sup>3</sup>University of São Paulo, São Paulo 05508-000, Brazil. <sup>4</sup>Bioqual, Rockville, MD 20852, USA. <sup>5</sup>Ragon Institute of MGH, MIT and Harvard, Cambridge, MA 02139, USA. <sup>6</sup>Henry M. Jackson Foundation, Bethesda, MD 20817, USA.

\*These authors contributed equally to this work. †These authors contributed equally to this work. ‡Corresponding author. Email: [dbarouch@bidmc.harvard.edu](mailto:dbarouch@bidmc.harvard.edu)



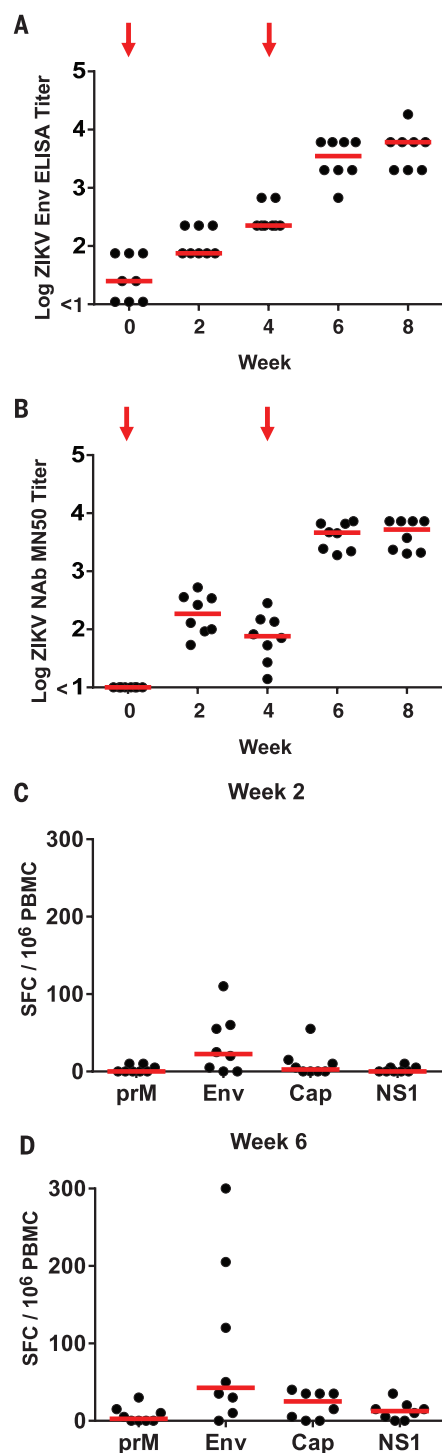


**Fig. 1. Immunogenicity of the ZIKV PIV vaccine.** (A) ZIKV Env-specific ELISA titers and (B) ZIKV-specific MN50 titers after immunization of rhesus monkeys by the subcutaneous route with 5 µg of PIV vaccine at weeks 0 and 4 (red arrows). The maximum measurable log MN50 titer in this assay was 3.86. NAb, neutralizing antibody. (C) Cellular immune responses measured by IFN-γ ELISPOT assays for prM, Env, Cap (capsid), and NS1 (nonstructural protein 1) at week 2 and (D) week 6. Red bars reflect medians. SFC, spot-forming cells. PBMC, peripheral blood mononuclear cells.

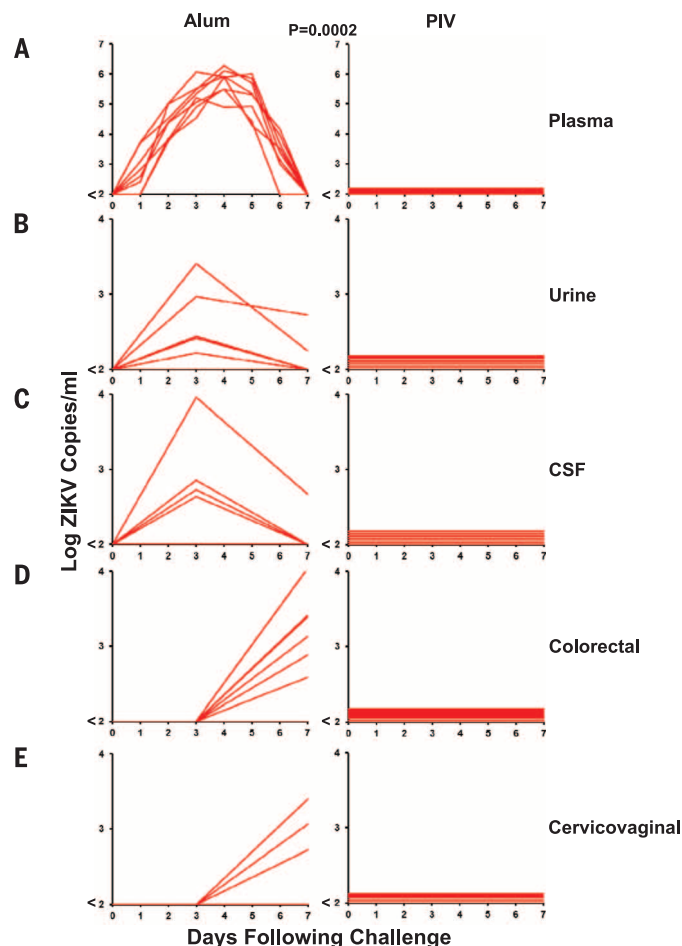


**Fig. 2. Protective efficacy of the ZIKV PIV vaccine.** PIV-vaccinated and sham control (alum-vaccinated) rhesus monkeys ( $n = 8$  per group) were challenged by the subcutaneous route with  $10^6$  vp ( $10^3$  PFU) of ZIKV-BR or ZIKV-PR. Each group contained six female and two male animals. Viral loads are shown for (A) plasma, (B) urine, (C) CSF, (D) colorectal secretions, and (E) cervicovaginal secretions. Viral loads were determined on days 0, 1, 2, 3, 4, 5, 6, and 7 for the plasma samples (A) and on days 0, 3, and 7 for the other samples [(B) to (E)]. Data are shown for all eight animals, except in the case of cervicovaginal secretions (E), where data for the six females are shown. The  $P$  value was determined by Fisher's exact test.

Using protein G affinity chromatography, we purified immunoglobulin G (IgG) from plasma from PIV-vaccinated monkeys at week 8. Vaccine-elicited, ZIKV-specific IgG was then infused into four groups of naïve Balb/c mice ( $n = 5$  per group) as fivefold serial dilutions of the purified IgG preparation, which had a log ELISA titer of 3.30 and a log MN50 titer of 3.30. After infusion, these groups of recipient mice (designated I, II, III, and IV) had median log ELISA titers of 2.83, 2.35, 1.40, and  $<1.00$  (Fig. 3A) and median log MN50 titers of 2.93, 1.77, 1.14, and  $<1.00$  (Fig. 3B), respectively. Mice were then challenged by the intravenous route with  $10^5$  vp ( $10^2$  PFU) of ZIKV-BR, as we have previously described (15). The higher two doses of purified IgG provided complete protection after ZIKV challenge, whereas the lower two doses of purified IgG resulted in reduced viremia compared with sham-infused control mice (Fig. 3, C to E).

Vaccine-elicited, ZIKV-specific IgG was also infused into two groups of naïve rhesus monkeys ( $n = 2$  per group). After infusion, these groups of recipient monkeys (designated I and II) had respective median log MN50 titers of 2.11 and 1.22 (Fig. 4A). Monkeys were then challenged with  $10^6$  vp ( $10^3$  PFU) of ZIKV-BR. In the animals that received the higher IgG dose, one animal was completely protected and the other showed a blip of viremia on days 3 to 5 (Fig. 4B). No en-

hancement of viral replication was observed at subtherapeutic IgG concentrations. Taken together, these data demonstrate that purified IgG from PIV-vaccinated rhesus monkeys provided passive protection against ZIKV challenge after adoptive transfer to both rodents and primates.

### ZIKV DNA and adenovirus vaccine study

To evaluate the immunogenicity and protective efficacy of DNA- and vector-based ZIKV vaccines, we immunized 12 rhesus monkeys with a plasmid DNA vaccine (15) or a rhesus adenovirus serotype 52 (RhAd52) vector-based vaccine (16) (fig. S1). Monkeys were immunized by the intramuscular route with 5 mg of DNA vaccine expressing prM-Env at weeks 0 and 4 ( $n = 4$ ), with  $10^{11}$  vp of RhAd52 vector expressing prM-Env as a single immunization at week 0 ( $n = 4$ ), or with sham vaccine at weeks 0 and 4 ( $n = 4$ ). The DNA-prM-Env vaccine induced ZIKV-specific neutralizing antibody titers in all animals after the week 4 boost immunization, although only minimal MN50 titers were detected after the initial priming immunization (Fig. 5A). In contrast, the RhAd52-prM-Env vaccine induced ZIKV-specific neutralizing antibody responses in all animals at week 2 after the initial priming immunization (Fig. 5A). Moreover, the RhAd52-prM-Env vaccine induced a substantial breadth of antibody responses against linear ZIKV Env epitopes, as measured by peptide

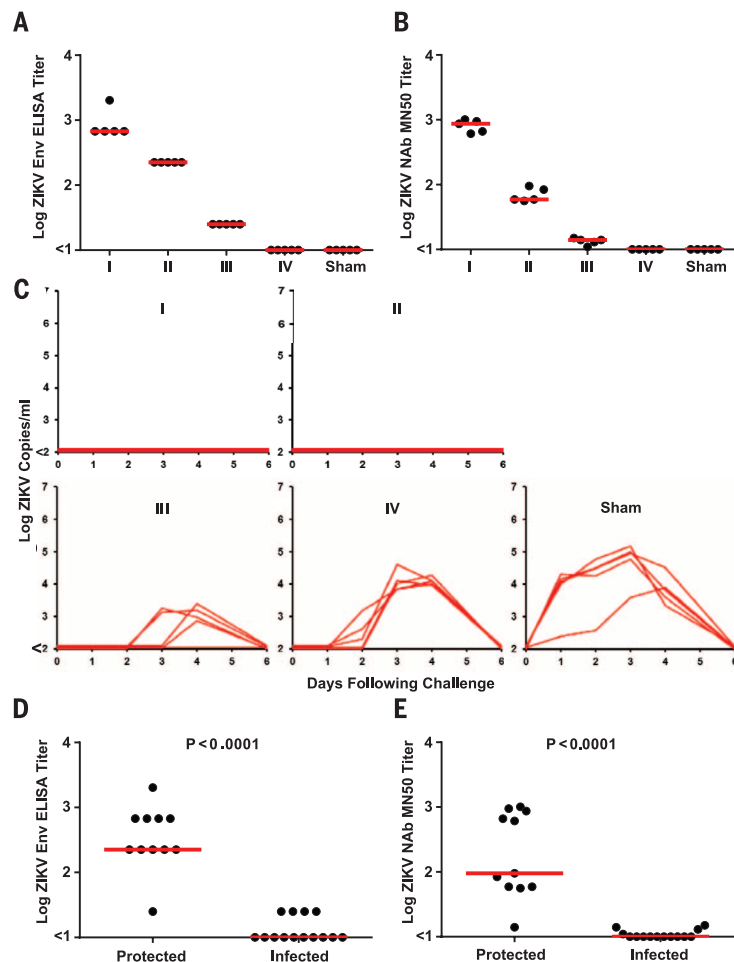


**Fig. 3. Adoptive transfer studies in mice.** (A) ZIKV Env-specific ELISA titers and (B) ZIKV-specific MN50 titers in serum from recipient Balb/c mice ( $n = 5$  per group), measured 1 hour after adoptive transfer of fivefold serial dilutions of IgG purified from PIV-vaccinated rhesus monkeys (groups I, II, III, and IV) or sham controls. (C) Plasma viral loads in mice after challenge with  $10^5$  vp ( $10^2$  PFU) of ZIKV-BR. (D and E) Immune correlates of protection and infection. Red bars reflect medians.  $P$  values were determined by  $t$  tests.

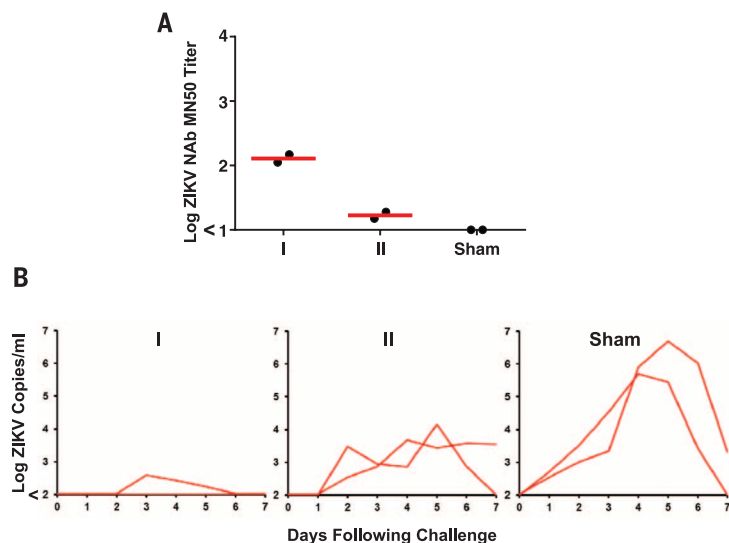


**Fig. 4. Adoptive transfer studies in rhesus monkeys.** (A) ZIKV-specific MN50 titers in serum from recipient rhesus monkeys ( $n = 2$  per group), measured 1 hour after adoptive transfer of fivefold dilutions of IgG purified from PIV-vaccinated rhesus monkeys (groups I and II) or sham controls. (B) Plasma viral loads in rhesus monkeys after challenge with  $10^6$  vp ( $10^3$  PFU) of ZIKV-BR. Red bars reflect medians.

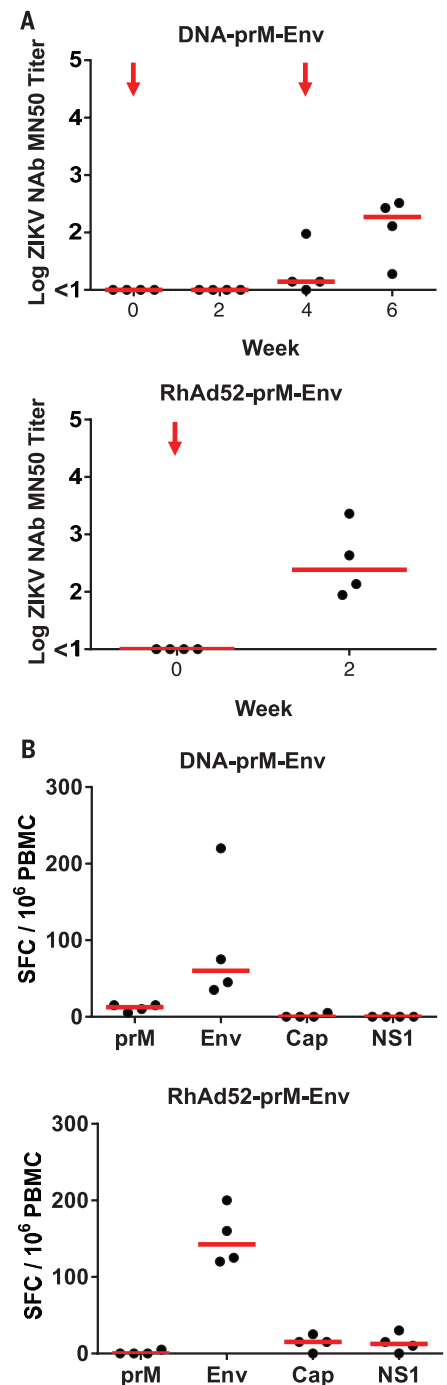


**Fig. 5. Immunogenicity of the ZIKV DNA-prM-Env and RhAd52-prM-Env vaccines.** (A) ZIKV-specific MN50 titers measured after immunization of rhesus monkeys by the intramuscular route with 5 mg of DNA-prM-Env vaccine at weeks 0 and 4 (red arrows) or with  $10^{11}$  vp RhAd52-prM-Env as a single immunization at week 0. (B) Cellular immune responses measured by IFN- $\gamma$  ELISPOT assays for prM, Env, Cap, and NS1 at week 6 for the DNA-prM-Env vaccine or at week 4 for the RhAd52-prM-Env vaccine. Red bars reflect medians.

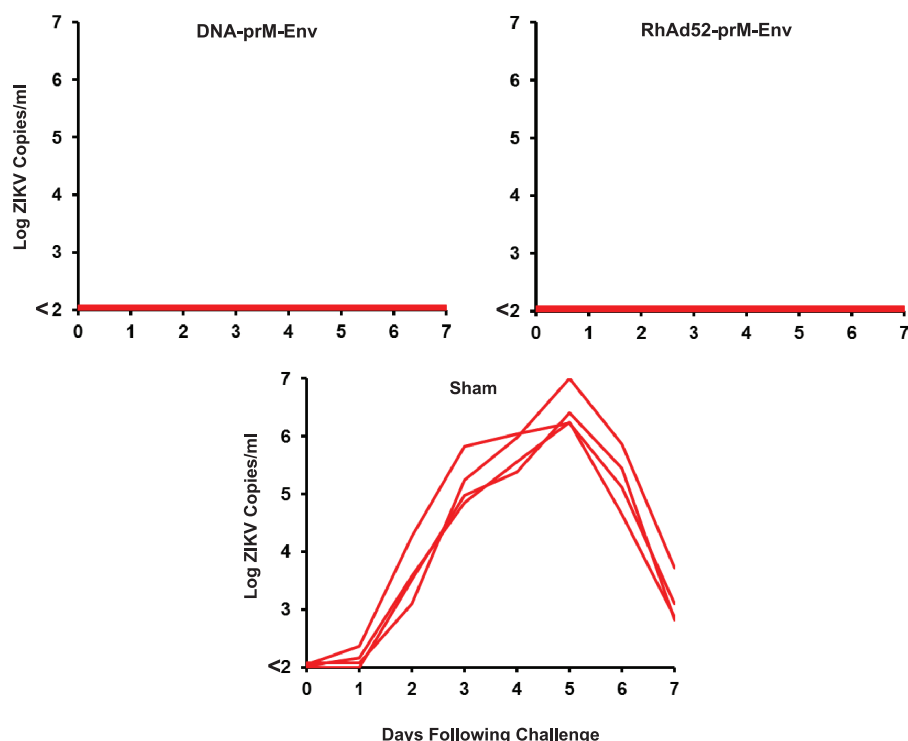


**Fig. 6. Protective efficacy of the ZIKV DNA-prM-Env and RhAd52-prM-Env vaccines.** Rhesus monkeys vaccinated with the DNA-prM-Env vaccine, the RhAd52-prM-Env vaccine, or sham vaccine ( $n = 4$  per group) were challenged by the subcutaneous route with  $10^6$  vp ( $10^3$  PFU) of ZIKV-BR. Plasma viral loads are shown.

microarray assays, compared with the other vaccines tested (17) (fig. S7). The DNA-prM-Env vaccine also induced detectable Env-specific IFN- $\gamma$  ELISPOT responses after the week 4 boost immunization, and the RhAd52-prM-Env vaccine induced Env-specific cellular immune responses after the initial week 0 priming immunization (Fig. 5B). Monkeys were challenged 4 weeks after the final vaccination. Both the DNA- and the RhAd52-prM-Env vaccines provided complete protection against subcutaneous challenge with  $10^6$  vp ( $10^3$  PFU) of ZIKV-BR, as measured by plasma viral loads (Fig. 6).

## Discussion

We demonstrate that three different vaccine platforms provide complete protection against ZIKV challenge in rhesus monkeys. No specific clinical safety adverse effects related to the vaccines were observed. We recently reported the protective efficacy of the PIV vaccine and the DNA-prM-Env vaccine in mice (15). The present data confirm and extend these prior studies by demonstrating robust protection against ZIKV challenge in nonhuman primates and specifically using the vaccination doses, routes, and schedules that are typically evaluated in clinical trials. Although the PIV vaccine and the DNA-prM-Env vaccine appeared comparably immunogenic in mice (15), the former proved more potent in rhesus monkeys under the conditions tested (Figs. 1 and 5). To generalize these observations to a vector-based vaccine, we also evaluated the RhAd52-prM-Env vaccine, which proved highly immunogenic and afforded complete protection after a single

immunization in monkeys (Fig. 5). Rhesus adenovirus vectors have the potential advantage of minimal baseline vector-specific neutralizing antibodies in human populations (16).

The adoptive transfer studies demonstrate that vaccine-elicited antibodies are sufficient for protection against ZIKV challenge. Moreover, passive protection in mice and rhesus monkeys was observed at relatively low antibody titers (Figs. 3 and 4). Such antibody titers are likely achievable in humans with these vaccine platforms, thus raising optimism for the development of a ZIKV vaccine for humans. Future preclinical and clinical studies will need to address the potential impact of cross-reactive antibodies against dengue virus and other flaviviruses. Secondary infection with a heterologous dengue serotype can be clinically more severe than initial infection, which may or may not reflect antibody-dependent enhancement (18, 19). Cross-reactive antibodies for ZIKV and dengue virus have also been described (20, 21), and dengue-specific antibodies have been reported to increase ZIKV replication in vitro (22). The relevance and implications of these findings for ZIKV vaccine development remain to be determined.

The consistent and robust antibody-based correlates of vaccine protection against ZIKV challenge in both rodents and primates suggest the generalizability of these findings. Similar correlates of protection, and specifically neutralizing antibody titers  $>10$ , have been reported for other flavivirus vaccines in humans (23–25). Together, these data suggest a path forward for clinical development of ZIKV vaccines in humans. PIV

vaccines have been evaluated previously in clinical trials for other flaviviruses, including dengue virus, tick-borne encephalitis virus, and Japanese encephalitis virus (26–30). Phase 1 clinical trials with the ZIKV PIV vaccine, as well as other candidate ZIKV vaccines, are expected to begin later this year.

## REFERENCES AND NOTES

1. A. S. Fauci, D. M. Morens, *N. Engl. J. Med.* **374**, 601–604 (2016).
2. L. R. Petersen, D. J. Jamieson, A. M. Powers, M. A. Honein, *N. Engl. J. Med.* **374**, 1552–1563 (2016).
3. J. Mlakar et al., *N. Engl. J. Med.* **374**, 951–958 (2016).
4. P. Brasil et al., *N. Engl. J. Med.* 10.1056/NEJMoal602412 (2016).
5. S. A. Rasmussen, D. J. Jamieson, M. A. Honein, L. R. Petersen, *N. Engl. J. Med.* **374**, 1981–1987 (2016).
6. M. A. Johansson, L. Mier-y-Teran-Romero, J. Reefhuis, S. M. Gilboa, S. L. Hills, *N. Engl. J. Med.* **375**, 1–4 (2016).
7. C. Li et al., *Cell Stem Cell* **19**, 120–126 (2016).
8. J. J. Miner et al., *Cell* **165**, 1081–1091 (2016).
9. F. R. Cugola et al., *Nature* **534**, 267–271 (2016).
10. P. Brasil et al., *Lancet* **387**, 1482 (2016).
11. R. W. Driggers et al., *N. Engl. J. Med.* **374**, 2142–2151 (2016).
12. D. M. Dudley et al., *Nat. Commun.* **7**, 12204 (2016).
13. P. P. Garcez et al., *Science* **352**, 816–818 (2016).
14. X. Qian et al., *Cell* **165**, 1238–1254 (2016).
15. R. A. Larocca et al., *Nature* 10.1038/nature18952 (2016).
16. P. Abbink et al., *J. Virol.* **89**, 1512–1522 (2015).
17. K. E. Stephenson et al., *J. Immunol. Methods* **416**, 105–123 (2015).
18. T. P. Endy et al., *Am. J. Epidemiol.* **156**, 40–51 (2002).
19. D. H. Libraty et al., *PLoS Med.* **6**, e1000171 (2009).
20. G. Barba-Spaeth et al., *Nature* 10.1038/nature18938 (2016).
21. K. Stettler et al., *Science* 10.1126/science.aaf8505 (2016).
22. W. Dejnirattisai et al., *Nat. Immunol.* 10.1038/ni.3515 (2016).
23. J. Hombach, T. Solomon, I. Kurane, J. Jacobson, D. Wood, *Vaccine* **23**, 5205–5211 (2005).
24. T. R. Kreil, I. Burger, M. Bachmann, S. Fraiss, M. M. Eibl, *Clin. Exp. Immunol.* **110**, 358–361 (1997).
25. R. A. Mason, N. M. Tauraso, R. O. Spertzel, R. K. Ginn, *Appl. Microbiol.* **25**, 539–544 (1973).
26. L. J. Martinez et al., *Am. J. Trop. Med. Hyg.* **93**, 454–460 (2015).
27. S. Fernandez et al., *Am. J. Trop. Med. Hyg.* **92**, 698–708 (2015).
28. V. Demicheli, M. G. Debalini, A. Rivetti, *Cochrane Database Syst. Rev.* **2009**, CD000977 (2009).
29. V. Demicheli, P. Graves, M. Pratt, T. Jefferson, *Cochrane Database Syst. Rev.* **2000**, CD000977 (2000).
30. E. O. Erra, A. Kantele, *Expert Rev. Vaccines* **14**, 1167–1179 (2015).

## ACKNOWLEDGMENTS

We thank J. Masciola, B. Graham, H. Marston, P. Vasconcelos, N. Collins, R. Olson, K. Kabra, C. Springer, G. Ballarini, N. Botero, K. Chandrika, G. Donofrio, M. Robb, D. Weiss, A. Cook, J. Campbell, S. Hetzel, U. Reimer, H. Wenschuh, T. Susovich, C. Linde, R. Lu, L. Peter, J. Le Suer, P. Gandhi, M. Iampietro, K. Visitsunthorn, A. Badamchi-Zadeh, L. Maxfield, and F. Stephens for generous advice, assistance, and reagents. The data from this study are tabulated in the main paper and in the supplementary materials. P.A., R.A.L., D.H.B., R.G.J., K.H.E., and S.J.T. are co-inventors on pending patent applications related to ZIKV vaccines, antigens, and vectors, and licensure discussions with industry partners are currently ongoing. P.A. and D.H.B. are cofounders and equity holders in AVVI Biotech. ZIKV challenge stocks and vaccine constructs are available with appropriate material transfer agreements. We acknowledge support from the U.S. Military Research and Materiel Command and the U.S. Military HIV Research Program through its cooperative agreement with the Henry M. Jackson Foundation (W81XWH-11-2-0174); the National Institutes of Health (grants AI095985, AI096040, AI100663, and AI124377); the Ragon Institute of MGH, MIT, and Harvard; and the São Paulo Research Foundation (FAPESP; grants 2011/18703-2 and 2014/17766-9). The views expressed in this manuscript are those of the authors and do not represent the official views of the Department of the Army or the Department of Defense.

## SUPPLEMENTARY MATERIALS

www.sciencemag.org/content/353/6304/1129/suppl/DC1  
Materials and Methods  
Figs. S1 to S7

21 July 2016; accepted 28 July 2016  
Published online 4 August 2016  
10.1126/science.aah6157



## REPORTS

## GEOPHYSICS

# Local near instantaneously dynamically triggered aftershocks of large earthquakes

Wenyuan Fan\* and Peter M. Shearer

Aftershocks are often triggered by static- and/or dynamic-stress changes caused by mainshocks. The relative importance of the two triggering mechanisms is controversial at near-to-intermediate distances. We detected and located 48 previously unidentified large early aftershocks triggered by earthquakes with magnitudes between  $\geq 7$  and 8 within a few fault lengths (approximately 300 kilometers), during times that high-amplitude surface waves arrive from the mainshock (less than 200 seconds). The observations indicate that near-to-intermediate-field dynamic triggering commonly exists and fundamentally promotes aftershock occurrence. The mainshocks and their nearby early aftershocks are located at major subduction zones and continental boundaries, and mainshocks with all types of faulting-mechanisms (normal, reverse, and strike-slip) can trigger early aftershocks.

Earthquake occurrence is modulated by complex fault interactions that often involve static- or dynamic-stress triggering mechanisms (1), which can trigger earthquakes over a variety of spatial and temporal scales (2–4). Aftershock sequences are thought to result from either or both of these mechanisms (1, 5). Static-stress triggering is most important for near-field aftershocks, whereas dynamic triggering is dominant in the far field. However, it is challenging to quantitatively separate the effects of static and dynamic triggering in the near-to-intermediate field (6, 7), leaving their relative importance controversial (8, 9).

Dynamic triggering is most clearly seen at large distances from earthquakes, where earthquakes and/or nonvolcanic tremors sometimes occur during the passage of surface waves, which are generally the highest-amplitude wave arrivals from shallow sources (10–12). However, observing possible dynamic triggering close to earthquakes is hampered by the mainshock coda, leaving existing catalogs incomplete and the local dynamic triggering effects uncertain (13–15). More complete catalogs would help in understanding local tectonics, constraining fault strength, and forecasting potential host faults for large earthquakes (16). Local dynamic triggering can facilitate multiple-fault ruptures for a single earthquake, which can pose a much higher seismic risk than that of single-fault ruptures (17, 18). Recently, local near-instantaneous dynamic triggering has been observed at both subduction zones (19) and continental plate boundaries (20, 21). But it is unclear how com-

monly this type of triggering occurs. We performed a comprehensive global search for early aftershocks of  $7 \leq \text{magnitude } (M) < 8$  earthquakes and found that local near-instantaneous dynamic triggering is common and that multiple-fault systems often dynamically interact with each other within a few fault lengths of the mainshocks within the first  $\sim 200$  s.

We analyzed teleseismic  $P$  waves from 88 large earthquakes [ $7.0 \leq \text{moment magnitude } (M_w) < 8.0$ ] from January 2004 to September 2015, with Global Centroid Moment Tensor (GCMT) centroid depths shallower than 40 km (Fig. 1) (22). We did not examine 12 larger earthquakes ( $M_w \geq 8.0$ ) in the same period because of their duration and complexity. We applied back-projection to detect and locate early aftershocks. Back-projection has proven to be effective to resolve complex spatiotemporal evolution of large earthquakes because the method requires few prior assumptions (23), and it has been successfully implemented to detect and locate both sub-events (24–27) and early aftershocks (19–21, 28, 29).

Our data are from global stations distributed by the Data Management Center (DMC) of the Incorporated Research Institutions for Seismology (IRIS). The  $P$  waves are filtered between 0.05 and 0.5 Hz for back-projection and are aligned for each event so as to reduce the effect of three-dimensional velocity structure (30). No post-smoothing or post-processing was applied to the back-projection images. We searched with a three-step screening criteria for potential early aftershocks that occurred within 200 s and between 50 and  $\sim 300$  km from the target earthquakes (30). We have validated our detection algorithm with three tests (30), which include confirming that our detected early aftershocks can be seen in high-frequency regional array

data (fig. S7), detecting and locating five cataloged mainshock–early-aftershock pairs within 100 km (fig. S8), and performing back-projection on 15 local  $M_w$  5.5 to 6.5 earthquakes located 200 to 400 km away from mainshocks, using the same corrections as we used on the mainshocks (figs. S9 and S10).

Twenty-seven of the 88 target earthquakes clearly triggered early aftershocks and include events at most of Earth's subduction zones and continental boundaries (Fig. 1 and figs. S1 to S3). None of the 88 target earthquakes have cataloged aftershocks in the time/distance window that we examined for this study (31). Earthquakes with all types of faulting mechanisms are capable of triggering early aftershocks (16 reverse-faulting, 4 strike-slip, and 7 normal-faulting) (Figs. 1 and 2 and table S1). Normal-faulting earthquakes have the highest triggering rate (50%), whereas triggering rates of reverse-faulting (28.1%) and strike-slip (23.5%) earthquakes are similar. For robustness, our back-projection approach focuses on the phase of the  $P$  wave arrivals, at the cost of losing absolute  $P$  wave amplitudes (30), which makes estimating the magnitudes of the very early aftershocks challenging. Nevertheless, by comparing with historical nearby earthquakes, the triggered early aftershocks are likely to be  $M$  5 to 6.5 earthquakes (30).

Within the Sunda arc subduction zone, a 24 July 2005 earthquake ( $M_w$  7.2) occurred near the northwestern boundary of the great 2004 Sumatra-Andaman earthquake (Fig. 2A) (23). The earthquake was a strike-slip event, which likely ruptured a different fault than the megathrust. The earthquake triggered two early aftershocks  $\sim 177$  and  $\sim 221$  km away from the epicenter and  $\sim 68$  and 120 s after its initiation at the landward region of the subduction zone. The triggered events strongly correlate with the surface-wave arrivals from the mainshock. The exact focal mechanisms, magnitudes, and depths of the triggered events are difficult to determine with only teleseismic  $P$  waves (19), but the triggered events must be at least  $M$  5 to be observed in the far field (19). Within 100 km of the 24 July 2005 earthquake, a 26 December 2004 reverse-faulting earthquake ( $M_w$  7.2) triggered an event in the seaward region (fig. S1E). Both  $M$  7 earthquakes may be aftershocks of the 2004 Sumatra-Andaman earthquake yet have very different focal mechanisms. Their triggered events are located in both the seaward and landward regions of the trench, indicating that the region is potentially critically stressed at both sides of the trench.

Within the Japan subduction zone, a 25 October 2013 normal-faulting earthquake ( $M_w$  7.1) broke the shallow part of the Pacific plate mantle 2 years after the 2011 Tohoku earthquake (Fig. 2B). The earthquake is seaward of the trench and triggered an early aftershock landward of the trench axis  $\sim 40$  s later. The triggered event is  $\sim 133$  km away from the epicenter, close to the 2011 Tohoku earthquake centroid location, and can be either an interplate or intraplate earthquake (32). This triggered event underlines that stress

Scripps Institution of Oceanography, University of California, San Diego, La Jolla, CA 92093-0225, USA.

\*Corresponding author. Email: w3fan@ucsd.edu

can be near instantaneously dynamically transferred within complex multiple fault systems, in a region with long-term plate-bending and converging deformation.

At the New Britain trench, the 29 March 2015 and 5 May 2015  $M_w$  7.5 doublet occurred on or near the subduction interface 130 km away from Kokopo, Papua New Guinea (Fig. 2C). The doublet events share similar focal mechanisms (22), and the 5 May 2015 event triggered two early aftershocks within the first 2 min after its initiation. The rupture propagated northeastward, toward the two triggered events (Fig. 2C). The first early aftershock is triggered ~40 s after

the mainshock origin time, located ~120 km northeast of the mainshock epicenter, and is close to the 29 March 2015  $M_w$  7.5 earthquake epicenter. Even though the first early aftershock struck within the trench-parallel region, its clear spatiotemporal separation from the mainshock and spatial correlation with the 29 March 2015 earthquake suggest that it is an early aftershock rather than part of the mainshock. The second triggered early aftershock is located further north of the mainshock, which we refer to as the horizontal down-dip direction of the mainshock. The second triggered event is located by the Manus trench, where the Australian and

Pacific plates converge at more than 70 mm year<sup>-1</sup> (33). The convergence dominates the local tectonic evolution (34), and the triggered early aftershock implies that the interplate fault of the two plates might be critically stressed.

In total, the 27 large earthquakes triggered 48 early aftershocks with epicentral distances ranging from 54 to 334 km (Fig. 3). For each triggered event, the triggering time is taken as the delay from the origin time to the peak amplitude time within a 20-s stacking window at the triggered location, ranging from 29.7 to 193.3 s, from which a triggering velocity can be derived from the epicentral distance divided by

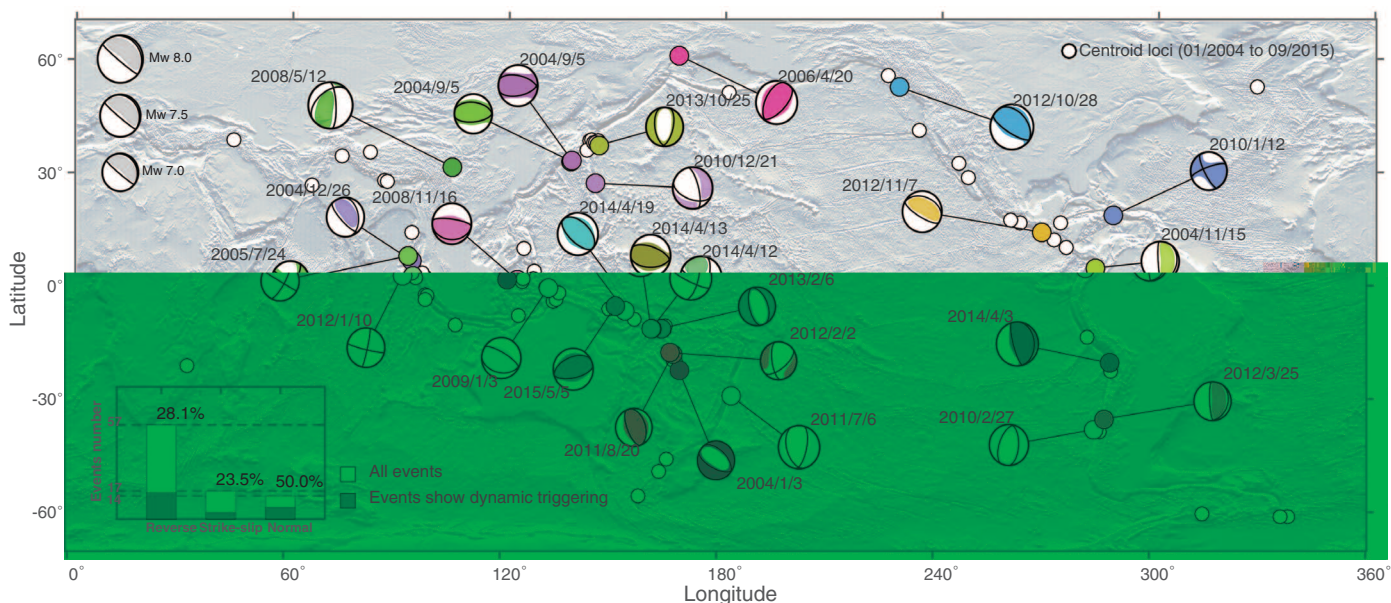


**Fig. 1. Twenty-seven early-aftershock-triggering mainshocks and their focal mechanisms.** The 27 triggering mainshocks are color-coded at their GCMT centroid locations (colored circles). The white circles show the rest of the 88 large earthquakes ( $7 \leq M_w < 8$ ) that we investigated with back-projection. Strike-slip earthquakes are defined when the rakes of both nodal planes are within 45° deviation of 0° or 180°. Normal- and reverse-faulting earthquakes have rakes within 45° deviation of -90° and 90°, respectively. (Inset) Triggering rates for the three types of earthquakes.

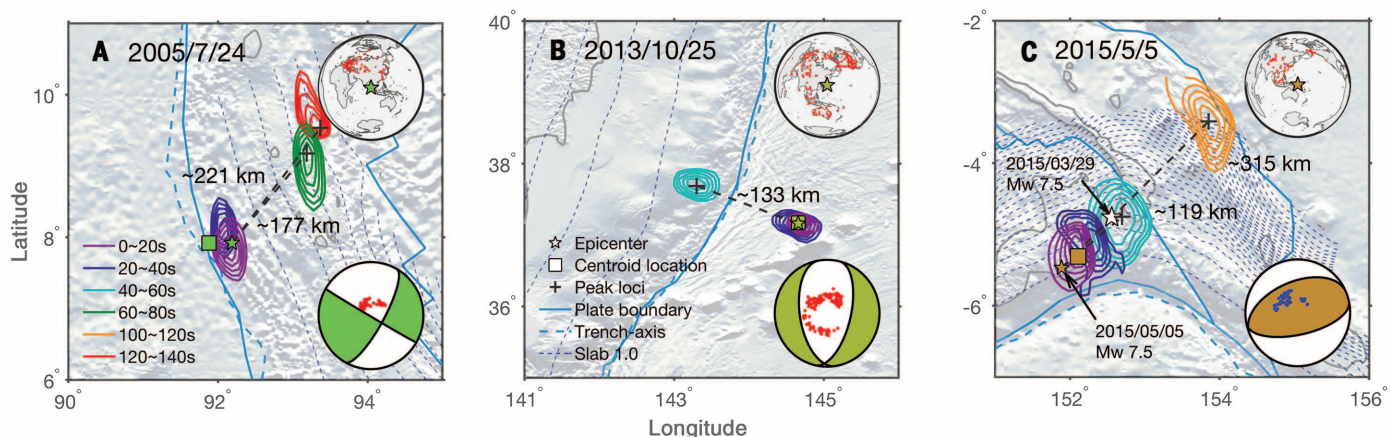


**Fig. 2. Back-projection results for three earthquakes with different focal mechanisms (60% normalized energy contours).** (A) Rupture evolution of the 24 July 2005,  $M_w$  7.2 strike-slip earthquake in the Sunda arc. Stations used for back-projection and their  $P$  wave polarity with the GCMT focal mechanism are shown as insets. Negative polarities are red, and positive polarities are blue. (B) Rupture evolution of the 25 October 2013,  $M_w$  7.1 normal-faulting earthquake in the Japan subduction zone. The insets are the same as in (A). (C) Rupture evolution of the 5 May 2015,  $M_w$  7.5 reverse-faulting earthquake in the New Britain trench. The insets are the same as in (A).



the triggering time. To assess standard errors (SEs) in the epicentral distances and triggering times, we implemented jackknife resampling for each earthquake with the records used for the back-projection (30). Within 1 SE, all the triggered early aftershocks occurred after the surface wave passed through (at 3 to ~4 km/s) (Fig. 3). This strong correlation shows that the 48 early aftershocks were triggered by the mainshocks and suggests that dynamic stress was the physical process that drove the observed triggering. Assuming that the  $M$  7 earthquakes ruptured for ~40 s, then 26 triggered early aftershocks coincide with the passing surface waves (Fig. 3). The rapid-onset dynamic triggering events with small delay time indicate frictional failures caused by dynamic stress changes induced by the transient surface waves (10). In addition, 22 triggered events are delayed for seconds to minutes, which might reflect nonlinear friction behavior or a hydraulic response of the receiver faults (35–37). The diversity of the triggered responses suggests the heterogeneity of the stress field and the variability of the frictional strength at each given fault (38). These observations imply that dynamic triggering modulates near-to-intermediate field seismicity and commonly promotes large early aftershocks in a near-instantaneous fashion.

There are 11 triggered early aftershocks that occurred within 50 s of the origin time, with the remainder occurring within 200 s. The short temporal delay has two implications. First, a large portion of the early aftershocks are missing from global catalogs, which do not have these events, despite being large enough to be detected in teleseismic records. Second, the transition time from mainshock to aftershocks is near instantaneous at most of the subduction zones and plate boundaries via dynamic triggering. If the early aftershock sequence follows Omori's law, then the relative aftershock deficit, related to parameter  $c$ , will be pushed to as short as tens of seconds (30). If the aftershock activities are dominated by rate-and-state friction, then the derived  $c$  can be used to probe frictional properties of the local fault systems (39).

Most of the observed early aftershocks are unlikely to be on or near the mainshock slip surface. The early aftershocks have a distinctly different epicentral distance distribution than the aftershocks cataloged by the International Seismological Centre (ISC) (31) catalog or U.S. Geological Survey National Earthquake Information Center Preliminary Determination of Epicenters Bulletin (PDE) (Fig. 4A). The aftershock distribution of the ISC and PDE events can be used to estimate mainshock rupture areas. The majority of the catalog aftershocks are within ~90 km, whereas the majority of the dynamically triggered early aftershocks are more than ~90 km away from the epicenters (Fig. 4A) (30).

Fifteen of the 27 large earthquakes were reverse-faulting earthquakes at subduction zones, seven were normal-faulting earthquakes at subduction zones, four were strike-slip, and one was the 2008 China Wenchuan continental earthquake (reverse-faulting). All the subduction zone

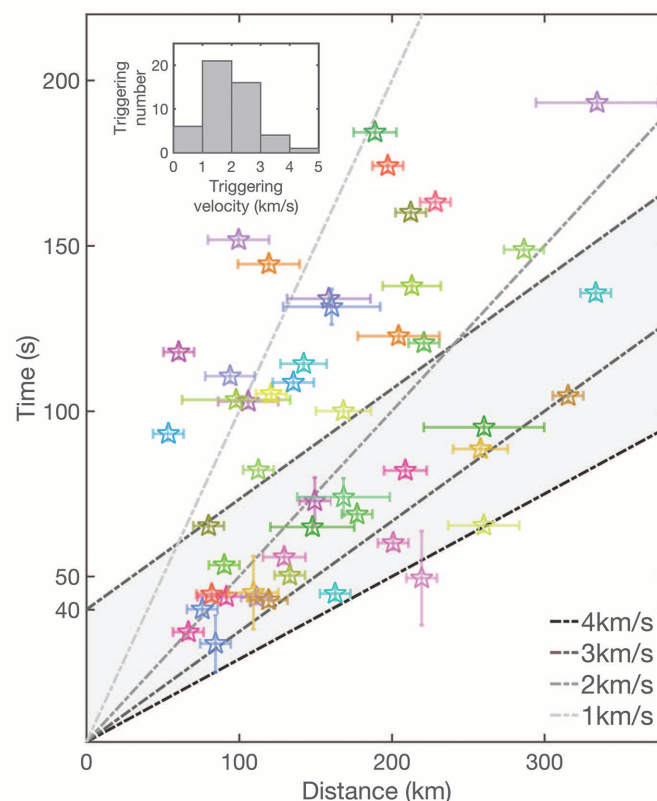


**Fig. 3. Time versus distance plot of triggered events.** Forty-eight triggered early aftershocks are shown as stars with the same color of their triggering large earthquakes. The colored bars for each triggered early aftershock show 1 SE of the epicentral distances and triggering times (table S1). The shaded region shows the likely influence of passing surface waves of a ~40 s duration  $M$  7 earthquake. (Inset) The distribution of the triggering velocity for the 48 triggered events.

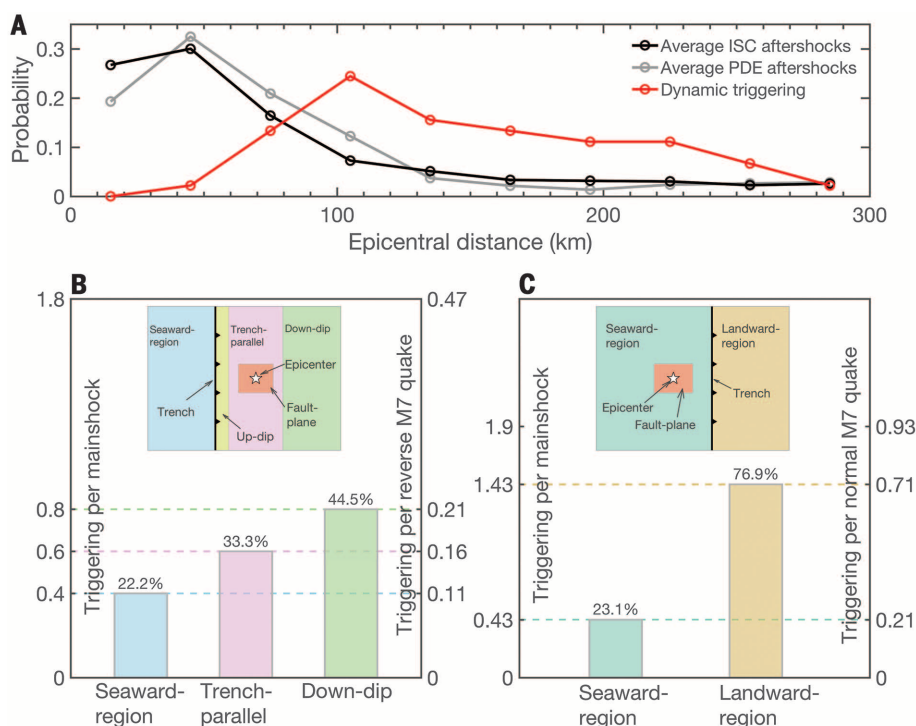


**Fig. 4. Aftershock distribution and relative locations of the triggered early aftershocks.** (A) The averaged ISC aftershock distribution of 18 mainshocks (30) is shown as the black line. Average PDE aftershock distribution from five mainshocks is shown as the gray line. The dynamically triggered early aftershock distribution is shown as the red line. The distribution is obtained from partitioning the triggered early aftershocks into 30-km-wide bins in epicentral distance. The probabilities are placed in the middle of the center of each epicentral bin. (B) Triggering rate and distribution for reverse-faulting mainshocks. (C) Triggering rate and distribution for normal-faulting mainshocks. (Insets) The divisions of the relative locations of triggered early aftershocks.



reverse-faulting earthquake centroid locations were within the landward region, whereas all the normal-faulting earthquakes were in the seaward region of the subduction zone (figs. S1 to S3). To better understand the triggering mechanisms, we horizontally divided the triggered locations as down-dip region, trench-parallel region, up-dip region, and seaward region for reverse-faulting earthquakes with respect to the mainshock and trench axis; we divided the triggered locations as landward and seaward regions for normal-faulting earthquakes with respect to the trench axis (Fig. 4, B and C). For the reverse-faulting earthquakes, the dynamically triggered early aftershocks tend to occur in the down-dip region (44.5%), rather than the trench-parallel region (33.3%) or the seaward region (22.2%). We did not observe any triggered early aftershocks in the up-dip region for reverse-faulting earthquakes. For the normal-faulting earthquakes, occurrence of the triggered early aftershocks in the landward region is three times higher than in the seaward region (landward region, 76.9%; seaward region, 23.1%). In total, the faults in the landward region, either on or near the megathrust, are more susceptible to near-field dynamic triggering. Although tsunami earthquakes often rupture the shallowest portion of the megathrust (40), the material or the faults in that region may be too weak to accumulate enough strain to be dynamically triggered. Generally, extensional regions are more easily triggered than compressional regions (41, 42). If this holds true, some of the triggered earthquakes in the landward region are likely normal-faulting instead of reverse-faulting.

The detected early aftershocks all radiated less energy than that of the mainshocks and are likely moderate in size ( $M$  5 to 6.5) (30). Although observed remotely triggered earthquakes to date have been relatively small (43), it is possible on rare occasions that remote dynamic triggering could cause damaging earthquakes (44). Near-to-intermediate field triggering has been observed before (24–27, 45–48)—and occurs in physics-based rupture models that show that multiple-fault systems can rupture together in a single earthquake (17, 18, 49–51)—but is often considered to be part of the mainshock rupture process, which may involve multiple subevents, some triggered in response to both static- and dynamic-stress changes. Because the majority of the triggered early aftershocks are seen in the landward region of the trenches (Fig. 4), which could be on or near the megathrust, it is possible that this type of early dynamic triggering could lead to a great earthquake ( $M \geq 8.0$ ), with contributions from both static and dynamic triggering (49, 51, 52). However, in the absence of known fault geometries for the triggered earthquakes we observed, it is difficult to perform stress calculations in order to explore the triggering mechanisms in more detail.

Early dynamically triggered aftershocks can also be seen in standard earthquake catalogs in favorable circumstances. To compare with our back-projection-detected events, we systematically searched through the ISC catalog from

1993 to 2013 to find earthquakes occurring in the same space/time window that we searched using back-projection, which follow target events of varying sizes (30). The local near-instantaneous triggering rate drawn from the ISC catalog for  $M$  7 earthquakes (4 of 198) is much lower than what we observed with back-projection (27 of 88), highlighting the difficulty in detecting these early aftershocks with standard methods (fig. S11). The catalog results are most likely to be complete in cases in which the triggered event is larger than the target event—the target event is a foreshock to the later event. This occurs globally in our space/time window for 3 of 1532 (0.2%) of  $M > 6$  earthquakes. Assuming that the dynamically triggered earthquake magnitudes are drawn randomly from a  $b = 1$  Gutenberg-Richter distribution and that aftershock triggering rates are self-similar with magnitude (53), a 0.2% rate of triggering a larger event implies a 20% rate of  $M$  5 to 7 early aftershocks following  $M$  7 mainshocks in the same space/time window. This is comparable with our observed rate of 30%.

Our analysis represents a lower limit on the number of near-source dynamically triggered earthquakes that are large enough to be seen teleseismically because we likely missed many events owing to our conservative selection criteria and the poor station coverage for some mainshocks. Thus, fault interactions and triggering may be a relatively common feature for large earthquakes near subduction zones and continental boundaries. The near-zero to short delay time of the observed dynamic triggering suggests that in a large complex fault system, such as exists in most subduction zones, a few faults will always be critically stressed and close to failure. By studying where triggered events are most common, it may be possible to infer properties of the interacting faults in specific regions. Last, early aftershocks can potentially illuminate unknown faults, and the observed fault interactions of earthquake sequences can inform future hazard assessment.

## REFERENCES AND NOTES

1. R. A. Harris, *J. Geophys. Res.* **103**, 24347–24358 (1998).
2. D. P. Hill et al., *Science* **260**, 1617–1623 (1993).
3. G. C. P. King, R. S. Stein, J. Lin, *Bull. Seismol. Soc. Am.* **84**, 935–953 (1994).
4. J. Gomberg, P. A. Reasenberg, P. Bodin, R. A. Harris, *Nature* **411**, 462–466 (2001).
5. A. M. Freed, *Annu. Rev. Earth Planet. Sci.* **33**, 335–367 (2005).
6. C. Voisin, M. Campillo, I. R. Ionescu, F. Cotton, O. Scotti, *J. Geophys. Res.* **105**, 21647–21659 (2000).
7. J. Deciem et al., *Geophys. J. Int.* **181**, 1128–1146 (2010).
8. K. R. Felzer, E. E. Brodsky, *Nature* **441**, 735–738 (2006).
9. K. Richards-Dinger, R. S. Stein, S. Toda, *Nature* **467**, 583–586 (2010).
10. D. Kilb, J. Gomberg, P. Bodin, *Nature* **408**, 570–574 (2000).
11. K. Obara, *Science* **296**, 1679–1681 (2002).
12. A. A. Velasco, S. Hernandez, T. O. M. Parsons, K. Pankow, *Nat. Geosci.* **1**, 375–379 (2008).
13. Y. Y. Kagan, *Bull. Seismol. Soc. Am.* **94**, 1207–1228 (2004).
14. Z. Peng, J. E. Vidale, H. Houston, *Geophys. Res. Lett.* **33**, L17307 (2006).
15. Z. Peng, P. Zhao, *Nat. Geosci.* **2**, 877–881 (2009).
16. S. G. Wesnousky, *Bull. Seismol. Soc. Am.* **84**, 1940–1959 (1994).
17. R. A. Harris, R. J. Archuleta, S. M. Day, *Geophys. Res. Lett.* **18**, 893–896 (1991).

18. R. A. Harris, J. F. Dolan, R. Hartleb, S. M. Day, *Bull. Seismol. Soc. Am.* **92**, 245–255 (2002).
19. W. Fan, P. M. Shearer, *Geophys. Res. Lett.* **43**, 1934–1942 (2016).
20. E. Nissen et al., *Nat. Geosci.* **9**, 330–336 (2016).
21. D. Wang et al., *J. Geophys. Res.* **121**, 1948–1961 (2016).
22. G. Ekström, M. Nettles, A. Dziwowski, *Phys. Earth Planet. Inter.* **200–201**, 1–9 (2012).
23. M. Ishii, P. M. Shearer, H. Houston, J. E. Vidale, *Nature* **435**, 933–936 (2005).
24. B. P. Allmann, P. M. Shearer, *Science* **318**, 1279–1283 (2007).
25. E. Kiser, M. Ishii, *Geophys. Res. Lett.* **38**, L07301 (2011).
26. H. Yue, T. Lay, K. D. Koper, *Nature* **490**, 245–249 (2012).
27. L. Meng, J.-P. Ampuero, A. Sladen, H. Rendon, *J. Geophys. Res.* **117**, 2156–2202 (2012).
28. S. D'Amico, K. D. Koper, R. B. Herrmann, A. Akinci, L. Malagnini, *Geophys. Res. Lett.* **37**, L03301 (2010).
29. E. Kiser, M. Ishii, *J. Geophys. Res.* **118**, 5564–5576 (2013).
30. Materials and methods are available as supplementary materials on Science Online.
31. International Seismological Centre, *On-line Bulletin* (ISC, 2013).
32. W. Nakamura, N. Uchida, T. Matsuzawa, *J. Geophys. Res.* **121**, 2591–2607 (2016).
33. C. DeMets, R. G. Gordon, D. F. Argus, S. Stein, *Geophys. Res. Lett.* **21**, 2191–2194 (1994).
34. T. Johnson, P. Molnar, *J. Geophys. Res.* **77**, 5000–5032 (1972).
35. J. Gomberg, M. L. Blanpied, N. M. Beeler, *Bull. Seismol. Soc. Am.* **87**, 294–309 (1997).
36. T. Parsons, *Geophys. Res. Lett.* **32**, L04302 (2005).
37. A. Nur, J. R. Booker, *Science* **175**, 885–887 (1972).
38. L. Rivera, H. Kanamori, *Geophys. Res. Lett.* **29**, 12–11 (2002).
39. Z. Peng, J. E. Vidale, M. Ishii, A. Helmstetter, *J. Geophys. Res.* **112**, B03306 (2007).
40. H. Kanamori, *Phys. Earth Planet. Inter.* **6**, 346–359 (1972).
41. S. Prejean, D. Hill, Dynamic triggering of earthquakes, in *Encyclopedia of Complexity and Systems Science* (Springer, 2009), pp. 2600–2621.
42. R. M. Harrington, E. E. Brodsky, *Bull. Seismol. Soc. Am.* **96**, 871–878 (2006).
43. T. Parsons, J. O. Kaven, A. A. Velasco, H. Gonzalez-Huizar, *Geochim. Geophys. Geosyst.* **13**, Q06016 (2012).
44. F. F. Pollitz, R. S. Stein, V. Sevilgen, R. Bürgmann, *Nature* **490**, 250–253 (2012).
45. D. Eberhart-Phillips et al., *Science* **300**, 1113–1118 (2003).
46. D. D. Oglesby, D. S. Dreger, R. A. Harris, N. Ratchkovski, R. Hansen, *Bull. Seismol. Soc. Am.* **94**, S214–S233 (2004).
47. B. Delouis, M. Pardo, D. Legrand, T. Monfret, *Bull. Seismol. Soc. Am.* **99**, 87–94 (2009).
48. S. Peyrat et al., *Geophys. J. Int.* **182**, 1411–1430 (2010).
49. G. Anderson, B. Aagaard, K. Hudnut, *Science* **302**, 1946–1949 (2003).
50. D. D. Oglesby, *Bull. Seismol. Soc. Am.* **95**, 1604–1622 (2005).
51. J. C. Lozos, *Sci. Adv.* **2**, e1500621 (2016).
52. D. C. Agnew, L. M. Jones, *J. Geophys. Res.* **96**, 11959–11971 (1991).
53. K. R. Felzer, R. E. Abercrombie, G. Ekström, *Bull. Seismol. Soc. Am.* **94**, 88–98 (2004).

## ACKNOWLEDGMENTS

The facilities of IRIS Data Services, and specifically the IRIS DMC, were used for access to waveforms used in this study (National Science Foundation grant EAR-1261681). Hi-net data were obtained from the National Research Institute for Earth Science Disaster Prevention in Japan (NIED). The earthquake catalogs were downloaded from the Global Centroid Moment Tensor project (GCMT) (22), U.S. Geological Survey National Earthquake Information Center PDE, and ISC (31). The data used in the study are publicly available at DMC and NIED, and the processed data are available from the authors upon request. This work was supported by National Science Foundation grant EAR-1111111.

## SUPPLEMENTARY MATERIALS

www.sciencemag.org/content/353/6304/1133/suppl/DC1  
Materials and Methods  
Supplementary Text  
Figs. S1 to S11  
Table S1 to S3  
References (54–75)

29 April 2016; accepted 11 August 2016  
10.1126/science.aag0013

## MATERIALS SCIENCE

# Electromagnetic interference shielding with 2D transition metal carbides (MXenes)

Faisal Shahzad,<sup>1,2\*</sup> Mohamed Alhabeab,<sup>3\*</sup> Christine B. Hatter,<sup>3\*</sup> Babak Anasori,<sup>3</sup> Soon Man Hong,<sup>1</sup> Chong Min Koo,<sup>1,2†</sup> Yuri Gogotsi<sup>3†</sup>

Materials with good flexibility and high conductivity that can provide electromagnetic interference (EMI) shielding with minimal thickness are highly desirable, especially if they can be easily processed into films. Two-dimensional metal carbides and nitrides, known as MXenes, combine metallic conductivity and hydrophilic surfaces. Here, we demonstrate the potential of several MXenes and their polymer composites for EMI shielding. A 45-micrometer-thick  $\text{Ti}_3\text{C}_2\text{T}_x$  film exhibited EMI shielding effectiveness of 92 decibels (>50 decibels for a 2.5-micrometer film), which is the highest among synthetic materials of comparable thickness produced to date. This performance originates from the excellent electrical conductivity of  $\text{Ti}_3\text{C}_2\text{T}_x$  films (4600 Siemens per centimeter) and multiple internal reflections from  $\text{Ti}_3\text{C}_2\text{T}_x$  flakes in free-standing films. The mechanical flexibility and easy coating capability offered by MXenes and their composites enable them to shield surfaces of any shape while providing high EMI shielding efficiency.

Electronic devices are getting smarter, being made smaller, and growing in number every day. Any electronic device that transmits, distributes, or uses electrical energy creates electromagnetic interference (EMI) that has detrimental impacts on device performance and the surrounding environment. As electronics and their components operate at faster speeds and smaller size, a substantial increase in EMI results, which can lead to malfunctioning and degradation of electronics (1–4). This increase in electromagnetic pollution can also affect human health, as well as the surrounding environment, if no shielding is provided (5).

An effective EMI shielding material must both reduce undesirable emissions and protect the component from stray external signals. The primary function of EMI shielding is to reflect radiation using charge carriers that interact directly with the electromagnetic (EM) fields (6). As a result, shielding materials need to be electrically conductive. However, conductivity is not the only requirement. The secondary mechanism of EMI shielding requires absorption of EM radiation due to the material's electric and/or magnetic dipoles interacting with the radiation. High electrical conductivity is the primary factor determining reflectivity and absorption characteristics of the shield (7). However, a third mechanism accounting for mul-

multiple internal reflections is less studied but contributes substantially to EMI shielding effectiveness. These internal reflections arise from scattering centers and interfaces or defect sites within the shielding material, resulting in scattering and then absorption of EM waves (EMWs) (1, 8, 9).

Previously, metal shrouds were the material of choice to combat EMI interference (1–4) (6–10), but with smaller devices and components, adding additional weight coupled with susceptibility to corrosion makes metals less desirable (8). Lightweight, low-cost, high-strength and easy-to-fabricate shielding materials are therefore needed. Polymer-matrix composites with embedded conductive fillers have become a popular alter-

native for EMI shielding because of high processability and low densities (10). Carbon-based fillers, particularly carbon nanotubes and graphene in combination with magnetic constituents, have attracted much interest in recent years (11), but no breakthrough has been reported thus far. New EMI shielding materials that can exceed the requirements of next-generation portable equipment and wearable devices are strongly needed.

MXenes are a unique family of two-dimensional (2D) transition metal carbides and/or nitrides with the formula  $\text{M}_{n+1}\text{X}_n\text{T}_x$ , where M is an early transition metal (e.g., Ti, Zr, V, Nb, Ta, or Mo) and X is carbon and/or nitrogen. Owing to the aqueous medium used during synthesis, MXene flakes are terminated with surface moieties ( $\text{T}_x$ ), such as a mixture of  $-\text{OH}$ ,  $=\text{O}$ , and  $-\text{F}$  (12). Metallic conductivity and good mechanical properties coupled with hydrophilicity make MXenes a good candidate for use in polymer composites (12) and energy storage devices (13) as they can intercalate organic molecules and ions. About 20 different MXenes have already been reported (12, 14, 15). Thus far, the most commonly studied MXene,  $\text{Ti}_3\text{C}_2\text{T}_x$ , has been incorporated into different polymer matrices such as ultrahigh-molecular weight polyethylene (UMWPE), polypyrrole (PPy), and polyvinyl alcohol (PVA). The MXene-polymer composites exhibited improved tensile strength, but good conductivity was maintained at low polymer loadings (16, 17). A previous study incorporating a naturally occurring polymer, sodium alginate (SA), as a binder for Li-ion batteries (18) showed retention of electrode conductivity, the primary component for EMI shielding. SA is a linear polysaccharide copolymer derived from seaweed. Natural biomaterials, like SA, are potentially ideal candidates for polymeric matrices because they are abundant, do not harm the environment, and are mechanically robust. SA has oxygen-containing functional groups ( $-\text{OH}$ ,  $-\text{COO}$ , and  $=\text{O}$ ), which can potentially facilitate the formation of hydrogen bonding with the termination

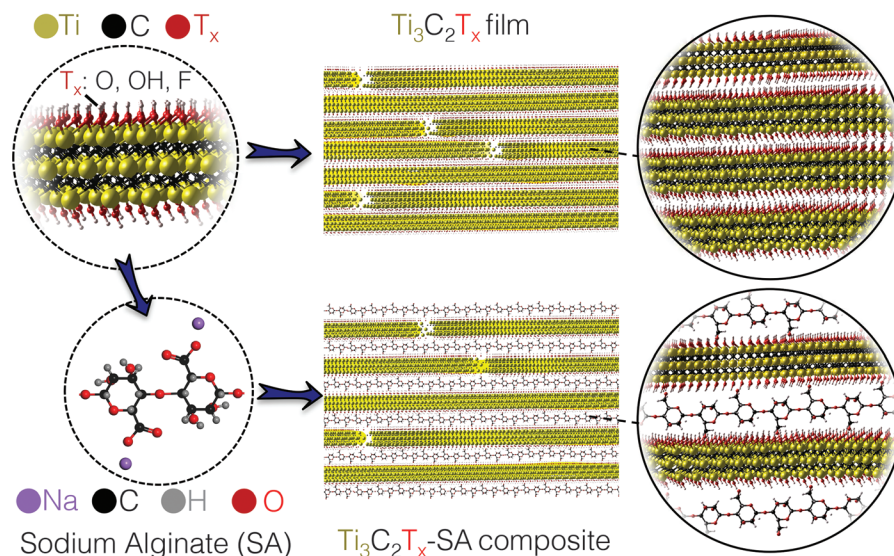


Fig. 1. Schematic of  $\text{Ti}_3\text{C}_2\text{T}_x$  and  $\text{Ti}_3\text{C}_2\text{T}_x$ -SA composite films.

<sup>1</sup>Materials Architecturing Research Center, Korea Institute of Science and Technology, 5, Hwarang-ro 14-gil, Seongbuk-gu, Seoul 02792, Republic of Korea. <sup>2</sup>Nanomaterials Science and Engineering, University of Science and Technology, 217, Gajung-ro, Yuseong-gu, Daejeon 34113, Republic of Korea. <sup>3</sup>Department of Materials Science and Engineering, and A. J. Drexel Nanomaterials Institute, Drexel University, 3141 Chestnut Street, Philadelphia, PA 19104, USA.

\*These authors contributed equally to this work. †Corresponding author. Email: gogotsi@drexel.edu (Y.G.); koo@kist.re.kr (C.M.K.)



groups of MXenes. To date, no MXene-SA composites have been reported in the literature.

Here we report highly flexible MXene films ( $\text{Ti}_3\text{C}_2\text{T}_x$ ,  $\text{Mo}_2\text{TiC}_2\text{T}_x$ , and  $\text{Mo}_2\text{Ti}_2\text{C}_3\text{T}_x$ ) and nacre-like MXene-polymer composite films ( $\text{Ti}_3\text{C}_2\text{T}_x$ -SA) with excellent EMI shielding performance. All free-standing films were made by vacuum-assisted filtration starting from colloidal solutions of pure MXenes or its composites (fig. S1). The schematic representation of the layered structure for MXene-SA composites is displayed in Fig. 1. Both  $\text{Ti}_3\text{C}_2\text{T}_x$  film (45  $\mu\text{m}$ ) and  $\text{Ti}_3\text{C}_2\text{T}_x$ -SA [8  $\mu\text{m}$ , 10 weight % (wt %) SA], in particular, exhibit extraordinary EMI shielding effectiveness (SE) of 92 and 57 dB, respectively. These MXene films have additional advantages such as high conductivity, easy processing, relatively low density, and mechanical flexibility. To our knowledge, this is the highest EMI SE performance reported for synthetic materials of similar thickness and is comparable to the EMI SE performance of pure metals. This finding paves the way for the development of a large family of EMI shielding materials.

The scanning electron microscopy (SEM) image of a  $\text{Ti}_3\text{C}_2\text{T}_x$  MXene flake (size range from 1 to 5  $\mu\text{m}$ ) on an alumina filter is shown in Fig. 2A, in which the MXene flake is almost transparent to the electron beam. The cross-sectional SEM images of the 50 wt %  $\text{Ti}_3\text{C}_2\text{T}_x$ -SA, and pristine  $\text{Ti}_3\text{C}_2\text{T}_x$  are shown in Fig. 2, B and C, respectively. In all composite loadings, the nacre-like layered stacking of the  $\text{Ti}_3\text{C}_2\text{T}_x$  remains; similar to that of the pristine  $\text{Ti}_3\text{C}_2\text{T}_x$  films. This characteristic is also confirmed by the presence of the  $\text{Ti}_3\text{C}_2\text{T}_x$  (002) peak in all the  $\text{Ti}_3\text{C}_2\text{T}_x$ -SA x-ray diffraction (XRD) patterns (Fig. 2D). The intensity of all the (001)  $\text{Ti}_3\text{C}_2\text{T}_x$  peaks in the composite samples is decreased compared to that of the pristine  $\text{Ti}_3\text{C}_2\text{T}_x$ , owing to the presence of SA between the layers. The introduction of SA adds disorder in stacking and separates MXene flakes. Additionally, a new peak around  $\sim 4.4^\circ$  appears after the addition of SA, and its intensity increases with SA content

(compare the top two patterns in Fig. 2D). This peak corresponds to a  $\text{Ti}_3\text{C}_2\text{T}_x$  interlayer spacing of  $\sim 10$  Å, a result of SA presence between MXene layers. In the case of 30 wt %  $\text{Ti}_3\text{C}_2\text{T}_x$ -SA, the broad (002) peak is between  $\leq 4.4^\circ$  and  $6.5^\circ$ , which is due to the variable interlayer spacings between MXene layers, ranging from  $>10$  to 3.5 Å. This shows that although SA molecules are intercalated between MXene layers, the latter still retains the ordered layered structure.

Cross-sectional transmission electron microscopy (TEM) images of the  $\text{Ti}_3\text{C}_2\text{T}_x$ -SA composite films confirm the intercalation of SA layers in-between MXene flakes. At higher  $\text{Ti}_3\text{C}_2\text{T}_x$  contents, mostly stacks of  $\text{Ti}_3\text{C}_2\text{T}_x$  flakes, with some individual flakes separated with SA, are observed (Fig. 2E). This feature could be due to MXene restacking during filtration. At lower  $\text{Ti}_3\text{C}_2\text{T}_x$  concentrations, more individual  $\text{Ti}_3\text{C}_2\text{T}_x$  flakes are separated with SA, and a variety of different interlayer spacings are present (Fig. 2F). However, some MXene restacking does occur even at lower MXene concentrations (fig. S2). This combination of different spacing between layers can explain the very broad range of the (002) peaks observed in 30 wt %  $\text{Ti}_3\text{C}_2\text{T}_x$ -SA XRD patterns from  $\leq 4.4^\circ$  to  $6.5^\circ$ .

Materials with large electrical conductivity are typically needed to obtain high EMI SE values. Figure 3A presents the electrical conductivity of three different types of MXenes. A higher electrical conductivity in  $\text{Mo}_2\text{Ti}_2\text{C}_3\text{T}_x$  was observed compared to  $\text{Mo}_2\text{TiC}_2\text{T}_x$ , which is in agreement with previously reported results (19).  $\text{Ti}_3\text{C}_2\text{T}_x$  films showed the highest electrical conductivity among the studied samples, reaching  $4600 \text{ S cm}^{-1}$ . Such excellent electrical conductivity arises from the high electron density of states near the Fermi level  $[N(E_F)]$  as predicted from density functional theory (DFT) (20), making this MXene metallic in nature. By contrast,  $\text{Mo}_2\text{TiC}_2\text{T}_x$  and  $\text{Mo}_2\text{Ti}_2\text{C}_3\text{T}_x$  exhibited lower electrical conductivity values of 119.7 and  $297.0 \text{ S cm}^{-1}$ , respectively, and semiconductor-

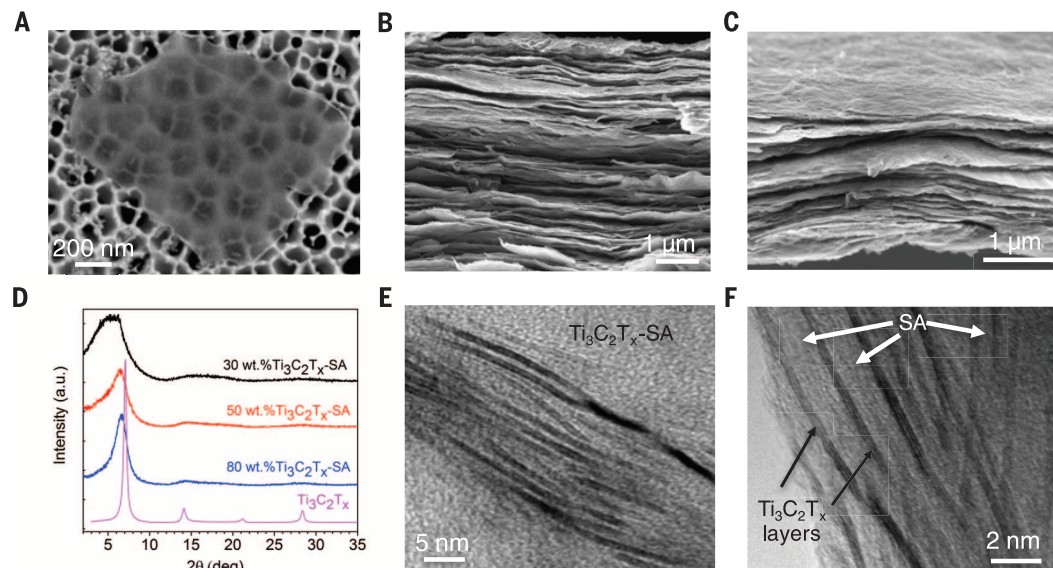
like temperature dependence of conductivity (15, 19).

Electrical conductivities of  $\text{Ti}_3\text{C}_2\text{T}_x$ -SA polymer composites are plotted in Fig. 3B. With the addition of only 10 wt %  $\text{Ti}_3\text{C}_2\text{T}_x$ , the conductivity of SA polymer rises to  $0.5 \text{ S cm}^{-1}$ . The large aspect ratio of  $\text{Ti}_3\text{C}_2\text{T}_x$  flakes likely provides a percolation network at low filler loading, thereby increasing electrical conductivity of the composite sample. As filler content is increased, electrical conductivity increases and reaches  $3000 \text{ S cm}^{-1}$  for the 90 wt %  $\text{Ti}_3\text{C}_2\text{T}_x$ -SA composite.

To explore the EMI shielding properties of MXenes, we compared three MXene film compositions with an average thickness of  $\sim 2.5 \mu\text{m}$  in Fig. 3C. EMI SE is directly proportional to electrical conductivity (eq. 2, supplementary materials). Consequently,  $\text{Ti}_3\text{C}_2\text{T}_x$ , with the best electrical conductivity, gives the highest EMI SE among the studied MXenes. Because thickness plays a crucial role in EMI SE of any material, EMI SE can be improved simply by increasing the thickness. To investigate this effect, we measured the EMI SE of six  $\text{Ti}_3\text{C}_2\text{T}_x$  films with different thicknesses in Fig. 3D. The highest EMI SE value, 92 dB, was recorded for a 45- $\mu\text{m}$ -thick film, enough to block 99.99999994% of incident radiation with only 0.00000006% transmission (table S1). Experimental results of a  $\text{Ti}_3\text{C}_2\text{T}_x$  film in the X-band are comparable to the theoretically calculated values using eq. 2 (supplementary materials) that predicts high EMI SE values of  $\text{Ti}_3\text{C}_2\text{T}_x$  films at lower frequencies, as well (see fig. S3A). Experimental measurements on a laminated spray-coated 4- $\mu\text{m}$ -thick film (fig. S1) confirmed the prediction, showing similar EMI SE values at high and low frequencies. Thus, MXene films maintain excellent EMI SE shielding capability over a broad frequency range (fig. S3B).

In general, adequate shielding can be achieved by using thick conventional materials; however, material consumption and weight put such materials at a disadvantage for use in aerospace and

**Fig. 2. Morphological and structural characterization of  $\text{Ti}_3\text{C}_2\text{T}_x$  and  $\text{Ti}_3\text{C}_2\text{T}_x$ -SA composites.** (A) SEM image of a  $\text{Ti}_3\text{C}_2\text{T}_x$  flake on a filter. (B and C) SEM images of (B) 50 wt %  $\text{Ti}_3\text{C}_2\text{T}_x$ -SA composite and (C) pure  $\text{Ti}_3\text{C}_2\text{T}_x$ . (D) XRD patterns of pristine  $\text{Ti}_3\text{C}_2\text{T}_x$  and its composite with SA at different loadings. (E and F) TEM images of 80 and 30 wt %  $\text{Ti}_3\text{C}_2\text{T}_x$ -SA composite films, respectively.





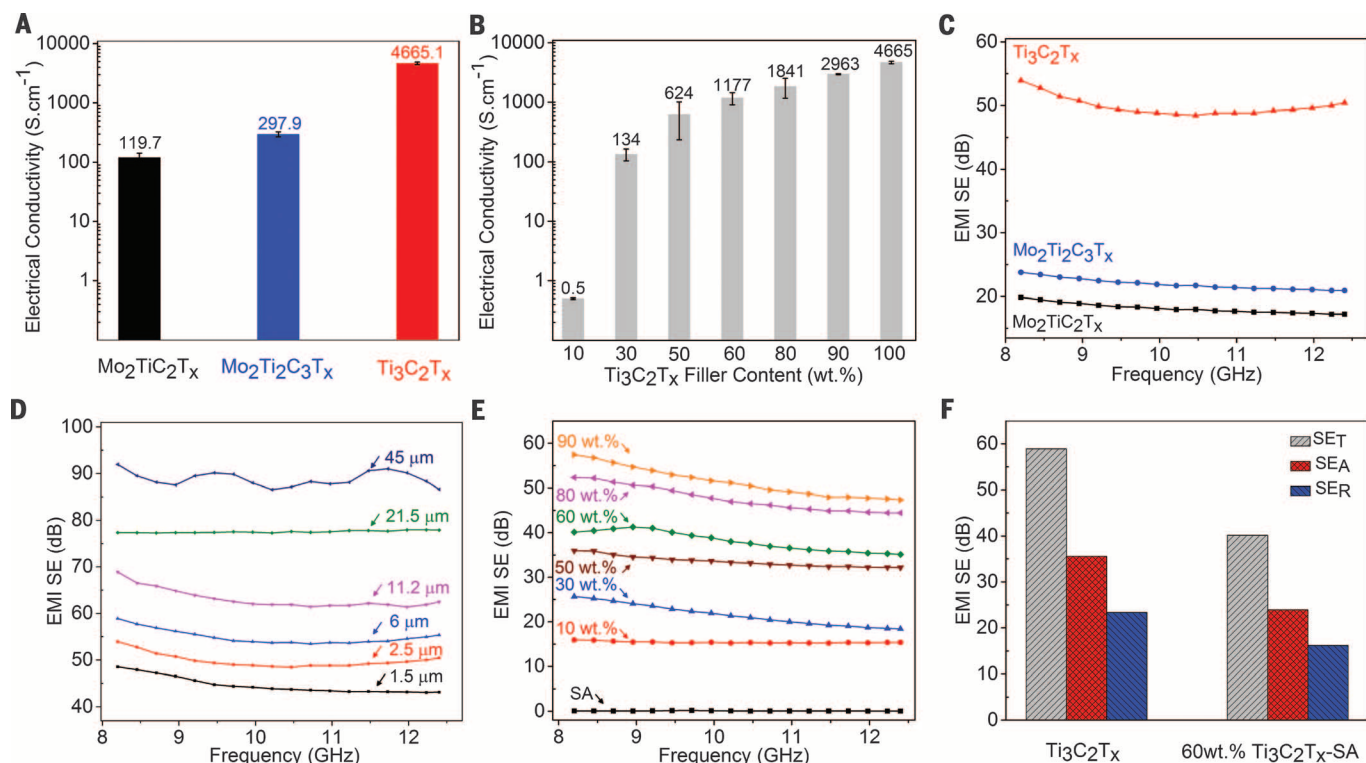


**Fig. 3. Electrical conductivity and EMI SE of MXene and MXene composites.** (A) Electrical conductivity of Mo<sub>2</sub>TiC<sub>2</sub>T<sub>x</sub>, Mo<sub>2</sub>Ti<sub>2</sub>C<sub>3</sub>T<sub>x</sub>, and Ti<sub>3</sub>C<sub>2</sub>T<sub>x</sub>. (B) Electrical conductivity of Ti<sub>3</sub>C<sub>2</sub>T<sub>x</sub>-SA composites. Filler content varies from 10 to 90 wt % Ti<sub>3</sub>C<sub>2</sub>T<sub>x</sub> in SA matrix. (C) EMI SE of Mo<sub>2</sub>TiC<sub>2</sub>T<sub>x</sub>, Mo<sub>2</sub>Ti<sub>2</sub>C<sub>3</sub>T<sub>x</sub>, Ti<sub>3</sub>C<sub>2</sub>T<sub>x</sub> at a thickness of ~2.5 μm. (D) EMI SE of Ti<sub>3</sub>C<sub>2</sub>T<sub>x</sub> at different thicknesses. (E) EMI SE of Ti<sub>3</sub>C<sub>2</sub>T<sub>x</sub>-SA composites at a thickness of 8 to 9 μm. (F) Total EMI SE (EMI SE<sub>T</sub>) and its absorption (SE<sub>A</sub>) and reflection (SE<sub>R</sub>) mechanism in Ti<sub>3</sub>C<sub>2</sub>T<sub>x</sub> and 60 wt % Ti<sub>3</sub>C<sub>2</sub>T<sub>x</sub>-SA samples at 8.2 GHz.

telecommunication applications. Therefore, it is important to achieve high EMI SE values with relatively thin films. As discussed above, to further improve MXenes mechanical properties and environmental stability, and to reduce their weight, we can embed them in polymer matrices. As an example, we investigated the Ti<sub>3</sub>C<sub>2</sub>T<sub>x</sub>-SA composites for EMI shielding. Here, the thickness of composite films was fixed between 8 and 9 μm. With increasing MXene content, EMI SE increased, to a maximum of 57 dB for the 90 wt % Ti<sub>3</sub>C<sub>2</sub>T<sub>x</sub>-SA sample (Fig. 3E). To obtain a clearer picture, we plotted the influence of filler content on EMI SE at a constant frequency of 8.2 GHz (see Fig. S4). Shielding mechanism from absorption (SE<sub>A</sub>) and reflection (SE<sub>R</sub>) in the Ti<sub>3</sub>C<sub>2</sub>T<sub>x</sub> (6 μm) and 60 wt % Ti<sub>3</sub>C<sub>2</sub>T<sub>x</sub>-SA (~8 μm) films were plotted in Fig. 3F at 8.2 GHz. Shielding due to absorption was the dominant mechanism, rather than reflection in pristine MXene and its composites.

A comprehensive literature review of previously studied materials for EMI SE (table S2) clearly indicates that MXenes and their composites are the best EMI shielding materials known to date. So far, most research has focused on graphene (11, 21, 22), carbon nanotubes (23), iron oxides (24), ferrites (25), iron-aluminum-silicon alloys (26), and metallic-based filler (27) polymer composites. However, to satisfy the common commercial EMI shielding requirements (above 30 dB) (2), large thicknesses, usually more than 1 mm, are needed. Ultrathin MXene films clearly outperform all of

the known synthetic materials and rank at the top of the comparison chart (Fig. 4A).

Recently, the concept of foam structures has gained tremendous interest as a way to reduce the density of shielding materials. Lightweight materials are a necessity for aerospace applications; therefore, some metals (such as copper and silver) that possess high EMI SE values are less useful (1, 28–30). When considering a material's density, specific EMI shielding effectiveness (SSE) is used as a criterion to evaluate different materials. However, SSE alone is not a sufficient parameter for understanding overall effectiveness, as a higher SSE can simply be achieved at a larger thickness, which directly increases the weight of the final product. Therefore, a more realistic parameter is to divide SSE by the material thickness (SSE/*t*) (27, 31). Such a parameter is highly valuable for determining the effectiveness of a material by incorporating three important factors: EMI SE, density, and thickness. Interestingly, SSE/*t* values for MXene and MXene-SA composites are much higher than those for other materials of different categories (table S3). As a representative example, a 90 wt % Ti<sub>3</sub>C<sub>2</sub>T<sub>x</sub>-SA composite sample gives a SSE/*t* of 30,830 dB cm<sup>2</sup> g<sup>-1</sup>, which is several times higher than those of the other materials studied thus far (Fig. S5). This finding is notable because several commercial requirements for an EMI shielding product are engrained in a single material, such as high EMI SE (57 dB), low density (2.31 g cm<sup>-3</sup>), small thickness (8 μm,

reducing net weight and volume), oxidation resistance (due to polymer binder), high flexibility (a feature of 2D films), and simple processing (mixing and filtration or spray-coating). Going a step further, Ti<sub>3</sub>C<sub>2</sub>T<sub>x</sub> and Ti<sub>3</sub>C<sub>2</sub>T<sub>x</sub>-SA composites were compared with pure aluminum (8 μm) and copper (10 μm) foils (Fig. S6). Ti<sub>3</sub>C<sub>2</sub>T<sub>x</sub>, which has two orders of magnitude lower electrical conductivity than these metals, shows EMI SE values similar to those of metals (tables S2 and S3). For comparison, thermally reduced graphene oxide film (8.4 μm) that possessed lower electrical conductivity is also plotted and fell far below the other materials (32).

The massive EMI SE of MXene can be understood from several proposed mechanisms shown in Fig. 4B. The EMI shielding originates from the excellent electrical conductivity of MXene and partially from the layered architecture of the films. A potential mechanism can be explained as follows: As EMWs strike the surface of a MXene flake, some EM waves are immediately reflected because of abundant free electrons at the surface of the highly conductive MXene (9, 10). The remaining waves pass through the MXene lattice structure where interaction with the high electron density of MXene induces currents that contribute to ohmic losses, resulting in a drop in energy of the EMWs. The surviving EMWs, after passing through the first layer of Ti<sub>3</sub>C<sub>2</sub>T<sub>x</sub> (marked as "I" in Fig. 4B), encounter the next barrier layer (marked as "II"), and the phenomenon of EMW attenuation repeats. Simultaneously, layer II acts as a

**Fig. 4. Comparison of EMI SE with the previous literature and shielding mechanisms.** (A) EMI SE versus thickness of different materials. Each symbol indicates a set of material category as follows:  $\text{Ti}_3\text{C}_2\text{T}_x$  MXenes (red star),  $\text{Ti}_3\text{C}_2\text{T}_x$ -SA composite (purple star), molybdenum MXenes (green filled circle), copper and aluminum foils (black diamond), metals (blue diamond), graphene (open circle), carbon fibers and nanotubes (open square), graphite (black filled circle), other materials (blue filled circle). A detailed

description of each data point is presented in table S2. (B) Proposed EMI shielding mechanism. Incoming EM waves (green arrows) strike the surface of a MXene flake. Because reflection occurs before absorption, part of the EM waves is immediately reflected from the surface owing to a large number of charge carriers from the highly conducting surface (light blue arrows), whereas induced local dipoles, resulting from termination groups, help with absorption

of the incident waves passing through the MXene structure (dashed blue arrows). Transmitted waves with less energy are then subjected to the same process when they encounter the next MXene flake, giving rise to multiple internal reflections (dashed black arrows), as well as more absorption. Each time an EM wave is transmitted through a MXene flake, its intensity is substantially decreased, resulting in an overall attenuated or completely eliminated EM wave.

reflecting surface and gives rise to multiple internal reflections. The EMWs can be reflected back and forth between the layers (I, II, III, and so on) until completely absorbed in the structure. This is in marked contrast to pure metals that have a regular crystallographic structure and no interlayer reflecting surface available to provide the internal multiple reflection phenomenon. Thus, the nacre-like (or laminated) structure provides MXene with the ability to behave as a multilevel shield. The SEM image (Fig. 2C) shows well-aligned MXene layers in both pure  $\text{Ti}_3\text{C}_2\text{T}_x$  and its composites. Considering a 45- $\mu\text{m}$ -thick  $\text{Ti}_3\text{C}_2\text{T}_x$  film, thousands of 2D  $\text{Ti}_3\text{C}_2\text{T}_x$  sheets act as barriers to EMWs. As the overall EMI value goes above 15 dB, it is generally assumed that the contribution from internal reflections is minimal (1). However, in the layered structure of MXenes, multiple internal reflections cannot be ignored. The multiple reflection effect, nevertheless, is included with absorption because the re-reflected waves get absorbed or dissipated in the form of heat within the material (8, 9, 27). Furthermore, MXene flake surface terminations may play a role as well. Local dipoles between Ti and terminating groups ( $-\text{F}$ ,  $=\text{O}$ , or  $-\text{OH}$ ) may be created when subjected to an alternating electromagnetic field. Fluorine, in particular, being highly electronegative, can induce this kind of dipole polarization. The ability of each element to interact with incoming EMWs leads to polarization losses, which in turn improve the overall shielding.

We have shown here that flexible  $\text{Ti}_3\text{C}_2\text{T}_x$  films with thicknesses ranging from 1 to 45  $\mu\text{m}$  exhibit excellent electrical conductivity and EMI shielding capabilities. The reported EMI SE values are the highest of any known synthetic materials with similar thickness. Moreover, excellent shielding ability is maintained after adding SA to create polymer composite films. This allows the use of

very thin films for device shielding to help eliminate EM radiation as miniaturization of electronics progresses. This study is set to pave the way for a large family of 2D materials that are far superior in performance compared to currently used materials in EMI shielding applications. The 2D structure, combined with high electrical conductivity and good electronic coupling between the layers, is responsible for the extremely high EMI shielding efficiency of MXenes.

## REFERENCES AND NOTES

1. Z. Chen, C. Xu, C. Ma, W. Ren, H. M. Cheng, *Adv. Mater.* **25**, 1296–1300 (2013).
2. X. Yan et al., *Adv. Funct. Mater.* **25**, 559–566 (2015).
3. N. Yousefi et al., *Adv. Mater.* **26**, 5480–5487 (2014).
4. Y. Zhang et al., *Adv. Mater.* **27**, 2049–2053 (2015).
5. A. H. Frey, *Environ. Health Perspect.* **106**, 101–103 (1998).
6. D. D. L. Chung, *Carbon* **39**, 279–285 (2001).
7. N. C. Das et al., *Polym. Eng. Sci.* **49**, 1627–1634 (2009).
8. M. H. Al-Saleh, W. H. Saadeh, U. Sundararaj, *Carbon* **60**, 146–156 (2013).
9. H. B. Zhang, Q. Yan, W. G. Zheng, Z. He, Z. Y. Yu, *ACS Appl. Mater. Interfaces* **3**, 918–924 (2011).
10. J.-M. Thomassin et al., *Mater. Sci. Eng. Rep.* **74**, 211–232 (2013).
11. M.-S. Cao, X.-X. Wang, W.-Q. Cao, J. Yuan, *J. Mater. Chem. C* **3**, 6589–6599 (2015).
12. M. Naguib, V. N. Mochalin, M. W. Barsoum, Y. Gogotsi, *Adv. Mater.* **26**, 992–1005 (2014).
13. M. R. Lukatskaya et al., *Science* **341**, 1502–1505 (2013).
14. B. Anasori et al., *ACS Nano* **9**, 9507–9516 (2015).
15. J. Halim et al., *Adv. Funct. Mater.* **26**, 3118–3127 (2016).
16. Z. Ling et al., *Proc. Natl. Acad. Sci. U.S.A.* **111**, 16676–16681 (2014).
17. M. Boota et al., *Adv. Mater.* **28**, 1517–1522 (2016).
18. I. Kovalenko et al., *Science* **334**, 75–79 (2011).
19. B. Anasori et al., *Nanoscale Horizons* **1**, 227–234 (2016).
20. M. Khazaei et al., *Adv. Funct. Mater.* **23**, 2185–2192 (2013).
21. J. J. Liang et al., *Carbon* **47**, 922–925 (2009).

22. F. Shahzad, P. Kumar, Y.-H. Kim, S. M. Hong, C. M. Koo, *ACS Appl. Mater. Interfaces* **8**, 9361–9369 (2016).
23. Z. Zeng et al., *Carbon* **96**, 768–777 (2016).
24. S. Varshney, A. Ohlan, V. K. Jain, V. P. Dutta, S. K. Dhawan, *Ind. Eng. Chem. Res.* **53**, 14282–14290 (2014).
25. P. Xu et al., *J. Phys. Chem. B* **112**, 2775–2781 (2008).
26. L. Liu et al., *J. Magn. Magn. Mater.* **324**, 1786–1790 (2012).
27. A. Ameli, M. Nofar, S. Wang, C. B. Park, *ACS Appl. Mater. Interfaces* **6**, 11091–11100 (2014).
28. B. Shen, Y. Li, W. Zhai, W. Zheng, *ACS Appl. Mater. Interfaces* **8**, 8050–8057 (2016).
29. Y. Yang, M. C. Gupta, K. L. Dudley, R. W. Lawrence, *Nano Lett.* **5**, 2131–2134 (2005).
30. Y. Chen et al., *Adv. Funct. Mater.* **26**, 447–455 (2016).
31. Z. Zeng et al., *Adv. Funct. Mater.* **26**, 303–310 (2016).
32. B. Shen, W. Zhai, W. Zheng, *Adv. Funct. Mater.* **24**, 4542–4548 (2014).

## ACKNOWLEDGMENTS

This work was supported in part by the U.S. National Science Foundation under grant DMR-1310245. F.S., M.A., C.B.H., B.A., S.M.H., C.M.K., and Y.G. are inventors on patent application 62/326,074 submitted by Drexel University that covers MXene films and composites for EMI shielding. M.A. was supported by the Libyan North America Scholarship Program funded by the Libyan Ministry of Higher Education and Scientific Research. This work was also supported by the Fundamental R&D Program for Core Technology of Materials and the Industrial Strategic Technology Development Program funded by the Ministry of Trade, Industry and Energy, and the Disaster and Safety Management Institute by the Ministry of Public Safety and Security of Korean Government, Republic of Korea, and partially by the Korea Institute of Science and Technology.

## SUPPLEMENTARY MATERIALS

www.sciencemag.org/content/353/6304/1137/suppl/DC1  
Materials and Methods  
Supplementary Text  
Figs. S1 to S6  
Tables S1 to S3  
References (33–112)

29 May 2016; accepted 10 August 2016  
10.1126/science.aag2421

## GEOCHEMISTRY

# Highly siderophile elements were stripped from Earth's mantle by iron sulfide segregation

David C. Rubie,<sup>1\*</sup> Vera Laurenz,<sup>1</sup> Seth A. Jacobson,<sup>1,2</sup> Alessandro Morbidelli,<sup>2</sup> Herbert Palme,<sup>3</sup> Antje K. Vogel,<sup>1</sup> Daniel J. Frost<sup>1</sup>

Highly siderophile elements (HSEs) are strongly depleted in the bulk silicate Earth (BSE) but are present in near-chondritic relative abundances. The conventional explanation is that the HSEs were stripped from the mantle by the segregation of metal during core formation but were added back in near-chondritic proportions by late accretion, after core formation had ceased. Here we show that metal-silicate equilibration and segregation during Earth's core formation actually increased HSE mantle concentrations because HSE partition coefficients are relatively low at the high pressures of core formation within Earth. The pervasive exsolution and segregation of iron sulfide liquid from silicate liquid (the "Hadean matte") stripped magma oceans of HSEs during cooling and crystallization, before late accretion, and resulted in slightly suprachondritic palladium/iridium and ruthenium/iridium ratios.

The formation of Earth's metallic core resulted from the segregation of liquid iron from silicates during accretion. This process partially removed siderophile (metal-loving) elements from the mantle by transporting them into the core. Moderately siderophile elements (MSEs), such as Ni, Co, W, and Mo, are variably depleted in the bulk silicate Earth (BSE) as a consequence of metal-silicate equilibration, because of their differing metal-silicate partition coefficients (1, 2). In contrast, the highly siderophile elements (HSEs; Re, Os, Ir, Ru, Rh, Pt, Pd, and Au) are present in near-chondritic relative abundances, even though their metal-silicate partition coefficients (measured over the pressure range 0 to 18 GPa) vary by orders of magnitude (3). This has led to the widely accepted hypothesis that the HSEs were stripped from the mantle by metal-silicate segregation and that the present concentrations were added by the late accretion of chondritic material after core formation had ceased (4–6). The mass of late-accreted material, as estimated from HSE concentrations, has also been used to determine the age of the Moon (6).

Unlike simple geochemical models of core formation, which unrealistically treat core-mantle equilibration as a single event (7), we modeled core formation as a multistage process because metal was delivered to Earth by accreting bodies throughout its accretion history. We followed the approach of (8), in which evolving MSE abundances in Earth's mantle and core were modeled by integrating the dynamics of planetary accretion with the chemistry of core-mantle differentiation. In this approach, Earth's

growth history comes from state-of-the-art *N*-body accretion simulations based on the "Grand Tack" scenario (9–12), which start with a protoplanetary disk consisting of 80 to 220 roughly Mars-sized embryos and several thousand smaller planetesimals distributed initially over heliocentric distances of 0.7 to 10 astronomical units (AU). For the HSE modeling presented here, the results are not dependent on the choice of the Grand Tack scenario because planets grow through embryo-embryo and embryo-planetesimal collisions in all accretion scenarios. Each collision is an accretion event, which delivers mass and energy to the growing planets, resulting in

melting, magma ocean formation, and an episode of core formation. Embryos and most planetesimals are assumed to have undergone early core-mantle differentiation. Unlike previous core formation models, the metal of projectile cores equilibrates with only a fraction of the target's mantle, which is determined from a hydrodynamic model (12, 13). The compositions of metal and silicate produced in each core formation event are determined by a mass balance–element partitioning approach (8, 14). Five parameters are fit by least squares minimization so that the composition of the model Earth's mantle matches that of the BSE (8). Metal-silicate equilibration pressures are fit assuming that they are a constant proportion (refined by least squares to be ~0.7) of the target's core-mantle boundary pressure ( $P_{\text{CMB}}$ ) at the time of each impact, which on average is consistent with calculations of impact-induced melting during Earth's accretion (15). A heliocentric oxidation gradient model defines the bulk compositions of all starting bodies and is defined by four of the five fitting parameters (8) (fig. S1A).

We investigated the evolution of mantle Ir, Pt, Pd, and Ru concentrations during Earth's accretion and differentiation using our accretion–core formation model (8). Metal-silicate partition coefficients for the HSEs decrease with increasing pressure and temperature (*P*–*T*) conditions (3). In addition, we have shown experimentally that increasing the sulfur content in the metal has a similar effect (12, 16). It is therefore essential to include sulfur in the initial bulk compositions of accreting bodies. Sulfur is a volatile element with a low 50% condensation temperature of 655 K at

<sup>1</sup>Bayerisches Geoinstitut, Bayreuth, Germany. <sup>2</sup>Observatoire de la Côte d'Azur, Nice, France. <sup>3</sup>Forschungsinstitut und Naturmuseum Senckenberg, Frankfurt, Germany.

\*Corresponding author. Email: dave.rubie@uni-bayreuth.de

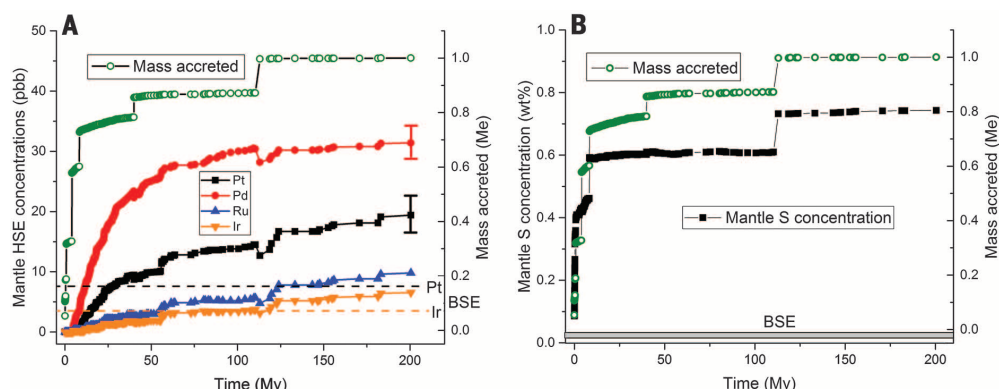


**Fig. 1. Evolution of HSE and sulfur concentrations in the mantle during Earth's accretion, based on metal-silicate equilibration and segregation.** Shown are mantle concentrations of (A) HSEs and (B) sulfur over time. Each symbol represents an impact, and "mass accreted" is the accumulated mass after each impact, normalized to Earth's current mass ( $M_{\oplus}$ ). The final giant impact, at 113 My, increases Earth's mass from 0.872 to 0.997  $M_{\oplus}$ . BSE abundances (21) are shown by dashed lines in (A) and the gray bar in (B). Error bars, based on the propagation of uncertainties in the partitioning parameters, are shown for the final Pt and Pd concentrations (A); propagated uncertainties for Ru and Ir are  $\pm 0.6$  and  $\pm 1.7$  parts per billion (ppb), respectively. Results obtained when only 50% of each batch of accreted metal equilibrates with silicate, as a result of incomplete emulsification of impacting cores (23), are presented in fig. S2. Although the oblique lines connecting the symbols show the general trends of mass and composition with time, they do not accurately represent the evolution paths, which in reality always involve a series of vertical steps.



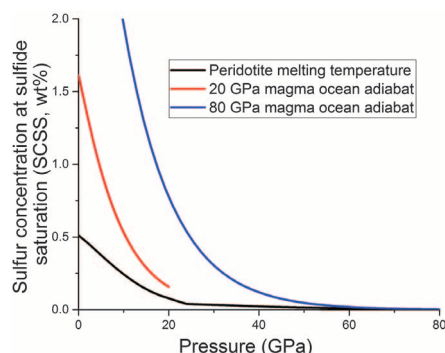


**Fig. 2. Sulfur concentrations at sulfide saturation (SCSS) in peridotite liquid, as a function of pressure.** Equation 1 (16) has been used to calculate concentrations at temperatures about midway between the peridotite liquidus and solidus (8) and along adiabatic temperature profiles for magma oceans with basal pressures of 20 and 80 GPa.

$10^{-4}$  bar (17). We therefore assumed that concentrations of S increased systematically with decreasing temperature and increasing heliocentric distance (18). We assumed that, before giant planet migration, fully oxidized bodies that formed beyond Jupiter and Saturn ( $>6$  AU) contained the full complement of S [corresponding to 5.35 weight % (wt %) in a CI chondrite composition], with concentrations decreasing along a linear gradient toward the Sun (fig. S1B). We adjusted the heliocentric distance at which the S concentration becomes zero to 0.8 AU in order to obtain Earth's bulk sulfur content (0.64 wt %). Although there are potential problems with this simple concentration-distance model, our main results do not depend on it (12). We used a partitioning model to determine the distribution of S between metallic and silicate liquids during each metal-silicate equilibration event (12, 19). Our ultimate objective was to obtain 1.7 to 2.0 wt % S in Earth's core (20) and 200 to 250 parts per million (ppm) in the mantle (21) at the end of accretion.

Using high-pressure metal-silicate partition coefficients (3, 16), we considered the effects of metal-silicate equilibration and segregation on the evolution of Pt, Ru, Pd, and Ir concentrations by including the modeled S abundances in the metallic liquid (table S1). The final HSE concentrations were high and variably fractionated because of differing partition coefficients (3, 16), with the result that relative abundances in the mantle were strongly nonchondritic (Fig. 1A). Pd and Pt concentrations started to become especially high after the model Earth had accreted ~60% of its mass and increased to strongly exceed BSE values by the end of accretion. Contrary to the conclusions of previous studies, accreted metal in these growth models actually added HSEs to Earth's mantle rather than removing them. In the case of differentiated planetesimals that underwent early [e.g.,  $<3$  million years (My)] core-mantle differentiation as a result of heating caused by the rapid decay of  $^{26}\text{Al}$  (22), HSE partition coefficients were extremely high ( $10^6$  to  $10^{11}$ ) (3) at

the low  $P$ - $T$  conditions of planetesimal differentiation ( $\leq 0.3$  GPa and  $\leq 1900$  K). This means that the HSEs partitioned almost entirely into the metallic cores of planetesimals, and to a lesser extent into embryo cores, during differentiation. In contrast, at the high  $P$ - $T$  conditions of metal-silicate equilibration after Earth had accreted ~60% of its mass, HSE partition coefficients were lower by two to five orders of magnitude than under the conditions of planetesimal differentiation (3). This resulted in HSEs in impactor cores being transferred to Earth's mantle by metal-silicate equilibration so that mantle concentrations increased to exceed BSE values (Fig. 1A). High HSE abundances also resulted from the accretion of fully oxidized bodies and from the oxidation of accreted metal (delivered as small planetesimal cores and as dispersed metal in undifferentiated bodies) by water in the magma ocean (8, 12).

The results shown in Fig. 1A are based on the assumption that 100% of the accreted metal equilibrated with the silicate liquid. If only a limited fraction of metal equilibrated because of incomplete emulsification (23), concentrations of all four HSEs would become even higher (fig. S2A); this is because higher equilibration pressures would then be required to reproduce the MSE concentrations of Earth's mantle, causing further reductions in the HSE metal-silicate partition coefficients.

The final calculated mantle S content exceeded the BSE concentration by a factor of ~30 (Fig. 1B) and, in addition, the S content of the core was very low (0.36 wt %). The high mantle concentrations that developed were not removed by metal-silicate equilibration and segregation (Fig. 1B) (12). To achieve a low BSE concentration ( $<200$  ppm before late accretion) and a core concentration of 1.7 to 2.0 wt %, FeS liquid must be exsolved and segregated to the core, an event that has been termed the "Hadean matte" (24, 25).

Sulfide liquid exsolves from a magma ocean when a solubility saturation level, termed the

sulfur concentration at sulfide saturation or SCSS, has been exceeded (26). We have experimentally determined the SCSS for peridotite liquid at 7 to 21 GPa and 2373 to 2673 K (16), thus enabling concentrations in S-saturated magma oceans to be estimated by extrapolation using

$$\ln(\text{SCSS}) = 14.2(\pm 1.18) - \frac{11032(\pm 3119)}{T} - \frac{379(\pm 82)P}{T} \quad (1)$$

where SCSS is in parts per million,  $T$  is in kelvin, and  $P$  is in gigapascals. Average values along magma ocean adiabats are much higher than the concentrations shown in Fig. 1B (Fig. 2). However, SCSS decreases strongly with decreasing temperature and becomes much lower close to the peridotite melting curve (Fig. 2). Thus, droplets of immiscible FeS liquid exsolve from the silicate melt structure in a deep S-bearing magma ocean as it cools toward crystallization temperatures. This effect is enhanced as the melt fraction is reduced by crystallization; because of its high density, the exsolved FeS segregates by sinking to the core (12).

We considered two end-member scenarios when modeling sulfide segregation, depending on magma oceans being either short-lived (27) or long-lived (28): (i) Sulfide segregation took place in multiple stages and occurred after each giant impact, provided SCSS was exceeded close to the peridotite melting curve, and (ii) FeS segregation took place in a single stage and occurred only after the final giant impact and before late accretion. The final results from these two scenarios are almost identical, although the evolutionary paths are different.

The strong  $P$ - $T$  and depth dependences of SCSS in a deep convecting magma ocean (Fig. 2) require a simple modeling approach because of the challenges in determining the amount of FeS liquid that exsolves and equilibrates chemically in such conditions (29). We thus defined empirically an effective pressure  $P_{\text{eq-S}}$  that describes the SCSS (using Eq. 1) and equilibration pressure for the entire magma ocean, assuming that

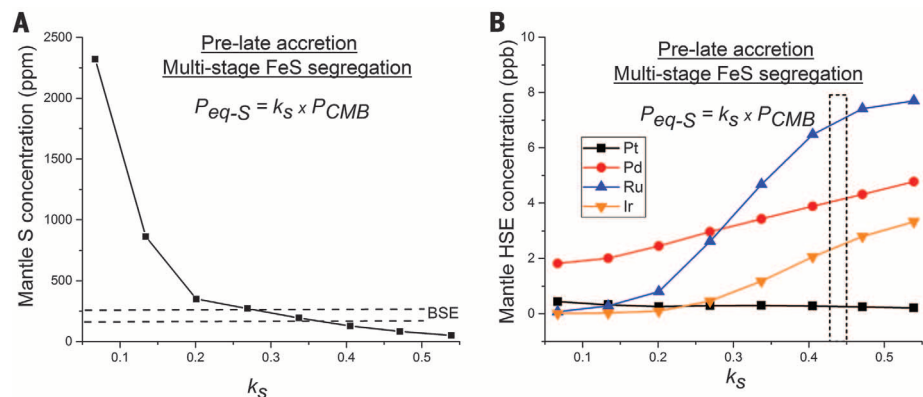


**Fig. 3. Final mantle concentrations after multistage sulfide segregation but before late accretion.**

Shown are the final concentrations of (A) sulfur (with the BSE concentration shown by the horizontal dashed-outline bar) and (B) HSEs that result from multistage sulfide segregation, without late accretion, as a function of  $k_S$  (Eq. 2). When late accretion is also modeled, BSE abundances of both sulfur and HSEs are best reproduced with  $k_S \approx 0.44$  [vertical dashed-outline bar in (B)] (see Fig. 4). The concentrations of Pd and Ru are elevated because these elements are the least chalcophile at high  $P$ - $T$ . A similar result is obtained for single-stage sulfide segregation.

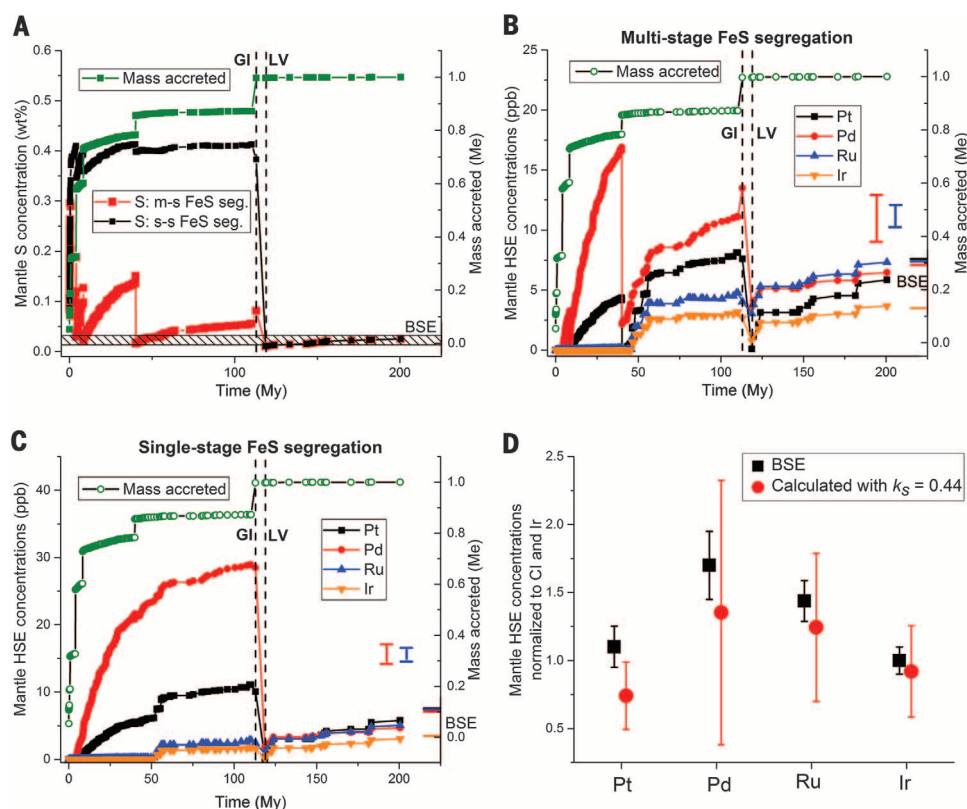


**Fig. 4. Final results based on metal-sulfate segregation, sulfide segregation, and late accretion.** The evolution of (A) sulfur and (B and C) HSE concentrations with time is shown for  $k_S = 0.44$  (Eq. 2). The accretion history is shown in (A) to (C). Results are shown for multistage FeS segregation (m-s FeS seg.) and late single-stage segregation (s-s FeS seg.) at 118 My. Mass accreted is as in Fig. 1. The vertical dashed lines in (A) to (C) show the time of the final giant impact (GI) at 113 My and the start of late veneer accretion (LV) at 119 My. Horizontal bars show BSE concentrations. Error bars, based on the propagation of uncertainties in the partitioning parameters, are shown in (B) and (C) for the final Pd and Ru concentrations; propagated uncertainties for Pt and Ir are  $\pm 0.3$  and  $\pm 0.6$  ppb, respectively. As in Fig. 1, the oblique lines connecting the symbols show the general trends of mass and composition with time, but they do not accurately represent the stepwise progression of the evolution paths. (D) Final calculated HSE values for multistage FeS segregation, normalized to Ir and CI chondrite composition, compared with BSE values (32). The error bars on the calculated values are based on propagating the partitioning parameter uncertainties (tables S1 and S2).

the corresponding temperature lies between the liquidus and solidus of peridotite (8)

$$P_{eq-S} = k_S \times P_{CMB} \quad (2)$$

Here  $P_{CMB}$  is the core-mantle boundary pressure at the time of each FeS exsolution and segregation event, and  $k_S$  is a constant so that  $P_{eq-S}$  increases as Earth accretes. The amount of FeS that exsolves is the excess that is present above the SCSS value calculated using Eqs. 1 and 2.

Because HSEs dissolve in S-bearing silicate melts as HSE-S species, they are fractionated into sulfide liquid that exsolves from a magma ocean (30). We modeled the effect of segregating FeS liquid on mantle HSE concentrations, using our experimental data on the partitioning of Pt, Pd, Ru, and Ir between FeS and peridotite liquids [obtained at 7 to 21 GPa and 2373 to 2673 K (16)] (table S2). We assumed that equilibration between sulfide and silicate liquids occurs simultaneously with sulfide exsolution at pressure  $P_{eq-S}$  (Eq. 2). Because of high convection velocities (several meters per second), combined with a time scale of at least 1000 years to cool to crystallization temperatures (27, 29), sulfur should be well mixed in the magma ocean before exsolution starts. We therefore assumed that droplets of FeS liquid exsolve pervasively and equilibrate with the entire mantle at pressure  $P_{eq-S}$ , in contrast to the metallic liquid that segregated earlier, which equilibrates with only a limited fraction of the mantle at the base of the magma ocean (8).

The value of the adjustable parameter  $k_S$  (Eq. 2) determines the final mantle S and HSE concen-

trations before late accretion (Fig. 3). Optimal results are obtained with  $k_S \approx 0.44$ . This fit requires the accretion of a late veneer to increase HSE concentrations to BSE values (12). Late accretion is modeled by terminating the segregation of sulfide liquid, which ends as a result of magma ocean solidification, because FeS liquid cannot percolate efficiently through crystalline mantle (12, 31).

The models that include both sulfide segregation and late accretion predict Ir, Pt, and S concentrations that are close to BSE values, irrespective of whether FeS segregation occurred in a single stage or multiple stages (Fig. 4 and fig. S3). Furthermore, we reproduced suprachondritic Pd/Ir and Ru/Ir ratios for the BSE (4, 32) (Fig. 4D). Sulfide segregation is very efficient at depleting the mantle in Pt and Ir, but it is less efficient at depleting Pd and Ru because these elements are less chalcophile than Pt and Ir at high  $P$ - $T$  (16). This contrasts with metal-sulfate partitioning behavior, in which Pd and Pt are the least siderophile (3). However, a number of other explanations have been proposed for suprachondritic Pd/Ir and Ru/Ir ratios (4, 33) that cannot readily be dismissed, especially considering the uncertainties on our results (Fig. 4D).

Accretion of a late veneer depends on the mantle being largely crystalline, because otherwise sulfide segregation in a magma ocean would simply continue, and HSE concentrations would never increase to BSE levels (12). The mixing of HSEs into convecting crystalline mantle is expected to have been a slow process, perhaps consistent with a previously estimated mixing time of  $\sim 1.5$  billion years (34), and also may not have been complete

(35). The age of the Moon has recently been determined using correlations between the time of the final giant impact and the mass of late-accreted material, derived from a large number of accretion simulations (6). Our results indicate that this correlation provides only a lower limit on the age of the Moon because it actually dates Earth's final magma ocean crystallization.

It has been argued that Earth accreted from the same reservoir before and after core formation because of correlated isotopic signatures of Mo and Ru; this argument is based on the assumption that Mo was added to the mantle mainly before late accretion, whereas Ru was added only with the late veneer (36). Here we show that this assumption is not valid because modeled Ru concentrations increased in the mantle at an early stage of Earth accretion and long before the addition of the late veneer, especially in the case of single-stage sulfide segregation (Fig. 4, B and C).

We conclude that the addition of sulfur to Earth occurred over the entire history of accretion (Fig. 4A), refuting the assumption that all sulfur was added during late accretion (37). Although our results are based on assumptions about the distribution of S in the early solar system (12), it is unlikely that a plausible distribution could be found that would change our conclusion. The addition of S throughout accretion affects core formation models that use the elements W and Mo because S strongly influences their partitioning behavior (38). Last, we speculate that a possible low-density layer at the top of Earth's liquid outer core (39) could be the result of late FeS enrichment due to sulfide segregation.

## REFERENCES AND NOTES

- B. J. Wood, M. J. Walter, J. Wade, *Nature* **441**, 825–833 (2006).
- D. C. Rubie, F. Nimmo, H. J. Melosh, in *Evolution of the Earth*, D. J. Stevenson, Ed., vol. 9 of *Treatise on Geophysics*, G. Schubert, Ed. (Elsevier, ed. 2, 2015) pp. 43–79.
- U. Mann, D. J. Frost, D. C. Rubie, H. Becker, A. Audétat, *Geochim. Cosmochim. Acta* **84**, 593–613 (2012).
- R. J. Walker et al., *Chem. Geol.* **411**, 125–142 (2015).
- C.-L. Chou, *Proc. Lunar Planet. Sci.* **9**, 219–230 (1978).
- S. A. Jacobson et al., *Nature* **508**, 84–87 (2014).
- M. J. Walter, E. Cottrell, *Earth Planet. Sci. Lett.* **365**, 165–176 (2013).
- D. C. Rubie et al., *Icarus* **248**, 89–108 (2015).
- D. P. O'Brien, K. J. Walsh, A. Morbidelli, S. N. Raymond, A. M. Mandell, *Icarus* **239**, 74–84 (2014).
- S. A. Jacobson, A. Morbidelli, *Philos. Trans. A Math. Phys. Eng. Sci.* **372**, 20130174 (2014).
- K. J. Walsh, A. Morbidelli, S. N. Raymond, D. P. O'Brien, A. M. Mandell, *Nature* **475**, 206–209 (2011).
- Materials and methods are available as supplementary materials on Science Online.
- R. Deguen, P. Olson, P. Cardin, *Earth Planet. Sci. Lett.* **310**, 303–313 (2011).
- D. C. Rubie et al., *Earth Planet. Sci. Lett.* **301**, 31–42 (2011).
- J. de Vries et al., *Prog. Earth Planet. Sci.* **3**, 7 (2016).
- V. Laurenz, D. C. Rubie, D. J. Frost, A. K. Vogel, *Geochim. Cosmochim. Acta* **10.1016/j.gca.2016.08.012** (2016).
- K. Lodders, *Astrophys. J.* **591**, 1220–1247 (2003).
- P. Cassen, *Meteor. Planet. Sci.* **31**, 793–806 (1996).
- A. Boujibar et al., *Earth Planet. Sci. Lett.* **391**, 42–54 (2014).
- G. Dreibus, H. Palme, *Geochim. Cosmochim. Acta* **60**, 1125–1130 (1996).
- H. Palme, H. St. C. O'Neill, in *The Mantle and Core*, R. W. Carlson, Ed., vol. 3 of *Treatise on Geochemistry*, H. D. Holland, K. K. Turekian, Eds. (Elsevier-Pergamon, ed. 2, 2014), pp. 1–39.
- T. S. Kruijer et al., *Geochim. Cosmochim. Acta* **99**, 287–304 (2012).
- T. W. Dahl, D. J. Stevenson, *Earth Planet. Sci. Lett.* **295**, 177–186 (2010).
- H. St. C. O'Neill, *Geochim. Cosmochim. Acta* **55**, 1159–1172 (1991).
- P. S. Savage et al., *Geochem. Persp. Lett.* **1**, 53–64 (2015).
- J. A. Mavrogenes, H. St. C. O'Neill, *Geochim. Cosmochim. Acta* **63**, 1173–1180 (1999).
- V. S. Solomatin, in *Origin of the Earth and Moon*, R. M. Canup, K. Righter, Eds. (Univ. of Arizona Press, 2000), pp. 323–338.
- Y. Abe, *Phys. Earth Planet. Inter.* **100**, 27–39 (1997).
- D. C. Rubie, H. J. Melosh, J. E. Reid, K. Liebske, K. Righter, *Earth Planet. Sci. Lett.* **205**, 239–255 (2003).
- V. Laurenz et al., *Geochim. Cosmochim. Acta* **108**, 172–183 (2013).
- H. Terasaki, D. J. Frost, D. C. Rubie, F. Langenhorst, *Earth Planet. Sci. Lett.* **273**, 132–137 (2008).
- H. Becker et al., *Geochim. Cosmochim. Acta* **70**, 4528–4550 (2006).
- M. Fischer-Gödde, H. Becker, *Geochim. Cosmochim. Acta* **77**, 135–156 (2012).
- W. D. Maier et al., *Nature* **460**, 620–623 (2009).
- H. Rizo et al., *Science* **352**, 809–812 (2016).
- N. Daughas, A. M. Davis, B. Marty, L. Reisberg, *Earth Planet. Sci. Lett.* **226**, 465–475 (2004).
- F. Albarède, *Nature* **461**, 1227–1233 (2009).
- J. Wade, B. J. Wood, J. Tuff, *Geochim. Cosmochim. Acta* **85**, 58–74 (2012).
- G. Helffrich, S. Kaneshima, *Nature* **468**, 807–810 (2010).

## ACKNOWLEDGMENTS

D.C.R., V.L., S.A.J., A.M., and H.P. were supported by the European Research Council Advanced Grant ACCRETE (Accretion and Early Differentiation of the Earth and Terrestrial Planets; contract number 290568). A.K.V. was supported by the German Science Foundation (DFG) Priority Programme SPPI385, “The first 10 million years of the solar system – a planetary materials approach” (grant Ru1323/2). We thank H. J. Melosh and R. J. Walker for discussions and three reviewers for their helpful and constructive comments. Data files with final results are available in the supplementary materials.

## SUPPLEMENTARY MATERIALS

www.sciencemag.org/content/353/6304/1141/suppl/DC1  
Materials and Methods  
Supplementary Text  
Figs. S1 to S4  
Tables S1 and S2  
References (40–62)  
Databases S1 and S2

5 April 2016; accepted 17 August 2016  
10.1126/science.aaf6919

## ORGANIC CHEMISTRY

## Dirhodium-catalyzed C-H arene amination using hydroxylamines

Mahesh P. Paudyal,<sup>1</sup> Adeniyi Michael Adebisin,<sup>1</sup> Scott R. Burt,<sup>2</sup> Daniel H. Ess,<sup>2</sup> Zhiwei Ma,<sup>3</sup> László Kürti,<sup>3</sup> John R. Falck<sup>1\*</sup>

Primary and *N*-alkyl arylamine motifs are key functional groups in pharmaceuticals, agrochemicals, and functional materials, as well as in bioactive natural products. However, there is a dearth of generally applicable methods for the direct replacement of aryl hydrogens with NH<sub>2</sub>/NH(alkyl) moieties. Here, we present a mild dirhodium-catalyzed C-H amination for conversion of structurally diverse monocyclic and fused aromatics to the corresponding primary and *N*-alkyl arylamines using NH<sub>2</sub>/NH(alkyl)-O-(sulfonyl)hydroxylamines as aminating agents; the relatively weak RSO<sub>2</sub>O-N bond functions as an internal oxidant. The methodology is operationally simple, scalable, and fast at or below ambient temperature, furnishing arylamines in moderate-to-good yields and with good regioselectivity. It can be readily extended to the synthesis of fused *N*-heterocycles.

Arylamine motifs (**1**, **2**) are prevalent in natural products, pharmaceuticals, agrochemicals, functional materials, and dyestuffs, as well as in many synthetic reagents and catalysts (**3–5**). Most traditional methods for their synthesis from a corresponding C(sp<sup>2</sup>)-H bond involve multistep sequences and/or harsh conditions (**6–8**). In many instances, the initial product (nitro, azide, azo, nitroso, chloronitroso, amide/imide/sulfonamide, or imine) requires one or more additional steps before arriving at a free amine (**6**). The amination of organic anions is a useful and direct alternative (**9**), but is generally restricted to the introduction of NR<sub>1</sub>R<sub>2</sub> (R<sub>1</sub>, R<sub>2</sub> ≠ H) and is not applicable to base-sensitive substrates. The seminal studies of Ullmann and Goldberg into metal-mediated arene C(sp<sup>2</sup>)-N bond formation at the beginning of the 20th century were harbingers (**10**) of more efficient palladium-catalyzed cross-couplings between aromatic halides/sulfonates and ammonia or nitrogen surrogates developed independently by Hartwig (**11**) and Buchwald (**12**) in the early 1990s. In turn, a steady succession of technical improvements, up to the present time, has been offered with the aim of mitigating the original stringent Hartwig-Buchwald reaction conditions (**13–16**). All of these procedures, however, are restricted by the need for a prefunctionalized arene.

In more recent years, much attention has been paid to catalytic, direct arene aminations (**17–19**).

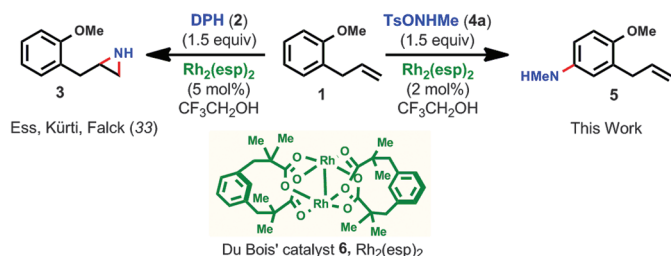
Many elegant atom- and step-efficient protocols have been introduced, but virtually all require a directing group, while others need an excess of arene, require high temperatures, or generate amides, imides, and sulfonamides instead of free amines (**20–31**). A noteworthy exception is the photoredox-driven process of Nicewicz (**32**) and colleagues that circumvents many of the preceding limitations.

Extensive density functional theory (DFT) calculations of the dirhodium-catalyzed olefin aziridination reported previously by our laboratories (**33**) suggested that the reactive rhodium-nitrene complex might exist in a protonated form in the presence of a weakly basic counterion and that this species could follow a different reaction manifold. This was corroborated by analysis of minor by-products from the aziridination of different substrates and the behavior of structurally varied nitrogen donors. After a systematic investigation, proof-of-principle for arene amination versus aziridination was demonstrated (Fig. 1). Treatment of 1-allyl-2-methoxybenzene (*o*-allylanisole, **1**) with *O*-(2,4-dinitrophenyl)-

**Fig. 1. A marked shift in chemoselectivity arises with different aminating agents.**

*o*-Allylanisole (**1**)

undergoes chemoselective olefin aziridination in the presence of catalytic Rh<sub>2</sub>(esp)<sub>2</sub> (**6**) and aminating agent



DPH (**2**) in 2,2,2-trifluoroethanol (TFE = CF<sub>3</sub>CH<sub>2</sub>OH) to give **3**. Changing the aminating agent to TsONHMe (**4a**) furnishes the corresponding *N*-Me aniline (**5**).

<sup>1</sup>Division of Chemistry, Department of Biochemistry, University of Texas Southwestern Medical Center, Dallas, TX 75390, USA. <sup>2</sup>Department of Chemistry and Biochemistry, Brigham Young University, Provo, UT 84602, USA. <sup>3</sup>Department of Chemistry, Rice University, BioScience Research Collaborative, Houston, TX 77005, USA.

\*Corresponding author. Email: j.falck@utsouthwestern.edu



hydroxylamine (**2**; DPH) (**34**) and catalytic  $\text{Rh}_2(\text{esp})_2$  (Du Bois' catalyst, **6**; 5 mol %) in 2,2,2-trifluoroethanol (TFE) at 0°C afforded the corresponding aziridine (**3**) as the sole product, whereas use of *N*-methyl-*O*-tosylhydroxylamine (**4a**) (**35**) as the aminating agent under otherwise identical conditions furnished exclusively the arene amination adduct 3-allyl-4-methoxy-*N*-methylaniline (**5**). Consequently, a more detailed study of the C-H arene amination was begun and ultimately led to a versatile, regioselective, operationally simple and mild dirhodium-catalyzed direct arene amination suitable for both intermolecular and intramolecular applications. The relatively weak N-O bond of the aminating agents, many of which are commercial or readily prepared (33–37), functions as an internal oxidant when

cleaved during the catalytic amination process, thus obviating the need for addition of an external oxidant to the reaction mixture. Also, the synchronous release of a stoichiometric amount of arylsulfonic acid during the amination is critical because it protonates the arylamines, which would otherwise inactivate the Rh catalyst. In some instances, acid-sensitive functionality such as epoxides and acetals do not survive.

Mesitylene (**7a**) was selected as a model arene to optimize reaction parameters. Use of 2 mol %  $\text{Rh}_2(\text{esp})_2$  and 1.5 equivalents of aminating agent **4a** in TFE as solvent smoothly generated *N*-methylaniline **8a** (75%) in just 30 min at 0°C (Fig. 2, entry 1); comparable yields were obtained with 1 and 0.5 mol % catalyst, except that the latter required 1 hour for complete consumption of

starting material. Combinations of TFE with  $\text{CH}_2\text{Cl}_2$  or MeOH in ratios up to 1:1 were suitable, but aminations run in EtOH or MeOH as the only solvent delivered poor yields (~10 to 20%) and those run in only DMF,  $\text{CH}_3\text{CN}$ , THF, toluene, and dioxane failed. Among alternative Rh-catalysts,  $\text{Rh}_2(\text{OAc})_4$  and  $\text{Rh}_2(\text{C}_8\text{H}_{15}\text{O}_2)_4$  were the next best with moderate yields (~40 to 45%), whereas the performance by  $\text{Rh}_2(\text{TFA})_4$  was poor. Results from other catalysts are summarized in table S1. Generally, reactions were quenched as soon as the substrate was completely consumed to minimize by-product formation. Air and water (5% v/v) were well tolerated, making this methodology operationally convenient.

The successful transfer of a *n*BuNH- unit to **7a** from TsONH*n*Bu (**4b**), affording **8b** in 52% yield

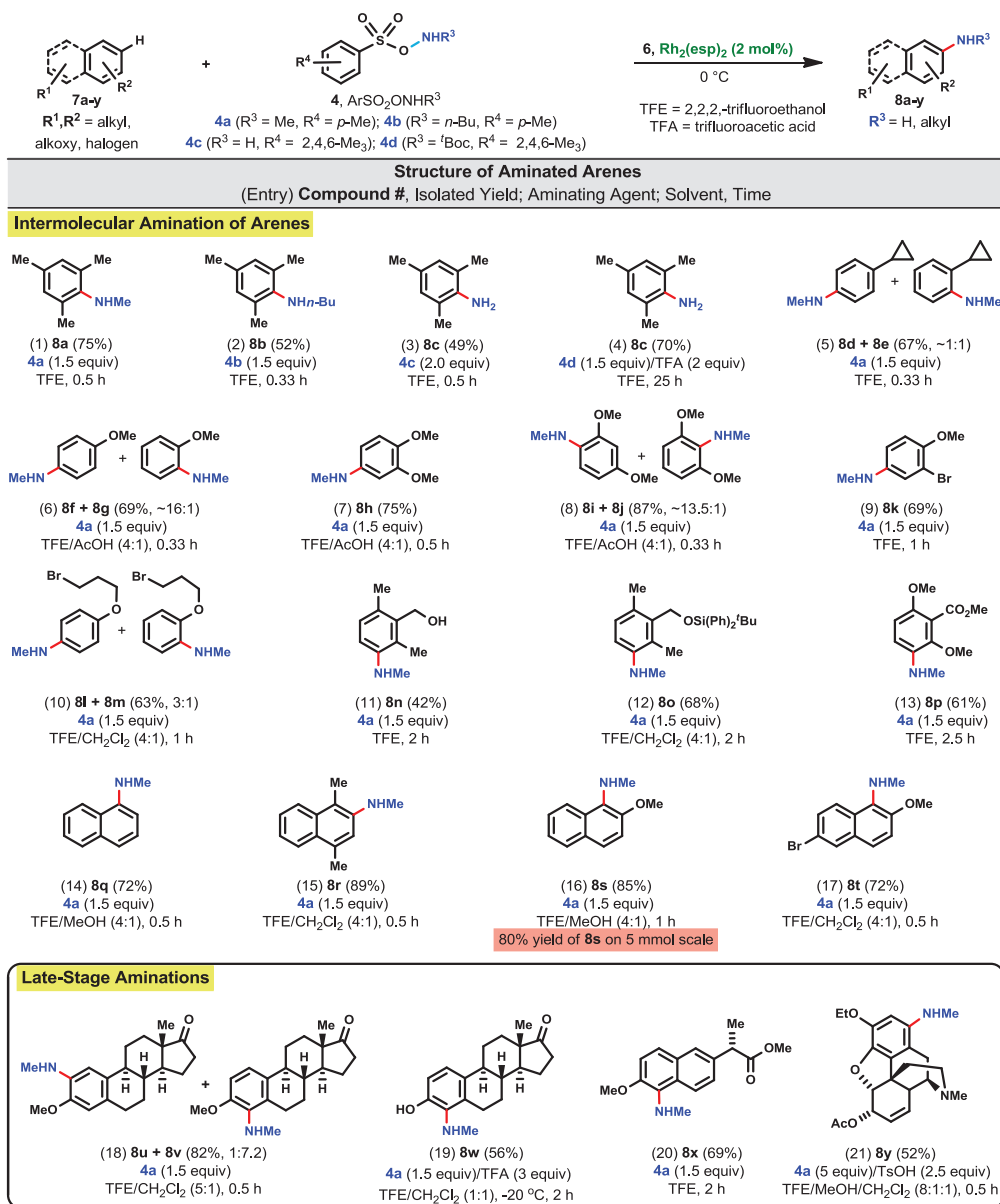


**Fig. 2. Direct intermolecular amination of arenes.** Reactions were conducted on a 0.1- to 0.5-mmol scale at 0.1 M using 2,2,2-trifluoroethanol (TFE =  $\text{CF}_3\text{CH}_2\text{OH}$ ) as solvent or using mixtures of TFE and other solvents as indicated.

(Fig. 2, entry 2), suggested that more complex amino moieties should also be suitable. For the introduction of  $\text{NH}_2$  into **7a**, we used 2,4,6- $\text{Me}_3\text{C}_6\text{H}_2\text{S}(\text{O})_2\text{ONH}^t\text{Boc}$  (**4d**, 2 equiv.) as aminating agent because of its greater stability at room temperature compared with  $\text{TsONH}_2$  (**37**). Although all of **4c** was consumed, a considerable amount of unreacted **7a** was recovered and a modest yield (49%) of **8c** was realized (entry 3). By contrast, the simple and expedient generation of the aminating agent in situ from 2,4,6- $\text{Me}_3\text{C}_6\text{H}_2\text{S}(\text{O})_2\text{ONH}^t\text{Boc}$  (**4d**, 1.5 equiv.) and  $\text{CF}_3\text{CO}_2\text{H}$  (2 equiv.) proved quite effective and boosted the yield of **8c** to 70% (entry 4), although the reaction was much slower than in the case of aminating agent **4c** (entry 3) and appeared to be dependent on the rate of  $t$ -Boc cleavage.

The results from other representative arenes are also summarized in Fig. 2. Despite having only a single aliphatic substituent, cyclopropylbenzene (**7d**) was well behaved, affording a 1:1 *para*/*ortho*-mixture (**8d** and **8e**) in 20 min at 0°C with no evidence of addition to the strained three-membered ring (entry 5). The directing effect in favor of the *para*-isomer was more pronounced with anisole (**7f**) and led to a 16:1 distribution of **8f** and **8g** (entry 6). This effect completely dominated in veratrole (**7h**) that gave **8h** as the predominant regioisomer (entry 7) and was equally evident in the conversion of 1,3-dimethoxybenzene (**7i**) into **8i**, although a minor amount (6%) of the *ortho*-isomer **8j** was found despite the increased steric congestion at this site (entry 8). Addition of acetic acid to the reaction solvent for the latter three examples (entries 6 to 8) improved the yields and suppressed the formation of mauve-colored by-products that we assume arose from further oxidation of the aminated adducts. The *ortho*/*para*-directing effect

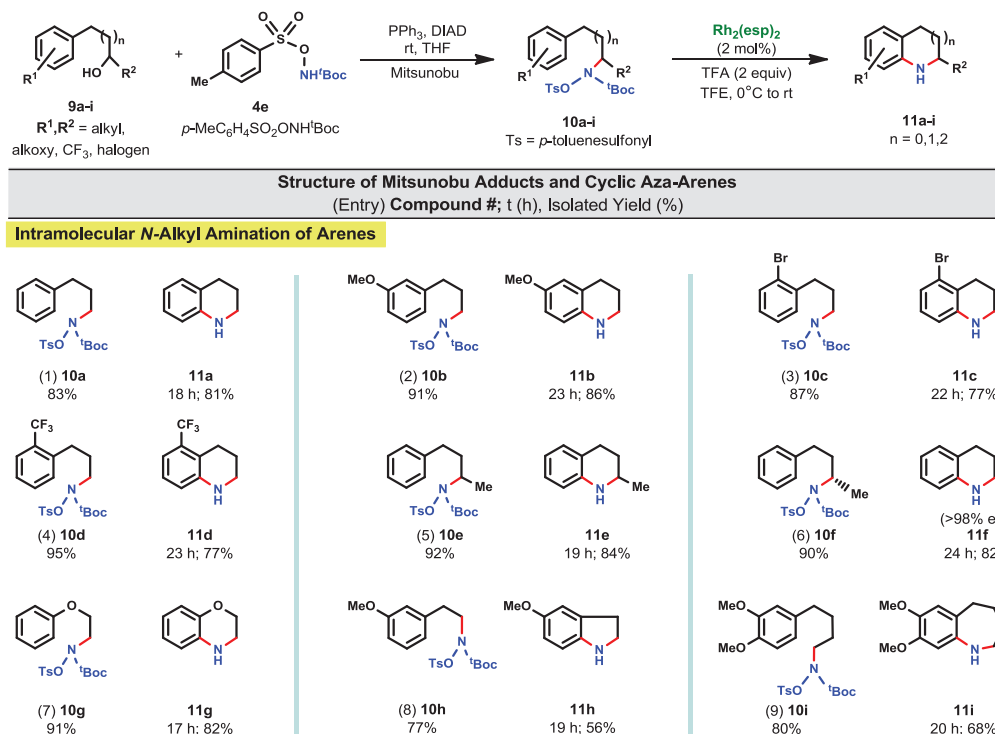


**Fig. 3. Direct intramolecular cyclization (aza-annulation) of arenes.** Cyclizations were conducted at 0.1 M using 2,2,2-trifluoroethanol (TFE = CF<sub>3</sub>CH<sub>2</sub>OH) as solvent on a 0.1- to 0.3-mmol scale unless otherwise indicated.

of electron-donating substituents is typical for electrophilic aromatic additions; the preference for the *para*- versus *ortho*-isomer might reflect the steric demand of the Rh-nitrenoid complex. Consistent with these results, aromatics with only electron-withdrawing substituents (e.g., CF<sub>3</sub> and CN) fail to aminate under these reaction conditions.

Aryl bromide **7k** (entry 9) and terminal alkyl bromide **7l** (entry 10) endured to deliver **8k** and a mixture of **8l**/**8m** (3:1), respectively, leaving the halogens available for further manipulation, if desired. The presence of some functional groups, however, partially retard amination; e.g., exposure of benzyl alcohol **7n** to the standard amination conditions generated a modest amount of **8n** (42%) after 2 hours (entry 11); by contrast, protection as silyl ether **7o** resulted in a much improved yield of **8o** (68%) (entry 12). Fortunately, a synthetically useful yield of amine could be obtained even in the presence of an electron-withdrawing substituent, e.g., **7p**→**8p** (entry 13). The amination process was also extended to fused aromatics: Naphthalene (**7q**) and 1,4-dimethylnaphthalene (**7r**) gave rise to *N*-methyl-1-naphthylamine (**8q**, entry 14) and *N*-methyl-1,4-dimethyl-2-naphthylamine (**8r**, entry 15), respectively, and 2-methoxynaphthalene (**7s**) readily underwent amination to give **8s** in 85% yield on a 0.5-mmol scale and in 80% yield on a 5-mmol scale (entry 16). The smooth amination of 2-methoxy-6-bromonaphthalene (**7t**) into *N*-methyl-2-methoxy-6-bromo-1-naphthylamine (**8t**, entry 17) succinctly illustrates the chemo- and regioselectivities of this methodology.

To validate the suitability of this methodology for late-stage functionalization of complex molecules, *O*-methylestrone (**7u**) was smoothly converted to a mixture of **8u** and **8v** (1:7.2, entry 18)

withdrawing functionality, **10c**→**11c** (entry 3) and **10d**→**11d** (entry 4). Control studies of the reaction of **10b** confirmed that there was less than 2% of the *ortho*-annulation product,

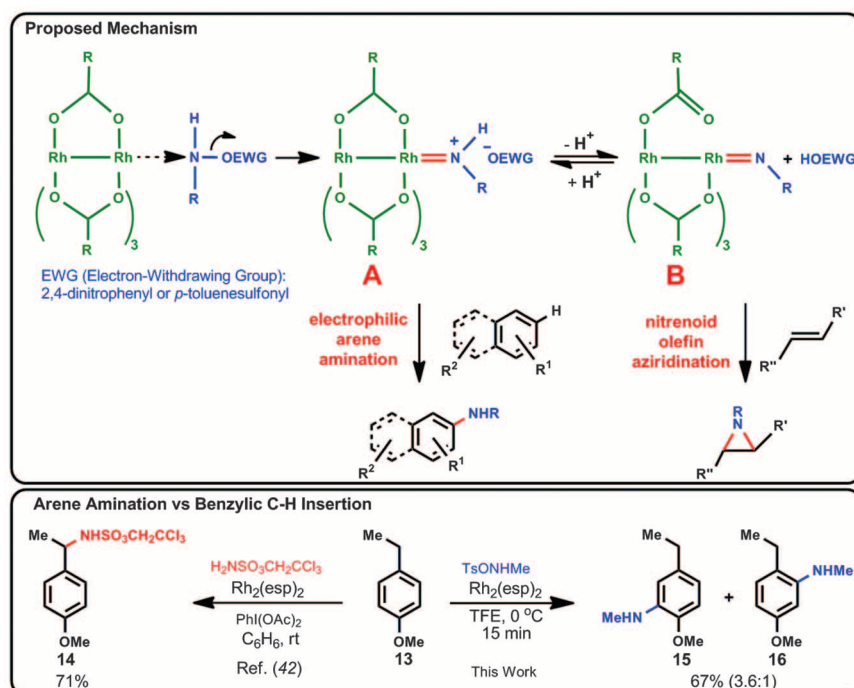


**Fig. 4. Proposed intermediates leading to amination versus aziridination and control study of arene amination versus benzylic C-H insertion.**

8-methoxy-1,2,3,4-tetrahydroquinoline, based on  $^{13}\text{C}$ -nuclear magnetic resonance analysis of the crude reaction product (figs. S5 and S6). Secondary alcohols likewise participated readily in the Mitsunobu and aza-annulation reactions, **9c**→**10c**→**11c** (entry 5). This two-step sequence, when conducted using the chiral alcohol **9f**, showed no loss of stereochemical integrity (entry 6). Incorporation of a heteroatom into the ring closure, e.g., **9g**→**10g**→**11g** (entry 7), did not perturb the chemistry and provided easy access to the dihydrobenzoxazine class of heterocycles. The yield declined somewhat for making the five-membered dihydroindole **11h** from alcohol **9h** (entry 8), but improved for the seven-membered tetrahydrobenzazepine **11i** from **9i** (entry 9).

As a beginning toward gaining insight into the mechanism of the amination, a 1:1 mixture of naphthalene (**7q**) and **7q-d<sub>8</sub>** was treated with a limited amount of amination reagent (**4a**, 0.5 equiv.) under otherwise standard reaction conditions. Samples were taken and quenched at 10, 20, 30, and 40 min. Analysis via selected ion monitoring–liquid chromatography–mass spectrometry revealed that the product ratios remained constant at ~1:1, a ratio inconsistent with an organometallic C–H activation pathway, which would typically manifest ~3:1 or higher ratios (**40**, **41**). Based on DFT calculations, we previously suggested that aziridination of alkenes involves the dirhodium-nitrenoid intermediate **B** shown in Fig. 4 that arises from overall NH transfer from the DPH-aminating reagent to the dirhodium catalyst (**33**). In contrast, reaction of *O*-tosylhydroxylamine reagents with the dirhodium catalyst favor intermediate **A** because  $\text{TsO}^-$  is weakly basic and the equilibrium with intermediate **B** lies far to the left. The chemoselectivity might be explained by the more electrophilic nature of intermediate **A** versus nitrenoid **B**. This preliminary hypothesis is consistent with the observation that moderate-to-strong bases such as  $\text{K}_2\text{CO}_3$ ,  $\text{Et}_3\text{N}$ , and pyridine completely inhibit amination, but not aziridination. Moreover, addition of  $\text{TsOH}$  (1.5 equiv.) to the reaction of **1** with 2,4-DNPNHMe (**12**) produced only the arene amination adduct **5** and no aziridine. As an additional control, it was shown that the presence of 2,4-DNP-OH (1.5 equiv.) did not alter the reaction manifold in favor of aziridination when **4a** was used as the aminating reagent and only **5** was observed.

It was also instructive to compare our methodology with the intermolecular Rh-catalyzed amination procedure of Du Bois to gain a perspective on their respective complementary chemoselectivities (Fig. 4) (**42**). Both have similar efficiency using *p*-ethylanisole (**13**), but the Du Bois procedure leads to benzylic C–H insertion only, whereas our methodology gives arene amination exclusively, providing **15** and **16** in a combined 67% yield.

The influence of ligands and counterions on the reactivity of organometallics is well predated (**43**, **44**). However, examples of such dramatic bifurcation of the reaction manifold are rare and warrant closer study to understand the energetics and full synthetic potential of this metalloid-nitrogen umpolung for direct arene aminations.

## REFERENCES AND NOTES

- R. Hili, A. K. Yudin, *Nat. Chem. Biol.* **2**, 284–287 (2006).
- A. Ricci, Ed., *Amino Group Chemistry: From Synthesis to the Life Sciences* (Wiley-VCH, 2008).
- R. J. Angelici, *Reagents for Transition Metal Complex and Organometallic Synthesis* (Wiley-Interscience, New York, 1990), vol. 28.
- A. Dalla Cort et al., *J. Org. Chem.* **70**, 8877–8883 (2005).
- N. R. Candeias, L. C. Branco, P. M. P. Gois, C. A. M. Afonso, A. F. Trindade, *Chem. Rev.* **109**, 2703–2802 (2009).
- J. F. Hartwig, S. Shekhar, Q. Shen, F. Barrios-Landeros, *Chem. Anilines* **1**, 455–536 (2007).
- Y.-S. Xie et al., *Tetrahedron Lett.* **54**, 5151–5154 (2013).
- J. Yu, P. Zhang, J. Wu, Z. Shang, *Tetrahedron Lett.* **54**, 3167–3170 (2013).
- T. Daskapan, *ARKIVOC* **2011**, 230–262 (2011).
- K. Kunz, U. Scholz, D. Ganzer, *Synlett* (15): 2428–2439 (2003).
- J. F. Hartwig, *Acc. Chem. Res.* **41**, 1534–1544 (2008).
- D. S. Surry, S. L. Buchwald, *Angew. Chem. Int. Ed.* **47**, 6338–6361 (2008).
- N. Xia, M. Taillefer, *Angew. Chem. Int. Ed.* **48**, 337–339 (2009).
- X. Zeng, W. Huang, Y. Qiu, S. Jiang, *Org. Biomol. Chem.* **9**, 8224–8227 (2011).
- R. J. Lundgren, M. Stradiotto, *Aldrichim Acta* **45**, 59–65 (2012).
- T. Maejima et al., *Tetrahedron* **68**, 1712–1722 (2012).
- H. M. L. Davies, X. Dai, Synthetic reactions via C–H bond activation: Carbene and nitrene C–H insertion, in *Comprehensive Organometallic Chemistry III*, R. H. Crabtree, D. M. P. Mingos, Eds. (Elsevier, 2007), vol. 10, pp. 167–212.
- J. Jiao, K. Murakami, K. Itami, *ACS Catal.* **6**, 610–633 (2016).
- P. Starkov, T. F. Jamison, I. Marek, *Chemistry* **21**, 5278–5300 (2015).
- W. C. P. Tsang, N. Zheng, S. L. Buchwald, *J. Am. Chem. Soc.* **127**, 14560–14561 (2005).
- K. Inamoto, T. Saito, M. Katsuno, T. Sakamoto, K. Hiroya, *Org. Lett.* **9**, 2931–2934 (2007).
- G. Brasche, S. L. Buchwald, *Angew. Chem. Int. Ed.* **47**, 1932–1934 (2008).
- K. Inamoto, T. Saito, K. Hiroya, T. Doi, *J. Org. Chem.* **75**, 3900–3903 (2010).
- R. Shrestha, P. Mukherjee, Y. Tan, Z. C. Litman, J. F. Hartwig, *J. Am. Chem. Soc.* **135**, 8480–8483 (2013).
- Y. Xue et al., *Eur. J. Org. Chem.* **2014**, 7481–7488 (2014).
- Z. Chen et al., *Org. Chem. Front.* **2**, 1107–1295 (2015).
- Y. Park, K. T. Park, J. G. Kim, S. Chang, *J. Am. Chem. Soc.* **137**, 4534–4542 (2015).
- K. Shin, H. Kim, S. Chang, *Acc. Chem. Res.* **48**, 1040–1052 (2015).
- F. Sun, Z. Gu, *Org. Lett.* **17**, 2222–2225 (2015).
- C. Suzuki, K. Hirano, T. Satoh, M. Miura, *Org. Lett.* **17**, 1597–1600 (2015).
- K. Takamatsu, K. Hirano, T. Satoh, M. Miura, *J. Org. Chem.* **80**, 3242–3249 (2015).
- N. A. Romero, K. A. Margrey, N. E. Tay, D. A. Nicewicz, *Science* **349**, 1326–1330 (2015).
- J. L. Jat et al., *Science* **343**, 61–65 (2014).
- Z. Yang, *Synlett* **25**, 1186–1187 (2014).
- O. R. S. John et al., *Org. Lett.* **9**, 4009–4012 (2007).
- J. Mendiola et al., *Org. Process Res. Dev.* **13**, 263–267 (2009).
- L. A. Carpino, *J. Am. Chem. Soc.* **82**, 3133–3135 (1960).
- M. Cherest, X. Lusinch, *Tetrahedron Lett.* **30**, 715–718 (1989).
- M. Kawase, Y. Kikugawa, *Chem. Pharm. Bull. (Tokyo)* **29**, 1615–1623 (1981).
- W. D. Jones, *Acc. Chem. Res.* **36**, 140–146 (2003).
- E. M. Simmons, J. F. Hartwig, *Angew. Chem. Int. Ed.* **51**, 3066–3072 (2012).
- C. G. Espino, K. W. Fiori, M. Kim, J. Du Bois, *J. Am. Chem. Soc.* **126**, 15378–15379 (2004).
- L. S. Hegeudus, *Transition Metals in the Synthesis of Complex Organic Molecules* (University Science Books, 1994), pp. 16–22.
- C. G. Espino, J. Du Bois, *Angew. Chem. Int. Ed.* **40**, 598–600 (2001).

## ACKNOWLEDGMENTS

J.R.F. thanks NIH (grant HL034300, HL111392, DK038226) and the Robert A. Welch Foundation (grant I-0011) for funding. L.K. gratefully acknowledges the generous financial support of Rice University, NIH (grant R01 GM-114609-01), NSF (CAREER:SusChem CHE-1455335), the Robert A. Welch Foundation (grant C-1764), American Chemical Society Petroleum Research Fund (grant 51707-DN1), Amgen (2014 Young Investigators' Award to L.K.), and Biotech (2015 Young Principal Investigator Award). A provisional patent application (patent no. 62/360,859) has been submitted and assigned jointly to University of Texas Southwestern and Rice University.

## SUPPLEMENTARY MATERIALS

www.sciencemag.org/content/353/6304/1144/suppl/DC1  
Materials and Methods  
Figs. S1 to S4  
Table S1  
References (45–61)

12 April 2016; accepted 18 August 2016  
10.1126/science.aaf8713

## ANTIBIOTIC RESISTANCE

## Spatiotemporal microbial evolution on antibiotic landscapes

Michael Baym,<sup>1</sup> Tami D. Lieberman,<sup>1\*</sup> Eric D. Kelsic,<sup>1</sup> Remy Chait,<sup>1†</sup> Rotem Gross,<sup>2</sup> Idan Yelin,<sup>2</sup> Roy Kishony<sup>1,2,3‡</sup>

A key aspect of bacterial survival is the ability to evolve while migrating across spatially varying environmental challenges. Laboratory experiments, however, often study evolution in well-mixed systems. Here, we introduce an experimental device, the microbial evolution and growth arena (MEGA)–plate, in which bacteria spread and evolved on a large antibiotic landscape (120 × 60 centimeters) that allowed visual observation of mutation and selection in a migrating bacterial front. While resistance increased consistently, multiple coexisting lineages diversified both phenotypically and genotypically. Analyzing mutants at and behind the propagating front, we found that evolution is not always led by the most resistant mutants; highly resistant mutants may be trapped behind more sensitive lineages. The MEGA-plate provides a versatile platform for studying microbial adaption and directly visualizing evolutionary dynamics.

**T**he worldwide increase in antibiotic resistance has motivated numerous studies aimed at understanding the phenotypic and genotypic evolution of antibiotic resistance (*1–7*). These experiments have shed light on the trade-offs constraining adaptive evolution in single-

and multidrug environments (*5, 6, 8, 9*). However, most of our current knowledge about the evolution of resistance is based on laboratory setups with well-mixed environments (*1–7, 10, 11*).

In natural and clinical settings, bacteria migrate between spatially distinct regions of selection



(5, 6, 8, 9, 12, 13). Theoretical models show that spatially structured pressures change the nature of selection: Instead of competing with its neighbors for limited resources, an adapted individual needs only to be the first with the capability to venture and survive in a new region (14, 15). A pioneering study focusing on small population sizes showed that structured microenvironments increase the rate of adaptation to antibiotics through highly reproducible genetic changes (9). It is unknown how evolution is shaped by the diversification potential and differences in adaptive constraints of large populations in spatial environments.

Here, we present a device for the evolution of bacteria that allows migration and adaptation in a large, spatially structured environment. The microbial evolution and growth arena (MEGA)-plate consists of a rectangular acrylic dish, 120 × 60 cm, in which successive regions of black-colored agar containing different concentrations of antibiotics are overlaid by soft agar allowing bacterial motility (Fig. 1A). Motile bacteria inoculated at one location on the plate deplete nutrients locally and then spread by chemotaxis to other regions (16). Only increasingly resistant mutants can spread into sections containing higher levels of antibiotic. The large size of the plate serves two purposes: It provides for a large population and mutational supply, and it maintains the antibiotic gradient despite diffusion (drug diffusion time scales quadratically with distance while the bacterial front advances linearly; thus, the large plate size prevents the antibiotic gradient from equilibrating over the duration of the experiment). Once a mutant has exhausted the resources of a region of the plate, other mutants do not meaningfully migrate by chemotaxis to that region (because they move diffusively without a nutrient gradient). In this manner, mutational lineages can block each other physically—a phenomenon notably observed in biofilm formation (17). This partitioning of mutants into stable spatial domains also enables sampling of individual mutants for later analysis. Using periodic photography of the plate, we constructed time-lapse movies of evolution (movie S1). Combining these with analysis of isolates, this system allows reconstruction of the phenotypic and genotypic evolutionary histories of evolving bacteria.

Challenging bacteria in spatial gradients of antibiotics leads to large increases in resistance through sequential adaptive steps across competing lineages (Fig. 1 and movie S1). We first set up the MEGA-plate with symmetric four-step gradients of trimethoprim (TMP) or ciprofloxacin (CPR) proceeding inward with order-of-magnitude increases in concentration per step [Fig. 1A; TMP: 0, 3, 30, 300, and 3000 × wild-type minimum inhibitory concentration (MIC); CPR:

0, 20, 200, 2000, and 20,000 × MIC] and inoculated the drug-free regions with *Escherichia coli*. Bacteria swim and spread until they reach a concentration in which they can no longer grow (TMP, Fig. 1C and movies S1 and S2; CPR, movie S3). As resistant mutants arise in the population, their descendants migrate into the next step of drug concentration and fan out (Fig. 1C, 88 hours). Adjacent mutant lineages exclude each other and compete for limited space, resulting in some lineages entirely blocking off growth of others (Fig. 1C). When the winning lineages reach a further increased level of drug concentration at which they too are unable to grow, secondary mutations arise and the process repeats. Ultimately, the bacteria reach and overspread the highest drug concentration, showing marked increases in drug resistance: Phenotyping of sampled mutants from the highest-concentration region showed a factor of  $10^4$  increase in MIC for TMP (Fig. 1B) and a factor of  $10^5$  increase in MIC for CPR (fig. S1). The adaption time (10 days in TMP, 12 days in CPR) is consistent with evolution in well-mixed environments (4), yet is slower than reported adaptation rates in microspatial environments, likely because of the additional time required to swim between concentration steps (9). It is possible that at different dimensions, the MEGA-plate will yield different evolutionary dynamics;

a wider front would increase the effective population size and thus the mutational supply, whereas a longer run between steps would increase selection among adjacent lineages.

To test the importance of the size of intermediate steps in the evolution of high-level resistance, we set up a variant of the MEGA-plate in which bacteria go from no drug to a high level directly or through one middle region of variable magnitude (Fig. 2; TMP: high step 3000 × MIC, middle step 0, 3, 30, or 300 × MIC; CPR: high step 2000 × MIC, middle step 0, 2, 20, or 200 × MIC). Bacteria were unable to adapt directly from zero to the highest concentration of either drug. Diffusive smoothing of these large steps enabled the appearance of partially resistant mutants, but their lineages did not advance (Fig. 2A, left). The addition of an intermediate concentration step enabled adaptation, although this was impeded when this middle step was too high (Fig. 2B). Even across the permissive intermediate steps, evolution often proceeded through multiple mutations taking advantage of the local gradients formed by diffusion (TMP, movie S4; CPR, movie S5). Thus, by progressing through colonization of regions with moderately challenging selective pressures, intermediate-resistance mutants can expand to sufficient numbers to facilitate the rise of high-resistance mutants. Analogous to evolutionary

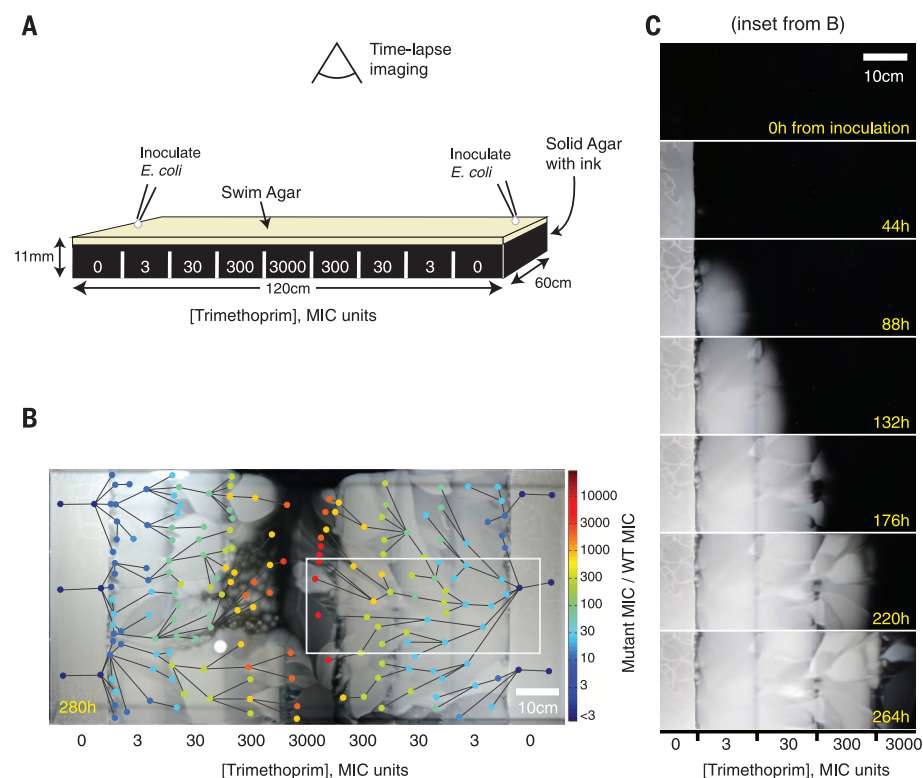


**Fig. 1. An experimental device for studying microbial evolution in a spatially structured environment.** (A) Setup of the four-step gradient of trimethoprim (TMP). Antibiotic is added in sections to make an exponential gradient rising inward. (B) The four-step TMP MEGA-plate after 12 days. *E. coli* appear as white on the black background. The 182 sampled points of clones are indicated by circles, colored by their measured MIC. Lines indicate video-imputed ancestry. (C) Time-lapse images of a section of the MEGA-plate. Repeated mutation and selection can be seen at each step. Images have been aligned and linearly contrast-enhanced but are otherwise unedited.

<sup>1</sup>Department of Systems Biology, Harvard Medical School, Boston, MA, USA. <sup>2</sup>Faculty of Biology, Technion-Israel Institute of Technology, Haifa, Israel. <sup>3</sup>Faculty of Computer Science, Technion-Israel Institute of Technology, Haifa, Israel. \*Present address: Massachusetts Institute of Technology, Cambridge, MA, USA. †Present address: IST Austria, Klosterneuburg, Austria. ‡Corresponding author. Email: rkishony@technion.ac.il

rescue in temporal selective gradients (18–20), a gradual spatial gradient allows adaptation to previously inhospitable environments. However, unlike in a temporal gradient, a spatial gradient does not impose a minimal time for a mutant's appearance and spread; at any time, a mutant appearing on the stalled front can expand and evolve further, provided it is sufficiently resistant to colonize the next step. Thus, concordant with theoretical predictions (21, 22), access to intermediate regions of moderate selection is critical for enabling a range of evolutionary paths to high-level resistance.

We next focused on the genotypic and phenotypic paths leading to high levels of resistance. We sequenced 21 isolates from the four-step TMP gradient experiment and 230 isolates from the multiple intermediate-step TMP experiment above. The samples separated into minimally and highly mutated (i.e., mutator phenotype) groups [ $>60$  single-nucleotide polymorphisms (SNPs) and indels for high,  $<12$  for low; Fig. 3A]. Similar separation was also seen when restricting the analysis to synonymous mutations to

minimize differential effects of selection (fig. S2). All highly mutated isolates, but none of the others, had mutations in *dnaQ* (also called *mutD*), which was the only gene for which the presence of a mutation correlated perfectly with the mutator phenotype. This gene encodes DNA polymerase III, which is critical to proofreading (23, 24). Isolates carrying mutated *dnaQ* alleles showed increased rates of mutations on rifampin disk diffusion assays (fig. S2) (25). These mutators appeared repeatedly in distinct locations on the plate and across experiments. On the basis of lineage reconstructions from the time-lapse video as well as genotypic relationships, the mutator phenotype emerged at least six times independently between the four-step and intermediate-step TMP experiments above [fig. S2; four different alleles of *dnaQ* were observed: Val<sup>96</sup> → Glu (V96E), Ile<sup>97</sup> → Asn (I97N), Ile<sup>97</sup> → Ser (I97S), and Ile<sup>97</sup> → Thr (I97T), where I97T appeared three independent times]. Although these mutator lineages accumulated mutations more rapidly, their rate of phenotypic adaption was similar to

that of the less mutated isolates, reaching the highest level of resistance at roughly the same time (fig. S3 and movie S4). Indeed, the highly mutated lineages had a close to neutral ratio of non-synonymous to synonymous substitutions (Fig. 3B). In contrast, the less mutated isolates showed a high bias toward coding mutations, indicating that most of these mutations were likely adaptive (Fig. 3B).

Focusing on the nonmutator isolates, we identified a wide spectrum of putatively adaptive mutations for TMP resistance. The most frequently mutated gene was the primary target of TMP, *folA* (26), which encodes dihydrofolate reductase (DHFR) (Fig. 3C), with more mutations appearing as resistance increased. We also observed several genes that were repeatedly mutated yet are not involved in the folate biosynthesis pathway, and thus are not primarily associated with TMP resistance. These included stress response genes, such as those of the *mar* and *sox* operons, known to be important in general antibiotic and toxin resistance (27), as well as genes involved in transcription and translation, which have been shown to affect TMP resistance (28). We also found that three genes not classically associated with TMP resistance were repeatedly mutated, often with a probable loss of function (frameshift or nonsense): a phosphate transporter (*pitA*), shikimate kinase I (*aroK*), and a negative regulator of the PhoQP system (*mgrB*). Knockout of these genes in the ancestral strain confirmed their resistance phenotypes (fig. S4).

Mutations that increased resistance often came with a cost of reduced growth, which was subsequently restored by additional compensatory mutations (29–31). Although some resistance-conferring mutations allowed colonization of regions of high drug concentration without affecting growth, many lineages capable of growing in these regions were deficient in yield, particularly during CPR resistance evolution (as measured by optical density: Fig. 4, A and B, for CPR; fig. S3 for TMP). These yield-deficient mutations were followed by compensatory mutations allowing growth to full density (Fig. 4, A and B, and movie S3; number of compensatory mutants observed in a single run:  $>50$  for TMP,  $>500$  for CPR). In the absence of a chemotaxis-inducing nutrient gradient, the compensatory mutants stayed localized behind the front, appearing in a characteristic pattern of localized spots spreading from single points (Fig. 4A and movie S3).

Focusing on evolution in CPR, we sampled and phenotyped compensatory mutants. We found that many of them had not only compensated for growth but had also increased in resistance, often beyond the resistance levels of the propagating front (Fig. 4C). Yet, as these mutants were engulfed by their parental lineage, they stayed constrained to the immediate vicinity in which they appeared and were unable to overtake the moving front. To test whether these compensatory mutants were capable of outcompeting the propagating front, we conducted an additional evolution experiment in

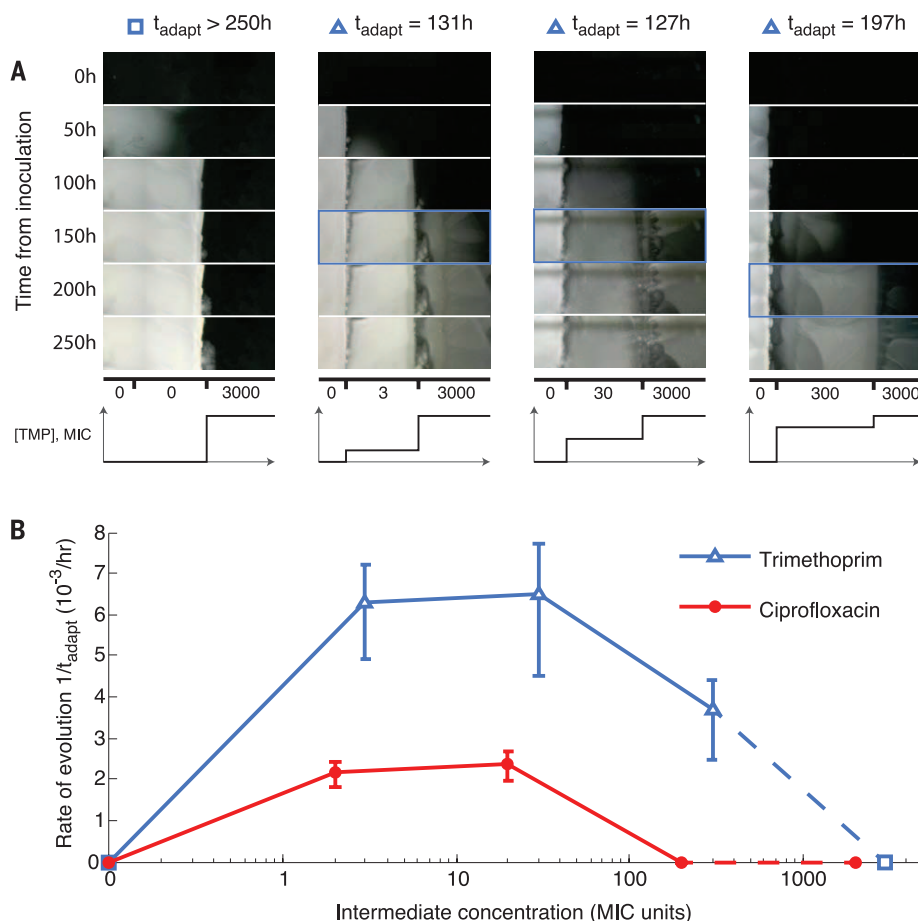


**Fig. 2. Initial adaptation to low drug concentrations facilitates later adaptation to high concentrations.** (A) Frames from a section of the TMP intermediate-step MEGA-plate over time (TMP, movie S4; CPR, movie S5). The first frame showing a mutant in the highest band is indicated by a blue box. (B) Rates of adaptation in the intermediate-step experiments across TMP and CPR, showing the necessity of intermediate adaptation for the evolution of high levels of resistance. Error bars show the appearance times of multiple lineages in the highest concentration. Because the intermediate step with no drug puts the highest and lowest concentrations adjacent, it serves as both the highest and lowest intermediate steps (dashed line).

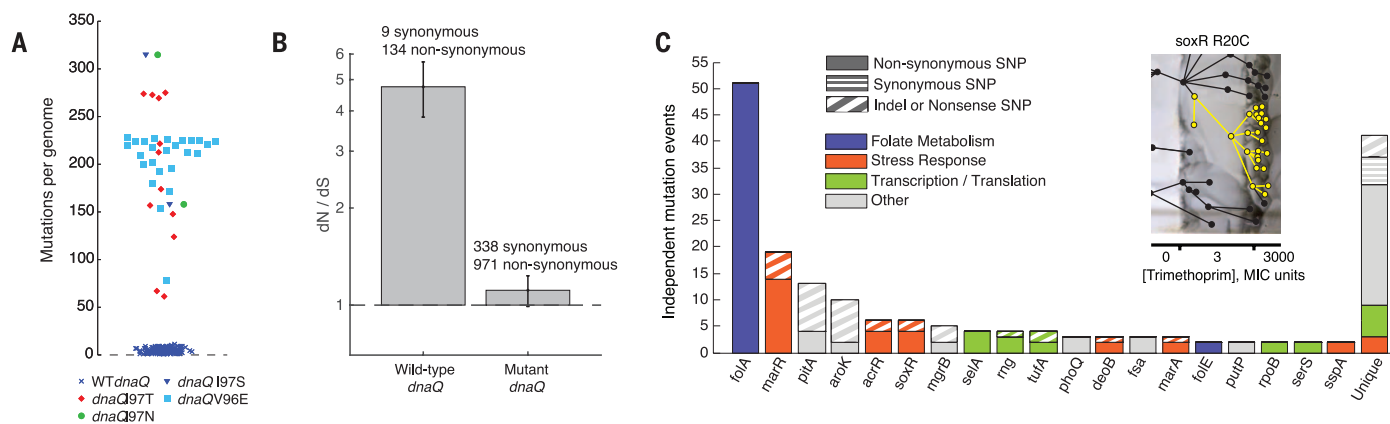


**Fig. 3. Diverse genotypic strategies for adaptation to trimethoprim.** (A) Numbers of observed mutations across individual isolates. Samples with a *dnaQ* mutation (solid symbols) consistently carried more mutations than those sampled with the wild-type *dnaQ* allele (crosses). Data points are horizontally jittered for clarity. (B) The normalized ratio of nonsynonymous to synonymous substitutions of isolates compared with the ancestor for samples with normal and highly mutated phenotypes. Error bars are the standard deviation of the Bayesian posterior estimate for the binomial parameter. (C) Numbers of dis-

tinct mutational events in genes that were mutated at least twice independently. Genes are colored by pathway per EcoCyc (37). Nonsynonymous, synonymous, and loss-of-function mutations (including indel and nonsense) are indicated. Genes that only had one mutation across all samples were combined into the “unique” column. Individual mutation events were inferred through ancestry (movies S1 and S4). Inset: The multistep MEGA-plate with samples containing the mutation *soxR* R20C (yellow) tracing mutational events from multiple samples and video.

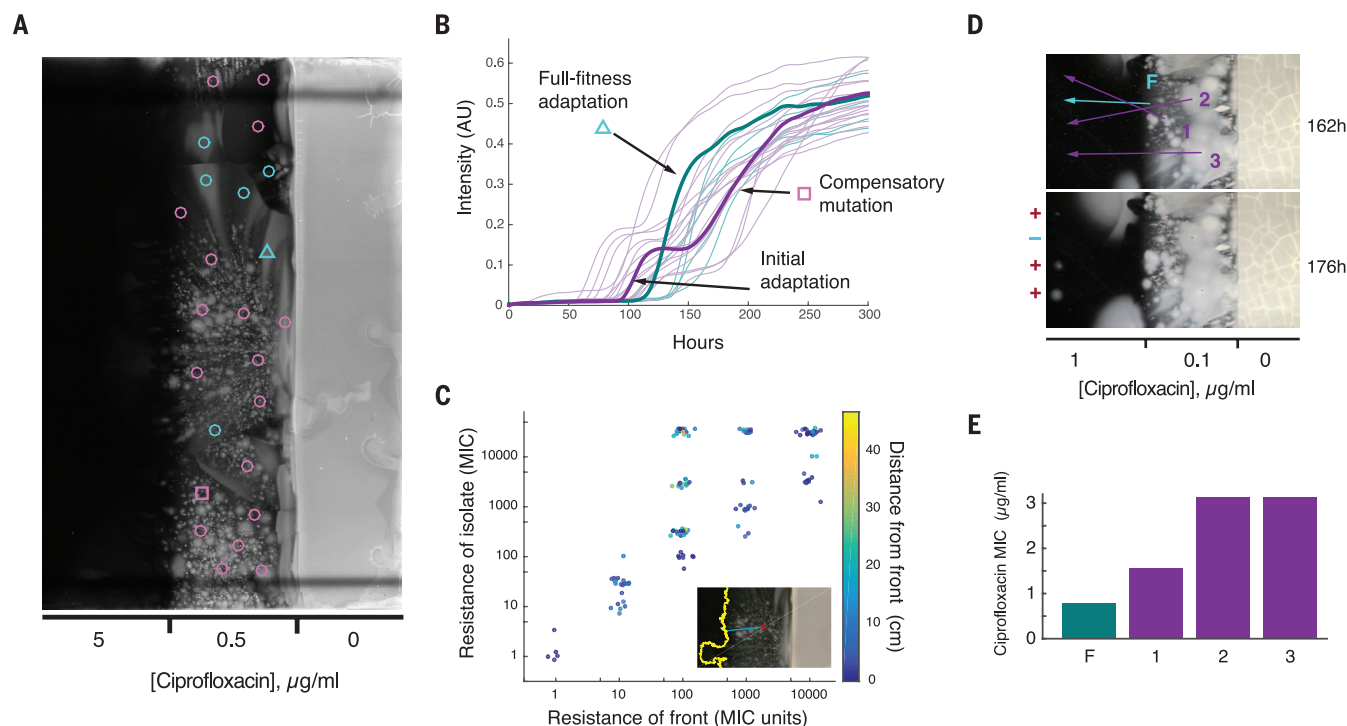


**Fig. 4. Compensatory mutations can be spatially trapped.** (A) Ciprofloxacin experiment still frame with locations of 24 isolates showing a full-fitness mutation (cyan) or yield-deficient mutation followed by a compensatory mutation (purple). (B) Optical density at the marked points in (A) over the course of the experiment. The two example traces (indicated by a square and triangle) correspond to the points marked by the same glyph in (A). (C) Mutants isolated behind the front can have markedly higher resistance than the front at the time it passed the same location. Resistance of the front was

measured by the concentration at which front progression stopped; isolate MICs were measured in vitro. (D) The front (marked F) and three compensatory mutants (marked 1 to 3) were sampled at 162 hours, and immediately inoculated ahead of the front as indicated by the arrows. Growth of the moved mutants is evident for the three compensatory mutants, despite being inoculated at a CPR concentration much higher than where they emerged, but not for the front. (E) Measured CPR MICs of the mutants from (D).

which we sampled the trapped compensatory mutants and moved them forward, reinoculating them ahead of the still-moving front. These compensatory mutants were able to grow in a

region where the front could not (Fig. 4D). Similarly, some trapped compensatory mutants were able to outcompete their parent when placed side-by-side on a fresh gradient plate (fig. S5).

Hence, as compensatory mutations often occur behind the front, they are spatially restricted from contributing to the ultimate evolutionary course of the population. Indeed, in the rare cases



when these compensatory mutations appeared at the front and were not physically blocked, they accelerated the adaptive process (fig. S3 and movie S3, 00:53). Thus, the fitness of the population is not driven by the fittest mutants (32–34), but rather by those that are both sufficiently fit and arise sufficiently close to the advancing front.

The MEGA-plate is not intended to directly simulate natural or clinical settings, but it does capture unique aspects of evolution during range expansion. Evolution of high levels of resistance is enabled by intermediate regions of moderate selective pressure. Furthermore, as multiple lineages evolve in parallel, the propagating front can be led by lineages less fit than those trapped behind it. It will be interesting to explore how adaptation rates and mutational diversity depend on other spatiotemporal parameters, including population density, mutation rate, and the relative expansion speed and spatial dimensions. Owing to the relaxed evolutionary constraints in range expansion dynamics, the MEGA-plate is likely to reveal novel mutational pathways to high-level multiantibiotic resistance. Further, the MEGA-plate can be adapted to a range of organisms and challenges beyond antibiotics. Differences in evolutionary dynamics between evolution under different selection pressures appear visually, simplifying both hypothesis generation and testing. Owing to this flexibility, the MEGA-plate is a platform for exploring the interplay of spatial constraints and evolutionary pressures. The MEGA-plate provides a physical analog of the otherwise abstract Muller plots of population genetics (35, 36) and of other elusive aspects of evolution, including diversification, compensatory mutations, and clonal interference. Its relative simplicity and ability to visually demonstrate evolution makes the MEGA-plate a useful tool for science education and outreach.

## REFERENCES AND NOTES

1. D. M. Weinreich, N. F. Delaney, M. A. Depristo, D. L. Hartl, *Science* **312**, 111–114 (2006).
2. H. H. Lee, M. N. Molla, C. R. Cantor, J. J. Collins, *Nature* **467**, 82–85 (2010).
3. P. G. Lane, A. Hutter, S. G. Oliver, P. R. Butler, *Biotechnol. Prog.* **15**, 1115–1124 (1999).
4. E. Toprak et al., *Nat. Genet.* **44**, 101–105 (2012).
5. L. Imamovic, M. O. A. Sommer, *Sci. Transl. Med.* **5**, 204ra132 (2013).
6. V. Lázár et al., *Mol. Syst. Biol.* **9**, 700–700 (2013).
7. O. Fridman, A. Goldberg, I. Ronin, N. Shores, N. Q. Balaban, *Nature* **513**, 418–421 (2014).
8. M. Hegreness, N. Shores, D. Damian, D. Hartl, R. Kishony, *Proc. Natl. Acad. Sci. U.S.A.* **105**, 13977–13981 (2008).
9. Q. Zhang et al., *Science* **333**, 1764–1767 (2011).
10. T. M. Conrad, N. E. Lewis, B. O. Palsson, *Mol. Syst. Biol.* **7**, 509–509 (2011).
11. T. J. Kawecki et al., *Trends Ecol. Evol.* **27**, 547–560 (2012).
12. J. L. Martinez, *Proc. Biol. Sci.* **276**, 2521–2530 (2009).
13. O. Hallatschek, P. Hersen, S. Ramanathan, D. R. Nelson, *Proc. Natl. Acad. Sci. U.S.A.* **104**, 19926–19930 (2007).
14. P. Greulich, B. Waclaw, R. J. Allen, *Phys. Rev. Lett.* **109**, 088101 (2012).
15. R. Hermesen, J. B. Deris, T. Hwa, *Proc. Natl. Acad. Sci. U.S.A.* **109**, 10775–10780 (2012).
16. H. C. Berg, D. A. Brown, *Nature* **239**, 500–504 (1972).
17. J. B. Xavier, K. R. Foster, *Proc. Natl. Acad. Sci. U.S.A.* **104**, 876–881 (2007).
18. G. Bell, A. Gonzalez, *Science* **332**, 1327–1330 (2011).
19. A. Gonzalez, G. Bell, *Philos. Trans. R. Soc. London Ser. B* **368**, 20120079 (2013).

20. H. A. Lindsey, J. Gallie, S. Taylor, B. Kerr, *Nature* **494**, 463–467 (2013).
21. J. R. Bridle, T. H. Vines, *Trends Ecol. Evol.* **22**, 140–147 (2007).
22. J. Polechová, N. H. Barton, *Proc. Natl. Acad. Sci. U.S.A.* **112**, 6401–6406 (2015).
23. R. G. Fowler, G. E. Degnen, E. C. Cox, *Mol. Gen. Genet.* **133**, 179–191 (1974).
24. H. Echols, C. Lu, P. M. Burgers, *Proc. Natl. Acad. Sci. U.S.A.* **80**, 2189–2192 (1983).
25. J.-C. Galán et al., *J. Clin. Microbiol.* **42**, 4310–4312 (2004).
26. D. R. Smith, J. M. Calvo, *Mol. Gen. Genet.* **187**, 72–78 (1982).
27. R. G. Martin, K. W. J. R. E. Wolf Jr., J. L. Rosner, *J. Bacteriol.* **178**, 2216–2223 (1996).
28. T. Bollenbach, S. Quan, R. Chait, R. Kishony, *Cell* **139**, 707–718 (2009).
29. R. E. Lenski, *Int. Microbiol.* **1**, 265–270 (1998).
30. B. R. Levin, V. Perrot, N. Walker, *Genetics* **154**, 985–997 (2000).
31. A. Handel, R. R. Regoes, R. Antia, *PLOS Comput. Biol.* **2**, e137 (2006).
32. C. O. Wilke, J. L. Wang, C. Ofria, R. E. Lenski, C. Adami, *Nature* **412**, 331–333 (2001).
33. R. Sanjuán, J. M. Cuevas, V. Furió, E. C. Holmes, A. Moya, *PLOS Genet.* **3**, e93 (2007).
34. F. M. Codoñer, J.-A. Darós, R. V. Solé, S. F. Elena, *PLOS Pathog.* **2**, e136 (2006).
35. H. J. Muller, *Am. Nat.* **66**, 118–138 (1932).
36. J. E. Barrick, R. E. Lenski, *Nat. Rev. Genet.* **14**, 827–839 (2013).
37. I. M. Keseler et al., *Nucleic Acids Res.* **41**, D605–D612 (2013).

## ACKNOWLEDGMENTS

Sequence data are available on NCBI SRA under accession number SRP077287. We thank X. R. Bao and A. C. Palmer for helpful discussions and the National BioResource Project (NIG, Japan) for providing the Keio collection. Supported by National Defense Science and Engineering Graduate fellowship 32 CFR 168a (E.D.K.), NIH grant R01-GM081617 (R.K.), and European Research Council FP7 ERC grant 281891 (R.K.).

## SUPPLEMENTARY MATERIALS

www.sciencemag.org/content/353/6304/1147/suppl/DC1  
Materials and Methods  
Figs. S1 to S6  
Tables S1 and S2  
Movies S1 to S5  
References (38–43)

6 May 2016; accepted 28 July 2016  
10.1126/science.aag0822

## INTERNET ACCESS

# Digital discrimination: Political bias in Internet service provision across ethnic groups

Nils B. Weidmann,<sup>1,\*</sup> Suso Benitez-Baleato,<sup>1,2</sup> Philipp Hunziker,<sup>3</sup> Eduard Glatz,<sup>4</sup> Xenofontas Dimitropoulos<sup>5,6</sup>

The global expansion of the Internet is frequently associated with increased government transparency, political rights, and democracy. However, this assumption depends on marginalized groups getting access in the first place. Here we document a strong and persistent political bias in the allocation of Internet coverage across ethnic groups worldwide. Using estimates of Internet penetration obtained through network measurements, we show that politically excluded groups suffer from significantly lower Internet penetration rates compared with those in power, an effect that cannot be explained by economic or geographic factors. Our findings underline one of the central impediments to “liberation technology,” which is that governments still play a key role in the allocation of the Internet and can, intentionally or not, sabotage its liberating effects.

In the wake of the Arab Spring, the Internet has often been portrayed as a “liberation technology” (1). Specifically, it has been argued that the Internet fosters transparency and accountability of nondemocratic governments worldwide and can help opposition movements organize for collective action (2). This expectation, however, is based on the assumption that political activists have sufficient access to the Internet in the first place.

The socioeconomic background of individuals affects their access to the Internet (3, 4). Also, there is evidence of a global digital divide: Countries with democratic institutions and higher levels of development have higher Internet penetration rates (5). Still, we do not know how the provision of Internet services varies across societal groups in a country or how it is driven by politics. This information is key if we are to assess whether the

Internet can indeed empower politically marginalized populations.

In most developing countries, governments are the major, if not the only, provider of telecommunication services (6). At the same time, in many of these countries, politics operates along ethnic lines, so that one or more groups hold

<sup>1</sup>Department of Politics and Public Administration, University of Konstanz, Universitätsstraße 10, 78457 Konstanz, Germany.

<sup>2</sup>Department of Political Science, University of Santiago de Compostela, Campus Vida, 15705 Compostela, Spain.

<sup>3</sup>International Conflict Research, ETH Zurich, Haldeneggsteig 4, 8092 Zurich, Switzerland. <sup>4</sup>Computer Engineering and Networks Laboratory, ETH Zurich, Gloriastraße 35, 8092 Zurich, Switzerland.

<sup>5</sup>Foundation for Research and Technology Hellas, Nikolaou Plastira 100, 71110 Heraklion, Crete, Greece. <sup>6</sup>Department of Computer Science, University of Crete, Voutes Campus, 70013 Heraklion, Crete, Greece.

\*Corresponding author. Email: nils.weidmann@uni-konstanz.de

political power at the expense of other, marginalized ones (7). This allows Internet technology to be implemented in a way that benefits certain groups while neglecting others. Two mechanisms can account for this: First, ethnic groups in power can foster economic and technological development in their home regions (8), a phenomenon typically referred to as “ethnic favoritism.” Second, governments can attempt to strategically exclude certain groups from access to communication technology because they are afraid of facilitating political mobilization and unrest. Either (or both) of these mechanisms can lead to digital discrimination, in which politically marginalized groups suffer from reduced access to modern information and communications technology (ICT). Our aim was to test whether less politically favored ethnic groups are systematically deprived of this access by governments. The biggest challenge in doing so was to rule out alternative explanations (such as uneven economic status across groups) for the potential correlation between political status and Internet penetration.

We based our analysis on the Ethnic Power Relations (EPR) list of politically relevant groups (7). EPR distinguishes between politically “included” and “excluded” groups. The former are groups that have access to (executive) political power at the national level, such as by having representatives in the government of a country. This access can take a variety of forms, ranging from participation in ethnically shared governments to complete ethnic monopolies, in which the entire executive apparatus is effectively controlled by a single group. Conversely, excluded groups do not participate in the executive apparatus at the national level,

but they may have different levels of regional power—or no power at all.

Typically, the main source of statistics about Internet penetration is the International Telecommunication Union’s World Telecommunications/ICT Indicators Database (9). This database provides more than 150 indicators of different aspects of ICT coverage, including access to and use of the Internet for 192 countries starting from 1992. However, it offers data only at the country level, making it useless for subnational analysis across ethnic groups. A source of subnational estimates could be the official statistics provided by the telecommunication ministries and regional operators, because they sometimes include data at the regional or local level. Unfortunately, this level of disaggregation is only available for a limited number of countries, mostly industrialized ones, which would severely limit the scope of our study. Yet another data source could be the large surveys that are periodically conducted by international agencies to describe trends in development, health, and demographics. For example, the Demographic and Health Surveys include questions about technological access, such as whether the Internet is available in a household, and about the use of certain Internet services (10). Some of these surveys also contain the (self-reported) ethnicities of the individuals interviewed. However, although these surveys are generally representative at the country level, this is not necessarily the case at the level of ethnic groups. Moreover, relying on surveys would restrict our sample considerably because they are available for a limited set of countries only.

Therefore, we estimated Internet penetration spatially using the method proposed in (11), which has shown that Internet penetration in countries and subnational administrative units (provinces or states) can be approximated by the number of active Internet subnetworks. We used subnetworks of size /24 (the slash notation refers to the number of bits used for the network address), which correspond to ~256 IP (Internet protocol) addresses each and are typically assigned to institutions or small providers.

Our estimation of Internet penetration from active subnetworks proceeded in three steps. First, we determined which were the active /24 subnetworks. This was necessary because large parts of the Internet address space are not used for digital communication. We did this in two different ways. One way was a passive measurement that relied on observed Internet traffic from a large Internet service provider in Switzerland. This data set included the outside IP addresses with which any host within the provider’s network communicated, from which we obtained a sample of 16 days for each year in our study period (2004–2012). The methodology for creating this data set is described in (12), and we refer to the subnetworks determined through this method as “observed” subnetworks. The other estimation approach used routing metadata (border gateway protocol data) collected by the Route Views project (13). This project provides daily snapshots of routing tables for the same annual samples as above. The IP addresses in these samples were collapsed to unique /24 subnetworks, and reserved addresses were removed. We retained those subnetworks that appeared on every day of the 16-day

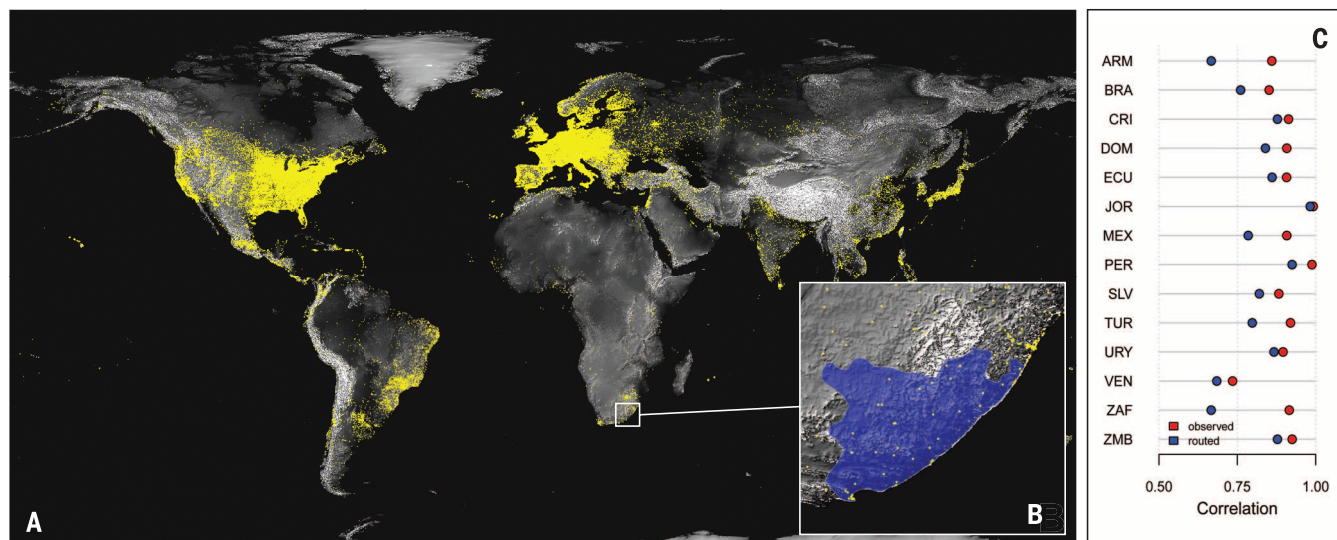


**Fig. 1. Estimating Internet penetration from active Internet subnetworks.**

(A) Global map of active Internet subnetworks for the year 2012, where each yellow dot represents the subnetwork’s location. The areas with the highest Internet penetration are North America, Europe, and parts of Asia. (B) Active subnetworks were assigned to ethnic groups by identifying whether they were located within the settlement region of that group. As an example, the close-up view shows this for the Xhosa group (blue) in South Africa. (C) Results of the validation study of the Internet penetration measure. Active subnetworks

were assigned to subnational administrative regions for which the Internet penetration was known. The plots show the correlations between the (log-transformed) number of subnetworks per 1000 capita (red, observed; blue, routed) and the Internet penetration across the subnational administrative divisions for 14 countries. ARM, Armenia; BRA, Brazil; CRI, Costa Rica; DOM, Dominican Republic; ECU, Ecuador; JOR, Jordan; MEX, Mexico; PER, Peru; SLV, El Salvador; TUR, Turkey; URY, Uruguay; VEN, Venezuela; ZAF, South Africa; ZMB, Zimbabwe.

period to filter out subnetwork leaks due to misconfigurations (17). We call these the “routed” subnetworks. This approach, however, does not take into account whether the routed subnetworks actually transmit any data and may thus overestimate the number of active ones. However, because it is based on publicly available data, it has the advantage of being applicable

to other projects and in other contexts. In our analysis, we used these two methods as alternative measurement approaches for subnational levels of Internet penetration.

Second, we used a geolocation database to find the geographic location of the observed subnetworks (14) (Fig. 1A). This database translates IP addresses into geographic coordinates that best

approximate where on the globe a network is located. We used the MaxMind database, which is one of the most accurate databases with coverage going back as far as 2004 (15).

Third, we aggregated the active subnetworks (observed or routed) to the level of subnational geographic units (see Fig. 1B for an example). For our main analysis, we combined ethnic group

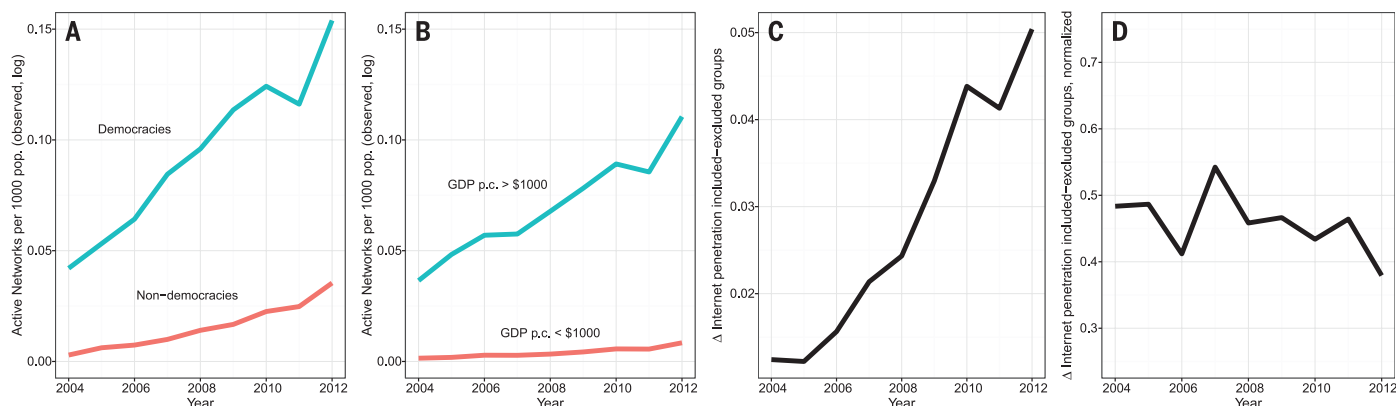


**Fig. 2. Trends in Internet penetration for a global sample of ethnic groups.** (A) Penetration rates in democracies and nondemocracies, the latter defined as having a democracy score of less than 6 according to (25). (B) Penetration rates in developed and less developed countries [gross domestic product (GDP) per capita (p.c.) data from (26)]. In (A) and (B), the log-transformed number of active subnetworks is shown per 1000 capita. (C) Yearly averages of the differences between included and excluded groups across all countries in the sample. (D) Differences between included and excluded groups, normalized by the country's average level of Internet penetration.

**Table 1. Regression results for Internet penetration as the dependent variable.** Coefficients are shown with uncertainties (standard errors) in parentheses. Models 1 to 3 capture the absolute level of Internet penetration; models 4 to 6 capture Internet penetration relative to the country average. Models 1 and 4 include only the main independent variable (exclusion); models 2 and 5 use the group GDP indicator based on the G-Econ data set (17) and the other control variables. Models 3 and 6 use the nighttime lights–based indicator of development rather than the one based on the G-Econ data set. These results are for observed subnetworks; results for routed subnetworks are shown in table S1.  $R^2$ , coefficient of determination.

Dependent variable	Internet penetration, absolute			Internet penetration, relative		
	1	2	3	4	5	6
Excluded	−0.027*** (0.003)	−0.021*** (0.003)	−0.019*** (0.003)	−0.725*** (0.094)	−0.481*** (0.094)	−0.539 (0.090)
Group GDP p.c.		0.025*** (0.005)			0.749*** (0.155)	
Nighttime lights p.c.			0.023*** (0.004)			1.665*** (0.145)
Ruggedness		−0.001*** (0.0001)	−0.0004 (0.0001)		−0.023*** (0.003)	−0.011*** (0.003)
Distance to capital		−0.006 (0.005)	−0.001 (0.004)		−0.942*** (0.133)	−0.703*** (0.130)
Road density		0.110*** (0.033)	0.077** (0.032)		4.068*** (0.833)	3.108 (0.809)
Urbanization		0.525*** (0.026)	0.479*** (0.026)		2.782*** (0.748)	3.285*** (0.695)
Intercept	0.028 (0.054)	0.098* (0.052)	0.001 (0.050)	1.418 (1.628)	5.562*** (1.593)	0.65 (1.542)
Country × year FEs	Yes	Yes	Yes	Yes	Yes	Yes
Observations	4663	4371	4581	2925	2811	2904
$R^2$	0.708	0.764	0.768	0.272	0.36	0.4
Adjusted $R^2$	0.623	0.694	0.698	−0.119	0.017	0.071

\* $P < 0.1$ ; \*\* $P < 0.05$ ; \*\*\* $P < 0.01$ .



settlement regions from the GeoEPR data set (16) with the location of the subnetworks from the previous step. Using a simple GIS (geographic information system) overlay operation, we calculated the number of (observed or routed) subnetworks per group and year.

In a validation study, we confirmed that our indicator is able to capture subnational variation in Internet penetration. We aggregated the active subnetworks to the level of administrative units (provinces or districts) for which the level of Internet penetration is known (details are provided in section 1 of the supplementary materials). This analysis reveals generally high correlations (Fig. 1C). Results in sections 1.2 to 1.15 of the supplementary materials show that the log-transformed number of observed subnetworks per population of 1000 achieves the best results, which is why we used this transformation for our main analysis (we provide additional results calculated using routed subnetworks as a robustness test in sections 3 to 6 of the supplementary materials). Because these tests were successful, we can assume that our method also works for ethnic group settlement regions, which in many cases are much larger than the administrative units in our validation analysis.

Our data illustrate that Internet penetration has increased for ethnic groups worldwide over time, but at higher rates in more democratic countries (Fig. 2A) and more developed ones (Fig. 2B). The “digital gap” between included and excluded groups within the same country widened over time in absolute terms (Fig. 2C). However, this increase was driven by the general increase in connectivity: The normalized difference between included and excluded groups (computed as the absolute difference as a proportion of the country’s average level of Internet penetration) actually decreased slightly (Fig. 2D). This suggests that excluded groups are catching up, if only slowly.

To determine the effect of political exclusion on Internet penetration at the level of groups, we used a regression analysis with the (log-transformed) number per 1000 capita of active subnetworks per group to measure the absolute level of Internet penetration. In addition, we computed a relative indicator of Internet penetration that captures the Internet coverage of a group in relation to the other groups in a country (see section 2.1 of the supplementary materials for details). We ran our models with a separate intercept (fixed effect) for each country-year to net out differences between countries that are due to different economic or political conditions or to country-specific temporal trends in Internet adoption. To exclude the possibility that a group’s level of Internet penetration was simply a result of its level of development, geographic location, or settlement pattern (urban versus rural), we included a number of GIS-derived control variables. Most importantly, we controlled for a group’s level of development by using either the disaggregated G-Econ data set (17) or the group’s nighttime light emissions (18). These emissions have recently been proposed as an indicator

of economic performance (18, 19) and have been shown to strongly predict wealth at the local level (20). We also controlled for whether the group is located in a remote and inaccessible area by including an indicator of terrain ruggedness as well as the group’s distance from their country’s capital. Similarly, we included a control variable for the group’s level of urbanization (details are given in sections 2.2 to 2.7 of the supplementary materials).

The regression results in Table 1 demonstrate that excluded groups’ political status leads to significantly lower Internet penetration rates compared with included groups in the same country. This result is not driven by the groups’ level of development, their geographic location and quality of infrastructure, or their urban-versus-rural settlement pattern. The coefficients indicate that on average, excluded groups have between 0.019 and 0.021 subnetworks fewer per 1000 capita than politically included groups in the same country (models 2 and 3). To put this result into context, models 5 and 6 indicate that exclusion leads to a reduction in relative Internet penetration by a factor of about 0.6 ( $e^{-0.481}$  and  $e^{-0.539}$ , respectively). This means that, all other factors being equal, an included group with an average level of Internet penetration for its country would receive only ~60% of that level if it were an excluded group. In additional analyses, we confirmed that this result is driven not only by lower penetration rates associated with exclusion (when comparing only groups that have some level of penetration) but also by excluded groups’ higher probability of having no Internet coverage at all (tables S2 and S3). Table S4 shows that, using the approach of (21), the inclusion of our control variables appears to be sufficient to remove bias from unobserved confounding variables. To study variation in the effect of exclusion across countries, we also used multilevel regression models (supplementary materials, section 6). These models fail to provide evidence that democracy alleviates the negative effect of exclusion on Internet coverage. Rather, they suggest that if democracies exclude groups politically, their level of digital discrimination is comparable to that of nondemocracies. Overall, however, because democratic countries have much lower percentages of excluded populations [on average 6%, compared with 21% in nondemocracies, according to the EPR data (7)], digital discrimination is a much more severe issue in nondemocratic countries.

What are the effects of reduced Internet coverage on excluded groups? Resource mobilization theories explain the emergence of social movements by their capability to mobilize a sufficient number of supporters (22), and the Internet should be a crucial technology to this end (23). If, however, politically excluded groups suffer from reduced levels of Internet access, as we have shown above, a group’s level of Internet penetration should be less important in determining whether it is able to mobilize collectively. We conducted additional regression analyses on the set of excluded groups to test whether a group’s level of Internet penetration helps to predict whether it engages in

collective violence against the government (supplementary materials, section 7). We found little evidence that it does. Overall, the effect of Internet penetration on the probability of collective mobilization was insignificant. When estimating the effect across different levels of development among ethnic groups (as measured by per capita light emissions), a positive and significant effect emerged for poor groups only, suggesting that the Internet can increase collective mobilization capacity if few other resources are available.

In sum, the politically motivated digital discrimination against ethnically marginalized groups that we identify in this analysis constitutes a challenge to proponents of liberation technology. In many countries, access to modern ICT, and in particular to the Internet, is determined by national governments. As we have shown, this can lead to selective provision of digital communication, with governments extending these services primarily to politically favored groups. Although the Internet clearly has the potential to foster collective organization and political change, governments can prevent this effect through their key role in the allocation and control of digital communication. This may be one explanation for the finding that Internet penetration is a weak predictor of collective mobilization at the level of ethnic groups.

This insight has important consequences for research and policy. First, students of the political effects of ICT will have to rethink if and under what circumstances the Internet can catalyze collective mobilization and political change. This scholarship needs to pay closer attention to the role of governments and the extent to which they can prevent these effects. Second, development policies aiming to promote peace and democratization through the Internet need to take into account the uneven provision of digital services within countries. Only if this digital inequality is alleviated can we expect these modern channels to empower people and societies in order to foster lasting political and economic development. Third, it is a frequent assumption that the uneven global distribution of digital technology can be mitigated by economic forces and incentives; for example, the recent *World Development Report 2016* suggests that more competition and better regulation of the ICT sector are necessary (24). Again, however, this suggestion needs to carefully consider the role of local political actors in shaping this process. If the allocation of digital services has become a means to reward loyalists and fend off challengers, improved connectivity for everyone may not be in the interest of governments.

## REFERENCES AND NOTES

1. L. Diamond, *J. Democracy* **21**, 69–83 (2010).
2. M. M. Hussain, P. N. Howard, *Int. Stud. Rev.* **15**, 48–66 (2013).
3. W. T. Kilenthong, P. Odton, *Telecomm. Policy* **38**, 1146–1159 (2014).
4. S. Mendonça, N. Crespo, N. Simões, *Telecomm. Policy* **39**, 192 (2015).
5. H. V. Milner, *Comp. Polit. Stud.* **39**, 176–199 (2006).
6. T. C. Boas, *How Revolutionary Was the Digital Revolution? National Responses, Market Transitions, and Global Technology*.

T1

- J. Zysman, A. Newman, Eds. (Stanford Univ. Press, 2006), pp. 361–378.
7. L.-E. Cederman, A. Wimmer, B. Min, *World Polit.* **62**, 87–119 (2010).
  8. R. Hodler, P. A. Raschky, Q. J. Econ. **129**, 995–1033 (2014).
  9. International Telecommunications Union, World Telecommunication/ICT Indicators Database (2013); [www.itu.int/en/ITU-D/Statistics/Pages/publications/wtid.aspx](http://www.itu.int/en/ITU-D/Statistics/Pages/publications/wtid.aspx).
  10. Demographic and Health Surveys Program, <http://dhsprogram.com/>.
  11. S. Benitez-Baleato, N. B. Weidmann, P. Gligis, X. Dimitropoulos, E. Glatz, B. Trammell, in *Proceedings of the Passive and Active Measurement Conference*, J. Mirkovic, Y. Liu, Eds. (Springer, 2015), pp. 220–231.
  12. A. Dainotti et al., *Comput. Commun. Rev.* **44**, 99–100 (2014).
  13. University of Oregon Route Views Project, [www.routeviews.org](http://www.routeviews.org).
  14. MaxMind, GeoIP2 Databases; [www.maxmind.com/en/geoip2-databases](http://www.maxmind.com/en/geoip2-databases).
  15. B. Huffaker, M. Fomenkov, K. Claffy, “Geocompare: A comparison of public and commercial geolocation databases” (CAIDA Tech Report, Center of Applied Internet Data Analysis, 2011); [www.caida.org/publications/papers/2011/geocompare-tr.pdf](http://www.caida.org/publications/papers/2011/geocompare-tr.pdf).
  16. J. Wucherpfennig, N. B. Weidmann, L. Girardin, L.-E. Cederman, A. Wimmer, *Conflict Manage. Peace Sci.* **28**, 423–437 (2011).
  17. W. D. Nordhaus, *Proc. Natl. Acad. Sci. U.S.A.* **103**, 3510–3517 (2006).
  18. J. V. Henderson, A. Storeygard, D. N. Weil, *Am. Econ. Rev.* **101**, 194–199 (2011).
  19. X. Chen, W. D. Nordhaus, *Proc. Natl. Acad. Sci. U.S.A.* **108**, 8589–8594 (2011).
  20. N. B. Weidmann, S. Schutte, *J. Peace Res.* 10.1177/0022343316630359 (2016).
  21. J. G. Altonji, T. E. Elder, C. R. Taber, *J. Polit. Econ.* **113**, 151–184 (2005).
  22. S. Tarrow, *Power in Movement: Social Movements, Collective Action and Politics* (Cambridge Univ. Press, 1994).
  23. J. Earl, K. Kimport, *Digitally Enabled Social Change: Activism in the Internet Age* (MIT Press, 2011).
  24. The World Bank, *World Development Report 2016: Digital Dividends* (The World Bank, 2016); [www.worldbank.org/en/publication/wdr2016](http://www.worldbank.org/en/publication/wdr2016).
  25. M. G. Marshall, T. R. Gurr, K. Jaggers, “Polity IV Project: Political regime characteristics and transitions, 1800–2015” (2015); [www.systemicpeace.org/polity/polity4.htm](http://www.systemicpeace.org/polity/polity4.htm).
  26. The World Bank, *World Development Indicators* (2016); <http://data.worldbank.org/data-catalog/world-development-indicators>.

## ACKNOWLEDGMENTS

We acknowledge financial support from the Alexander von Humboldt Foundation (Sofja Kovalevskaja Award to N.B.W.). We are grateful to M. Baum, M. Becher, L.-E. Cederman, D. Lazer, A. Little, and P. Selb for comments. We do not have any real or apparent conflicts of interest. Data for replication are available at <http://dx.doi.org/10.7910/DVN/Y3VPIG>. There are two restrictions. First, we cannot share the active subnetworks data because these are computed from traffic traces (netflow) captured from an Internet service provider. These traces were made available to us under a strict nondisclosure agreement that prevents further sharing or public release. However, we share the complete list of routed subnetworks (annual observations) because they were derived from a public source. The second restriction concerns the spatial coordinates for each subnetwork. MaxMind does not permit the publication of any information contained in their database, so we share a random sample of 5% of the routed subnetworks with truncated geographic coordinates, but without IP addresses, along with code that executes the spatial aggregation to the group polygons in SQL (structured query language).

## SUPPLEMENTARY MATERIALS

[www.sciencemag.org/content/353/6304/1151/suppl/DC1](http://www.sciencemag.org/content/353/6304/1151/suppl/DC1)  
Materials and Methods  
Supplementary Text  
Figs. S1 to S3  
Tables S1 to S8  
References (27–43)

29 February 2016; accepted 27 July 2016  
10.1126/science.aaf5062

## ANIMAL BEHAVIOR

# Optic flow odometry operates independently of stride integration in carried ants

Sarah E. Pfeffer and Matthias Wittlinger\*

*Cataglyphis* desert ants are impressive navigators. When the foragers roam the desert, they employ path integration. For these ants, distance estimation is one key challenge. Distance information was thought to be provided by optic flow (OF)—that is, image motion experienced during travel—but this idea was abandoned when stride integration was discovered as an odometer mechanism in ants. We show that ants transported by nest mates are capable of measuring travel distance exclusively by the use of OF cues. Furthermore, we demonstrate that the information gained from the optic flowmeter cannot be transferred to the stride integrator. Our results suggest a dual information channel that allows the ants to measure distances by strides and OF cues, although both systems operate independently and in a redundant manner.

The navigational skills of insects have engaged scientists for decades. *Cataglyphis* ants are one of the major model organisms used to study path integration, a navigation feat in which angles steered and distances travelled are combined to provide a direct link to the point of origin, a so-called home vector (1). While celestial cues are the main source for angular or compass information (2), distance information is derived from a pedometer, a stride integrator that accounts for stride number and the respective stride length (3, 4). It is well-known that optic flow (OF) is the means of estimating travel distance in flying hymenopterans, like bees or wasps (5–7). In ants, however, which are phylogenetically closely related, ventral OF has been shown to play only a minor role (8). Ants are walkers after all, so stride integration and OF integration are difficult to tease apart from each other experimentally (8, 9).

Social carrying behavior (10–13) gives us an opportunity to study how distance may be estimated without stride integration in nonwalking ants (Fig. 1). This behavior is common in *Cataglyphis bicolor* ants because of their polydomous nest structure, where the main nest with the single queen is surrounded by satellite nests. Experienced forager ants [here denoted as carrier (C) ants] frequently transport interior workers [here denoted as carried (Cd) ants] between the different nest sites. A C-Cd pair that is separated during transport will usually re-engage in social carrying behavior and continue its travel. However, if the Cd ant (which is inexperienced outside of the nest) stays lost, it can only use the path information acquired during transport to find its way back to the home nest. Cd ants do not locomote actively; therefore, the stride integrator will not receive any input. However, the visual

motion pattern generated during displacement can be exploited to gain information about the distance travelled.

In our first experiment, the OF experiment, we connected two nest entrances of neighboring nests with a walking channel. After a C-Cd pair had covered a distance of 10 m in the channel, we captured it and separated both ants carefully. The transported ant was then released in a distant test channel aligned in parallel, and its search behavior was examined. We recorded the search behavior as consecutive 180° turning points in the test channel (4, 6, 14). A Cd ant that fully exploits OF for odometry should be able to estimate the length of the travelled path and hence walk back to the nest from which it had departed. Our experiments show that Cd ants are able to gauge the distance to the nest (Fig. 2). After an initial search around the release point in the test channel (Fig. 2C), presumably to locate the absent C ant, the Cd ants eventually set out for the home nest and searched back and forth around the anticipated nest position [peak of second search phase at 9.6 m (Fig. 2C); peak of differential search at 9.7 m (Fig. 2D)].

To ensure that it is indeed the experienced OF mechanism that enables the Cd ants to estimate



Fig. 1. Body posture of a carrier-carried pair.

Institute of Neurobiology, Ulm University, 89081 Ulm, Germany.  
\*Corresponding author. Email: [matthias.wittlinger@uni-ulm.de](mailto:matthias.wittlinger@uni-ulm.de)

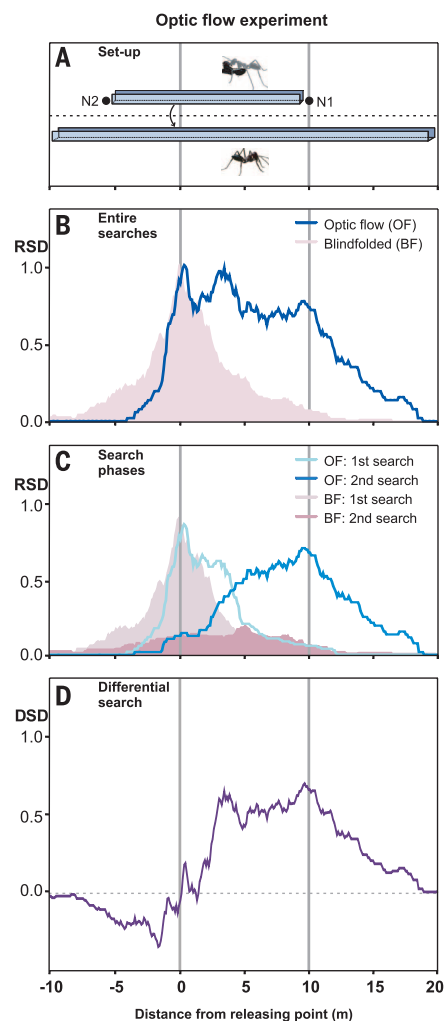


**Fig. 2. Optic flow experiment.** Distance was measured exclusively with OF cues. (A) Experimental procedure. Carrier-carried (C-Cd) pairs travel between two nests (N1 to N2) and were caught and separated at a walking distance of 10 m. The Cd ants were then released in the test channel, and their search behavior was recorded. (B) Relative search density (RSD). The performance of the OF group ( $n = 21$  ants) is depicted in blue and that of the BF group ( $n = 26$ ) is shown in shaded red. The ants of the BF group were prevented from perceiving OF cues during carrying and homing. (C) First and second search phases of the OF and BF groups. For the analysis of the two search phases, see (14). (D) Differential search density (DSD). The purple line indicates BF group data subtracted from that of the OF test group.

distances, we blindfolded the ventral part of the compound eyes of a separate test group. It has already been shown that ventral eye caps do not interfere with proper homing behavior in walking ants and thus ventral blindfolding does not affect correct distance estimation (9). The Cd ants of the blindfolded test group (BF group) did not obtain any distance information in the outbound journey because visual input was eliminated (covered eyes) and the stride integrator was also not effective

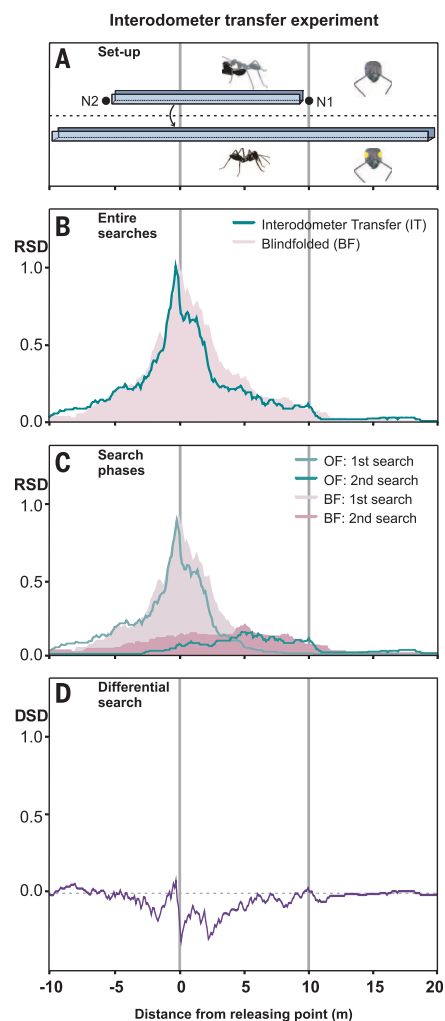


**Fig. 3. Interodometer transfer experiment.** No OF information was transferred to the stride integrator. (A) Experimental procedure. C-Cd pairs travel between two nests (N1 to N2) and were caught and separated at a walking distance of 10 m. The Cd ants were ventrally blindfolded and then released in the test channel, and their search behavior was recorded. (B) Relative search density (RSD). The performance of the IT group ( $n = 25$  ants) is depicted in green and that of the BF group ( $n = 26$ ) is shown in shaded red. The ants of the BF group were prevented from perceiving OF cues during carrying and homing. Thus, their search behavior did not extend beyond the point of release (0 m) (compare with fig. S1). (C) First and second search phases of the IT and BF groups. For the analysis of the two search phases, see (14). (D) Differential search density (DSD). The purple line indicates BF group data subtracted from that of the IT test group.

(carried mode). The blindfolded ants did not head for the home nest; their search was concentrated around the releasing point (Fig. 2). For additional experimental and control groups, see fig. S1.

*Cataglyphis* carry their conspecifics in a stereotyped formicine fashion where both ants are facing each other, with the Cd ant in a “pupal” posture (10) (Fig. 1 and movie S1). As such, the

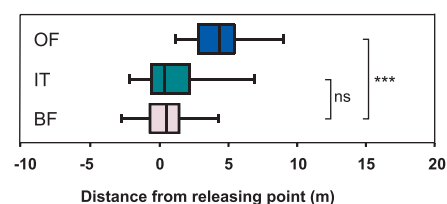


**Fig. 4. Statistical comparison of odometer performance.** Distributions of the search centers (medians of all turning points) of each test group (entire searches) are shown as box-and-whisker plots [OF experiment: median = 4.28 m, interquartile range (IQR) = 2.25 m; IT experiment: median = 0.30 m, IQR = 2.32 m; BF group: median = 0.42 m, IQR = 1.80 m]. The OF and the BF groups differ significantly ( $U$  test;  $***P \leq 0.001$ ). We found no significant (ns) difference between the IT and BF groups ( $U$  test;  $P = 0.742$ ).

orientations of the head and visual field of both ants are similar (12); however, the Cd ant's view is flipped antero-posteriorly, and it experiences reversed image motion (for head angles, see fig. S2). Our data show that the Cd ants cope well with this situation, suggesting the use of the absolute value of the perceived OF amount as odometer information. In two earlier papers, Duelli (11, 12) reports that the celestial compass system keeps the ants on track even though the compass input was reversed during transport and that, at least qualitatively, the ants have some idea about distance. In general, the reversing of celestial compass cues during homing does not seem to be a problem for navigating desert ants (15).

In a second experiment, the interodometer transfer (IT) experiment, we further investigated whether the distance information gained by the optic flowmeter can be used and exploited by the stride integrator. By using the term “interodometer transfer,” we do not necessarily mean that information is directly transferred from one system to another. Rather, information acquired by one system could be read off of some downstream integration stage by another system. At some stage, a transfer of information occurs (16). After 10 m of carrying, where the Cd ant visually perceived the transport, we disengaged the C-Cd pair. The ventral part of the Cd ant's eyes were then occluded, and we tested its ability to gauge the homing distance. Thus, after it was released into the test channel, the walking but blindfolded ant had no chance of running off its vector with the optic flowmeter but instead had to rely on the alternative odometer, the stride integrator, available for the homing task. If the stride integrator could make use of OF distance information, we would expect the Cd ants to exhibit a search peak at the virtual nest position. However, we saw no evidence of such IT (Fig. 3). Rather, the ants in this experiment seemed to be lost, pacing back and forth around the point of release, basically exhibiting just one distinct search phase.

The box-and-whisker plots of Fig. 4 contain the entire search phases of each experiment. Note that in the case of the OF group, as opposed to the IT and BF groups, two distinct search phases exist



(compare Figs. 2 and 3). The first is centered on the point of release and the second on the position of the nest location. Because both contribute to the entire data distribution, the median value lies around roughly half the distance between the releasing point and the nest position. The IT and BF groups do not show such a distinct second search phase; thus, the data are distributed around the point of release.

Our experiments show that the exclusive use of OF cues is sufficient for the ants to measure travel distances. Furthermore, active locomotion is not a prerequisite for distance estimation or path integration, provided that the transport happens in a naturally occurring behavior (17). There is ample evidence that the stride integrator can function without visual input. Ants walking in complete darkness (18), or with the ventral halves of their eyes covered (8, 9), are still able to gauge homing distance correctly. However, our results show that two separate and independent systems of distance measurement exist and operate redundantly.

#### REFERENCES AND NOTES

- M. Müller, R. Wehner, *Proc. Natl. Acad. Sci. U.S.A.* **85**, 5287–5290 (1988).
- R. Wehner, M. V. Srinivasan, in *The Neurobiology of Spatial Behaviour*, K. J. Jeffrey, Ed. (Oxford Univ. Press, 2003), chap. 1, pp. 9–30.
- M. Wittlinger, R. Wehner, H. Wolf, *Science* **312**, 1965–1967 (2006).
- M. Wittlinger, R. Wehner, H. Wolf, *J. Exp. Biol.* **210**, 198–207 (2007).
- H. E. Esch, J. E. Burns, *Naturwissenschaften* **82**, 38–40 (1995).
- M. V. Srinivasan, S. Zhang, M. Altwein, J. Tautz, *Science* **287**, 851–853 (2000).
- A. Ugolini, *Anim. Behav.* **35**, 590–595 (1987).
- B. Ronacher, R. Wehner, *J. Comp. Physiol. A* **177**, 21–27 (1995).
- M. Wittlinger, H. Wolf, *J. Physiol. Paris* **107**, 130–136 (2013).
- M. Möglich, B. Hölldobler, *Psyche* **81**, 219–236 (1974).
- P. Duelli, *Rev. Suisse Zool.* **83**, 413–418 (1976).
- P. Duelli, *Rev. Suisse Zool.* **80**, 712–719 (1973).
- A. Dabhi, J. Retana, A. Lenoir, X. Cerdà, *J. Ethol.* **26**, 119–126 (2008).
- Materials and methods are available as supplementary materials on Science Online.
- S. E. Pfeffer, M. Wittlinger, *J. Exp. Biol.* **219**, 2119–2126 (2016).
- F. Leibold, B. Ronacher, *J. Comp. Physiol. A* **201**, 599–608 (2015).
- T. Seidl, M. Knaden, R. Wehner, *J. Comp. Physiol. A* **192**, 1125–1131 (2006).
- M. Thiélin-Bescond, G. Beugnon, *Naturwissenschaften* **92**, 193–197 (2005).

#### ACKNOWLEDGMENTS

We thank H. Wolf for help during the initial experiments, discussions, and support; K. J. Kaiser and V. L. Wahl for help collecting data in the field; O. Stroh for measuring the head angles, and U. Seifert for editing the text. The University of Ulm provided financial support and infrastructure. M.W. developed the initial idea and concept. M.W. and S.E.P. planned and carried out the experiments, analyzed the data, and wrote the manuscript. Data are available on Dryad (doi:10.5061/dryad.8h3n).

#### SUPPLEMENTARY MATERIALS

www.sciencemag.org/content/353/6304/1155/suppl/DC1  
Materials and Methods  
Supplementary Text  
Figs. S1 and S2  
References (19–21)  
Movie S1

28 April 2016; accepted 17 August 2016  
10.1126/science.aaf9754

#### CELL MIGRATION

# Collective cell durotaxis emerges from long-range intercellular force transmission

Raimon Sunyer,<sup>1</sup> Vito Conte,<sup>1</sup> Jorge Escribano,<sup>2</sup> Alberto Elosegui-Artola,<sup>1</sup> Anna Labernadie,<sup>1</sup> Léo Valon,<sup>1</sup> Daniel Navajas,<sup>1,3,4</sup> José Manuel García-Aznar,<sup>2</sup> José J. Muñoz,<sup>5</sup> Pere Roca-Cusachs,<sup>1,3\*</sup> Xavier Trepát<sup>1,3,6,7\*</sup>

The ability of cells to follow gradients of extracellular matrix stiffness—durotaxis—has been implicated in development, fibrosis, and cancer. Here, we found multicellular clusters that exhibited durotaxis even if isolated constituent cells did not. This emergent mode of directed collective cell migration applied to a variety of epithelial cell types, required the action of myosin motors, and originated from supracellular transmission of contractile physical forces. To explain the observed phenomenology, we developed a generalized clutch model in which local stick-slip dynamics of cell-matrix adhesions was integrated to the tissue level through cell-cell junctions. Collective durotaxis is far more efficient than single-cell durotaxis; it thus emerges as a robust mechanism to direct cell migration during development, wound healing, and collective cancer cell invasion.

The ability of living cells to migrate following environmental gradients underlies a broad range of phenomena in development, homeostasis, and disease (1, 2). The best-understood mode of directed cell migration is chemotaxis, the well-established ability of cells to follow gradients of soluble chemical cues (1). Some cell types are also able to follow gradients in the stiffness of their extracellular matrix (ECM), a process known as durotaxis (3–10). Durotaxis has been implicated in development (11), fibrosis (12), and cancer (13), but its underlying mechanisms remain unclear.

Most of our understanding of directed cell migration has been obtained in single isolated cells. However, fundamental processes during development, wound healing, tissue regeneration, and some forms of cancer cell invasion are driven by directed migration of cell groups (14–16). Cell-cell interactions within these groups provide cooperative mechanisms of cell guidance that are altogether inaccessible to single cells (14–20). Here, we investigated whether cell groups undergo collective durotaxis and the cooperative nature of underlying mechanisms.

Using stencils of magnetic polydimethylsiloxane (PDMS), we micropatterned rectangular clusters (500  $\mu\text{m}$  in width) of human mammary epithelial cells (MCF-10A) on fibronectin-coated polyacrylamide gel substrates exhibiting either uniform stiffness or a stiffness gradient ( $56.6 \pm 2.1$  kPa/mm) (fig. S1) (21, 22). Upon removal of the PDMS stencil, clusters migrating on uniform gels displayed symmetric expansion (Fig. 1, A, C, E, and G; fig. S2A; and movie S1), whereas clusters migrating on stiffness gradients displayed a pronounced asymmetry characterized by faster, more persistent expansion toward the stiff edge (Fig. 1, B, D, F, and H; fig. S2, B to F; and movie S1). This

result was also observed in clusters of Madin-Darby canine kidney epithelial cells (MDCK) and three-dimensional spheroids of human epidermoid carcinoma cells (A431) (fig. S3).

Asymmetric expansion is not attributable to cell proliferation, because it was unaffected by inhibition of cell division and because the number of divisions in the cluster was independent of substrate stiffness (fig. S4). Importantly, it is not attributable to additive contribution of single-cell durotaxis either, because single MCF-10A cells did not durotax in isolation (Fig. 2, A to C and E, and movie S2). Taken together, these data establish an unanticipated mode of collective durotaxis driven by an emergent property of the cell cluster.

Even if single MCF-10A cells did not durotax in isolation, they exhibited faster randomly oriented velocity on stiffer gels (Fig. 2D) (13). In a close-packed system, this feature could explain collective durotaxis because volume exclusion would force cells to move persistently away from the cluster at a higher speed on the stiffer edge. To test the contribution of this mechanism, we perturbed cell-cell junctions independently of close packing by knocking down  $\alpha$ -catenin using small interfering RNA (siRNA). Like control cells,

<sup>1</sup>Institute for Bioengineering of Catalonia, 08028 Barcelona, Spain. <sup>2</sup>Aragon Institute of Engineering Research (I3A), University of Zaragoza, 50018 Zaragoza, Spain. <sup>3</sup>University of Barcelona, 08028 Barcelona, Spain. <sup>4</sup>Centro de Investigación Biomédica en Red en Enfermedades Respiratorias, 28029 Madrid, Spain. <sup>5</sup>Laboratory of Numerical Analysis (LaCaN), Polytechnic University of Catalonia (UPC-BarcelonaTech), 08036 Barcelona, Spain. <sup>6</sup>Institució Catalana de Recerca i Estudis Avançats (ICREA), Barcelona, Spain. <sup>7</sup>Centro de Investigación Biomédica en Red en Bioingeniería, Biomateriales y Nanomedicina, 28029 Madrid, Spain.  
\*Corresponding author. Email: roca-cusachs@ub.edu (P.R.-C.); xtrepát@ibecbarcelona.eu (X.T.)

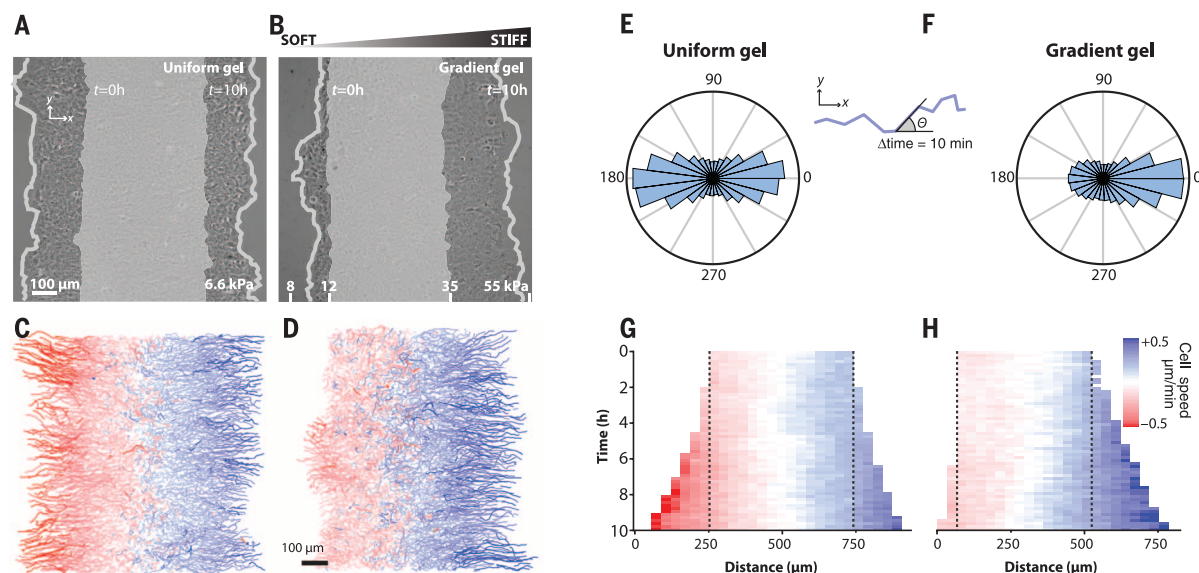
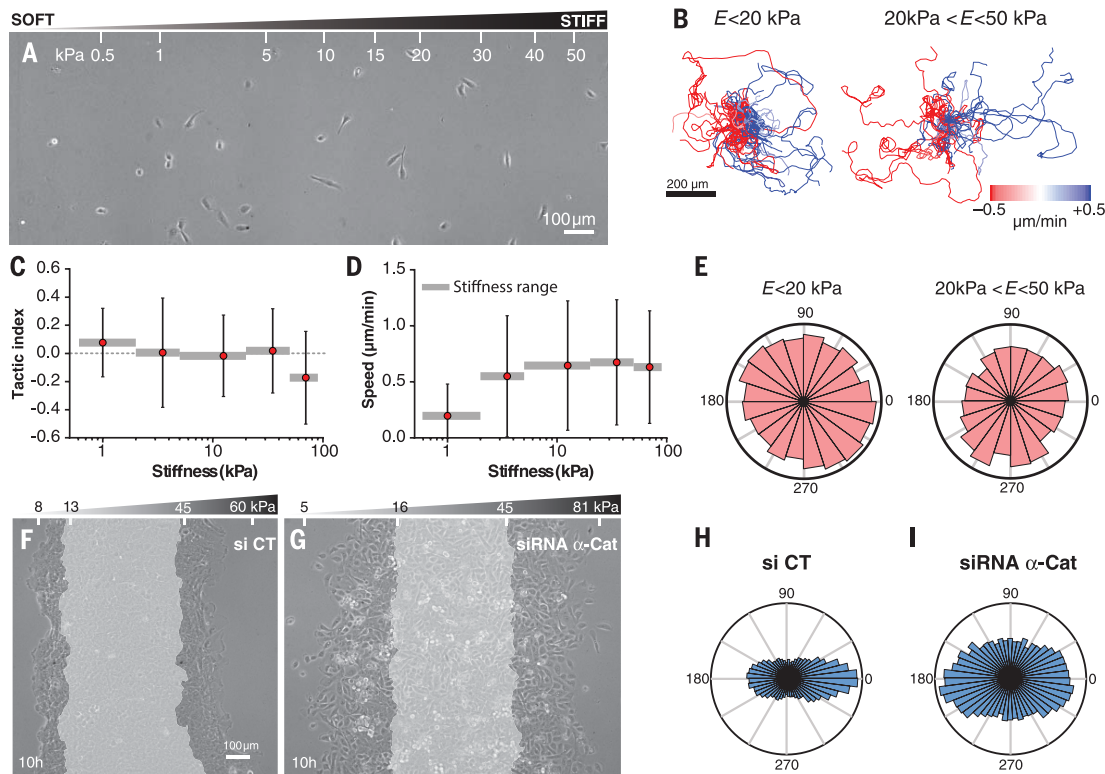


**Fig. 1. Cell clusters display durotaxis.** (A) A representative cell cluster expanding on a soft uniform gel of 6.6 kPa. The gray transparent area indicates initial cluster position ( $t = 0$  hours), and the phase-contrast image shows the cluster at 10 hours. Gray lines indicate cluster edges at 10 hours. (B) Example of a cell cluster expanding on a gradient gel. Gel stiffness increases toward the right of the panel. Numbers at the bottom indicate Young's modulus values measured with atomic force microscopy (AFM). (C and D) Individual cell trajectories corresponding to the experiments displayed in (A) and (B),

respectively. Color coding indicates mean cell speed for every track. (E and F) Distribution of the angle  $\theta$  between the instantaneous velocity vector and the  $x$  axis (see inset) for the experiments displayed in (A) and (B), respectively. (G and H)  $x$ - $t$  Kymographs of cell speed corresponding to the experiments displayed in (A) and (B), respectively. Dashed lines indicate initial cluster position. Kymographs were computed by averaging the speed of individual trajectories in the  $x$  direction over the  $y$  coordinate for every time point (methods).

## Fig. 2. Collective durotaxis is an emergent phenomenon.

(A) Phase-contrast image of MCF-10A cells seeded at low density on a gradient gel. Gel stiffness increases toward the right of the image. Numbers at the top of the panel indicate Young's modulus values measured with AFM. (B) Trajectories of individual cells located in different regions of the gradient gel. For the two regions of the gel, trajectories are plotted with the same origin. Color coding indicates mean cell speed. (C and D) Mean tactic index (C) and mean speed (D) of single cells located in different regions of the gradient gel (see Methods). Horizontal gray bars indicate the stiffness range of each bin. Error bars are SD of  $n = 24$  to 63 cells. (E) Angular distributions of cell trajectories in different regions of the gradient gels. (F and G) Example of a control cluster (F) and a cluster depleted of  $\alpha$ -catenin (G) expanding on a gradient gel. Gray area indicates initial cluster position ( $t = 0$  hours), and phase-contrast image shows the cluster at 10 hours. Western blot analysis showed that  $\alpha$ -catenin levels on the day of the experiment were  $57 \pm 13\%$  of those observed in control cells. (H and I) Angular distributions of cell trajectories for experiments shown in (F) and (G), respectively.





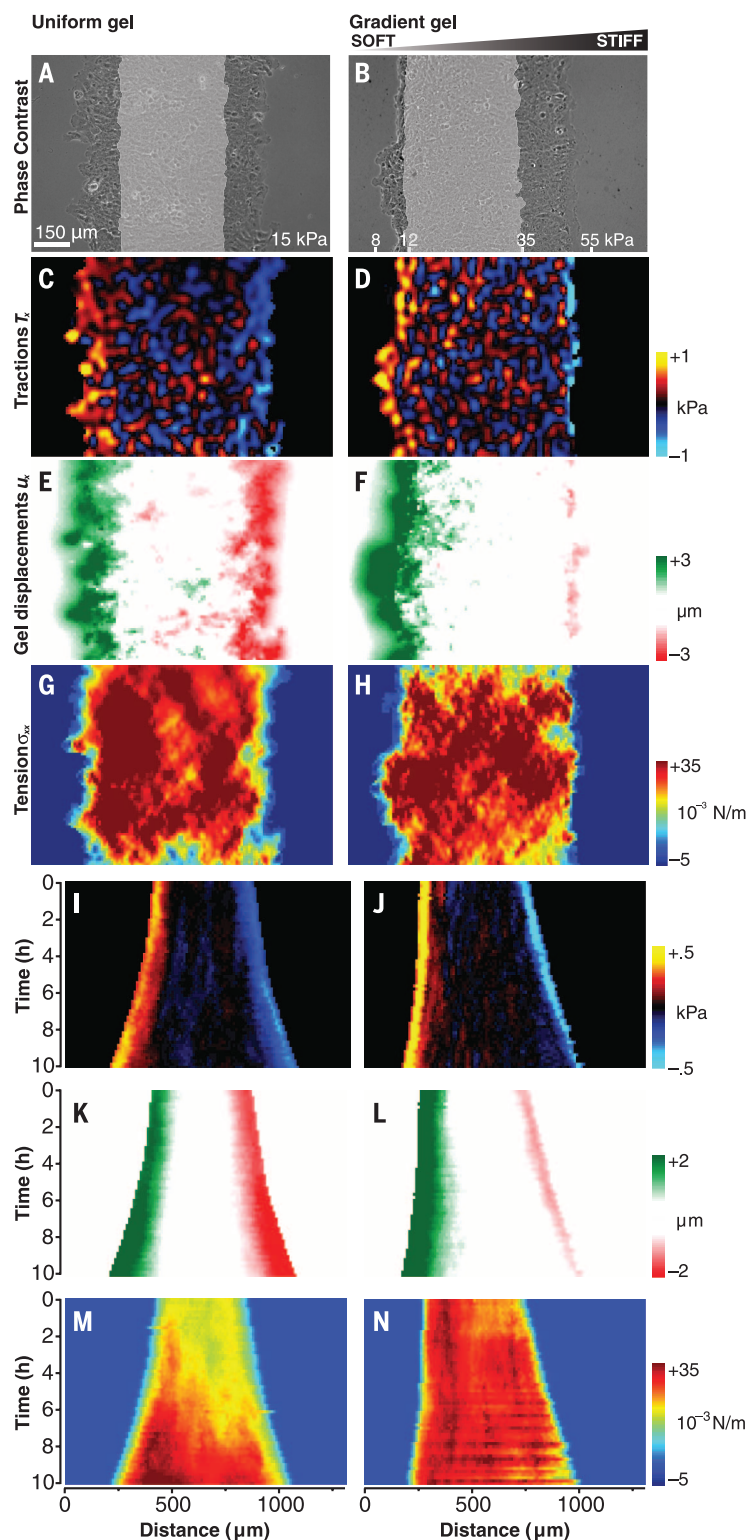


**Fig. 3. Traction force microscopy on gradient gels shows long-range intercellular force transmission within the clusters.** (A and B) Phase-contrast images of clusters migrating on a uniform gel (A) and on a gradient gel (B). (C and D) Maps of the traction component  $T_x$ . (E and F) Maps of the substrate displacement component  $u_x$ . (G and H) Maps of the intercellular tension component  $\sigma_{xx}$  for the clusters depicted in (A) and (B). (I and J) Kymographs of the traction component  $T_x$  for a uniform gel (I) and for a gradient gel (J). (K and L) Kymographs of the substrate displacement component  $u_x$ . (M and N) Kymographs of intercellular tension component  $\sigma_{xx}$ . See fig. S14 for all other components of tractions, intercellular stress tensor, and substrate displacements.

isolated cells depleted of  $\alpha$ -catenin migrated faster on stiffer regions but did not durotax (fig. S5, A to D, and movie S3). Unlike control clusters, however, close-packed clusters depleted of  $\alpha$ -catenin expanded nearly symmetrically (Fig. 2, F to I; fig. S5, E to M; and movie S4), thereby indicating that cell-cell adhesions are required for collective cell durotaxis. These findings rule out mechanisms solely based on local stiffness sensing and point to a long-range mechanism involving cell-cell adhesion.

We next studied whether this long-range mechanism involves transmission of physical forces across the cluster. To this end, we implemented a generalized traction force microscopy algorithm to map forces exerted by cells on substrates with arbitrary stiffness profiles (supplementary text 1). Clusters migrating on uniform gels (Fig. 3, A and C, and movie S5) and on gradient gels (Fig. 3, B and D, and movie S6) exhibited similar traction force maps. The highest tractions were localized at the edges and pointed toward the midline of the cluster, whereas relatively lower tractions in the bulk showed no particular orientation. To average out fluctuations and retain systematic traction patterns, we computed  $x$ - $t$  kymographs of traction component  $T_x$  (Fig. 3, I to J). Kymographs on uniform and gradient gels revealed two traction layers of similar magnitude and opposite sign at both edges of the clusters and negligible average tractions in the bulk. Interestingly, soft edges had cell-substrate forces similar to those of stiff edges but smaller and denser cell-matrix adhesions, consistent with previous findings that force levels are not necessarily linked to a specific adhesion size (fig. S6, A and B) (23). Unlike traction forces, substrate displacements on gradient gels were nearly one order of magnitude higher on the soft edge than on the stiff one (Fig. 3, E, F, K, and L, and movies S5 and S6).

To compute force transmission within the monolayer, we used monolayer stress microscopy and focused on the normal component of the stress tensor in the direction of expansion  $\sigma_{xx}$  (24, 25), which we hereafter refer to as intercellular tension (Fig. 3, G and H, and movies S5 and S6). Kymographs showed that intercellular tension increased up to a plateau within the first few cells at the monolayer edges and remained roughly constant in the monolayer bulk thereafter (Fig. 3, M and N).

Our force measurements establish that the monolayer expands by generating contractile traction forces of equal magnitude at both edges and that these forces are transmitted across the cluster. To explore how this physical scenario might lead to collective durotaxis, we developed a model that integrates clutchlike cell-ECM dynamics at focal adhesions (23, 26–28), long-range force transmission through cell-cell junctions, and actin polymerization at monolayer edges (Fig. 4, A and B, and supplementary text 2). For a monolayer attached to a substrate of uniform stiffness, the model predicts symmetric expansion; actin polymerization exceeds acto-myosin contraction to the same extent on both edges.



By contrast, on stiffness gradients, the substrate deforms and opposes polymerization more on the soft edge, tilting monolayer expansion toward the stiff one (Fig. 4B).

We next used the model to produce testable predictions. First, the model predicts that durotaxis should decrease upon reducing the difference in substrate deformation between the soft and stiff side (Fig. 4C). We confirmed this prediction by reducing the slope of the stiffness gradient (Fig. 4D), seeding clusters on progressively stiffer regions of the gradient gels (Fig. 4D), reducing cluster size (fig. S7), inhibiting myosin contractility with blebbistatin (Fig. 4, E to H; fig. S8; and movie S7), and reducing cell adhesion by decreasing fibronectin coating (fig. S9). Notably, clusters placed on the softest region of the gradient, where the model predicts highest durotaxis, exhibited directed migration toward the stiff edge as a single unit rather than asymmetric expansion (fig. S10 and movie S8). Second, impairing long-range force transmission should abrogate durotaxis. This prediction was confirmed

by knocking down  $\alpha$ -catenin (Fig. 2, F to I; fig. S11; and movie S9) and by laser-ablating clusters in the direction parallel to the midline (Fig. 4, I to L; fig. S12; and movie S10), which drastically reduced both intercellular force transmission and durotaxis. Third, the clutch mechanism implies that actin retrograde flow should be faster on the soft edge and that the differences in the speeds of actin flow and monolayer expansion between edges should be of the same order. This was indeed the case (fig. S6, C and D). Finally, the model predicts that in response to an extremely steep gradient, even single cells should generate sufficiently large differences in substrate deformation between their leading and trailing edges to enable durotaxis (10). As predicted, single MCF-10A cells exhibited weak but significant durotaxis in response to a step gradient ( $433.6 \pm 43.6$  kPa/mm) (fig. S13). Given the close agreement between model predictions and experiments, we conclude that local stiffness sensing at the cluster edges and long-range force transmission through intercellular junctions are sufficient

to explain the phenomenology of collective cell durotaxis.

Recent experimental and theoretical research has emphasized that some collective systems are more effective at responding to environmental gradients than their isolated constituents (19, 20, 29). This emergent phenomenon, often alluded to as “collective intelligence,” has been observed in cell clusters during chemotaxis (19, 20), fish schools during phototaxis (29), and human groups during online gaming (30). In the context of these phenomena, collective durotaxis is unique in that the very same machinery that senses the attractant—i.e., the actomyosin cytoskeleton—is responsible for propulsion toward it. As such, collective durotaxis might be the most rudimentary, and perhaps most primitive, mechanism by which a collective living system responds to a gradient. Rudimentary or not, collective durotaxis is robust, is general, and dramatically boosts single-cell responses, providing a new mechanism to organize directed cell migration during development, wound healing, and collective cancer cell invasion.

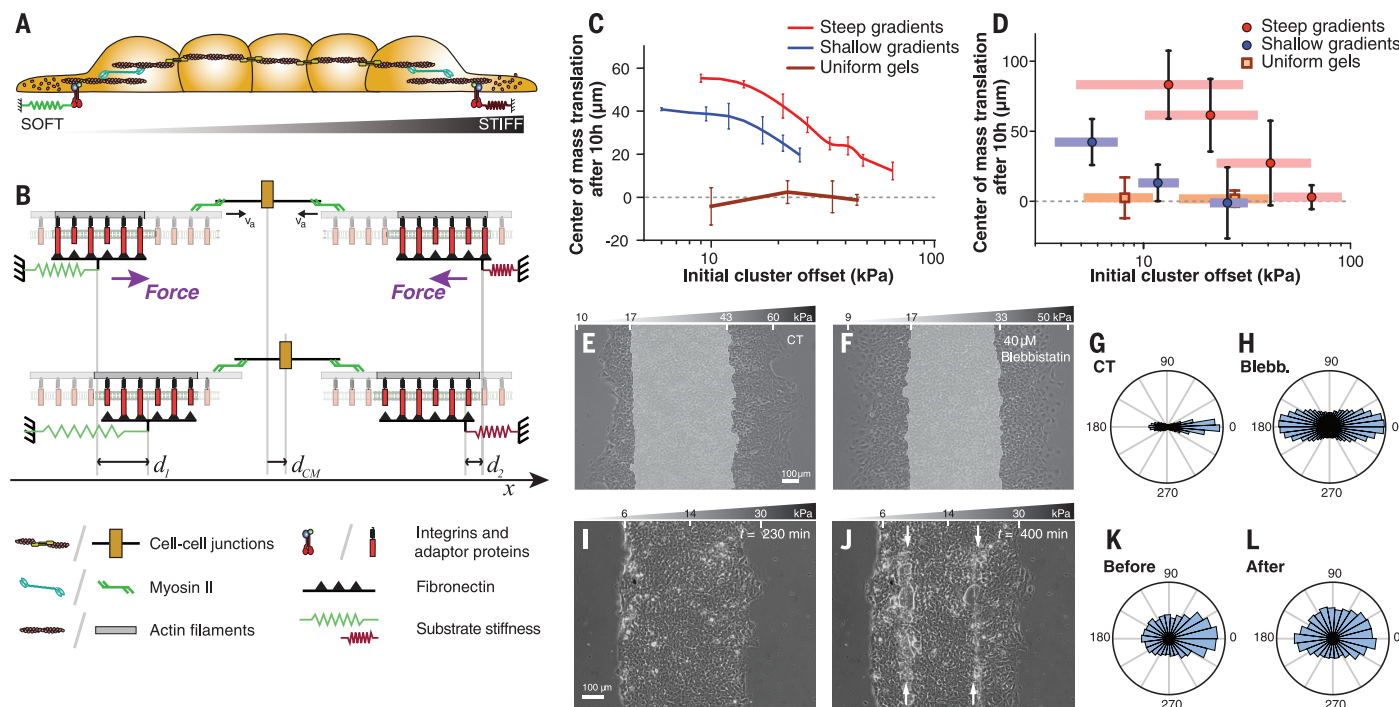


**Fig. 4. A generalized clutch model predicts collective durotaxis.** (A) The expanding cell monolayer is modeled as a one-dimensional contractile continuum that exerts forces on its underlying deformable substrate through discrete focal adhesions and viscous friction. (B) (Top) Each focal adhesion is modeled as a clutch. Actomyosin-driven contraction of the monolayer causes substrate deformation and actin retrograde flow according to the binding/unbinding dynamics of focal adhesion proteins under force. Substrate deformation is represented as a deformed discrete spring for simplicity, but the model is continuum (see supplementary text 2). (Bottom) To maintain force balance across the monolayer after each myosin-driven contraction step, the substrate is pulled by a larger amount on the soft side ( $d_1$ ) than on the stiff side ( $d_2$ ), thereby tilting overall expansion toward the stiff side ( $d_{CM} = d_1 - d_2$ ). (C) Model predictions. Durotaxis (quantified by the cluster center of mass translation after 10 hours) represented as a function of the initial stiffness of the center of the

cluster (i.e., stiffness offset). Error bars are SD of  $n = 5$  simulations. (D) Experimental data. Durotaxis [quantified as in (C)] represented as a function of the initial stiffness of the center of the cluster. For steep (red, 57 kPa/mm) and shallow (blue, 14 kPa/mm) gradients, horizontal bars indicate the mean values of the soft and the stiff edge at  $t = 0$  hours. For uniform stiffness gels (orange), horizontal bars represent the stiffness SD of the gels in the group. Error bars are SD of  $n = 3$  to 9 clusters. (E and F) Example of a control cluster (E) and a blebbistatin-treated cluster (F) expanding on a gradient gel. (G and H) Angle distribution of cell trajectories for control experiments (G) and blebbistatin (H). (I and J) An expanding cluster on a gradient gel before (I) and after (J) being severed by two laser cuts parallel to the midline applied at  $t \sim 260$  min (white arrows). (K and L) Angular distributions of cell trajectories before (K) (140 to 230 min) and after (L) (400 to 490 min) laser ablation. See also fig. S12 and movie S10.

## REFERENCES AND NOTES

1. R. Majumdar, M. Sixt, C. A. Parent, *Curr. Opin. Cell Biol.* **30**, 33–40 (2014).
2. P. Roca-Cusachs, R. Sunyer, X. Trepat, *Curr. Opin. Cell Biol.* **25**, 543–549 (2013).
3. C.-M. Lo, H.-B. Wang, M. Dembo, Y. L. Wang, *Biophys. J.* **79**, 144–152 (2000).
4. B. C. Isenberg, P. A. Dimilla, M. Walker, S. Kim, J. Y. Wong, *Biophys. J.* **97**, 1313–1322 (2009).
5. M. Raab et al., *J. Cell Biol.* **199**, 669–683 (2012).
6. S. V. Plotnikov, A. M. Pasapera, B. Sabass, C. M. Waterman, *Cell* **151**, 1513–1527 (2012).
7. T. Kawano, S. Kidoaki, *Biomaterials* **32**, 2725–2733 (2011).
8. J. R. Tse, A. J. Engler, *PLOS ONE* **6**, e15978 (2011).
9. L. G. Vincent, Y. S. Choi, B. Alonso-Latorre, J. C. del Álamo, A. J. Engler, *Biotechnol. J.* **8**, 472–484 (2013).
10. L. Bollmann et al., *Front. Cell. Neurosci.* **9**, 363 (2015).
11. L. A. Flanagan, Y.-E. Ju, B. Marg, M. Osterfield, P. A. Janmey, *Neuroreport* **13**, 2411–2415 (2002).
12. F. Liu et al., *J. Cell Biol.* **190**, 693–706 (2010).
13. T. A. Ulrich, E. M. de Juan Pardo, S. Kumar, *Cancer Res.* **69**, 4167–4174 (2009).
14. D. Cai et al., *Cell* **157**, 1146–1159 (2014).
15. E. Donà et al., *Nature* **503**, 285–289 (2013).
16. A. Haeger, K. Wolf, M. M. Zegers, P. Friedl, *Trends Cell Biol.* **25**, 556–566 (2015).
17. A. Bianco et al., *Nature* **448**, 362–365 (2007).
18. B. A. Camley, J. Zimmermann, H. Levine, W.-J. Rappel, *Phys. Rev. Lett.* **116**, 098101 (2016).
19. G. Malet-Engra et al., *Curr. Biol.* **25**, 242–250 (2015).
20. E. Thevenneau et al., *Dev. Cell* **19**, 39–53 (2010).
21. R. Sunyer, A. J. Jin, R. Nossal, D. L. Sackett, *PLOS ONE* **7**, e46107 (2012).
22. Materials and methods are available as supplementary materials on Science Online.
23. A. Elosegui-Artola et al., *Nat. Mater.* **13**, 631–637 (2014).
24. D. T. Tambe et al., *Nat. Mater.* **10**, 469–475 (2011).
25. E. Bazellieres et al., *Nat. Cell Biol.* **17**, 409–420 (2015).
26. C. E. Chan, D. J. Odde, *Science* **322**, 1687–1691 (2008).
27. A. Elosegui-Artola et al., *Nat. Cell Biol.* **18**, 540–548 (2016).
28. J. Escribano, M. T. Sánchez, J. M. García-Aznar, *Comput. Part. Mech.* **1**, 117–130 (2014).
29. A. Berdahl, C. J. Torney, C. C. Ioannou, J. J. Faria, I. D. Couzin, *Science* **339**, 574–576 (2013).
30. P. M. Krafft, R. X. Hawkins, A. S. Pentland, N. D. Goodman, J. B. Tenenbaum, in *Proceedings of the 37th Conference of the Cognitive Science Society* (Cognitive Science Society, 2015).

## ACKNOWLEDGMENTS

The authors acknowledge X. Serra-Picamal, V. Romaric, R. Alert, J. Cadademunt, and all members of the X.T. and P.R.-C. laboratories for stimulating discussions; N. Castro for technical assistance; and G. Charras, G. Scita, and E. Sahai for providing cells. This work was supported by the Spanish Ministry of Economy and Competitiveness (BFU2015-65074-P to X.T., BFU2011-23111 and BFU2014-52586-REDT to P.R.-C., DPI2015-64221-C2-1-R to J.M.G.-A., DPI2013-43727-R to J.J.M., PI14/00280 to D.N., RYC-2014-15559 to V.C., FPI BES-2013-063684 to J.E., IJCI-2014-19156 to A.E.-A., and IJCI-2014-19843 to A.L.), the Generalitat de Catalunya (2014-SGR-927), the European Research Council (CoG-616480 to X.T. and StG 306571 to J.M.G.-A.), Obra Social “La Caixa,” Marie-Curie Action (CAFFORCE 328664 to A.L.), EMBO Long-Term Fellowship (EMBO ALTF 1235-2012 to A.L.), a Career Integration Grant within the seventh European Community Framework Programme (PCIG10-GA-2011-303848 to P.R.-C.), and Fundació la Marató de TV3 (project 20133330 to P.R.-C.).

## SUPPLEMENTARY MATERIALS

www.sciencemag.org/content/353/6304/1157/suppl/DC1  
Materials and Methods  
Supplementary Text  
Figs. S1 to S16  
Tables S1 and S2  
Movies S1 to S10  
References (31–43)

22 March 2016; accepted 27 July 2016  
10.1126/science.aaf7119

## TUMOR METABOLISM

# Tissue of origin dictates branched-chain amino acid metabolism in mutant *Kras*-driven cancers

Jared R. Mayers,<sup>1,2\*</sup> Margaret E. Torrence,<sup>1,2\*</sup> Laura V. Danai,<sup>1</sup> Thales Papagiannakopoulos,<sup>1†</sup> Shawn M. Davidson,<sup>1,2</sup> Matthew R. Bauer,<sup>1</sup> Allison N. Lau,<sup>1</sup> Brian W. Ji,<sup>3</sup> Purushottam D. Dixit,<sup>3</sup> Aaron M. Hosios,<sup>1,2</sup> Alexander Muir,<sup>1</sup> Christopher R. Chin,<sup>1</sup> Elizaveta Freinkman,<sup>1,2,4,5,6</sup> Tyler Jacks,<sup>1,2,6</sup> Brian M. Wolpin,<sup>7</sup> Dennis Vitkup,<sup>3</sup> Matthew G. Vander Heiden<sup>1,2,5,7‡</sup>

Tumor genetics guides patient selection for many new therapies, and cell culture studies have demonstrated that specific mutations can promote metabolic phenotypes. However, whether tissue context defines cancer dependence on specific metabolic pathways is unknown. *Kras* activation and *Trp53* deletion in the pancreas or the lung result in pancreatic ductal adenocarcinoma (PDAC) or non-small cell lung carcinoma (NSCLC), respectively, but despite the same initiating events, these tumors use branched-chain amino acids (BCAAs) differently. NSCLC tumors incorporate free BCAAs into tissue protein and use BCAAs as a nitrogen source, whereas PDAC tumors have decreased BCAA uptake. These differences are reflected in expression levels of BCAA catabolic enzymes in both mice and humans. Loss of *Bcat1* and *Bcat2*, the enzymes responsible for BCAA use, impairs NSCLC tumor formation, but these enzymes are not required for PDAC tumor formation, arguing that tissue of origin is an important determinant of how cancers satisfy their metabolic requirements.

The development of new cancer therapeutics relies on underlying genetic features to identify sensitive patients (1). Mutations in both *KRAS* and *TP53* are common genetic events found in tumors arising from many tissues, and cancers with these mutations are often difficult to treat (2, 3). These genetic events, as well as others associated with cancer, contribute to the metabolic changes that support biomass accumulation and cancer cell proliferation (4). Oncogenic *RAS* signaling increases glucose and glutamine consumption to support anabolic processes including nucleotide, lipid, and nonessential amino acid biosynthesis and can also drive extracellular protein and lipid scavenging (5). *TP53* mutations increase glucose consumption and glycolytic flux, whereas inactivation of *TP53* renders cancer cells more dependent on serine uptake and metabolism (6).

*KRAS* and *TP53* mutations are found in most human pancreatic tumors (7) and are also common in lung adenocarcinoma (8). What is known of how mutant *KRAS* or disruption of *TP53* affects

cancer metabolism is based on cell culture studies in defined medium, although in vivo nutrient availability varies widely between tissues, and vasculature changes can limit nutrient access within tumors (9, 10). The inability to model these differences in culture has therefore limited understanding of how tissue of origin influences tumor metabolism (11). Furthermore, environment can influence metabolic phenotypes in vitro (12–14), and metabolic dependencies in vivo can differ from those found in vitro (15). Metabolic differences between tumor types may also result from cell-autonomous effects, and tumor metabolic gene expression more closely resembles that of its tissue of origin than that of other tumors (16). The same oncogenic driver can also cause different metabolic phenotypes in lung and liver tumors (17). This raises the possibility that tumor type is a major determinant of some tumor metabolic dependencies in vivo.

Elevated plasma branched-chain amino acid (BCAA) levels are found in early pancreatic ductal adenocarcinoma (PDAC) but not in non-small cell lung carcinoma (NSCLC), even when the tumors are initiated by the same genetic events (18). To confirm that tumor tissue of origin influences whole-body BCAA metabolism, we used *LSL-Kras<sup>G12D/+</sup>;Trp53<sup>fllox/fllox</sup>* (KP) mice. We crossed KP mice to mice harboring a *Cre-recombinase* allele driven by a *Pdx-1* promoter (KP<sup>-/-C</sup> model) (19) or delivered viral *Cre* to the lungs of these mice (20) in order to generate models of PDAC and NSCLC, respectively. Consistent with prior reports (18), mice with early PDAC have increased levels of plasma BCAAs, whereas mice with early NSCLC exhibit decreased plasma BCAA levels (fig. S1, A to D). When cells derived from these tumors

<sup>1</sup>Koch Institute for Integrative Cancer Research, Massachusetts Institute of Technology, Cambridge, MA 02139, USA. <sup>2</sup>Department of Biology, Massachusetts Institute of Technology, Cambridge, MA 02139, USA. <sup>3</sup>Center for Computational Biology and Bioinformatics and Department of Systems Biology, Columbia University, New York, NY 10027, USA. <sup>4</sup>Whitehead Institute for Biomedical Research, Nine Cambridge Center, Cambridge, MA 02142, USA. <sup>5</sup>Broad Institute, Seven Cambridge Center, Cambridge, MA 02142, USA. <sup>6</sup>Howard Hughes Medical Institute, Massachusetts Institute of Technology, Cambridge, MA 02139, USA. <sup>7</sup>Dana-Farber Cancer Institute, Boston, MA 02115, USA.

\*These authors contributed equally to this work.

†Present address: School of Medicine, New York University, New York, NY 10016, USA. ‡Corresponding author. Email: mvh@mit.edu

are implanted subcutaneously into syngeneic hosts, tumors derived from PDAC cells did not affect plasma BCAA levels (fig. S1E) (18), whereas tumors derived from NSCLC cells led to decreased plasma BCAAs (fig. S1F). These results suggest that tumor formation from NSCLC cells can cause depletion of circulating BCAAs.

To trace tissue-specific differences in BCAA metabolism in animals with pancreatic or lung tumors, mice were fed an amino acid–defined diet in which 20% of leucine and valine were  $^{13}\text{C}$ -labeled. All groups of mice exhibited similar levels of plasma  $^{13}\text{C}$ -BCAA enrichment after 1 week of exposure to labeled diets (figs. S2, A and B). Whereas PDAC tumors contained slightly decreased free BCAAs relative to normal pancreas, NSCLC tumors displayed a significant increase in labeled free BCAAs compared with normal lung (Fig. 1A and fig. S2, C and D). These differences are not a reflection of different amino acid compositions of normal or tumor tissue in either the PDAC or NSCLC models (fig. S3). Because BCAAs are essential amino acids that animals cannot synthesize *de novo* (21), these results suggest that unlike PDAC tumors, NSCLC tumors display enhanced BCAA uptake.

BCAAs have several potential metabolic fates in tissues (Fig. 1B). They can be directly incorporated into protein or reversibly transaminated by BCAA transaminase (Bcat) to produce branched-chain  $\alpha$ -ketoacids (BCKAs) and glutamate. BCKAs can regenerate BCAAs, be secreted, or be oxidatively decarboxylated by the branched-chain ketoacid dehydrogenase (Bckdh) complex to allow further oxidation of the carbon skeleton (21). In agreement with increased BCAA uptake in NSCLC tumors, lung tumors displayed increased labeled BCAA incorporation into protein compared with normal lung, whereas PDAC tumors incorporated less labeled BCAAs relative to normal pancreas (Fig. 1C and fig. S2, E and F). Analysis of metabolites derived from BCAA catabolism revealed that NSCLC tumors also had more labeled  $\alpha$ -ketoisocaproate (KIC), the leucine-derived BCKA, whereas no change was observed in levels of this labeled metabolite in PDAC tumors (Fig. 1D and fig. S2G). No other differences in labeled BCAA catabolite levels were observed in NSCLC compared with normal tissues, but PDAC tumors showed decreased labeling of the tricarboxylic acid (TCA) cycle intermediate citrate relative to normal pancreas from labeled BCAAs (Fig. 1E and fig. S2, G to I). This is consistent with recent work demonstrating minimal catabolism of BCAAs to TCA intermediates in proliferating cells (22). We then explored whether excess KIC may be excreted by NSCLC tumors for further metabolism by other tissues, such as liver, which has limited Bcat but high Bckdh activity (21, 23). Consistent with this hypothesis, we observed increased labeling of downstream leucine metabolites in the livers of mice with lung tumors (fig. S4). Taken together, these data suggest that BCAA uptake and transamination, but not their subsequent catabolism, may provide a benefit to NSCLC tumors, potentially by acting as a source of nitrogen.

To examine whether NSCLC tumors, but not PDAC tumors, use BCAAs as a source of nitrogen,

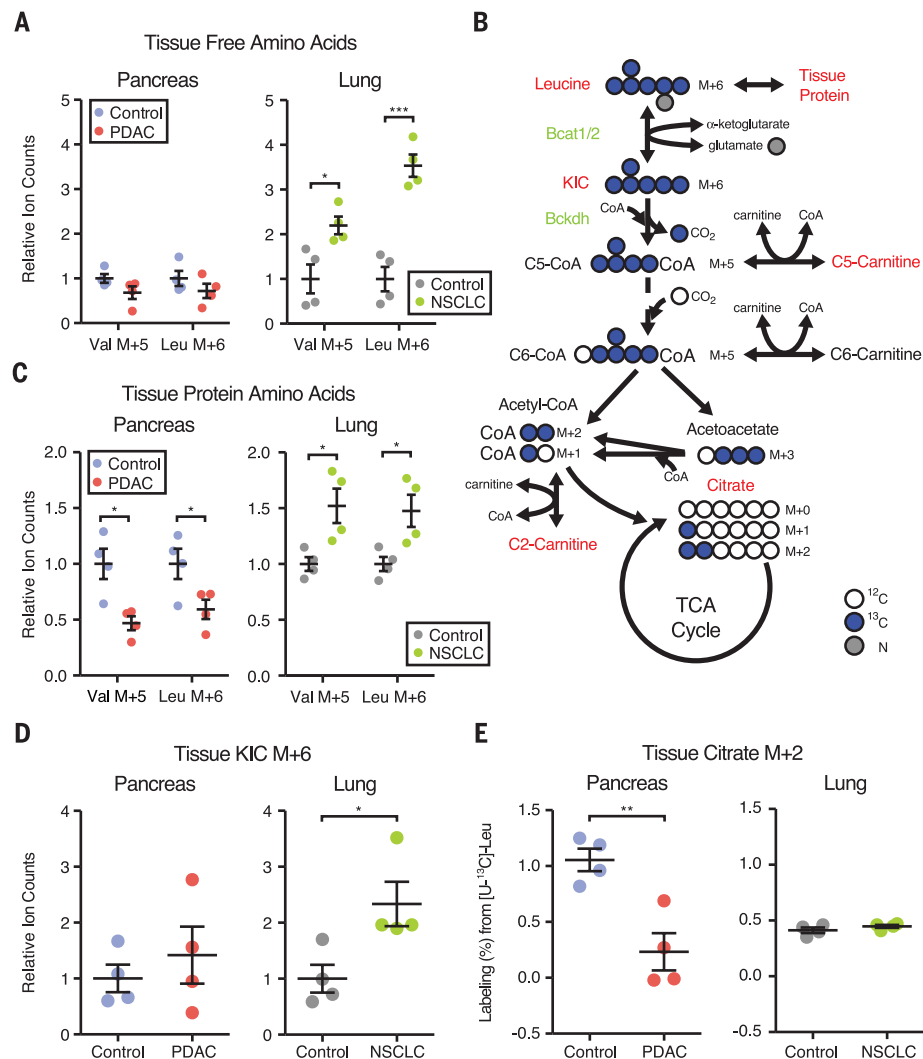


**Fig. 1. Mice with NSCLC display increased BCAA uptake and metabolism.** (A and C to E) Mice were fed  $^{13}\text{C}$ -BCAA-containing diet for 7 days. (A) Relative ion counts by means of liquid chromatography–mass spectrometry (LC–MS) analysis of fully labeled, free BCAAs in tumors from PDAC and NSCLC mice and normal tissues from their respective control mice. Data are presented as mean  $\pm$  SEM;  $n = 4$  control and  $n = 4$  PDAC;  $n = 4$  control and  $n = 4$  NSCLC. (B) Diagram of the leucine catabolic pathway. Red labels indicate metabolites measured with mass spectrometry. Blue circles indicate  $^{13}\text{C}$ -labeled carbons. KIC,  $\alpha$ -ketoisocaproate. (C) Relative ion counts by means of gas chromatography (GC)–MS analysis of fully labeled BCAAs from protein acid hydrolysates of tumors from PDAC and NSCLC mice and normal tissues from their respective control mice. Data are presented as mean  $\pm$  SEM;  $n = 4$  control and  $n = 4$  PDAC;  $n = 4$  control and  $n = 4$  NSCLC. (D) Relative ion counts by means of LC–MS analysis of fully labeled KIC in tumors from PDAC and NSCLC mice and normal tissues from their respective control mice. Data are presented as mean  $\pm$  SEM;  $n = 4$  control and  $n = 4$  PDAC;  $n = 4$  control and  $n = 4$  NSCLC. (E) Citrate M+2 labeling (%) from  $[\text{U}-^{13}\text{C}]$ -leucine by means of GC–MS analysis in tumors from PDAC and NSCLC mice and normal tissues from their respective control mice. Data are presented as mean  $\pm$  SEM;  $n = 4$  control and  $n = 4$  PDAC;  $n = 4$  control and  $n = 4$  NSCLC. Two-tailed  $t$  test was used for all comparisons between two groups. \* $P < 0.05$ , \*\* $P < 0.01$ , \*\*\* $P < 0.001$ .

we fed mice a modified amino acid diet in which 50% of leucine was labeled with  $^{15}\text{N}$ , allowing the fate of leucine-derived nitrogen to be traced (Fig. 2A). In agreement with  $^{13}\text{C}$ -tracing, mice with PDAC demonstrated no differences in free  $^{15}\text{N}$ -labeled leucine in tumors compared with control pancreas (fig. S5A) and had less  $^{15}\text{N}$  incorporation into other amino acids (fig. S5B). In contrast, increased levels of  $^{15}\text{N}$ -leucine were found in

NSCLC tumors compared with normal lung (fig. S5C) with decreased plasma enrichment of  $^{15}\text{N}$ -leucine in mice with NSCLC tumors (Fig. 2B and fig. S5D). A relative increase in  $^{15}\text{N}$ -labeling of nonessential amino acids, as well as valine and isoleucine, was observed in both the free and tissue-protein amino acid pools of NSCLC compared with control lung (Fig. 2C and fig. S5, C and E). Given the reduced plasma enrichment of



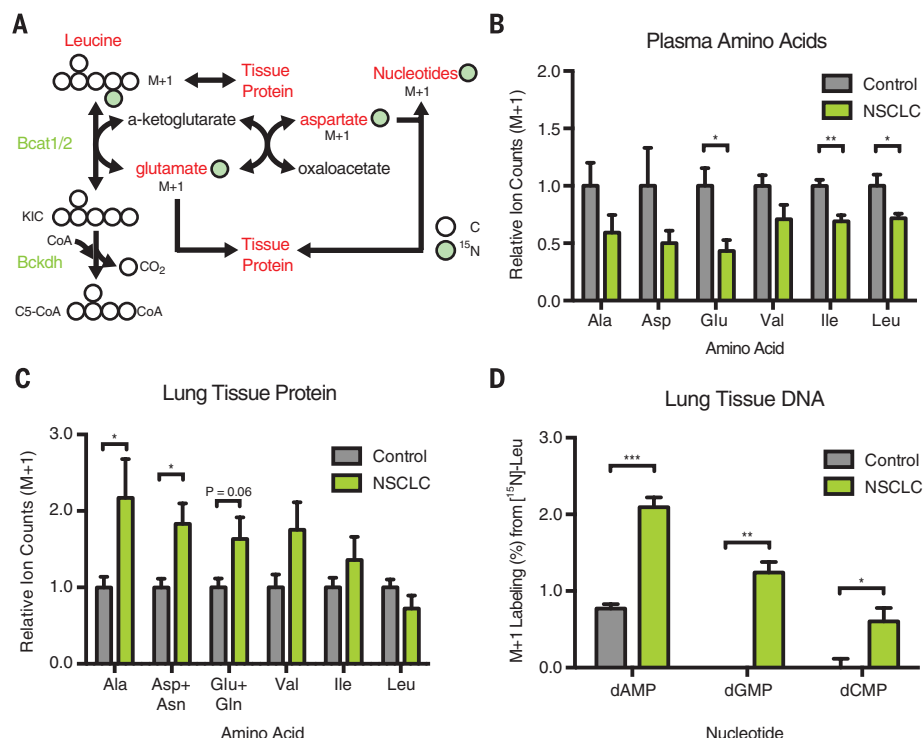


**Fig. 2. BCAA-derived nitrogen supports non-essential amino acid and DNA synthesis in NSCLC tumors.** (A) Diagram of leucine transamination by Bcat and nitrogen (green circles) fate after transamination. (B to D) NSCLC mice were fed <sup>15</sup>N-leucine containing diet for 6 days. (B) Relative ion counts by means of GC-MS analysis of M+1-labeled amino acids in plasma of control and NSCLC mice. Data are presented as mean ± SEM; n = 5 control and n = 6 NSCLC. (C) Relative ion counts by means of GC-MS analysis of M+1-labeled amino acids from protein acid hydrolysates of control mouse lung tissue and NSCLC mouse tumors. Data are presented as mean ± SEM; n = 6 control and n = 6 NSCLC. (D) M+1 labeling (%) from <sup>15</sup>N-leucine of deoxynucleic acids from nucleic acid digest of control mouse lung tissue and NSCLC mouse tumors. Data are presented as mean ± SEM; n = 6 control and n = 6 NSCLC. Two-tailed t test was used for all comparisons between two groups. \*P < 0.05, \*\*P < 0.01, \*\*\*P < 0.001.

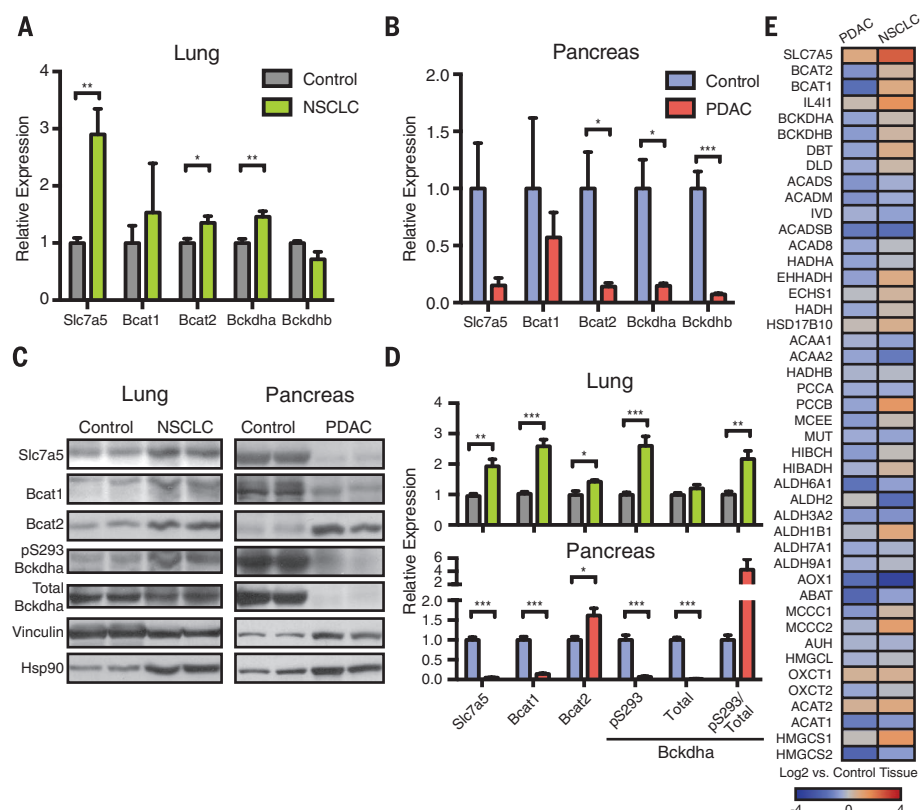


**Fig. 3. Gene expression in both mouse and human tumors reflects tumor tissue-specific BCAA metabolism.** (A) Relative expression of BCAA metabolic pathway genes in normal lung and NSCLC tumors from KP mice. Data are presented as mean ± SEM; n = 6 control and n = 6 NSCLC. (B) Relative expression of BCAA metabolic pathway genes in normal pancreas and PDAC tumors from KP mice. Data are presented as mean ± SEM; n = 7 control and n = 5 PDAC. (C) Immunoblots of proteins involved in BCAA metabolism in representative normal lung and NSCLC tumors (left) and representative normal pancreas and PDAC tumors (right) from KP mice. (D) Quantification of (C). Data are presented as mean ± SEM; n = 6 control and n = 6 NSCLC; n = 4 control and n = 4 PDAC. (E) Comparison of BCAA metabolic pathway gene expression in human NSCLC and PDAC tumors relative to their adjacent paired normal tissues. Overall expression of BCAA metabolism genes is significantly decreased in PDAC (P < 0.0001). Two-tailed t test was used for all comparisons between two groups unless otherwise stated. \*P < 0.05, \*\*P < 0.01, \*\*\*P < 0.001.

<sup>15</sup>N-amino acid species (Fig. 2B and fig. S5D), this <sup>15</sup>N-labeling pattern argues that BCAA-transamination mediated by Bcat isoforms is active in NSCLC tumor tissue. Evidence for increased BCAA transamination in NSCLC compared with PDAC cells

is also evident in vitro across a range of glutamine concentrations; however, tissue culture does not recapitulate the same phenotypes observed in tumors (fig. S6). Downstream of nonessential amino acid biosynthesis, this nitrogen can also

be used to generate nucleotides, primarily if aspartate is synthesized de novo in these tumors. Consistent with this possibility, we found increased incorporation of <sup>15</sup>N-label in both aspartate and nucleotides (Fig. 2, C and D, and fig. S5E). In

some contexts, aspartate production is limiting for nucleotide biosynthesis and proliferation (24, 25), indicating that BCAA metabolism may be important for tumor growth.

To test whether gene expression differences might contribute to differential BCAA metabolism, we used quantitative reverse transcription polymerase chain reaction (RT-PCR) to analyze mRNA levels in NSCLC and PDAC tumors compared with their respective normal tissues. Consistent with increased BCAA uptake and KIC generation in NSCLC tumors, these tumors displayed increased expression of the primary BCAA transporter *Slc7a5* (also called the neutral amino acid transporter *Lat1*) and increased levels of *Bcat2* and *Bckdh* (Fig. 3, A, C, and D). In contrast, PDAC exhibited decreased expression of these genes relative to normal pancreas (Fig. 3, B to D). We also observed increased inhibitory phosphorylation of the Bckdh complex in lung tumors (Fig. 3, C and D). *Bcat* expression enables use of BCAAs as a source of nitrogen by lung tumors, and inhibition of Bckdh prevents further catabolism of these amino acids.

The expression changes observed in PDAC are not specific to this model; the related KPC mouse model (26), which is initiated by a point mutation in *Trp53*, showed similar changes in gene expression (fig. S7A). Furthermore, these decreases in gene expression do not appear to be a consequence of the relative decrease in cancer cellularity of PDAC tumors (7) because sorted pancreatic cancer cells showed similar expression of genes involved in proximal BCAA catabolism relative to whole tumor extracts (fig. S7B). In further agreement with neither lung nor pancreatic cancers showing evidence of downstream BCAA-carbon oxidation, the expression of enzymes from this pathway was not markedly different in either of these cancers (fig. S7, C and D). In contrast, glycolytic gene expression was increased in both tumor types (fig. S7, E and F), which is consistent with known increases in glycolysis in each tumor type (27–29). Last, to relate these data to tissue of origin, we performed principal component and clustering analyses, which demonstrated segregation of each tumor with the normal tissue from which it arose (figs. S7, G and H).

To ascertain whether similar changes in gene expression were also found in human cancers, we examined expression of BCAA catabolic enzymes in NSCLC and PDAC relative to their respective normal tissues in publicly available data sets (30). Consistent with our observations in mice, human NSCLC had increased expression of *SLC7A5*, *BCAT*, and *BCKDH*, whereas expression of BCAA catabolism pathway enzymes was decreased in human PDAC ( $P < 0.0001$  for the pathway) (Fig. 3E and tables S1 and S2). The distinct expression patterns for each tumor type were highly correlated across multiple data sets (fig. S7I and tables S3 to S6). The similarity between human NSCLC and the mouse model of NSCLC was observed despite *KRAS* and *TP53* mutations occurring in <50% of human tumors (8), and similar expression patterns were also seen in squamous cell lung cancer (fig. S7I and table S6),

further supporting the notion that tissue of origin can dictate metabolic phenotype.

The increased contribution of plasma BCAAs to biomass in NSCLC tumors suggests that these tumors may rely on BCAA metabolism for growth. To test this possibility, we used clustered regularly interspaced short palindromic repeats (CRISPR)–

Cas9-mediated genome editing to disrupt exon sequences present in both the *Bcat1* (cytosolic) and the *Bcat2* (mitochondrial) isoforms (fig. S8A) in cancer cell lines derived from KP mice with NSCLC (*Bcat* null clones A and B) or PDAC (*Bcat* null) (fig. S8B). Expression analysis and  $^{15}\text{N}$ -leucine tracing studies confirmed functional deletion of

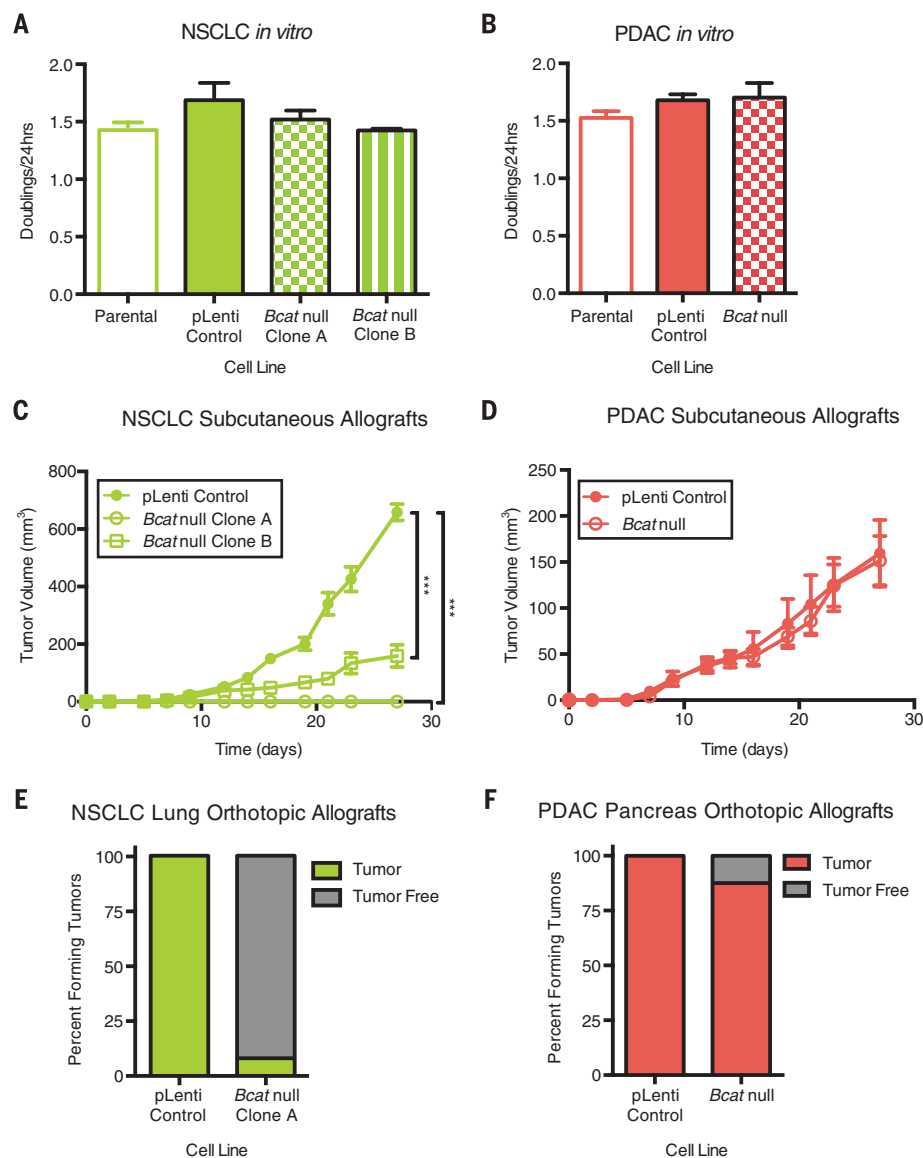


**Fig. 4. Bcat activity is required for NSCLC tumor growth.** (A) Doubling time of parental, control CRISPR-Cas9 vector infected (pLenti), and NSCLC *Bcat* null cell lines in vitro. Data are presented as mean  $\pm$  SEM;  $n = 3$  per group. Representative experiment from  $\geq 2$  repeats. (B) Doubling time of parental, control CRISPR-Cas9 vector infected, and PDAC *Bcat* null cell lines in vitro. Data are presented as mean  $\pm$  SEM;  $n = 3$  per group. Representative experiment from  $\geq 2$  repeats. (C) Estimated tumor volume (cubic millimeters) of subcutaneous allograft of control infected and *Bcat* null syngenic NSCLC cell lines into C57BL/6J mice. Data are presented as mean  $\pm$  SEM;  $n = 6$  per group. Two-way repeated measures analysis of variance (ANOVA) was used for comparison between groups. (D) Estimated tumor volume (cubic millimeters) of subcutaneous allograft of control infected and *Bcat*-null syngenic PDAC cell lines into C57BL/6J mice. Data are presented as mean  $\pm$  SEM;  $n = 5$  pLenti control and  $n = 6$  *Bcat* null. Two-way repeated measures ANOVA was used for comparison between groups. (E) Lung orthotopic allograft of control infected and *Bcat*-null syngenic NSCLC cell lines into C57BL/6J mice;  $n = 23$  vector control and  $n = 13$  *Bcat* null Clone A. (F) Pancreatic orthotopic allograft of control infected and *Bcat* null syngenic PDAC cell lines into C57BL/6J mice.  $n = 8$  mice per group. \* $P < 0.05$ , \*\* $P < 0.01$ , \*\*\* $P < 0.001$ .

*Bcat* in both the NSCLC and PDAC cancer cells (fig. S8, C to F). Despite loss of both *Bcat* isoforms, these cells proliferate at a rate that is similar to the parental and vector control infected cell lines in vitro (Fig. 4, A and B). When *Bcat*-null NSCLC cells were implanted subcutaneously in vivo, however, the ability of these cells to form tumors was impaired, and one clone failed to produce tumors (Fig. 4C and fig. S8G). In contrast, *Bcat*-null PDAC cells implanted subcutaneously generated tumors (Fig. 4D and fig. S8H). Additionally, orthotopic transplantation of NSCLC *Bcat*-null cells failed to form lung tumors (Fig. 4E), whereas PDAC *Bcat*-null cells formed tumors in the pancreas (Fig. 4F). Unlike subcutaneously implanted PDAC cells in which both *Bcat* isoforms were knocked out, these cells formed smaller tumors in the pancreas than did control cells (fig. S8I). Taken together, these data suggest that although KP lung tumors require *Bcat* activity for growth, this enzyme activity is dispensable for KP pancreas tumor formation, although PDAC tumor growth may be aided by *Bcat* activity in some tissue environments.

Proliferating cells need to acquire amino acids, both to make protein and as a source of nitrogen for nucleotide and nonessential amino acid synthesis. Prior work has shown that macropinocytosis plays a role in filling this requirement in mutant *RAS*-driven PDAC tumors and cells (12, 14, 31). The data presented here argue that this process might be less active in mutant *Ras*-transformed NSCLC tumors that acquire nitrogen in part from free BCAAs. Indeed, we observed less macropinocytosis in cells derived from mouse NSCLC relative to mouse PDAC cells (fig. S9). The decreased reliance of PDAC on free BCAAs, however, does not necessarily imply that uptake of these amino acids would be toxic for this cancer. Overexpressing *Slc7a5* in PDAC cells is sufficient to increase leucine uptake (fig. S10, A and B) but has minimal effects on proliferation in vitro (fig. S10C) or tumor growth in vivo (fig. S10, D and E).

A role for free BCAAs in supplying nitrogen to lung cancers is intriguing in light of recent studies in glioblastoma and NSCLC indicating that glutamine, which is the most abundant plasma amino acid and serves as the major free amino acid substrate for nitrogen and carbon in culture (32), contributes less to tumor metabolism in vivo (33, 34). Indeed, glucose-tracing studies in humans and mice demonstrate that glutamine is net syn-

thesized from glucose (15, 33–37), and alternative sources of nitrogen are required to support glutamine production. Thus, in these contexts, extraction of nitrogen from BCAAs for de novo amino acid and nucleotide biosynthesis in vivo may explain how lung tumors satisfy their nitrogen requirements. Consistent with this possibility, *BCAT1* expression is known to be important for glioblastoma growth (38), suggesting that tumors arising in tissues other than the lung may also use BCAAs as a source of nitrogen. Multiple factors—including local environment, tumor cell of origin, and genetic mutations—can lead to convergent metabolic adaptations in disparate tumor types.

Elevations in plasma BCAA levels are associated with early PDAC and result from increased tissue protein breakdown (18). The finding that PDAC tumors have decreased use of circulating BCAAs contributes to this phenotype as well. In contrast, NSCLC tumors actively use BCAAs, leading to plasma BCAA depletions, particularly because the liver does not regulate levels of these amino acids (23). Many patients with PDAC and NSCLC tumors develop cachexia with end-stage disease (39). Our findings suggest that differential use of amino acids by tumors and the resulting impact on whole-body metabolism might play a role in the initiation and natural history of cachexia. In addition, as personalized medicine plays a larger role in the clinical management of cancer, it will be critical to understand how cell of origin and tissue environment interact with genetic events to influence metabolic dependencies of tumors and select the right treatment approaches for patients.

## REFERENCES AND NOTES

1. L. A. Garraway, *J. Clin. Oncol.* **31**, 1806–1814 (2013).
2. N. Vasan, J. L. Boyer, R. S. Herbst, *Clin. Cancer Res.* **20**, 3921–3930 (2014).
3. P. A. Muller, K. H. Vousden, *Cancer Cell* **25**, 304–317 (2014).
4. L. K. Borroughs, R. J. DeBerardinis, *Nat. Cell Biol.* **17**, 351–359 (2015).
5. E. White, *Development* **27**, 2065–2071 (2013).
6. F. Kruiswijk, C. F. Labuschagne, K. H. Vousden, *Nat. Rev. Mol. Cell Biol.* **16**, 393–405 (2015).
7. A. V. Biankin et al., *Nature* **491**, 399–405 (2012).
8. E. A. Collisson et al., *Nature* **511**, 543–550 (2014).
9. P. Vaupel, F. Kallinowski, P. Okunieff, *Cancer Res.* **49**, 6449–6465 (1989).
10. A. Hirayama et al., *Cancer Res.* **69**, 4918–4925 (2009).
11. J. R. Mayers, M. G. Vander Heiden, *Trends Biochem. Sci.* **40**, 130–140 (2015).

12. C. Commisso et al., *Nature* **497**, 633–637 (2013).
13. J. J. Kamphorst et al., *Proc. Natl. Acad. Sci. U.S.A.* **110**, 8882–8887 (2013).
14. W. Palm et al., *Cell* **162**, 259–270 (2015).
15. S. M. Davidson et al., *Cell Metab.* **23**, 517–528 (2016).
16. J. Hu et al., *Nat. Biotechnol.* **31**, 522–529 (2013).
17. M. O. Yuneva et al., *Cell Metab.* **15**, 157–170 (2012).
18. J. R. Mayers et al., *Nat. Med.* **20**, 1193–1198 (2014).
19. N. Bardeesy et al., *Proc. Natl. Acad. Sci. U.S.A.* **103**, 5947–5952 (2006).
20. M. DuPage, A. L. Dooley, T. Jacks, *Nat. Protoc.* **4**, 1064–1072 (2009).
21. A. E. Harper, R. H. Miller, K. P. Block, *Annu. Rev. Nutr.* **4**, 409–454 (1984).
22. C. R. Green et al., *Nat. Chem. Biol.* **12**, 15–21 (2016).
23. J. T. Brosnan, *J. Nutr.* **133** (suppl. 1), 2068S–2072S (2003).
24. K. Birsoy et al., *Cell* **162**, 540–551 (2015).
25. L. B. Sullivan et al., *Cell* **162**, 552–563 (2015).
26. S. R. Hingorani et al., *Cancer Cell* **7**, 469–483 (2005).
27. H. Friess et al., *Gut* **36**, 771–777 (1995).
28. K. Kubota et al., *J. Nucl. Med.* **31**, 1927–1932 (1990).
29. K. B. Nolop et al., *Cancer* **60**, 2682–2689 (1987).
30. T. Barrett et al., *Nucleic Acids Res.* **39** (database), D1005–D1010 (2011).
31. J. J. Kamphorst et al., *Cancer Res.* **75**, 544–553 (2015).
32. R. J. DeBerardinis et al., *Proc. Natl. Acad. Sci. U.S.A.* **104**, 19345–19350 (2007).
33. I. Marin-Valencia et al., *Cell Metab.* **15**, 827–837 (2012).
34. K. Sellers et al., *J. Clin. Invest.* **125**, 687–698 (2015).
35. E. A. Maher et al., *NMR Biomed.* **25**, 1234–1244 (2012).
36. S. Tardito et al., *Nat. Cell Biol.* **17**, 1556–1568 (2015).
37. C. T. Hensley et al., *Cell* **164**, 681–694 (2016).
38. M. Tonjes et al., *Nat. Med.* **19**, 901–908 (2013).
39. W. D. Dewys et al., *Am. J. Med.* **69**, 491–497 (1980).

## ACKNOWLEDGMENTS

J.R.M. acknowledges support from U.S. NIH National Cancer Institute (NCI) grant F30CA183474 and National Institute of General Medical Sciences grant T32GM007753. A.N.L. is a Robert Black Fellow of the Damon Runyon Cancer Research Foundation, DRG-2241-15. M.G.V.H. acknowledges support from NCI grants P30CA1405141, R01CA168653, and R01CA201276; the Burroughs Wellcome Fund; the Eisen and Chang Families; the Ludwig Center at Massachusetts Institute of Technology; Stand Up To Cancer; and the Lustgarten Foundation. M.G.V.H. is a paid scientific adviser for Agios Pharmaceuticals and for Aeglea Biotherapeutics, biotechnology companies that are developing drugs targeting cellular metabolism to treat cancer and other diseases.

## SUPPLEMENTARY MATERIALS

www.sciencemag.org/content/353/6304/1161/suppl/DC1  
Materials and Methods  
Figs. S1 to S10  
Tables S1 to S8  
References (40–49)

21 February 2016; accepted 29 July 2016  
10.1126/science.aaf5171





### Automation-Ready Blowdown Evaporator

The Ultravap Levante is a nitrogen-blowdown evaporator used for removing chromatography solvents such as dichloromethane, acetonitrile, methanol, and hexane. It can be operated from an in-house supply of nitrogen/clean dry air or from a gas cylinder. The Ultravap Levante comes with an RS232 connection and a remote command set, enabling it to connect to and be operated from most commercially available robotic liquid-handling systems. In addition, it is equipped with full-color touchscreen graphic displays, an integrated auto-ranging power supply, and built-in solvent fume venting. Offering multistep ramped programming with full alphanumeric program naming, it can automatically handle even complex evaporation protocols effortlessly. Designed around a standard ANSI/SLAS plate "nest" to accept most microplate formats and tube racks, the Ultravap Levante can accommodate tubes up to 80 mm in height and allows the use of 2-dram vials, 1.5-mL HPLC vials, barcoded tubes in racks, and many other common formats.

#### Porvair Sciences

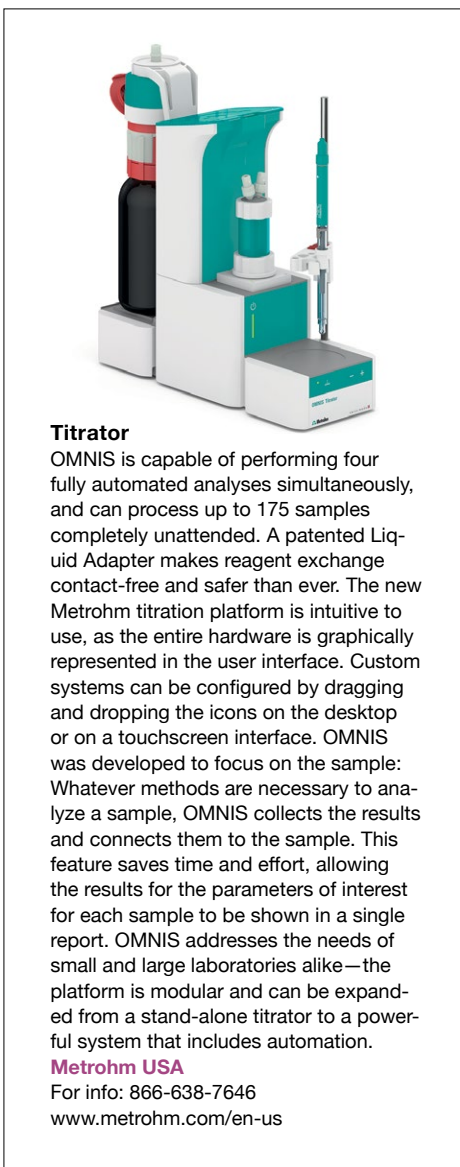
For info: +44-(0)-1978-666222  
[www.porvair-sciences.com](http://www.porvair-sciences.com)

### TF3 System

The Postnova TF2000 is an advanced thermal field-flow fractionation (TF3) system that provides an efficient method of separating and characterizing complex polymer samples such as natural or synthetic rubbers, starches, and paints from approximately 10 kDa up to 100 MDa and more, in organic and aqueous solvents. The TF2000 uses a temperature gradient as the driving force for its separation of polymers and particles. This unique feature allows the separation of different materials having the same molar mass. Separation can be further optimized by the use of different eluents and various temperature programs. Unlike traditional gel permeation chromatography/size-exclusion chromatography separation, samples can be injected without prefiltration, allowing the characterization of complex polymer and nanoparticulate samples without any potential alteration and damage. The TF2000 also has no size-exclusion limit—even ultrahigh molar mass, branched, and crosslinked polymers can be separated, as well as gels, aggregates, and particles.

#### Postnova Analytics

For info: +44-(0)-1885-475007  
[www.postnova.com/tf2000-overview.html](http://www.postnova.com/tf2000-overview.html)



### Titritator

OMNIS is capable of performing four fully automated analyses simultaneously, and can process up to 175 samples completely unattended. A patented Liquid Adapter makes reagent exchange contact-free and safer than ever. The new Metrohm titration platform is intuitive to use, as the entire hardware is graphically represented in the user interface. Custom systems can be configured by dragging and dropping the icons on the desktop or on a touchscreen interface. OMNIS was developed to focus on the sample: Whatever methods are necessary to analyze a sample, OMNIS collects the results and connects them to the sample. This feature saves time and effort, allowing the results for the parameters of interest for each sample to be shown in a single report. OMNIS addresses the needs of small and large laboratories alike—the platform is modular and can be expanded from a stand-alone titrator to a powerful system that includes automation.

#### Metrohm USA

For info: 866-638-7646  
[www.metrohm.com/en-us](http://www.metrohm.com/en-us)

### Pipettes

INTEGRA's VOYAGER II pipettes feature unique motorized tip spacing, enabling parallel transfer of multiple samples between labware of different sizes and formats. The tip spacing can be changed by the simple push of a button. Due to varying requirements in their sample processing, different labware vessels are typically used for sample storage, processing, and analysis tasks. Traditional multichannel pipettes were not designed to accommodate the wide variety of labware formats used today, because their tip-to-tip spacing is optimized for use with standard 96-well microplates. The VOYAGER II can adjust its tip spacing anywhere between 4.5 mm and 33 mm. Lab scientists choosing to download the new application guide can learn how to significantly reduce the hours they spend pipetting, and how to minimize transfer errors when pipetting liquids between tubes, vials, and microplates. Applications covered in the guide include screening compound libraries, genotyping, quantitative PCR, and cell seeding.

#### Integra Biosciences

For info: 603-578-5800  
[www.integra-biosciences.com](http://www.integra-biosciences.com)

### Benchtop-Scale Fermentation Systems

proSET is a range of benchtop-scale fermentation systems designed to provide an optimized cell cultivation solution for applications including the growth of sensitive and fragile mammalian and insect cells. Incorporating a large, color touchscreen panel with an intuitive software interface, these systems are very user friendly. The proSET One combines space-saving design with operational versatility and affordability. The heating system in the proSET One allows use of any fermentation vessel type up to 20 L. The fermentation temperature, antifoam, pH, and dissolved oxygen probe are all included in the standard package. Drawing upon its ability to accommodate vessels from 0.5 L to 20 L, the proSET Evo System enables productive cultivation of cell lines, including aerobic and anaerobic bacterial, yeast, plant, algae, fungal, mammalian, and insect lines. The proSET Parallel System allows you to run up to two thermostat-heating and two dry-heating experiments simultaneously.

#### Cleaver Scientific

For info: +44-(0)-1788-565300  
[www.cleaverscientific.com](http://www.cleaverscientific.com)

Electronically submit your new product description or product literature information! Go to [www.sciencemag.org/about/new-products-section](http://www.sciencemag.org/about/new-products-section) for more information.

Newly offered instrumentation, apparatus, and laboratory materials of interest to researchers in all disciplines in academic, industrial, and governmental organizations are featured in this space. Emphasis is given to purpose, chief characteristics, and availability of products and materials. Endorsement by *Science* or AAAS of any products or materials mentioned is not implied. Additional information may be obtained from the manufacturer or supplier.

# Made in Foshan with wisdom builds the first-tier city of Chinese manufacturing >>>>>>

Foshan has an obvious advantage of industrial cluster. On the one hand, strategically emerging industries have grown dramatically, such as New IT, LED, new energy, advanced materials, advanced medicines, Internet of Things and so on, which gradually develop the industrial agglomerations. On the other hand, there are a number of well-known industrial parks here, such as Nationally High-tech Industrial Development Zone, Sino-German Industrial Services Zone, Guangdong High Tech Service Zone for Financial Industrious, Guangdong (Foshan) Software Park, Foshan Creative Industry Park, 1506 Creative City and so on.

Foshan is one of the most important manufacturing bases across the country and even across the world. It possesses the biggest ceramic industry cluster with the most perfect industry chain nationwide and even worldwide. It is the national largest stainless steel base for production, processing and sales, the nationwide major production base and distributing center of knitwear. Therefore, we can find the label of "made in foshan" all over the world.

As one of the most dynamic regions of the private economy in China, Foshan owns 170,255 private enterprises, which account for 88.44% of the companies in the city, with a batch of key private enterprises, such as Midea, Galanz, Vanward, Chigo and Country Garden.

Nowadays, Foshan is aiming at the first-tier city of Chinese manufacturing, national manufacturing innovation center and leading city of equipment manufacturing in the west bank of Pearl River. Moreover, it also strives for playing a leading role in transformation and upgrading of industry and innovation-driven development in the whole province or even the whole country, as well as exploring a unique way with characteristics of Foshan, which is called "Made in China 2025" .



## Relevant Data of Foshan in 2015

Total area	Resident population	GDP of Foshan	Total industrial output value	Gross output value of advanced equipment manufacturing
3797.72km2	7.4306 million	800.392 billion	1977.493 billion	593.3 billion



Since the reform and opening-up policy, Foshan has adapted to the environment of the reform and opening-up policy and law of international industrial development. It has also developed domestic-oriented and external-oriented economy and formed a well-known manufacturing city in China, in which private economy is the principal part, and the professional towns and industrial parks are the supporters.



Made in Foshan with Wisdom

## Lead the equipment manufacturing in the west bank of Pearl River >>>>>>

As one of the most famous manufacturing base, the Foshan's economic aggregation of industrial economy is ranked No.6 among large and medium-sized cities in 2015, and No.2 among the cities in Guangdong. The equipment manufacturing industry has a distinct advantage in Foshan. The main reasons are as follows. Firstly, there is an integrated chain of machinery and equipment for manufacturing in Foshan, and the equipment industry has a good industrial base. The overall level of technology development is relatively high. Secondly, the domestic market share and influence of the traditional preponderantly equipment products are rising steadily in Foshan. For examples, The production and sales of ceramic machinery, woodworking machinery has accounted for about 85% and 50% in national market, the production and sales of plastic machinery and pressing machine has accounted for about 30% and 40% in the market of Guangdong.

As the leading city of the advanced equipment manufacturing in the west bank of pearl river, Foshan seized the opportunities, starts industrial base

construction of the advanced equipment manufacturing with trillions investment, and leads to build industry zones of advanced equipment manufacturing in the west bank of pearl river. In 2015, the total output value of advanced equipment manufacturing reached 593.3 billion yuan in Foshan, which accounts for half of the "Six City Area" in the west bank of Pearl River.

In order to implement the policies promoted by ministry of industry and information technology, the Guangdong Provincial People's Government jointly promote strategic deployment of the construction of advanced equipment manufacturing industry zones in the west bank of Pearl River, fully integrate the high-quality resources in the west bank of pearl river, show the achievement in the development of advanced equipment manufacturing industry, and jointly promote industrial transformation and upgrading. The second session of the advanced equipment manufacturing investment and trade symposium in the west bank of pearl river is scheduled on September 28-29, 2016, and will be held in Foshan.



Innovation-driven development

## Build the "innovation center of national manufacturing" >>>>>>

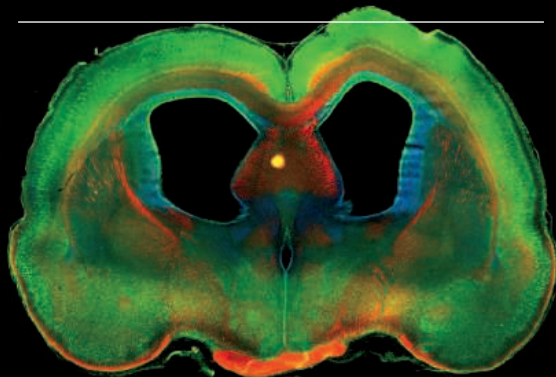
In recent years, the government of Foshan has invested heavily in technological innovation, and established a number of innovation platforms and supporters successively, such as scientific and technological enterprises, large incubator, Guangdong-Guangxi-Guizhou High-speed Rail Demonstration Zone for Economic Cooperation, Sino-German Industrial Services Zone and so on, which become an important innovation-driven engine. Moreover, Foshan has possessed 215 enterprise technical centers, 10 world-class high-tech business incubators, 716 national high-tech

enterprises, and 7067 valid patent for invention. Furthermore, it has introduced 32 experts from the "Thousand Talents Programs" and set up 37 academician studios.

In the meanwhile, it guides the combination of industry and finance actively, plays a role in the industry transformation lead by financial innovation and builds a number of major financial platforms like Foshan Folk Finances Street, Guangdong Equity Exchange.



# DOES YOUR LAB ANALYZE THE MECHANISMS THAT MEDIATE COMMUNICATION BETWEEN CELLS?



Kong-Yan Wu *et al.* (Zhen-Ge Luo), "Semaphorin 3A activates the guanosine triphosphatase Rab5 to promote growth cone collapse and organize callosal axon projections", *Sci. Signal.* 7, ra81 (2014). Photo Credit: Rat Brain Slice. Photo Credit: Kong-Yan Wu and Zhen-Ge Luo, Chinese Academy of Sciences.

**ScienceSignaling** | AAAS  
CELL SIGNALING IN PHYSIOLOGY AND DISEASE

Find out more about the scope of the journal and submit your research today. [ScienceSignaling.org](http://ScienceSignaling.org)

## AAAS *Travels* SOUTH GEORGIA

the Falklands & Antarctica  
December 14-January 4, 2017



With 20%  
Discount!

Breathtaking, extraordinary, and "The Most Beautiful Place In the World!" A rare opportunity on board *M/V Ortelius* with a 20% discount! See wildlife and walk in the footsteps of Shackleton. Spaces are limited, so please call Taunya immediately if you want to go.

**For a detailed brochure, call (800) 252-4910**

All prices are per person twin share + air



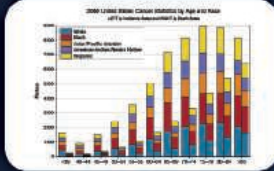
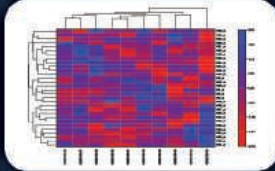
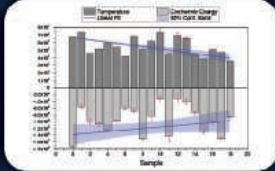
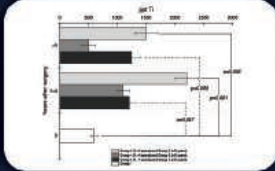
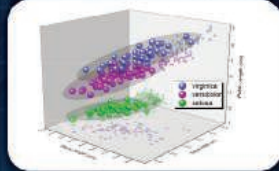
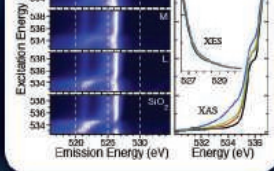
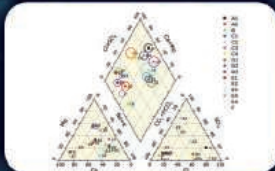
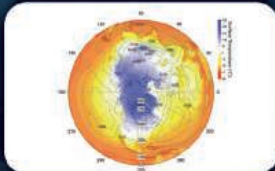
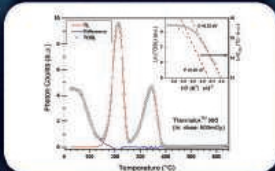
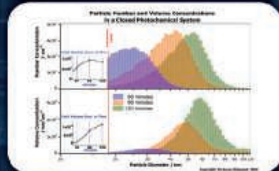
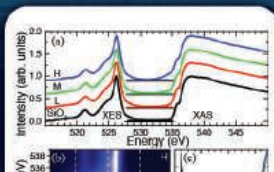
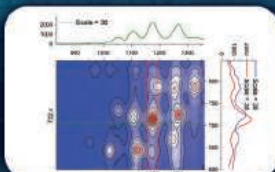
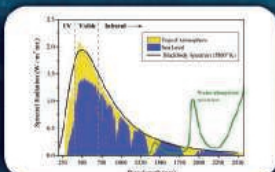
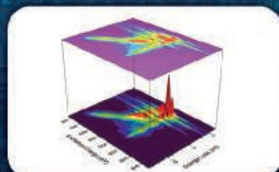
BETCHART EXPEDITIONS Inc.  
17050 Montebello Rd, Cupertino, CA 95014  
Email: [AAASInfo@betchartexpeditions.com](mailto:AAASInfo@betchartexpeditions.com)  
[www.betchartexpeditions.com](http://www.betchartexpeditions.com)



# ORIGIN® 2016

Graphing & Analysis

New Version!



Over 100 new features & improvements in Origin 2016!

**FOR A FREE 60-DAY EVALUATION,  
GO TO [ORIGINLAB.COM/DEMO](http://ORIGINLAB.COM/DEMO)  
AND ENTER CODE: 7564**

Over 500,000 registered users worldwide in:

- 6,000+ Companies including 120+ Fortune Global 500
- 6,500+ Colleges & Universities
- 3,000+ Government Agencies & Research Labs

**OriginLab®**

20+ years serving the scientific & engineering community

advantage New Promotion September 1 – December 31, 2016



# Perfect Teamwork

Your expertise + our equipment. Save now with our new special offers!

Our new Eppendorf Advantage™ special offers complement your expertise with matching Eppendorf equipment for crucial work steps in your laboratory.

Save up to 20 % on select products and enjoy perfect teamwork!

Advantage offers are available for:

- > Multipette® M4 (US/CAN: Repeater® M4)
- > Combitips advanced®
- > Eppendorf ThermoMixer® C
- > Eppendorf BioPhotometer® D30
- > Centrifuge 5424/5424 R
- > Innova® 44/44R incubator shakers

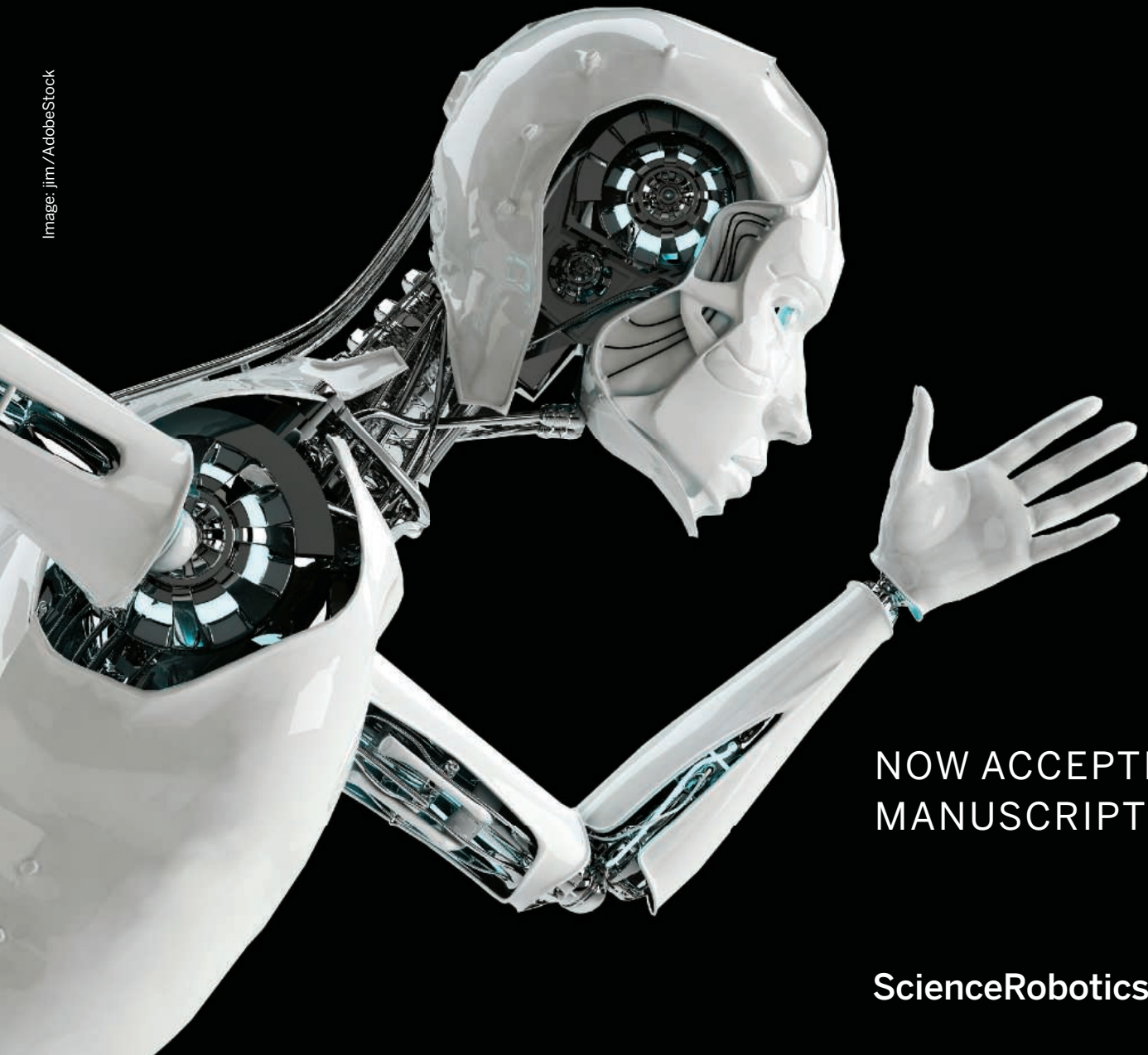
[www.eppendorf.com/advantage](http://www.eppendorf.com/advantage)

Eppendorf®, the Eppendorf logo, Combitips advanced®, Eppendorf BioPhotometer®, Eppendorf ThermoMixer®, Multipette®, Repeater® are registered trademarks of Eppendorf AG, Germany. Eppendorf Advantage™ is a trademark of Eppendorf AG, Germany. Innova® is a registered trademark of Eppendorf, Inc., USA. U.S. Design Patents are listed on [www.eppendorf.com/ip](http://www.eppendorf.com/ip). Offers may vary by country. All rights reserved, including graphics and images.



# Be Among the First to Publish in ***Science Robotics***

Image: jim / AdobeStock



NOW ACCEPTING  
MANUSCRIPTS

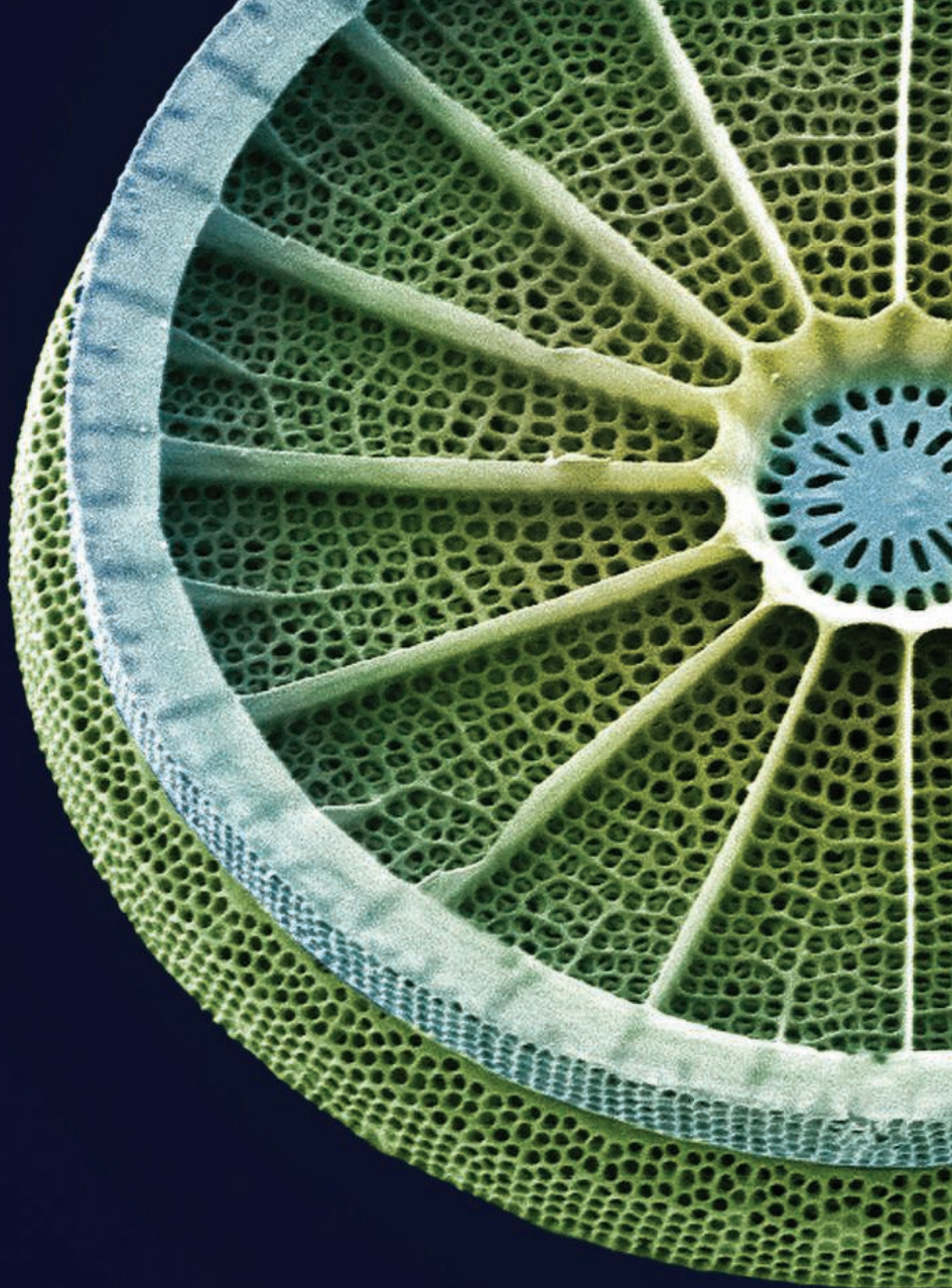
[ScienceRobotics.org](http://ScienceRobotics.org)

*Science Robotics* is a unique journal created to help advance the research and development of robotics for all environments. *Science Robotics* will provide a much-needed central forum to share the latest technological discoveries and to discuss the field's critical issues.

Join in the excitement for the Fall 2016 debut!

**ScienceRobotics**  
AAAS





# Target with precision.

## Introducing the NEBNext Direct<sup>™</sup> Cancer HotSpot Panel

Using a unique approach, the NEBNext Direct Cancer HotSpot Panel enriches for 190 common cancer targets from 50 genes prior to next generation sequencing. Combining a novel method for hybridization-based target enrichment with library preparation, the NEBNext Direct technology reduces processing time and minimizes sample loss. Ideal for automation, NEBNext Direct enables highly-specific deep sequencing of genomic regions of interest for the discovery and identification of low frequency variants from challenging sample types.

Visit **NEBNextDirect.com** to learn more and to inquire about sampling this product.

### TARGETS INCLUDE REGIONS FROM THE FOLLOWING CANCER-RELATED GENES, INCLUDING >18,000 COSMIC FEATURES:

ABL1	EGFR	GNAQ	KRAS	PTPN11
AKT1	ERBB2	GNAS	MET	RB1
ALK	ERBB4	HNF1A	MLH1	RET
APC	EZH2	HRAS	MPL	SMAD4
ATM	FBXW7	IDH1	NOTCH1	SMARCB1
BRAF	FGFR1	IDH2	NPM1	SMO
CDH1	FGFR2	JAK2	NRAS	SRC
CDKN2A	FGFR3	JAK3	PDGFRA	STK11
CSF1R	FLT3	KDR	PIK3CA	TP53
CTNNB1	GNA11	KIT	PTEN	VHL

*For research use only; not intended for diagnostic use.*

NEW ENGLAND BIOLABS<sup>®</sup> and NEB<sup>®</sup> are registered trademarks of New England Biolabs, Inc.  
NEBNext DIRECT<sup>™</sup> is a trademark of New England Biolabs, Inc.

By E. S. Levine

# Newton and the Big Apple

**W**hen I graduated from college 15 years ago, I had the same goal as many beginning astrophysicists: to become a tenured professor. I was living at my parents' house in the New York City suburbs, preparing to pursue a master's degree in England followed by a Ph.D. at the University of California (UC), Berkeley, when the 9/11 attacks happened. I frantically tried to contact friends and family while military jets flew over my childhood home. Over the next few days, I saw my hometown covered in fliers for the missing, which soon turned into makeshift memorials. It felt like the entire world was changing.

It was hard to leave for England just a few weeks after the attacks. I tried to focus on my classwork, which had been such a source of excitement for me as an undergraduate, but it was difficult to concentrate with all the news coming out of the United States. Nonetheless, I earned my degree and moved on to my doctoral studies at UC Berkeley, where I found an adviser and a sub-field that seemed like a good fit.

I was fascinated by the methods I was using—the data analysis, the programming, the mathematics—but about halfway through grad school, I began to understand that my passion didn't extend to the actual subject matter of astronomy. I increasingly felt a disconnect between the work I was doing in my graduate studies—making maps of the Milky Way's spiral arms—and what I actually cared about: national security policy, the Afghanistan and Iraq wars, the intelligence community, and counterterrorism. How could I focus on something so distant when we had so many problems nearer to home?

One year away from finishing my dissertation, I realized that I wanted to spend my career working on security issues. I considered leaving graduate school without finishing my degree, but it seemed foolish to waste the effort I had already invested, and I didn't want to disappoint my adviser or my family. Also, I didn't have any contacts in national security or counterterrorism, so I thought the best way to get my foot in the door would be through one of a small number of fellowships, which only accepted recent graduates. I worried that my adviser would be upset that I was not following his path, but to my surprise, he supported my decision and wrote strong letters of reference.

So, after completing my Ph.D., I moved on to a fellow-



***“How could I focus on something so distant?”***

ship that placed me in a small office at the U.S. Department of Homeland Security, analyzing risks from terrorism, natural disasters, and public health emergencies. I felt confident in my understanding of the math behind the analysis, but other parts of the job had no analog in my scientific education. Bringing dozens of policymakers to consensus on a mathematical methodology, for example, was a significant challenge in persuasion. Luckily, I had help from a team of professionals in my office who had strong communication and leadership skills.

I also had the opportunity to support the Counterterrorism Bureau of the New York City Police Department (NYPD). It was thrilling to see the connection between my analysis and the NYPD's operations, and I eventually transitioned to working directly for the NYPD. Now, I write algorithms to increase patrol effectiveness and design tools that help officers understand crime trends. Issues in policing are on the front pages of U.S. newspapers every day, and I believe that using analytics to help police officers make better-informed decisions is one way to make New York City safer and fairer. These are the real-world problems I dreamed of solving when I was in graduate school.

*Evan S. Levine is the assistant commissioner of data analytics for the New York City Police Department. Send your career story to [SciCareerEditor@aaas.org](mailto:SciCareerEditor@aaas.org).*





There's only one **Science**

## Science Careers Advertising

For full advertising details, go to [ScienceCareers.org](http://ScienceCareers.org) and click For Employers, or call one of our representatives.

### Tracy Holmes

Worldwide Associate Director  
Science Careers  
Phone: +44 (0) 1223 326525

### THE AMERICAS

E-mail: [advertise@sciencecareers.org](mailto:advertise@sciencecareers.org)  
Fax: +1 (202) 289 6742

### Tina Burks

Phone: +1 (202) 326 6577

### Nancy Toema

Phone: +1 (202) 326 6578

### Online Job Posting Questions

Phone: +1 (202) 312 6375

### EUROPE / INDIA / AUSTRALIA / NEW ZEALAND / REST OF WORLD

E-mail: [ads@science-int.co.uk](mailto:ads@science-int.co.uk)  
Fax: +44 (0) 1223 326532

### Sarah Lelarge

Phone: +44 (0) 1223 326527

### Kelly Grace

Phone: +44 (0) 1223 326528

### Online Job Posting Questions

Phone: +44 (0) 1223 326528

### JAPAN

### Katsuyoshi Fukamizu (Tokyo)

E-mail: [kfukamizu@aaas.org](mailto:kfukamizu@aaas.org)  
Phone: +81 3 3219 5777

### Hirofumi Mashiki (Kyoto)

E-mail: [hmashiki@aaas.org](mailto:hmashiki@aaas.org)  
Phone: +81 75 823 1109

### CHINA / KOREA / SINGAPORE / TAIWAN / THAILAND

### Ruolei Wu

E-mail: [rwu@aaas.org](mailto:rwu@aaas.org)  
Phone: +86 186 0082 9345

### Danny Zhao

E-mail: [dzhao@aaas.org](mailto:dzhao@aaas.org)  
Phone: +86 131 4114 0012

All ads submitted for publication must comply with applicable U.S. and non-U.S. laws. *Science* reserves the right to refuse any advertisement at its sole discretion for any reason, including without limitation for offensive language or inappropriate content, and all advertising is subject to publisher approval. *Science* encourages our readers to alert us to any ads that they feel may be discriminatory or offensive.

**ScienceCareers**

FROM THE JOURNAL SCIENCE 

[ScienceCareers.org](http://ScienceCareers.org)



University of  
Zurich <sup>UZH</sup>

## Faculty of Science

The Faculty of Science at the University of Zurich invites applications for a

## Professor of Ecology

in order to join our team of experts at the Department of Evolutionary Biology and Environmental Studies.

We seek innovative applicants with a strong record in research and teaching, who will strengthen our existing expertise in ecology and/or biodiversity. Applicants with interests in theory, experiments or field based observations to assess different ecological and evolutionary interactions generating and maintaining biodiversity, ecosystem function and their interactions with global change drivers are particularly encouraged to apply.

The successful applicant is expected to develop a complementary and independent research program in ecology, and strengthen our profile in ecology and/or biodiversity research, broadly defined to encompass population, community, evolutionary, and ecosystem ecology in the context of global change. Contributing to the existing undergraduate and graduate teaching efforts in Ecology and Environmental Sciences will also constitute an integral part of the position. The successful applicant will be located at the University of Zurich and is further expected to acquire external funding. The position is advertised on the level of assistant professor tenure track or associate professor with preference for early career scientists.

The University of Zurich provides generous research support, including dedicated funds for personnel and running expenses and competitive start-up packages. Zurich's scientific environment includes a rich spectrum of research activities in ecology and life sciences and provides extensive opportunities for collaborations with research groups at the Faculty of Science of the University of Zurich, as well as teams at the nearby ETH Zurich. The University of Zurich and the city of Zurich also offer a stimulating cultural environment and are family-friendly.

Application packages should include a motivation letter, a full curriculum vitae, a vision statement of research and teaching interests outlining major unsolved problems and how they could be tackled and the names and addresses of three potential referees. Documents should be addressed to Prof. Dr. Michael Schaepman, Dean of the Faculty of Science, University of Zurich, and uploaded as a single PDF file to <http://jobs.mnf.uzh.ch/es> by October 7, 2016. A brief questionnaire will have to be filled out at the beginning of the upload process. For further information, please contact Prof. Dr. Andreas Wagner at [Andreas.Wagner@ieu.uzh.ch](mailto:Andreas.Wagner@ieu.uzh.ch).

The University of Zurich is an equal opportunities employer.





## JOIN US!

### Drug Discovery Project Leader in Neuropsychiatry

We are looking for a highly-motivated scientific leader with skills in project management and the ability to translate emerging scientific knowledge on Proteinopathies into novel drug candidates for the improved treatment of Alzheimer's, Parkinson's and other neurodegenerative diseases.

Working in the Neuropsychiatry Department, you will lead a dedicated project either derived from internal programs, or sourced from outside institutions. You will coordinate multidisciplinary work with internal and external partners from the phase of target validation through to the proposition of preclinical candidates.

Your mission, mirroring our "R and D" working spirit, will be articulated around the principles of Entrepreneurship, Collaboration, Performance and Communication.

#### Major requirements:

- Ph.D. and Post-Doc in Neuroscience: Expertise in the fields of Proteinopathies and Neurodegenerative disorders of the CNS.
- 2-5 years' experience after your PhD, preferably involving a drug discovery-related position in a Biotech or Pharmaceutical company.
- Strong organizational skills and the ability to design and run a unique project.
- Excellent interpersonal relations and a well-developed sense of team-work.
- Perfectly fluent in English - French would be a plus.

**Joining Servier** means working in a stimulating environment and contributing to an innovative, research-based and people-oriented organization.

Servier is the leading French independent pharmaceutical company, located in 144 countries with 21 000 employees and a turnover in 2015 of about 4 billion euros.

25% of Servier's annual turnover is reinvested in Research & Development, reflecting the company's dedication to its mission of innovation and discovery for improved treatment of unmet medical needs.

Organized as a foundation, we guarantee our independence toward stock exchange market. Our founder Doctor Jacques Servier used to say: "a company is a group of human beings, so it has no price".

Servier is well known for staff care, with particular attention to career evolution within the Group, and to an agreeable and productive working environment.

Together with international experts, for over 30 years we have been investing in programs to improve the control of neuropsychiatric and neurodegenerative diseases like Alzheimer's, Parkinson's, multiple sclerosis and depression. Our Research Center in Neuropsychiatry is located near Paris, in Croissy-sur-Seine, France.

To apply or to acquire more details concerning the position, please contact [geoffroy.bellet@servier.com](mailto:geoffroy.bellet@servier.com) - Ref. 115



## SERVIER ONCOLOGY RECRUITS

We are looking for **DRUG DISCOVERY PROJECT LEADERS** in order to further advance towards our goal of positioning Servier as a significant and dynamic player in Oncology.

Internationally recognized for our expertise in Cardiology, Rheumatology and Diabetes Therapeutic Areas, we decided in 2014 to focus on the reinforcement of our Oncology effort, to contribute in a major way to the fight against Cancer. Consequently, we decided to dedicate 50% of our Research efforts (which represent 25% of our global turnover) to Oncology and more precisely in the areas of immune-oncology, apoptosis and cancer cell signaling.

To succeed in that exciting challenge, we are looking for highly motivated **TALENTS!**

- You are motivated by turning basic research into innovative cancer treatments (from target validation up to preclinical candidate selection), timely leading Drug Discovery projects, managing internal and external multidisciplinary teams, participating in due diligences of external opportunities (licensing-in, partnerships, etc.);
- You are result-oriented and able to think out of the box; you are willing to federate a group of scientists with diverse expertise and to enter an environment where you can fulfill yourself by fulfilling your projects;
- You have a Ph.D in biological sciences and a strong track record in basic research in one of the following research fields:
  - Tumor immune microenvironment (checkpoints and activators)
  - Tumor Immunology et Immunotherapy
  - Cell Therapy
  - Apoptosis and cancer cell signaling
- Preferably, you have previous experience in Drug Discovery;
- You are perfectly fluent in English and have strong communication skills,

## Join us NOW!

#### About Servier

Joining Servier means working in a stimulating environment and contributing to an innovative, research-based and people-oriented organization.

Servier is the leading French independent pharmaceutical company, located in 144 countries with 21 000 employees and a turnover in 2015 of about 4 billion euros.

25% of Servier's annual turnover is reinvested in Research & Development, reflecting the company's dedication to its mission of innovation and discovery for improved treatment of unmet medical needs.

Organized as a foundation, we guarantee our independence from the stock exchange. As our late founder Doctor Jacques Servier said: "a company is a group of human beings, so it has no price".

Servier is well known for its attention to the wellbeing of the staff, with particular importance placed on career evolution within the Group, and to an agreeable and productive working environment.

To know more, visit [www.servier.com](http://www.servier.com)

#### About Servier Oncology

Our journey in oncology started in the 90s with Muphoran, a chemotherapy drug used to treat melanoma. In 2014, we launched Pixuvri in multiple relapsed or refractory aggressive non-Hodgkin B-cell lymphomas. On April 27th, 2016, we received marketing approval for LONSURF® (trifluridine/tipiracil) in the field of advanced metastatic colorectal cancer.

Currently, there are eight new molecular entities in clinical development for oncology respectively in breast, lung and other solids tumors as well as various leukemias and lymphomas.

This portfolio of innovative cancer treatments is being developed with various partners worldwide, and includes different class of anti-cancer drugs such as cytotoxics, kinase inhibitors, apoptosis inducers, immune and cell therapies.

To know more, visit <http://servier-oncology.com>

To apply and for more details about the positions:  
[Geoffroy.bellet@servier.com](mailto:Geoffroy.bellet@servier.com) - Ref. 994



**BAYLOR**  
UNIVERSITY

### **Faculty Positions in Tropical Disease Biology and Evolutionary Medicine**

Baylor University is a private Christian university and a nationally ranked research institution, consistently listed with highest honors among The Chronicle of Higher Education's "Great Colleges to Work For." Chartered in 1845 by the Republic of Texas through the efforts of Baptist pioneers, Baylor is the oldest continuously operating university in Texas. The university provides a vibrant campus community for over 15,000 students from all 50 states and more than 80 countries by blending interdisciplinary research with an international reputation for educational excellence and a faculty commitment to teaching and scholarship. Baylor is actively recruiting new faculty with a strong commitment to the classroom and an equally strong commitment to discovering new knowledge as we pursue our bold vision, Pro Futuris.

The Department of Biology is pleased to announce a significant expansion of its research and education mission. The recruitment of two initial faculty positions is described below. To ensure full consideration, complete applications must be submitted by **October 30, 2016**. Regardless of rank and area of specialization, enthusiasm for interdisciplinary research and development of new collaborations within and beyond Baylor University is essential to these positions. For position details and application information please visit: [www.baylor.edu/hr/facultypositions](http://www.baylor.edu/hr/facultypositions) or contact the Search Committee Chair.

- 1) A tenured/tenure-track position (open rank) in Tropical Disease Biology. Candidates with one or more of the following specific research foci are especially encouraged to apply: tropical disease pathogens (Malaria, Dengue, Zika, Chikungunya, etc.), virology, parasitology, bacteriology, microbiology or vector biology. We seek an outstanding scientist who will establish competitive and externally funded research program in an area of science relevant to human health and which contributes to broader departmental goals. Committee Chair, **Cheolho\_Sim@baylor.edu**.
- 2) A tenured/tenure-track associate/assistant professor in Evolutionary Medicine. The Department of Biology seeks an evolutionary biologist with research expertise related to phenotype-genotype relationships. Preference will be given to applicants studying this relationship within the context of animal development, metabolism, virulence, disease, behavior, or comparative genomics. Applicants should have a strong research background in an area of evolutionary biology with relevance to medicine or human biology, that complements our faculty's strengths in organismal and evolutionary biology, molecular and population genetics, ecology, developmental biology, animal physiology and biomedical science. Committee Chair: **Myeongwoo\_Lee@baylor.edu**.

*Baylor University is a private not-for-profit university affiliated with the Baptist General Convention of Texas. As an Affirmative Action/Equal Opportunity Employer, Baylor is committed to compliance with all applicable anti-discrimination laws, including those regarding age, race, color, sex, national origin, marital status, pregnancy status, military service, genetic information, and disability. As a religious educational institution, Baylor is lawfully permitted to consider an applicant's religion as a selection criterion. Baylor encourages women, minorities, veterans and individuals with disabilities to apply.*

UNIVERSITY OF CALIFORNIA  
**UC RIVERSIDE**



# Opportunity awaits.

[clusterhiring.ucr.edu](http://clusterhiring.ucr.edu)



## Head of Department Bioinformatics & Computational Biology

In order to successfully meet the challenges presented by large-scale 'omics' data in biomedical research, we are actively seeking a highly motivated and experienced leader to head the Department of Bioinformatics & Computational Biology.

We indeed offer an exceptional opportunity, to further develop an existing team focused on analysis of genomics & proteomics data coupled with bioinformatics & computational analysis. The position is of highest importance to support biomarker, target discovery & validation and translational research in multiple therapeutic areas, notably oncology.

Our working spirit is based on entrepreneurship, collaboration, result orientation and communication.

### Key roles and activities:

- Leading a team of bioinformaticians, you will build strong collaborations with R&D teams within and beyond the company and will lead the design, analysis and interpretation of biomedical studies.
- Working within a pluridisciplinary team of molecular and cellular biologists, you will participate to innovation by focusing on dissecting the gene regulatory networks and signaling pathways in human diseases, such as cancer.
- You will contribute in reconstructing genome-wide and context-specific predictive network models to interrogate impact of underpinning biological process, to the development of both physiological and pathological phenotypes and generate in-silico hypothesis in combination with laboratory validations.

### Skills and experience:

- PhD degree in bioinformatics/biostatistics, computational sciences or biological sciences.
- Demonstrate experience in handling, processing and analyzing omics data.
- Demonstrate experience of genome-wide genetic, genomic, pathway and network methods.
- Strong collaboration skills and ability to work effectively in multidisciplinary teams.
- Strong communication and presentation skills, both written and oral.
- management experience

## Join us NOW!

### About Servier

Joining Servier means working in a stimulating environment and contributing to an innovative, research-based and people-oriented organization.

Servier is the leading French independent pharmaceutical company, located in 144 countries with 21 000 employees and a turnover in 2015 of about 4 billion euros.

25% of Servier's annual turnover is reinvested in Research & Development, reflecting the company's dedication to its mission of innovation and discovery for improved treatment of unmet medical needs.

Organized as a foundation, we guarantee our independence from the stock exchange. As our late founder Doctor Jacques Servier said: "a company is a group of human beings, so it has no price".

Servier is well known for its attention to the wellbeing of the staff, with particular importance placed on career evolution within the Group, and to an agreeable and productive working environment.

To know more, visit [www.servier.com](http://www.servier.com)

To apply and for more details about the positions: [Geoffroy.bellet@servier.com](mailto:Geoffroy.bellet@servier.com) - réf. 991



UNIVERSITÄT  
HEIDELBERG  
ZUKUNFT  
SEIT 1386

The Medical Faculty Mannheim, Heidelberg University, offers the position of an

## ASSOCIATE PROFESSOR (W3) FOR EXPERIMENTAL AND TRANSLATIONAL GYNAECOLOGIC ONCOLOGY

in the Department of Gynaecology and Obstetrics  
(Director: Prof. Dr. M. Sütterlin).

The future holder of the position (male/female) must fully represent the area of Experimental and Translational Gynaecologic Oncology with regard to research and teaching. Given the appropriate qualification, clinical care as a consultant of the department with the focus on gynaecologic cancer patients is desirable.

The successful candidate should intensively support the core research program of the Faculty regarding Oncology and/or Vascular Biology. He/she is expected to take an active role in the establishment of novel extramurally funded collaborative research programs and to support already existing programs such as SFB-TRR 23, IRTG 1874, RTG 2099, SFB 873, Exzellenzcluster CellNetworks, and M<sup>2</sup>OLIE. Thereby, the scientific focus should be directed to the expansion and strengthening of experimental and/or translational gynaecologic research. He/she should intensively collaborate with research groups at extramural research institutions of the Metropol-region Rhein-Neckar such as the German Cancer Research Center (DKFZ) or the European Molecular Biology Laboratory (EMBL) and participate in the establishment of a Comprehensive Cancer Center in Mannheim. In addition, an extensive involvement in gynaecologic teaching within the scope of the model curriculum MaReCuM<sup>plus</sup> is essential.

Prerequisites for application are a university degree and doctoral degree and (in accordance with Article 47, paragraph 2 of the Higher Education Law of the state of Baden-Württemberg) a Habilitation, a successfully evaluated junior professorship or equivalent qualifications. The successful candidate should have outstanding, internationally acknowledged academic credentials and a distinguished record of basic or translational research in gynaecologic oncology. Additionally, apart from a strong record of extramural funding and networking in thematically related research consortia and research programs, leadership ability, cooperation, mentoring and teaching skills, including active participation in MaReCuM<sup>plus</sup>, and participation in academic self-management are expected.

Clinical expertise in the care of cancer patients is desirable. However applications of physicians, preferably with board certification for gynaecology, gynaecologic oncology or hematology and oncology, and of natural scientists are likewise welcome.

The position is tenured and, by observing the legal regulations, the appointment will normally be made on the basis of a lifetime civil servant status (Beamtenverhältnis auf Lebenszeit).

The University of Heidelberg is an Equal Opportunity/Affirmative Action Employer. The faculty intends to increase the number of women in teaching and research. Women are therefore explicitly invited to apply. Handicapped persons with the same qualifications will be given preference.

Candidates should submit a full CV with copies of certificates, a list of publications and selected reprints (please follow the applicants' guidelines for the full CV and fill in both the applicants' forms found on our webpage at [www.umm.uni-heidelberg.de/dekanat/berufungen](http://www.umm.uni-heidelberg.de/dekanat/berufungen)) **within 4 weeks of publication of this advertisement** to Prof. Dr. med. Sergij Goerdts, Dean of the Medical Faculty Mannheim, University of Heidelberg, University Medical Center Mannheim, 68135 Mannheim, Germany.





**Announcement and call for nominations  
– deadline December 1, 2016**

## **The 2017 Gunnerus Award in Sustainability Science**

The Gunnerus Award in Sustainability Science is conferred by the Royal Norwegian Society of Sciences and Letters (DKNVS) and NTNU – Norwegian University of Science and Technology. The Award winner will receive NOK 1 million (approximately USD 190,000), a gold medal, and a diploma.

The Award will be presented to a scholar who has made outstanding contributions to sustainability science within the fields of natural sciences, social sciences, humanities, or technological sciences, either through interdisciplinary work or through work within one of these fields.

Scientific academies, universities, research institutions, university professors, and senior researchers are encouraged to submit nominations before **December 1, 2016**.

For further information and to make nominations: <http://www.dknvs.no/english/the-gunnerus-sustainability-award/>



**BAYLOR**  
UNIVERSITY

faculty with a strong commitment to the classroom and an equally strong commitment to discovering new knowledge as we pursue our bold vision, *Pro Futuris* ([www.baylor.edu/profuturis/](http://www.baylor.edu/profuturis/)).

Baylor seeks to fill the following **full-time Lecturer** faculty position within the Department of Biology, in the College of Arts & Sciences. The successful candidate for this position will provide outstanding undergraduate teaching and leadership in the broad areas of general biology, genetics, and/or health-related bioscience. The department is committed to implementing quantitative inquiry-based methods of teaching and laboratory experiences for undergraduate students, both for specified classes and individualized independent research experiences. The candidate should be prepared to develop and implement discovery-based introductory courses in biology that will complement similar courses already offered in the department. The department is currently comprised of 20 research and 9 lecturer faculty members.

Candidates should possess an earned doctorate by the time of application in the field of biology, including genetics, molecular biology, or an allied area. You will be asked to provide a letter of interest; curriculum vitae; and official transcripts showing highest degree conferred, and a list of three references in the application process. Salary is commensurate with experience and qualifications.

To learn more about the Department of Biology or the above position, please visit the appropriate URL: <http://www.baylor.edu/biology/> or [www.baylor.edu/hr/facultypositions](http://www.baylor.edu/hr/facultypositions).

*Baylor University is a private not-for-profit university affiliated with the Baptist General Convention of Texas. As an Affirmative Action/Equal Opportunity Employer, Baylor is committed to compliance with all applicable anti-discrimination laws, including those regarding age, race, color, sex, national origin, marital status, pregnancy status, military service, genetic information, and disability. As a religious educational institution, Baylor is lawfully permitted to consider an applicant's religion as a selection criterion. Baylor encourages women, minorities, veterans and individuals with disabilities to apply.*



### **Two Faculty Positions in Evolutionary Genomics**

The Department of Biology at Texas A&M University invites applications for two tenure-track Assistant Professor positions in evolutionary genomics, starting in the fall of 2017.

We will consider candidates pursuing innovative research in any area of evolutionary genomics, including empirical, theoretical or computational approaches applied to any taxonomic group. The criteria for selection will be uniqueness, creativity and excellence in research and scholarship. We require all candidates to have a Ph.D. and strongly encourage applications from candidates who will increase the exposure of our students to a diverse culture.

Successful candidates will be expected to develop externally funded research programs and to teach undergraduate and graduate courses. The Department of Biology ([www.biology.tamu.edu](http://www.biology.tamu.edu)) is part of an interactive and collegial research environment, offering a modern infrastructure and competitive startup packages. The broader Texas A&M research community includes a number of exciting interdepartmental programs, such as the new Ecology and Evolutionary Biology Doctoral Program ([eeb.tamu.edu](http://eeb.tamu.edu)), the Texas A&M Institute for Genome Sciences and Society ([genomics.tamu.edu](http://genomics.tamu.edu)), and the Genetics Interdisciplinary Graduate Program ([genetics.tamu.edu](http://genetics.tamu.edu)). Applicants should email a letter of intent, *curriculum vitae*, statements of research and teaching interests, and should arrange to have three letters of recommendation sent to [evosearch@bio.tamu.edu](mailto:evosearch@bio.tamu.edu). Review of applications will begin **November 1, 2016**.

Questions regarding this research should be directed to **Dr. Adam G. Jones**, chair of the search committee, at [evosearch@bio.tamu.edu](mailto:evosearch@bio.tamu.edu).

*Texas A&M University is an Equal Opportunity/Affirmative Action Employer that is dedicated to the goal of building a culturally diverse and pluralistic faculty and staff who are committed to teaching and working in a multicultural environment. We strongly encourage applications from women, minorities, veterans, individuals with disabilities, and the LGBTQ community. In addition, the University is responsive to the needs of dual career couples.*



**UNITED NATIONS  
UNIVERSITY**

### **DIRECTOR (D-1 LEVEL) UNU-INTERNATIONAL INSTITUTE FOR GLOBAL HEALTH (UNU-IIGH) (DUTY STATION: KUALA LUMPUR, MALAYSIA)**

UNU is searching for a highly qualified director for its Institute in Kuala Lumpur which undertakes solution-oriented policy-relevant research on global health issues. The Institute contributes to the development and strengthening of health services policy frameworks and management actions, particularly for people in developing countries, and supports implementation of promotive approaches to human health.

The Director is the chief academic and administrative officer of UNU-IIGH and has overall responsibility for the direction, organization, administration and programmes of the Institute under the direction of the Rector of UNU. The Director's qualifications should lend to UNU-IIGH the necessary prestige in the international scholarly community. The Director will need to develop and manage a programme of policy-oriented research of the highest quality and provide leadership and guidance for the conduct of UNU-IIGH activities.

**Qualifications:** A doctoral qualification in health systems and policies, public health, epidemiology or another health-related discipline.

**Experience:** An established track record of effective leadership in global health or in the health sciences with demonstrable global health influence and a strong research background with publications in areas related to emerging problems in global health.

Candidates should possess excellent management and communications skills with fluency in English. Knowledge of other official languages of the United Nations is desirable.

Applications from suitably qualified women candidates are particularly encouraged.

**CLOSING DATE: 15 OCTOBER 2016**

For the complete information about this position, please visit <http://unu.edu/about/hr>. The successful candidate is expected to take up the position in August/September 2017.



# Faculty Careers

Issue date: October 7

Book ad by September 20

Ads accepted until Sept 30 if space allows

For recruitment in science, there's only one *Science*.

**Hiring Faculty?** Whatever your timing, we've got two special features for your faculty ads this fall! The September 16 feature offers advice on how to develop skills for reviewing grants and papers. The October 7 feature covers business principles for researchers. Reach *Science* readers and share opportunities at your university.

## What makes *Science* the best choice for recruiting?

- Read and respected by 400,000 readers around the globe
- 62% of our weekly readers work in academia and 65% are Ph.D.s. *Science* connects you with more scientists in academia
- Your ad dollars support AAAS and its programs, which strengthens the global scientific community.

## Why choose these Faculty Features for your advertisement?

- Relevant ads lead off these career sections with a special Faculty banner
- October 7 issue will be distributed at the American Society of Human Genetics meeting, 18–22 October, Vancouver.

## Expand your exposure by posting your print ad online:

- Link on the job board homepage directly to Faculty jobs
- Dedicated landing page for faculty positions.

Deliver your message to a global audience of targeted, qualified scientists.

## 129,574

subscribers in print every week

## 352,966

monthly unique browsers on ScienceCareers.org

## 65 %

of our weekly readers are Ph.D.s



Produced by the *Science*/AAAS Custom Publishing Office.

SCIENCECAREERS.ORG

# Science Careers

FROM THE JOURNAL SCIENCE  AAAS

To book your ad: [advertise@sciencecareers.org](mailto:advertise@sciencecareers.org)

The Americas  
+202 326 6582  
Japan  
+81 3 3219 5777

Europe/RoW  
+44 (0) 1223 326500  
China/Korea/Singapore/Taiwan  
+86 186 0082 9345



**University of  
Zurich**<sup>UZH</sup>

## Faculty of Science

The Faculty of Science at the University of Zurich invites applications for an

# Assistant Professor Tenure Track of Earth System Science

in order to join our team of experts of the University Research Priority Program on «Global Change and Biodiversity» co-hosted at the Department of Geography.

We seek innovative applicants with a strong record in research and teaching, who will strengthen our expertise in Earth System Science. Applicants with interests in interdisciplinary research between and amongst the Earth's spheres focusing on theory, experiments, observations, or modeling to assess different interaction and feedback mechanisms on global change drivers (including climate change and human dimensions) are encouraged to apply. Preference is given to candidates with a focus on more than one sphere, of which one is the biosphere.

The successful applicant is expected to develop a complementary and independent research program in Earth System Science, and strengthen our profile in assessing global change drivers, their feedbacks and interactions. Contributing to the existing undergraduate and graduate teaching efforts in Earth System Science and Geography will also constitute an integral part of the position. The successful applicant will be located at the University of Zurich and is further expected to acquire external funding. The position is advertised on the level of assistant professor tenure track.

The University of Zurich provides generous research support, including dedicated funds for personnel and running expenses and competitive start-up packages. Zurich's scientific environment includes a rich spectrum of research activities in ecology and life sciences and provides extensive opportunities for collaborations with research groups at the Faculty of Science of the University of Zurich, as well as teams at the nearby ETH Zurich. The University of Zurich and the city of Zurich also offer a stimulating cultural environment and are family-friendly.

Application packages should include a motivation letter, a full curriculum vitae, a vision statement of research and teaching interests outlining major unsolved problems and how they could be tackled and the names and addresses of three potential referees. Documents should be addressed to Prof. Dr. Michael Schaepman, Dean of the Faculty of Science, University of Zurich, and uploaded as a single PDF file to <http://jobs.mnf.uzh.ch/ess> by October 7, 2016. A brief questionnaire will have to be filled out at the beginning of the upload process. For further information, please contact Prof. Dr. Michael Schmidt at [Michael.Schmidt@geo.uzh.ch](mailto:Michael.Schmidt@geo.uzh.ch).

The University of Zurich is an equal opportunities employer.



**University of  
Zurich**<sup>UZH</sup>

## Faculty of Science

The Faculty of Science at the University of Zurich invites applications for an

# Assistant Professor of Ecological Modeling

in the framework of the University Research Priority Program «Global Change and Biodiversity», to join our team of experts at the Department of Evolutionary Biology and Environmental Studies. The position is advertised at the level of assistant professor non-tenure track with 6-year term.

We seek innovative applicants with a strong and innovative record in research and teaching, who will strengthen our expertise in Ecological Modelling. Applicants with interests in interdisciplinary research focusing on linking theory and data to understand feedbacks among environmental change, biodiversity, ecosystem processes and services are encouraged to apply.

The successful applicant is expected to develop a complementary and independent research program in Ecological Modeling, and strengthen our profile in drivers of environmental change, their ecological feedbacks and interactions. Contributing to the existing undergraduate and graduate teaching efforts in Ecology, Environmental Science and Earth System Science will also constitute an integral part of the position. The successful applicant will be located at the University of Zurich and is further expected to acquire external funding.

The University of Zurich provides generous research support, including dedicated funds for personnel and running expenses and competitive start-up packages. Zurich's scientific environment includes a rich spectrum of research activities in ecology and life sciences and provides extensive opportunities for collaborations with research groups at the Faculty of Science of the University of Zurich, as well as teams at the nearby ETH Zurich. The University of Zurich and the city of Zurich also offer a stimulating cultural environment and are family-friendly.

Application packages should include a motivation letter, a full curriculum vitae, a vision statement of research and teaching interests outlining major unsolved problems and how they could be tackled and the names and addresses of three potential referees. Documents should be addressed to Prof. Dr. Michael Schaepman, Dean of the Faculty of Science, University of Zurich, and uploaded as a single PDF file to <http://jobs.mnf.uzh.ch/em> by October 7, 2016. A brief questionnaire will have to be filled out at the beginning of the upload process. For further information, please contact Prof. Dr. Owen Petchey at [Owen.Petchey@ieu.uzh.ch](mailto:Owen.Petchey@ieu.uzh.ch).

The University of Zurich is an equal opportunities employer.